



Universidad de Granada



UNIVERSIDAD DE GRANADA
Programa de Doctorado en Bioquímica y Biología Molecular

"Nuevos aspectos estructurales y funcionales de los dominios I al VI de la región 5' del RNA del Virus de la Hepatitis C"

Memoria presentada por la Licenciada M^a Ascensión Ariza Mateos
para optar al grado de Doctor.

V^o. B^o. del Director:

Doctorando:

Fdo.: Jordi Gómez Castilla
Investigador Científico (CSIC)

Fdo.: M^a Ascensión Ariza Mateos

Editor: Universidad de Granada. Tesis Doctorales
Autora: María Ascensión Ariza Mateos
ISBN: 978-84-9125-773-8
URI: <http://hdl.handle.net/10481/43500>

ÍNDICE 15

INTRODUCCIÓN 16

El virus de la hepatitis C 16

Generalidades 16

Cuasiespecies 16

Genoma 18

Regiones reguladoras de la replicación y traducción del virus en la región 5' no traducible (5'UTR) 19

IRES 21

Motivo tipo-tRNA 22

Interacciones terciarias en el RNA de HCV 24

Pseudonudo 24

Anillamiento a larga distancia 26

Elementos celulares relacionados con la traducción y replicación del virus 28

Inicio de traducción en RNA de HCV 28

Subunidad ribosomal 40S 29

microRNAs 31

Generalidades 31

microRNAs que interactúan directamente con la región 5'UTR de HCV 33

miR-122 34

let-7b 38

miR-199a* 39

RNAsas específicas de estructuras tipo-tRNA 39

Mimetismo molecular 39

Biosíntesis de los tRNAs 40

RNasa P 41

RNasa Z 46

Virus de la Peste porcina clásica (CSFV) 49

Generalidades 49

Genoma 51

Radiación Ultravioleta 52

Generalidades 52

Efectos de la radiación UV en el DNA 53

Lesiones en el DNA 54

Dímeros de pirimidinas 54

Otros fotoproductos 55

Formación de *crosslink* 56

Rotura del DNA 56

Mecanismos de reacción por UV 56

Fotoionización 57

Fotosensibilización 57

Efectos de la radiación UV en el RNA 58

Lesiones en el RNA	58
Fotoproductos de RNA	58
Formación de crosslink	59
Rotura del RNA	59
Mecanismos de reacción por UV	59
Fotoionización	60
Fotosensibilización	61
Lazo-E	62

Virus como señales 63

OBJETIVOS 67

MATERIALES Y MÉTODOS 72

Materiales 72

Tampones 72

Tampones y soluciones generales	72
Tampones para preparar bacterias competentes	72
Tampones de electroforesis	73
Tampones de electroforesis para geles de poliacrilamida en condiciones desnaturalizantes	73
Tampones de electroforesis para geles de poliacrilamida en condiciones nativas	73
Tampón de carrera para geles de proteínas en condiciones desnaturalizantes	73
Tampones de carga para electroforesis	74
Soluciones para teñir y lavar geles de proteínas	75
Tampones y soluciones para la purificación de la RNasa Z de <i>Escherichia coli</i>	75
Tampones para la cromatografía de afinidad	76
Tampones para la purificación de las subunidades ribosomales de células HeLa	77
Tampones para la lisis celular	77
Tampones para la extracción ribosomal	77
Tampones para gradiente de sacarosa	78
Purificación de subunidades ribosomales 40S y 60S	78
Reacciones de protección con la RNasa A	78
Tampones y soluciones de reacción	79
Tampones para reacciones con nucleasas	79
Tampones para estudiar el cambio conformacional del RNA en función de la concentración de magnesio	80

Resina de celulosa fosfato CF-11 81

Agua 82

Medios de cultivo bacteriano 82

Medio de cultivo celular 83

Cepas bacterianas 83

Líneas celulares 83

Medio de congelación de líneas celulares 84

Construcciones de DNA empleadas para las reacciones de transcripción 84

Isótopos radiactivos 86

Marcadores de peso molecular para electroforesis 86

Oligonucleótidos de DNA sintéticos 87

Oligonucleótidos de RNA sintéticos 89

Métodos 90

Métodos generales de microbiología 90

Cultivos bacterianos 90

Criopreservación de cepas bacterianas 90

Preparación de células termocompetentes 90

Ligación de insertos de DNA en plásmidos bacterianos 91

Transformación de *E. coli* con plásmidos recombinantes mediante choque térmico 92

Selección de colonias recombinantes de *E. coli* 92

Extracción de DNA plasmídico 93

Secuenciación de DNA 93

Métodos generales de biología celular 94

Descongelación de células 94

Mantenimiento de una línea celular (pases) 94

Congelación y recuento de células 95

Métodos generales de biología molecular 96

Electroforesis de ácidos nucleicos 96

Geles de agarosa 96

Geles de poliacrilamida desnaturalizantes 96

Geles de poliacrilamida nativos 97

Autorradiografía 97

Electroforesis de proteínas 98

Purificación de ácidos nucleicos 98

Fenolización 98

Precipitación con etanol 99

Transcripciones *in vitro* 99

Transcripción estándar 99

Transcripción a partir de oligonucleótidos de DNA 100

Digestión del DNA molde con DNasa RQ1 100

Purificación de los productos de transcripción 100

Marcaje radiactivo de ácidos nucleicos 103

Marcaje interno 103

Marcaje en el extremo 5' 104

Marcaje en 5' de RNAs largos durante la reacción de transcripción 104

Marcaje en 5' de oligonucleótidos de DNA o RNA 104

Marcaje en el extremo 3' 106

Amplificación de ácidos nucleicos: Reacción en cadena de la polimerasa (PCR) 106

Retrotranscripción (RT) 107

Cuantificación de ácidos nucleicos 107

Cuantificación de DNA y RNA no marcados radiactivamente 108

Cuantificación del RNA marcado internamente con GTP[α -³²P] 108

Cuantificación de proteínas 108

Digestión de ácidos nucleicos: DNA 108

Digestión de proteínas: tratamiento con proteinasa K y SDS 109

Métodos para la detección de la naturaleza química de extremos 5' y 3' en el RNA 109

Fosforilación de extremos 5'-P 110

Ligación de moléculas de RNA con extremos 5'-P y 3'-OH 110

Reacción poliadenilación del RNA 110

Reacción de poliuridinación del RNA 110

Reacción de fenton	111
Espectrometría de masas (MALDI-TOF)	111
<i>Métodos para el estudio de la estructura del RNA</i>	112
Reacciones con la RNasa H	112
Nucleasas específicas de estructuras tipo-tRNA	112
Reacciones con la ribozima de la RNasa P de <i>Synechocystis sp.</i> (RZ6803)	112
Reacciones con la RNasa P humana	113
Reacciones con la RNasa Z de <i>E. coli</i>	113
<i>Métodos enzimáticos y químicos para el estudio de la estructura del RNA</i>	114
RNasa T1	114
RNasa V1	115
RNasa A	116
Hidrólisis alcalina del RNA	117
Dimetil sulfato (DMS)	117
Reacción de corte específico en RNA con luz UV	118
<i>Métodos de asociación con el RNA</i>	118
Ensayos de asociación en geles nativos	118
Unión de un oligonucleótido	119
Unión de la subunidad ribosomal 40S	119
<i>Método de extracción y purificación de la RNasa Z de E. coli</i>	120
<i>Método de extracción y purificación de subunidades ribosomales 40S de células HeLa</i>	121
<i>Análisis bioinformática</i>	123
Cuantificación de los ensayos obtenidos	123
Análisis de ensayos termodinámicos	123
Análisis de ensayos cinéticos	124
Predicciones in silico de dianas para microRNAs	124
RESULTADOS	125
<i>"In vitro characterization of a miR-122-sensitive double-helical switch element in the 5' region of hepatitis C virus RNA"</i>	126
<i>"RNA self-cleavage activated by ultraviolet light-induced oxidation"</i>	150
<i>"A magnesium-induced RNA conformational switch at the internal ribosome entry site of hepatitis C virus genome visualized by atomic force microscopy"</i>	183
<i>"Key role of IRES structural context and its dynamic transformations promoted by miR-122 in the formation of the hepatitis C virus IRES-40S binary complex"</i>	213
<i>"Virus is a Signal for the Host Cell"</i>	269
DISCUSIÓN	278
CONCLUSIONES	288
BIBLIOGRAFÍA	292

ABREVIATURAS

Ago *Argonaute* Proteína Argonauta del complejos RISC

AMV *Avian Myeloblastosis Virus*. Virus de la mieloblastosis avial

base^{•+} Radical base catiónica.

base^{•-} Radical base aniónica.

BDV *Borna Disease Virus*. Virus de la enfermedad de borna (VEB)

BMV *Brome Mosaic Virus*. Virus del mosaico del bromo.

BVDV *Bovine Viral Diarrhea Virus*. Virus de la diarrea viral bovina.

Cap Modificación en 5' de los mRNA eucariotas que consiste en una guanosina invertida y metilada en posición N7 unida al primer nucleótido transcrito.

cDNA DNA copia.

CIAP *Calf Intestinal Alkaline Phosphatase*. Fosfatasa alcalina intestinal de ternera.

CPS Cuentas por segundo.

CRE *Cis Replication Element*. Elementos de replicación en *cis*-.

Crio-EM *Cryo-electron microscopy (Cryo-EM)*. Crio-electromicroscopía

CrPV *Cricket paralysis virus*. Virus de la parálisis del grillo.

CSFV *Classical Swine Fever Virus*. Virus de la peste porcina clásica (PPC).

D.O. Densidad óptica.

DAA *Direct-Acting Antiviral*. Antivirales de acción directa.

DMS Dimetil sulfato.

DMSO Dimetil sulfóxido.

DNA *Deoxyribonucleic acid*. Acido desoxirribonucleico (ADN).

DNasa Desoxirribonucleasa.

dNTP desoxirribonucleótido.

dsRNA *double stranded RNA*. RNA de doble cadena perfecta.

DTT Dithiothreitol.

e- electrón.

EMCV *Encephalomyocarditis virus*. Virus de la encefalomiocarditis.

EMSA *Electrophoretic movility shift assay*. Geles de movilidad electroforética en geles nativos.

FMDV *Foot and Mouth Disease Virus*. Virus de la fiebre aftosa.

FRET *Fluorescence Resonance Energy Transfer*. Transferencia de Energía de Resonancia de Förster.

GBV-B *GB virus B*. Hepacivirus GB del tipo B. Hepacivirus de primates Tamarinos.

GHV *Guereza hepacivirus*. Hepacivirus Guereza. Hepacivirus que infecta roedores norteamericanos y murciélagos africanos.

GTP Guanosín trifosfato.

H Hidrógeno.

HBV *Hepatitis B virus*. Virus de la hepatitis B.

HCV *Hepatitis C virus*. Virus de la hepatitis C.

hnRNA *Heterogeneous nuclear RNA*. RNA heterogéneo nuclear.

IC50 Concentración de competidor al alcanzar el 50% de inhibición en la reacción.

IRES *Internal Ribosome Entry Site*. Entrada interna de unión al ribosoma.

Kd Constante de disociación.

KDa KiloDalton.

Kobs Constante de velocidad observada.

Leader Guía.

Let-7 *Lethal-7*. microRNA let-7.

LNA *Locked nucleic acid*. Ácido nucleico bloqueado. es un nucleótido análogo que presenta un puente de metileno entre C2' y C4' del anillo ribosa, incrementando la afinidad por su DNA o RNA diana. Se utiliza para secuestrar miRNAs.

LRA *Long Range Annealing*. Hibridación RNA:RNA a larga distancia.

Mg²⁺ Cation magnesio.

min Minutos.

miRNA microRNA.

mRNA *messenger RNA*. RNA mensajero.

ncRNA *Non coding RNA*. RNA no codificante.

nm nanometros.

NPHV *Non primate hepacivirus*. Hepacivirus de animales no primates (caballos y perros)

nt Nucleótido.

ODN Oligodesoxinucleótido.

OH• Radical hidroxilo.

ORF *Open Reading Frame*. Marco abierto de lectura.

pb Pares de bases.

PCR *Polymerase Chain Reaction*. Reacción en cadena de la polimerasa.

PEG Polietilenglicol.

PK *Pseudoknot*. Pseudonudo.

PNK T4 Polinucleótido Quinasa.

pre-miRNA *precursor miRNA*. Precursor del microRNA.

pretRNATyr precursor del tRNA tirosina.

pri-miRNA *primary miRNA transcript*. Transcrito primario de RNA.

PRORP *Protein-only RNase P*. RNasa P formada únicamente por subunidades protéicas.

PSTV *Potato spindle tuber viroid*. Viroide del tubérculo fusiforme de la patata.

PTB *Polypyrimidine tract-binding protein*. Proteína de unión a tramos de polipirimidina.

rcf *relative centrifugal force*. Fuerza centrífuga relativa. Representado también como "g".

RHV *Rodent hepacivirus*. Hepacivirus de roedores.

Riboswitch Estructura reguladora en el mRNA que sufre un cambio conformacional inducido por la unión de un metabolito.

RISC *RNA-induced silencing complex*. Complejo de silenciamiento inducido por RNA.

RMN Resonancia magnética nuclear (NMR).

RNA *Ribonucleic acid*. Ácido ribonucleico (ARN).

RNasa H Ribonucleasa H.

RNasa III Ribonucleasa III.

RNasa P Ribonucleasa P.

RNasa Ribonucleasa.

rNTP ribonucleótido.

RPM revoluciones por minuto.

RPR *RNase P RNA*. Subunidad RNA de la RNasa P.

RRL *Rabbit Reticulocyte Lysate*. Lisado de reticulocitos de conejo.

rRNA *ribosomal RNA*. RNA ribosómico.

RT *Reverse transcriptase*. Transcriptasa reversa, también llamada retrotranscriptasa.

SAP *Shrimp alkaline phosphatase*. Fosfatasa alcalina de gamba.

SDS Dodecilsulfato sódico.

SDS-PAGE *sodium dodecyl sulfate polyacrylamide gel electrophoresis*. Electroforesis en gel de poliacrilamida con dodecilsulfato sódico.

Secuencia seed Secuencia semilla: referida a los microRNAs, secuencia de 7 nucleótidos en la región 5' responsable del reconocimiento de su mRNA diana. Está especialmente conservada y permite el agrupamiento de los microRNAs en familias.

seg segundos.

SFB Suero Fetal Bovino.

SGE Secuencia guía externa.

SHAPE *2'-hydroxyl acylation analyzed by primer extension*. Acilación en 2' hidroxilo analizado por primer extension. Técnica que incorpora grupo acilo al C2' de la ribosa de los ribonucleótidos que se analiza mediante primer extension.

siRNA *short interfering RNA*. Pequeños RNAs interferentes.

SL *Stem-Loop*. Tallo-lazo.

snRNA *small nuclear RNA*. RNA pequeño nuclear.

Splicing En las células eucariotas proceso postranscripcional, autocatalítico, de corte y empalme de RNA para eliminar intrones.

SRP *Signal Recognition Particle*. Partícula de reconocimiento señal.

Switch Cambio, intercambio estructural.

T7 R1.1RNA RNA mensajero policistrónico temprano del bacteriófago T7; sustrato natural de la RNasa III.

TAP *tobacco acid pyrophosphatase*. Pirofosfatasa ácida de tabaco.

tmRNA *transfer-messenger RNA*. RNA transferente-mensajero.

TRBP *TAR RNA binding protein*. Proteína de unión al RNA TAR. Proteína que forma parte del complejo RISC.

tRNA *transfer RNA*. RNA transferente.

tRNA_i^{Met} tRNA aminoacilado con la metionina iniciadora de la traducción.

tRNasa ribonucleasa de tRNA.

Trz tRNasa Z o RNasa Z.

TYMV *Turnip Yellow Mosaic Virus*. Virus del mosaico amarillo del nabo.

UTR *Untranslated region*. Región no traducible.

UV Ultravioleta.

Xrn *5'-3' Exoribonuclease*. 5' → 3' exorribonucleasa.

Z^L Forma larga de la RNasa Z.

Zn²⁺ Ión Zinc.

Z^S Forma corta de la RNasa Z.

RESUMEN

El virus de la hepatitis C (HCV) es un virus hepatotrópico, perteneciente al género *Hepacivirus* dentro de la familia *Flaviviridae*. Infecta a más de 185 millones de personas en el mundo y ha sido reconocido como la principal causa de infección hepática crónica en humanos. HCV es un virus envuelto, que contiene un genoma de RNA de cadena sencilla y polaridad positiva, que presenta un único marco de lectura abierto de 9.6 Kb flanqueado por dos regiones no traducible (UTR) en sus extremos 5' y 3'. En la región 5' UTR se encuentra un elemento para la entrada interna del ribosoma (IRES), constituido por varios dominios estructurales muy conservados, esenciales para el reclutamiento interno del ribosoma en la traducción independiente de 5'-cap. Mediante ensayos de corte con la RNasa P se determinó que el dominio IV del IRES incluye un motivo estructural tipo-tRNA, en torno al codón de inicio de la traducción AUG. En el dominio II del IRES se encuentran dos bucles-E, altamente sensibles a la radiación UV y uno de ellos es responsable del doblamiento del dominio hacia el dominio IV, favoreciendo el posicionamiento del codón AUG en el surco de descodificación en la subunidad ribosomal 40S en el inicio de traducción.

En el desarrollo de esta Tesis, se ha trabajado con el fragmento 1-570 del RNA de HCV, que incluye toda la región 5'UTR y el primer tercio de la secuencia que codifica para la proteína *core*. En trabajos previos de este laboratorio se determinó, mediante ensayos de corte de la RNasa III, que la secuencia comprendida entre los dominios I y II del 5'UTR, interacciona con la secuencia basal del dominio VI (428-442) formando un anillamiento a larga distancia que deja al IRES en una forma cerrada. En este trabajo se ha estudiado los efectos del magnesio en los cambios conformacionales que experimenta este fragmento del RNA de HCV. Se demostró mediante ensayos de corte con la RNasa T1 en condiciones nativas y mediante ensayos de movilidad electroforética en geles nativos, que el magnesio es esencial en la formación de estructuras terciarias en el IRES, como la formación del pseudonudo ya descrito con anterioridad, y en la formación y estabilidad de la forma cerrada que experimenta el IRES en presencia de sus secuencias flanqueantes (dominios I y V-VI), a una concentración final de magnesio entre 0-2 mM.

A continuación nos focalizamos en el microRNA hepático miR-122, relacionado con el tropismo, la estabilidad, la replicación y la traducción del virus. El miR-122 presenta dos dianas ampliamente estudiadas entre los dominios I y II (S1 y S2). Recientemente,

una tercera diana (S3) fue preliminarmente descrita en el dominio IV, incluyendo al codón AUG, sin función, parámetros termodinámicos o cinéticos aún determinados; y una cuarta diana (S4) en el dominio V, fue descrita por nosotros en la elaboración de este trabajo. Formando dos sitios de unión en tándem a ambos flancos del IRES, la unión del miR-122 en cada flanco presentó diferencias termodinámicas y cinéticas. Las dianas localizadas en el flanco 3' del IRES (S3 y S4) interaccionaron con menor afinidad, pero con mayor rapidez que en las dianas del flanco 5' (S1 y S2). De manera que, aparte del cambio conformacional de la forma abierta a cerrada por la formación del anillamiento a larga distancia, la interacción directa del miR-122 en el flanco 3' del IRES (S3) es capaz de provocar un cambio conformacional local, desestabilizando el tallo del dominio IV. Por tanto, el mir-122 presentaría un efecto opuesto al magnesio, en lo que respecta este cambio conformacional. La aparición de la forma cerrada en presencia del miR-122, necesitó una concentración superior de magnesio (3 mM).

El cambio conformacional observado en geles nativos, tanto en presencia como en ausencia de miR-122, o bien de Mg^{2+} , se ha correlacionado con dos formas de migración del RNA 1-570 incubado con la subunidad 40S, una rápida y otra lenta. Indicativo de que las formas cerradas y abiertas del RNA, interaccionan de manera distinta con el ribosoma. Mediante ensayos de digestión total con la RNasa A se detectaron diferencias en las regiones del RNA-HCV que interaccionan con la subunidad 40S entre las formas abierta y cerrada. Concretamente, en la forma abierta estarían protegidos de la RNasa A los dominios II y III, mientras que en la forma cerrada únicamente el dominio III.

Mediante ensayos de corte con RNasas específicas de estructuras tipo-tRNA (RNasas P y RNasa Z), hemos detectado mayor rendimiento de corte de la RNasa P humana en la estructura tipo-tRNA en el fragmento del RNA de HCV que presenta la forma cerrada (HCV1-570). Sin embargo, la presencia del miR-122 en la reacción de la RNasa P humana, contribuyó negativamente en el corte de la forma cerrada, mientras que los fragmentos que no presentaron anillamiento a larga distancia incrementaron su accesibilidad.

Otro elemento estructural a resaltar en el IRES de HCV, fueron los bucles-E presentes en el dominio II del IRES. Ante la irradiación con UV-C, ambos bucles-E formaron un

enlace covalente (*crosslink*) entre las cadenas opuestas. presumiblemente, mostrándose como dos productos de migración retardada en geles de poliacrilamida desnaturalizante. Sorprendentemente, la radiación de la luz UV-C (254 nm) en el bucle-E apical provocó un auto-corte específico del RNA-HCV en las posiciones U₇₈ y C₇₉, mediante un mecanismo oxidativo independiente de la generación de radicales libres del medio, obteniéndose mayoritariamente una serie de productos con nuevos extremos generados 5'P y 3'P, y en menor medida 3'OH. La generación de un auto-corte específico por acción de la radiación UV se demostró también en el dominio Ib del IRES del RNA del virus de la peste porcina clásica (CSFV) en las posiciones C₄₃ y U₄₄, indicando que no se trata de un fenómeno exclusivo del RNA de HCV.

Cada una de las estructuras que componen la región en estudio, 1-570 del RNA de HCV, serían una serie de señales que son reconocidas de manera específica por los diferentes factores biológicos que se encuentran dentro de la célula. De manera que la especificidad que presentan esos elementos celulares por las diferentes estructuras presentes en los RNAs virales es la información que resulta de interés.

INTRODUCCIÓN

El Virus de la Hepatitis C

Generalidades

El virus de la hepatitis C (HCV) es un virus hepatotrópico que infecta a humanos y primates (Pfaender, Brown et al. 2014), y ha sido reconocido como la principal causa de enfermedad hepática crónica en humanos, afectando a más de 185 millones de personas en el mundo (3% de la población mundial) (Catanese and Dorner 2015). Su forma de transmisión es por vía sanguínea y la epidemia ocasionada por HCV fue mayormente ocasionada por la imposibilidad de la detección del virus en transfusiones sanguíneas, y trasplantes, además de la reutilización de jeringas en tratamientos parenterales, vacunas y en individuos drogodependientes. Sin embargo, la transmisión por contacto sexual o vertical de madre a hijo parece ser poco frecuente (Simmonds 2013). La infección persistente ocurre en más del 70% de los individuos infectados, permaneciendo asintomática durante un periodo de tiempo muy variable. La enfermedad está asociada a hepatitis crónica, esteatosis hepática, resistencia a insulina, cirrosis y hepatocarcinoma (Catanese and Dorner 2015). Y además, es capaz de alterar la función de otros órganos pertenecientes a los sistemas endocrino, hematopoyético y nervioso (Joyce and Tyrrell 2010). La infección por HCV es la principal causa de trasplante hepático a nivel mundial.

HCV pertenece al género *Hepacivirus* y está clasificado dentro de la familia *Flaviviridae*. Se han determinado 7 genotipos distintos (diferencias a nivel de nucleótido 30-35%), incluyendo 67 subtipos (diferencias a nivel de nucleótido <15%) grados de virulencia (Messina, Humphreys et al. 2014). Los subtipos de HCV son diferentes a nivel epidemiológico, entre los distintos grupos de riesgo y están distribuidos geográficamente de forma diferente (Simmonds 2013).

Quasispecies

La existencia de numerosos tipos y subtipos del HCV es la consecuencia a largo plazo de la evolución del virus. En paralelo a esa diversificación, en cada hepatocito infectado se está produciendo en cada momento un repertorio de variantes que pasaran al

torrente sanguíneo para mezclarse con el conjunto de variantes de otras células infectadas. Esta heterogeneidad es conferida por la alta tasa de replicación viral, entre 10^{10} - 10^{12} viriones por día, y la carencia de sistema de reparación de errores por parte de la RNA polimerasa del virus (tasas de mutación 10^{-4} - 10^{-3}), así como la frecuente y alta tasa de renovación de virus en suero, presentando una vida media de 2-3 horas (Hoofnagle 2002; Barth 2015). La variabilidad genética del virus del mismo individuo alcanza diferencias entre 1-5% de la secuencia. Este es un fenómeno común a los virus de RNA, que hace que sea imposible definir el genoma del virus con una secuencia única, y para el cual se adoptó el concepto de "cuasiespecies virales". La diversidad de cuasiespecies podría estar contribuyendo al desarrollo de la infección crónica, evadiendo al sistema inmune (Martell, Esteban et al. 1992).

Históricamente, los primeros tratamientos usados eran parcialmente efectivos (eficacia en 15% casos) y consistían en la administración por vía intravenosa de interferón. Primeramente fue administrado solo, luego en combinación con ribavirina (nucleósido de RNA análogo) y después α -pegilado combinado con ribavirina. Una década después se empezó a combinar esta terapia con una serie de fármacos conocidos como antivirales de acción directa (DAA), dirigidos a inhibir las dos enzimas esenciales para la replicación del virus: una Serin-proteasa (NS3/4A) y una RNA polimerasa (NS5B); y una proteína no-enzimática NS5A, esencial para el ciclo viral, aumentando el éxito de los tratamientos hasta un 75%. Sin embargo, el uso de todos estos tratamientos ha generado con frecuencia efectos secundarios severos, además de resistencia viral. La continua búsqueda de un tratamiento mejorado ha dado a luz a una nueva generación de DAAs dirigidos contra la RNA polimerasa del virus NS5B y la proteína NS5A, y que junto con ribavirina, llegan a curar a más del 95% de los casos. Estos nuevos tratamientos están presentando mínimos efectos secundarios y son altamente eficaces frente a la aparición de resistencias. Este hecho parece esperanzador, sin embargo, aún existen muchas personas infectadas con los diferentes genotipos que presentan tantas variantes que pueden seguir originándose resistencias. El coste del tratamiento asciende a 60000 € administrado en 12 semanas, aunque se espera que en unos años descienda por la alta presión de los gobiernos a las empresas farmacéuticas. Una vacuna sería la herramienta más adecuada para la protección contra el virus, sin embargo, aún no hay ninguna vacuna suficientemente eficaz contra

HCV debido a la estructura en cuaasiespecies del genoma de HCV (Rice and Saeed 2014; Barth 2015).

Genoma

El virus de la hepatitis C es un pequeño virus de RNA de cadena sencilla y polaridad positiva que va acompañado de una envuelta proteica. Su genoma tiene aproximadamente 9600 nucleótidos de longitud y presenta un único marco de lectura abierto (ORF) que codifica para una poliproteína de unos 3010 aminoácidos. El ORF está flanqueado por dos regiones no traducibles en sus extremos 5' y 3' que son requeridas para la encapsidación, replicación y el inicio de traducción del virus. Tras la traducción, el precursor poliproteico es procesado a nivel post-traduccional para dar lugar a 10 proteínas estructurales y no estructurales. Las proteínas estructurales forman la partícula viral y corresponden a la proteína core, que modula la expresión génica viral y celular, y da lugar a la nucleocápsida del virus; y las glicoproteínas de la envuelta E1 y E2, que controlan la entrada mediada por receptor del virus en la célula. Las proteínas no estructurales incluyen la viroporina p7, que actúa como canal iónico; la proteasa NS2; las proteínas que conforman el complejo macromolecular de la replicasa: el complejo proteasa NS3-4A (serín proteasa y RNA helicasa), las proteínas NS4B y NS5A; y la RNA polimerasa NS5B dependiente de RNA (Suzuki, Ishii et al. 2007; Joyce and Tyrrell 2010; Pineiro and Martinez-Salas 2012; Moradpour and Penin 2013)

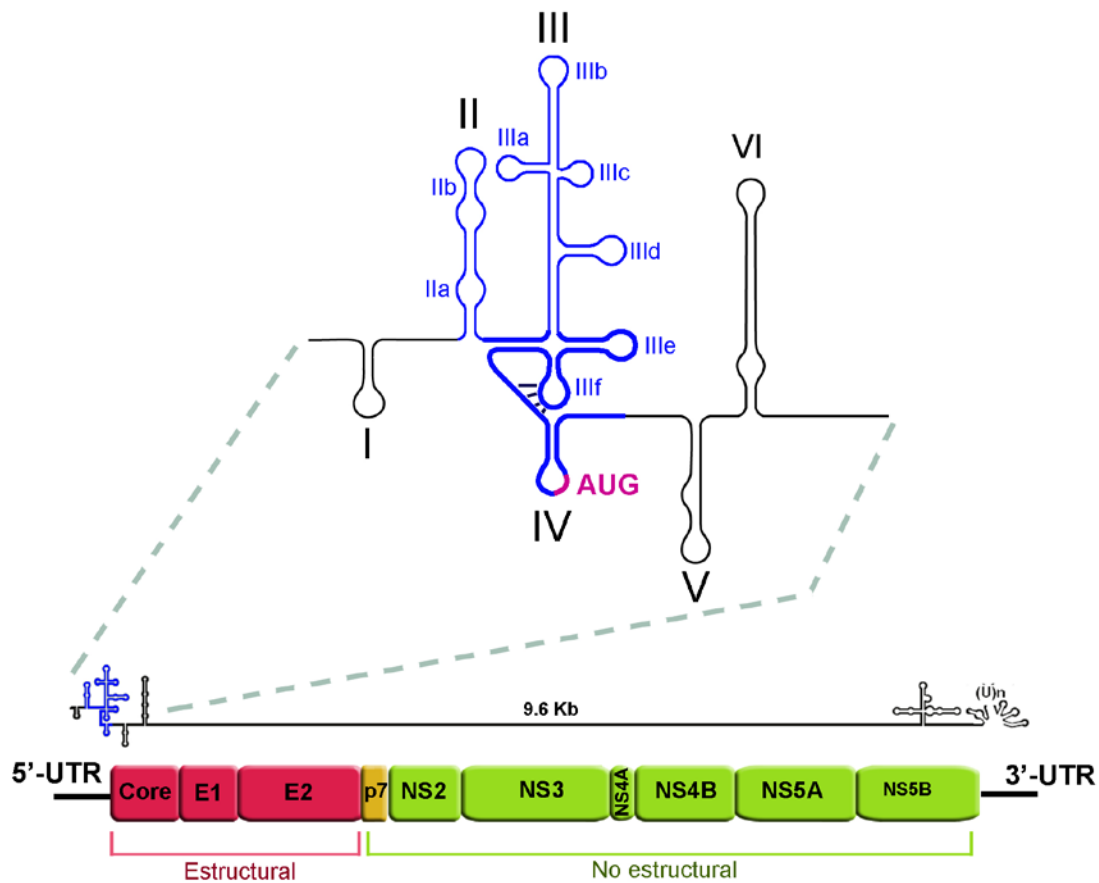


Figura 1: Representación esquemática del genoma de RNA del HCV. Las diferentes proteínas que codifica el RNA de HCV son mostradas en rosa (Proteínas estructurales) y en verde (proteínas no estructurales). El ORF está flanqueado por las dos zonas no traducibles (5'-UTR y 3'-UTR). La ampliación muestra la región 5'-UTR y los primeros 230 nucleótidos que codifican para la proteína del Core. En azul se resalta el elemento IRES (dominios II-IV) que incluye el motivo tipo-tRNA con trazo azul más grueso (dominios IIIef y IV).

Regiones reguladoras de la replicación y traducción del virus en la región 5' no traducible (5'UTR)

Los principales elementos del RNA que actúan regulando el ciclo replicativo de HCV en *cis*- se localizan fundamentalmente en las regiones no traducibles de los extremos 5' y 3' de la cadena positiva. También se han encontrado otros elementos reguladores en el extremo 3' de la cadena negativa y dentro del ORF, en las secuencias que codifican para la proteína core y la RNA polimerasa NS5B(Sagan, Chahal et al. 2015).

La región 5'-UTR del RNA viral contiene cuatro estructuras principales organizadas en tallo-lazo, separadas por pequeñas regiones espaciadoras, denominadas dominios I, II, III y IV.

El dominio I (5-20 nt) es esencial para la replicación viral, requiriendo la totalidad del tallo-lazo para incrementar la replicación (Friebe, Lohmann et al. 2001). Aunque hay datos en los que parece no implicar al dominio I con la traducción, existen trabajos en cultivo celular donde la delección de este dominio la favorecería (Rijnbrand, Bredenbeek et al. 1995; Honda, Brown et al. 1996).

El dominio II está formado por dos subdominios: IIa y IIb. El subdominio IIa posee dos bucles internos asimétrico que corresponde a dos lazos-E, capaz de formar interacciones no canónicas entre sus nucleótidos enfrentados. El subdominio IIb presenta también un bucle-E y un bucle apical, que están conservados en diferentes virus de la familia *Flaviviridae* (Peste porcina clásica y Diarrea viral bovina). Mediante ensayos de crio-electromicroscopía (crio-EM) y resonancia magnética nuclear (RMN), se ha visto que el bucle asimétrico del subdominio IIa es capaz de doblarse en un ángulo de aproximadamente 90° dando lugar a una estructura en forma de L extendida. Este doblamiento se produce también cuando forma parte de la molécula del IRES, pero es estabilizado por la interacción de la subunidad ribosomal 40S. Este dominio II imprescindible para la traducción del virus. (Spahn, Kieft et al. 2001; Lukavsky, Kim et al. 2003). El dominio II, junto con el dominio I forman la unidad mínima requerida para que se lleve a cabo la replicación viral (Friebe, Lohmann et al. 2001). Recientemente se ha demostrado que este dominio podría mediar la conexión de traducción a replicación (Sagan, Chahal et al. 2015).

El dominio III es altamente complejo a nivel de estructura secundaria. Está formado por seis subdominios (IIIabcdef) implicados directamente en la traducción del virus. Los subdominios IIIabc forman una unión en cruz que aporta flexibilidad a la molécula. IIIad interaccionan directamente con la superficie de la subunidad ribosomal 40S, mientras que los subdominios IIIbc interaccionan con el factor de inicio de traducción eIF3 favoreciendo la formación del complejo 40S-IRES (Kieft, Zhou et al. 1999). Los subdominios IIIef están interaccionando con el dominio IV formando un doble pseudonudo (Wang, Le et al. 1995; Berry, Waghray et al. 2010) (Berry, Waghray et al.

2011) siendo esencial para el posicionamiento del codón de inicio de traducción en el sitio P de la subunidad ribosomal 40S(Berry, Waghray et al. 2010). Recientemente se ha propuesto que podría conferirle un papel biológico alternativo disociando el IRES del ribosoma para permitir la encapsidación del genoma en una nueva partícula vírica(Fricke, Dunnes et al. 2015).

El dominio IV incluye el codón de inicio de traducción AUG en la posición 342 y los 10 primeros nucleótidos del ORF. La estabilidad de este dominio es imprescindible para la traducción, favoreciéndose el proceso en condiciones donde este dominio se encuentra desestabilizado(Honda, Brown et al. 1996). También, forma un doble pseudonudo con los subdominios IIIef, esencial para el posicionamiento del codón de inicio en el surco de descodificación en la subunidad ribosomal 40S. Mediante ensayos de corte con distintas RNAsas P se ha descrito que las regiones que incluyen el pseudonudo y el dominio IV forman un motivo tipo-tRNA(Nadal, Martell et al. 2002; Lyons and Robertson 2003; Sabariego, Nadal et al. 2004).

Los distintos dominios del 5'UTR se organizan en una serie de elementos estructurales capaces de regular las diferentes funciones del virus. Entre estos elementos, cabe destacar el IRES, esencial para iniciar la traducción viral, y que incluye un motivo tipo-tRNA.

- IRES:

Los IRES (Sitio de Entrada Interna del Ribosoma) son elementos de RNA cuya estructura y función están altamente conservados entre miembros de los géneros pestivirus y hepacivirus, a pesar de sus diferencias a nivel de secuencia(Brown, Zhang et al. 1992; Hellen and Pestova 1999; Honda, Beard et al. 1999). Fueron descritos por primera vez en el virus de la polio (Pelletier, Kaplan et al. 1988) y posteriormente fueron encontrados en otros RNAs virales como HCV (Tsukiyama-Kohara, Iizuka et al. 1992) y pestivirus animales relacionados(Poole, Wang et al. 1995), y también están presentes en mensajeros celulares (Macejak and Sarnow 1991). Su principal función consiste en el reclutamiento interno del ribosoma y el inicio del proceso de traducción por un mecanismo no canónico independiente de un extremo 5'-cap. La traducción mediada por IRES requiere menor número de factores canónicos del inicio de traducción del hospedador, debido a su complejidad estructural. Según el número de

factores necesarios para la traducción pueden ser clasificados en diferentes tipos, incluyendo a HCV dentro de los IRES de tipo 2, donde los factores necesarios para el inicio de traducción son eIF2 y eIF3 (Kieft 2008).

El IRES de HCV lo forman los dominios II, III y IV (nucleótidos 39-371)(Perard, Leyrat et al. 2013), incluyendo al codón de inicio de la traducción en la posición 342 y los primeros 30-40 nucleótidos de la secuencia que codifica para la proteína core. (Rijnbrand, Bredenbeek et al. 1995; Honda, Ping et al. 1996; Sagan, Chahal et al. 2015). Mediante ensayos de difracción de rayos-x se ha determinado que el IRES de HCV en solución es una estructura articulada formada por diversos dominios que se mueven unos respecto de los otros gracias a las regiones de simple cadena que los separan(Perard, Leyrat et al. 2013). Al igual que ocurre en otros IRES, funciona por un mecanismo más similar al bacteriano que al de eucariotas, basado en el reconocimiento de secuencias Shine-Dalgarno (2-10 nts), donde los nucleótidos -15 a +20 respecto del codón de inicio de traducción son imprescindibles por la estructura que adoptan para la exposición del codón de inicio de traducción, sin haberse encontrado secuencia consenso entre ellos. En HCV la subunidad ribosomal pequeña se recluta aguas arriba del codón de inicio. En la interacción participan las secuencias entre la región conservada de la hélice 26 del rRNA 18S de la subunidad ribosomal 40S (triplete CCC) que aparean con el bucle apical del dominio IIIId del IRES de HCV (triplete GGG). A diferencia de que son elementos más largos, discontinuos y estructurados que los presentes en bacterias y donde la estructura terciaria tiene un importante papel(Fletcher, Ali et al. 2002; Malygin, Kossinova et al. 2013; Panek, Kolar et al. 2013). Este apareamiento también es esencial para que se lleve a cabo el inicio de la traducción *in vivo* (Matsuda and Mauro 2014).

Ha sido descrito que el IRES de HCV es necesario también para conectar el inicio de traducción con el proceso de elongación(Filbin, Vollmar et al. 2013).

- Motivo tipo-tRNA:

Son motivos que mimetizan diversas características de los tRNAs. Los primeros motivos tipo-tRNA fueron descritos en el extremo 3' del RNA de virus de plantas, concretamente el primero fue en el virus del mosaico del nabo (TYMV) con la

capacidad de incorporar un aminoácido por la valil-tRNA sintetasa (Yot, Pinck et al. 1970). Muy posteriormente han sido descritos en otros virus de RNA animales y mensajeros celulares (Diaz-Toledano and Gomez 2015). Las principales propiedades que caracterizan a las estructuras tipo-tRNA son la capacidad de aminoacilación (con valina, histidina y tirosina), la formación de un complejo ternario con los factores eEF1A-GTP, la adenilación de extremos 3'-CC por la CCA-nucleotidiltransferasa para mantener los extremos 3'-CCA intactos y presentar pseudonudos en su estructura. Aunque también existen otras propiedades: modificación de base, capacidad de ser procesado por la RNasa P y la eliminación del aminoácido cargado mediante la peptidil-tRNA hidrolasa. Entre las funciones que aportan los motivos tipo-tRNA, se encuentra la estimulación de la traducción, el incremento de la estabilidad del extremo 3', actuar de promotor de la cadena negativa, encapsidación de genomas virales, interacción con los ribosomas (Dreher 2010). Concretamente en virus, aunque pueden incorporar un aminoácido, no pueden donarlo a su síntesis proteica, por lo que destaca el papel esencial en replicación de la secuencia 1-3... (Dreher 2009).

Dentro del genoma de HCV se han identificado dos estructuras tipo-tRNA mediante ensayos de corte con la RNasa P humana, nucleasa celular implicada de forma natural en la maduración del extremo 5' de los precursores del tRNA. Se utiliza como herramienta molecular para la identificación de este tipo de motivos. Una de ellas se encuentra dentro de la región 5' UTR dentro del IRES, en torno al codón de inicio de traducción, confirmada mediante *análisis in silico* (Lavender, Ding et al. 2010) y la otra está incluida en la secuencia que codifica para la proteína NS2. El motivo tipo-tRNA presente en el IRES, presenta la estructura secundaria en forma de hoja de trébol característica de los tRNAs mediante los dominios IIIdef. Psee un doble pseudonudo cerca de la posición de corte de la RNasa P humana (Berry, Waghray et al. 2011), que favorece la estructura terciaria característica en forma de L. Forma dos dominios en hélice separados por un lazo espaciador, que corresponden al brazo T y al brazo aceptor del tRNA. Aunque su función es aún desconocida, su localización cercana al triplete iniciador podría favorecer el reclutamiento de la maquinaria traduccional en ausencia de un 5'-cap (Nadal, Martell et al. 2002). Recientemente se ha identificado un motivo tipo-tRNA en el mensajero del interferón α -5, con el que presenta parecido (Diaz-Toledano and Gomez 2015). Se han identificado otras estructuras tipo-tRNA mediante

ensayos de corte con la RNasa P, en los IRES de pestivirus relacionados con HCV (CSFV y PPC), el picornavirus EMCV y el miembro de la familia *Dicistroviridae* CrPV. Indicando que las estructuras tipo-tRNA podrían ser elementos característicos de los IRES cuyo reconocimiento favorecería el posicionamiento del AUG en el sitio P del ribosoma (Lyons and Robertson 2003).

Interacciones terciarias en el RNA de HCV

Las estructuras terciarias formadas por las interacciones RNA-RNA confieren una serie de funciones relacionadas con el ciclo de replicación y traducción del virus. La estructura secundaria de las regiones implicadas en estas interacciones está altamente conservada y está focalizada en las regiones no traducibles 5' y 3', regiones próximas a éstas (secuencia de la proteína Core y NS5B) y en los extremos 5' y 3' de la hebra negativa.

El apantallamiento de las cargas negativas del RNA por los iones divalentes, y concretamente del ión magnesio, es crucial para la formación y estabilización de las estructuras terciarias que se forman en el RNA de HCV (Kieft, Zhou et al. 1999).

– *Pseudonudo*

Mediante ensayos de cristalografía, difracción de rayos-x y SHAPE se ha descrito un doble pseudonudo en la base del dominio III (IIIe-f) del IRES. Es el dominio estructural más complejo en el IRES y está localizado en el centro de él conectando los dominios II y III con el dominio IV, que contiene el codón de inicio AUG. Consiste en una estructura compleja que incluye 3 tallos (SI, SII y SII/J) unidos por tres lazos de uridinas (L1, L2 y L3), y el cruce que conecta SI, SII/J, dominio IIIe y el tallo que parte hacia el resto del dominio III. El subdominio IIIe posee un lazo apical de cuatro nucleótidos cuya secuencia está altamente conservada entre los diferentes genotipos del virus. Los cambios de accesibilidad observados en IIIe en diferentes condiciones de iones magnesio y en presencia de la subunidad ribosomal 40S, han confirmado la formación de esta interacción terciaria, que es imprescindible para una eficaz traducción (Honda, Brown et al. 1996; Kieft, Zhou et al. 1999; Berry, Waghray et al. 2011). El plegamiento que origina el pseudonudo en el IRES, favorece el

posicionamiento y la orientación necesarios del codón de inicio en la subunidad ribosomal 40S (Berry, Waghay et al. 2010).

Otro pseudonudo está descrito en el extremo 3' de la secuencia que codifica para la RNA polimerasa NS5B, entre la secuencia conservada del lazo apical del tallo-lazo 5BSL3.2 y la cola-X del 3'UTR. Es una interacción dinámica entre los dos lazos apicales de ambas estructuras, cuya disrupción inhibe la replicación y traducción viral (Friebe, Boudet et al. 2005; Tuplin, Struthers et al. 2015).

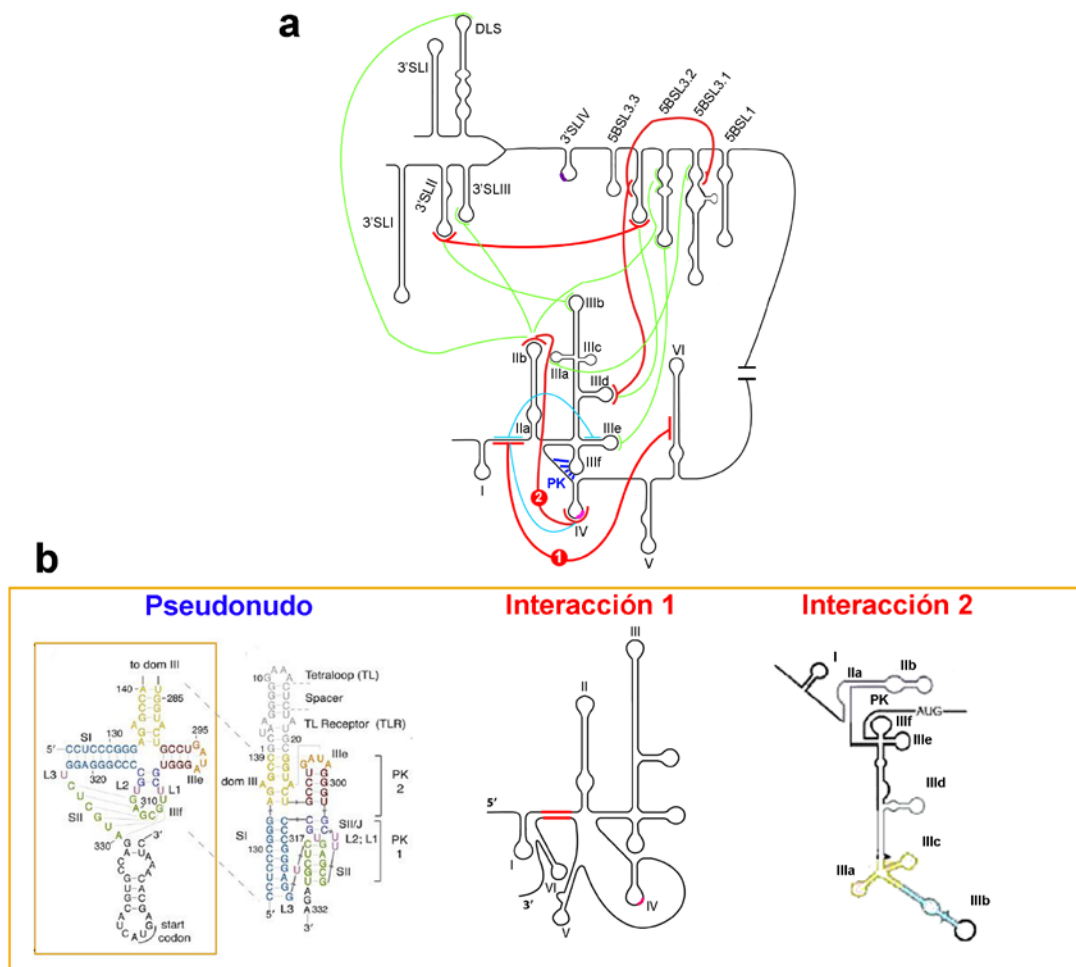


Figura 2: Representación esquemática de las diferentes interacciones terciarias relacionadas con el IRES de HCV. **(a)** Anillamientos a media y larga distancia entre los diferentes dominios de la región 3'UTR y 5'UTR. En rojo se muestran las interacciones ya descritas y ampliamente estudiadas; en celeste las predicciones *in silico* de interacciones entre dominios del IRES y en verde las predicciones para interacciones entre elementos del 3'UTR con el IRES. En azul se muestra el pseudonudo (PK) del 5'UTR. En rosa se muestra el codón de inicio de traducción AUG en 5'UTR y en violeta el codón de parada en 3'UTR. **(b)** Representación más detallada de los nucleótidos implicados en el nuevo doble pseudonudo

descrito por (Berry, Waghray et al. 2010); de las interacciones ampliamente estudiadas 1 (entre la región espaciadora de los dominios I y II con el dominio VI) y 2 (entre dominios IIb y IV)(Boehringer, Thermann et al. 2005).

– *Anillamiento a larga distancia:*

El RNA de HCV tiende a favorecer el acoplamiento de la traducción con la replicación para aumentar la eficacia de ambos procesos, al igual que ocurre en otros virus de RNA de polaridad positiva. Una serie de interacciones a larga distancia conectan y estabilizan la interacción de regiones distantes cuya proximidad favorece la regulación tanto de replicación como de traducción. Las secuencias y estructuras implicadas en estas interacciones son conservadas (Fricke, Dunnes et al. 2015).

Mediante análisis estructural con SHAPE y cribaje con oligonucleótidos antisentido, se ha descrito la circularización del genoma del RNA de HCV interaccionando el tallo-lazo 5BSL3.2 de la secuencia que codifica la RNA polimerasa NS5B (extremo 3' del ORF) con el subdominio IIIId del IRES. La circularización de genomas virales se ha descrito en virus de RNA de polaridad positiva y está presente de forma frecuente en flavivirus, siendo importante para la traducción, transcripción y replicación viral (Edgil and Harris 2006). Esta interacción entre los extremos 5' y 3' del RNA de HCV, posiblemente aporte un papel regulador de la traducción y tenga un papel crítico en replicación (Romero-Lopez, Barroso-Deljesus et al. 2012). El tallo-lazo 5BSL3.2 también interacciona con la secuencia 9110 de 5BSL2 (dentro de la secuencia que codifica para NS5B) (Tuplin, Struthers et al. 2012) y con el tallo-lazo SLII de la cola-X del 3'-UTR (Friebe, Boudet et al. 2005), resaltando el papel regulador y conector de 5BSL3.2 en los procesos de replicación y traducción viral (Fricke, Dunnes et al. 2015).

En la región 5' del RNA de HCV se produce un anillamiento a larga distancia entre las secuencias que flanquean el IRES (Honda, Rijnbrand et al. 1999; Beguiristain, Robertson et al. 2005). Mediante ensayos de corte con la RNasa III de *Escherichia coli* y de mutagénesis *in vitro*, se ha determinado que la secuencia de simple cadena presente entre los dominios I y II del 5'UTR (24-38 nt) interacciona con la base del dominio VI del genoma (428-442 nt), cuya secuencia es muy conservada y se localiza dentro de la secuencia codificante para la proteína core (Honda, Rijnbrand et al. 1999; Kim, Lee et al. 2003; Beguiristain, Robertson et al. 2005). Este anillamiento a larga distancia

mantiene al IRES en una conformación cerrada. En ensayos de traducción *in vitro* en lisado de reticulocito y células HepG2 se ha determinado que esta interacción inhibe la traducción viral (Honda, Rijnbrand et al. 1999; Wang, Rijnbrand et al. 2000; Kim, Lee et al. 2003). Sin embargo, en células Huh-7 no se ha podido evaluar adecuadamente el efecto del anillamiento a larga distancia debido a los niveles internos de microRNA hepático miR-122, que al favorecer la traducción viral, contrarrestaría los efectos negativos del anillamiento a larga distancia (McMullan, Grakoui et al. 2007; Roberts, Lewis et al. 2011; Goergen and Niepmann 2012). Por tanto, existen discrepancias en el papel de este anillamiento a larga distancia en traducción, por lo que generalmente la mayoría de estudios relacionados con la traducción dependiente de IRES de HCV se lleven a cabo sin los dominios V y VI.

Mediante ensayos de movilidad electroforética en geles nativos (EMSA) (Lafuente, Ramos et al. 2002), SHAPE (Filbin and Kieft 2011) y análisis *in silico* (Fricke, Dunnes et al. 2015) se ha identificado otro anillamiento a larga distancia dentro del propio IRES, entre los lazos apicales de los dominios II y IV. Esta interacción es la más estudiada debido a que está estrechamente relacionada con el codón de inicio de traducción AUG. A través de mutaciones y deleciones en el dominio II, se ha determinado que el dominio II sufre un doblamiento a nivel del subdominio IIa, orientando el lazo apical del subdominio IIb hacia el codón de inicio de traducción AUG, dentro del dominio IV (Lukavsky, Kim et al. 2003; Filbin and Kieft 2011). Sin embargo, distintas consideraciones indican que: la poca conservación de secuencia a nivel filogenético del lazo apical de subdominio IIb, la conflictiva competición con el tRNA por el sitio P del ribosoma, el desplazamiento del AUG lejos del sitio P que se originaría por esta interacción impidiendo su unión con el tRNA iniciador y las discrepancias en valores de densidad de crio-EM, indican que estos dominios estarían aproximados espacialmente, debido al doblamiento del dominio II, sin llegar a producirse apareamiento de bases entre ellos (Filbin and Kieft 2011).

Una interacción entre los dominios IIIId y IV del IRES se también fue identificada mediante ensayos de cribaje con oligonucleótidos antisentido y EMSA (Lafuente, Ramos et al. 2002). Mediante ensayos con SHAPE se ha visto que la interacción del miR-122 en el 5'UTR produce cambios estructurales que incrementan la accesibilidad

del dominio I, IIa y el bucle apical IIb, pudiendo facilitar interacción entre I y IIa (Mortimer and Doudna 2013). Recientemente, mediante análisis bioinformático han sido confirmadas cada una de estas interacciones a larga distancia, y además se han predicho otras posibles interacciones que implican a las regiones 5' y 3'-UTR. Dentro del elemento IRES se han encontrado nuevos anillamientos a larga distancia entre la región de simple cadena que conecta los dominios I y II con el subdominio IIIId y con el dominio IV (Fricke, Dunnes et al. 2015).

Elementos celulares relacionados con la traducción y replicación del virus

Inicio de traducción en RNA de HCV

La traducción de la poliproteína de HCV es llevada a cabo en el citoplasma de hepatocitos mediante un elemento IRES, donde simplemente requiere de dos factores proteicos de la célula hospedadora para el inicio de traducción: eIF2 y eIF3 (Figura 3).

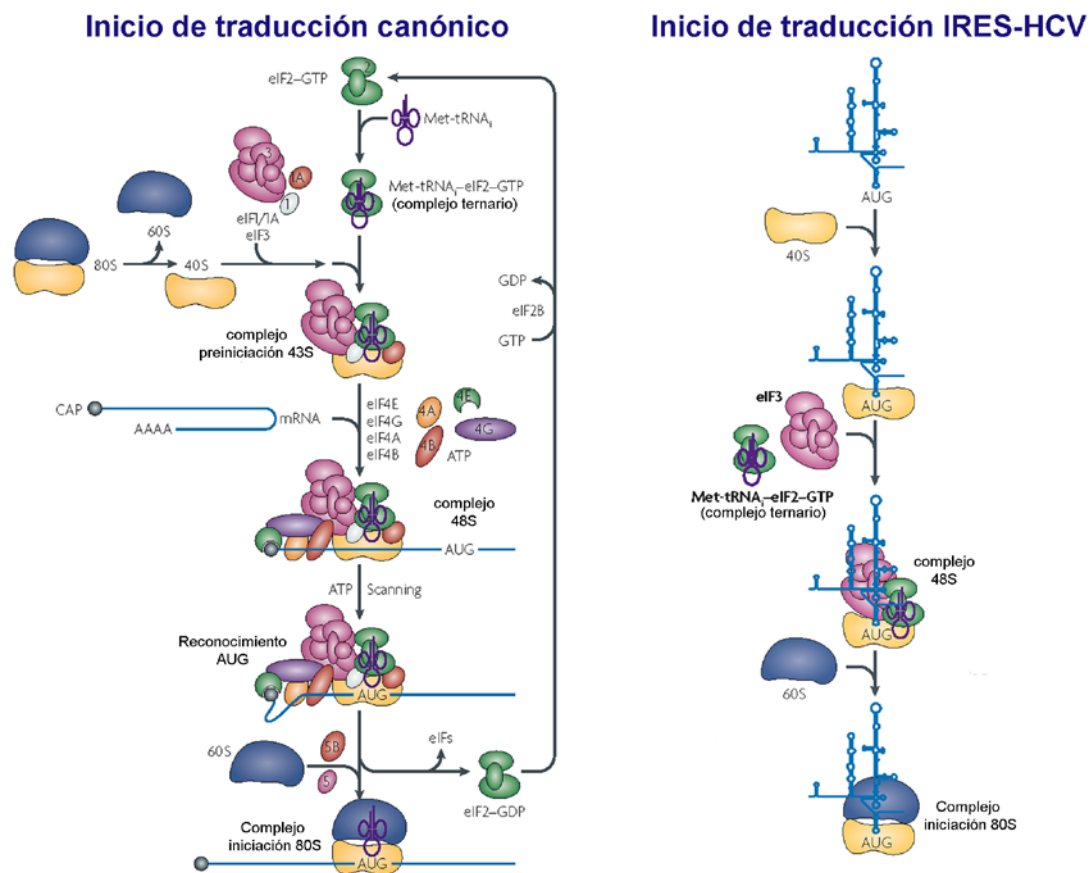


Figura 3: Representación esquemática del inicio de traducción canónico, en mayoría de mRNAs celulares y el inicio de traducción de los IRES tipo 2, concretamente de HCV. A diferencia del mecanismo de traducción canónico de eucariotas, la traducción en el RNA de HCV no se inicia con el reconocimiento de una 7-metil Guanosina (cap) en su extremo 5', seguido de un escaneo desde el extremo 5' para localizar el codón de inicio de traducción como sucede en la traducción canónica. En este caso, el IRES de HCV sustituye a esos factores implicados en el reconocimiento del 5'cap (eIF4F) y en el escaneo de la secuencia en búsqueda del codón de inicio de traducción (eIF1 y eIF1A), por lo que recluta y posiciona directamente a la subunidad ribosomal 40S en el codón de inicio de traducción AUG sin necesidad de ningún factor de inicio de traducción. El IRES de HCV unido a la subunidad 40S (IRES-40S) es conocido como complejo binario.

Existe una vía alternativa de traducción en IRES de HCV en condiciones de estrés, en la que el factor eIF2 (implicado en el complejo ternario) se inactiva por fosforilación y es sustituido por eIF5B, asemejándose aún más al inicio de traducción de procariotas (Terenin, Dmitriev et al. 2008).

A continuación, se une directamente el factor de inicio de traducción eucariota eIF3 en el subdominio IIIb del IRES y también el complejo ternario formado por eIF2-GTP-tRNA_i^{Met}, formándose el complejo de pre-iniciación de la traducción. La hidrólisis del GTP a GDP favorece la liberación del factor eIF2 y eIF3, y la interacción de la subunidad ribosomal mayor 60S para formar un complejo 80S eficiente, esencial para que se inicie la síntesis proteica (Spahn, Kieft et al. 2001; Boehringer, Thermann et al. 2005; Khawaja, Vopalensky et al. 2014) (Kieft 2008)

Subunidad ribosomal 40S

El ribosoma humano contiene cuatro rRNAs y 80 proteínas ribosomales organizados en dos subunidades: las subunidades ribosomales pequeña 40S y grande 60S, nombradas en función de su coeficiente de sedimentación.

La subunidad ribosomal 40S contiene un único rRNA 18S de aproximadamente 1900 nucleótidos de longitud y 30-50 proteínas ribosomales. El rRNA 18S es sintetizado por la RNA polimerasa I en el nucleolo celular como un precursor mayor 47S, presente en repeticiones en tandem en los cromosomas 13, 14, 15, 21 y 22, y que contiene también la secuencia para dos de los rRNAs de la subunidad 60S (5.8S y 28S). El rRNA 18S es procesado y modificado en el nucleoplasma y es exportado al citoplasma para el ensamblaje con las diferentes proteínas ribosomales que dan lugar a la subunidad ribosomal 40S. (Jackson, Hellen et al. 2010; Lafontaine 2015).

Morfológicamente, la subunidad 40S posee dos partes: La cabeza, que presenta un saliente o pico; y el cuerpo, que incluye a su vez la plataforma por donde se desplaza el RNA mensajero durante la traducción.

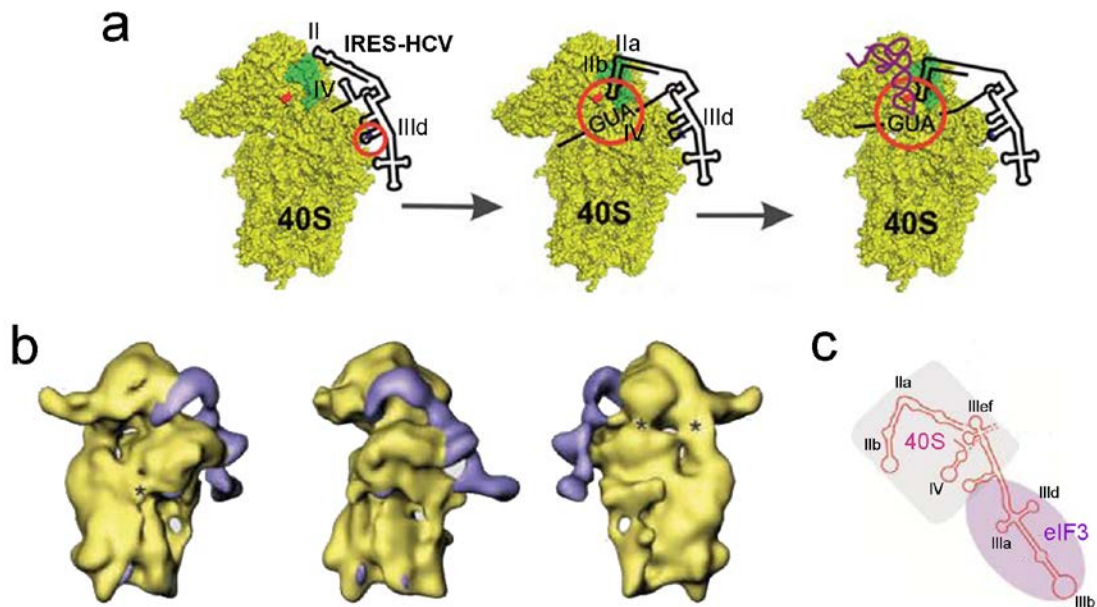


Figura 4: (a) Modelo del proceso de formación del complejo de preiniciación 48S. En verde se muestra la posición de la proteína ribosomal rpS5. 1- Interacción inicial entre IIIId y el bucle 7 del rRNA 18S; 2- Doblamiento de II e interacción IIb con proteína rpS5, desnaturalización IV y posicionamiento de AUG en el sitio P en el surco de descodificación; 3- Interacción del complejo ternario y formación del complejo de preiniciación 48S. En amarillo se muestra el 40S y en morado el IRES-HCV (Malygin, Kossinova et al. 2013). (b) Imagen de crioelectromicroscopía desde tres ángulos diferentes de la unión del IRES-HCV al 40S. (c) estructura secundaria del IRES de HCV unido a 40S y al factor eIF3(Perard, Leyrat et al. 2013).

Durante el inicio de traducción del mRNA de HCV, el IRES interacciona con la subunidad 40S mediante sus dominios II y III a través de interacciones con diferentes proteínas ribosomales; y mediante el subdominio IIIId con el rRNA 18S(Lytle, Wu et al. 2002; Malygin, Kossinova et al. 2013). La afinidad de unión del 40S con el IRES de HCV es alta, $K_d = 1.9$ nM, y requiere de la presencia de iones Mg^{2+} (hasta aproximadamente 2mM) para favorecer las estructuras terciarias del IRES, que son esenciales para la estabilización de la unión con el 40S (Kieft, Zhou et al. 2001). Mediante análisis de crio-EM(Spahn, Kieft et al. 2001) y transferencia de energía de resonancia de Förster (FRET) (Fuchs, Petrov et al. 2014) se ha determinado que cuando el 40S interacciona con el IRES, este sufre un cambio donde el dominio II se dobla, ocupando el sitio E del ribosoma y se orienta hacia el codón de inicio AUG,

quedando conectados los lazos apicales de los dominios II y IV mediante la interacción con la proteína RPS5 de la subunidad ribosomal 40S (Filbin and Kieft 2011; Barth 2015). La aproximación del dominio II al AUG origina un segundo cambio conformacional en el dominio IV, que con ayuda del pseudonudo presente en el IRES (Berry, Waghray et al. 2010), se produce la desestabilización del tallo del dominio IV y se favorece el posicionamiento del AUG en el sitio P dentro del surco de descodificación (Honda, Brown et al. 1996). Recíprocamente, la interacción del IRES con el 40S origina otro cambio conformacional en la propia subunidad ribosomal, mediante un giro de la cabeza de la subunidad que conduce al cierre del surco de descodificación en torno al mensajero a traducir (Spahn, Kieft et al. 2001).

Mediante ensayos de unión y de crosslink se ha determinado recientemente que la subunidad ribosomal 40S interacciona también con la región 3'-UTR de HCV. Esta región estaría captando subunidades 40S para cederlas al IRES, mediante la interacción a larga distancia entre el 3'UTR y el 5'UTR, para incrementar la eficiencia de las sucesivas rondas de traducción (Bai, Zhou et al. 2013).

microRNAs

Generalidades

Los microRNAs (miRNAs) son pequeñas moléculas de RNA no codificante de cadena sencilla de 21-23 nucleótidos de longitud, implicados en la regulación de la expresión génica.

Los primeros microRNAs descritos fueron *lin-4* y *let-7b* en el nematodo *Caenorhabditis elegans*, y desde entonces se han determinado y aislado miles de estas moléculas codificadas en organismos eucariotas (plantas, algas verdes y animales) y en virus, existiendo en muchos casos conservación entre especies (Griffiths-Jones, Saini et al. 2008). Hay descritos alrededor de 2600 miRNAs en humanos y regulan una tercera parte de los genes del genoma. Se les ha relacionado con muchas enfermedades humanas, siendo utilizados para el diagnóstico clínico y como dianas terapéuticas.

La secuencia diana para los miRNAs animales se suele encontrar en los 3'-UTRs de los mRNAs, pero cada vez es más frecuente dianas en las regiones 5'-UTRs o en ORFs,

capaces de inhibir o favorecer con la misma eficacia la expresión génica. Entre los diferentes efectos en regulación génica encontramos: Regulación post-transcripcional, regulación transcripcional, alteraciones epigenéticas, desregulación del ciclo celular, supresión de la apoptosis, alteración de las vías de señalización celular y regulación de la replicación y traducción viral.

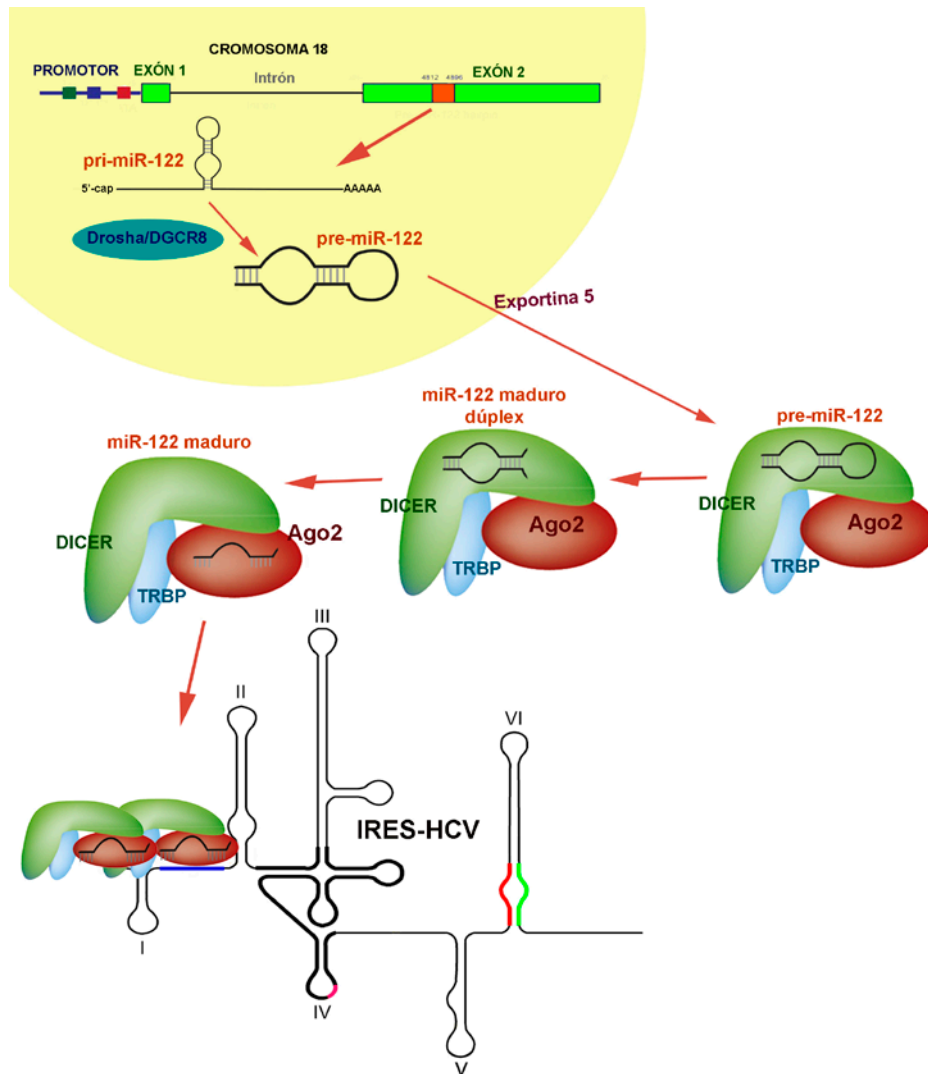


Figura 5: Biosíntesis del miR-122 y e interacción en las dianas S1 y S2 del IRES de RNA de HCV mediante las proteínas del complejo RISC:Dicer, Ago2, TRBP. Los miRNAs son sintetizados generalmente por la RNA polimerasa II en el núcleo celular como un transcrito precursor denominado pri-miRNA. Contiene la secuencia para un único miRNA o varios con funciones relacionadas, presentes en forma de horquilla de doble cadena en ese precursor. Los pri-miRNAs pueden ser transcritos únicos o proceder de un intrón de un pre-RNA mensajero. El pri-miRNA es procesado en el núcleo celular por la RNasa III Droscha (DCL1 en plantas), asociada con la proteína DGCR8, que reconoce y corta el RNA de

doble cadena, dando una horquilla de menor tamaño correspondiente al precursor del miRNA (pre-miRNA) de aproximadamente 70 nucleótidos de longitud. El pre-miRNA es exportado al citoplasma por la Exportina 5 y allí termina de ser procesado por la RNasa III Dicer, produciendo un RNA de doble cadena de 21-23 pares de bases, con 2 nt protuberantes en los extremos 3'. El miRNA duplex es introducido en los cuerpos-P donde es cargado en el complejo de silenciamiento inducido por RNA (RISC), asociado a una proteína Argonauta (Ago). Se retiene la hebra con el extremo 5' más débil, que corresponde al miRNA maduro, y la otra hebra es eliminada (Czech and Hannon 2011; Hammond 2015).

Los miRNAs son presentados por RISC a la secuencia complementaria del RNA mensajero diana, presente generalmente en la región 3'-UTR. Los miRNAs de plantas hibridan de manera perfecta con el mRNA diana, produciendo el corte del mensajero por acción de la RNasa III y la no expresión del mismo (conocidos como siRNA); sin embargo, en el reino animal la hibridación de los miRNAs con la secuencia diana del mRNA es imperfecta, dirigiendo a la represión de la expresión génica.

Los miRNAs presentan una secuencia diana de seis nucleótidos altamente conservada, conocida como secuencia "seed". Corresponde a los nucleótidos 2 al 7 del extremo 5' del miRNA. Inicialmente era asumido que los miRNAs efectúan su papel regulador uniéndose a sus secuencias dianas a través de la secuencia *seed*. De manera que han sido determinados muchos miRNAs y sus funciones mediante la identificación de sitios dianas para las secuencias *seed*. Sin embargo, a medida que se han ido identificando nuevos miRNAs, se ha visto que la interacción y la funcionalidad del miRNAs no tienen que ser exclusivamente de la secuencia *seed*. La hibridación con sus mRNAs dianas puede realizarse a través de la secuencia en 3' y/o regiones centrales del miRNA ("no-*seed*") dependiente e independientemente de la secuencia *seed* (Brodersen and Voinnet 2009; Roberts, Lewis et al. 2011).

microRNAs que interactúan directamente con la región 5'UTR de HCV:

Actualmente hay descritos muchos microRNAs relacionados con el ciclo de replicación del HCV, ya se favoreciendo y/o reprimiendo su propagación. La mayoría de ellos intervienen indirectamente (miR-29, miR-296...) y unos pocos son capaces de interactuar directamente con el RNA de HCV (miR-448 hacia la secuencia del core, miR-196 con la secuencia de NS5A), pero sólo los microRNAs miR-122, let-7b y miR-199a* presentan secuencias dianas en la región 5'-UTR de HCV (Conrad and Niepmann 2013).

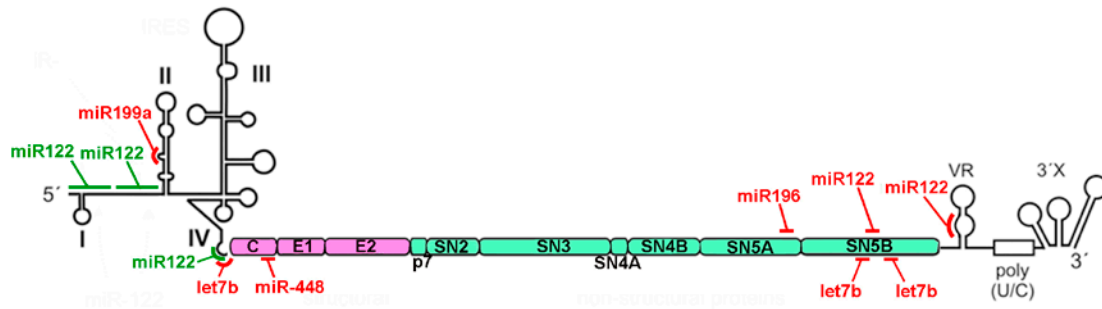


Figura 6: Posicionamiento de los microRNAs de interacción directa con el genoma de RNA de HCV. En verde se muestran los miRNAs con papel positivo sobre el virus y en rojo a los miRNAs con papel inhibitorio.

– *microRNA-122*

El microRNA-122 (miR-122) es específico de vertebrados, estando presente al menos en 18 especies diferentes (ranas, pez cebra, humanos...). Su secuencia completa (*seed* y *no-seed*) se encuentra altamente conservada, indicando que toda su secuencia es imprescindible para su función. En el ser humano, es específico del hígado y seguramente sea el factor que confiere al HCV el tropismo por este órgano. El miR-122 se expresa a partir de un único locus genómico en el cromosoma 18 de humanos, en un exón de RNA no codificante. La expresión del miR-122 es mucho mayor que del resto de microRNAs del hígado humano (72% de los miRNAs totales). Su expresión está muy regulada: a nivel transcripcional sobre sus precursores pri-miR-122 y pre-miR122 por los ciclos circadianos; y a nivel post-transcripcional, por la adición de adeninas en su extremo 3', confiriéndole una gran estabilidad y originándose diferentes isoformas del miRNA. Está presente en aproximadamente 66000 copias/célula en el hígado sano de un humano adulto. (Jopling 2012; Cox, Sagan et al. 2013; Wilson and Huys 2013).

En el hígado sano, el miR-122 regula más de 100 dianas en diferentes genes de hepatocitos (~60% genes). Regulando funciones fisiológicas implicadas en la síntesis de ácidos grasos y del colesterol, respuesta a estrés, regulación de la homeostasis y supresión de tumores(Fernandez-Hernando, Ramirez et al. 2013).

miR-122 está sorprendentemente implicado en el ciclo de vida de HCV dentro de hepatocitos infectados, sin afectar a su papel en el metabolismo lipídico del hospedador(Wilson and Sagan 2014). Siendo considerado el miRNA más importante asociado con HCV. Se le ha relacionado con el incremento de estabilidad, de replicación

y traducción viral, y con el tropismo hepático, aunque aún no se conoce con toda exactitud el mecanismo por el cual ejerce su función (Conrad and Niepmann 2013; Wilson and Huys 2013; Wilson and Sagan 2014).

El miR-122 tiene dos sitios diana en tandem en el flanco 5' del IRES de HCV, entre los dominios I y II (Jopling, Schutz et al. 2008). Estos sitios de unión se conocen como **S1** (5'-¹GCC³-²²ACACUCC²⁸-3') y **S2** (5'-²⁹UGGUA³³-³⁸CACUCC⁴³-3') e hibridan con el RNA de HCV a través de su secuencia *seed* y *no-seed*, siendo ambos esenciales para la función del miR-122 (Shimakami, Yamane et al. 2012). Estas secuencias dianas están conservadas entre los diferentes genotipos de HCV y en hepacivirus relacionados (2 dianas en GBV-B y 1 en hepacivirus animales NPHV, RHV, GHV) (Conrad and Niepmann 2013; Sagan, Sarnow et al. 2013; Wilson and Huys 2013; Wilson and Sagan 2014). Recientemente se ha propuesto de forma preliminar un nuevo sitio de unión para el miR-122 en el dominio IV del IRES, para el que no se ha atribuido todavía ninguna función (Pang, Pham et al. 2011). También se ha encontrado una diana para el miR-122 en la región codificante (secuencia para NS5B) que es la diana con mayor afinidad por el miR-122, pero parece ser inactivo (Nasheri, Singaravelu et al. 2011; Wilson and Huys 2013); y otras dos en el 3'-UTR (Niepmann 2009).

El miR-122 se presenta a sus sitios diana en la región 5' del RNA de HCV, unido a algunas de las proteínas que forman parte del complejo RISC: Ago2 (en menor medida Ago1), Dicer y TRBP. Estas proteínas interactúan previamente con el miR-122 dúplex y seleccionan la hebra madura para presentar a sus secuencias dianas, pudiendo tener un papel adicional colaborando con el miR-122 en su función (Shimakami, Yamane et al. 2011; Shimakami, Yamane et al. 2012; Zhang, Huys et al. 2012; Conrad, Giering et al. 2013). Por este motivo, el miR-122 administrado exógenamente para estudios funcionales varía sus efectos *in vitro*, miR-122 maduro de cadena sencilla (lisado de reticulocito) e *in vivo*, miR-122 dúplex (células HeLa y Huh-7) (Goergen and Niepmann 2012). Sigue siendo un importante tema de estudio en que fases del ciclo del virus interactúa el miR-122 (Wilson and Sagan 2014).

Mediante ensayos *in vitro* de calorimetría y de SHAPE se ha determinado que dos moléculas de miR-122 son capaces de interactuar simultáneamente en S1 y S2, existiendo mayor afinidad por S2 ($Kd_{S1}=120$ nM; $Kd_{S2}=2.3$ nM) (Mortimer and Doudna 2013). Sin embargo, está pendiente de demostrar *in vivo*, ya que el miR-122

interacciona unido a las proteínas del complejo RISC, que podrían eclipsar el segundo sitio de unión(Conrad and Niepmann 2013). Al igual que ocurre en el silenciamiento génico de mRNAs por varios miRNAs cuyas dianas están separadas una distancia de 8-40 nucleótidos, se ha visto que existe cooperatividad entre S1 y S2 (Wilson and Huys 2013). Sin embargo, existe controversia en los ensayos realizados para estudiar el tipo de cooperatividad que puede haber entre ellos. Por un lado, ambas moléculas de miR-122 competirían por parte de la secuencia diana, existiendo un fenómeno de cooperatividad negativo(Mortimer and Doudna 2013); mientras que la unión en S1 podría relajar la estructura del dominio I, favoreciendo la entrada de la segunda molécula de mir-122 en S2(Nasheri, Singaravelu et al. 2011). *In vivo*, en células HepB3 y Huh-7.5, presenta cooperatividad positiva para la función de replicación(Thibault, Huys et al. 2015). La interacción del miR-122 a S1 y S2 necesita de forma diferencial iones Mg^{2+} , que resulta ser esencial para la unión a S1 y no así para S2 (Mortimer and Doudna 2013).

La unión del miR-122 en S1 y S2 aumenta la estabilidad del genoma de HCV frente a: la degradación por 5' exonucleasas Xrn1 y Xrn2 del citoplasma celular(Li, Masaki et al. 2012); y al reconocimiento de proteínas antivirales de la respuesta inmune innata (cita). El papel estabilizador es mayoritariamente por unión a S1, debido a que el extremo 3' del miR-122 sobresale respecto del extremo 5' del RNA de HCV, ocultándolo del reconocimiento de las exonucleasas celulares y sistema inmune. Tanto S1 como S2 podrían estar también implicados en desplegar la estructura del RNA de HCV y desplazar o reclutar proteínas de unión a RNA(Wilson and Sagan 2014). La estabilización del genoma de HCV es independiente de los procesos de replicación y traducción viral(Shimakami, Yamane et al. 2011). En hepatocitos infectados participan menos moléculas de Ago en la represión de mensajeros regulados por miR-122, de manera que el miR-122 estaría siendo secuestrado por HCV, funcionando como una esponja de moléculas de miR-122. Los niveles de miR-122 caen a la mitad y esa des-represión global de dianas del miR-122 del hospedador, proporciona unas condiciones propicias para la propiedad oncogénica de HCV a largo plazo(Luna, Scheel et al. 2015).

El RNA de HCV es capaz de llevar a cabo su replicación independientemente de miR-122, en células HEK-293, Hep3B y Huh-7.5(Bradrick, Nagyal et al. 2013) (Wilson and

Huys 2013; Thibault, Huys et al. 2015). Sin embargo, la interacción del miR-122 incrementa los niveles de replicación(Jopling, Yi et al. 2005; Wilson and Sagan 2014).

El papel del miR-122 en traducción está sometido a debate. Varios grupos han determinado que el miR-122 estimula la traducción de HCV, donde las dianas S1 y S2 contribuyen por igual (Jangra, Yi et al. 2010) y los requisitos mínimos son la presencia de IRES y de extremo 3' del miR-122 y la ausencia de un extremo 5'cap(Roberts, Lewis et al. 2011). Mediante ensayos de unión con la subunidad ribosomal 40S, miR-122 forma parte y participa en la formación del complejo 48S en lisado de reticulocito, células HeLa y Huh-7(Henke, Goergen et al. 2008); el enmascaramiento de S1 y S2 en un tallo-lazo artificial evita la unión de Ago y dificulta el incremento de traducción por el miR-122, apoyando su papel estimulante en traducción(Conrad, Giering et al. 2013). No obstante, otros estudios funcionales no han encontrado un papel estimulador de traducción por parte del mir-122, indicativo de que posiblemente sea debido al uso de unos sistemas celulares no apropiados(Jopling, Yi et al. 2005)(Jopling, Schutz et al. 2008). Recientemente se ha descrito que el aumento de traducción si ocurre, pero es un efecto secundario de las funciones de protección y estabilización del RNA de HCV por el miR-122 (Li, Masaki et al. 2013; Wilson and Huys 2013; Thibault, Huys et al. 2015) o como consecuencia del aumento en replicación. La replicación y la traducción están acopladas y el miR-122 regularía el balance de los genomas de HCV comprometidos con replicación respecto de traducción. Siendo necesario primero el aumento de replicación por el miR-122 para que se incremente la traducción, y una traducción activa para que se incremente replicación(Masaki, Arend et al. 2015). El efecto del miR-122 en traducción varía según la fase del ciclo celular, siendo mayor en G₁ y G₀, donde los niveles de miR-122 alcanzan los valores más altos y son las fases en las que generalmente están los hepatocitos y es mantenida por la proteína core del propio virus (Fehr, Conrad et al. 2012).

La relación del miR-122 con el ciclo infectivo del virus hace que sea considerada una diana para el tratamiento de la enfermedad. Se ha diseñado un fármaco anti-miR-122 (SPC3649), llamado "Miravirsen". Consiste en una molécula de RNA antisentido (LNA) que está dirigido a secuestrar los precursores del miR-122(Gebert, Rebhan et al. 2013). Tiene reducida toxicidad, alta estabilidad y no produce resistencias. Sin embargo, este tipo de tratamiento debe ser usado con cautela ya que el secuestro de miR-122 puede

conducir a la disminución de la expresión de los genes implicados en la producción del colesterol, esteatosis por la desregulación del metabolismo lipídico y hepatocarcinoma(Wilson and Sagan 2014).

– *let-7b*

Let-7 (*lethal-7*) fue el primer microRNA identificado en humanos. La misma secuencia let-7 se expresa en múltiples localizaciones genómicas en tándem, y su secuencia y funciones están altamente conservadas entre especies. Los diferentes miembros de la familia let-7b corresponden a diferentes isoformas del mismo miRNA, designadas con una letra minúscula. En humanos aparecen 10 miembros dentro de esta familia, que se producen tras la maduración de 13 precursores diferentes (let-7a madura a partir de 3 precursores let-7a-1, let-7a-2 y let 7a-3; let-7f a partir de 2 precursores let7f-1 y let-7f-2; el resto de isoformas a partir de un único precursor). La expresión génica de let-7 está regulada a nivel post-transcripcional.

Let-7 en vertebrados está implicado en la diferenciación celular. En *C. elegans* también está asociado a procesos de desarrollo, aunque en organismos superiores sus niveles de expresión aumentan en la embriogénesis, no se ha visto efecto directo en desarrollo(Roush and Slack 2008).

De todos los miembros de esta la familia, let-7b está directamente relacionado con HCV. El papel celular de let-7b está asociado a la supresión tumoral y la expresión deficiente de let-7b conduce a la desdiferenciación celular, desarrollando un proceso canceroso.

Mediante predicción *in silico* y ensayos celulares en Huh-7 han sido determinadas dos dianas para la unión de let-7b en el RNA de HCV. Una diana está en el dominio IV del 5'-UTR (5'⁻³³⁸C-A³⁶⁵-3'), interaccionando mediante la secuencias *seed* y la *no-seed*, compartiendo parte de la secuencia diana con el miR-122; y otras dos dianas en la secuencia que codifica NS5B (5'⁻⁸⁷⁴⁵G-A⁸⁷⁶⁶-3') (5'⁻⁸⁹⁷⁷A-A⁸⁹⁹⁵-3'). Estas dianas están conservadas entre varios de los genotipos de HCV (1b y 2a). Let-7b es presentado a sus dianas unido a Ago2. La interacción de let-7b conduce a la represión de la replicación viral, siendo indiferente para el proceso de traducción. Indirectamente, let-7b también puede regular hasta 79 genes asociados con la infección de HCV. De manera que

durante la infección, let-7b presenta bajos niveles de expresión(Cheng, Yeh et al. 2012).

– *miR-199a**

La familia miR-199 está formada por dos miembros: mir-199a y miR-199b. miR-199a* es el miRNA maduro y posee un papel anti-tumoral en humanos y también se le ha relacionado con la progresión de la fibrosis hepática y como agente antiviral, reprimiendo la replicación del virus(Hoffmann, Duverlie et al. 2012).

miR-199a* presenta una secuencia diana en la región 5'-UTR de HCV (genotipos 1b y 2a), concretamente en dominio II del IRES, interaccionando a través de la secuencia *seed* y *no-seed*. La unión de miR-199a* parece estar relacionada con la alteración de la estructura secundaria del dominio II, esencial para replicación y traducción del virus, aunque aún no hay datos experimentales. Además, se le relaciona con el tropismo celular de HCV debido a que los niveles de este miRNA son inferiores en hepatocitos que en células de cualquier otro tejido(Murakami, Aly et al. 2009; Conrad and Niepmann 2013).

RNAsas específicas de estructuras tipo-tRNA

Mimetismo molecular

El mimetismo en biología es considerado una semejanza entre organismos o características de diversas clases. Ese parecido debe llevar alguna funcionalidad, que se mantenga de forma repetitiva en la escala temporal a nivel evolutivo u ontogénico.

La mimesis ocurre cuando una señal o característica de un individuo (el mimo o imitador), simula las propiedades de la señal de un segundo individuo (el modelo), de manera que ese parecido entre las señales tiene que ser recurrente y engañoso para un tercer participante (el operador), aportando alguna ventaja para el mimo (Maran; Vane-Wright 1976).

El mimetismo molecular ha sido observado principalmente en la semejanza de muchas proteínas con los ácidos nucleicos, en cuanto a la forma y a la función. También aparece en el reconocimiento de la superficie celular por virus o parásitos, la unión de agonistas y antagonistas a receptores, y las reacciones cruzadas en las respuestas inmunes (Nissen, Kjeldgaard et al. 2000).

Es de destacar el mimetismo del tRNA, uno de los mejores ejemplos descritos a nivel del RNA. Las estructuras de RNA semejantes al tRNA han sido denominadas estructuras tipo-tRNA y han sido identificadas gracias a enzimas implicadas en el metabolismo del tRNA (Mans, Pleij et al. 1991; Giege, Frugier et al. 1998), como son las aminoacil-tRNA sintetasas, las RNasas P (Nadal, Martell et al. 2002; Lyons and Robertson 2003) y posiblemente la RNasa Z (aún no descrito).

Biosíntesis de los tRNAs

Los tRNAs se sintetizan principalmente mediante la RNA polimerasa III, en el núcleo celular como pre-tRNA, quedando una serie de nucleótidos adicionales en sus extremos 5' y 3' que deben ser eliminados para dar lugar al tRNA maduro.

El pre-tRNA naciente debe terminar de transcribirse y ser liberado de la RNA polimerasa para que comience su procesamiento (Maraia and Lamichhane 2011).

Generalmente, el pre-tRNA es procesado en primer lugar, en su extremo 5' por la RNasa P, mediante un corte endonucleolítico. A continuación, se lleva a cabo el procesamiento del extremo 3', en un único paso mediante corte endonucleolítico con la RNasa Z; o en ciertos casos, mediante 3'-exonucleasas, dependiendo de la disponibilidad, el acceso de ciertos factores auxiliares y otras condiciones particulares (Maraia and Lamichhane 2011). En la mayoría de arqueas, muchas bacterias y en todos los eucariotas, los genes de los tRNAs no codifican la secuencia CCA en el extremo 3', donde posteriormente se incorporará el aminoácido. Esta secuencia es añadida por la enzima tRNA nucleotidil transferasa (Weiner 2004).

El orden de procesamiento de los extremos 5' y 3' viene regido por la proteína "La", necesaria a su vez para estabilizar el pre-tRNA naciente. El extremo 3' del pre-tRNA naciente es secuestrado por la proteína La que lo incluye en un bolsillo interno,

bloqueando la degradación por 3' exonucleasas y por tanto, favoreciendo que ocurra en primer lugar el procesamiento en el extremo 5' y posteriormente en extremo 3'. La desfosforilación o ausencia de la proteína *La* favorecería el procesamiento del extremo 3' por exonucleasas antes que el 5' (Maraia and Lamichhane 2011).

Se han determinado eucariotas inferiores que no poseen genes de la RNasa P, de manera que la RNA polimerasa presenta como sitio de inicio de traducción el primer nucleótido del tRNA maduro (Waters, Hohn et al. 2003).

La RNasa P y la proteína *La* se han localizado con la maquinaria de la pol III y en los genes de tRNAs (consistente con su función en las fases tempranas de procesamiento del tRNA).

Los siguientes pasos en la biosíntesis de los tRNAs varían según el organismo. En eucariotas puede ocurrir: splicing de los tRNAs que presenten intrones, modificaciones nucleotídicas específicas de ciertos tRNAs y la aminoacilación (Maraia and Lamichhane 2011).

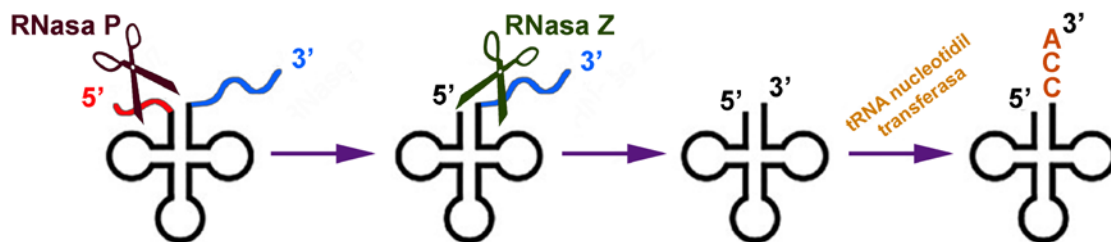


Figura 7: Procesamiento y maduración de los tRNA mediante las endonucleasas RNasa P y RNasa Z. Se muestra la posterior incorporación de la secuencia CCA por la nucleotidil transferasa esencial para la aminoacilación de los tRNAs.

RNasa P

La RNasa P es una ribonucleoproteína esencial en la inmensa mayoría de organismos, cuya función principal es la de catalizar la maduración del extremo 5' en los precursores del tRNA (pre-tRNA) mediante corte endonucleolítico. A diferencia de la RNasa Z, no existe otra enzima capaz de llevar a cabo esta reacción. Es considerada una de las actividades ribozimas más antiguas (Maizels and Weiner 1994). La actividad de la RNasa P fue identificada por primera vez en *E. coli* en el año 1972 al intentar elucidar la biosíntesis de los precursores del tRNA (Robertson, Altman et al. 1972). Esta enzima está muy conservada en todos los organismos, estando presente en los

tres reinos de la vida: arqueas, procariotas y eucariotas (Walker and Engelke 2006), y en esta última, en los diferentes compartimentos celulares: núcleo celular, mitocondria (Rossmann and Karwan 1998) y cloroplastos (Jarrous, Wolenski et al. 1999; Thomas, Li et al. 2000). En humanos (células HeLa), la subunidad de RNA (H1) se acumula principalmente en el citoplasma y tras un ensamblaje dinámico con las diferentes subunidades proteicas procedentes de los diferentes compartimentos celulares, es transportado al núcleo celular (Jarrous 2002).

Generalmente la RNasa P está formada por una subunidad de RNA (RPR) y un número variable de subunidades proteicas, dependiendo del organismo al que pertenezca: desde una subunidad en procariotas, cuatro o cinco en arqueas, a nueve o diez en eucariotas (Hall and Brown 2002; Jarrous 2002; Evans, Marquez et al. 2006). Recientemente se han identificado casos de RNasa P formada únicamente por proteínas en cloroplastos y mitocondrias de plantas terrestres y humanas (Holzmann, Frank et al. 2008; Gobert, Gutmann et al. 2010).

La actividad catalítica de la RNasa P reside en la subunidad de RNA, realizando su función en ausencia de subunidades proteicas. Por tanto, estaría incluida dentro de la categoría de ribozimas. No obstante, tanto el RNA como las proteínas son imprescindibles para que la enzima lleve a cabo su función *in vivo*.

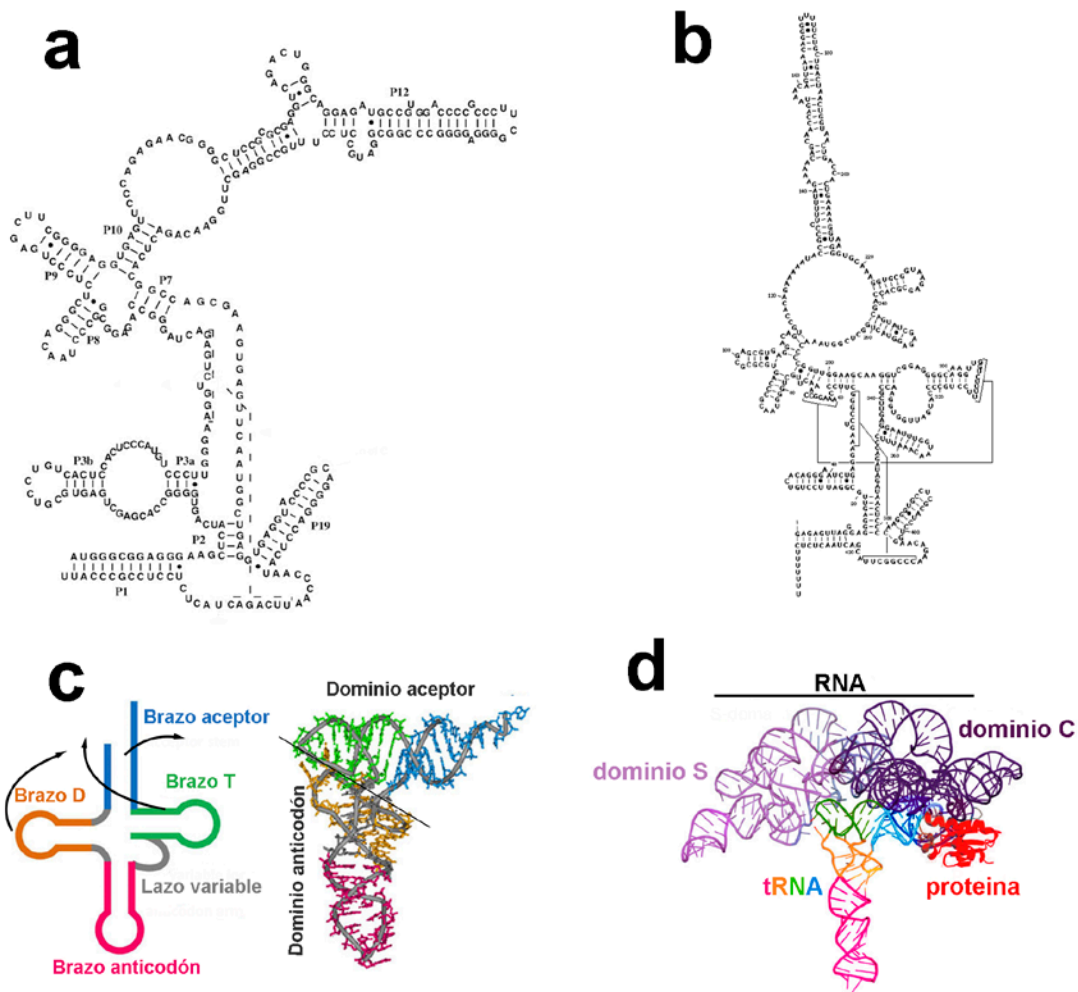


Figura 8: (a) (b) Ejemplos de estructura secundaria de la subunidad RNA de la RNasa P de *Synechocystis sp* y humana (H1), respectivamente. (c) Diagrama de la estructura secundaria en forma de trébol (izquierda) y de su plegamiento de forma tridimensional en forma de L (derecha) propios de los tRNAs. (d) Estructura cristalina de la interacción de una RNasa P bacteriana con el tRNA, mostrando los diferentes dominios de la subunidad RNA unidos con la subunidad proteica.

Subunidad RNA (RPR):

El tamaño de la subunidad de RNA varía entre organismos, en bacterias posee un tamaño de 350-400 nucleótidos de longitud, siendo de menor tamaño y más simple en el caso de eucariotas, gracias a la participación de mayor número de subunidades proteicas que sustituyen a esos elementos estructurales de RNA dan estabilidad a la molécula (Kazantsev and Pace 2006).

En bacterias, existen dos subtipos de estructura secundaria para la RPR: el tipo A (ancestral), representado por la RPR de *E. coli*, conocida como M1; y el tipo B, siendo su

prototipo *B. subtilis* (Pace and Brown 1995; Haas, Banta et al. 1996; Haas and Brown 1998).

Las RPRS están muy conservadas y presentan dos dominios estructurales: el dominio catalítico y el dominio de la especificidad. Se pliegan de forma independiente uno del otro, y se combinan formando un complejo bimolecular catalíticamente activo (Pan, Loria et al. 1995; Loria and Pan 1996; Masquida and Westhof 2011). El dominio de especificidad interacciona con el brazo T del pre-tRNA, crucial para el posicionamiento y la afinidad de sustrato; En el dominio catalítico están incluidos todos los elementos estructurales que forman el sitio activo y la zona de unión de la subunidad proteica. Ambos son esenciales para un corte eficiente en el sitio correcto (Lai, Vioque et al. 2010; Wu, Kikovska et al. 2012).

Al igual que otras ribozimas, la RPR pertenece a la familia de las metaloenzimas y requiere la presencia en su sitio activo de iones metálicos divalentes, preferentemente de magnesio, y una elevada fuerza iónica para ser catalíticamente activa *in vitro* (Gardiner, Marsh et al. 1985; Brannvall and Kirsebom 2001). Los cationes metálicos apantallan las fuerzas electrostáticas de repulsión establecidas entre moléculas de RNA y van a favorecer un adecuado plegamiento del RNA en ausencia de proteínas (Tinoco and Bustamante 1999). En bacterias es capaz de catalizar la maduración del tRNA en el sitio correcto *in vitro*, en ausencia de su cofactor proteico, estando presente iones mono- y divalentes en altas concentraciones (Guerrier-Takada, Gardiner et al. 1983).

EL reconocimiento de sustrato por la RNasa P no es dependiente de secuencia, en su lugar, reconoce la estructura terciaria en forma de "L" de los tRNAs, que presentan de forma prematura los pre-tRNAs (Swerdlow and Guthrie 1984; Lee and Knapp 1985). El pre-tRNA debe estar bien plegado, presentando una estructura tipo-tRNA, para que pueda ser reconocido por la RNasa P y lo procese (mutaciones que alteren esa estructura tipo-tRNA impiden el reconocimiento y procesamiento por la P) (Maraia and Lamichhane 2011).

En procariotas, la RPR necesita para cortar eficazmente una horquilla de RNA donde el tallo acceptor y el brazo T del tRNA estén apilados coaxialmente, con o sin subunidad proteica. La reducción de esta estructura disminuye la eficacia de corte. Generalmente, la secuencia NCCA del extremo 3' del pre-tRNA interacciona mediante apareamientos

Watson-Crick con el motivo desapareado GGU de la hélice P15 del dominio catalítico (Svard, Kagardt et al. 1996) y el dominio de especificidad reconoce los bucles de los brazos D y T Ψ C. Esto produce la desnaturalización parcial del tallo aceptor del pre-tRNA, dejando más accesible el sitio de corte. Además, en muchas bacterias, los nucleótidos -1 y -2 respecto del sitio de corte, influyen en la eficacia y precisión del procesamiento. Sin embargo, esta interacción es irrelevante en organismos cuyos pre-tRNAs no presentan la secuencia CCA en su extremo 3' (por ejemplo: la cianobacteria *Synechocystis sp*, humanos, utilizados en esta tesis) donde otras interacciones de la hélice P15 son necesarias para el correcto posicionamiento del punto de corte (Mondragon 2013). En eucariotas, la RNasa P localiza el punto de corte en el sustrato, "midiendo" la longitud de la hélice coaxial formada por el apilamiento del tallo aceptor y el brazo T (Yuan and Altman 1995). Tras el corte, se genera un extremo 5' P en el tRNA maduro y un extremo 3'-OH en la secuencia 5'-*leader* (Mondragon 2013).

Subunidades proteicas (RPPs):

En bacterias únicamente hay una subunidad proteica que es codificada por el gen *rnpA*, de aproximadamente 14 KDa y unos 120 aminoácidos (10% de la masa total de la holoenzima). La RPP bacteriana es esencial para la función de la RNasa P *in vivo*. Entre sus funciones destaca: facilitar la interacción con el fragmento 5' leader del pre-tRNA, incrementando la afinidad por el sustrato y acelerando la liberación del tRNA maduro; mejorar la eficacia del corte por la ribozima; disminuyendo la fuerza iónica del medio, permite la actividad de la RPR en condiciones fisiológicas; aportar estabilidad al plegamiento de la ribozima; permitir la interacción a sustratos (Niranjanakumari, Stams et al. 1998; Buck, Kazantsev et al. 2005); y compensar las diferencias estructurales de los tRNAs para que el proceso de catálisis sea uniforme en todos los casos. (Hartmann, Gossringer et al. 2009).

En arqueas y en eucariotas aún queda más por conocer a cerca de las subunidades proteicas. Sin embargo, desde el punto de vista evolutivo, las RNasas P han ido incrementando su contenido proteico de 10% (bacterias) a 70% (eucariotas). Esto ha supuesto incrementar el rango de sustratos diferentes al pre-tRNA reconocidos por la RNasa P para ser procesados, además de permitir la aparición de nuevas funciones adicionales a la biosíntesis de los tRNAs (Jarrous and Gopalan 2010). En arqueas, la

subunidad RNA es más similar a bacterias y la parte proteica a eucariotas(Hall and Brown 2002).

Recientemente se ha determinado una nueva categoría de RNAsas P que carecen de subunidad RNA (llamada PRORP), implicada igualmente en la maduración de los pre-tRNAs(Rossmann 2011), pero realizando su catálisis por un mecanismo diferente(Pavlova, Gossringer et al. 2012).

La RNasa P presenta otras funciones adicionales a la de procesar los extremos 5' de los pre-tRNAs: actuar como factor de transcripción de la RNA polimerasa III y procesamiento de otros RNAs no codificantes (Jarrous and Reiner 2007); Evolutivamente parece haber estado sujeta a duplicación, selección y divergencia génica para generar dos nuevas ribonucleoproteínas: MRP y MRP-TERT, relacionadas con el procesamiento de los rRNAs (Chu, Archer et al. 1994) y en la regulación del ciclo celular(Jarrous and Gopalan 2010). La RNasa P ha sido utilizada en biología molecular para la detección de estructuras tipo-tRNA (Nadal, Martell et al. 2002; Lyons and Robertson 2003; Sabariego, Nadal et al. 2004) y posee potencial terapéutico empleándose con secuencias guías externas para inactivar mRNAs mediante digestión dirigida (Werner, Rosa et al. 1998; Nadal, Martell et al. 2002; Lyons and Robertson 2003; Lundblad and Altman 2010).

RNasa Z

La RNasa Z es una endorribonucleasa proteica implicada en el procesamiento del extremo 3' de los pre-tRNA esencial para la viabilidad celular. Ha sido caracterizada en arqueas, bacterias y eucariotas, estando presente incluso en mitocondrias y cloroplastos. Es conocida por diversos nombres: tRNasa Z, 3'-tRNasa, pre-tRNasa, Trz, ElaC, ZiPD y RNasa BN. El primer gen de la RNasa Z fue clonado en 2002 en *Xenopus laevis* (Castano, Tobian et al. 1985), de aproximadamente 97 KDa. Es capaz de incorporar dos iones Zn^{2+} en su centro catalítico o dos iones Fe, pero sólo presenta actividad fosfodiesterasa en presencia de Zn^{2+} . De manera que está clasificada dentro de la familia de las metalo- β -lactamasas de las metalohidrolasas dependientes de Zn^{2+} (Vogel, Schilling et al. 2002).

La RNasa Z puede presentarse en dos formas: forma corta Z^S (ElaC1) y larga Z^L (ElaC2). La secuencia de la RNasa Z está altamente conservada entre los diferentes reinos.

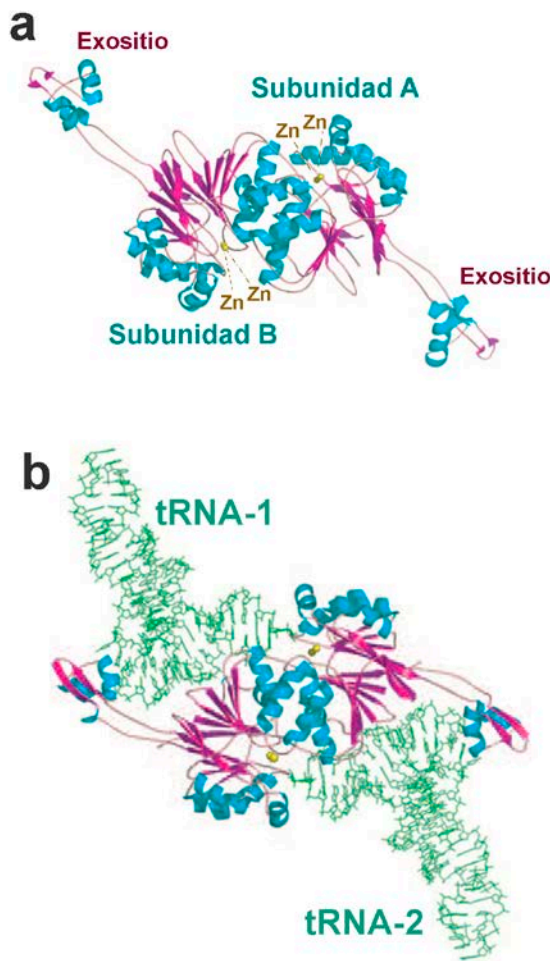


Figura 9: (a) Estructura cristalina dimérica de la RNasa Z de *E. coli*. En color azul se muestran las hélices α y en rosa las láminas β . (b) Modelo del complejo formado por la unión de la RNasa Z de *E. coli* con dos moléculas de tRNA (Redko, Li de la Sierra-Gallay et al. 2007).

La estructura cristalina de la RNasa Z ha sido estudiada en unos pocos organismos: *E. coli* (Kosteleccky, Pohl et al. 2006), *B. subtilis* (Li de la Sierra-Gallay, Pellegrini et al. 2005) y *T. maritima* (Ishii, Minagawa et al. 2005). La RNasa Z de *B. subtilis* es homodimérica y ambos monómeros (A y B) se presentan de forma asimétrica, similar a las metalo- β -lactamasas dependientes de Zn. El dominio central de cada monómero consiste en dos motivos de 7 láminas β cubiertas a modo de sándwich por hélices alfa a cada lado ($\beta\beta\beta\beta\alpha\beta\alpha\beta$). Su estructura se caracteriza por tener un brazo largo y flexible denominado

exosito, que la diferencia del resto de metalo- β -lactamasas y sin ninguna similitud a proteínas de estructura conocida. Las dos subunidades no son

equivalentes, en la subunidad B está el exosito, esencial para el reconocimiento del tRNA y en la subunidad A reside el centro catalítico de la enzima, formado por una hélice α adicional, dos átomos de Zn^{2+} y un ión fosfato (Li de la Sierra-Gallay, Pellegrini et al. 2005). La unión entre los dos monómeros forma la hendidura del sitio activo que acomoda al RNA monocatenario del pre-tRNA. En el caso de *E. coli*, cada monómero presenta un exosito y un sitio catalítico que incorpora 2 iones Zn cada uno; en *T. maritima* está ausente el exosito, pero presenta dos centros activos que incorporan 1 único ión Zn cada uno (Redko, Li de la Sierra-Gallay et al. 2007).

El reconocimiento de sustrato por parte de la RNasa Z se lleva a cabo mediante un dominio flexible, que contacta con el brazo T y el tallo aceptor del pre-tRNA. Estos dos dominios del pre-tRNA son los esenciales para el corte de la RNasa Z *in vitro*. Z^L presenta un espectro más amplio de sustratos que Z^S y además no necesitaría todo el pre-tRNA para reconocer el sustrato. Un número concreto de pares de bases del tallo aceptor, 7 pares de bases, es imprescindible para el buen procesamiento de la enzima. Delecciones o adiciones de más de un nucleótido reducen mucho la eficacia de corte y además desplazan el sitio de corte en el brazo aceptor (Schiffer, Rosch et al. 2003). Sin embargo, ciertas RNasas Z pueden requerir alguna región adicional del pre-tRNA, estando aún por esclarecer el sustrato mínimo de la enzima (Vogel, Schilling et al. 2005).

Generalmente, la RNasa Z procesa aquellos tRNAs que carecen de la secuencia CCA en su extremo 3' tras el nucleótido discriminador en eucariotas (Schiffer, Rosch et al. 2003) y procariotas (Pellegrini, Nezzar et al. 2003), funcionando como mecanismo para evitar el procesamiento de los tRNAs maduros. Además, la presencia de un residuo de arginina, dirigido hacia el sitio catalítico, interacciona con los residuos de citosina del CCA inhibiendo a la RNasa Z. La unión a la primera citosina inhibe la actividad del enzima y a la segunda citosina interfiere en la estabilidad del tRNA maduro. Ambos factores inhibidores son necesarios para impedir la entrada del pre-tRNA al sitio activo e inhibir al enzima (Dutta, Malhotra et al. 2013). Sin embargo, el comportamiento ante la presencia de CCA varía entre las RNasas Z de cada organismo (Minagawa, Takaku et al. 2004; Redko, Li de la Sierra-Gallay et al. 2007).

Tras el reconocimiento de la enzima sobre sus sustrato, se produce un corte del enlace fosfodiéster entre los nucleótidos 73- y 74 del pre-tRNA, dejando un extremo 3'-OH en el tRNA procesado y un extremo 5'-P en el otro fragmento generado tras el corte (Li de la Sierra-Gallay, Pellegrini et al. 2005). Z^L procesa un único pre-tRNA a la vez, mientras que Z^S hasta dos (Vogel, Schilling et al. 2005). Aunque el corte se produce después del nucleótido discriminador, existe heterogeneidad en la selección del sitio de corte *in vitro*. Además, el sitio de corte puede ser desplazado de manera dependiente de secuencia (Minagawa, Takaku et al. 2004).

Si bien la principal función de la RNasa Z es la del procesamiento de los pre-tRNAs en su extremo 3', principalmente en ausencia de la secuencia CCA, otras funciones

fisiológicas adicionales son posibles. Sin embargo, el estudio de la actividad de esta enzima en los diferentes organismos *in vivo*, indica que otras funciones son posibles. La RNasa Z de *E. coli* intervendría en el metabolismo de otros RNAs (rRNA y mRNA) (Peng, Robinson et al. 2003; Perwez and Kushner 2006). También presenta actividad de corte sobre sustratos cromogénicos (sustratos modelo para la actividad fosfodiesterasa). La RNasa Z de ratón y cerdo adicionalmente procesa aquellos RNAs acomplexados con tRNAs truncados, conocido como actividad RNasa 65 (Takaku, Minagawa et al. 2004; Vogel, Schilling et al. 2005). La RNasa Z conocida como BN presenta además actividad exonucleasa, para eliminar los nucleótidos aguas abajo del CCA (Dutta, Malhotra et al. 2013). De forma directa o indirecta, la RNasa Z está implicada en la regulación del ciclo celular: en *C. elegans* estimula la división celular y en humanos se asocia al cáncer de próstata (Tavtigian, Simard et al. 2001; Vogel, Schilling et al. 2005).

Virus de la Peste porcina clásica (CSFV)

Generalidades

El virus de la peste porcina clásica pertenece al género *Pestivirus*, dentro de la familia *Flaviviridae*. Es el agente causante de una enfermedad altamente contagiosa a nivel mundial en cerdos y jabalíes conocida como peste porcina clásica. El principal problema de esta enfermedad es la gran pérdida económica que ocasiona en la industria ganadera del cerdo. Su medio de transmisión es mediante contacto directo entre cerdos vivos a través de secreciones corporales, abrasiones de la piel, aerosoles, material contaminado y por la ingesta de carne contaminada (Paton, McGoldrick et al. 2000). Una vez en el animal, el virus se reproduce en las amígdalas (infección oral o nasal) o en ganglios linfáticos regionales (infección vaginal o piel) y seguidamente pasa a la sangre y se disemina a diversos órganos: bazo, ganglios, riñón, pulmón y médula ósea (Newcomer and Givens 2013). Se han identificado 3 genotipos y 10 subgenotipos del virus con diferentes grados de virulencia, desde cepas asintomáticas a cepas altamente virulentas cuya tasa de mortalidad está próxima al 100% de los casos (Paton, McGoldrick et al. 2000). La enfermedad suele manifestarse de forma aguda con

depresión, anorexia, conjuntivitis exudativa severa, decoloración púrpura de orejas, abdomen y cara interna de extremidades, y fiebre hemorrágica severa hiperaguda, acompañada de afecciones respiratorias, gastrointestinales y neurológicas, que conducen a una tasa alta de mortalidad tras 5 a 15 días. Existe también una posible infección congénita persistente, que conduce a malformaciones, aborto o muerte antes de año de edad. La severidad de la enfermedad está condicionada por la edad, la condición física del hospedador, y sobre todo por la virulencia de la cepa del virus (Leifer, Ruggli et al. 2013; Newcomer and Givens 2013).

Se han desarrollado vacunas eficaces dirigidas hacia las glicoproteínas de la envuelta E^{rns} y E2, que evitan el contagio de CSFV ante brotes de la enfermedad en países endémicos. Sin embargo, la dificultad para distinguir entre animales inmunizados e infectados hace necesaria la búsqueda de vacunas mejoradas. Hasta el momento, sólo se ha determinado un fármaco que reduce los niveles de CSFV, dirigido contra la RNA polimerasa dependiente de RNA del virus, pero aún está en estudio (Moennig 2000).

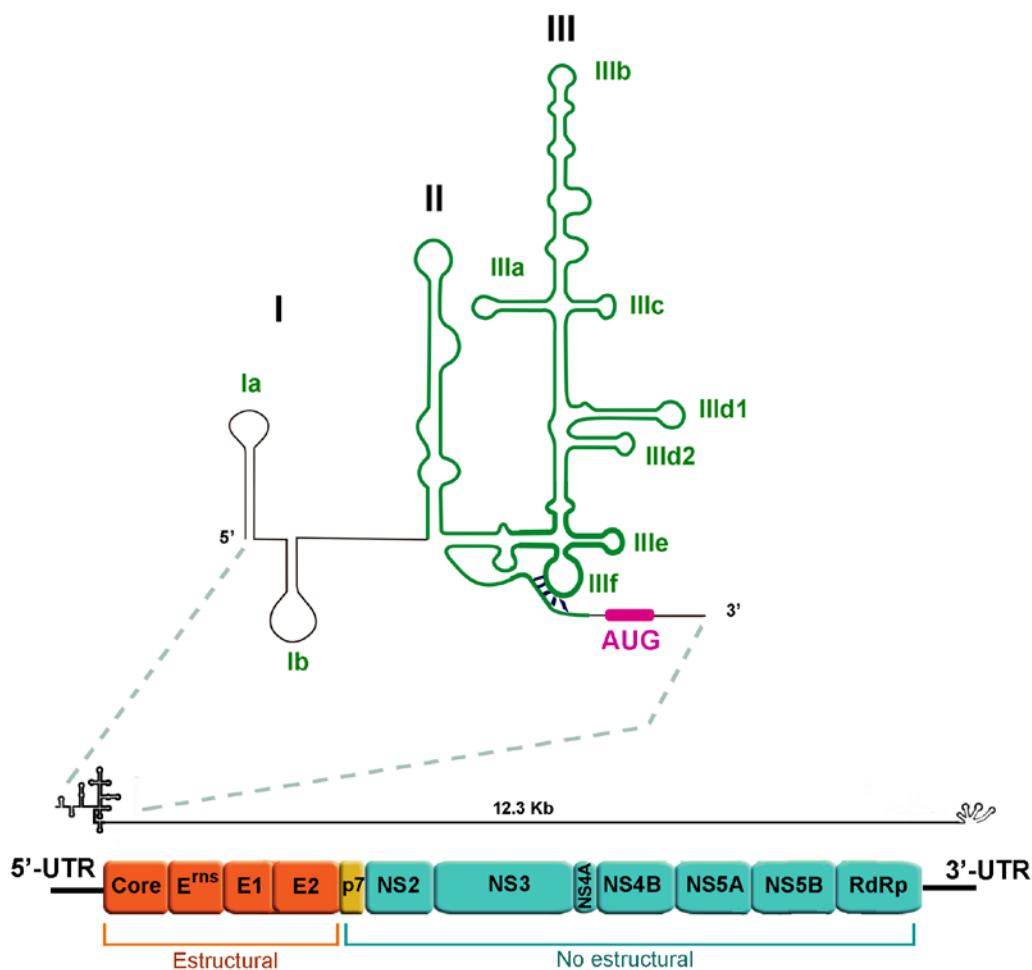


Figura 10: Representación esquemática del genoma de RNA del CSFV. Las diferentes proteínas que codifica el RNA de HCV se muestran en naranja (Proteínas estructurales) y en azul (proteínas no estructurales). El ORF está flanqueado por las dos zonas no traducibles (5'-UTR y 3'-UTR). La ampliación muestra la región 5'-UTR. En el verde se resalta el elemento IRES (dominios II y III) que incluye el motivo tipo-tRNA con trazo verde más grueso (dominios IIIef).

Genoma

El virus de la peste porcina clásica es un virus cubierto por una envuelta proteica que incluye una molécula de RNA de cadena sencilla y de polaridad positiva de aproximadamente 12.3 kb de longitud. Su genoma posee un único ORF que codifica para una única poliproteína de 3898 aminoácidos que tras su procesamiento por proteasas virales y del hospedador da lugar a 12 proteínas: estructurales (N^{pro} , C, E^{ms} , E1 y E2) esenciales para la envuelta y la cápsida del virus; y proteínas no estructurales (p7, NS2, NS3, NS4A, NS4B, NS5A y NS5B) para la replicación viral. El ORF está flanqueado por dos regiones no traducibles en sus extremos 5' y 3', que al igual que en HCV, son esenciales para la replicación y la traducción (Deng and Brock 1993) (Wu, Liu et al. 2015).

Figura 10: (Friis 2012)

La región 5' UTR tiene 374 nucleótidos y su secuencia presenta un alto grado de conservación con los otros miembros del género *Pestivirus* (BVDV y BDV) (Deng and Brock 1993) (Hsu, Chen et al. 2014). Está formado por tres dominios estructurales tallo-lazo denominados I, II y III. Los dominios II y III forman el elemento IRES (nucleótidos 65-427), esencial para que CSFV pueda llevar a cabo la traducción independiente de un 5'cap. El IRES de CSFV pertenece a los IRES del grupo II, de manera que comparte muchas características estructurales y funcionales con HCV (Brown, Zhang et al. 1992) (Deng and Brock 1993) (Kieft 2008).

En relación a la similitud que presenta con HCV (Le, Liu et al. 1998), las características estructurales del IRES, las regiones que interaccionan con el 40S y el inicio de traducción mediado por éste son prácticamente los mismos (Kolupaeva, Pestova et al. 2000). Cabe destacar la presencia de un pseudonudo entre el dominio III y la secuencia aguas abajo del codón de inicio de traducción, esencial para el posicionamiento del AUG en el sitio P del ribosoma y un funcionamiento apropiado del IRES (Rijnbrand, van der Straaten et al. 1997). Al igual que el resto de pestivirus y hepacivirus, el

dominio II del IRES es capaz de sufrir el doblamiento en forma de L que es imprescindible para un correcto inicio de la traducción (Boerneke and Hermann 2015), y para la hidrólisis del GTP y liberación del eIF2 necesarios para la formación del 80S (Lukavsky, Kim et al. 2003; Locker, Easton et al. 2007). También es capaz de reclutar directamente la subunidad ribosomal 40S para formar el complejo binario, sin la necesidad de ningún factor del inicio de traducción (Kolupaeva, Pestova et al. 2000; Hsu, Chen et al. 2014).

Sin embargo, existen una serie de características estructurales que lo diferencian de HCV: El dominio II de HCV es ligeramente más largo que en pestivirus; a nivel del pseudonudo, existen ligeras diferencias de longitudes entre los tallos-lazos, aunque sin perder su implicación en la actividad del IRES; El dominio III presenta un subdominio IIIId₂ que está carente en HCV; y PPCV carece del dominio IV donde reside el codón de inicio en HCV, de manera que el AUG se encuentra en un segmento monocatenario (Fletcher and Jackson 2002; Friis, Rasmussen et al. 2012).

La región 3'UTR de 230 nucleótidos de longitud, presenta tres dominios tallo-lazo altamente estructurados: SLI, SLII y SLIII directamente relacionados con el 5' UTR en regulación de la traducción del virus, que a diferencia de HCV, SLI presenta un papel inhibidor de la traducción (Hsu, Chen et al. 2014).

Radiación Ultravioleta

Generalidades

La luz ultravioleta (UV) forma parte de la energía electromagnética irradiada por el sol y constituye la porción más energética del espectro electromagnético que incide en la superficie de la Tierra. Está comprendida en el espectro de luz entre longitudes de onda de 400-100 nm, dividida en tres bandas: UV-A (400-320 nm), UV-B (320-280 nm) y UV-C (280-100 nm). Generalmente es considerada un tipo de radiación no ionizante, pero las radiaciones UV más energéticas del UV-C, conocido como UV lejano o de vacío (200-100 nm) si producen ionización.

En un “mundo RNA” prebiótico, gobernado por moléculas de RNA con funciones catalíticas, la cantidad de radiación UV que incidía sobre la Tierra era muchísimo mayor que la actual (100 veces mayor) debido a la carencia de protección atmosférica y un Sol más radiante. Estas condiciones ambientales desfavorables para la mayoría de moléculas orgánicas podrían haber servido para seleccionar a los ácidos nucleicos como estructuras prebióticas primordiales debido al poder amortiguador de las bases nitrogenadas en el esqueleto de azúcar-fosfato, además de la participación del UV en las reacciones de condensación para formar oligonucleótidos (Mulkidjanian, Cherepanov et al. 2003). Las moléculas de RNA al poseer 2'-OH en lugar de 2'-H en el azúcar son más lábiles que el DNA a la hidrólisis, pero más resistentes a los efectos del UV (Thorp 2000). Sin embargo, a medida que fue surgiendo la vida, los organismos vivos tuvieron que luchar contra efectos de la radiación UV solar capaces de dañar el DNA (efectos genotóxicos). La aparición de la capa de ozono hace 3.5-0.5 miles de millones de años permitió la atenuación de esta radiación, reteniendo la mayoría de radiaciones inferiores a 320 nm y posibilitando la vida tal y como la conocemos (González-Pumariega M. 2009) (Berkner LV. 1964).

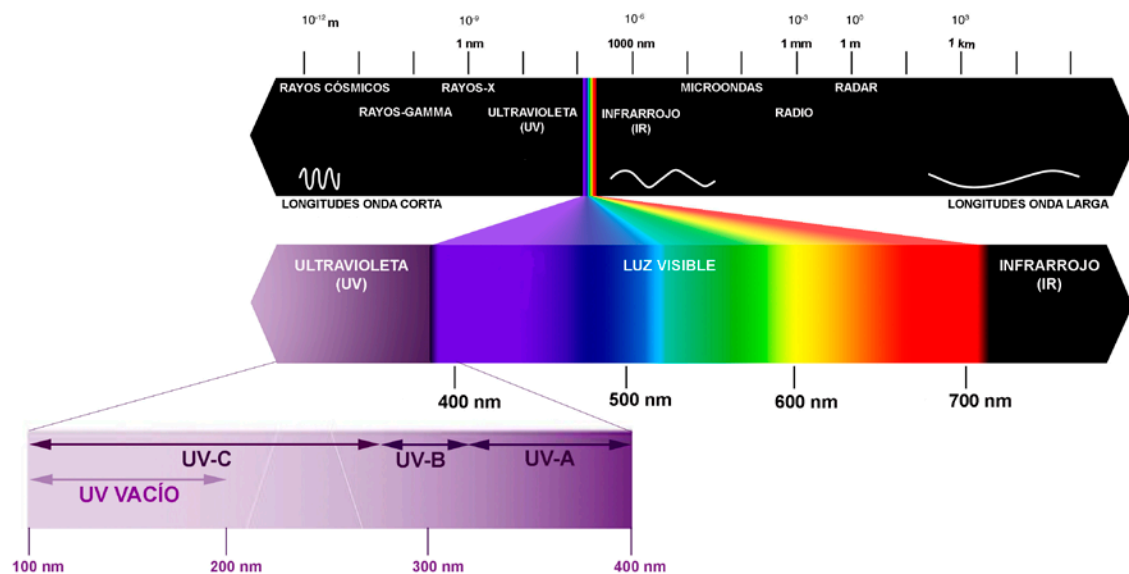


Figura 11: Espectro electromagnético. La parte inferior muestra la banda de la radiación UV con sus diferentes tipos: UV-A, UV-B, UV-C y de vacío.

Efectos de la radiación UV en el DNA

Los estudios para conocer los efectos de la radiación UV en los ácidos nucleicos, han estado centrados principalmente en el DNA: efectos biológicos, mecanismos de

reparación del daño y tolerancia. En la mayoría de situaciones, la radiación recibida se disipa en forma de calor sin producir daño, sin embargo, dependiendo de la longitud de onda a la que sea irradiado el DNA, las lesiones que origina son de naturaleza muy diferente (Burrows and Muller 1998). Dentro del DNA están sujetos a daño las bases, el azúcar y los enlaces fosfodiéster.

Lesiones en el DNA

La mayoría de lesiones del DNA ocasionadas directamente por la irradiación UV superior a 180 nm (UV-B y UV-C) son fotoproductos de diferente naturaleza:

– Dímeros de pirimidinas

• *Pirimidinas ciclobutano:*

Son la principal lesión en el DNA por la exposición a la luz UV. Se originan cuando el DNA es expuesto a la radiación UV próximo a su máximo de absorción (máximo 260 nm), aunque también se origina en longitudes de onda inferiores (193 nm) (Gorner 1994). Consiste en la unión de dos pirimidinas adyacentes por enlace covalente, formándose una estructura en anillo entre las pirimidinas por la saturación de sus dobles enlaces C-5 y C-6. Estos dímeros existen en dos isoformas diferentes: *cis-syn* (en DNA de doble cadena) y *trans-cys* (DNA de cadena sencilla, desnaturalizados, entre pirimidinas no adyacentes de DNA de cadena sencilla y en DNA dúplex con la conformación DNA-Z:DNA-B). Son extraordinariamente estables a temperatura y pH extremos, resistentes a la hidrólisis de DNA y reversibles durante la irradiación. La formación de dímeros de pirimidinas no es aleatoria, dependiendo de la composición nucleotídica (generalmente Timina:Timina) y de la secuencia que flanquea al dímero (preferentemente Adeninas en flancos 5' y 3').

• *Fotoproductos (6-4)pirimidina-pirimidona:*

Son dímeros de pirimidinas donde se forma un enlace covalente entre el carbono-6 de una pirimidina y el carbono 4 de otra pirimidina (generalmente entre citosinas). Se produce una torsión en el dúplex de DNA al girar 90° la base en 3' respecto de la pirimidina de 5'. Son 50% menos frecuentes que los anteriores e inestables por calentamiento en presencia de un álcali.

– Otros fotoproductos

- *Hidratos de pirimidinas*: Consiste en la adición de una molécula de agua en el doble enlace 5,6 entre dos pirimidinas de un DNA de cadena sencilla originando 5,6-dihidro-6-hidroxido, generalmente de citosina. Se producen en DNA de cadena sencilla y dúplex. Son inestables y revierten con facilidad a la forma original.
- *Lesiones en purinas*: La irradiación de poli(dA) origina dímeros de Adenas por enlace 8,8 de los anillo de imidazol. Es sensible a pH alto y ocurre específicamente en secuencias ACA, potenciado por la presencia de dos o más pirimidinas contiguas en su flanco 5'.
- *Glicoles de timina*: Se producen por la saturación de los dobles enlaces 5 y 6 de algunas pirimidinas. Suele ser una de las principales formas de daño del DNA por radiación ionizante, aunque también se generan por la radiación UV.
- *Fotoproductos de esporas*: hasta un 30% de las Timinas pueden adoptar esta forma. Puede originarse incluso en DNA deshidratado.

La formación de fotoproductos puede afectar a la unión de proteínas específicas de secuencia, mutaciones y producir anomalías reguladoras; lesiones distorsionantes de la hélice impidiendo su codificación y a la detención de la replicación al no poder incorporar ninguna base que forme un puente de hidrógeno de razonable estabilidad. Las células poseen enzimas y cofactores fotosensibles para reparar este tipo de lesiones (Chinnapen and Sen 2004).

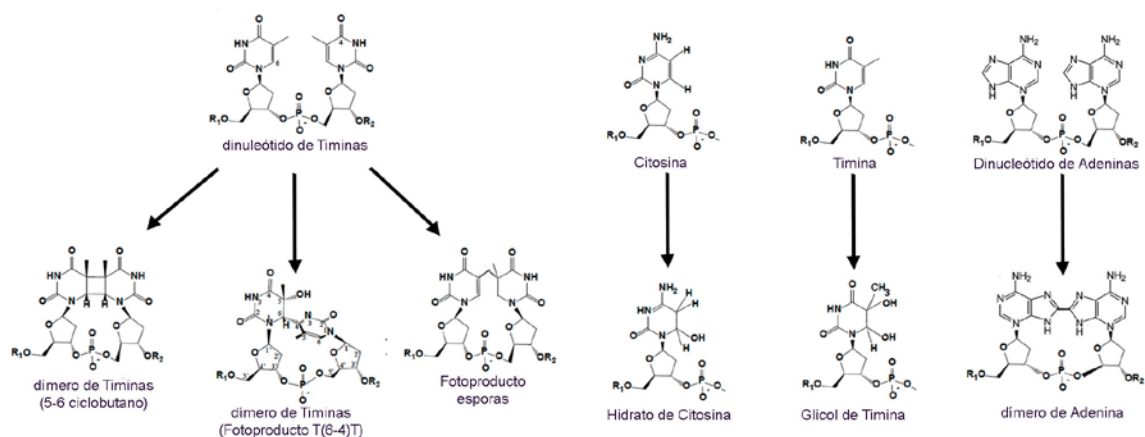


Figura 12: Fotoproductos generados por la radiación UV en el DNA.

– Formación de crosslink

Se producen por la formación de enlace covalente entre DNA-proteínas y DNA-DNA, entre las bases de la misma hebra o de la hebra complementaria. Es favorecido cuando el DNA está en estado seco, en un estado extremadamente denso que empaqueta el DNA o en otras conformaciones especiales. Es altamente estable, siendo resistente al calor y a la formamida. Interfiere con la replicación de la hebra de DNA (Marmur and Grossman 1961; Gorner 1994).

– Rotura del DNA

La rotura de DNA puede ser causada por la irradiación directa de la luz UV a 254 nm (UV-C) o de forma indirecta como consecuencia de otros daños en el DNA, como pueden ser los dímeros de pirimidinas o la fotoionización. Los picos de absorción para producir escisión son 265 y 450 nm. La frecuencia de rotura de las hebras de DNA es incrementada por la irradiación a longitudes de onda más cortas y de mayor intensidad (Candeias, O'Neill et al. 1992). A λ inferior de 180 nm en solución acuosa, la rotura del DNA es ocasionado de manera indirecta por la fotólisis de las moléculas de agua que generan radicales libres que ionizan el DNA, cortándolo (Takakura, Ishikawa et al. 1987). La rotura del DNA está condicionada al tipo de nucleótido (más sensibles las timinas) y a la secuencia flanqueantes (más vulnerable flanqueado por citosinas en 5' y 3', siendo más determinante la 3') (Kundu, Linne et al. 2004). La destrucción de nucleótidos (más frecuente en pirimidinas) y liberación de bases nitrogenadas (generalmente citosina) son otros efectos que pueden encontrarse como consecuencia de la irradiación del DNA a longitudes de onda de 272, 254 y 193 nm (Rosenstein and Ducore 1983; Gorner 1994).

Mecanismos de reacción por UV

La radiación UV que incide en el DNA se transfiere energéticamente hasta ciertas posiciones más susceptibles que acumularían la excitación energética (fotoexcitación) y provocarían el daño. Sin embargo, si esa posición excitada recibe excitación adicional o directamente recibe intensidad alta UV (~ 193 nm) se produce transferencia de carga a otras posiciones (fotoionización) pudiendo producirse rotura de hebra. La transferencia se ve favorecida por la presencia de adeninas, y de la cercanía al sitio

vulnerable a la excitación. Y puede darse hasta a 100 nucleótidos de distancia en sentido 5'→3', 3'→5' y cruzada de una hebra a la otra (Nordlund 2007).

– Fotoionización (=fotooxidación):

Consiste en la excitación de una molécula por los fotones de la radiación UV que conduce al desprendimiento de un electrón (e-) y la subsiguiente formación de un radical. La fotoionización puede ser directa y monofotónica, donde el fotón incide en un nucleótido o nucleósido, desprende un e- y produce una base radical catiónica (base^{•+}) que es capaz de dañar el DNA (rotura en la mayoría de los casos). Generalmente se origina a radiación UV muy energética (193 nm) en solución acuosa, aunque las bases de purina pueden ionizarse a 266 nm (bifotónica) (Crespo-Hernandez and Arce 2002). La guanina es la base más sensible a la fotoionización (G>A>C>T), concretamente el triplete 5'-GG-3', y conduce a la rotura de la hebra de DNA (Burrows and Muller 1998; Melvin, Cunniffe et al. 1998; Odom and Barton 2001). También pueden oxidarse todos los hidrógenos (-H) del azúcar en DNA de cadena sencilla (excepto los del C-2') y los -H de C-5' y C-4' de nucleótidos en surco menor, y C-3' del surco mayor del DNA dúplex (Pogozelski and Tullius 1998). Pero también existe una fotoionización indirecta que se origina por la fotólisis de las moléculas de agua, al ser irradiadas por UV a λ inferior a 180 nm (Candeias, O'Neill et al. 1992). Se genera el radical hidroxilo (\bullet OH) y un e-, y se forma una base radical aniónica (base^{•-}) (Melvin, T 1996).

– Fotosensibilización:

Las diferentes lesiones en el DNA por acción del UV pueden ser originadas partir de otras especies moleculares, llamadas fotosensibilizadores, que absorben los fotones a otras longitudes de onda diferentes a la del DNA y que tras su excitación transfieren su energía a la base del DNA. Destaca la fotosensibilización enzimática, donde estarían incluidas aquellas enzimas que implicadas en reparar ciertos daños en el DNA ocasionados por el UV (se activan con UV entre 300-600 nm), representadas por las DNA ligasas (Chinnapen and Sen 2004). Sin embargo, este mismo mecanismo puede ser utilizado para producir daño en el DNA: Es el que utiliza la radiación UV-A, que fotosensibiliza endo- o exosensibilizadores (enzimas, proceso inflamatorio) que producen radicales libres del oxígeno y del nitrógeno, transfiriendo energía al DNA y

produciendo su fragmentación (Cadet, Douki et al. 2015). Entre los fotosensibilizadores endógenos destacan las riboflavinas, porfirinas, flavinas mononucleótido (FMN y FAD) y aminoácidos aromáticos (Burgstaller, Hermann et al. 1997).

Efectos de la radiación UV en el RNA

La mayoría de estudios clásicos para conocer los mecanismos de reacción y los daños ocasionados por la radiación UV en ácido nucleicos, han estado centrados en el DNA y en muchos casos eran atribuidos por igual a DNA y RNA.

Lesiones en el RNA

La variedad de daños ocasionados por la radiación UV en el RNA es mucho menor que en DNA. Esto es debido a las diferencias en el azúcar de ribonucleótidos y desoxirribonucleótidos. El C2'-OH en ribonucleótidos es el elemento responsable de la labilidad del RNA, pero le confiere estabilidad al azúcar frente a la oxidación, y por tanto frente a la fotoionización por radiación UV (Thorp 2000) (Kupfer and Leumann 2007). Por otro lado, el RNA dúplex (incluso en dúplex DNA-RNA) adopta una conformación tipo A, mientras que el DNA es tipo B. Esto permite que las hélices tipo A sean mucho más resistentes a la radiación UV (Kundu, Linne et al. 2004). Por otro lado, hay que tener en cuenta que la célula posee de cuatro a seis veces más RNA que DNA, por lo que no hay que menospreciar los efectos en el RNA (Wurtmann and Wolin 2009). Con todo ello, las principales lesiones en el RNA son:

- Fotoproductos de RNA:

Pueden formarse dímeros de uridinas, que modifican la secuencia de codificación en la síntesis de proteínas, pudiendo ser codificados como UU o GU. Y también se producen hidratos de uridinas, que son codificados como citosinas (Ottensmeyer and Whitmore 1968). En el bacteriofago de *E. coli* R17 se han detectado hidratos de uridinas y de citidinas, implicados en la inhibición de la traducción y la inactivación de R17 (Cerutti, Miller et al. 1969). Los fotoproductos son más frecuentes en RNA de cadena sencilla que en dúplex RNA-RNA, de manera que el incremento de Mg^{2+} disminuye su

formación. Para que se generen los fotoproductos se necesita que el RNA sea irradiado con UV-C entre 200-290 nm(Wurtmann and Wolin 2009).

– Formación de crosslink:

La radiación UV (254 nm) es capaz de formar crosslink entre moléculas de RNA y proteínas (Dobrov, Arbieva et al. 1989) y entre RNA-RNA, destacando los bucles-E, donde se forma crosslink entre dos bases no apareadas pero muy cercanas espacialmente (Branch, Benenfeld et al. 1985). Éstos son descritos más a delante con más detalle. Otro ejemplo es el crosslink formado en los tRNAs de *E. coli*, donde la citosina forma crosslink con la pseudouridina, disminuyendo la tasa de aminoacilación de los tRNAs. La frecuencia de crosslink RNA-RNA correlaciona con la distancia y el ángulo entre nucleótidos (Wurtmann and Wolin 2009).

– Rotura del RNA:

Es la principal lesión en el RNA por acción de la radiación UV. En los primeros estudios sobre los daños causados por UV (254 nm) mostraban únicamente cortes inespecíficos en las moléculas de RNA, pero incluso con menor rendimiento que en el DNA. El corte inespecífico es producido por la absorción de fotones por el esqueleto azúcar-fosfato, siendo independiente de las bases nitrogenadas (Jericevic, Kucan et al. 1982). Sin embargo, los mecanismos de corte son muy similares al DNA y la radiación UV es capaz de cortar el RNA en posiciones concretas (directa e indirecta). Tal es el caso del par de bases G:U dentro de una hebra de RNA, cuyo corte se produce en el extremo 3' de la U por un mecanismo oxidativo, de manera dependiente de iones metálicos divalentes(Burgstaller, Hermann et al. 1997). La sensibilidad a la radiación UV también varía con la temperatura, debido a que el calentamiento (65-70°C) rompe la estructura secundaria de las moléculas de RNA(Coahran, Buzzell et al. 1962).

Mecanismo de reacción por UV

Los mecanismos de reacción son similares a los del DNA, aunque existen algunos detalles concretos y específicos al RNA que resultan interesantes destacar.

Al incidir la radiación UV en el RNA, el estado excitado de un nucleótido dura más tiempo en bases apiladas que en nucleótidos libres(Takaya, Su et al. 2008). El estado excitado y los electrones desprendidos de los ribonucleótidos se transfieren a lo largo

de la cadena de RNA hasta llegar a un sitio más vulnerable que sufre algún tipo de alteración o corte. La transferencia electrónica se basa en el potencial reductor de las bases nitrogenadas, siendo más fácil reducir las pirimidinas ($U > C \gg A > G$) y por tanto ser las principales responsables de ese movimiento electrónico. La distancia de migración depende del número de pares de bases A:U, detectando transferencia hasta de 10 pares de bases A:U en RNA dúplex (Takada, Otsuka et al. 2011).

– Fotoionización:

La fotoionización es el mecanismo de reacción más importante de la radiación UV en RNA. El mecanismo de corte ha sido profundamente estudiado en relación a la ionización por acción del radical $\bullet\text{OH}$ (y $\bullet\text{H}$). $\bullet\text{OH}$ conduce a la formación de una base radical en el 90% de interacciones con el RNA y de ellas el 40% sufren rotura del RNA. La base radical suele generarse en el C-5 de pirimidinas y se estabiliza extrayendo un H de la ribosa (generalmente el C-2'-OH), del mismo nucleótido ionizado o del nucleótido adyacente en 5'. La existencia del grupo -OH en C-2' de ribonucleótidos favorece la escisión de la hebra de RNA porque estaría facilitando la transferencia de la base al azúcar, susceptible de rotura. Los productos de corte generados dejan extremos 5'-P y 3'-P o 3'-P+fragmentos del nucleótido. En RNA de cadena sencilla más del 80% de escisión sucede en el nucleótido donde se genera la base radical y en RNA dúplex el 85% de corte es en el nucleótido adyacente en 5'. La rotura de hebra sucede tanto en RNA de cadena sencilla (con mayor rapidez) como dúplex y se favorece en condiciones anaerobias. En aerobiosis los radicales $\bullet\text{OH}$ son atrapados por el oxígeno compitiendo con la base por su captación (Jacobs, Resendiz et al. 2010; Jacobs, Resendiz et al. 2011).

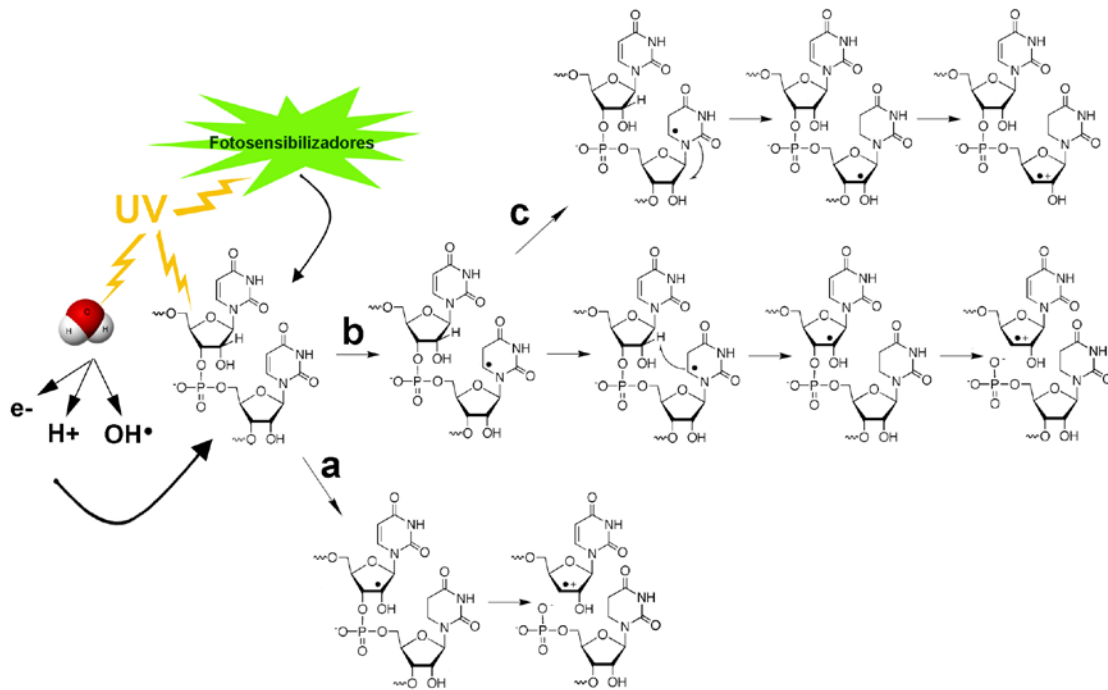


Figura 13: Fotoionización por acción de la radiación UV en moléculas de RNA. A la izquierda se muestran los tres mecanismos de oxidación de un nucleótido: directamente por UV, mediante radicales libres generados por fotólisis de moléculas de agua o mediante fotosensibilización. La ionización puede producirse en (a) la ribosa o en (b) la base nitrogenada (base radical) y producir rotura de la hebra de RNA. La base radical ioniza la ribosa de su mismo nucleótido (b) o la ribosa del nucleótido adyacente en 5' (c) conducir a rotura.

In vivo, los productos de la oxidación en RNA son 1.4 veces más abundantes que los de DNA (14-25 veces a nivel de nucleósido). Esto es debido a que las tasas de oxidación incrementan en la proximidad de la mitocondria (metabolismo del oxígeno más activo) y el DNA está limitado al núcleo (menos niveles de oxígeno); las proteínas unidas preservan de la oxidación y las moléculas de cadena sencilla son más vulnerables. También pueden apreciarse diferencias en los niveles de oxidación entre RNAs codificantes y no codificantes, y entre diferentes especies de mRNAs. Las consecuencias de la oxidación del RNA son a nivel de la traducción y plegamiento anómalo de proteínas (Wurtmann and Wolin 2009).

– Fotosensibilización:

Al igual que en el DNA, las moléculas de RNA pueden ser excitadas por fotosensibilizadores que absorben una longitud de onda diferente a la necesaria para excitar al RNA. Destacan igualmente los derivados de flavinas, NADPH y porfirinas.

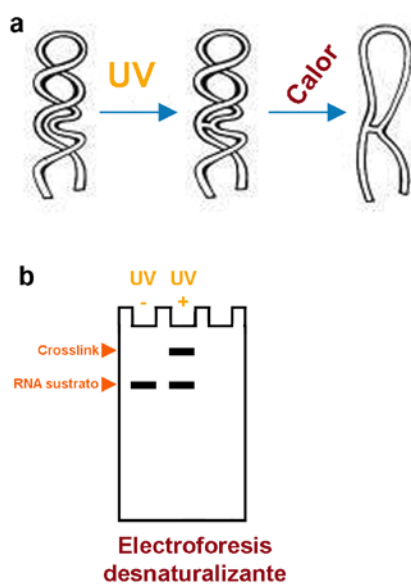
Igualmente, la radiación UV-A es suficiente para excitar a los fotosensibilizadores que posteriormente excitan o ionizan al RNA (Burgstaller, Hermann et al. 1997) (Wurtmann and Wolin 2009).

Lazo-E

Los lazos-E son elementos de estructura local terciaria que presentan una serie de características a nivel de secuencia y de estructura que les confiere una alta sensibilidad a la formación de un enlace covalente por irradiación de la luz UV entre bases muy próximas espacialmente (*crosslink*) (Branch, Benenfeld et al. 1985). Los lazos-E están presentes en el RNA de los tres reinos de la vida. En procariotas se encuentran en lazos internos simétricos, como es el caso del lazo-E del rRNA 5S de *E. coli* (Correll, Freeborn et al. 1997). En eucariotas y algunos grupos de arqueas los lazos-E se encuentran en lazos asimétricos, que están relacionados con los de bacterias pero que difieren en su estructura (Leontis and Westhof 1998). Los modelos más estudiados son los rRNAs 5S y 23S de eucariotas (*Xenopus laevis*, HeLa). También están presentes en virus (HCV y virus de la hepatitis delta HDV) y viroides de plantas (viroide del tubérculo fusiforme de la patata (PSTV)) (Branch, Benenfeld et al. 1985).

Los diferentes lazos-E han sido ampliamente estudiados a través de cristalografía de rayos-X y RMN. Esto ha permitido identificar una serie de características estructurales propias de estos motivos. A nivel de secuencia, en PSTV y en rRNA 5S de HeLa, se han determinado 8 bases que se conservan en el lazo interno asimétrico: en una hebra 5'-GGGAA-3' y en la otra 5'-UAC-3'. Los residuos G y U (purina con pirimidinas) enfrentados en el lazo son capaces de formar un *crosslink* por la luz UV. El lazo está flanqueado por regiones compuestas de 7-9 bases apareadas. A pesar de que estas 8 bases aparecen en más RNAs relacionados, a veces sólo 6 bases se conservan (Branch, Benenfeld et al. 1985). Sin embargo, lo que caracteriza a un lazo-E es su estructura terciaria, favorecida por el apilamiento de apareamientos no-canónicos (no Watson:Crick) entre las bases del lazo. Estos apareamientos no-canónicos provocan una torsión del esqueleto de azúcar-fosfato hacia el interior del lazo, aproximando las bases implicadas en la formación del *crosslink* y aportando estabilidad al RNA. Generalmente, entre estos apareamientos aparecen: apareamientos Hoogsteen,

Hoogsteen reverso, apareamientos G-A, ect. (Wimberly, Varani et al. 1993; Branch, Levine et al. 1995). No se limitan a los lazos internos, han sido identificados también en uniones multihélices que son sitios de gran importancia funcional en los RNAs largos (Leontis and Westhof 1998).



Los crosslinks al ser enlaces covalentes, son termoestables, resistentes al glioxal y a nucleasas específicas de RNA de simple cadena, como la RNasa T1 (Branch, Benenfeld et al. 1985; Branch, Levine et al. 1995). Los lazos-E presentes en ribozimas, al formarse el crosslink no pierden la actividad enzimática (Leontis and Westhof 1998). La re-irradiación un crosslink con UV a 248 nm sufren fotorreversibilidad (Shapkina, Lappi et al. 2004).

Figura 14: (a) Representación esquemática de un bucle-E en RNA. Se muestra la formación de un crosslink por la radiación UV y la desnaturalización de la estructura secundaria con calor, mostrándose resistente el crosslink. (b) Patrón comparativo de migración de un RNA irradiado (derecha) o no (izquierda) con UV con formación de crosslink.

Los lazos-E son motivos que participan en la organización y estructuración de múltiples uniones RNA-RNA (ribozimas) y RNA-proteínas (RNAs ribosomales, factor de transcripción TFIIIA), de manera, que son sitios de interacción con proteínas y otros RNAs que están directamente relacionados con funciones biológicas (Leontis and Westhof 1998).

En la región 5'-UTR de HCV se han identificado dos motivos lazo-E asimétricos, en los dominios IIB y IIId. El lazo-E del dominio IIB incluye parte de la secuencia implicada en el inicio de traducción (Lyons, Lytle et al. 2001). Ambos lazos-E son esenciales para la funcionalidad del IRES de HCV, contribuyendo a la estabilidad de la estructura terciaria o mediante interacciones intermoleculares con el 40S (Klinck, Westhof et al. 2000; Lukavsky, Otto et al. 2000).

Virus como señales

La biosemiótica es la ciencia que resulta de aplicar la semiótica a los sistemas vivos. Semiótica viene de la raíz griega *Semeion*, que significa «signo» y constituye el estudio de los signos. Los signos se estudian desde la Antigüedad. A su vez, el término «signo» proviene del griego *signum*, que significa prueba, indicio, síntoma. Desde Aristóteles, hacia el siglo IV a.C. hasta el presente, el signo ha sido objeto de estudio, pudiéndose clasificar en dos categorías fundamentales, aquellas que dividen el signo en dos componentes, por ejemplo: el nombre y el concepto, y los que lo dividen en tres. Nos centramos en esta última pues la complejidad del tema desborda ampliamente esta Tesis, y porque tal vez esta última es la que mas consenso ha ido ganando para su aplicación en biología. Aunque la fórmula triádica ya es propuesta por San Agustín y cultivada por filósofos castellanos medievales, la nueva tradición semiótica parte de los escritos del filósofo y matemático norteamericano Charles Sanders Peirce (1839-1914), aunque el autor nunca los publicó, y estos han sido recopilados a *posteriori*. La definición más popular de «signo» para Peirce es la de «aquello que está en lugar de algo para alguien». Peirce defiende para el signo una estructura triádica o de signo compuesto de tres elementos: representamen (lo que está en lugar de), objeto (aquello por lo que está) e interpretante (que concibe la relación entre ambos). El esquema característico de esta relación se presenta como se indica en la figura ().

Thomas Sebeok fue el primero en proponer una síntesis entre la ciencia de los signos y las ciencias de la vida que conduce a la biosemiótica. Y esto pasa, por un lado, por las relaciones semióticas del lingüista Pierce y, por otro, por las investigaciones de la percepción del teórico de la biología alemán Jacob von Uexküll. Sebeok insiste en que no hay modelo semiótico sin interpretación. Muchos biosemióticos adoptarán esta teoría, como la Escuela de Copenhague o la Escuela de Praga. El entendimiento de Sebeok de los sistemas vivos es fundamentalmente hermenéutico. Siguiendo al filósofo alemán Hans-Georg Gadamer, los organismos vivos siempre cuentan con una situación actual de memoria y de interpretación, cosas que ni la lógica matemática ni las máquinas, por el momento, llegan a integrar. Es posible descomponer los procesos básicos de la expresión génica (tanto la mecánica de la transcripción y la traducción, como el desciframiento del código genético) en series triádicas como las de la figura 1, pero también los procesos mediados por hormonas y neurotransmisores. En los virus, un ejemplo semiótico es la mimesis, tanto en relación con el sistema inmune del

organismo, como en la interacción con la maquinaria celular. Por ejemplo, el caso del mimetismo del tRNA: a diferencia de lo que comúnmente se tiende a pensar, la mimesis no se refiere a la arquitectura de la cadena de RNA, tal y como al podríamos dibujar tras averiguar todas las distancias y ángulos entre sus átomos, sino directamente al lenguaje y a la comunicación molecular. Los motivos estructurales de RNA encontrados empleando enzimas cuyo reconocimiento depende de características estructurales, constituyen potenciales señales de significación, pues dichos motivos estructurales son informativos para los enzimas en el contexto celular, donde se las considera intérpretes. Es decir, el elemento estructural vírico que se parece al tRNA, es la señal, que está en lugar del verdadero tRNA (objeto), y es interpretado por la RNasa P o los enzimas del metabolismo.

La gran ventaja que supone el mimetismo a nivel molecular es que permite economizar, en cuanto que requiere un menor número de interacciones macromoleculares para desarrollar procesos biológicos muy diversos. En el caso de los virus, serviría para aprovechar la maquinaria de la célula hospedadora, suplantando la identidad de sus componentes. El original y la copia no tienen por qué ser extraordinariamente parecidos para desencadenar una respuesta biológica. Por ejemplo, la estructura tipo tRNA encontrada en el extremo 3' del virus del mosaico del bromo (BMV) (Verificar) no muestra la arquitectura típica en forma de L del tRNA, que, sin embargo, sí exhibe el virus del mosaico amarillo del nabo (TYMV). Sin embargo ambas estructuras son reconocidos por las aminoacil-tRNA sintetasas.

Todas las versiones de la biosemiótica concluyen con la idea de que la semiosis es fundamental para la vida y que todas las criaturas vivas son sistemas semióticos, propiedad que las distingue de la materia inerte. Es decir, la semiótica sería ese algo más que deberíamos añadir a la física y la química para la total comprensión de los sistemas vivos. La biosemiótica en cuestión es un genuino y nuevo paradigma para ambas, biología y semiosis, pero su futuro es impredecible. Y es, verdaderamente, como un nuevo continente cuya exploración acaba de empezar. En la actualidad los estudios de biosemiótica se recopilan en una revista que lleva este mismo nombre "Biosemiotics" y esta conducida por una sociedad que realiza un congreso internacional anualmente.

Una postura radical que se explora en esta tesis es si se puede considerar al virus, no como un organismo, sino como una señal; una señal compleja, sin duda, que induciría una práctica divisoria de las relaciones moleculares del interior celular.

OBJETIVOS

La región 5' del genoma del virus de la hepatitis C que comprende los (dominios I-VI) es una de las más estudiadas en sus aspectos estructurales y funcionales del conjunto de los RNAs víricos. Estudios estructurales realizados en laboratorio receptor de este trabajo han identificado una serie de facetas del IRES que pueden participar en el posicionamiento adecuado del triplete AUG en la subunidad 40S del ribosoma o en la eficacia de esa unión, estos incluyen : (a) una estructura tipo tRNA-like identificada usando la actividad RNasa P; que podría participar en el anclaje de la subunidad ribosomal 40S, directa o indirectamente (b) una estructura de RNA de doble cadena detectada con la actividad RNasa III, que representa el anillamiento a larga distancia entre los dominios I y IV que flanquean los lados distal y proximal del IRES dejando este en una conformación cerrada. Esta estructura podría determinar la presentación de los motivos que interactúan con la subunidad 40S (c) usando la luz UV se observó un lazo-E en el dominio II, esencial para el doblamiento de este dominio hacia el codón de inicio de traducción que se estabiliza mediante la unión de la subunidad ribosomal 40S (d) trabajos de otros grupos han identificado un nuevo sitio de unión para el miR-122 en el dominio IV del IRES, aún por caracterizar. Teniendo en cuenta estos antecedentes, los objetivos en el desarrollo de esta Tesis doctoral fueron los siguientes:

- Describir los cambios estructurales en la región 5' UTR del RNA de HCV por la interacción del microRNA específico del hígado humano miR-122.
- Analizar la importancia de las regiones que flanquean al IRES del RNA de HCV en sus extremos 5' (dominio I) y 3' (dominio V y VI) en la organización estructural.
- Estudiar los cambios conformacionales que se originan en la región 5' UTR del RNA de HCV por la presencia del ión Magnesio.
- Determinar si la estructura del motivo tipo-tRNA se modifica cuando cambia la conformación de la región 5' UTR del RNA del virus de la hepatitis C.
- Detectar si hay cambios en la accesibilidad de las subunidades ribosomales 40S al IRES del RNA de HCV por la interacción del miR-122 a esa región, y en ese caso, determinar los cambios estructurales que se producen en el RNA de HCV 1-570.

- Ensayos preliminares del laboratorio han detectado que durante la formación del *crosslink* en el dominio II del IRES del RNA-HCV por la luz UV, se origina un corte específico en el RNA de HCV en ese mismo. De manera que se propone caracterizar si el corte es específico en el RNA-HCV y si es directamente dependiente de la luz UV-C o de radicales libres generados en el medio.

-

MATERIALES Y MÉTODOS

Materiales

Tampones

Tampones y soluciones generales:

Tampón TSE 10X:

Tris-HCl pH 7.5.....	0.5M
NaCl.....	1M
EDTA pH 7.5	10mM

Tampón de elución T1 10X:

Tris-HCl pH 7.5	100mM
EDTA pH 7.5	10mM

Solución de precipitación de Acetato de sodio + glicógeno:

AcNa pH 5.2	3M
Glicógeno	0.2µg/µl

Solución de siliconización 4%:

Dimetil-diclorosilano.....	4% (vol/vol)
Cloroformo	99%

Tampones para preparar bacterias competentes:

TFBI

AcOK	2.9 g/l
MnCl ₂	9.9 g/l
CaCl ₂	1.47 g/l
RbCl	12.09 g/l
Glicerol 87%.....	172 ml/l

Filtrar por filtro de 0.22 µm y ajustar pH a 5.8.

TFBII

MOPS	2.9 g/l
------------	---------

CaCl ₂	11.03 g/l
RbCl	1.21 g/l
Glicerol 87%.....	172 ml/l

Filtrar por filtro de 0.22 µm y ajustar pH a 7.

Tampones de electroforesis:

Tampones de electroforesis para geles de poliacrilamida en condiciones desnaturizantes:

Tampón Tris-Borato-EDTA (TBE) 10X:

Disolución de paquete comercial de Ambion en 1 litro de agua.

Composición 1X:

Tris-Borato	89mM
Na ₂ EDTA	2mM

Tampón Tris-Acetato-EDTA (TAE) 25X:

Disolución de paquete comercial de Ambion en 1 litro de agua.

Composición 1X:

Tris-Acetato	40mM
Na ₂ EDTA	1mM

Tampones de electroforesis para geles de poliacrilamida en condiciones nativas:

Tampón Tris-Acetato 10X:

Tris-Acetato	500mM
Ac ₂ Mg	100mM

Tampón Tris-Acetato (sin Magnesio) 10X:

Tris-Acético	500mM
Acetato de amonio	100mM

Tampón Tris-Borato-Magnesio 10X:

Tris-Base.....	220mM
Ácido Bórico	880mM
MgCl ₂	10mM

Tampón de carrera para geles de proteínas en condiciones desnaturizantes 5X:

Tris-Base.....	125mM
SDS	0.05 % (v/v)
Glicina	960 mM

Tampones de carga para electroforesis:

Tampón para geles de poliacrilamida en condiciones desnaturizantes (1.5X):

Formamida desionizada	97.5% (v/v)
EDTA pH 7.5	10mM
Azul de bromofenol	0.03% (p/v)
Xilencianol	0.03% (p/v)

Tampón para geles de poliacrilamida en condiciones nativas (2x):

Glicerol	30% (v/v)
TMN 5X.....	20% (v/v)
tRNA levadura.....	4% (p/v)
Azul de bromofenol	0.03% (p/v)
Xilencianol	0.03% (p/v)

Tampón para geles de poliacrilamida condiciones nativas sin Magnesio (2x):

Glicerol	30% (v/v)
TMN 5X (sin Mg ²⁺)	20% (v/v)
tRNA levadura.....	4% (p/v)
Azul de bromofenol	0.03% (p/v)
Xilencianol	0.03% (p/v)

Tampón TMN 5X:

Tris-Acetato pH 7.6	100mM
Ac2Mg	50mM
NaCl.....	500mM

Tampón para geles de poliacrilamida para reacciones de unión con ribosomas en condiciones nativas (2x):

Glicerol	6% (v/v)
Xilencianol	0.03% (p/v)

Tampón para geles de agarosa en condiciones nativas (6x):

Sacarosa.....	20% (p/v)
EDTA	10mM
Tris-HCl pH 8.....	50mM
Azul de bromofenol	0.03% (p/v)
Xilencianol	0.03% (p/v)

Tampón para geles de poliacrilamida para proteínas (2x):

Tris-HCl pH 6.8.....	250 mM
SDS	4% (v/v)
Glicerol	20% (v/v)
DTT.....	200 mM
Azul de bromofenol	0.03% (p/v)

Soluciones para teñir y lavar geles de proteínas

Solución Fairbanks A:

Ácido acético	10%
Isopropanol.....	25%
Azul de coomassie.....	0.05%

Solución Fairbanks B:

Ácido acético	10%
Isopropanol.....	10%
Azul de coomassie.....	0.005%

Solución Fairbanks C:

Ácido acético	10%
Azul de coomassie.....	0.002%

Solución Fairbanks D:

Ácido acético	10%
---------------------	-----

Tampones y soluciones para la purificación de la RNasa Z de *Escherichia coli*

Buffer de resuspensión y lisis:

Tris-HCl pH 7.8.....	20 mM
----------------------	-------

NaCl	500 mM
Glicerol	10% (v/v)
Tritón X-100	0.1%

Buffer de resuspensión y lisis suplementado:

Tris-HCl pH 7.8.....	20 mM
NaCl	500 mM
Glicerol	10% (v/v)
Tritón X-100	0.1%
Imidazol	5 mM
DTT.....	2mM
Inhibidor de proteasas	

Tampones par la cromatografía de afinidad

Tampón de lavado 1:

Tris-HCl pH 7.8.....	20 mM
NaCl	300 mM
Imidazol	20 mM
DTT.....	2mM

Tampón de lavado 2:

Fosfato de sodio pH 6.....	50 mM
NaCl	300 mM
DTT.....	2mM

Tampón de elución:

Tris-HCl pH 7.8.....	20 mM
NaCl	300 mM
Imidazol	250 mM
DTT.....	2mM

Tampón de diálisis:

Tris-HCl pH 7.5.....	50 mM
DTT	2 mM
Glicerol	25% (v/v)

Tampones para la purificación de las subunidades ribosomales de células HeLa

Tampones para la lisis celular

Tampón isotónico:

HEPES-KOH pH 7.6	35 mM
NaCl	146 mM
Glucosa	11 mM

Tampón isotónico:

HEPES-KOH pH 7.6	20 mM
AcO ₂ Mg	1.5 mM
KCl	10 mM
DTT.....	1 mM

Tampón S10:

HEPES-KOH pH 7.6	100 mM
AcO ₂ Mg	20 mM
KAcO	600 mM
DTT.....	25 mM

Tampones para la extracción ribosomal

Tampón A:

Tris-HCl pH 7.5	20 mM
AcO ₂ Mg	6 mM
KCl	500 mM
Sacarosa.....	1 M
DTT.....	2 mM

Tampón B:

Tris-HCl pH 7.5.....	20 mM
AcO ₂ Mg	6 mM
KCl	150 mM
Sacarosa.....	100 mM
DTT.....	2 mM

Tampón C:

Tris-HCl pH 7.5.....	20 mM
EDTA	0.2 mM
KCl	10 mM
MgCl ₂	1 mM
Sacarosa.....	1 M
DTT.....	1 mM

Tampones para gradiente de sacarosa

Purificación de subunidades ribosomales 40S y 60S

Tampón para gradiente con sacarosa 10%:

Tris-HCl pH 7.5.....	20 mM
KCl	500 mM
AcO ₂ Mg	6 mM
EDTA	0.1 μM
DTT.....	1 mM
Sacarosa.....	10% (p/v)

Tampón para gradiente con sacarosa 30%:

Tris-HCl pH 7.5.....	20 mM
KCl	500 mM
AcO ₂ Mg	6 mM
EDTA	0.1 μM
DTT.....	1 mM
Sacarosa.....	30% (p/v)

Reacciones de protección con la RNasa A

Tampón de dilución:

Tris-HCl pH 7.5.....	10 mM
KCl	25 mM
MgCl ₂	1 mM

NaCl..... 10 mM
DTT..... 1 mM

Tampón para gradiente con sacarosa 15%:

Tris-HCl pH 7.5..... 10 mM
KCl 25 mM
MgCl₂ 1 mM
NaCl..... 10 mM
DTT..... 1 mM
Sacarosa..... 15% (p/v)

Tampón para gradiente con sacarosa 30%:

Tris-HCl pH 7.5..... 10 mM
KCl 25 mM
MgCl₂ 1 mM
NaCl..... 10 mM
DTT..... 1 mM
Sacarosa..... 30% (p/v)

Tampones y soluciones de reacción

Tampones para reacciones con nucleasas

Tampón P humana 5X: (estándar)

HEPES-KOH pH 7.5 50mM
Ac₂Mg 50mM
AcNH₄ 500mM

Tampón P humana 5X: (20 mM Mg²⁺)

HEPES-KOH pH 7.5 50mM
Ac₂Mg 20mM
AcNH₄ 500mM

Tampón Ribozima RNasa P *Synechocystis* sp 5X:

Tris-HCl pH 7.5..... 250mM
MgCl₂ 500mM

Tampón RNasa Z 5X:

Tris-HCl pH 7.1.....	50 mM
KCl.....	50 mM
MgCl ₂	5 mM
ZnCl ₂	5 μM
DTT.....	7.5 mM

Tampones para estudiar el cambio conformacional del RNA en función de la concentración de magnesio

Tampón sin Magnesio 3X:

HEPES pH 7.5	300 mM
NaCl.....	300 mM

Tampón con 6 mM Mg²⁺ 3X:

HEPES pH 7.5	300 mM
NaCl.....	300 mM
MgCl ₂	6 mM

Tampón con 12 mM Mg²⁺ 3X:

HEPES pH 7.5	300 mM
NaCl.....	300 mM
MgCl ₂	12 mM

Tampón con 18 mM Mg²⁺ 3X:

HEPES pH 7.5	300 mM
NaCl.....	300 mM
MgCl ₂	18 mM

Tampón con 30 mM Mg²⁺ 3X:

HEPES pH 7.5	300 mM
NaCl.....	300 mM
MgCl ₂	30 mM

Tampón quelante de Mg²⁺ 3X:

HEPES pH 7.5	300 mM
NaCl.....	300 mM
Na ₂ EDTA	6 mM

Tampón para la reacción de corte con UV 1X:

Tris-HCl pH 7.5.....	10 mM
MgCl ₂	10 mM

Tampón para la reacción de Fenton 1X:

(NH ₄) ₂ Fe(SO ₄) ₂	100 µl
Na-EDTA	900 µl

Tampón para degradación con RNasa T1 en condiciones desnaturalizantes 2X:

Citrato sódico pH 4.5.....	20mM
EDTA	1mM
Urea	7M
Azul de bromofenol	0.03% (p/v)
Xilencianol	0.03% (p/v)

Solución para hidrólisis alcalina de RNA 10X:

Carbonato sódico	100mM
Bicarbonato sódico	100mM
pH 9.5	

Resina de celulosa fosfato CF-11

La resina CF-11 se emplea en la purificación de RNA para eliminar rNTPs no incorporados, sales y DNA. Permite separar RNA de simple y doble cadena según las condiciones de elución.

Preparación de la resina CF-11:

1. Pesar 130 gr de resina CF-11 (Whatman). Lavar en un litro de solución 0.1M NaOH durante 30 min en agitación. Dejar reposar 30 minutos. Transcurrido este tiempo retirar el sobrenadante.

2. Realizar 10 lavados empleando un 1 litro de agua bidestilada (30 minutos de agitación, 30 minutos de reposo y eliminación del sobrenadante). En los últimos lavados el sobrenadante debe de ser transparente.

Tras el último lavado, conservar en 1 litro de EDTA 2 mM pH 8 a 4°C hasta su utilización.

Agua

Para la preparación de tampones y soluciones que están en contacto con el RNA se utilizó agua estéril para inyectables adquirida de la casa comercial Braun Medical.

Para el resto de soluciones se utilizó agua bidestilada.

Medios de cultivo bacteriano

Medio líquido LB (Luria-Bertani)

NaCl 5 gr/l

Triptona..... 10 gr/l

Extracto de levadura 5 gr/l

Tras su disolución se autoclave durante 20 mi a 121°C.

Medio sólido LA (LB-Agar):

Preparado a partir de LB-Agar en polvo de la casa comercial Conda. Disolución de 35 g de LB-Agar en polvo en 1L de agua destilada mediante agitación y calor hasta llevar a ebullición. Finalmente autoclavar a 121°C durante 20 min.

Composición:

NaCl 5 gr/l

Triptona..... 10 gr/l

Extracto de levadura 5 gr/l

Agar bacteriológico..... 15 gr/l

Placas LA-Amp-IPTG-Xgal:

Ampicilina 50 µg/ml

IPTG 150 µg/ml

Xgal 40 µg/ml

Placas LA-Kan:

Kanamicina..... 50 µg/ml

Medio de cultivo celular

DMEM (Medio basal de Agle modificado por Dulbecco) con alto contenido en glucosa. Es suministrado por el servicio de cultivos del Instituto de Parasitología y Biomedicina “López-Neyra”.

Composición 1X:

D-glucosa 4.5 g/l
L-glutamina..... 580 mg/l
Rojo fenol 15 mg/l

Es suplementado en condiciones de esterilidad en cabina de flujo laminar con:

Piruvato sódico 1 mM
Suero fetal bovino (SFB)..... 10% (v/v)
(SFB debe estar inactivado previamente durante 30 min a 55°C)

Tras su preparación se filtra mediante un sistema de filtración por vacío a través de una membrana PES de 0.2 µm. Conservación a 4°C.

Cepas bacterianas

Las diferentes construcciones plasmídicas utilizadas fueron introducidas por choque térmico en la cepa bacteriana *Escherichia coli* DH5, con genotipo:

φ80dlacZΔM15, *recA1*, *endA1*, *gyrA96*, *thi-1*, *hsdR17* (r_k^- , m_k^+), *supE44*, *relA1*, *deoR*, Δ(*lacZYA-argF*) U169, *phoA*.

Líneas celulares

Células Hela: Procedentes una muestra de cáncer cérvico-uterino de la paciente Henrietta Lacks. En este trabajo fueron utilizadas para la obtención y purificación de las subunidades ribosomales 40S y 60S.

Medio de congelación de líneas celulares

DMEM alto en glucosa..... 10 gr/l
SFB 50% (v/v)
DMSO 10% (v/v)

Tras su preparación se filtra a través de un filtro de 0.22 μ m y se conserva a -20°C.

Construcciones de DNA empleadas para las reacciones de transcripción.

1. ***pN(1-4728) Bluescript***: contiene los 4728 primeros nucleótidos del genoma del virus de la hepatitis C, genotipo 1b. Esta secuencia está precedida por el promotor de la T7 RNA polimerasa (cedido por el Dr. Stanley M. Lemon). Empleando el plásmido como molde para PCR se obtuvieron los diferentes tamaños de HCV que permiten la transcripción de cada uno de los transcritos empleados en este trabajo. Para la obtención del fragmento HCV1-570 se utilizaron los oligonucleótidos 1b-pT7-HCV1-16(+) y HCV553-570(-); HCV1-402: 1b-pT7-HCV1-16(+) y HCV402-381(-); 1-370: 1b-pT7-HCV1-16(+) y HCV 370-351(-); 44-570: pT7+3Gs+HCV44-59(+) y HCV553-570(-); 44-370: pT7+3Gs+HCV44-59(+) y HCV370-351(-); 44-312: pT7+3Gs+HCV44-59(+) y HCV312-293(-). En caso de los fragmentos 1-249 y 1-130, fueron digeridos a partir del mismo plásmido con los enzimas de restricción NheI y NciI, respectivamente, y los productos de transcripción resultantes poseen los 249 y 130 primeros nucleótidos del genoma de RNA de HCV.
2. ***pGEM3Z-Non complementary y pGEM3Z-Restoring***: contiene los primeros 542 nucleótidos del genoma de HCV bajo el promotor de la T7 RNA polimerasa y fueron clonados dentro del vector pGEM[®]-3Zf(-) (Promega) entre las dianas de restricción EcoRI y HindIII. Presenta mutaciones en el dominio IV del IRES de HCV las posiciones 5'-A³³²CC³³⁴-3' por 5'-U³³²AA³³⁴-3' para el mutante Non y 5'-A³³²CC³³⁴-3' por 5'-G³³²UU³³⁴-3' en el mutante Rest. La mutagénesis dirigida fue realizada por la casa comercial GenScript a partir de un plásmido vector con la secuencia salvaje aportado por nosotros.

3. **pUC19Tyr**: contiene el precursor del tRNA para la tirosina de *E.coli* (sustrato natural de la RNasa P de *E.coli*) clonado bajo el promotor de la T7 RNA polimerasa. Tras digestión con el enzima de restricción Fok I proporciona un molde para la transcripción de un RNA de 131 nucleótidos de longitud. Se utiliza como sustrato control de las reacciones de corte con las RNasas P humana y de *Synechocystis sp.*
4. **pT76803**: contiene el gen de la subunidad de RNA de la RNasa P de la cianobacteria *Synechocystis sp.* PPC 6803 bajo el promotor de la T7 RNA polimerasa clonado dentro del vector pUC19 {Vioque, 1992 #92; Pascual, 1996 #591}. Tras digestión con el enzima de restricción Dra I proporciona un molde para la transcripción del RNA catalítico RZ6803 de 437 nt de longitud.
5. **pUGK3**: contiene el gen que expresa para la RNasa Z de *E. coli*, cepa SK3188 (F-) clonado en el plásmido pET-28a (cedido por el Dr. Sydney Kushner). Presenta una cola de 6 Histidinas que se induce en presencia de IPTG. y presenta el gen de resistencia a kanamicina. La expresión de este plásmido produce RNasa Z activa en presencia de IPTG y kanamicina, para su posterior extracción y purificación.
6. **pGemT easy-trnD-leu2**: contiene el precursor del tRNA de la leucina de *B. subtilis* (sustrato control para la RNasa Z) clonado bajo el promotor de la T7 RNA polimerasa (cedido por el Dr. Sidney Kushner). Tras digerir el plásmido con la enzima de restricción NcoI se obtiene molde para la transcripción del fragmento de RNA correspondiente a los 235 nucleótidos que forman el pre-tRNA-Leu.
7. **pcDNA3.1 DNAX**: consiste en el plásmido comercial pcDNA3.1 (cedido por la Dra. Sunnie Thompson) sin ningún inserto adicional que se utiliza de molde para la enzima de restricción EcoRI. El producto de digestión sirve de molde para la transcripción con la T7 RNA polimerasa para la obtención de un fragmento de RNA de 85 nucleótidos de longitud que se utiliza en la reacción de unión de la subunidad 40S con HCV para impedir interacciones inespecíficas.

8. **pGL3(IRES-CrPV)-Luc:** contiene el IRES del virus de la parálisis del grillo (CrPV) que consiste en los primeros 185 nucleótidos del genoma viral. Está clonado bajo el promotor de la T7 RNA polimerasa. Mediante PCR con los oligonucleótidos PT7+CrPV1-16(+) y CrPV185-165(-) se obtiene el DNA molde para la transcripción del RNA 1-185.
9. **pGEM-1 (T7 CSFV):** contiene los primeros 442 nucleótidos (secuencia Alfort) del genoma del virus de la peste porcina clásica, fusionado a la proteína NS1 del virus de la gripe (Cedido por el Dr. Richard Jackson). El inserto fue clonado bajo el promotor de la T7 RNA polimerasa y la diana de restricción HindIII. Tras la digestión con la enzima XhoI, el producto sirve de molde para la transcripción del fragmento de RNA que contiene los primeros 218 nucleótidos del genoma viral.

Isótopos radiactivos.

Los isótopos radiactivos empleados para el marcaje de los RNAs fueron suministrados por la casa comercial Perkin Elmer.

1. **GTP[α -³²P]:** con una actividad específica de 3000Ci/mmol, 250 μ Ci a una concentración de 10mCi/ml. Para marcaje interno del RNA.
2. **pCp[5'-³²P]:** con una actividad específica de 3000Ci/mmol, 250 μ Ci a una concentración de 10mCi/ml. Para marcaje del extremo 3' del RNA.
3. **GTP[γ -³²P]:** con una actividad específica de 6000Ci/mmol, 250 μ Ci a una concentración de 10mCi/ml. Para marcaje del extremo 5' de DNA y RNA.
4. **ATP[γ -³²P]:** con una actividad específica de 6000Ci/mmol, 250 μ Ci a una concentración de 10mCi/ml. Para marcaje del extremo 5' de DNA y RNA.

Marcadores de peso molecular para electroforesis.

1. **RNA Century™ Marker-Plus (Ambion):** marcador de peso molecular para RNA. Se preparó según las indicaciones del fabricante. Su transcripción, en presencia

de GTP[α -³²P], origina siete transcritos marcados radiactivamente de 100, 200, 300, 400, 500, 750 y 1000 nucleótidos de longitud.

2. **Decade™ Marker System** (Ambion): marcador de peso molecular para RNA. Se preparó según las indicaciones del fabricante. El tratamiento con T4 polinucleótido quinasa (PNK) en presencia de ATP[γ -³²P] o GTP[γ -³²P] da lugar a diferentes fragmentos de RNA marcados radiactivamente de 10, 20, 30, 40, 50, 60, 70, 80, 90, 100 y 150 nucleótidos de longitud.
3. **2-Log DNA Ladder** (NEB): marcador de peso molecular para electroforesis en gel de agarosa que contiene fragmentos de DNA comprendidos entre 100-10000 pares de bases.

Oligonucleótidos de DNA sintéticos

Los oligodesoxirribonucleótidos utilizados en este trabajo fueron sintetizados por el servicio de síntesis de oligonucleótidos del Instituto de Parasitología y Biomedicina “López-Neyra” de Granada. La síntesis se llevó a cabo en el sintetizador 3400 DNA Synthesizer (Applied Biosystems), siendo purificados posteriormente por HPLC.

Nombre oligonucleótido	Secuencia (5'→3')
1b-pT7-HCV1-16(+)	TAA TAC GAC TCA CTA TAG GGC CAG CCC CCG ATT GG
pT7+3Gs+HCV44-59(+)	TAA TAC GAC TCA CTA TAG GGC CTG TGA GGA ACT ACT
HCV 41->22(-)	AGT GAT CTA TGG TGG AGT GT
HCV 370->351(-)	TTT CTT TGA GGT TTA GGA TT
HCV 553-570 (-)	CCC AGG CCC TGC CCT CGG
HCV 381-402 (-)	CCT GTG GGC GGC GGT TGG TGT
Oligo d(A)-anchor primer	GAC CAC GCG TAT CGA TGT CGA CAA AAA AAA AAA AAA AAA

PCR anchor primer	GAC CAC GCG TAT CGA TGT CGA C
Semi-caset	GAA CCG GAC CGA AGC CCG
caset+HCV402->383 (-)	GAA CCG GAC CGA AGC CCG ATT TGG ATC CGG CGA ACC GGA TCG ACC TGT GGG CGG CGG TTG GTG
HCV312-293(-)	ACT CGC AAG CAC CCT ATC AG
HCV 542->522(-)	CTT GGG GAT AGG CTG TCG CCT
HCV121-140(-)	TGG CTC TCC CGG GAG GGG GG
HCV332-313(-)	TCT ACG AGA CCT CCC GGG GC
HCV336-317(-)	ACG GTC TAC GAG ACC TCC CG
HCV338->319(-)	GCA CGG TCT ACG AGA CCT CC
HCV 358->339(-)	TTA GGA TTC GTG CTC ATG GT
HCV 370->351(-)	TTT CTT TGA GGT TTA GGA TT
HCV 390->371(-)	GGT TTG TGT TAC GTT TGG TT
CSFV63-34(-)+T7(19-1)	CTA GAC CAA ATC GAA ATT TAG TGT ATC CAA CCT ATA GTG AGT CGT ATT A
mir-122 DNA	TGG AGT GTG ACA ATG GTG TTT GT
T7-miR122	ACA AAC ACC ATT GTC ACA CTC CAC TAT AGT GAG TCG TAT TA
T7+miR122 (MUT19-20)	ACA AAC ACC ATT GTC ACA TAC CAC TAT AGT GAG TCG TAT TA
T7+miR122 (MUT19-22)	ACA AAC ACC ATT GTC ACA TAT TAC TAT AGT GAG TCG TAT TA
T7+miR122 (MUT16-22)	ACA AAC ACC ATT GTC TAT TAT TAC TAT AGT GAG TCG TAT TA
Let-7b DNA	TGA GGT AGT AGG TTG TGT GGT T
T7+3Gs+CrPV 1-16 (+)	TAA TAC GAC TCA CTA TAG GGA TGT GAT CTT GCT TGT
CrPV 185-165 (-)	AGC AGG TAA ATT TCT TAG GT

--	--

Oligonucleótidos de RNA sintéticos

Los oligorribonucleótidos utilizados fueron sintetizados por las casas comerciales IDT (miR-122 y Seed1 mir-122), Dharmacon (HCV 68-100) y Exiqon (let-7b) purificados por HPLC.

Nombre oligonucleótido	Secuencia (5'→ 3')
miR-122	UGG AGU GUG ACA AUG GUG UUU GU
Seed1 miR122	UGG AGU GUG A
Let-7b	UGA GGU AGU AGG UUG UGU GGU U
HCV 68-100	GCAGAAAGCGUCUAGCCAUGGCGUUAGUAUGAG

Métodos

Métodos generales de microbiología

Cultivos bacterianos

En este trabajo se utilizó *E. coli* para todos los cultivos bacterianos. Los medios de cultivo líquidos consistieron en LB suplementado con un antibiótico para favorecer exclusivamente el crecimiento de las colonias portadoras del plásmido de interés. Los inóculos se incubaron en agitación a 37°C durante aproximadamente 16 horas. Los cultivos en medio sólido fueron sembrados en placas Petri de LB-agar suplementada con el antibiótico correspondiente, que fue administrado previo a su solidificación. Las placas sembradas fueron incubadas boca arriba durante 16 horas en una cámara termostaticada a 37°C.

En la mayoría de cultivos bacterianos líquidos y sólidos, el antibiótico suplementado fue Ampicilina a una concentración final de 50 µg/ml. A excepción de la cepa cultivada para extraer y purificar la RNasa Z que fue suplementada con kanamicina a una concentración final de 50 µg/ml y los cultivos de células competentes que no fueron suplementados con ningún antibiótico.

Criopreservación de cepas bacterianas

Para la congelación de cepas bacterianas se cultivaron 2-3 ml de medio LB durante 16 horas aproximadamente y conservadas en crioviales de 2 ml con glicerol al 30%. A -80°C.

Preparación de células termocompetentes.

1. Sembrar por estrías una alícuota de células competentes *E.coli* cepa DH5α en una placa de LB-agar sin antibiótico e incubar 14-16 horas a 37°C.
2. A partir de varias colonias aisladas, inocular 300 ml de LB sin suplementar y crecer en agitación a 37°C hasta que el cultivo alcance un valor de densidad óptica medido a 600nm de 0.6 unidades (tiempo aproximado de 3 horas).

3. Repartir el cultivo en botellas de polipropileno para centrifuga de 250 ml de capacidad atemperadas en hielo. Centrifugar las células a 4300 rpm durante 10 minutos a 4 °C.
4. Descartar el sobrenadante. Resuspender y lavar el pelet de células con 6 ml de tampón TFBI/botella a 4°C y pasar a un tubo para centrífuga de 15 ml.
5. Incubar durante 10 minutos en hielo. Centrifugar a 4300 rpm durante 10 minutos a 4°C.
6. Eliminar muy bien el sobrenadante. Resuspender y lavar el pelet de células con 6 ml de tampón TFBII a 4°C.
7. Hacer alícuotas de 100µl y congelar en un baño de nieve carbónica-etanol. Almacenar a -80°C hasta su utilización.

Ligación de insertos de DNA en plásmidos bacterianos

La ligación de un inserto dentro de vectores plásmídicos se llevó a cabo mediante la enzima T4 DNA ligasa. Esta enzima cataliza la formación de un enlace fosfodiéster entre los extremos 5'-P y 3'-OH de moléculas de DNA de doble cadena. Generalmente, tanto el inserto de DNA y el vector, son digeridos con la misma enzima de restricción previo a la reacción de ligación.

A lo largo de todo el trabajo experimental, la mayoría de reacciones de ligación han sido llevadas a cabo para clonar un fragmento de DNA y posteriormente ser secuenciado, utilizándose para la ligación el vector *pGEM[®]-T Easy* (Promega). Este vector posee

El fragmento a secuenciar fue amplificado mediante PCR y purificado por extracción con fenol-cloroformo y precipitación con AcONa+glicógeno y etanol. La reacción de ligación se llevó a cabo en un volumen de 10 µl, siguiendo las instrucciones del fabricante: 50ng de *pGEM[®]-T Easy* vector en tampón de ligación rápida 1X (30mM Tris-HCl pH 7.8, 10mM MgCl₂, 10mM DTT, 1mM ATP, y un 5% de PEG), y 3U de T4 DNA ligasa (Promega). La relación molar entre inserto vector fue 5:1. La reacción se incubó durante toda la noche a 4°C.

Antes de proceder a la transformación de bacterias el enzima T4 DNA ligasa se inactivó mediante tratamiento por calor a 65°C durante 15min.

Transformación de *E. coli* con plásmidos recombinantes mediante choque

térmico

1. Descongelar en hielo una alícuota de bacterias competentes y añadir 10-100 ng del producto de ligación plasmídico de interés. Mezclar bien por pipeteo evitando la formación de burbujas.
2. Incubar en hielo durante 30 minutos, mezclando bien por pipeteo cada 10 minutos.
3. Someter las bacterias a un choque de calor incubando a 42°C durante 2 minutos e inmediatamente colocar en hielo. Incubar en hielo 10 minutos.
4. Recuperar las células con 400 µl de medio LB previamente atemperado a 37°C. Pasar la muestra a un tubo de cultivo.
5. Incubar en agitación (200rpm) a 37°C durante una hora. Este tiempo es necesario para que las bacterias expresen el gen de resistencia al antibiótico codificado por el plásmido. Sembrar en césped en placa Petri con medio selectivo (LA-Amp-IPTG-Xgal) un volumen comprendido entre 25-100µl del cultivo bacteriano. Incubar a 37°C durante unas 16 horas. Apareceran colonias blancas y azuladas, y las colonias blancas son las portadoras de nuestro plásmido con el inserto ligado.

Selección de colonias recombinantes de *E.coli*:

Para la selección de bacterias transformadas con un vector que porta el inserto de interés, sembraron en medio LA conteniendo ampicilina 50µg/ml, X-gal 40µg/ml e IPTG 150µg/ml.

Las bacterias transformadas fueron seleccionadas por la resistencia al antibiótico conferida por el plásmido, creciendo únicamente aquellas colonias que han incorporado el plásmido.

Las colonias recombinantes, que portaban el plásmido con el inserto ligado, se identificaron en función de su coloración, causado por la expresión diferencial del gen de la β -galactosidasa. La cepa bacteriana DH5 α es defectiva para la síntesis de $\beta\beta$ -galactosidasa al presentar deleciónado el gen que codifica para uno de sus péptidos, el péptido α . Los plásmidos que portan este gen restauran la expresión en las células transformadas mediante complementación genética. De manera que en presencia del sustrato cromogénico X-gal y del agente inductor del operón lactosa IPTG, las células transformadas expresan $\beta\beta$ -galactosidasa correctamente y procesan el X-gal, generando un compuesto insoluble de color azul, apareciendo colonias azules. El sitio de clonación múltiple plásmidos vectores, se sitúa dentro del marco abierto de lectura del gen del péptido α , por lo que en los plásmidos recombinantes que contienen un inserto, la pauta de lectura del gen *lacZ* se encuentra alterada y no se expresa la $\beta\beta$ -galactosidasa, apareciendo colonias que crecen con su habitual color blanco.

Extracción de DNA plasmídico.

La extracción y purificación de plásmidos de la cepa bacteriana correspondiente fueron realizadas mediante minipreparación:

- Utilizando el kit comercial *High Pure plasmid Isolation kit* (Roche) según las instrucciones del fabricante.
- A través del servicio de secuenciación del Instituto de Parasitología y Biomedicina “López-Neyra” de Granada, mediante el kit comercial *QIAprep Spin Miniprep kit* (Qiagen).

Secuenciación de DNA

La secuenciación de las muestras de DNA fue realizada por el servicio de secuenciación del Instituto de Parasitología y Biomedicina “López-Neyra” de Granada. Se realizó mediante el procedimiento de secuenciación cíclica utilizando la química *BigDye Terminator v3.1* y electroforesis en sistema de capilar múltiple automático. El equipo utilizado fue el secuenciador *3130XL-Genetic Analyzer* de *Applied Biosystems*.

A lo largo de este trabajo únicamente se utilizó la línea celular HeLa. El crecimiento a gran escala de células HeLa se llevó a cabo para la extracción y purificación de subunidades ribosomales.

Descongelación de células

1. Descongelar un vial de células, conservado en un tanque de nitrógeno líquido, durante 2 minutos en un baño a 37°C. Tener cuidado de no dejar descongeladas mucho tiempo las células debido a la presencia de DMSO en el medio de congelación, que resulta mortal para las células en estado líquido.
2. Llevar las células a un tubo de plástico para centrífuga e inmediatamente diluir y lavar con 10 ml de medio de cultivo, añadido muy despacio para evitar que sufran las células. Mezclar muy bien.
3. Centrifugar durante 1500 rpm a temperatura ambiente (aproximadamente 21°C).
4. Descartar sobrenadante mediante aspiración por vacío. Resuspender el pelet de células con 5-6 ml de medio, añadido despacio y sin formar burbujas.
5. Pasar los 5-6 ml de células a una placa de petri 6 cm de diámetro, tratada para la adecuada adhesión de células. Esta placa fue llamada pase 0 (P.0).
6. Incubar en un incubador de células a 37°C con un aporte continuo de CO₂.

Mantenimiento de una línea celular (pases)

Los cultivos celulares en crecimiento fueron chequeados diariamente mediante un microscopio de transmisión, para ser transferido a otro contenedor (flask) cuando alcanzaron una confluencia de aproximadamente 90-95%. Se debe trabajar con células en condiciones de esterilidad y para ello todo el material debe estar autoclavado y trabajar en una cabina de flujo laminar. Todas las soluciones deben estar atemperadas a 37°C.

Se muestra el ejemplo para el pase de un flask T25 a otro flask T25:

1. Retirar el medio de cultivo del flask mediante aspiración por vacío, por la cara opuesta a la crecen las células.

2. Lavar las células con 5 ml de PBS 1X y retirarlo por la cara opuesta a las células.
3. Despegar células con 0.5 ml de tripsina, incubada durante 3-5 minutos en el incubador a 37°C, sin exceder ese tiempo debido a que la tripsina es una proteasa y puede dañar las membranas celulares. Para facilitar el desprendimiento de células de la cara del flask donde están adheridas, dar unos pequeños golpes en los laterales del flask.
4. Inactivar la tripsina añadiendo 10 veces el volumen añadido de tripsina (5 ml). Mezclar bien.
5. Tomar aproximadamente 1 ml de medio con células y pasar a otro flask T25 (volumen para obtener el óptimo de confluencia aproximadamente tras 3 días de incubación). Completar con medio de cultivo hasta 10 ml. Incubar a 37°C.

Según el tamaño del flask utilizado (T25, T75 y T175), los volúmenes en el pase varían:

	Volumen PBS	Volumen Tripsina	Volumen medio cultivo	Volumen medio cultivo total
T25	5 ml	0.5 ml	5 ml	10 ml
T75	10 ml	1 ml	10 ml	20 ml
T175	20 ml	2 ml	20 ml	40 ml

Congelación y recuento de células

1. Se partió de un cultivo celular con una confluencia del 90-95% de números de pases bajos (P.2-P.4), para disminuir las probabilidades de contaminación.
2. Eliminación del medio mediante aspiración por vacío. Lavar las células con PBS.
3. Retirar el PBS y despegar las células con tripsina.
4. Inactivar tripsina con medio de cultivo.
5. Llevar todo el medio de cultivo con células a un tubo de plástico estéril y contar el número de células mediante una cámara de Neubauer. Para ello se toman 10 μ l de cultivo y se coloca en la cámara. Deben contarse el número de células que hay en las cuatro cuadrículas que posee la cámara y hacer la media de las cuatro

medidas. Ese valor multiplicado por 10^4 corresponde al número de células que hay por ml de cultivo.

6. Centrifugar todo el cultivo celular a 1500 rpm durante 5 minutos a 20°C .
7. Eliminar el sobrenadante por aspiración con vacío. Resuspender el pelet celular con tanto volumen como sea necesario para repartir todo el pelet celular en crioviales con $1.5 \cdot 10^6$ células:
8. Inmediatamente incubar los crioviales durante 30 minutos en hielo.
9. Congelar los crioviales durante 24 horas a -80°C y posteriormente preservar en nitrógeno líquido.

Métodos generales de biología molecular

Electroforesis de ácidos nucleicos

Geles de agarosa

Los geles de agarosa se prepararon del 1-2% (p/v) (Promega) en tampón TAE 1X. Las muestras se cargaron en presencia de tampón de carga no desnaturizante 1X para geles de agarosa. La electroforesis se desarrolló en tampón TAE 1X a un voltaje comprendido entre 80-150V. Una vez finalizada la electroforesis, los geles fueron teñidos con una solución de bromuro de etidio en agua a una concentración de $0.5 \mu\text{g/ml}$, desteñidos y visualizados en un transiluminador convencional con luz ultravioleta.

Geles de poliacrilamida desnaturizantes:

Para su elaboración se utilizó una solución de poliacrilamida al 40% compuesta por monoacrilamida:bisacrilamida en una proporción 19:1 (Sigma/National Diagnostics). Los geles se prepararon entre el 4-10% de poliacrilamida (p/v), en TBE 1X ó 0.5X y 7M de urea. El porcentaje del gel fue determinado en función del tamaño del fragmento sujeto a estudio. Como iniciadores de la reacción de polimerización se emplearon una solución de persulfato de amonio al 0.08% (p/v) (Sigma) y TEMED al 0.08% (v/v) (Sigma). Las muestras se prepararon en tampón de carga desnaturizante

1X. La electroforesis se desarrolló en tampón TBE 1X (reacciones de UV), ó 0.5X (para el resto de ensayos) a un amperaje de 25-35mA aproximadamente, durante un tiempo variable en función de la longitud del RNA analizado y la capacidad resolutive del gel.

Geles de poliacrilamida nativos:

Para la elaboración de los geles de acrilamida nativos se empleó la misma solución de monoacrilamida:bisacrilamida que para las condiciones desnaturalizantes, y se disolvió en cada uno de los tampones nativos 1X, según el ensayo a realizar. El porcentaje de acrilamida empleado fue del 4-6% (p/v). Como catalizadores de la reacción de polimerización se utilizaron persulfato de amonio y TEMED, tal y como se describe en el apartado anterior. Tras las diferentes reacciones, las muestras se prepararon en tampón de carga nativo 2X para los ensayos de interacción entre RNA de HCV y el miR-122, tampón de carga nativo sin magnesio 2X para los ensayos de cambios de conformación en función del Mg^{2+} y en tampón de carga formado exclusivamente por glicerol para los ensayos de unión con la subunidad ribosomal 40S. Fueron conservadas en hielo hasta su posterior carga en gel. Antes de cargar las muestras se realizó una pre-electroforesis de 30min con una intensidad de corriente de 12mA. La electroforesis se desarrolló en tampón nativo 1X, a 4°C en cámara termostatizada, manteniendo un amperaje constante de 12mA. El tiempo de carrera osciló entre 3-17 horas, según el ensayo.

Autorradiografía:

Los experimentos procedentes de geles de acrilamida con moléculas marcadas con P^{32} , fueron visualizados mediante autorradiografía. Fueron expuestos dentro de un casete BioMax (Kodak) con pantalla intensificadora BioMax MS (Kodak) en presencia de una película de doble emulsión Super-RX (FUJIFILM). Los casetes se almacenaron a -80°C el tiempo necesario para la observación de los resultados. Las películas de radiografía fueron reveladas en un revelador Curix 60 (Agfa). Los geles fueron secados sobre papel Whatman a 80°C en condiciones de vacío cuando fue necesaria la cuantificación de los resultados. En estos casos los geles secos se expusieron en un casete *Storage Phosphor Screen* (GE Healthcare) y se visualizaron usando el escáner *Typhoon 9400* (Amersham Biosciences). En el caso de geles de poliacrilamida de 155 o

superiores, no pudieron ser secados y fueron expuesto directamente sobre un soporte plástico inerte que adhiere perfectamente el gel.

Electroforesis de proteínas

Los geles de proteínas fueron preparados en condiciones desnaturalizantes para la detección y evaluación de la pureza de la RNasa Z en su proceso de purificación. Se utilizó una solución de poliacrilamida al 30% formada por monoacrilamida:bisacrilamida en una relación 29:1. Se utilizaron vidrios de electroforesis para geles de 10 cm x 10 cm x 0.75 mm. Los geles fueron preparados en dos fases con dos concentraciones diferentes de acrilamida para una mejor resolución de las proteínas. La fase inferior (fase de separación) fue preparada a una concentración del 10% en presencia de 1.5 M de Tris-HCl pH 8.8 y la fase superior (fase de concentración) a una concentración de 5% en presencia de 1 M de Tris-HCl pH6.8. Primero se polimerizó la fase de separación y luego sobre ella, fue polimerizada la fase concentradora. En ambos casos, la polimerización se llevó a cabo en presencia de 10% SDS en presencia de los catalizadores de la reacción de polimerización APS al 0.025% p/v) y TEMED al 0.004% (v/v). Las muestras se prepararon en tampón de carga para geles de proteínas 2X y la electroforesis se llevó a cabo en el tampón carrera para geles de proteínas 1X a 150 V constantes. Tras la carrera, las diferentes bandas proteicas fueron visualizadas al teñir y lavar los geles con las soluciones Fairbanks A, B, C y D.

Purificación de ácidos nucleicos

Los ácido nucleicos fueron purificados por extracción con fenol y precipitación con etanol. Ambas técnicas se utilizan para la eliminación de proteínas presentes en las reacciones, y para cambio de tampón.

Fenolización

La muestra se llevó a un volumen final de 100-200µl con agua estéril (Braun Medical). Se agregó un volumen igual de fenol saturado en cloroformo y alcohol isoamílico (Invitrogen), en el caso de tratarse de moléculas de DNA, o fenol saturado

en agua (Invitrogen), para el caso de moléculas de RNA. Las dos fases se mezclaron mediante agitación con *vortex* durante 1min, y fueron nuevamente separadas por centrifugación a 12000 rpm, durante 4 min a temperatura ambiente. Se tomó la fase acuosa, la superior, y se pasó a un tubo limpio. Seguidamente se realizó un lavado de la fase orgánica con otros 100-200 μ l de agua, repitiendo el proceso descrito.

Precipitación con etanol

La fase acuosa resultante fue precipitada añadiendo en este orden: 10% del volumen de reacción con acetato de sodio 3M pH 5.2 con 0.2 μ g/ μ l de glicógeno, y 2.5 volúmenes de etanol absoluto frío (Merck). La mezcla se mantuvo a -20°C toda una noche o durante 1 hora a -80°C. Transcurrido este tiempo se centrifugó a 12000 xg durante 1hora. Se retiró el sobrenadante y el precipitado se secó por centrifugación a vacío durante 5min. El sedimento fue resuspendido en un volumen apropiado de agua estéril durante 2 minutos con vórtex.

Transcripciones *in vitro*

Transcripción estándar

La reacción de transcripción se llevó a cabo en un volumen final de 25 μ l. La mezcla de reacción incluye 1-2 μ g de DNA molde, 1.4U/ μ l de T7 RNA polimerasa (Promega) en el tampón de reacción suministrado por la casa comercial 1X (40mM Tris-HCl pH 7.9, 6mM MgCl₂, 2mM espermidina, 10mM NaCl), 0.4mM de cada uno de los rNTPs (Promega), 4mM DTT (Promega), y 20U de RNasin® Plus (Promega). La reacción fue incubada durante un tiempo comprendido entre 1-4 horas a una temperatura de 37°C.

Para fragmentos de RNA comprendidos entre 20-500 nucleótidos de longitud, que no fueron necesarios tener marcados internamente con radiactividad, se empleó el kit comercial *MEGAscript® T7* (Ambion) siguiendo las recomendaciones del fabricante, mejorando el rendimiento de la reacción de transcripción.

En los casos en los que se precisó la síntesis de cantidades elevadas de RNA sin marcaje radiactivo, se hizo uso del kit *AmpliScribe™ T7-Flash™ Transcription Kit* (Epicentre) siguiendo las recomendaciones del fabricante.

Transcripción a partir de oligonucleótidos de DNA

En las transcripciones para obtener el miR-122 y sus respectivos mutantes mut1, mut-2 y mut-3, se emplearon oligonucleótidos de DNA que portaron la secuencia completa del promotor de la T7 RNA polimerasa (T7-miR122 *wt*, T7-miR122 (Mut 1), T7-miR122 (Mut 2), T7-miR122 (Mut 3)) hibridados como molde para la reacción de transcripción. En estos casos las reacciones se realizaron en un volumen final de 50µl. Se partió de 2µg del oligonucleótido molde correspondiente y del oligonucleótido promotor T7 complementario. La cantidad de ambos oligonucleótidos se ajustó para estar presentes en cantidades equimoleculares. Los dos oligonucleótidos fueron calentados durante 1 minutos a 90°C de forma paralela al tampón de transcripción. Se agregó el tampón caliente sobre la mezcla de oligonucleótidos, y se mantuvo a temperatura ambiente durante 15 minutos para un correcto plegamiento. Transcurrido este tiempo se incorporaron el resto de componentes para una reacción de transcripción estándar.

Digestión del DNA molde con DNasa RQ1

Tras la reacción de transcripción en cualquiera de los casos anteriores, se llevo a cabo la digestión del molde de DNA incubando la reacción de transcripción en presencia de la enzima DNasa RQ1 (Promega) durante 15 minutos a 37°C. Se empleó 1U de DNasa por cada microgramo de DNA molde utilizado en la reacción de transcripción. En los casos de transcripciones con kits comerciales se utilizó la propia DNasa suministrada en cada uno de los kits.

Purificación de los productos de transcripción

Los productos de transcripción fueron purificados siguiendo el protocolo que se detalla a continuación:

1. Fenolización: tras la reacción de digestión con la DNasa RQ1 añadir 975µl de TSE 1X y 500µl de fenol saturado en agua (Invitrogen) en tubos *eppendorfs* siliconizados de 2ml. Agitar en *vortex* durante 1min y posteriormente centrifugar a 11000rpm, a temperatura ambiente durante 4 minutos. Recoger la fase acuosa e incorporar 1 volumen de etanol frío (~1ml). Mezclar bien.

2. Cromatografía de afinidad en columnas de CF-11: La purificación a través de columnas de celulosa fosfato CF-11 (Whatman) permite eliminar sales, nucleótidos no incorporados en la reacción y seleccionar para su elución exclusivamente el RNA de simple cadena. Se llevó a cabo tras todas las transcripciones excepto para los oligonucleótidos de RNA, que presentan un tamaño demasiado pequeño para ser retenidos por la resina. Siendo exclusivamente purificados a partir de un gel de poliacrilamida. En aquellos oligonucleótidos de RNA que no pudieron ser purificados mediante gel (RNA-X para reacción de unión con ribosomas), se realizó una cromatografía por exclusión de tamaños con través de columnas de Sephadex-G25.

Preparación de las columnas: Se introduce en una jeringa de vidrio de 1 ml (RUTHE-Normax) introducir algodón hidrófobo estéril (horneado). Fijar la jeringa sobre un soporte y añadir aproximadamente 0.2 ml de resina CF-11 (Whatman) convenientemente preparada. Dejar compactar por decantación durante 20 min evitando que se seque. Transcurrido este tiempo la columna se equilibra dejando pasar las siguientes soluciones, previamente desgasificados a vacío durante 20 min, en este orden:

- a) 1ml de TSE 1X
- b) 1ml de agua
- c) 3ml de TSE-1X:EtOH (relación 1:1)

Elución del RNA:

- a) Pasar los 2ml de muestra de uno en uno e ir recogiendo fracciones de 1ml en *ependorfs* normales.
- b) Lavar la columna con 3ml de TSE-1X:EtOH. Recoger los 3 ml en otros 3 tubos *ependorf* normales.
- c) Eluir el transcrito con 2ml de agua en dos tubos *ependorfs* de plástico siliconizado. Cuando se hayan recogido las 7 fracciones de la columna, para el caso de las moléculas de RNA marcadas radiactivamente con ^{32}P , chequear los tubos con un contador Geiger-Müller. Una elución

correcta implica el siguiente orden de recuperación del material radiactivo medido en cuentas por segundo (CPS): la obtención de la mayor cantidad de CPS en los dos primeros mililitros de elución (lo que corresponde a nucleótidos radiactivos no incorporados), un descenso acusado durante los lavados, con un mínimo de CPS en el quinto mililitro de elución. Finalmente el número de CPS debe ascender de forma acusada en el sexto y séptimo tubo, lo cual corresponde a la molécula de RNA marcada eluída en agua.

Los dos últimos eppendorfs recogidos tras la cromatografía (~ 2 ml)tubo), donde el RNA está eluido en agua, se pasaron a un tubo COREX siliconizado para la precipitación de RNA con 10% de su volumen de acetato sódico 3M pH 5.2 con glicógeno a 0.2µgr/µl, y 2.5 volúmenes de etanol frío. Mezclar bien y dejar 1 noche a -20°C ó 1 hora a -80°C. Centrifugar a 4°C durante 90 min a una velocidad de 10000 rcf. Eliminar el sobrenadante y secar el precipitado de RNA en un frasco secador conectado a vacío durante 5-10 minutos. Resuspender el precipitado en 10µl de agua y 20µl de tampón desnaturalizante de carga en geles de acrilamida, mediante agitación en *vortex* durante 10 minutos.

3. Purificación en gel de poliacrilamida desnaturalizante:

La muestra de transcripción resuspendida en agua y tampón de carga desnaturalizante se cargó en un gel de poliacrilamida 7M urea de 0.4mm de grosor. Los vidrios de electroforesis fueron previamente siliconizados para facilitar el desmolde del gel. Para aquellos RNAs marcados radiactivamente Las bandas se visualizaron por autorradiografía y se recortaron del gel como se detalla a continuación:

- a) Una vez terminada la electroforesis desmontar el gel retirando una sola placa de vidrio. Cubrir la superficie del gel con film transparente y fijar con cinta adhesiva los bordes. Hacer unas etiquetas con tinta radiactiva y repartirlas por los márgenes del gel, junto con las flechas que indiquen el fondo de los pocillos y la migración de los colorantes.

- b) Exponer el gel con 2 películas de doble emulsión Super RX (FUJIFILM) superpuestas dentro de un casete durante el tiempo necesario para su observación (5-10 minutos). Revelar las películas de autorradiografía.
- c) Enmarcar con un rotulador, en una de las dos películas, las bandas que interesa recortar. Cortar el trozo de película para dejar una ventana. Solapar la película con el gel original haciendo uso de las etiquetas. Recortar las bandas de acrilamida usando un bisturí estéril. Las bandas de acrilamida se sumergen en 2ml de tampón T1-1X en un tubo COREX (para depositarlas dentro del líquido se emplean espátulas horneadas). Los tubos se dejan en agitación toda una noche a temperatura ambiente.

Aquellos RNAs que no fueron marcados con radiactividad, fueron purificados de gel utilizando una placa de silicagel forrada con un plástico tipo Saran-wrap donde fue desmoldado el gel. Tras una corta exposición de pocos segundos con una lámpara de radiación UV a 254 nm (UV-C) fueron visualizadas y extraídas las bandas de RNA. Las bandas fueron eluidas en tampón T1-1X, como se describió en el párrafo anterior.

Finalmente, se pasaron los 2ml de tampón T1-1X, que contienen el RNA eluido de las bandas de acrilamida, utilizando una pipeta Pasteur de vidrio estirada y siliconizada. Precipitar en tubo COREX añadiendo un 10% de su volumen de AcNa 3M pH 5 con glicógeno a 0.2µgr/µl, y 2.5 volúmenes de EtOH frío. Mezclar y dejar 1 noche a -20°C o 1 hora a -80°C. Centrifugar a 4°C durante 90min a una velocidad de 10000rcf. Eliminar el sobrenadante y secar el precipitado de RNA en un frasco secador conectado a vacío durante 10 minutos. Resuspender el precipitado en 20µl de agua y guardar a -20°C hasta su posterior utilización.

Marcaje radiactivo de ácidos nucleicos

Marcaje interno:

El marcaje a lo largo de la cadena de RNA se realizó mediante la incorporación de 40µCi (4µl) del isótopo radiactivo GTP[α-³²P], a la mezcla de reacción para la transcripción estándar. El producto de transcripción se purificó según se detalla en el apartado anterior.

Marcaje en el extremo 5':

Marcaje en 5' de RNAs largos durante la reacción de transcripción

El marcaje de RNAs largos en su extremo 5' se realizó mediante la incorporación de 40 μ Ci (4 μ l) del isótopo radiactivo GTP[γ -³²P] a la mezcla de reacción de transcripción estándar, acompañado de una disminución en la concentración de rGTP (0.1mM) dentro de la mezcla de rNTPs. El producto de transcripción se purificó como se detalló anteriormente.

Marcaje en 5' de oligonucleótidos de DNA o RNA

- Oligonucleótidos sintéticos: Los oligonucleótidos de DNA o RNA sintéticos no contienen fosfato en su extremo 5' por lo que es innecesaria su desfosforilación previa. La reacción de fosforilación se realizó en un volumen final de 10 μ l, conteniendo entre aproximadamente 60pmoles de oligonucleótido a marcar, 1U/ μ l de T4 polinucleótido quinasa (NEB) en el tampón suministrado por la casa comercial 1X (70mM Tris-HCl pH 7.6, 10mM MgCl₂, y 5mM DTT), y 30 μ Ci (3 μ l) del isótopo ATP[γ -³²P] o GTP[γ -³²P]. La reacción se incubó durante 1hora a 37°C, tiempo tras el cual se inactivó el enzima por calor a 65°C durante 20min. La purificación de las moléculas marcadas se realizó como se detalló anteriormente.

- Productos de digestión de RNA y RNAs procedentes de transcripción *in vitro* que deben ser marcados en su extremo 5': En estos casos los RNAs presentan un extremo 5'-fosfato o 5'-trifosfato, respectivamente, por lo que deben ser desfosforilados previo a su marcaje mediante fosforilación.
 - Las reacciones de desfosforilación se llevaron a cabo de dos maneras:
 - Mediante la fosfatasa alcalina intestinal de ternera (CIAP) (*Promega*) para la eliminación de todos los fosfatos en 5'. Los productos de reacción a desfosforilar fueron incubados durante 30 minutos a 37°C con 0.4 U/ μ l de CIAP en presencia de un

tampón de reacción que contenía 10 mM MgCl₂, 100mM Tris-HCl pH7.4.

- Mediante la fofafasa alcalina de gamba (USB) para la eliminación de un único fosfato en 5', de manera que en extremos 5'-trifosfato debe realizarse un tratamiento previo con la pirofosfatasa ácida de tabaco (TAP) (*Epicentre*). La reacción se llevó a cabo con 0.5 U/μl de la TAP en un volumen final de 50μl, incluyendo una fracción del producto de digestión de RNA con extremo 5'-trifosfato, en presencia de un tampón suministrado por la casa comercial a 37°C durante 1h. El tratamiento con la SAP realizó en un volumen final de 10μl sobre el RNA 5' monofosfato, 0.1U/μl de SAP y el tampón de reacción suministrado por la casa comercial 1X (20mM Tris-HCl pH 8, 10mM MgCl₂). La reacción fue incubada durante 7 minutos a 37°C para evitar efectos degradativos en el RNA por acción de la fosfatasa.

Al finalizar las reacciones de desfosforilación, tanto la CIAP como la TAP fueron inactivadas mediante extracción fenólica con fenol:cloroformo y la SAP fue inactivada por tratamiento a 65°C durante 15 minutos. En todos los casos, el producto de reacción fue precipitado y resuspendido en 10μl de agua antes de realizar la fosforilación del RNA.

- La reacción de fosforilación se efectuó en un volumen final de 10μl. La mezcla de reacción consistió en 5μl de la reacción de desfosforilación anterior, 1U/μl de T4 polinucleótido quinasa (NEB) en el tampón suministrado por la casa comercial a concentración 1X (70 mM Tris-HCl pH 7.6, 10 mM MgCl₂, y 5 mM DTT), y 15 μCi (1.5μl) de ATP[γ-³²P]. La reacción fue incubada durante 7 minutos a 37 °C. Se inactivó el enzima calentando a 65°C durante 20 min. El producto de reacción fue precipitado y resuspendido en 10 μl de agua.

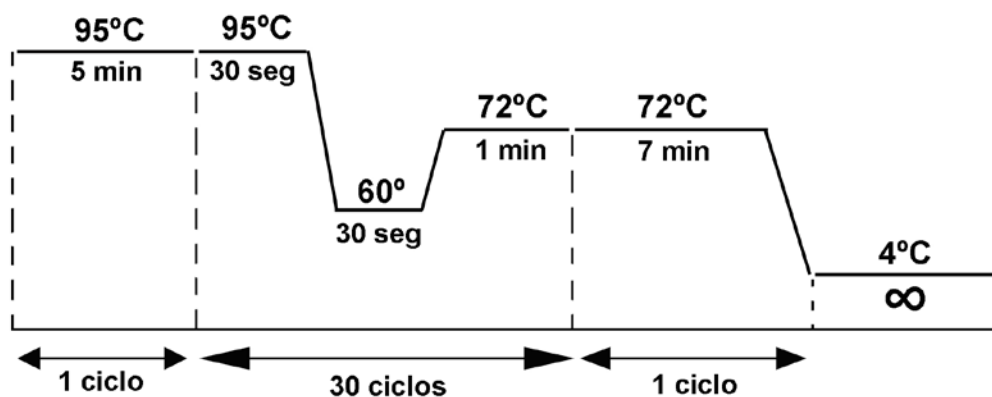
Marcaje en el extremo 3'.

El marcaje del RNA en su extremo 3' se llevó a cabo en un volumen final de 10µl, mediante incorporación de 40µCi (4µl) del isótopo radiactivo pCp[5'-³²P] en una mezcla de reacción que incluyó 2-3µg de RNA, 2U/µl de T4 RNA ligasa (Promega) en el tampón de reacción suministrado por la casa comercial 1X (50mM Tris-HCl pH 7.8, 10mM MgCl₂, 5mM DTT, y 1mM ATP), 2U/µl de RNasin®Plus (Promega), 0.01% BSA, y 1% PEG. La reacción se mantuvo durante 4 días a 4°C. Transcurrido este tiempo, la reacción se sometió a tratamiento con proteinasa K (descrito a continuación) y posterior precipitación con etanol. Después se llevó a un volumen final de 100µl con agua, se añadieron 900µl de TSE 1X y 1000µl de etanol y se sometió a cromatografía de afinidad con la resina CF11 y posterior purificación a partir de gel de poliacrilamida, como fue detallado anteriormente para el proceso de transcripción *in vitro*.

Amplificación de ácidos nucleicos: Reacción en cadena de la polimerasa (PCR)

Las reacciones de amplificación de DNA mediante PCR se llevaron a cabo en el termociclador iCycler (Bio-Rad) a partir de 10-50 ng de DNA molde en un volumen de reacción de 50-100 µl. En la mezcla de reacción se incluyó 1.5 U de la enzima DNA polimerasa AmpliTaq®Gold (*Applied Biosystems*) en el tampón de reacción *PCR Buffer II* 1X (10mM Tris-HCl pH 8.3, 50mM KCl) suministrado por la casa comercial, 1.5mM de MgCl₂ (Roche), 0.2mM de cada uno de los dNTPs (mezcla de Roche) y 20 pmoles de cada uno de los oligonucleótidos que actúan como cebadores en la reacción.

El protocolo estándar de amplificación empleado fue el siguiente:



No obstante, cada uno de los parámetros de la reacción de PCR fueron optimizados según las condiciones para cada reacción: el número de ciclos de desnaturalización, anillamiento y extensión, la temperatura de hibridación de los cebadores, y los tiempos de anillamiento y extensión.

Los productos de PCR fueron visualizados en gel de agarosa TAE 1X teñido con bromuro de etidio y purificados mediante extracción fenólica y precipitación con etanol.

Retrotranscripción (RT)

La reacción de retrotranscripción se llevó a cabo en un volumen final de 20 μ l sobre una fracción de RNA molde en presencia de 1 μ M de un oligonucleótido de DNA específico de secuencia que actúa de cebador. El RNA molde y el oligonucleótido fueron desnaturalizados juntos durante 1 min a 90°C y renaturalizados en presencia del tampón de reacción 1X (50mM Tris-HCl pH 8.5, 8mM MgCl₂, y 30mM KCl) (Roche) durante 15 min a temperatura ambiente. Transcurrido ese tiempo se añadió 20U de RNasin®Plus (Promega), mezcla de dNTPs a 1 mM (Roche), 10 ng/ μ l del RNA MS2 (Roche), y 10 U de retrotranscriptasa (Roche). La incubación se desarrolló a 55°C durante 30 min y al finalizar se inactivó el enzima calentando 5min a 85°C.

En los casos en los que la temperatura de anillamiento del oligonucleótido cebador fue demasiado baja con respecto a la temperatura de incubación de la RT de Roche, se empleó la transcriptasa inversa del virus de la mieloblastosis aviar (AMV). Este fue el caso concreto de los productos de las reacciones de poliadenilación y poliuridilación, donde se emplearon los oligonucleótidos dT-Pst y dA-Pst para la síntesis del cDNA, respectivamente. En estas ocasiones las reacciones se llevaron a cabo en un volumen de 20 μ l con la siguiente composición: 5 μ l de producto de la reacción de poliadenilación o poliuridilación, 1 μ M del oligonucleótido cebador, 20 U de RNasin®Plus (Promega), mezcla de dNTPs a 1mM (Roche), y 15 U de enzima AMV RT (USB) en el tampón proporcionado por el fabricante 1X (50mM Tris-HCl pH 8.3, 8mM MgCl₂, 50mM NaCl, 1mM DTT). La incubación se realizó a 37°C durante 30min.

Cuantificación de ácidos nucleicos

Cuantificación de DNA y RNA no marcados radiactivamente

La concentración de los ácidos nucleicos en solución fue determinada mediante el espectrofotómetro *NanoDrop*[®] ND-1000 (Nucliber) gracias a la capacidad cromófora que presentan los anillos aromáticos de las bases nitrogenadas a 260 nm. La concentración se calculó por determinación de la D.O. a 260 nm de la muestra problema.

Cuantificación del RNA marcado internamente con GTP[α -³²P]

La concentración de los transcritos radiactivos marcados internamente con GTP[α -³²P] se determinó calculando la cantidad de isótopo radiactivo incorporado en la reacción, en base a las medidas en CPM (cuentas por minuto) obtenidas en el contador de radioisótopos *Quick Count 2000* (Bioscan). Para ello se aplicó la siguiente fórmula matemática:

$$\frac{\mu\text{gr } rNTPs}{\frac{CPM}{\mu\text{l}} \text{ GTP} [\alpha -^{32} P] \times \mu\text{l GTP} [\alpha -^{32} P]} = \frac{\mu\text{gr transcrito}}{\frac{CPM}{\mu\text{l}} \text{ transcrito}}$$

La primera parte de la ecuación corresponde a los microgramos de ribonucleótidos no radiactivos agregados a la reacción de transcripción, y el valor en CPM/ μl del GTP[α -³²P] incorporado en la reacción de transcripción. La segunda parte de la ecuación corresponde a los datos del RNA transcrito *in vitro*: el valor en microgramos del transcrito sintetizado (incógnita a despejar), y el valor en CPM/ μl obtenido para dicho transcrito.

Cuantificación de proteínas

La cuantificación de proteínas se realizó mediante espectrofotometría con el espectrofotómetro *NanoDrop*[®] ND-1000 (Nucliber). A diferencia de los ácidos nucleicos, las proteínas absorben a 280 nm, de manera que la concentración de las proteínas problema se calculó a una D.O de 280 nm.

Digestión de ácidos nucleicos: DNA

El DNA puede ser degradado de manera inespecífica mediante DNasas, concretamente en la realización de este trabajo, se utilizó exclusivamente la DNasa RQ1, que ya fue descrita anteriormente en el apartado de transcripción; y de manera específica

mediante enzimas de restricción que cortan en secuencias dianas específicas de cada tipo de enzima:

- Finalidad puramente analítica (ej. Determinación de plásmidos recombinantes): Se partió de 300 ng de DNA sustrato.
- Finalidad preparativa (molde de transcripción *in vitro*): Se emplearon 10 ng de DNA.

Por regla general se usaron 3U de enzima por microgramo de DNA a digerir, teniendo en cuenta que el volumen de enzima no excediese el 10% del volumen total de la reacción. El tampón de reacción fue el suministrado por la casa comercial (NEB, Fermentas y ROCHE) a concentración 1X. La reacción de incubación se realizó en estufa a 37°C en un tiempo comprendido entre 1hora-1 noche y transcurrido este tiempo os enzimas fueron inactivados por tratamiento con calor según las indicaciones del fabricante. Se chequeó la digestión del DNA mediante electroforesis en gel de agarosa y tinción con bromuro de etidio de una alícuota de la reacción antes de proceder a su purificación. La purificación se realizó mediante extracción fenólica y precipitación con etanol.

Digestión de proteínas: tratamiento con proteinasa K y SDS

La proteinasa K es una serín proteasa de amplio espectro que se utilizó en combinación con el dodecilsulfato sódico (SDS), un surfactante empleado como detergente, en la eliminación de proteínas capaces de interferir en la visualización de los resultados por electroforesis en gel de poliacrilamida, y garantizar la inactivación de diferentes enzimas. La proteinasa K fue diluida a una concentración final de 1µg/µl y activada por calor a 63°C durante 5 min. Tras la activación, la reacción se llevó a cabo en un volumen final de 10µl de reacción con 0.6µl de proteinasa K (1µg/µl) en presencia de 5µg de tRNA de levadura (Ambion), 0.7µl de SDS al 10%, 0.7µl de EDTA a 100mM pH 8. Tras 12 minutos de incubación a 63°C, la mezcla fue precipitada con etanol y resuspendida en 10µl de agua.

Métodos para la detección de la naturaleza química de extremos 5' y 3' en el RNA

Fosforilación de extremos 5'-P

La naturaleza 5'-OH de los extremos de RNA se determinó mediante la reacción de fosforilación con la T4 PNK en presencia de ATP[γ - 32 P], previamente descrita en el apartado de marcajes en extremo 5'.

Ligación de moléculas de RNA con extremos 5'-P y 3'-OH

La determinación de fragmentos de RNA que poseen extremos 5'-P y 3'-OH se realizó mediante ligación con la T4 RNA ligasa, mediante la ligación de dos fragmentos de RNA o la circularización de un fragmento largo de RNA con extremos 5'-P y 3'-OH. La reacción se llevó a cabo como se mostró en el apartado de marcaje de extremos 3' del RNA. Tras el periodo de incubación de la reacción, se realizó un tratamiento con proteinasa K y SDS.

Reacción poliadenilación del RNA

La enzima Poli(A)-RNA polimerasa de *E.coli* cataliza la incorporación de AMP en el extremo 3'-OH de un RNA, a partir de ATP. Esta técnica fue utilizada para la determinación de la composición química de los extremos 3' tras el autocorte del RNA de HCV en presencia de la luz UV-C. Los fragmentos de RNA sujetos a análisis fueron tratados con 5U de Poli(A) polimerasa (NEB) en el tampón de reacción suministrado por el fabricante 1X (50mM Tris-HCl pH 7.9, 250mM NaCl, 10mM MgCl₂) en presencia de ATP[α - 32 P] en un volumen final de 20 μ l. La mezcla de reacción fue incubada durante 10 min a 37°C y tras finalizar ese tiempo, fue llevada a un volumen total de 100 μ l con agua para ser sometida a extracción fenólica y precipitación con etanol.

Esta reacción también se utilizó para la identificación de la región de corte de la RNasa Z y las posiciones de corte de la RNasa H para la determinación de las nuevas regiones de unión del microRNA miR-122. En estos casos, las reacciones de poliadenilación se llevaron a cabo de manera idéntica, pero se utilizó 1 mM de ATP.

Reacción de poliuridinación del RNA.

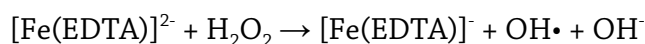
La enzima Poli(U) polimerasa cataliza la adición independiente de molde de UMP al extremo 3' de un RNA, a partir de UTP. En este caso el enzima recombinante

en *E.coli* procede de *Schizosaccharomyces pombe*. En el presente trabajo se empleó en paralelo a las reacciones de la Poli(A) RNA polimerasa en los mismos ensayos.

Los fragmentos de RNA sometidos a análisis fueron incubados con 2U de Poli(A) polimerasa (NEB) en el tampón de reacción suministrado por el fabricante 1X (10mM Tris-HCl pH 7.9, 50mM NaCl, 10mM MgCl₂, y 1mM DTT) en presencia de UTP[α-³²P] ó 0.5 mM UTP, según el tipo de ensayo, en un volumen final de 25 µl. Tras 10 min a 37°C se llevó a un volumen total de 100 µl con agua para ser sometida a extracción fenólica y precipitación con etanol.

Reacción de fenton

La reacción de Fenton consiste en la generación de radicales libres OH• y OH⁻ a partir del H₂O₂ al reaccionar con una solución de [Fe(EDTA)]²⁻:



Estos ensayos fueron realizados para determinar si el autocorte específico producido en el RNA de HCV por radiación de la luz UV-C fue ocasionado por la generación de radicales libres en el ambiente molecular del RNA o por acción directa en el RNA de HCV.

La reacción de fenton se llevó a cabo en un volumen final de 10 µl en un RNA sustrato precalentado en agua durante 1 min a 90°C en paralelo al tampón de reacción P humana 5X y seguidamente se pusieron en contacto. La mezcla se dejó renaturalizar a temperatura ambiente durante 15min y trascurrido ese tiempo se incorporó a la reacción 100mM de MgCl₂ y 2-4 µg/µl de tRNA de levadura. A continuación se añadieron los reactivos de la reacción fenton con la mayor rapidez posible respetando el orden siguiente: solución Fe(II)EDTA, H₂O₂ y ascorbato de sodio. La mezcla se incubó durante 2 min a temperatura ambiente y se paró con 1 µl de Tiourea y 9 µl de tampón de carrera para geles de poliacrilimida desnaturalizantes 2X. Los productos de reacción fueron visualizados en gel en paralelo a las reacciones de corte del UV-C en RNA-HCV.

Espectrometría de masas (MALDI-TOF)

La espectrometría de masas es una técnica que permite conocer la composición química de moléculas orgánicas mediante un proceso de ionización producido por un láser que permite la fragmentación de los elementos químicos. La naturaleza de los extremos generados en el RNA de HCV por el corte específico con la radiación UV-C fue analizada por el servicio de proteómica del Instituto de Parasitología y Biomedicina “López-Neyra” de Granada, utilizando un MALDI-TOF Voyager DE-PRO (Applied Biosystems)

Métodos para el estudio de la estructura del RNA

Reacciones con la RNasa H

La ribonucleasa H corta de manera específica el RNA de dúplex DNA/RNA con una extensión mínima de 4 pares de bases, produciendo extremos 5'-P y 3'OH {Donis-Keller, 1979 #790; Eun, 1996 #791}.

Lo ensayos de corte con la RNasa H se realizaron para la determinación de las nuevas posiciones de unión del miR-122 y para estudios conformacionales locales según la accesibilidad del enzima. Las reacciones se realizaron con oligonucleótidos de DNA de aproximadamente 20 nucleótidos de longitud complementarios a las regiones sujetas a estudio, en un volumen final de 10 µl que incluía 0.6 nM del RNA sustrato en tampón P humana 1X, 20U de RNasin® Plus (Promega), 2µg de tRNA de levadura (Ambion), 0.5U/µl de RNasa H de *E.coli* (Ambion). Los oligonucleótidos de DNA fueron utilizados a tres concentraciones finales: 15nM, 150nM y 1500nM. Algunos ensayos se realizaron en presencia de oligonucleótidos de RNA que fueron utilizados en las mismas concentraciones que los oligonucleótidos de DNA. Tras un periodo de incubación de 1 hora a 37°C, se detuvo la reacción añadiendo tampón de carga para geles de poliacrilamida desnaturalizantes. Los productos fueron desnaturalizados y resueltos por electroforesis en geles de poliacrilamida desnaturalizantes. Los resultados se visualizaron por autorradiografía.

Nucleasas específicas de estructuras tipo-tRNA

Reacciones con la ribozima de la RNasa P de *Synechocystis sp.* (RZ6803)

La ribozima de la cianobacteria *Synechocystis sp.* (RZ6803) se obtuvo por transcripción *in vitro* a partir del DNA plasmídico pT76803-Dra I empleando el kit comercial MEGAscript®T7 (Ambion).

Previo a la reacción de corte, el RNA sustrato se desnaturalizó por calor durante 1min a 90°C y fue replegado en presencia del tampón P humana 5X durante 15 min a temperatura ambiente. La reacción se realizó en un volumen final de 15.5 µl compuesto por tampón RZ Cianobacteria 1X, 20U de RNasin®Plus (Promega), un 4% de PEG, 1M KCl, el RNA sustrato a una concentración de 1.8nM final y la ribozima a concentración de 1.2 nM y 67.5nM final para el RNA sustrato natural y HCV, respectivamente. La ribozima precisó de una preincubación de 15 min a 37°C, en el medio de reacción sin sustrato, para su correcto plegamiento. Transcurrido este tiempo se incorpora el RNA sustrato y se incuba a 37°C durante 1 hora. Las reacciones se detuvieron en hielo con tampón de carga para geles de poliacrilamida desnaturalizantes. Debido a la gran cantidad de sales del medio reactivo, no se realizó desnaturalización previa a la carga en gel.

Reacciones con la RNasa P humana

Las reacciones de corte con la RNasa P humana se realizaron en un volumen final de 10 µl, conteniendo 0.9nM del RNA sustrato en tampón P humana 1X, 20U de RNasin®Plus (Promega), un 4% de PEG, y 0.5µl del extracto purificado con actividad RNasa P humana. El RNA sustrato y el tampón de reacción fueron precalentados durante 1min a 90°C de forma paralela antes de ser puestos en contacto. Tras su unión, la mezcla se dejó renaturalizar a temperatura ambiente durante 15min. Transcurrido este tiempo se incorporaron el resto de componentes de reacción. Tras un periodo de incubación de 1 hora a 30°C, las muestras fueron sometidas a un tratamiento con proteinasa K y SDS a 63°C, como se describió anteriormente. Los productos de corte fueron resuspendidos en agua y tampón de carga y desnaturalizados antes de ser resueltos por electroforesis en geles de poliacrilamida desnaturalizante. Los resultados se visualizaron por autorradiografía.

Reacciones con la RNasa Z de *E. coli*

Cada reacción de corte con la RNasa Z se realizó en un volumen final de 10 μ l. 4.2 nM del RNA sustrato y el tampón de reacción RNasa Z 5X se calentaron en paralelo durante 1 min a 90°C y fueron puestos en contacto para la renaturalización del RNA durante 15 min a temperatura ambiente. Transcurrido ese tiempo se añadió 40U de *RNasin[®] Plus* (Promega) y 1 μ l de una dilución 1/9 del extracto de purificación de la RNasa Z. La mezcla fue incubada durante 1 hora a 37°C y los productos de corte fueron desnaturalizados durante 1 min a 90°C antes de ser resueltos por electroforesis en geles de poliacrilamida desnaturalizante. Se visualizó mediante autorradiografía.

Métodos enzimáticos y químicos para el estudio de la estructura del RNA

Para la determinación de cambios en la estructura secundaria y terciaria del RNA se emplearon diferentes agentes:

- Enzimáticos: RNasa T1, RNasa V1 y RNasa A
- Químicos: Dimetil sulfato e hidrólisis alcalina

La finalidad de estos ensayos fue conocer los cambios en la accesibilidad de cada uno de estos agentes por el RNA de HCV para determinar cambios conformacionales en su estructura y la determinación de nuevas posiciones de unión del miR-122.

Para este tipo de ensayos se emplearon transcritos *in vitro* marcados radiactivamente en su extremo 5' ó 3'. La concentración concreta de cada enzima se determinó mediante ensayos previos de calibración. Los productos de degradación se separaron por electroforesis en geles de poliacrilamida desnaturalizantes al 10 ó 15% 0.4 mm de grosor, manteniendo una potencia constante de 25W durante la carrera. Para evitar el sobrecalentamiento durante la carrera, se utilizaron unas placas de aluminio disipadoras de calor. Los geles fueron sometidos a una pre-electroforesis de 20min antes de cargar la muestra en cada pocillo. Tras la carrera, los geles fueron secados a vacío y visualizados mediante autorradiografía.

RNasa T1

La RNasa T1 procede de *Aspergillus oryzae*. Cataliza la hidrólisis en 3' del enlace fosfodiéster de las guaninas desapareadas, generando extremos 5'-OH y 3'-P, a través de intermediarios 2'-3'-P cíclico {Ehresmann, 1987 #789;Eun, 1996 #791}.

La digestión del RNA con la RNasa T1 se realizó de manera parcial en condiciones nativas o desnaturizantes. En ambos casos el protocolo seguido es diferente.

En la digestión parcial en condiciones nativas se utilizó 300CPM de RNA sustrato marcado radiactivamente que se precalentó en paralelo al tampón de reacción durante 1min a 90°C antes de ser puestos en contacto. Tras su unión, se dejó renaturalizar la mezcla a temperatura ambiente durante 15min. La reacción se realizó en un volumen final de 10 µl, e incluyó el RNA sustrato en tampón P humana 1X, 2 µg de tRNA de levadura (Ambion), y RNasa T1 (Calbiochem) a una concentración final 0.0001-0.0005 µg/µl de, según el tamaño del fragmento utilizado en cada ensayo. Transcurrido este tiempo se incorporaron el resto de componentes. La reacción se incubó a 37°C durante 20min, y se detuvo inmediatamente en un baño de nieve carbónica en etanol después de añadir tampón de carga para geles de poliacrilamida desnaturizante.

Las reacciones de degradación parcial con RNasa T1 en condiciones desnaturizantes (escalera de T1) se realizaron en un volumen final de 10µl, compuesto por 100-300 CPM de RNA sustrato, 6 µl de tampón para degradación con RNasa T1 en condiciones desnaturizantes, 1 µg de tRNA de levadura (Ambion) y RNasa T1 a una concentración final de 0.001µg/µl. La reacción fue incubada durante 5 min a 55°C, e inmediatamente después precipitada agregando 90µl de agua, dos volúmenes y medio de etanol y un 10% de acetato de sodio con glicógeno. Después de 60min a -20°C, la muestra fue centrifugada a 4°C durante 60min a 13200rcf. Los precipitados se resuspendieron en tampón de carga para geles de poliacrilamida desnaturizantes.

RNasa V1

La RNasa V1 procede de veneno de cobra (*Naja oxiana*). Es una endonucleasa que procesa regiones de RNA de doble cadena con un tamaño mínimo aproximado de 4-5 pares de bases, sin preferencia de secuencia. También reconoce ribonucleótidos desapareados en conformación apilada {Knapp, 1989 #745;Ehresmann, 1987 #789}.

Los productos de corte poseen extremos 5'-P y 3'-OH {Ehresmann, 1987 #789; Lowman, 1986 #416}.

La reacción de digestión se realizó de manera parcial en condiciones nativas en un volumen final de 10 µl. Previo a la reacción, 100-300 CPM de RNA sustrato y el tampón de reacción P humana 1X (concentración final) fueron precalentados durante 1min a 90°C de forma paralela antes de ser puestos en contacto. Transcurrido este tiempo se incorporaron el resto de componentes de la reacción: 2µg de tRNA de levadura (Ambion), y 0.001U/µl de RNasa V1 (Ambion). La reacción se incubó a 37°C durante 30min y se paró en un baño de nieve carbónica en etanol después de añadir tampón de carga para geles de poliacrilamida desnaturizantes.

RNasa A

La RNasa A procede de páncreas bovino y cataliza la hidrólisis del enlace fosfodiéster en 3' de las bases pirimidínicas C y U que se encuentren desapareadas. Los productos de corte generados son 5'-OH y 3'-P a través de intermediarios 2'-3'-P cíclico {Eun, 1996 #791}.

La reacción de digestión con la RNasa A se realizó de manera parcial y total.

La digestión parcial se llevó a cabo para la determinación de cambios estructurales por la unión del miR-122. Al igual que en las reacciones de digestión con T1 y V1, en antes de nada, el 100 CPM del RNA sustrato se precalentó y renaturalizó en el tampón P humana 1X. A continuación, se incluyeron el resto de componentes: 2 µg de tRNA de levadura (Ambion), y 0.0005ng/µl de RNasa A (Ambion) en un volumen total de 10µl. La reacción se incubó a 37°C durante 2min, y se detuvo inmediatamente en un baño de nieve carbónica en etanol después de añadir tampón de carga para geles de poliacrilamida desnaturizante.

La reacción de digestión total con la RNasa A se llevó a cabo para determinar la secuencia del RNA de HCV unida a la subunidad ribosomal 40S. Para ello, se añadió 0.05 µg/µl de RNasa A en el producto de unión del RNA sustrato con la subunidad 40S en volumen final de 40 µl. La reacción fue incubada durante 7.5 min en hielo. El producto de digestión fue suplementado con 250 µl el tampón de dilución y cargado en un gradiente de sacarosa de 15-30%. Tras una centrifugación a 45000 rpm a 4°C

durante 2 h, se fraccionó y se determinaron las fracciones protegidas mediante el contador de radioisótopos *Quick Count 2000 (Bioscan)*, recogiendo las medidas en CPM.

Hidrólisis alcalina del RNA

La reacción de hidrólisis alcalina sobre el RNA se realizó en un volumen final de 10 μ l que incluyó 200-600CPM del RNA sustrato marcado en uno de sus extremos, 1 μ g de tRNA de levadura (*Ambion*) y en último lugar se incorporó 1 μ l de una solución de carbonato-bicarbonato sódico 100mM a pH 9.5. La reacción se incubó a 95°C durante 60-120 seg, según el tamaño del RNA a analizar y se detuvo inmediatamente en un baño de nieve carbónica en etanol tras añadir tampón de carga para geles de poliacrilamida desnaturalizante.

Dimetil sulfato (DMS)

El dimetil sulfato es un agente químico capaz de incorporar un grupo metilo en las bases nitrogenadas de adenina y citosina, e incluso en ciertas guaninas muy reactivas, que se encuentren en simple cadena, e impidiéndose en el caso de aquellas bases hibridadas en doble cadena o unidas con otro tipo de moléculas (proteínas, RNAs, DNAs...). El uso de DMS permite el estudio de la estructura secundaria y terciaria del RNA, además de posibles interacciones con otras moléculas.

La reacción de metilación con DMS se llevó a cabo en un volumen final de 20 μ l e incluyó 2 μ g de RNA sustrato sin marcar en tampón P humana 1X, 2 μ g de tRNA de levadura (*Ambion*) y 1 μ l de una dilución 1/5 (v/v) de DMS (*Sigma*) en etanol, preparada inmediatamente antes de su uso. El RNA sustrato y el tampón de reacción fueron precalentados durante 1 min a 90°C por separado y puestos en contacto para su retaturalización durante 20 min a temperatura ambiente. Transcurrido este tiempo se añadió el resto de componentes de la mezcla. La reacción se incubó durante 1 min a 20°C e inmediatamente se detuvo en hielo. Tras subir el volumen total de la reacción a 100 μ l con agua, se realizó una precipitación con etanol y dos lavados con etanol al 70%. Finalmente se resuspendió en 10 μ l de agua (Fernández-Miragall O. RNA 2003) (Romero-López C. Nucleic Acids Research 2012).

Los productos de reacción del tratamiento con DMS fueron analizados mediante “*Primer Extension*”. Para ello, se realizó una retrotranscripción con la

retrotranscriptasa *Superscript III* (Invitrogen) en presencia de un oligonucleótido de DNA marcado en su extremo 5'. La reacción se realizó en 1-2 µl de RNA metilado, previamente incubado con 1 pmol de oligonucleótido de DNA durante 2 min a 70°C. La temperatura de la reacción se hizo bajar hasta 52°C y se incorporó 2 U de RNasin® Plus (Promega), 0.5 mM dNTPs, 5mM DTT, tampón de retrotranscripción 5X y 10 U de retrotranscriptasa *SuperScript III*. La reacción se incubó durante 1h a 52°C y transcurrido ese tiempo se inactivó la enzima durante 15 min a 70°C. Los productos de la retrotranscripción fueron resueltos en gel de 10% de acrilamida desnaturante en paralelo a una secuenciación realizada mediante el kit *Termo Sequenase Cycle Sequencing* (USB) según las indicaciones del fabricante.

Reacción de corte específico en RNA con luz UV

La reacción de corte del RNA con la luz UV se hizo siguiendo el protocolo clásico para inducir *crosslink* en el RNA. Para su realización se utilizó una lámpara de radiación UV-C *UVP Inc. Mineralight®* (modelo UVG-11, de emisión de UV-C a 254 nm, 220V, 60Hz y 0.16 A).

La reacción se llevó a cabo en 250-1000 CPM de RNA sustrato marcado radiactivamente disuelto en 10 µl de tampón de corte con UV 1X. La mezcla se depositó en forma de gota sobre la lámpara de UV, previamente recubierta por un plástico saran-wrap (que deje pasar la luz UV) y enfriada durante 20 min. Las gotas fueron sometidas a 6 ciclos de 30 seg de exposición intercalados por 30 seg sin exposición para evitar el calentamiento de la muestra. Transcurrido este tiempo, el producto irradiado fue resuelto en gel de acrilamida desnaturante del 4-15% y visualizado mediante autorradiografía. En algunos casos, los productos irradiados fueron purificados de gel para posteriores análisis.

Métodos de asociación con el RNA

Ensayos de asociación en geles nativos

Unión de un oligonucleótido

Para caracterizar los cambios conformacionales que experimentan algunas moléculas estudiadas en este trabajo, se realizaron ensayos de unión con diferentes oligonucleótidos.

La reacción de hibridación se llevó a cabo en un volumen de 10 μ l compuesto por 0.6nM del RNA sujeto a estudio en tampón P humana 1X y el oligonucleótido indicado a concentración variable. El RNA sustrato fue desnaturizado y renaturalizado en el tampón de reacción del mismo modo descrito en los protocolos anteriores. En ciertos casos la molécula portadora del marcaje radiactivo fue el RNA sustrato y en otros ensayos fue el oligonucleótido. Transcurrido el tiempo de hibridación se añadió tampón de carga no desnaturizante para geles de poliacrilamida e inmediatamente se dejó en hielo a la espera de ser cargado en gel de electroforesis en condiciones nativas en una cámara refrigerada a 4°C. El cambio conformacional se apreció como un retraso en la movilidad electroforética de las moléculas marcadas.

En ensayos de asociación en geles nativos sin magnesio, el procedimiento fue el mismo, pero utilizando tampones y soluciones en ausencia de magnesio.

Unión de la subunidad ribosomal 40S

Los ensayos de unión de un RNA sustrato con subunidades ribosomales 40S se llevaron a cabo en condiciones nativas. Las condiciones de reacción fueron ajustadas para estudiar los cambios conformacionales del RNA de HCV al interactuar con la subunidad 40S. Para ello, se utilizó un tampón de reacción P humana 1X con 4mM AcO_2Mg . La reacción de unión se realizó en un volumen final de 10 μ l en un RNA sustrato a concentración final de 0.6 nM, previamente desnaturizado durante 1 min a 90°C y renaturalizado durante 15 min a temperatura ambiente en el tampón de reacción precalentado en paralelo. Transcurrido ese tiempo se añadió extracto de purificación de la subunidad ribosomal 40S de células HeLa a una concentración final comprendida entre 0.5 nM y 180 nM, y 500 ng del RNA-X sin marcar, para evitar resultados de interacciones inespecíficas. La reacción de hibridación se incubó durante 20 min a 37°C, excepto para el RNA-CrPV que se realizó a temperatura ambiente. Transcurrido ese tiempo, se añadió tampón de carga para geles de unión con 40S 2X e

inmediatamente, se dejó en hielo para ser cargado con la mayor brevedad posible en un gel de acrilamida en condiciones nativas al 4% de 0.8 mm de grosor, realizado con tampón TBM 1X. La electroforesis se llevó a cabo durante 3 h a 12 mA constantes en una cámara refrigerada a 4°C. El resultado se visualizó mediante autorradiografía.

Método de extracción y purificación de la RNasa Z de *E. coli*

Para la purificación de la RNasa Z se utilizaron 400 ml de cultivo de *E. coli* recombinante con el plásmido pUGK3, en LB+Kan. Cuando el cultivo alcanzó una D. O. de 0.6, se reincubó con IPTG durante 3 h a 37°C, para inducir la síntesis de la proteína. Transcurrido ese tiempo se llevó a cabo la lisis celular, extracción y purificación de la RNasa Z siguiendo el siguiente procedimiento:

1. Centrifugar a 6000 rpm durante 15 min a 4°C. Decantar y lavar el *pellet* bacteriano en 50 ml de tampón de resuspensión y lisis, previamente enfriado en hielo.
2. Centrifugar en las mismas condiciones anteriores. El *pellet* puede ser congelado en este punto a -20°C. Resuspender el *pellet* en 2 ml de tampón de resuspensión y lisis suplementado por gramo de *pellet*..
3. Sonicar las suspensiones con un sonicador, con mucho cuidado de no realizar espuma, a 20W en tres ciclos de 20 seg con intervalos de descanso de 60 seg.
4. Centrifugar a 15000 rpm durante 30 min a 4°C. Incubar el sobrenadante durante 1 h a 4°C. Guardar 40 µl en tampón de carga para proteínas para analizar en gel SDS-PAGE.
5. Realizar una cromatografía de afinidad mediante columna de resina Ni-NTA Agarosa (Qiagen) a una temperatura de 4°C:
 - 5.1. Acondicionar y equilibrar la resina:
 - Mezclar 35 ml de resina homogeneizada en 3 ml de tampón de resuspensión/lisis suplementado (sin inhibidor de proteasas)
 - Centrifugar la mezcla a durante... a 4°C. Eliminar el sobrenadante.
 - Mezclar e incubar el lisado durante 1 h a 4°C.
 - Preparar la columna en una jeringa de plástico estéril. Dejar precipitar durante... a 4°C.

- 5.2. Lavar la resina con 15 ml de tampón de lavado 1. Conservar a 4°C para analizar en gel SDS-PAGE.
 - 5.3. Lavar la resina con 15 ml de tampón de lavado 2. Conservar a 4°C para analizar en gel SDS-PAGE.
 - 5.4. Eluir la columna con 2 ml de tampón de elución y recoger en dos tubos *eppendorf*.
 6. Dializar la elución en bolsas de diálisis en tampón B durante toda una noche a 4°C. Transcurrido ese tiempo, guardar a -20°C (nunca a -80°C debido a que la RNasa Z se desnaturaliza e inactiva a temperaturas inferiores a -20°C).
- El grado de pureza se analizó en gel de proteínas desnaturizante SDS-PAGE, donde se resolvieron cada una de las fracciones obtenidas durante la purificación.

Método de extracción y purificación de subunidades ribosomales 40S de células HeLa

La purificación de las subunidades ribosomales se realizó a partir de 400-500 ml de cultivo de células HeLa (12 flasks de T175) cuando alcanzó una confluencia de 100%. Se llevó a cabo la **lisis celular** siguiendo el protocolo que se detalla a continuación:

1. Lavar las células con PBS 1X
2. Extraer células mediante tratamiento con tripsina.
3. Inactivar la tripsina con medio DMEM suplementado.
4. Obtener el pelet celular mediante centrifugación a 1500 rpm durante 5 min a temperatura ambiente. Retirar el sobrenadante mediante extracción por vacío.
5. Resuspender y lavar el pelet en 10 volúmenes de tampón Isotónico refrigerado a 4°C y suplementado con un cuarto de pastilla de inhibidor de proteasas *Complete* (Roche).. 1 volumen equivale al volumen de pelet obtenido tras la anterior centrifugación. A partir de este punto el protocolo se realiza en hielo
6. Centrifugar la suspensión a 1500 rpm durante 5 min a 4°C. Retirar el sobrenadante mediante extracción por vacío.
7. Resuspender el pelet en 1.5 volúmenes de tampón hipotónico e incubar en hielo durante 20 min.
8. Romper las células mediante un homogenizador *Dounce* con 25 strokes del émbolo. Recoger el lisado celular y suplementar con 0.2 volúmenes de tampón S10.

9. Centrifugar a 10000 rcf durante 10 min a 4°C para eliminar los núcleos y otros restos de membrana celular.
10. Recoger el sobrenadante y medir la concentración de proteínas del lisado S10, que debe estar comprendida entre 35-50 mg/ml con aspecto lechoso y viscoso. En este punto pueden congelarse las fracciones S10 en tubos *eppendorf* a -80°C.

A partir del lisado S10 se realizó la **extracción de ribosomas**:

1. Añadir el lisado S10 (~2 ml) a dos tubos tipo 42 con tapón de titanio de 12 ml que contiene en este orden: 2 ml de tampón A, 2 ml de tampón hipotónico, los 2 ml de lisado S10 y tampón hipotónico hasta completar el tubo. Cada una de las soluciones se deben añadir gota a gota con extremo cuidado para que no lleguen a mezclarse.
2. Centrifugar a 42000 rpm durante 4 h a 4°C en un rotor fijo ss-34 (70 Ti) y eliminar el sobrenadante. Se obtendrá un pelet transparente por tubo que contiene los ribosomas.
3. Resuspender cada pelet en 1 ml de tampón B, con cuidado de no realizar espuma.
4. Tratar la resuspensión con promicina una concentración final de 4 mM. Incubar durante 10 min en hielo. La Puromicina es aminonucleósido inhibidor de la traducción, conduciendo a la terminación del proceso y liberación de los mensajeros.
5. Incubar de nuevo a 37°C durante 40 min.
6. Suplementar con KCl a concentración final de 500 mM. Mezclar por inversión del tubo.
7. Separar las subunidades ribosomales en gradiente continuo de sacarosa del 10-30% de 12 ml:
 - 7.1. Añadir la solución con ribosomas en la parte superior del gradiente, con mucho cuidado de no romper el gradiente.
 - 7.2. Centrifugar en un rotor vasculante a 28000 rpm durante 17 h a 4°C.
8. Fraccionar el gradiente de sacarosa tomando fracciones de 400 µl desde arriba del tubo, con cuidado de no mezclar.
9. Medir la concentración de RNA de cada fracción mediante el espectrofotómetro *NanoDrop*[®] *ND-1000* (Nucliber) y detectar los picos correspondientes a las subunidades 40S y 60S, con valores $A_{260}/230 \geq 1.45$ y $A_{260}/280 \geq 1.85$.

10. Reunir y concentrar las fracciones correspondientes a la subunidad 40S en un filtro Amicon de 4 ml con un tamaño de poro de 10K, y las fracciones correspondientes al 60S en otro filtro amicon de 4 ml con tamaño de poro de K. Centrifugar a 4000 rcf durante 1h a 4°C.
11. Al alcanzar un volumen concentrado de 200 µl, añadir 4 ml de tampón C, y centrifugar a 4000 rcf a 4°C durante el tiempo necesario para tener un volumen final de 250 µl.

Al final de todo el proceso, las soluciones con 40S y 60S fueron cada una de ellas alicuotadas en tubos *ependorf* mantenidos en hielo y almacenadas a -80°C. La pureza de 40S y 60S se examinó mediante la detección de los rRNA mediante gel de agarosa al 1%.

Análisis bioinformático

Cuantificación de los ensayos obtenidos:

Para realizar la cuantificación del porcentaje de producto de digestión con las diferentes nucleasas y para conocer el porcentaje de complejo formado en los ensayos de unión de moléculas, se obtuvieron las imágenes necesarias usando el escáner *Typhoon 9400* (*Amersham Biosciences*). Los datos fueron analizados mediante el *software ImageQuant 5.2* (*Molecular Dynamics*). El porcentaje de corte o complejo fue calculado como el cociente:

$$\left(\frac{\text{productos de corte}}{\text{material de partida} + \text{productos de corte}} \right) \times 100$$

En caso de referirse a una banda producto particular:

$$\left(\frac{\text{banda producto Y}}{\text{material de partida} + \text{resto de bandas producto}} \right) \times 100$$

La normalización de los datos y la representación gráfica se realizó con ayuda del *software SigmaPlot 8.0* (*Systat*).

Análisis de ensayos termodinámicos:

Para la evaluación de la interacción entre dos moléculas de RNA, se calculó la constante de disociación (Kd) empleando el *software SigmaPlot 8.0*, los datos se ajustaron a una

hiperbola; y mediante el software *GraphPad 5.01* (Prism), los diferentes datos fijados fueron normalizados y representados en una curva sigmoïdal *Klotz plot* (*semi-log plot*)

Análisis de ensayos cinéticos:

Se realizaron análisis cinéticos de la unión del mir-122 con el RNA de HCV. Para ello, se evaluó la constante de velocidad observada (Kobs) a lo largo del tiempo respecto de la concentración de miR-122 libre. Los valores obtenidos fueron ajustados a una curva hiperbólica mediante la siguiente ecuación:

$$[Complexes] = [complexes\ max] * (1 - e^{-kobs * t})$$

Los valores de Kobs fueron determinados y representados mediante el *software SigmaPlot 8.0*.

Predicciones *in silico* de dianas para microRNAs:

Las predicciones de interacciones de miRNAs en la secuencia de RNA-HCV en estudio, se utilizó el servidor web *RNA hybrid* (Bibiserv).

RESULTADOS

***In vitro* characterization of a miR-122-sensitive double-helical switch element in the 5' region of hepatitis C virus RNA**

Rosa Díaz-Toledano^{1,2}, Ascensión Ariza-Mateos¹, Alex Birk³, Belén Martínez-García¹
and Jordi Gómez^{1,2,*}

¹Laboratorio de Arqueología del RNA, Departamento de Bioquímica y Biología Molecular, Instituto de Parasitología y Biomedicina 'López Neyra' Armilla 18100, Granada, Spain, ²CIBERehd and ³Institute for Hepatitis and Virus Research, Doylestown, Pennsylvania, 18902, USA

Received November 26, 2008; Revised June 12, 2009; Accepted June 12, 2009

ABSTRACT

It has been proposed that the hepatitis C virus (HCV) internal ribosome entry site (IRES) resides within a locked conformation, owing to annealing of its immediate flanking sequences. In this study, structure probing using *Escherichia coli* dsRNA-specific RNase III and other classical tools showed that this region switches to an open conformation triggered by the liver-specific microRNA, miR-122. This structural transition, observed *in vitro*, may be the mechanistic basis for the involvement of downstream IRES structural domain VI in translation, as well as providing a role of liver-specific miR-122 in HCV infection. In addition, the induced RNA switching at the 5' untranslated region could ultimately represent a new mechanism of action of micro-RNAs.

INTRODUCTION

In a linear genomic map, the hepatitis C virus (HCV) internal ribosome entry site (IRES) (domains II–IV, bases 40–368) (1) is flanked upstream by domain I (bases 1–40), which is recognized by a liver-specific microRNA (miR-122) that acts as an enhancer of replication (2) (Figure 1A). Evidence accumulated over the last 10 years indicates that IRES downstream sequences in the coding region, particularly in domains V and VI (bases 368–510) are important for viral viability (3–6) through an unknown RNA structure-dependent mechanism.

In the secondary structure representation, functional (5), structural (7) and phylogenetic (6) studies indicate that bases 428–442 within the coding region interact with the complementary 5' unstructured sequence, 24–38, forming a long-range annealing (LRA) motif that constrains the IRES in a closed 'C' conformation (Figure 1B and C) known to inhibit viral translation (5,6).

Alternatively, earlier work suggested a structure within the core-coding domain, called stem-loop VI, in which bases 428–442 are paired with bases 495–508 (8) (Figure 1B and C), yielding an open conformation, which is designated 'O' herein in contraposition to the 'C' conformation.

We hypothesized that switching between the alternative 'C' and 'O' structures could regulate the ability of an HCV RNA molecule to participate in various biological processes (7). This idea was favored by subsequent descriptions of interactions between the most abundant liver microRNA, miR-122 and the 22–28 HCV region (2). Because this region overlaps with sequence 24–38, which anneals at long distance with 428–442, we hypothesized that miR-122 would inhibit LRA formation and thus promote the structural transition to stem-loop VI. This study investigates this possibility.

MATERIALS AND METHODS

RNA transcripts

The DNA templates for HCV RNA transcripts were derived from the plasmid vector pN(1–4728) Bluescript, which contains nt 1–4728 of HCV, under the T7 promoter. All RNA transcripts include the first base of the HCV genome and end at positions 402 (Aat II NEB), 466 (PCR product) and 570 (Bln I NEB). The PCR product ending at base 466 was generated by amplification of pN(1–4728) with the upstream primer 5'-CGCGGATCC TAATACGACTCACTATAGGCGCCCGCCCGATTGGG GGCGA (which serves to introduce the T7 promoter in the PCR product) and the downstream primer 5'-GGGCC CCTGCGCGGCAACAG.

***In vitro* transcription and internal labeling**

To obtain internally labeled substrates for the cleavage assays, 1–2 µg of DNA template was transcribed *in vitro*

*To whom correspondence should be addressed. Tel: 958181647; Fax: 958181632; Email: jgomez@ipb.csic.es

for 1 h at 37°C with T7 RNA polymerase (Promega) and [α - 32 P]GTP (Perkin Elmer) followed by a 10-min treatment with 0.04 U/ μ l RNase-free RQ1 DNase I (Promega) at 37°C (9). Cellulose CF11 chromatography was used to eliminate DNA, dsRNA fragments and unincorporated nucleotides (10). Transcripts were then purified by gel electrophoresis under denaturing conditions on 4% polyacrylamide gels containing 7 M urea. Bands were visualized by autoradiography, excised from the gel and eluted in buffer (100 mM Tris-HCl, pH 7.5 and 10 mM EDTA, pH 7.5). The concentration of radioactive transcripts was determined by calculating the amount of incorporated [α - 32 P]GTP based on quick count measures.

The 21-base transcripts representing the wt miR-122 and mutants were synthesized according to a T7 RNA polymerase transcription protocol in a 50 μ l reactions overnight at 37°C (9). Synthetic DNA oligodeoxynucleotides used as transcription templates were obtained from the Instituto de Parasitología y Biomedicina (C.S.I.C) facility. Transcripts were labelled by the inclusion of a [α - 32 P]GTP labeled in the reaction mixture. Transcription reactions were subsequently subjected to RQ1 DNase I treatment, phenol extraction and ethanol precipitation. The transcripts were purified by electrophoresis in 10% polyacrylamide gel containing 7 M urea, and eluted and measured identically to larger *in vitro* transcripts.

5' end labeling

5' end-labeled RNA transcript was obtained in a standard transcription reaction with two differences, the labeled triphosphate nucleotide was [γ - 32 P]GTP (Perkin Elmer), and the concentration of cold GTP in the nucleotide reaction mix was lowered to a quarter of the standard amount. Subsequent purification was performed as described above.

3' end labeling

Unlabeled transcripts prepared in standard transcription reactions were subsequently reacted as follows: aliquots containing a molar ratio of 2:1 pmol of 5' [32 P]pCp (Perkin Elmer) with respect to unlabeled RNA were incubated with T4 RNA ligase (Amersham Bioscience). The reaction was carried out in 10 μ l of 50 mM Tris-HCl (pH 7.5), 10 mM MgCl₂, 10 mM DTT, 1 mM ATP, 0.01% BSA, 0.1% PEG, 20 U RNasin (Promega) and 4 U/ μ l T4 RNA ligase. The reaction mixture was incubated for 4 days at 4°C. The labeled RNA was purified again using the electrophoretic procedure described above.

RNase III cleavage assay

Escherichia coli RNase III is a nuclease specific for dsRNA (11,12). The salt and buffer conditions used in all our experiments on HCV RNA cleavage by RNase III were the same as those used previously to detect RNase P cleavage of a tRNA-like structure near the AUG start triplet (13); these are known as secondary conditions of cleavage for RNase III (14). HCV RNA substrate was pre-heated at 90°C for 1 min before addition of reaction buffer (10 mM HEPES-KOH [pH 7.5],

10 mM Mg[AcO]₂ and 100 mM NH₄[AcO]) and then left to cool down to room temperature. Cleavage reactions were performed with 20 U RNasin, and 0.0005 U/ μ l or 0.001 U/ μ l (final concentration [FC]) of *E. coli* RNase III (Ambion) in the presence of 2 μ g/ μ l of yeast tRNA (Ambion), and were carried out in a volume of 10 μ l at 37°C for 1 h. These optimal conditions were used in all the experiments and are referred to throughout the text as 'standard conditions'. However, when the reactions were performed in the presence of rabbit reticulocyte lysate (supplemented with a mixture of 0.01 mM aa minus Cys), RNA was extracted successively with phenol and chloroform/isoamyl alcohol and precipitated. The cleavage products were separated on 4% denaturing polyacrylamide gels and visualized by autoradiography on Kodak BioMax MR or Fuji Super RX film.

For the kinetic studies, samples were treated as above and scaled-up to 100 μ l reaction volumes. Aliquots of 10 μ l were drawn at 0, 10, 20, 30, 40, 50 and 60 min and analyzed on polyacrylamide gels, as described above. Product bands were quantified using a Storm PhosphorImager (Amersham-Pharmacia Biotech) as follows: percent RNase III cleavage product (A) = (A product)/(starting material + \sum products) \times 100. Fold increase of PIX was measured as: PIX product at 60 min in the desired conditions divided by PIX product in the control lane at 60 min, run in the same gel.

RNase H cleavage assay

The salt and buffer conditions used for *E. coli* RNase H (Ambion) digestion were the same as those used in the RNase III cleavage assay. HCV RNA substrate was pre-treated identically. Cleavage reactions were performed in the presence of 20-mer DNA oligodeoxynucleotides (15, 150 and 1500 nM) with 20 U RNasin in the presence of 2 μ g/ μ l of yeast tRNA (Ambion) and 0.5 U/ μ l of RNase H, and were carried out in a volume of 10 μ l at 37°C for 1 h. Cleavage products were separated on 4% denaturing polyacrylamide gels and visualized by autoradiography.

Analysis on non-denaturing gels

HCV RNA was prepared as described above. We compared the buffer and salt conditions commonly used for RNA conformation assays, which contain 20 mM Tris-Ac (pH 7.6), 10 mM MgAcO and 100 mM NaCl (TMN 1X), with our standard conditions. Our conditions provided similar or even better results; hence, they were selected for the subsequent reactions. In all cases, just before addition of the probe, 2 μ g of carrier tRNA was added per reaction. Annealing reactions were incubated for 1 h at 37°C and transferred to an ice bucket. The RNA was left on ice for at least 10 min before re-suspending in loading buffer, consisting of 60% glycerol, TMN 1 \times , 0.4 μ g/ μ l yeast tRNA, 0.4% (w/v) xylene cyanol, and 0.4% (w/v) bromophenol blue, and was then used for gel analysis. Non-denaturing gels were 0.8 mM thick and contained 6% polyacrylamide, 50 mM Tris-Ac, pH 8.3 and 10 mM MgAcO. The gels were run at constant amperage of 12 mA for 24 h at 4°C, and autoradiographed.

Structural mapping with the single- or double-stranded RNases, T1 and V1

Various concentrations were prepared of RNase T1 (Calbiochem) (0.01, 0.001, 0.0001, 0.00001 $\mu\text{g}/\mu\text{l}$) and RNase V1 (Ambion) (0.0005 and 0.001 U/ μl). Analytical amounts of 3' end-labeled ^{32}pCp 1–570 RNA with and without different probes were digested with these RNase fractions and the digestion products electrophoresed on a denaturing 4% and 10% 7 M urea-containing polyacrylamide gel. The optimal RNase T1 and V1 digestion conditions were found to be 0.0005 $\mu\text{g}/\mu\text{l}$ in a 20-min reaction and 0.001 U/ μl in a 30-min reaction at 37°C, respectively. Adequate band separation to detect all differences between the electrophoretic lanes was achieved when bromophenol blue dye reached 80% of the length of a 4% polyacrylamide-urea gel. These conditions were used for the subsequent analyses of 1–570 RNA alone or preincubated with the DNA or RNA probes at several concentrations before adding the nucleases T1 or V1. Preincubation was performed for 1 h at 37°C.

To allow identification of the cleavage sites, a parallel run was performed with a 3' end-labeled 1–570 RNA ladder generated with either limited alkaline hydrolysis or RNase T1 degradation in denaturing conditions. In the alkaline hydrolysis reactions, aliquots containing 10^4 c.p.m. of 3' end-labeled RNA were incubated with 2 μg of carrier tRNA in 0.2 M NaHCO_3 – Na_2CO_3 (pH 9) and 1 mM EDTA for 5 min at 90°C. The RNase T1 reaction in denaturing conditions was performed with similar amounts of labeled substrate in the presence of 7 M urea at 55°C for 5 min. All reactions were stopped with one volume of loading buffer and maintained in dry ice until loading on 4% polyacrylamide-urea sequencing gel.

RNA sequencing using RACE

Two bands from T1 RNase digestion gel were purified and sequenced by the Rapid Amplification of cDNA Ends (RACE) procedure (ROCHE 5'/3'RACE kit 2nd generation). 5' RACE reactions were performed according to the manufacturer's recommendations. The HCV-specific oligonucleotide used for first-strand cDNA synthesis was 5'-₅₄₂CTTGGGGATAGGCTGTGCGCT₅₂₂, and the one used for PCR was 5'-₅₂₁TCCACGGGGTTGCGACC GCT₅₀₂.

Synthetic RNA oligonucleotides

The complete miR-122 RNA sequence is 5'-UGGAGUG UGACAAUGGUGUUUGU. The underlined portion (5'-UGGAGUGUGA) is a 10-mer oligoribonucleotide containing the 7 nt of the seed sequence. The remaining portion (5'-CAAUGGUGUUUGU) is miR-122 RNA minus the seed sequence. All oligoribonucleotides used were synthesized by IDT Integrated DNA Technologies.

Protein quantification

Protein concentration was determined using the Bio-Rad protein microassay procedure (Bio-Rad Laboratories).

RESULTS

Detection of a new RNase III cleavage event in 1–570 RNA indicates the potential of this region to form an alternative RNA structure

Previous RNase III cleavage experiments involved a 570-base HCV RNA transcript (nt 1–570). Figure 1A is a schematic drawing of the 1–570 RNA fragment showing the final reaction products characterized (P1, P2 and P3), located according to their corresponding positions. The autoradiogram in Figure 2, lane 2, reproduces an RNase III cleavage of a 1–570 RNA substrate resulting in partial digestion products (P2P3 and P1P2) and complete digestion products (P1, P2 and P3). It was demonstrated that these cleavages are only possible after annealing of both IRES flanking sequences (7). In the course of that experiment, we observed an additional minor band that appeared in a time-dependent manner [Figure 7 in reference (7)], but was not examined at that time. The band, which has a mobility between the two large partial product bands, P2P3 and P1P2, becomes a prominent band in the gel when, as in the present case, the reaction is performed at a higher RNase III concentration. The appearance of this band, referred to herein as band 'X', and its partner product, band Y, which comprise the total 1–570-base transcript, can only be observed when nearly all the 1–570 substrate has been processed and P2P3 becomes a dominant high molecular weight band. We propose two possible explanations for this: (i) Band X may correspond to a less sensitive site for RNase III in 1–570 RNA fragments, or (ii) Band X could be the result of an additional cleavage of P2P3 by RNase III, which does not occur in the 1–570 RNA substrate. This second option would indicate the presence of alternative structures within 1–570 RNA.

To investigate potential structural transitions within 1–570 RNA, we set up a parallel enzymatic reaction of 1–570 RNA and a 5' truncated ~36–570 HCV RNA transcript (nearly identical in size to P2P3) with RNase III. We found that band X was the main product of the reaction with the truncated transcript, where LRA formation is impeded (Figure 2, lanes 3 and 4). This is the key result that indicates that band X is not a direct product of 1–570 RNA cleavage, but instead, is a product of P2P3 cleavage.

Additional support was provided by titration experiments with RNase III on 1–570 RNA and purified P2P3. These fragments were incubated in the presence of increasing concentrations of RNase III, and the resulting products were analyzed in parallel migration in gel electrophoresis. As is shown in Figure 3A lanes 3–6, RNase III cleaves 1–570 RNA to produce P2P3 at an enzyme concentration 10-fold lower than the concentration needed to release band X. In contrast, both gel-purified and endogenously produced P2P3 incubated with RNase III releases the X band at an enzyme concentration similar to that producing P2P3 from 1–570 RNA (Figure 3A). In addition, a correlation was found between P2P3 decrease and band X formation curves. This demonstrates that both the LRA motif and its alternative conformation form stable helices, equally sensitive to RNase III, and strongly indicates that band X derives from P2P3.

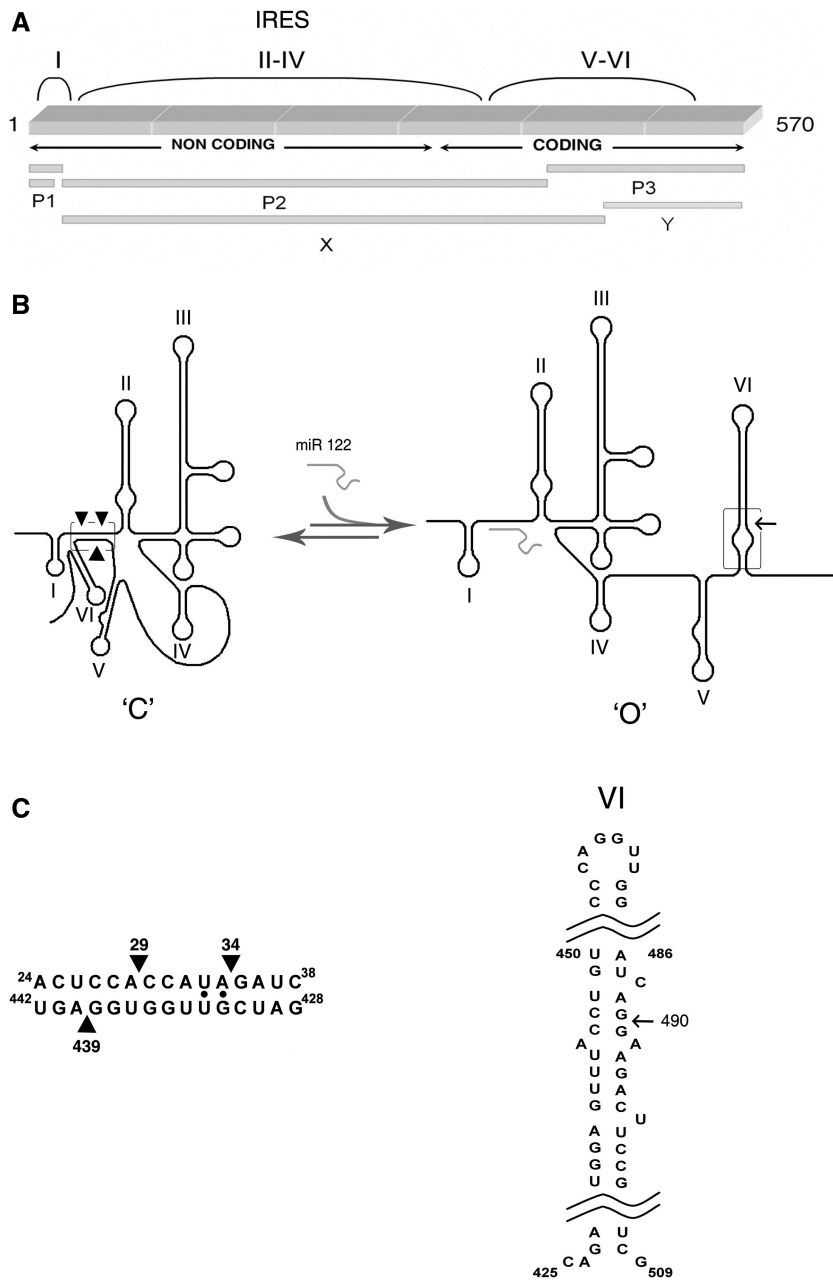


Figure 1. Schematic representation of 1–570 RNA. (A) Primary structure, where mapping of band X is indicated relative to 1–570 RNA and previously published products of the RNase III reaction with RNA in the closed conformation (‘C’). (B) Proposed secondary structures. Left: closed (‘C’) conformation. Solid arrowheads indicate the RNase III cleavages in the LRA. Right: linear open (‘O’) conformation; new cleavage in stem-loop VI indicated with an arrow; (C) detailed sequences of the double helical elements recognized by RNase III.

It also further supports our previous data that the LRA within 1–570 RNA is the major structural conformation.

The new RNase III cleavage event is specific

Since HCV RNA is not a canonical large dsRNA substrate for RNase III, it must be proven that band X is the specific result of RNase III activity and not of ssRNase-specific contaminant activities or otherwise non-canonical actions of the commercial RNase III preparation. Therefore, for band X, we identified the

characteristic RNase III chemistry of cleavage, which leaves the 5’ P and 3’ OH end groups in the newly generated termini, using three different assays that included phosphatase, kinase and ligase treatment, as described in the Supplementary Figure 1A, B and C.

Sequence determination of band X

The exact 5’ and 3’ termini of band X were determined by cyclization of band X RNA, followed by reverse transcription and sequencing across the ligated RNA junction.

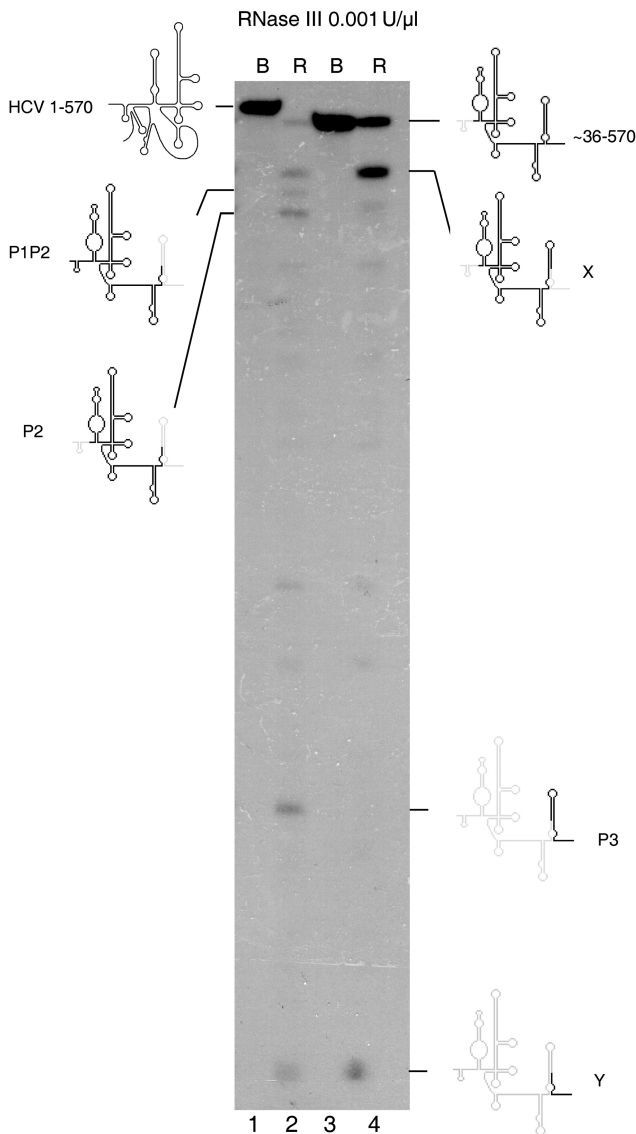


Figure 2. The new RNase III cleavage band detected in 1–570 RNA transcript (lanes 1–2) is indicated by X, and is shown to be highly promoted in a 5' truncated fragment ~36–570 (lanes 3–4). Lanes 1 and 3 are 1–570 and ~36–570 RNA transcripts incubated in buffer, and lanes 2 and 4 are the same transcripts incubated with 0.001 U/μl of RNase III.

Cleavage positions were 5' A29/A34 and 3' G490, which concurred with the results of direct RNA fingerprinting analysis of band X (Supplementary Figure 2B). Fingerprinting analysis (Supplementary Figure 2A) of the rest of the larger RNase III cleavage products demonstrated that their sequence corresponded to the already characterized bands (P2 P3, P1P2, p2 and P3), and that there is any new band product.

The A29/A34 position corresponds to a dsRNA region formed by the described LRA that produces RNase III cleavage at a low enzyme concentration. The new cleavage event between G489 and G490 maps approximately across from the 428–442 sequence in the secondary structure of stem-loop VI (Figure 1C). This suggests that stem-loop VI

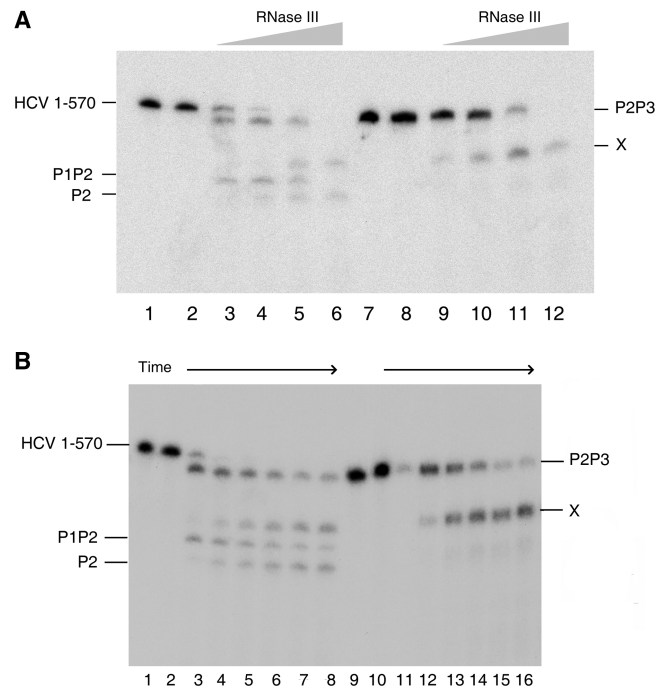


Figure 3. (A) A new RNase III cleavage detected in 1–570 RNA (lanes 1–6) is highly promoted in its larger cleavage product, P2P3 (lanes 7–12). 1–570 RNA and P2P3 were titrated for cleavage by *E. coli* RNase III at four concentrations: 0.0001 U/μl (lanes 3 and 9), 0.0005 U/μl (lanes 4 and 10), 0.001 U/μl (lanes 5 and 11) and 0.005 U/μl (lanes 6 and 12). Lanes 1 and 7 are RNA alone, whereas 2 and 8 are RNA incubated with reaction buffer alone. The new cleavage band is indicated by X. (B) Parallel kinetic analysis of *E. coli* RNase III cleavage of 1–570 RNA (lanes 1–8) and P2P3 RNA (lanes 9–16). Lanes 1 and 9, respectively, show 1–570 RNA and P2P3 transcripts alone, incubated on ice; Lanes 2–8 represent sequentially 10, 20, 30, 40, 50 and 60 min of incubation at 0.0005 U/μl of RNase III; Lanes 10–16 represent the same incubation times as two to eight at the same enzyme concentration.

is an alternative conformation to the LRA when LRA formation is impaired.

Factors involved in switching between alternative structures

The results described in the preceding paragraphs suggest that the 428–442 sequence can switch between two mutually exclusive base pairing conformations, either interacting with a ssRNA sequence in domain I of the LRA motif (allowing RNase III to recognize the LRA) or forming the basal part of stem-loop VI (allowing X cleavage). Because destabilization of the ‘C’ conformation and stabilization of the new alternative structure have to be achieved mechanically to allow switching, we subsequently assessed the role of *cis*-acting and *trans*-acting sequences on switching between the ‘C’ and ‘O’ conformations (Figure 1B).

Cis-acting elements. To delineate the sequence elements participating in the switch, two sets of RNase III and RNase H structure-dependent cleavage reactions were performed using an oligodeoxynucleotide ‘blocking’ assay and truncated fragments, as described below.

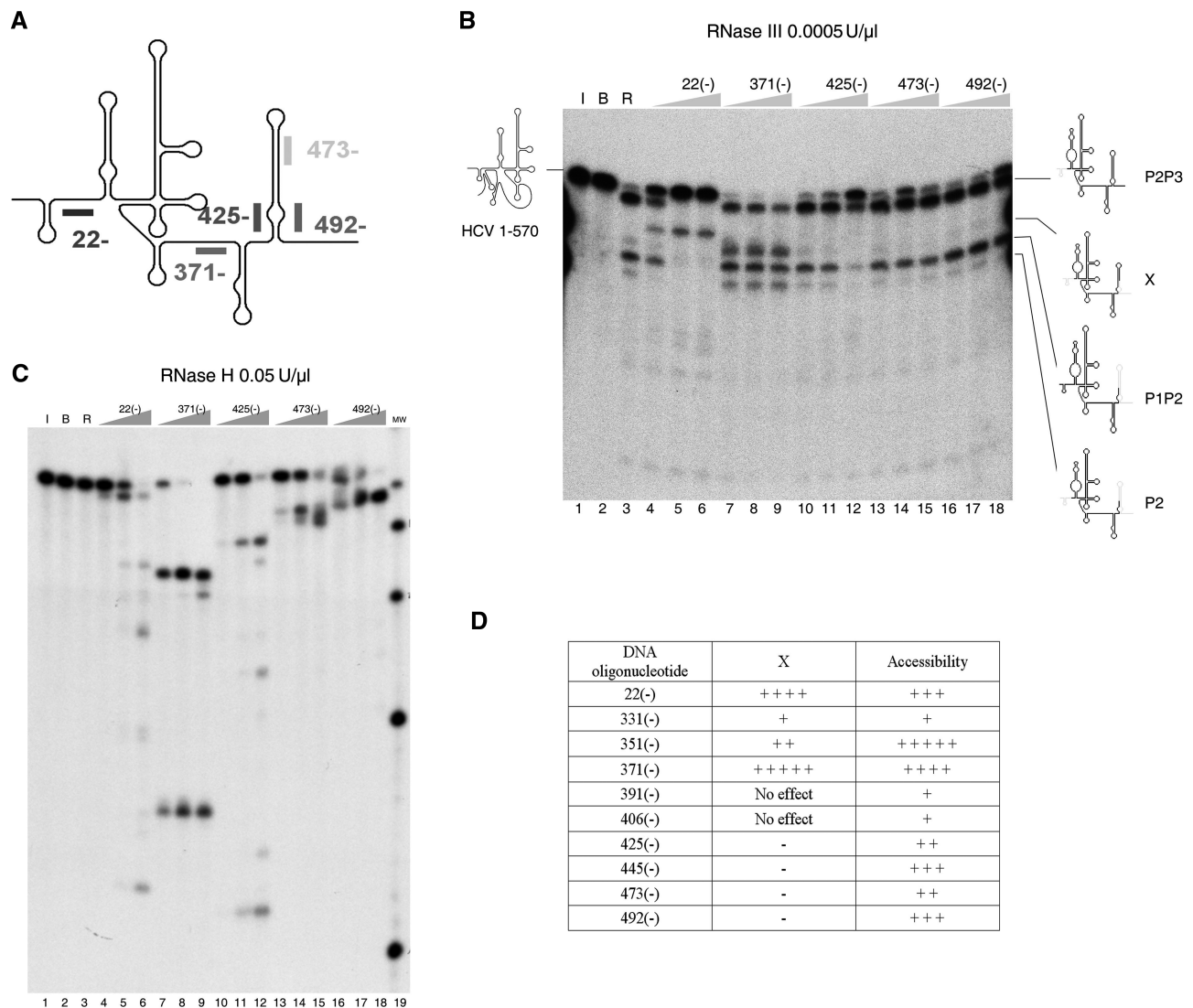


Figure 4. (A) Schematic drawing of 1–570 RNA, indicating a subset of 20-base ODNs, each complementary to an HCV IRES region beginning with the residue number shown; the (–) sign indicates complementary to the viral sequence. (B) Cleavage reaction of 1–570 RNA with *E. coli* RNase III in the presence of a set of ODNs complementary to the viral sequences: 22(–), 371(–), 425(–), 473(–) and 492(–). Cleavage reactions were performed at 0.0005 U/μl of RNase III. Lanes 1 and 2: 1–570 RNA alone incubated on ice and incubated with buffer, respectively. Lane 3: control cleavage reaction without oligonucleotide. Lanes 4–6: cleavage reaction in the presence of increasing concentrations of ODN 22(–); (lane 4: 15 nM; lane 5: 150 nM; lane 6: 1500 nM). The same for lanes 7–9, 10–12, 13–15 and 16–18 for ODN 371(–), 425(–), 473(–) and 492(–), respectively. RNA molecular weight markers of 1–502 and 1–466 nt in length are indicated by a line on the left of the gel fragments. (C) Analysis of *E. coli* RNase H digestion products of 1–570 RNA annealed with complementary ODNs. Lane 1 is RNA incubated on ice, lane 2 incubated in buffer and lane 3, buffer with 0.5 units of *E. coli* RNase H. Lanes 4 to 18: the annealing reaction was performed with a set of 20-mer ODNs, 22(–), 371(–), 425(–), 473(–) and 492(–), at increasing concentrations of 15, 150 and 1500 nM, as indicated at the top of the gel, and treated with 0.5 U/μl of RNase H. Lane 19 is a commercial radiolabeled ladder of RNA fragments of 100, 200, 300, 400, 500, 750 and 1000 bases in length, which will be referred to as ‘MW marker’ in the remaining figure legends. Only fragments 100–500 bases in size appear in this gel image. (D) Table summarizing the changes in reactivity of 1–570 RNA to RNase III in the presence of complementary ODNs. The ‘oligonucleotide’ column indicates the positions where DNA oligonucleotides hybridize to RNA. The ‘X’ column shows the relative activation of RNase III cleavage at the X site (including fragments X and PIX) in 1–570 RNA by the presence of ODNs. The ‘accessibility’ column indicates the relative sensitivities of 1–570 RNA to DNA-mediated RNase H cleavage.

We analyzed the RNase III cleavage pattern of 1–570 RNA in the presence of oligonucleotide (ODN) 22(–) and a consecutive set of 20-mer DNA oligonucleotides complementary to 1–570 RNA from domain IV to domain VI. The results are described in Figure 4B. ODN 22(–) inhibited LRA and promoted cleavage at the X site, producing a band containing fragments PIX that migrated more slowly than band X alone

(characterization is provided in the ‘*Trans-acting element: miR-122*’ section). ODNs 473(–) and 492(–) inhibited the small percentage of cleavage at the X site produced at 0.005 U/μl RNase III concentration and had no other effect on the cleavage pattern. ODNs 473(–) and 492(–) were not expected to cause any alteration in the ‘C’ conformation. When the experiment was repeated with a higher concentration of RNase III (0.001 U/μl), so that

the alternative 'O' structure is formed more quickly and in a higher percentage, the mix of ODN 473(-) and 492 (-) was then able to block band X formation (Supplementary Figure 3). The key result of this section is provided by ODN 425(-). The 428-442 sequence is theoretically involved in the formation of both structures, the LRA motif and stem-loop VI, and ODN 425(-) effectively inhibited production of all RNase III-dependent products. Unexpectedly, ODN 371(-) stimulates cleavage at both the LRA and X site (Figure 4B, lanes 7-9). The RNA folding application of the Mfold program (<http://mfold.bioinfo.rpi.edu/>) indicates possible folding of 1-570 RNA with an interaction between part of the sequence blocked by 371(-) and the key 'two partner' sequence, 428-442, which can hybridize with either 20-40 or the right arm of stem-loop VI. Specifically, the $_{372}\text{ACCAAAACG}_{379}$ sequence, which spans interdomains IV and V and is commonly drawn as an ssRNA region, might base pair with the $_{431}\text{CGUUGGU}_{437}$ sequence, which constitutes the basal part of the left strand of stem-loop VI in the 'O' form. If this interaction were to occur, it would disturb stem-loop VI and inhibit band X formation, or sequester the distal sequence for LRA formation, impeding cleavage at the LRA helix of the 'O' conformation. Thus, by blocking the 371-390 fragment, adequate formation of both the 'C' and 'O' structures would occur, favoring RNase III cleavage at both helices. Hence, the $_{372}\text{A-G}_{379}$ sequence may be an additional element participating in the switch. Additional information consistent with this hypothesis was obtained in the T1 analysis (see 'Results' section, 'Partial T1 and V1 digestions').

Oligonucleotides complementary to stem-loop IV and V had no effect on the LRA or switching (Figure 4D). A parallel RNase H analysis, performed for all the oligonucleotides used, indicated that (at least, at the highest concentration) the oligonucleotides were able to anneal to 1-570 RNA (Figure 4C) to saturation or, in the case of ODNs 473(-) (Figure 4C, lane 15), 331(-) and 391(-) (data not shown), to 80% of the starting material. This supports the conclusion that an absence of an effect of an oligonucleotide on RNase III activity is not due to an inability to hybridize to HCV RNA.

Parallel RNase III and RNase H analysis was performed on 1-570 RNA and transcripts consecutively shortened at their 3' ends (HCV RNA 1-466 and HCV RNA 1-402) in the presence of ODN 22(-) (Supplementary Figure 4). The results indicate that, in the absence of the right strand of stem-loop VI, RNase III cleavage in the LRA is faster and competition between ODN 22(-) and the LRA is more difficult, whereas the absence of both strands of stem-loop VI greatly favors ODN 22(-) annealing at its complementary site (Supplementary Figure 4B). Taken together, these experiments indicate a competitive interplay between sequence 20-40 and the right strand of stem-loop VI to anneal with sequence 425-445.

Trans-acting element: miR-122. As described above, two mutually exclusive and readily distinguishable conformations of 1-570 RNA are evident from the RNase III products. Because the proximal region of the LRA (bases 24-28) is involved in the interaction with specific liver

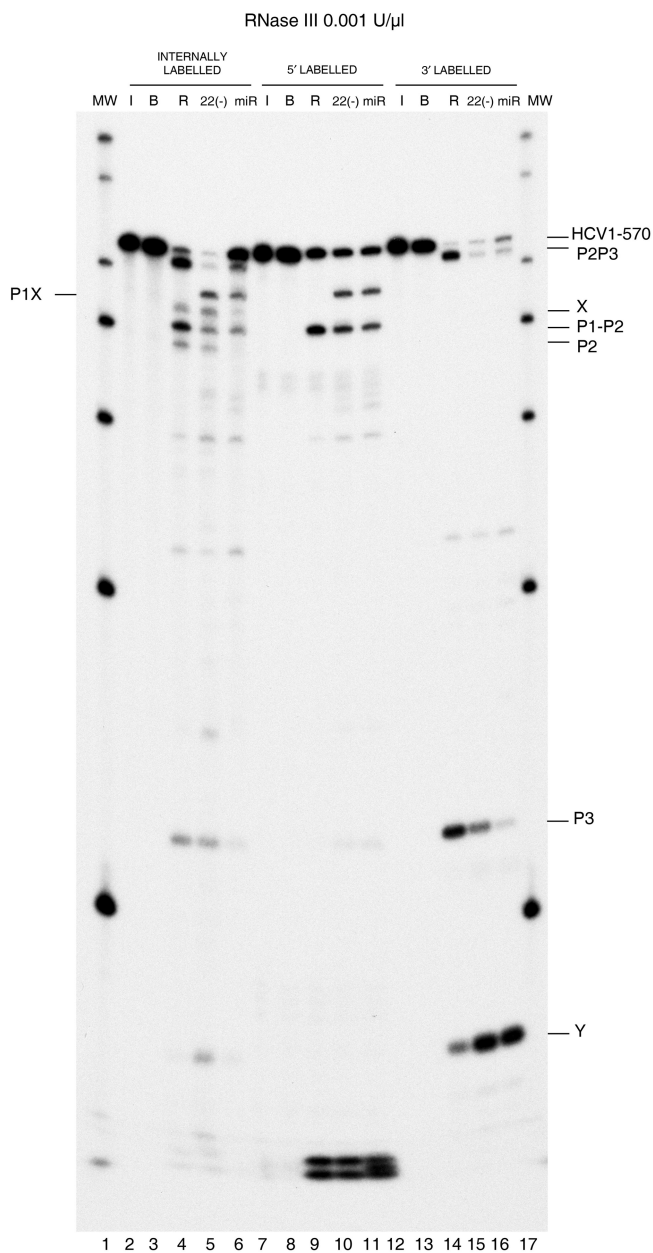


Figure 5. Characterization of an induced RNase III cleavage product of 1-570 RNA by ODN 22(-) and miR-122. Autoradiogram showing a parallel run of RNase III cleavage reaction and control reactions for differentially radiolabeled transcripts of 1-570 RNA: internally (lanes 2-6), in the 5' end (lanes 7-11), or in the 3' end (lanes 12-16). RNAs were either kept on ice (lanes 2, 7 and 12), incubated in standard conditions without the enzyme (lanes 3, 8 and 13), treated with RNase III alone (lanes 4, 9 and 14), or treated with RNase III plus either ODN 22(-) at 150 nM final concentration (lanes 5, 10 and 15) or miR-122 at 15 nM final concentration (lanes 6, 11 and 16). Previously identified RNA fragments are indicated on the right. Lanes 1 and 17 are MW markers.

miR-122 (2), this molecule is a good candidate to favor the alternative conformation by simple competition with the LRA. Examination of the RNase III products obtained after induction of the 'O' conformation with ODN 22(-) or miR-122 revealed a band pattern that indicated that cleavage positions were at similar positions as that obtained in the control reaction (Figure 5, lanes 4-6),

except for the appearance of a band that migrated more slowly than band X and was not present in the reactions without probes. This band could occur as follows: ODN 22(-) and miR-122 both carry complementary sequences in the 20–40 region of 1–570 RNA, and by annealing to it, the alternative ‘O’ conformation and cleavage at the X site are induced. However, concomitantly, the annealed DNA forms a hybrid DNA/RNA, and the miR-122 forms a short duplex miR-122/HCV RNA, which are no longer substrates for RNase III, and also partially abolish RNase III cleavage within the 20–40 sequence (i.e. between P1 and P2). Thus, in the presence of the probes, a new fragment starting at position 1 instead of at 27/34, and yielding a band length equivalent to P1X (1–490) is expected. The results of Figure 5 demonstrate that the new RNase III cleavage product band observed in the internally labeled transcript (lanes 5 and 6), contains the 5′ triphosphate group (lanes 10 and 11), as is visualized in the γ -³²P-labeled transcript. It also shows that the 3′ end position of the new band coincides with the previously characterized bands. In the lanes in which RNA was internally labeled or 3′ end-labeled, no differentiating product band appeared. In addition, attending to the 3′ end-labeled reactions, the band that joins band X to give the complete 1–570-base transcript (which we call band Y) increased in intensity in the ODN 22(-) and miR-122-treated lanes relative to the untreated sample (Figure 5, lanes 14–16). Taken together, these findings indicate that the new band contains nt 1 of HCV 1–570 RNA and the 3′ end of band X; therefore, the fragment is P1X.

Kinetic analysis of E. coli RNase III cleavage of 1–570 HCV RNA in the presence or absence of miR-122

We previously demonstrated that products P2P3 and P2 represent the ‘C’ conformation, and products X and P1X are characteristic of the ‘O’ conformation. Because several RNase III cleavage events occurred in the same molecule, we examined the efficiency of cleavage and order of events in the miR-122-induced transition from ‘C’ to ‘O’, using kinetic analysis.

Two concentrations of enzyme (0.0005 and 0.001 U/ μ l) were employed and three types of 1–570 HCV RNA substrate preparations: (i) alone; (ii) pre-incubated with different concentrations of miR-122 (1.5, 15 and 150 nM) during 60 min, with subsequent addition of RNase III; and (iii) without pre-incubation. The RNase III kinetic pattern of cleavage for a subset of experiments is shown in gels (Figure 6A and B). The results of these gels are summarized as the percentage formation of cleavage products: P2P3, P1X, P and X as a function of time (Figure 6C).

The fold increase on stimulating P1X band production in the presence of miR-122 was measured at the last time point of the reaction, as described in Material and methods section. 1–570 RNA pre-incubated with miR-122 in condition (ii) was cleaved by RNase III to produce P1X at a higher rate than 1–570 RNA alone (Figure 6). In reactions without preincubation, the effect of miR-122 on activating the P1X band was less pronounced

at 0.001 U/ μ l RNase III and undetectable at 0.005 U/ μ l (Figure 6).

The major RNase III single cleavage product of the ‘C’ conformation (P2P3) and the newly identified cleavage product induced in the presence of miR-122 (P1X) in the 0.001 U/ μ l RNase III and miR-122 15 nM reaction were compared in a kinetics analysis (Figure 6C). In the absence of miR-122, there was rapid production of P2P3 in the first 10 min. miR-122 significantly decreased the rate of P2P3 formation, suggesting that miR-122 competes with formation of the ‘C’ conformation. P1X can be only observed in the presence of miR-122. The initial kinetics of this effect was lower in miR-122 reactions without preincubation. These results are highly indicative that miR-122, after annealing with HCV 1–570 RNA induces the ‘O’ conformation.

Confirmation and characterization of the miR-122-induced RNA switch sequence by different methods

Because a secondary structure switch is at the basis of the 1–570 RNA conformational change, and there is evidence that the miR-122 sequence alone can induce switching, we evaluated the effect of miR-122 on the 1–570 RNA structure with three different methods that specifically respond to modifications of stable RNA:RNA duplexes. These include partial digestion with the single- and double-stranded nucleases T1 and V1, electrophoretic mobility in non-denaturing gels and the effect of mutated miR-122 on the RNase III cleavage pattern.

Partial RNase T1 and V1 digestion

Mapping the regions involved in the switch. Single- and double-stranded RNA-specific digestions were carried out under conditions leading to partial cleavage in order to evaluate whether conformational changes deduced from previous analyses could be visualized by this classical methodology and mapped to specific bases. We focused on the hypothetical key ‘two-partner’ sequence G₄₂₈-U₄₄₂, which should theoretically be displaced by competition from long range annealing with sequence A₂₄-C₃₈ by the ODN 22(-) or miR-122 sequences.

Comparative analysis of RNase T1 partial digestion of 1–570 RNA alone or pre-incubated with miR-122. RNase T1 partial digestions of the 3′ radiolabeled 1–570 RNA alone or pre-incubated with a miR-122 sequence at 150 nM were run in parallel with a sequence ladder of 1–570 RNA treated with alkali and heat or with RNase T1 in denaturing conditions (Figure 7A). In the analysis of the changes, base G428 showed a newly acquired sensitivity after miR-122 incubation. These results confirm the hypothesis that ODN 22(-) and miR-122 can induce changes in the ‘secondary status’ of 1–570 RNA at a long distance, which is consistent with the proposed RNA conformational switch.

While change G428 resides in the left strand of stem loop VI, there is another change at base G494, which maps across the helix in the complementary strand of the newly formed stem loop VI, indicated in Figure 7B. Decrease in cleavage at base G494 suggest an increase in

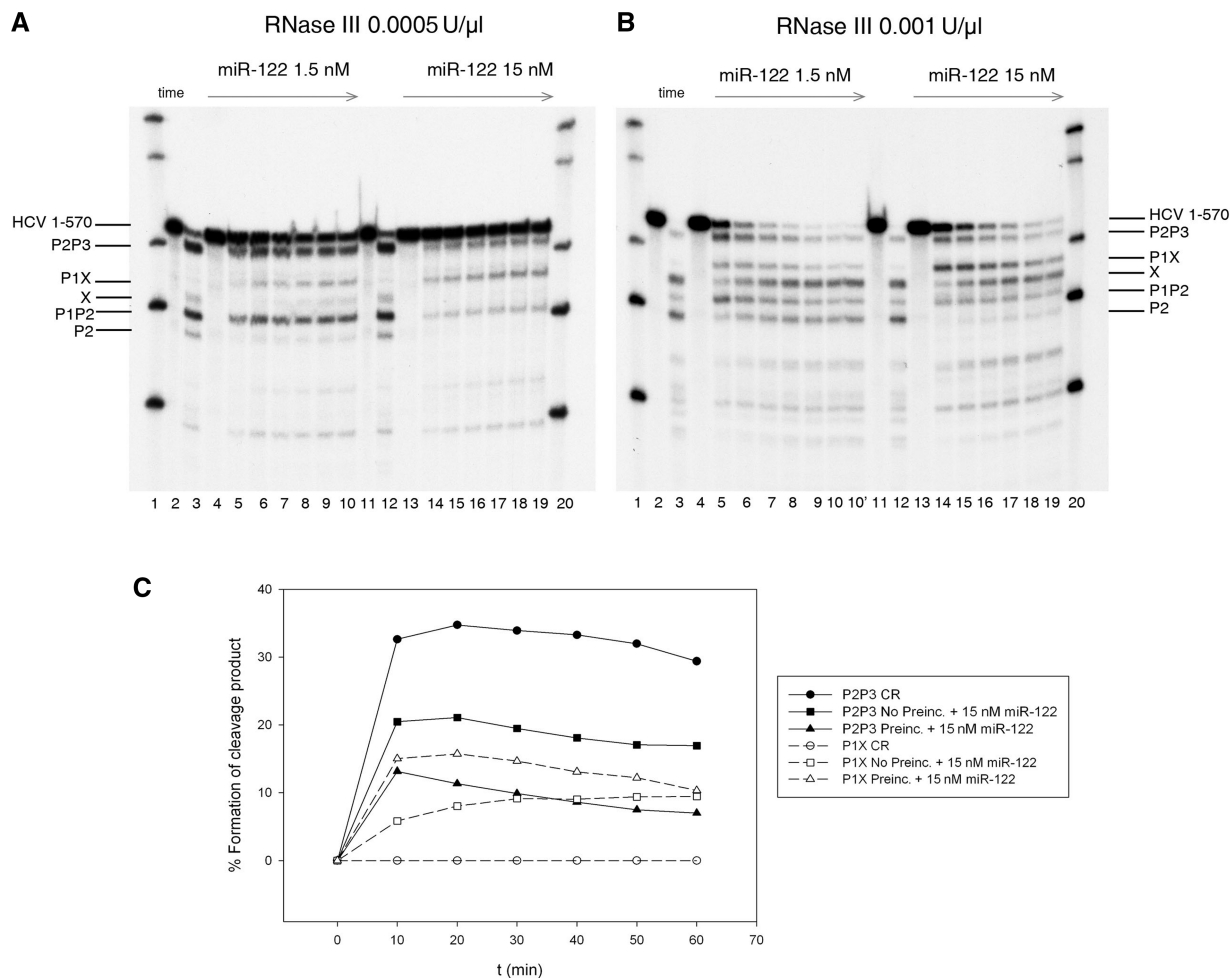


Figure 6. (A) Cleavage Kinetics of 1–570 RNA by *E. coli* RNase III at 0.0005 U/μl in the presence of 1.5 nM miR-122 (lanes 4–10) and 15 nM miR-122 (lanes 13–19). In this set of reactions, miR-122 was added to standard reaction, incubated for 1 hour at 37°C and then digested by the enzyme. In each individual reaction profile (lanes 4–10 and lanes 13–19) from left to right, each line represents time 0, 10, 20, 30, 40, 50 and 60 min incubation with RNase III. Lanes 2 and 11 RNA incubated on ice. Lanes 3 and 12 are control reactions without miR-122. Lanes 1 and 20 are MW century markers. (B) Same as panel A but reactions were performed at 0.001 U/μl *E. coli* RNase III. Bands are indicated by lines at the right of the figure. (C) Graphic representation of the time course processing of P2P3 and P1X by *E. coli* RNase III (0.001 U/μl) at different conditions: control reactions (CR), non-pre-incubated miR-122 reactions, or reactions pre-incubated with 15 nM miR-122.

stem loop VI formation as expected. Of particular interest is the increase in resistance of base G379 to RNase T1 attack after switch induction. This base forms part of the $_{372}\text{A-G}_{379}$ sequence, which appeared in the RNase III/RNase H analysis as a third element participating in the switch. Changes in reactivity at other positions indicate that other RNA fragments reorganize because of the switching. Further study is needed to determine the relationship between the overall conformational switch we propose and the specific secondary structure variation.

Effect of different concentrations of ODN 22(–), miR-122 and the miR-122 seed sequence on the pattern of RNases T1 and V1. Figure 7C and D show a comparative analysis pattern of RNase T1 and V1 reactivity on 1–570 RNA alone or pre-incubated with several probes. ODN 22(–) and miR-122 are observed to have nearly identical qualitative stimulatory effects on switching, although quantitatively, miR-122 was 10-fold more effective than ODN

22(–); both exerted a dose-dependent effect. Regarding the effects on the RNase V1 pattern, ODN 22(–) as well as miR-122 promote similar changes. In agreement with the RNase T1 results, the changes are concentrated in the region around G494 in the left and right strand of stem loop VI. The seed sequence alone was found to have a far less pronounced ability to promote changes in the T1 pattern. The effects were limited to slight V1 nuclease resistance around position 494 only when the highest concentration of seed sequence was used.

Non-denaturing gels

Native gels were used to investigate the conformational change from ‘C’ to ‘O’ of 1–570 RNA in the presence of specific probes. Three potential oligonucleotide inducers, ODN 22(–), miR-122 and miR-122 seed sequence and a theoretically unreactive control probe, truncated miR-122 (lacking the seed sequence) were added to 0.6-nM samples

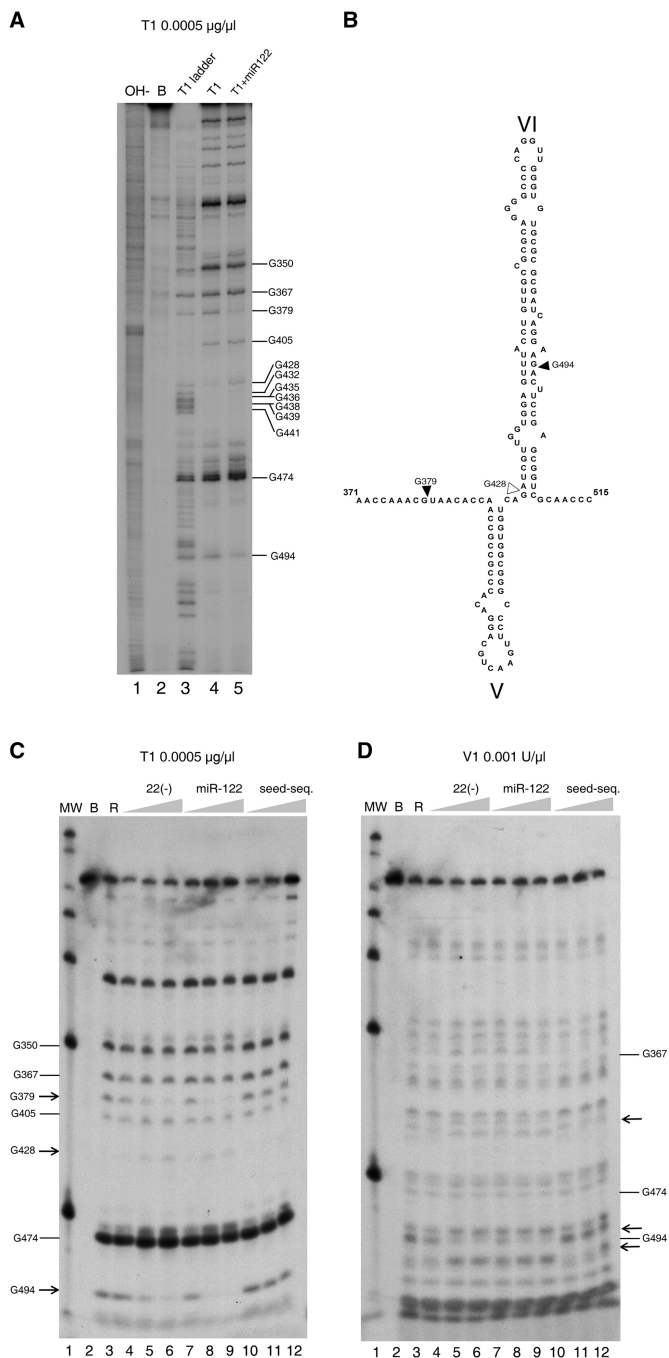


Figure 7. (A) 'G' sequence determination of 3' end-labeled 1–570 RNA in our standard conditions of cleavage by parallel running of RNA degradation with RNase T1 0.0005 $\mu\text{g}/\mu\text{l}$ in denaturing conditions (lane 3), in standard buffer (lane 4) and in the presence of miR-122 at 15 nM (lane 5). Lanes 1 is an alkali ladder degradation and lane 2, the RNA incubated in standard buffer alone. Gs are identified at the right of the gel. (B) Secondary structure of stem loop VI and its boundary regions summarizing the position with differential reactivity for RNase T1. Increased resistance is indicated by solid triangles and increased sensitivity by blank triangles. Nucleotide numbering is used, as in Figure 1. (C) Evaluation of the effect of increasing concentrations of probes on the T1 nuclease pattern of cleavage. Lane 1 is a MW marker. Control incubation of 1–570 RNA in the buffer (lane 2), or after addition 0.0005 $\mu\text{g}/\mu\text{l}$ of RNase T1 (lane 3). In subsequent lanes, before addition of the T1 RNase, RNAs were pre-incubated for 1h with increasing concentrations of ODN 22(–) of 15 nM, 150 nM and 1500 nM (lanes 4–6), or miR-122 at final concentrations of 1.5 nM,

of internally labeled 1–570 RNA, incubated and analyzed in non-denaturing acrylamide gels, as is described in Material and Methods section. As is seen in Figure 8A and B, addition of only buffer to the starting 1–570 RNA concentrates the radioactive label from a fuzzy smear to a more delineated band, consistent with a report demonstrating that Mg^{++} is required for the 5' region of HCV RNA to achieve proper folding (15). Incubation of HCV RNA with increasing concentrations of ODN 22(–) at 15, 150 and 1500 nM (Figure 8A, lanes 3–5) induced a band that migrated more slowly than the untreated samples, showing a sharp transition between 15 and 150 nM. Incubations with miR-122 at 1.5, 15 and 150 nM (Figure 8B, lanes 3–5) showed a similar position for the retarded band migration (Figure 8, lane 6), except that a very slow migrating band appeared at the highest miR-122 concentration used. Complete band mobility retardation was attained repeatedly at a final concentration of 15 nM. The miR-122 seed sequence alone had a faint effect. At the most concentrated condition, the band slowed to a slightly retarded smear (Figure 8B, lanes 8–10). The miR-122 sequence lacking the seed sequence had no effect at any concentration (Figure 8A, lanes 8–10).

In another experiment, we changed the annealing conditions between the probes and 1–570 RNA. We found that if 1–570 RNA were preheated to 90°C in water and slowly cooled with a mixture of our standard buffer plus miR-122 or seed sequence, miR-122 at 1.5 nM was able to promote mobility retardation of all of the 1–570 RNA counts (data not shown). Because we had previously shown that annealing of ODN 22(–) with HCV RNA was favored in these conditions (16), this result, together with the previous findings, confirmed that the limiting factor in promoting the RNA switch is the ability of the probe to anneal with the viral RNA target. However, the effect of the seed sequence alone on retardation was only slightly more evident than in the experiments that did not include annealing during the preheating step (data not shown).

A control was performed to rule out that 1–570 RNA retardation in the experiments above was due to the increase in weight contributed by the annealed probe, even though it represents only about 3.5% in mass and charge. A 20-mer DNA, ODN 188(–), which hybridizes to completion with 1–570 RNA in apical stem-loop III at positions 188–207, promoted no mobility changes (Supplementary Figure 5A).

Effect of miR-122 seed sequence mutations on 1–570 RNA cleavage by RNase III

We determined the effect of the presence of mutations within the miR-122 seed sequence on the RNase III reaction and native gel electrophoresis of 1–570 RNA. We used 15 nM of all the probes whose sequences are described in panel A of Figure 9. We found that

15 nM and 150 nM (lanes 7–9) and a 10-mer oligoribonucleotide carrying the 7 nucleotides of the miR-122 seed sequence to a final concentration of 1.5 nM, 15 nM and 150 nM (lanes 10–12). (D) Same as panel B, but the RNase used was double-stranded RNase VI. Arrows indicate the changes in sensitivity to the nuclease.

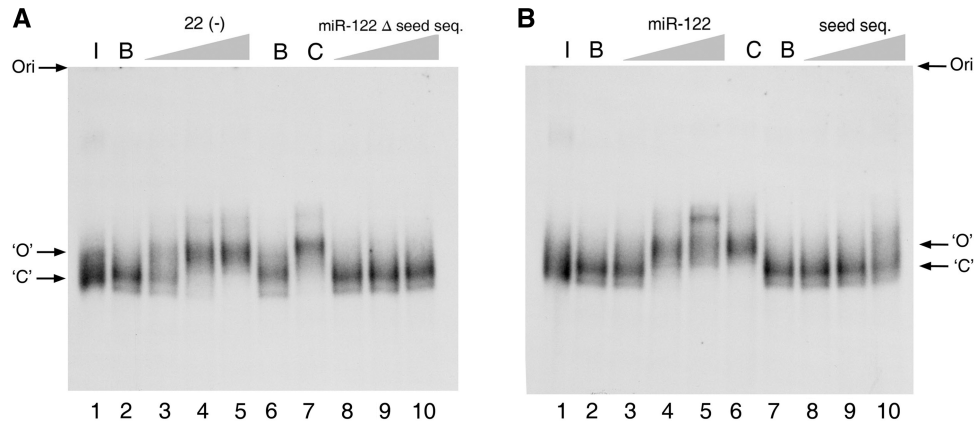


Figure 8. Analysis of induced conformational changes of 1–570 RNA on non-denaturing gel electrophoresis. (A) 1–570 RNA was resuspended at 0.6 nM in each of the following conditions: in water and kept on ice (lane 1), in standard buffer reaction alone (lanes 2 and 6), together with ODN 22(–) at a final concentration of 15 nM, 150 nM and 1500 nM (lanes 3–5), or with miR-122 minus seed sequence at increasing final concentrations of 1.5 nM, 15 nM or 150 nM (lanes 8–10). Lane 7, control ODN 22(–) at 1500 nM. (B) Ice-incubated control RNA is in lane 1, and buffer-incubated RNA controls are in lanes 2 and 7. RNA was incubated together with miR-122 at a final concentration of 1.5 nM, 15 nM and 150 nM (lanes 3–5). Lane 6, control 22(–) or together with seed sequence (5' U GGAGUGU GA 3') at concentrations of 1.5 nM, 15 nM and 150 nM (lanes 8–10). 'ORI' marks the origin of the electrophoresis. Arrows marked with 'O' and 'C' indicate open and close conformations respectively.

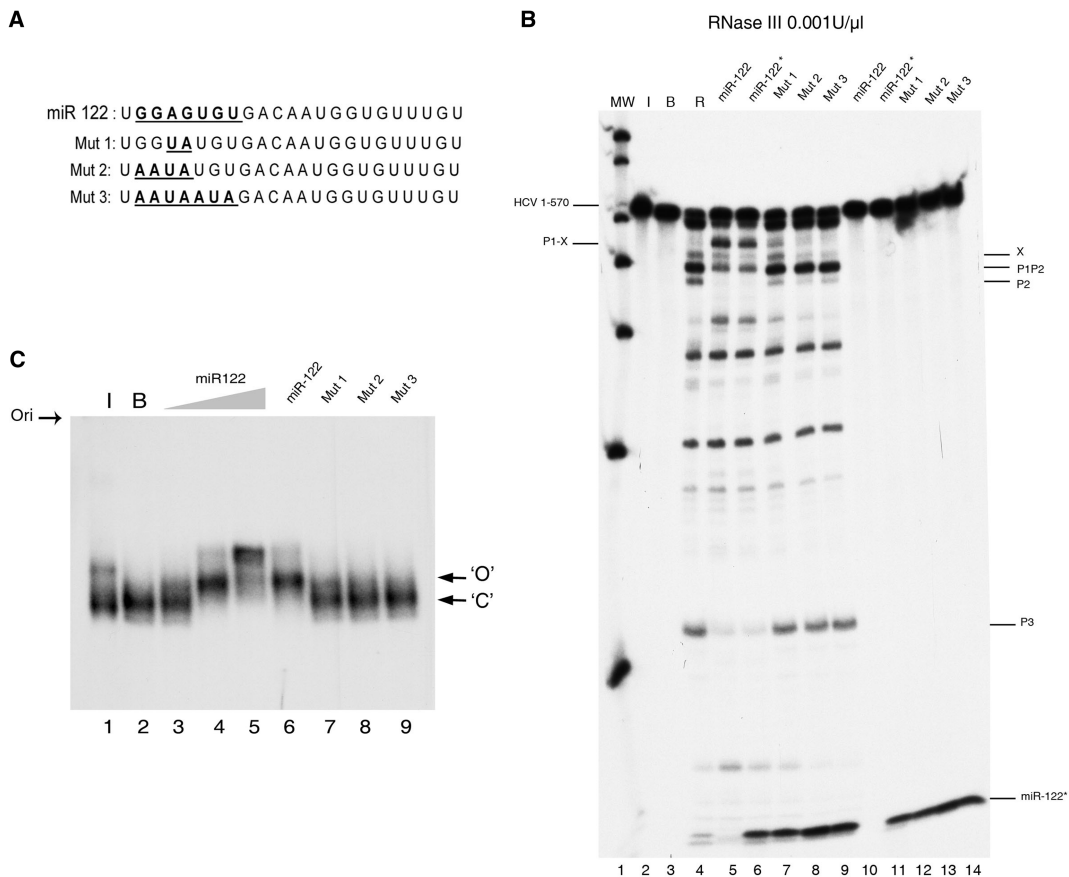


Figure 9. Effect of miR-122 seed sequence mutations on 1–570 RNA cleavage by RNase III (A) The miR-122 sequence and mutants 1, 2 and 3. Seed sequence mutations are indicated in bold and underlined. (B) Autoradiogram shows a 0.001 U/μl RNase III cleavage reaction of 1–570 RNA fragment alone (lane 4), or in the presence of 15 nM of an RNA sequence corresponding to the following: miR-122 (chemically synthesized and unlabeled in lane 5 or *in vitro*-transcribed from a DNA template and internally labeled in lane 6, referred to in the figures as miR-122*); or mutants of miR-122 transcribed from a DNA template and internally labeled: mut 1 (lane 7), mut 2 (lane 8), mut 3 (lane 9). Lane 1 is a MW marker, lane 2 is 1–570 RNA alone maintained on ice, and lane 3 is RNA incubated in reaction buffer. Lanes 10–14 are equivalent to lanes 6–8, but incubated in the absence of the enzyme. The miR-122-induced cleavage products are indicated at the left of the gel. The migration position of miR-122 and mutants are identified at the bottom of the gel. (C) Non-denaturing gel electrophoresis of 1–570 RNA alone incubated on ice (Lane 1) or in buffer (Lane 2); or incubated for 1 h at 37°C with increasing final concentrations of miR-122: 1.5 (lane 3), 15 nM (lane 4) and 150 nM (lane 5); or with 15 nM final concentrations of mut 1 (lane 6), mut 2 (lane 7), mut 3 (lane 8) or mut 4 (lane 9).

2 mutations in the middle of the seed sequence (mutant 1) sufficed to drastically reduce the switch induction effect of miR-122 (Figure 9B, lane 7). This effect was totally abolished in the variants carrying 4 or 7 mutations (mutants 2 and 3, Figure 9, lanes 8 and 9, respectively). It was also observed that, unlike miR-122, these probes were unable to stabilize the retarded band in the native gel electrophoresis (Figure 9C, lanes 7–9). These results indicate that switch induction is a highly specific result of miR-122 interaction with 1–570 RNA through its seed sequence.

DISCUSSION

In this study, the transition between two double-helical elements is characterized in the context of a conformational change of 1–570 HCV RNA and its dynamic *in vitro* modulation by the liver-specific microRNA, miR-122. These conformational changes involve the HCV IRES, which switches from a closed ‘circular’ conformation ‘C’ (5,7), formed by LRA (bases 24–38 in interdomains I-II with bases 428–442 in the basal part of domain VI) to an open ‘O’ form (where bases 428–442 interact with bases 494–508; i.e. those forming the basal part of stem-loop VI). The *in vitro* switch is governed by the interaction of miR-122, which disfavors the LRA. Liver miR-122 has been demonstrated to modulate viral abundance (2) and recently, to stimulate translation (17) when viral RNA fragments containing stem-loop VI are used. This led us to propose that the 1–570 RNA conformational change induced by miR-122 is an integral regulatory component of the viral genome.

The conformational switch we propose solves the apparent conflict between studies supporting the closed conformation (5–7) and the report describing stem-loop VI (8). Kinetic analysis in our previous study (7) showed that at least, 80% of the molecules were in the closed conformation. In apparent contrast, a structural study of RNA in the core coding region indicated that the G₄₂₈-U₄₄₂ sequence forms the basal part of the large stem-loop VI, whose presence is incompatible with the closed conformation (8). The conflict disappears if we consider that the RNA transcript fragment used in the study did not include the most proximal region of HCV RNA, which is needed for the closed conformation, and propose that 1–570 RNA is a conformationally dynamic molecule, able to switch between two conformations. A similar conflict was identically resolved with the discovery of two alternating structures in HIV leader RNA (18).

Upon miR-122 binding, changes in the accessibility of 1–570 RNA to RNase H, T1 and V1 are mostly located downstream of the IRES and are consistent with transition from the ‘C’ to ‘O’ conformation. Therefore, we conclude that the mobility changes seen on gel shift analysis are related to changes in the overall conformation. Thus, translation activation after miR-122 induction (17) might be related to increased accessibility to the small ribosomal subunit or to other initiation factors (i.e. eIFIII) in the ‘O’ conformation.

miR-122 is a viral inducer that interacts in tandem with the proximal 23–40 nt of the viral sequence (19),

coinciding with the region involved in the LRA. Regarding the influence of miR-122 on the population of the two conformers *in vitro*, several factors seem of interest: (i) the low ratio of miR-122 to 1–570 RNA (3:1) needed to induce the switch. This is consistent with the differing representation of these two molecules in infected hepatocytes [$>10^3$ for miR-122 (20) to <100 for positive-stranded HCV RNA (21)]; (ii) the seed sequence, which we proved to be essential for miR-122 activity, is unable to promote the switch alone (unless it is used at a high concentration); (iii) the miR-122-induced switch is reversible, whereas the switch induced by the complementary ODN 22(–) is not. These three points indicate that the switch is not promoted by simple Watson-Crick pairing competition. More complicated interaction of miR-122 by 1–570 RNA is suggested, through a process that may be more similar to bacterial riboswitches.

The results of the RNase III reaction in the presence of miR-122 and RRL suggest that the conformational switch is maintained in a specific biological context (Supplementary Figure 6). This prompted us to propose that the 1–570 RNA switch in the presence of miR-122 may represent the structural correlate of the recently described positive effect that miR-122 exerts on HCV translation in RRL and cell cultures (17). If this is the case, the data provide a role for RNA in the proximal part of the CORE region, whose unknown structure-dependent function has been described as essential for the virus in a chimpanzee model (3).

An intriguing question is whether the interaction of miR-122 with 1–570 RNA suffices for this biological effect (i.e. with miR-122 acting as a ligand in a manner similar to small molecule-induced riboswitches in bacteria) or protein factors are involved. In any case, the activity of miR-122 as a conformational switch-inducer departs from the concept of microRNA regulation of mRNA translation in eukaryotes. While that reported effect is inhibitory and occurs through direct binding to the 3′ UTR of mRNA, in the present case it involves activation at the 5′ UTR.

SUPPLEMENTARY DATA

Supplementary Data are available at NAR Online.

ACKNOWLEDGEMENTS

We thank Drs Encarnación Martínez-Salas, Josep Vilardell and Esteban Domingo for their helpful comments on the manuscript. We are grateful to Drs Cristina Romero and Francisco Muñoz for their help in the experimental procedures. Finally, the authors acknowledge the initial contribution to this study of Tchering Shorden and Dr Nerea Beguiristain, presented in Figure 2 of the Supplementary Data, which was done at Dr Hugh D Robertson’s laboratory in Cornell University, New York.

FUNDING

Ministerio de Ciencia e Innovación BIO2007-60106, BIO2004-06114 Proyecto Excelencia Comunidad

Autónoma de Andalucía CVI-03050; FISS (CIBERhd); FIPSE 36549/06 for work in Granada; National Institutes of Health grant NIH/NIDA K01 DAO18262 for work in Doylestown, Pennsylvania. Funding for open access charge: BIO-2007, 60106 (IPB-LN) CSIC. MCyT.

Conflict of interest statement. None declared.

REFERENCES

1. Reynolds, J.E., Kaminski, A., Carroll, A.R., Clarke, B.E., Rowlands, D.J. and Jackson, R.J. (1996) Internal initiation of translation of hepatitis C virus RNA: the ribosome entry site is at the authentic initiation codon. *RNA*, **2**, 867–878.
2. Jopling, C.L., Yi, M., Lancaster, A.M., Lemon, S.M. and Sarnow, P. (2005) Modulation of hepatitis C virus RNA abundance by a liver-specific MicroRNA. *Science*, **309**, 1577–1581.
3. McMullan, L.K., Grakoui, A., Evans, M.J., Mihalik, K., Puig, M., Branch, A.D., Feinstone, S.M. and Rice, C.M. (2007) Evidence for a functional RNA element in the hepatitis C virus core gene. *Proc. Natl Acad. Sci. USA*, **104**, 2879–2884.
4. Vassilaki, N., Friebe, P., Meuleman, P., Kallis, S., Kaul, A., Paranhos-Baccala, G., Leroux-Roels, G., Mavromara, P. and Bartenschlager, R. (2008) Role of the hepatitis C virus core+1 open reading frame and core cis-acting RNA elements in viral RNA translation and replication. *J. Virol.*, **82**, 11503–11515.
5. Kim, Y.K., Lee, S.H., Kim, C.S., Seol, S.K. and Jang, S.K. (2003) Long-range RNA-RNA interaction between the 5′ nontranslated region and the core-coding sequences of hepatitis C virus modulates the IRES-dependent translation. *RNA*, **9**, 599–606.
6. Honda, M., Rijnbrand, R., Abell, G., Kim, D. and Lemon, S.M. (1999) Natural variation in translational activities of the 5′ nontranslated RNAs of hepatitis C virus genotypes 1a and 1b: evidence for a long-range RNA-RNA interaction outside of the internal ribosomal entry site. *J. Virol.*, **73**, 4941–4951.
7. Beguiristain, N., Robertson, H.D. and Gomez, J. (2005) RNase III cleavage demonstrates a long range RNA: RNA duplex element flanking the hepatitis C virus internal ribosome entry site. *Nucleic Acids Res.*, **33**, 5250–5261.
8. Tuplin, A., Evans, D.J. and Simmonds, P. (2004) Detailed mapping of RNA secondary structures in core and NS5B-encoding region sequences of hepatitis C virus by RNase cleavage and novel bioinformatic prediction methods. *J. Gen. Virol.*, **85**, 3037–3047.
9. Milligan, J.F. and Uhlenbeck, O.C. (1989) Synthesis of small RNAs using T7 RNA polymerase. *Methods Enzymol.*, **180**, 51–62.
10. Franklin, R.M. (1966) Purification and properties of the replicative intermediate of the RNA bacteriophage R17. *Proc. Natl Acad. Sci. USA*, **55**, 1504–1511.
11. Robertson, H.D. (1967) A Nuclease Specific for Double-Stranded RNA. *Virology*, **12**, 718–719.
12. Nicholson, A.W. (1999) Function, mechanism and regulation of bacterial ribonucleases. *FEMS Microbiol. Rev.*, **23**, 371–390.
13. Nadal, A., Martell, M., Lytle, J.R., Lyons, A.J., Robertson, H.D., Cabot, B., Esteban, J.I., Esteban, R., Guardia, J. and Gomez, J. (2002) Specific cleavage of hepatitis C virus RNA genome by human RNase P. *J. Biol. Chem.*, **277**, 30606–30613.
14. Dunn, J.J. (1976) RNase III cleavage of single-stranded RNA. Effect of ionic strength on the fidelity of cleavage. *J. Biol. Chem.*, **251**, 3807–3814.
15. Kieft, J.S., Zhou, K., Jubin, R., Murray, M.G., Lau, J.Y. and Doudna, J.A. (1999) The hepatitis C virus internal ribosome entry site adopts an ion-dependent tertiary fold. *J. Mol. Biol.*, **292**, 513–529.
16. Lyons, A.J., Lytle, J.R., Gomez, J. and Robertson, H.D. (2001) Hepatitis C virus internal ribosome entry site RNA contains a tertiary structural element in a functional domain of stem-loop II. *Nucleic Acids Res.*, **29**, 2535–2541.
17. Henke, J.I., Goergen, D., Zheng, J., Song, Y., Schuttler, C.G., Fehr, C., Junemann, C. and Niepmann, M. (2008) microRNA-122 stimulates translation of hepatitis C virus RNA. *EMBO J.*, **27**, 3300–3310.
18. Huthoff, H. and Berkhout, B. (2001) Two alternating structures of the HIV-1 leader RNA. *RNA*, **7**, 143–157.
19. Jopling, C.L., Schutz, S. and Sarnow, P. (2008) Position-dependent function for a tandem microRNA miR-122-binding site located in the hepatitis C virus RNA genome. *Cell Host Microbe.*, **4**, 77–85.
20. Sarasin-Filipowicz, M., Krol, J., Markiewicz, I., Heim, M.H. and Filipowicz, W. (2009) Decreased levels of microRNA miR-122 in individuals with hepatitis C responding poorly to interferon therapy. *Nat. Med.*, **15**, 31–33.
21. Agnello, V., Abel, G., Knight, G.B. and Muchmore, E. (1998) Detection of widespread hepatocyte infection in chronic hepatitis C. *Hepatology*, **28**, 573–584.

ADDITIONAL MATERIAL

Additional Figure 1: Identification of the newly generated termini of band X by phosphatase, kinase, and ligase treatment in 3 different assays. One of the distinctive properties of RNase III is that it releases cleavage products containing 5' P and 3' OH end groups. 1-570 RNA substrate was labeled at low specific radioactivity to permit an increase of incorporated radioactivity in the subsequent end-labeling reactions, and cleaved with RNase III. Product bands X and P2 (used as the positive control) were gel-purified and the recovered radioactivity was divided into 3 aliquots. Each was subjected to specific enzymatic reactions to determine the chemical groups of the A) 5' end: lane 1, P2 control RNA alone; lane 2, P2 labeled with T4 polynucleotide kinase and [γ - 32 P] ATP; lane 3, P2 treated identically as before, with prior incubation with alkaline phosphatase; lane 4, X control RNA alone; lane 5, X labeled with T4 polynucleotide kinase and [γ - 32 P] ATP; lane 6, X treated exactly as before with prior incubation with alkaline phosphatase; B) 3' end: lane 1, X labeled with [32 P] pCp and T4 RNA ligase; lane 2, X alone; lane 3, control mobility bands 1-570, P2P3, X, and P2; lane 4, P2 labeled with [32 P] pCp and T4 RNA ligase; lane 5, P2 alone; and C) 3' and 5' ends: lane 1, P2 alone; lane 2, P2 circularization with T4 RNA ligase; lane 3, HCV control mobility bands 1-570, X, P1P2, and P2; lane 4, X alone; lane 5, X circularization with T4 RNA ligase. Bands corresponding to circularized bands migrate more slowly than the starting material.

Additional Figure 2: Characterization of RNase III cleavage pattern of 1-570 RNA at a high RNase III concentration of 0.001 U/ μ l through RNA fingerprinting analysis. RNase T1 fingerprints of 1-570 RNA and its reaction products with *E. coli* RNase III (0.001 U/ μ l). 32 P-labeled transcript was cleaved by RNase III and fractionated by gel electrophoresis. The 1-570 RNA substrate, and the 5 major products (bands P2P3, X, P1P2, P2 and P3) were eluted from excised gel bands and analyzed by 2-dimensional RNA fingerprinting. Arrows at the edge indicate the direction of migration in the first dimension by electrophoresis and in the second by ascending chromatography. Except for P3 band fingerprint, identification of spots was performed according to the rules of mobility, which are related to sequence length and base composition, and by comparison of relative

spot position with previous HCV RNA fingerprints. Spot fingerprints of the P3 band were identified after elution from the chromatography and secondary analysis (data not shown). Arrows indicate RNase T1-resistant oligonucleotides in the 5' end (spots 1 and 2), in the middle (spot 3), and in the 3' end (spots 4, 5 and 6) of the linear sequence of 1-570 RNA, respectively. Asterisks indicate absence of a spot in the various RNA fragment products. The sequence positions are as follows: for spots 1 and 2 at the 5' end, nt 22-33 and nt 36-47, respectively; for the middle spot numbered 3, nt 351-367; and for spots 4, 5 and 6 in the 3' end, nt 442-449, nt 510-517, and nt 531-542, respectively. The fingerprint patterns for product bands P2P3, P1P2, P2 and P3 are consistent with previous sequence data for partial cleavage products of RNase III bands P2P3, P1P2, and total digestion products P2 and P3, respectively. The fingerprint pattern of the new X band is similar to that of the 5' end of P2. Both contain spot 2 (nt 36-47) and lack spot 1 (nt 22-33), which moves to a similar fast migrating position in both cases, suggesting that the P2 and X fragments share very similar or identical 5' end mapping within the sequence between bases 22 to 33. With regard to the 3' end, the X band fingerprint has one spot more than P2, numbered 4 (nt 442-449), indicating that the X sequence extends further downstream than P2. Nonetheless, it lacks spots 5 (nt 510-517) and 6 (nt 531-542), present in the P2P3 and P3 products and the most 3' fragment of 1-570 RNA, indicating that the 3' end of band X is located somewhere between nt 449 and 510. B) Schematic representation of the cleavage positions after sequencing band X cDNA.

Additional Figure 3: RNase III cleavage in the presence of an ODN 473(-) and 492(-) mixture. *E. coli* RNase III digestion products of 1-570 RNA annealed with a mixture of antisense ODNs, 473(-) and 492(-) (complementary to the right strand of stem-loop VI). Lane 1 is RNA on ice, lane 2 RNA incubated in buffer, and lane 3 RNA incubated with 0.001 units of *E. coli* RNase III. In lanes 4 to 6, the annealing reaction was performed with 0.6 nM viral RNA substrate and 15, 150, and 1500 nM of the oligonucleotide mixture and digested with 0.001 U/ μ l of RNase III. These results are related to Figure 4B: when the RNase III units are increased favoring the 'O' conformation, the mixture of ODN 473(-) and 492(-) can impede band X formation.

Additional Figure 4: Effect of sequences on the 3' end of 1-570 RNA on 'C' conformation stability using consecutively truncated transcripts. A) We used RNase III to analyze the cleavage kinetics of the LRA in two transcripts either containing or lacking stem-loop VI. Transcripts included the 1-570 RNA and the 1-466 3' truncated transcript, which lacks the right strand of stem-loop VI, complementary to 428-442. 1-570 RNA (lanes 1-7) and 1-466 HCV (lanes 8-14), with 0.0005 U/ μ l of RNase III. Lanes 1 and 8: t=0, 2-7 and 9-14 are consecutive 10-minute time course reactions. The 1-466 HCV RNA fragment is cleaved to completion in the LRA by RNase III faster than 1-570 RNA. This result may indicate that the 3' sequence (corresponding to the region of stem-loop VI forming the "X signal") participates by competing with and destabilizing the more stable LRA conformation. Nevertheless, more steric impediments to the enzyme in the longer substrate cannot be ruled out.

B) Subsequently, we used *E. coli* RNase H 0.5 U/ μ l and 22(-) DNA oligonucleotide at 15 nM and consecutively 3' shortened HCV RNA transcripts, 1-570, 1-466, and 1-402, to determine the stability of the 'C' conformation. Lane 1, RNA alone; lane 2, t=0; lanes 3-8, aliquots removed from the reaction every 10 min. The 1-466 HCV RNA fragment is now less accessible to the complementary ODN 22(-) in the RNase H cleavage assay (16) (Figure 2B) than 1-570 RNA (containing the entire stem-loop VI) or 1-402 HCV (lacking stem-loops V and VI). Because the larger transcript 1-570 now cleaves more rapidly than the shorter 1-466, steric constraint is no longer a possible explanation for the RNase III cleavage kinetics described above. Thus, the RNase H cleavage data confirm the RNase III results in that the stem-forming sequences at the right part of stem-loop VI actively compromise LRA stability.

Additional Figure 5: ODN 188(-), unrelated to the switch, does not promote mobility retardation of the 1-570 RNA substrate. A) 6% non-denaturing gel analysis of 1-570 RNA incubated with ODN 188 (-) at a final concentration of 1500 nM (lane 1), control buffer (lane 2), and miR-122 at a concentration of 15 nM as a positive control (lane 3).

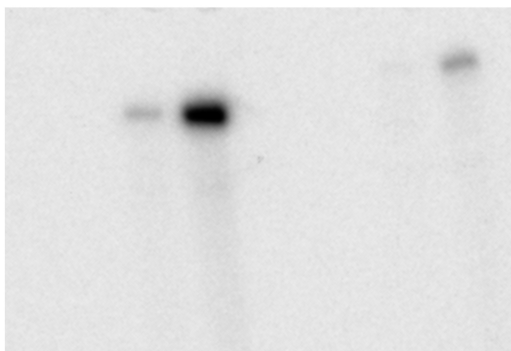
B) Complete accessibility of 1-570 RNA transcript to complementary ODN 188 (-) was tested by RNase H treatment of the hybrid and analysis of the products in 4% denaturing gel. 1-570 RNA is incubated on ice (lane 1), buffer (lane 2), and with the oligonucleotide at a final concentration of 1500 nM without (lane 3), or with 0.5 U/ μ l units of *E. coli* RNase H. Lane 4, with 150nM miR-122 and lane 6, with 1500 nM ODN 22(-).

Additional Figure 6: Determination of the effect of rabbit reticulocyte lysate on the stimulated switching reaction of RNase III by miR-122. A standard 0.001 U/ μ l RNase III reaction was performed on HCV RNA in the absence (Lanes 2-4) or presence of 1 μ l of RRL (lanes 5-9) or 0.5 μ l RRL (lanes 10-14). Control incubations without enzyme (Lanes 2, 5 and 10), with enzyme (Lanes 3, 6 and 11), and with increasing concentration of miR-122: 1.5 nM, 15 nM, or 150 nM are in consecutive lanes 7 to 9, and lanes 12 to 14. Lane 1 is RNA maintained on ice. Lane 15 is a MW marker.

To determine whether the 'O' conformation can be induced and maintain its distinctive RNase III cleavage pattern in a more relevant biological context, we assayed the reaction in the presence of rabbit reticulocyte lysate (RRL) at 5%, 10%, 20%, and 40% vol/vol, which represents a protein concentration in the reaction ranging from 1 μ g/ μ l to 8 μ g/ μ l. 1-570 RNA 0.6 nM in standard buffer was treated with increasing concentrations of miR-122 (1.5, 15 and 150 nM) at each of the RRL concentrations, and after 1 hour of pre-incubation, 0.001 U/ μ l of RNase III was added. Figure 10 shows the reaction at 5% and 10% RRL. A substantial proportion of RNA survived incubation with RRL for 60 minutes and thus accomplished the minimal requisite for the biochemical assay, a condition that we could not reach for the S20 fraction of the Hek-293 cell line (data not shown). Nevertheless, 2 factors made the analysis more difficult in the presence of RRL. One was the appearance of 2 new bands in the informative region of the gel by nucleases in the RRL, the upper one almost coinciding with P1X. The other was that RNase III cleavage of 1-570 RNA was partially prevented even at the lower RRL concentration and was further inhibited as the protein concentration

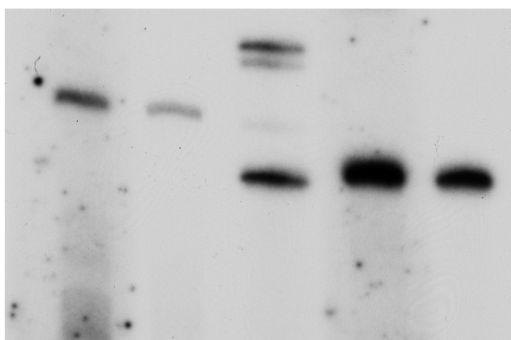
increased. The P2P3 and P2 bands characteristic of the 'C' conformation were nearly undetectable at 20% vol/vol reticulocyte extract, and the reaction was completely inhibited at 40% of RRL (data not shown). With these two restrictions, we could see that miR-122 was able to abrogate the different bands of the 'C' conformation P1P2, and P2, at 5% and at 10% vol/vol RRL, and to clearly increase the intensity of the band running near P1X. This band could be due to conversion to the 'O' form, followed by RNase III cleavage, and to RRL nuclease activity. The relevant point here is that as far as RNase III is able to cleave the viral RNA, miR-122 is active in promoting the band switch.

A



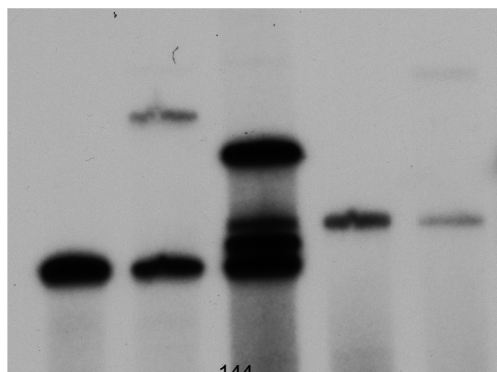
1 2 3 4 5 6

B

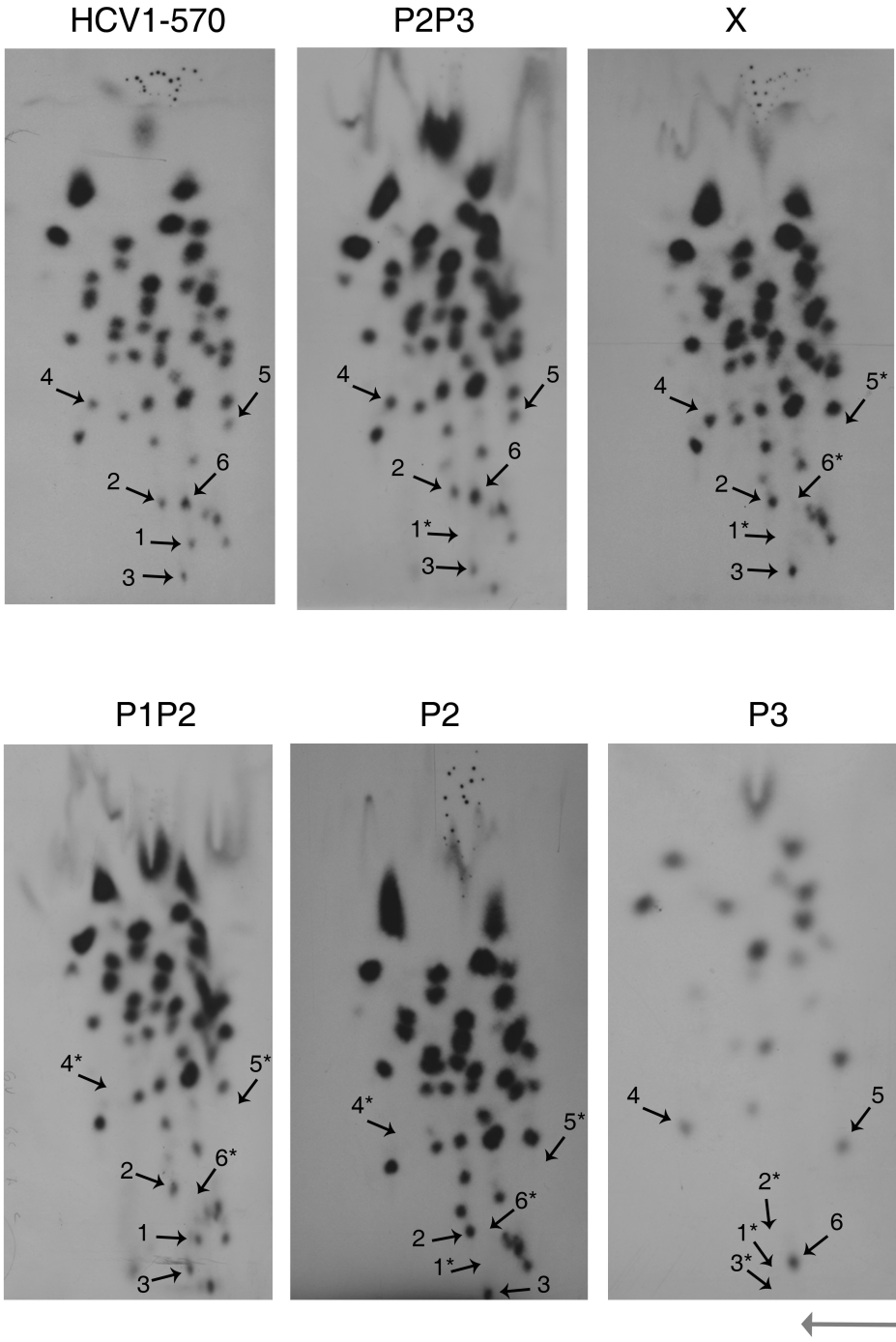
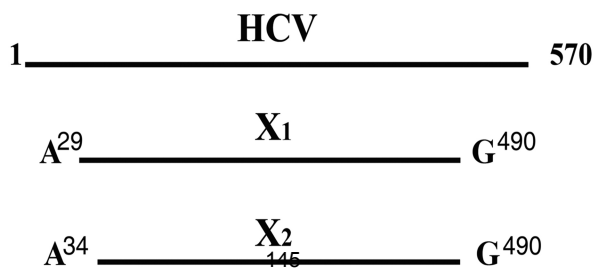


1 2 3 4 5

C

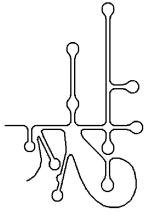


1 2 3 4 5

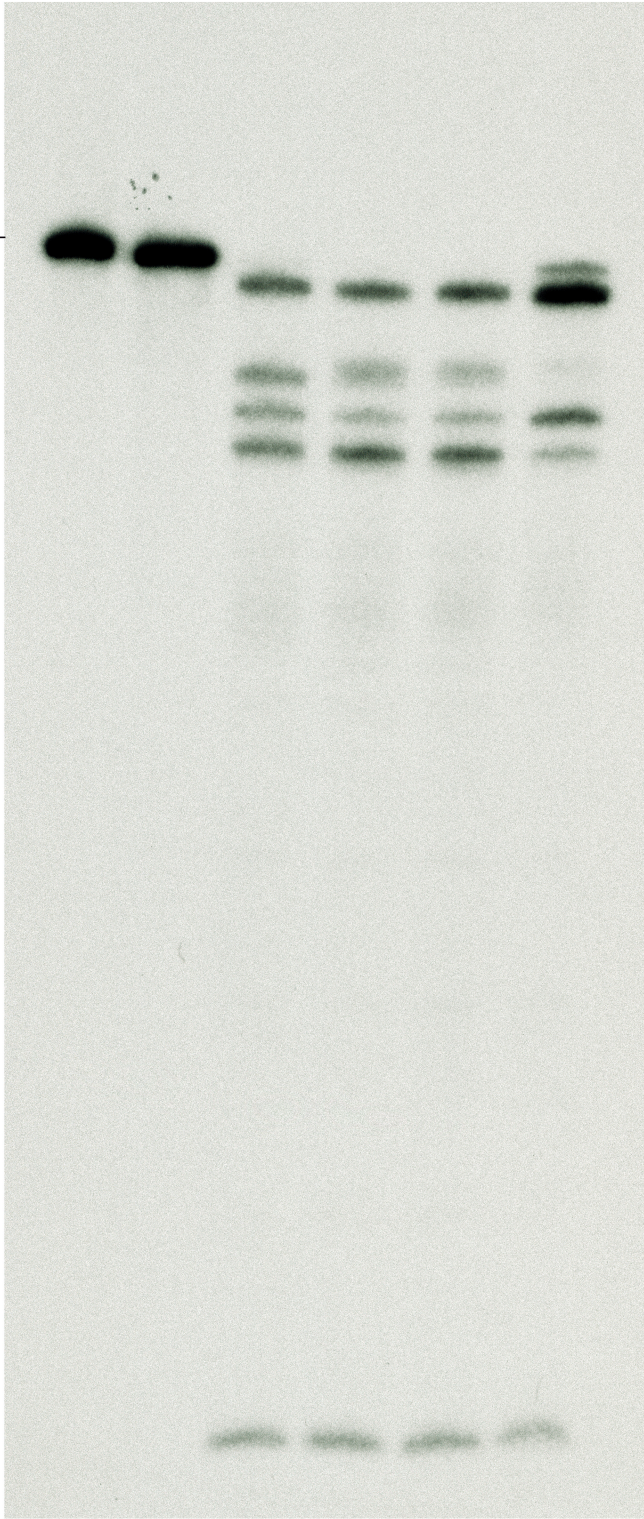
A**B**

473(-) + 492(-)

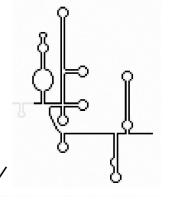
I B R



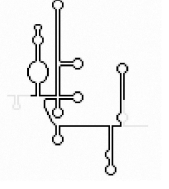
HCV 1-570



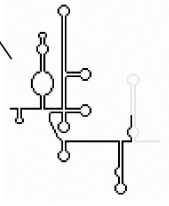
1 2 3 4₁₄₆ 5 6



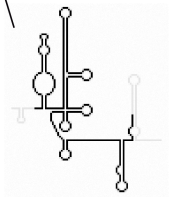
P2P3



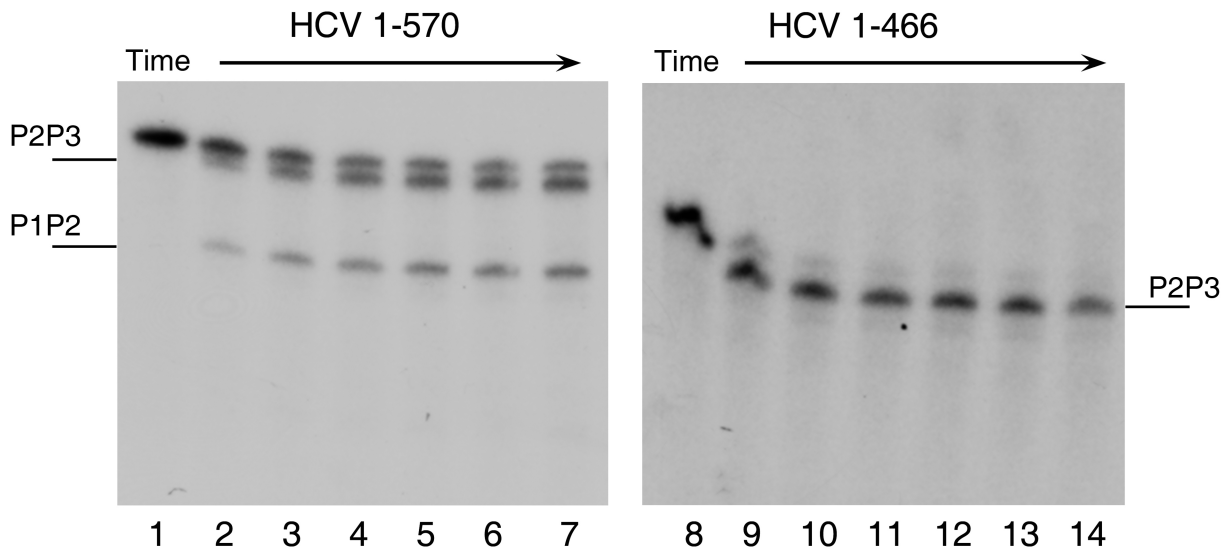
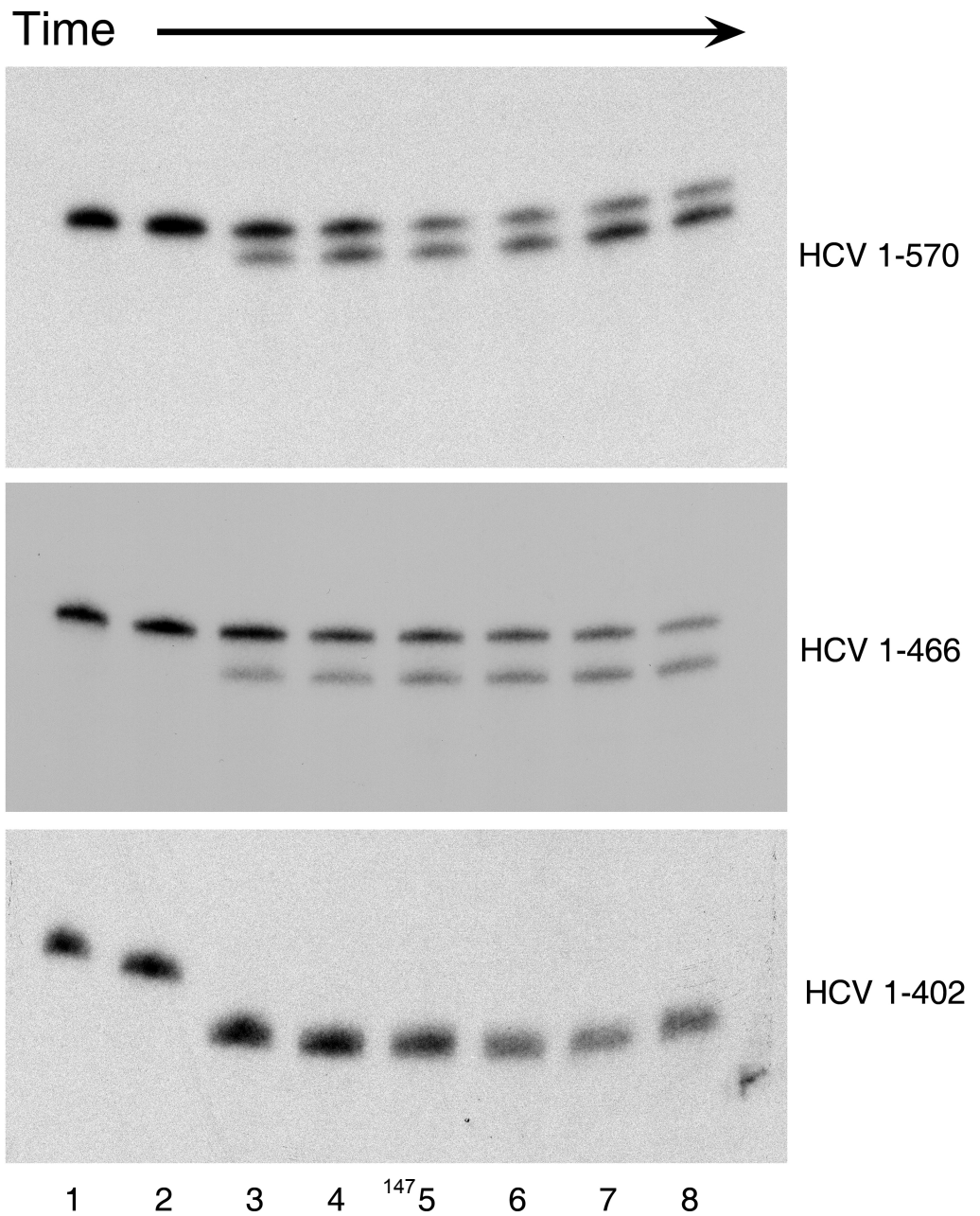
X

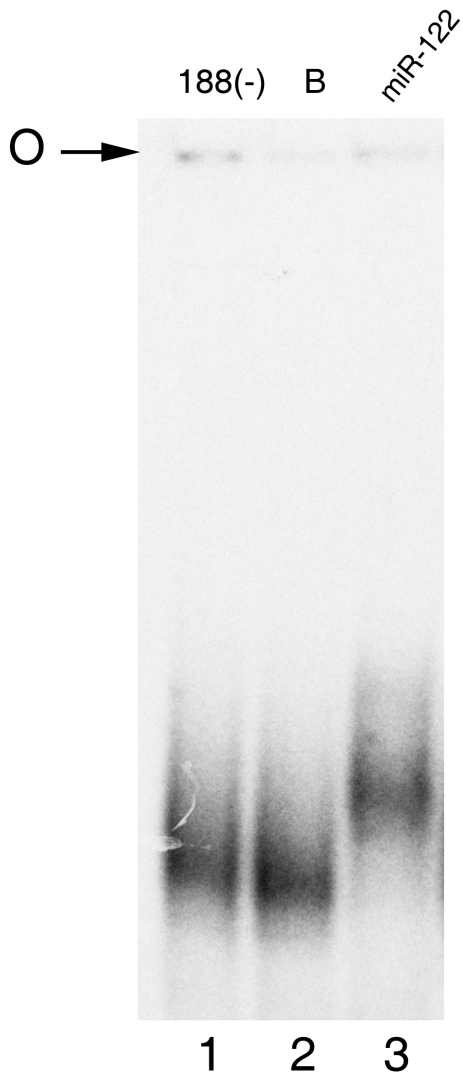
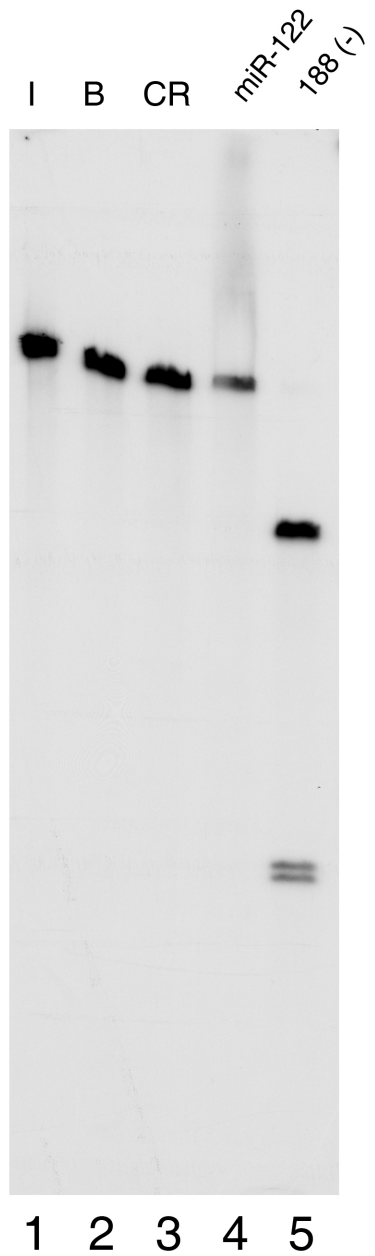


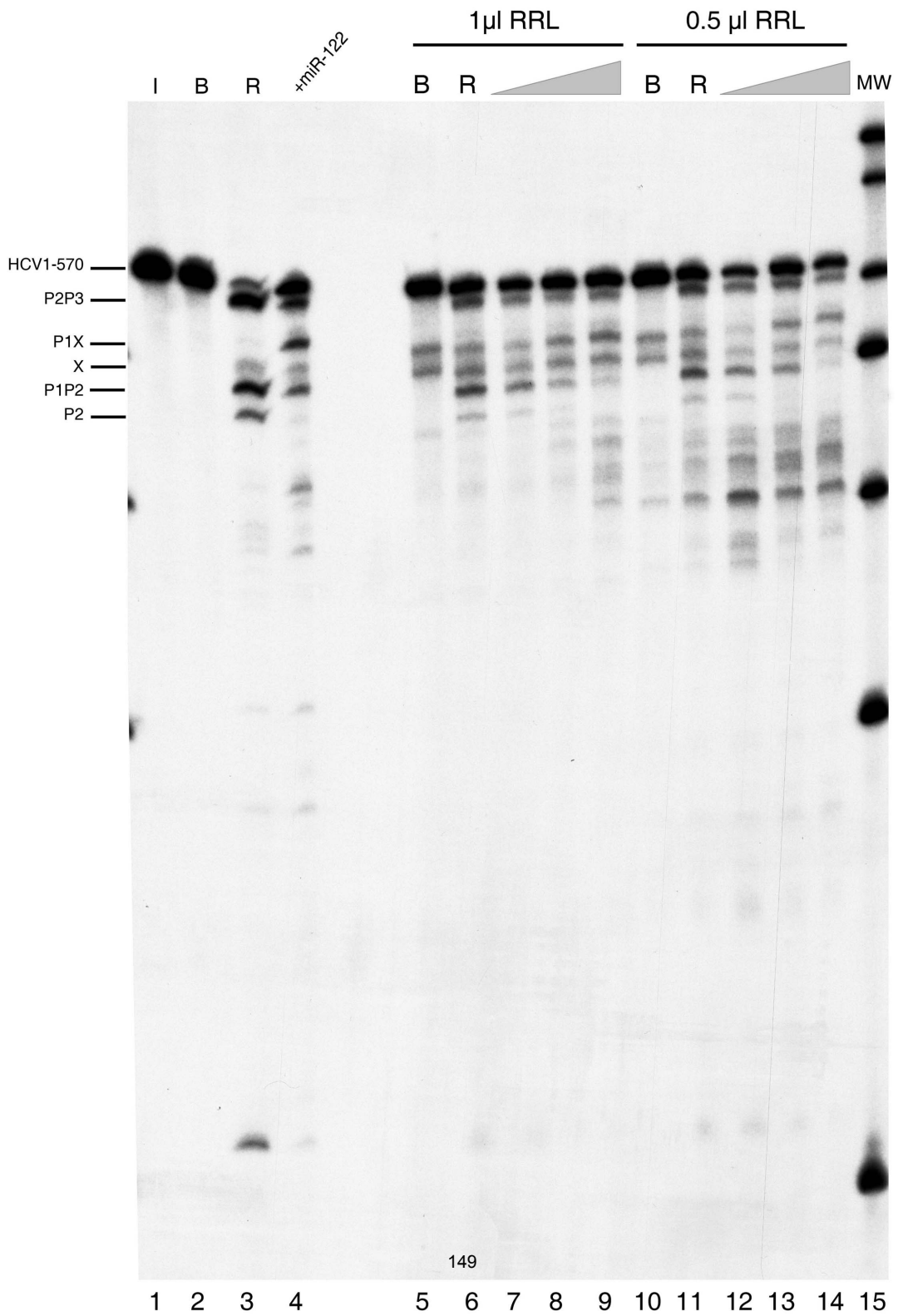
P1P2



P2

A**B**

A**B**



RNA self-cleavage activated by ultraviolet light-induced oxidation

Ascensión Ariza-Mateos¹, Samuel Prieto-Vega¹, Rosa Díaz-Toledano^{1,3}, Alex Birk^{4,*}, Hazel Szeto⁴, Ignacio Mena⁵, Alfredo Berzal-Herranz² and Jordi Gómez^{1,3,*}

¹Laboratory of RNA Archeology, Instituto de Parasitología y Biomedicina 'López-Neyra', CSIC, Armilla, 18100 Granada, ²Instituto de Parasitología y Biomedicina 'López-Neyra' IPBLN-CSIC, Armilla, 18100 Granada, ³Centro de Investigación Biomédica en Red de Enfermedades Hepáticas y Digestivas (CIBERehd), Spain, ⁴Department of Pharmacology, Weill Medical College of Cornell University, New York, NY 1002, USA and ⁵Centro de Investigación en Sanidad Animal (CISA-INIA), Valdeolmos, 28130 Madrid, Spain

Received April 26, 2010; Revised September 16, 2011; Accepted September 17, 2011

ABSTRACT

A novel UV-C-light-induced ribozyme activity was discovered within the highly structured 5'-genomic regions of both Hepatitis C Virus (HCV) and the related Classic Swine Fever Virus (CSFV). Cleavage is mediated by exposure to UV-C light but not by exogenous oxygen radicals. It is also very selective, occurring at base positions HCV C₇₉ and CSFV A₄₅ in some molecules and at the immediately adjacent 5'-positions HCV U₇₈ and CSFV U₄₄ in others. Among other reaction products, the majority of biochemically active products detected contained 3'-phosphate and 5'-phosphate-end groups at the newly generated termini, along with a much lower amount of 3'-hydroxyl end group. While preservation of an E-loop RNA structure in the vicinity of the cleavage site was a requisite for HCV RNA self-cleavage, this was not the case for CSFV RNA. The short size of the reactive domains (~33 nt), which are compatible with primitive RNA motifs, and the lack of sequence homology, indicate that as-yet unidentified UV-activated ribozymes are likely to be found throughout structured RNAs, thereby providing clues to whether early RNA self-cleavage events were mediated by photosensitive RNA structures.

INTRODUCTION

A significant number of novel functions, many of which have proven to be important in the study of gene function

and expression, have been attributed to RNA (1–4). This, in turn, has led to speculation among experts regarding the evolutionary role of RNA in early biological systems. Most of these non-canonical functions for RNA molecules take place in specific regions containing higher order and evolutionarily conserved structural elements. NMR and X-ray crystallographic analyses have provided invaluable insight into some of these tertiary structures and, in the case of certain ribozymes, have revealed their active sites (5,6). One class of RNA that is particularly rich in non-Watson:Crick interactions is the Internal Ribosome Entry Site (IRES) domain located at the 5'-ends of several single-stranded RNA viruses (7) such as Hepatitis C Virus (HCV) (8) and the related animal pestivirus Classical Swine Fever Virus (CSFV) (9) (Figure 1).

It is known that both DNA and RNA chains are affected by direct exposure to ultraviolet (UV) light (4), which in the case of DNA can result in the formation of pyrimidine dimers or random breaks (10–12). The effects of UV light on RNA are relatively unknown, although UV-C irradiation has been shown to induce mainly pyrimidine dimers and uridine hydrates (13) and, less frequently, unspecific chain breaks (14,15). Base-radicals are major reactive intermediates of RNA UV-mediated degradation (16,17). Using an oligoribonucleotide with a position-induced base-radical model (18), the mechanism of RNA oxidative degradation has recently been elucidated in two consecutive studies (19,20). These studies indicated that the cleavage occurred internal to the initial radical generation site, referred to as intra-nucleotidyl strand scission, and at the adjacent 5' nt, referred to as inter-nucleotidyl strand scission, as a consequence of migration of the radical from its original base to the upstream base. Nevertheless, a part of

*To whom correspondence should be addressed. Jordi Gomez. Tel: +34 958181647; Fax +34 958181632; Email: jgomez@ipb.csic.es
Correspondence may also be addressed to Alex Birk. Tel: +1 2127466232; Fax: +1 2127468835; Email: avbirk@med.cornell.edu
Present address:

Ignacio Mena. Microbiology Department, Mount Sinai School of Medicine. New York, NY 10029, USA.

unspecific degradation it should be emphasized that UV-C can also induce specific covalent bonds between bases in certain RNA regions containing structural motifs known as E-loops (21), an effect which has been utilized for the structural study of RNAs (21–26), including HCV RNA (27).

The biochemical mechanisms employed by RNA are surprisingly diverse (28–31). Nevertheless, the known chemistry promoted by natural RNAs alone is limited to transesterification and phosphate-bond hydrolysis, grouped together as nucleophilic cleavage reactions, or their reverse ligation reactions (30,31). One interesting exception, albeit in a DNA model, is the known ability of synthetic DNAs to promote self-repair of crosslinked thymine bases in a UV-dependent manner (32). It has been shown that a structural element involving four deoxy-G-residues (33) absorbs UV-light activating crosslink repair.

Whilst performing UV-C irradiation experiments on HCV RNA transcripts (27), we found that, somewhat surprisingly, UV-C site-selectively cleaved HCV genomic RNA in the presence of Mg^{2+} . We report here that UV-induced cleavage corresponds to a self-cleavage event specifically promoted by UV irradiation at a very specific location of HCV RNA. We also report the subset of key experiments which indicate that self-cleavage also occurs in the RNA of CSFV, thus making UV-C-induced self-cleavage a putatively general property of RNA.

This is the first evidence of a structure-dependent UV-activated selective self-cleavage of RNA in the absence of a photosensitizer (34).

MATERIALS AND METHODS

RNA transcription and purification

The plasmid pN(1–4728) which contains the first 4.7 kb of HCV sequence adjacent to a phage T7 promoter was a gift from Dr Stanley Lemon, University of Texas, Galveston. This DNA template was cleaved with restriction enzyme and then transcribed with phage T7 RNA polymerase *in vitro* in the presence of [α - ^{32}P]-labeled rNTPs (Perkin-Elmer) as previously described (35,36) to yield RNA transcripts of bases 1–130 (NciI), 1–249 (NheI) and 1–402 (AatII). A DNA plasmid encoding bases 1–442 of CSFV was a kind gift from Dr Richard Jackson of Cambridge University. This plasmid was digested and transcribed to yield RNA transcripts of bases 1–218 (XhoI). The set of sequentially deleted or mutated DNAs representing the wt or mutants for HCV and CSFV RNAs were obtained after digestion with plasmid polylinker enzymes. The transcripts used are smaller subdomains of the entire HCV and CSFV IRES structures shown in Figure 1. RNA transcriptions were followed by brief treatment with RNase-free DNase (RQ1) for 15 min at 37°C. A 1-ml aliquot of TSE 1× (50 mM Tris, pH 7.0, 100 mM NaCl, 10 mM EDTA) was then added and the samples extracted with phenol. Finally, 1 ml of absolute ethanol was added to give a 50% EtOH 0.5× TSE solution. The samples were layered carefully on a CF11 column equilibrated in 50%

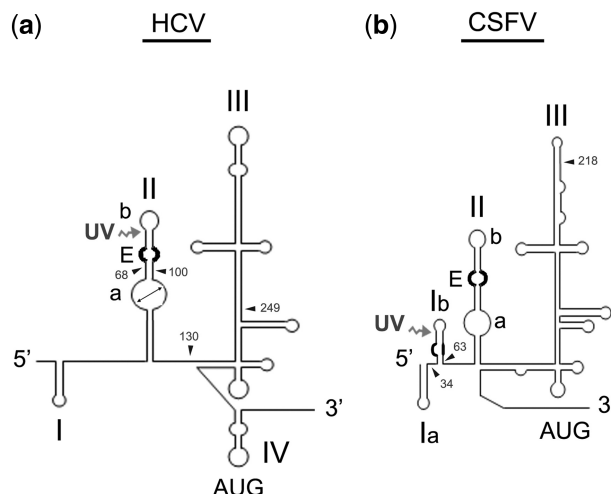


Figure 1. Secondary structure diagrams of the 5'-terminal regions of HCV and CSFV RNAs. Structural organization of the 5'-untranslated region (~400 bases long) of HCV and CSFV RNAs (43,44) (60). The main differences between the two viral RNAs are that HCV lacks stem-loop 1b of pestiviruses, and domain II is slightly longer in HCV than in the pestiviruses. A remarkable similarity is the presence of an E-loop structural motif in the stem-loop IIb (54,61). (a) Bases 1–402 of HCV RNA; (b) Bases 1–380 of CSFV RNA. Each RNA's 5'-end is on the left; major common structural domains are depicted as domains I–IV in HCV and I to III in CSFV. Domain I ('I') is bipartite in CSFV ('Ia' and 'Ib'). A UV-crosslinkable element previously described in HCV RNA is marked with a double arrowhead in stem-loop IIa. A characterized E-loop in the immediate vicinity, as well as an analogous motif at the same site in CSFV RNA, is drawn in bold. An uncharacterized internal loop in stem-loop Ib of CSFV RNA is also in bold. The position of AUG is indicated. Arrowheads locate the different transcripts size: 1–130, 1–249, 1–402 and 68–100 for HCV RNA and 1–218 and 34–63 for CSFV RNA. Cleavage site is indicated with an undulate arrow.

ethanol/TSE, and the 'flow-through' collected in a scintillation vial; three, 1 ml washes with 50% ethanol/TSE were then carried out. The fractions were collected in low retention Eppendorf tubes, using a 'standard' volume that was achieved by eye, as soon as the 50% ethanol/TSE had run dry, at which point 1 ml of water was added to the column. Significantly radioactive fractions were pooled and precipitated with sodium acetate and ethanol overnight at $-20^{\circ}C$.

The resuspended RNA transcripts were then purified by electrophoresis in 4–10% gel under denaturing conditions. Bands were visualized by autoradiography, excised from the gel, and eluted overnight in buffer (100 mM Tris-HCl, pH 7.5 and 10 mM EDTA, pH 7.5). The concentration of radioactive transcripts was determined by calculating the amount of incorporated [α - ^{32}P]GTP based on scintillation counting. The reactions yield RNAs at a specific radioactivity of 10^5 – 10^7 dpm/ μg , as noted in the text.

The synthetic DNA oligodeoxynucleotides used as transcription templates were obtained from the Instituto de Parasitología y Biomedicina 'López-Neyra' (CSIC). In three particular cases, the deleted and mutated HCV 130 RNA: ΔG_{94} and ${}_{93}AGA_{96}$, respectively, as well as the smaller substrate HCV RNA which correspond to the sequences 68–100 in the larger RNA were synthesized from

their cDNA copies cloned into EcoRI and HindIII sites of a plasmid under the T7 transcription promoter. As a consequence the corresponding transcripts have an increased length because they carry in their termini the additional sequences of the cloning sites. Transcripts were prepared as before except that no purification through CF11 chromatography was carried out.

UV-C cleavage reactions

A technique previously used to induce RNA cross-linking was used (22,27). Aliquots of the RNAs (1000–50 000 dpm) were dissolved in either ‘standard buffer’ (10 μ l of 0.01 M Tris–HCl, pH 7.6, containing 10 mM MgCl₂) or in water. RNA samples in water were then kept on ice (referred to in the figure footnotes as ‘ice’). RNA samples in standard buffer were incubated on ice without UV-C exposure (referred to in the figure footnotes as ‘buffer’), or exposed to UV-C light (wavelength: 254 nm) for increasing time periods (between 30 and 540 s). Briefly, 10 μ l drops were pipetted onto Saran Wrap covering the surface of a prechilled UVP Inc. Mineralight Lamp (model UVG-11, short-wave UV-C-254 nm, 220 V, 60 Hz, 0.16 A). These drops were irradiated for 30 s, with a 30 s break between intervals for cooling (22), for different periods of time and then electrophoresed on a 4–20% polyacrylamide gel in TBE buffer containing 7 M urea and autoradiographed. Cleavage products were isolated and eluted from the gel for further analysis.

Other assayed reaction conditions:

Human RNase P buffer (5 \times): 50 mM HEPES–KOH pH 7.5, 50 mM Ac₂Mg, 500 mM AcNH₄; RNase DICER buffer (5 \times): 100 mM HEPES, 250 mM Tris–HCl, pH 8, 1500 mM NaCl, 25 mM MgCl₂. Buffer RNase P ribozyme form cyanobacteria *Synechocystis* sp. (5 \times): 250 mM Tris–HCl, pH 8, 500 mM MgCl₂. The reaction is supplemented with KCl up to 1 M final concentration.

Phosphate buffer (1 \times): 150 mM NaCl, sodium phosphate pH 7.6, 10 mM, 1 mM Na₂EDTA, pH 6.5 [see Wimberly *et al.* (26)].

EDTA pre-incubations

RNAs were preheated for 1 min in 2 mM Na₂EDTA, 40 mM Tris–HCl, pH 7.6 at 90°C and then the pre-heated mixtures allowed to cool slowly to room temperature and subsequently to 4°C. RNA transcripts were incubated for either 2 h or overnight at 4°C in the same buffer. Transcripts were then exposed to 254 nm UV-C light for 3 min either with or without the addition of 20 mM MgCl₂, and then electrophoresed on a 6% polyacrylamide gel in TBE buffer containing 7 M urea and autoradiographed as before (27).

RNA fingerprinting

Isolated RNA molecules were dried with 10 μ g of tRNA, exhaustively digested for 40 min with 2 μ l of 1 mg/ml RNase T1 (CalBiochem) at 37°C, and the resulting oligonucleotides subjected to 2D separation by base

composition and size, as described by A.D. Branch and H.D. Robertson (22,37).

OH• radical RNA does not promote specific cleavage of viral RNAs *in vitro*

In order to investigate the possibility that cleavage could be mediated by OH• radicals generated in solution by the UV-C irradiation, we assayed the effect of this radical. The molecule was generated via the Fenton reaction [Fe(EDTA)]²⁻ + H₂O₂ → [Fe(EDTA)]⁻ + OH• + OH⁻ on the viral RNAs (38). Fenton reaction also give rise to superoxide species O₂⁻ (39). Probing experiments were carried out using internally labeled HCV RNA 1–130 and 1–249 and CSFV RNA 1–130 as substrate or end labeled minimal substrates. Reaction time of 2 min was assayed and the products electrophoresed in parallel to a standard UV-C cleavage reaction.

RNA sequencing reactions

To allow identification of the cleavage sites, a parallel run was performed with a 3'-end-labeled 1–570 RNA ladder generated by either limited alkaline hydrolysis or RNase T1 degradation under denaturing conditions. In the alkaline hydrolysis reactions, aliquots containing 5 \times 10² to 10⁴ dpm of 3'-end-labeled RNA were incubated with 1 μ g of carrier tRNA in 0.1 M NaHCO₃/Na₂CO₃ (pH 9) from 50 to 120 s at 95°C. The RNase T1 reaction under denaturing conditions was performed using similar amounts of labeled substrate in the presence of 1 μ g tRNA, 7 M urea at 55°C for 5 min. All reactions were quenched with one volume of loading buffer then maintained on dry ice until being loaded onto a 10–20% polyacrylamide–urea sequencing gel.

RNA endgroup analysis

RNA end-groups produced by UV-C-induced self-cleavage were analyzed by phosphatase, kinase, ligase and poly (A) or poly (U) polymerase treatment of UV-C-cleaved RNA transcripts. Calf alkaline phosphatase treatment was carried out as described by Knapp (40). Briefly, a 1000–50 000 dpm aliquot of the major cleavage product of either the CSFV or HCV transcript was incubated at 37°C for 30 min in a buffer containing 10 mM MgCl₂, 100 mM Tris–HCl, pH 7.4 and 0.4 U calf alkaline phosphatase. Artic phosphatase (AP) treatment was performed according to NEB catalog standard reaction. Phosphatase-dependent 5'-terminal labeling of RNAs containing newly created 5'-termini by polynucleotide kinase was carried out as follows: RNA aliquots were incubated at 37°C for 30 min in a buffer containing 10 mM MgCl₂, 40 mM Tris–HCl, pH 8.0, 5 mM dithiothreitol (DTT), 5% (v/v) glycerol, 0.4 mM spermidine, 10 U polynucleotide kinase (NEB) and [γ -³²P]ATP (Perkin-Elmer) with or without phosphatase pretreatment (35,40). RNA ligase was used to treat cleavage product bands, either previously phosphatase treated or not, as follows: RNAs were incubated at 4°C for 4 days in a buffer containing 10 mM MgCl₂, 50 mM HEPES, pH 8.3, 5 mM DTT, 0.12 mM ATP, 4 U of T4 RNA ligase (Promega) and [5'-³²P]pCp (Perkin-Elmer) (35,40). Poly (A) polymerase

(NEB) and Poly (U) polymerase (NEB) reaction was performed in the buffer provided by NEB and recommended conditions in the presence of [α - 32 P]ATP or [α - 32 P]UTP. Treated RNAs were subjected to proteinase K/SDS treatment. The volume was made up to 100 μ l with water and precipitated in EtOH and sodium acetate, in the absence of carrier and spun down in a microfuge at 12 500 rpm during 90 min at 4°C. The pellet was resuspended in 10–30 μ l of gel loading buffer.

Deletion analysis and *in vitro* mutagenesis

DNA templates corresponding to the 1–130 HCV and CSFV 1–218 RNA carrying deletions or mutations at different sites were obtained by synthesis of DNA oligonucleotides carrying the sequence for the T7 promoter. Those that were >100 nt templates were constructed partially from a cloned HCV sequence and a synthetic oligonucleotide carrying the modifications and subsequently cloned and sequenced.

CSFV infection under oxidative stress conditions

CSFV experiments were performed in the high security facilities at the animal health center: Centro de Investigación en Sanidad Animal CISA-INIA, in Valdeolmos, Madrid. Porcine PK15 cells were grown in either 24- (experiment 1) or 6-well (experiment 2) plates and infected with CSFV (strain Alfort) at a m.o.i. of approximately 1 TCID per cell in DMEM supplemented with glutamine, antibiotics and 2% serum. After 8 h the supernatant was replaced by a medium containing varying concentrations of H₂O₂ (experiment 1: 0, 0.2 and 1 mM H₂O₂; experiment 2: 0, 0.1, 0.2 and 0.5 mM H₂O₂). Total RNA was harvested 24 h post-infection using Trizol Reagent (Invitrogen) and used as template for the RACE reaction.

During RNA harvesting, cell cultures were visualized under a microscope in order to detect any toxic effects arising from the H₂O₂ treatment. In addition, equal quantities of the RNA obtained were analyzed by agarose gel electrophoresis. This was performed in order to visualize differences in RNA yield. Both techniques (data not shown) revealed that concentrations of H₂O₂ up to 0.2 mM had no detectable effects on cell survival or RNA yield, while higher concentrations (0.5 and 1 mM) had dramatic toxic effects.

Analysis of CSFV RNA from infected cells

The RACE reaction was performed using reagents from the 5'/3' RACE Kit, second Generation (Roche), following the manufacturer's instructions. Briefly, a cDNA was obtained by reverse transcription using primer Alf 751-R (5'-TCCGTCACCTGTCACC-3'). A poly (dA) tail was then added to the 3'-end of the cDNA using TdT enzyme and dATP. Finally, nested PCR was performed using virus specific primers Alf 601-R (5'-GCCTAGATG GTTGCCACTCC-3') and Pesti-D (5'-TCAACTCCATG TGCCATGTA-3') and primers specific for the poly (dA) tail. Fifteen microliters of the second PCR were analyzed by electrophoresis in a 2% agarose gel. The expected size of the PCR product from an intact viral RNA was 421 bp.

Mass spectrometry (MALDI-TOF)

A total of 100 drops (10 μ l, 15 nM synthetic RNA 68–100) were irradiated simultaneously, and the process repeated five times. The UV-C band products and substrate remaining after irradiation were purified on 15% polyacrylamide gels. UV-C-irradiated RNA labeled at its 3'- or 5'-end as a mobility reference. Untreated or treated RNAs were precipitated with 3 M ammonium acetate and 2.5 volumes of ethanol. After centrifugation, the precipitated material was dried in a vacuum chamber. The material was resuspended in water, and passed through a commercial micro-column (ZipTip U-C18 from Millipore) before mixing with the mass spectrometry matrix THAP (FLUKA). As external reference for mass calculation a ribo-oligonucleotide of 6356.79 Da was employed. The apparatus employed was a MALDI-TOF Voyager DE-PRO from Applied Biosystems.

Quantification

Product bands were scanned in a Phosphorimager (Storm 820, GE) and quantified with Image Quant 5.2 software (GE). The % formation of cleavage products was calculated as follows: percentage UV-C self-cleavage product = (product)/(starting material + Σ products) \times 100.

RESULTS

Detection and demonstration of a cleavage event in viral transcripts by UV-C irradiation and determination of cleavage position

Initial UV-C (254 nm) cleavage experiments involved a 249- and a 218-base sequence of HCV and CSFV RNA transcripts, respectively. The autoradiogram in [Figure 2](#) shows that UV-C light cleaved these substrate materials (SMs) with apparent specificity to produce two clearly defined cleavage products ('B1' and 'B2') in a denaturing electrophoresis gel.

The data shown in [Figure 2](#) were sufficiently novel that it was necessary to analyze the products resulting from this UV-mediated RNA cleavage directly, using different transcript lengths, by complementary methods that allowed mapping of the cleavage location. Thus, a fingerprint method was employed to map the cleavage specificity using internally labeled RNA chains ([Figure 3a](#)) and polyacrylamide sequencing gels for transcripts labeled asymmetrically at their ends ([Figure 3b](#)). A single band was identified in the sequence resolution gels at both sequencing polarities for both viral RNAs underlying the specificity of self-cleavage reaction. The electrophoretic mobility of the UV cleavage products in comparison with the mobility of RNase T1 partial digestion products allowed us to identify the appearance of new RNA fragments with termini located in the interval U₇₇-G₈₂ for HCV RNA and A₃₈-G₅₂ for CSFV RNA. Meanwhile, the fingerprinting of internally labeled RNA oligonucleotides after complete RNase T1 digestion highlighted the disappearance of the RNase T1 oligonucleotide that undergoes cleavage (5'₇₈UCUAG₈₂3' for HCV and

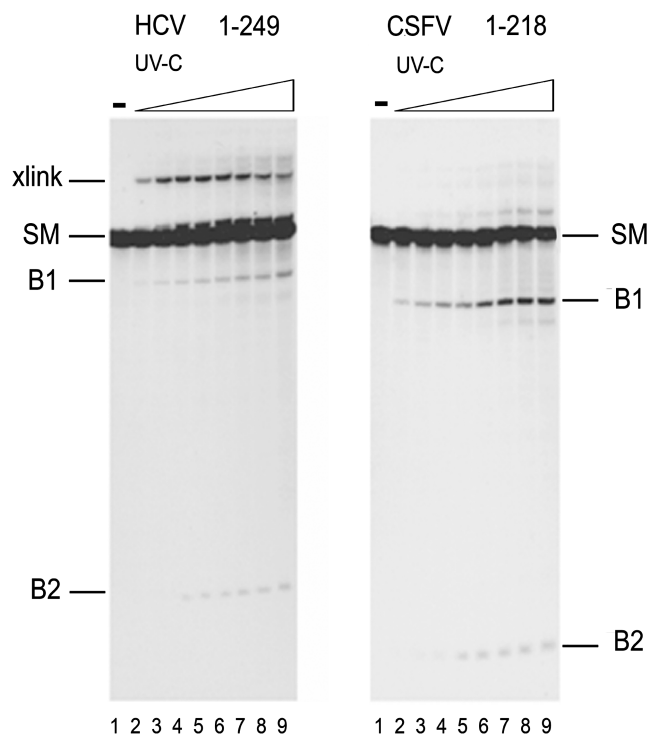


Figure 2. UV cleaves HCV and CSFV RNAs. Aliquots of HCV RNA 1–249 (left panel) or CSFV RNA 1–218 (right panel) (50000 dpm) (specific radioactivity 10^7 dpm/ μ g) were dissolved in 10 μ l of standard buffer (lane 1) or exposed to 254nm UV-C light for increasing times: 30, 60, 90, 120, 150, 180, 240 and 360 s (lanes 2–9). Samples were then electrophoresed on a standard 6% denaturing polyacrylamide gel and autoradiographed. The larger cleavage product is labeled as ‘B1’ and the smaller one ‘B2’. The starting material is referred to as ‘SM’. Previously characterized UV-crosslinked species (X-link 1) (27) migrate more slowly than the intense starting material band, a second uncharacterized crosslink band (X-link 2) is indicated.

5’₃₈AUACACUAAAUUUCG₅₂3’ for CSFV), thus confirming the results obtained by electrophoresis.

Both methods employing RNA transcripts (labeled either internally for fingerprinting or end-labeled for electrophoresis) coincided in the determination of the product fragments carrying the original 5’-PPP- and the original -3’-OH-ends, identified as B2 and B1, respectively, in Figure 2. This nomenclature, in other words B2 for the band carrying the newly generated 3’-end and B1 for the newly generated 5’-end, is maintained throughout this work irrespective of the length of the transcripts. These findings clearly demonstrate that the phenomenon involved in this UV-C-induced reaction is a cleavage reaction and that the electrophoretic band products B2 and B1 did not correspond to other potential UV-mediated side-reaction products as RNA adducts or rare crosslinked conformation with anomalous gel migration. They also locate the cleavage sites in the apical region of stem-loop II in HCV RNA and in the apical region of stem-loop I b in CSFV RNA (Figure 1).

The fact that cleavage specificity was maintained in RNAs with different transcript lengths (HCV RNA 1–130 and 1–402; Supplementary Figure S1) indicates that self-cleavage is not affected by the presence or absence of sequences from stem-loops III and IV (129–402).

Determination of cleavage site

In order to specifically determine the cleavage position with base-scale resolution, we performed a standard UV-C reaction and partial T1 digestion and alkali degradation using the minimum RNA fragment length that could retain the ability to act as a substrate G₆₈–G₁₀₀ for HCV and U₃₄–G₆₃ for CSFV) (Figure 4)—minimal fragment characterization is described below in the result section ‘Structural elements required for the self-cleavage reaction’: It was found that the main cleavages for HCV RNA occurred to leave fragments with new 3’-ends running as doublets at positions G₇₇ and U₇₈, with a smear of radioactive material reaching position C₇₉. The band carrying the new 5’-end ran as a wide band centered around C₇₉. The main band carrying the new 3’-end for CSFV RNA ran between U₄₄ and A₄₅ and was flanked by two faint bands, an upper band between A₄₅ and A₄₆ and a lower band that ran as U₄₄. The band for the new 5’-end was similar-shaped to that obtained for HCV RNA, in other words a very wide band that ran between U₄₄ and C₄₃.

Because RNA cleavage products migration in the electrophoresis is affected by the nature of the chemical end group, final assignment of each band to a specific base would wait until determination these end groups in the following results sections.

Characterization of UV-cleavage conditions

We decided to determine whether there was any UV-C dose-response behavior, substrate concentration dependence and whether Mg²⁺ participates in the reaction. The graphs in Figure 5 obtained from series of kinetic cleavage analysis as those shown in Supplementary Figure S2 show that the extent of HCV RNA 1–130 and CSFV RNA 1–218 self-cleavage is proportional to the dose of UV-C irradiation during most of the reaction period studied 540 s for HCV RNA 1–130 and 360 s for CSFV RNA 1–218. At the later time point assayed for each RNA (540 s for HCV RNA and 360 s for CSFV RNA), the intensity of the band products remained essentially the same or even began to decrease. It can be seen from the gel images in Supplementary Figure S2 that there was an increase in the background smear at these latter time points. This implies that the selective cleavage reaction is blurred by unspecific degradation. An irradiation time of 90–180 s was chosen for subsequent reactions as the reaction is clearly linear over this time period, in order to minimize potential secondary modifications and to use comparable conditions to UV-C RNA crosslinking studies that used the same standard UV-C source as employed here (22,27,41).

The rate of product formation over a 10- and 50-fold range of HCV and CSFV RNA substrate concentrations, respectively, was also examined. At the end of the reaction, the percentage of product formation for the most and least concentrated RNA samples was $6.5 \pm 1.8\%$ and $6.6 \pm 2.1\%$ for HCV and $14.2 \pm 5\%$ and 15 ± 3.1 for CSFV RNAs, respectively. The kinetic cleavage curve for each virus produced using the data for the distinct RNA concentrations tested and grouped

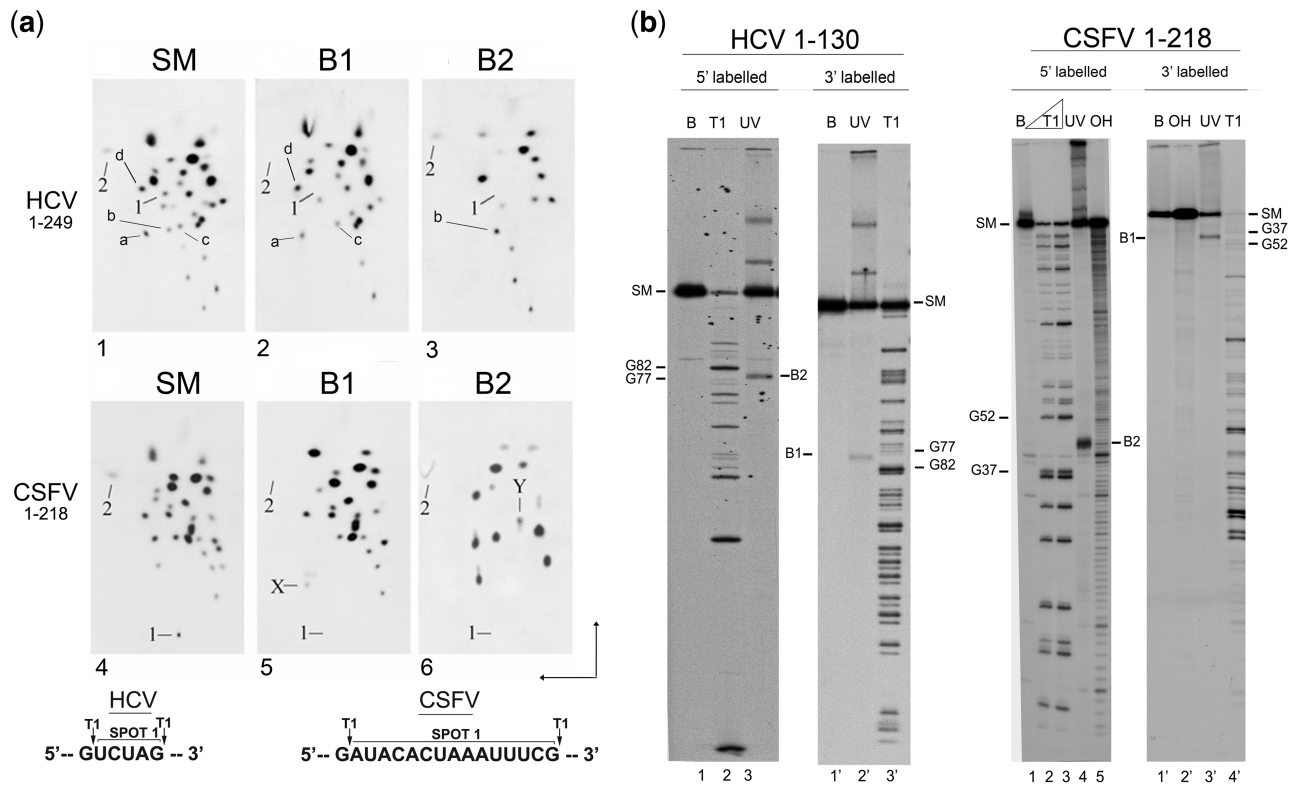


Figure 3. Characterization of UV-C cleavage of viral RNAs by fingerprinting and electrophoretic methods. **(a)** The RNA fingerprints of internally [α - 32 P] HCV (panels 1–3) and CSFV RNA (panels 4–6). Labeled SM, band B1 and band B2 were exhaustively digested with RNase T1 and the products subjected to 2D separation. **(1)** RNA fingerprint of HCV 1–249. A total of 500 000 dpm of HCV SM was fingerprinted. Spot 1: the HCV oligonucleotide 5'₇₈UCUAG₈₂3' within which cleavage takes place; Spot 2: this has the characteristic mobility of the 5'-terminal nucleotide 5'pppGp3'. **(2)** RNA fingerprint of HCV B1. A total of 300 000 dpm of RNA was fingerprinted as above. Spot 1 has disappeared, while the absence of the 5'-end (spot 2) shows that HCV B1 contains the 3'-portion of SM. **(3)** Fingerprint of HCV B2 (100 000 dpm). '1' indicates the loss of spot 1, while the presence of the HCV 5'-end ('2') shows that HCV B2 contains the 5'-portion of SM. **(4–6)**: RNA fingerprints of CSFV 1–218. SM (500 000 dpm), B1 (300 000 dpm) and B2 (100 000 dpm), transcribed with all four [α - 32 P]-labeled rNTPs. '1': the CSFV oligonucleotide 5'₃₈AUACACUAAAUUUCG₅₂3', which is present in SM but absent from B1 and B2; 'X' (a new CSFV B1 oligonucleotide) and 'Y' (the other new CSFV oligonucleotide) arise from cleavage within spot 1 (see text). '2': the 5'-end of CSFV, present in SM and B2, but not B1. Numbering according to Wang *et al.* (62) for HCV genotype 1b and Gene Bank J04358 for CSFV Alfort Isolate. The sequence of the spot numbered as 1 was identified by secondary RNase analysis and high voltage electrophoresis on DEAE and Whatmann paper by Hugh D. Robertson (data not available), as well as by superposition with previously resolved HCV fingerprints using secondary analysis and on the basis of the rules for RNA oligonucleotide mobility during 2D TLC. Briefly, these rules are: the larger the oligonucleotide, the slower the migration of the corresponding spot to the bottom. As far as composition is concerned, Us displace the spot to the left, Cs to the right, and As cause a slight delay, thus meaning that several As in the same oligo may cause it to behave as an oligo containing one or even two additional bases (37). As far as sequence is concerned, as HCV RNA was transcribed in the presence of [α - 32 P]GTP here, those T1 oligonucleotides in the original sequence that are followed by a (pG) carry a double label. In the case of HCV RNA several RNase T1 oligonucleotides are indicated as mobility reference: a: UCCUUUCUUGp(G); b: UCUUCAGp(C) 61:68; c: CUCAAUGp(G) 211–217; d: AUUUGp(G) 225–229. Spot 1 locates in the border of the triangle that can be formed by spots i, f and g. In CSFV, spot 1 is the slow migrating spot, and thus corresponded to the largest RNase T1 oligonucleotide. In both HCV and CSFV, band B2 contains the original 5'-terminal nucleotide, pppGp, of the substrate RNA transcript (indicated by '2'). The disappearance of spot 1 from both product band fingerprints (see Figure 1a, images 2, 3 and images 5, 6) suggests that self-cleavage occurs within this oligonucleotide and that this event is specific. Moreover, in the case of CSFV RNA two smaller oligomers (X and Y) that represent the fragment products of spot 1 are observed within the fingerprints of both product bands (B1 and B2) for CSFV. Indicated at the bottom is the sequence surrounding RNase T1 cleavage sites. **(b)** Electrophoresis analysis: Autoradiogram showing a parallel run of HCV RNA 1–130 and CSFV RNA 1–218 UV-cleavage reaction, with RNase T1 treated samples and control reactions for transcripts labeled at either the 5'-extreme with [γ - 32 P]GTP during transcription or the 3'-extreme with [γ - 32 P]pCp and T4 RNA ligase. HCV (lanes 1–6) and CSFV (lanes 1–9). HCV: Lanes 1 and 1': RNAs incubated in standard buffer; lanes 2 and 2': RNAs treated with RNase T1 under denaturing conditions; lanes 3 and 3': RNA irradiated with UV-C light for 180s. CSFV: Lanes 1 and 1': RNAs incubated under standard conditions; lanes 2, 3 and 4': RNA treated with RNase T1; lanes 4 and 3': RNA irradiated with UV-C light; Lanes 5 and 2' RNAs partially degraded with alkali. 'G' positions of a relevant size are indicated on either side of the gels. Lines indicate SM, and products B1 and B2.

together was found to fit a third degree polynomic equation (solid line) (Supplementary Figure S3) with an R^2 value of 0.999 for both viral RNAs. This indicates little variation in the extent of UV-C promoted cleavage in relation to RNA concentrations and therefore that the

reaction is intra-molecular. The parametric data of the equation is summarized in (Supplementary Figure S3).

The role of magnesium ions is traditionally addressed in RNA cleavage studies, therefore UV-C-induced cleavage assays were carried out under the magnesium-free

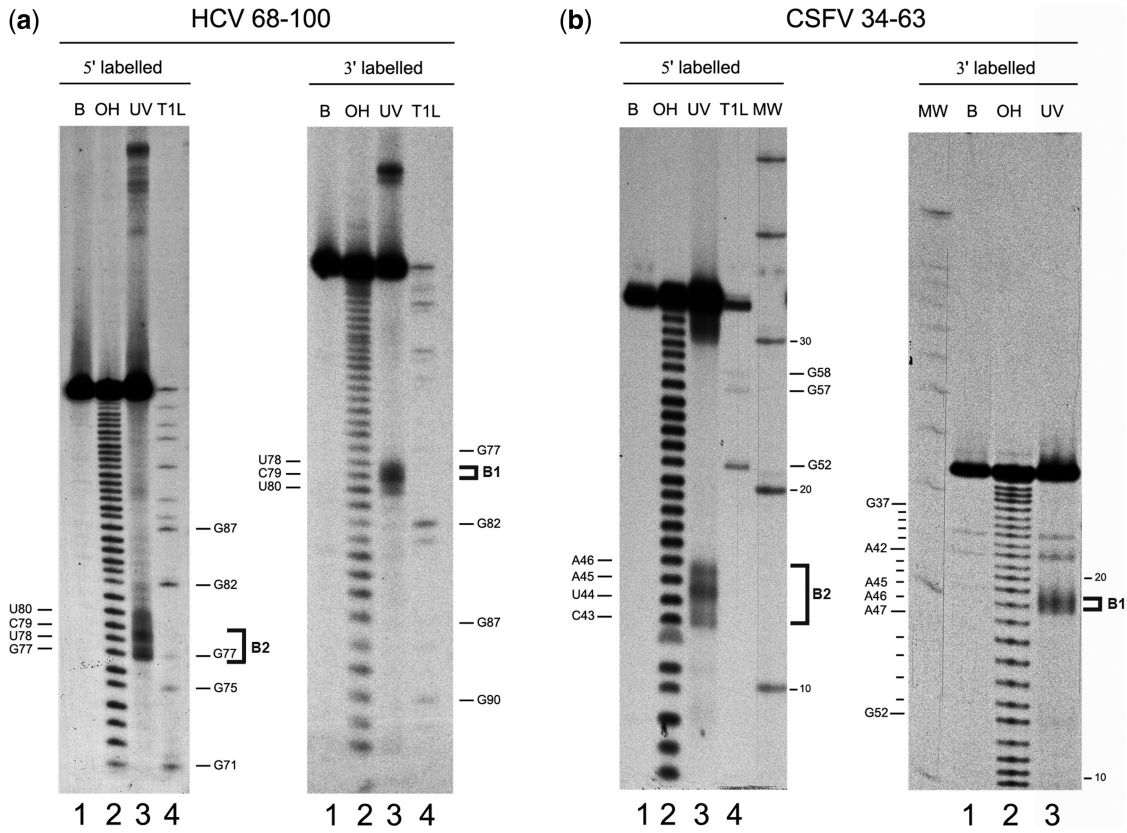


Figure 4. Determination of the UV-C cleavage sites in shortened HCV and CSFV RNA fragments. RNA sequencing reactions of HCV RNA 68–100 (a) and CSFV RNA 34–63 (b). RNAs were labeled at their 5'-end (left panels) or 3'-end (right panels). Lane 1: RNA incubated under standard buffer conditions. Lane 2: RNA partially degraded with alkali; Lane 3: RNA irradiated with UV-C light for 360 s. Lane 4: denatured RNA partially degraded with RNase T1. Base and cleavage sites are indicated on the left; the numbers refer to nucleotide positions in the HCV or CSFV transcript sequence. The numbers on the right refer to the electrophoretic position of RNase T1 deduced fragments, or of molecular weight markers (MW).

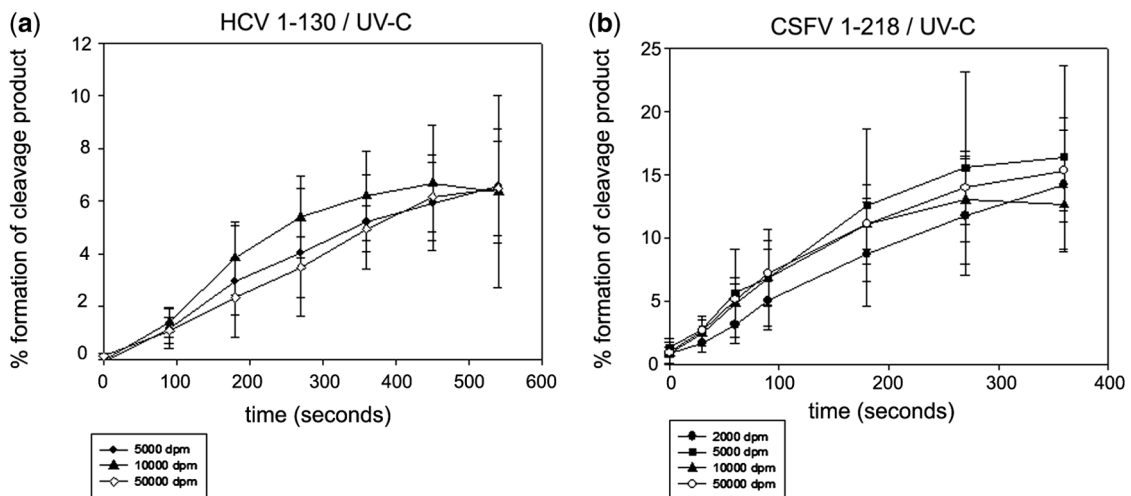


Figure 5. Viral RNA self-cleavage depends on UV-C dose but not on substrate concentration. A graphical representation of the time course of UV-C-induced self-cleavage of HCV RNA 1–130 (panel a) and CSFV RNA 1–218 (panel b) under standard conditions at increasing concentrations (5000, 10000 and 50000 dpm for HCV RNA 1–130 and 2000, 5000, 10000 and 50000 dpm for CSFV RNA 1–218). The length of the UV-C irradiation was limited to 540 s for HCV RNA and 360 s for CSFV RNAs due to non-specific degradation of the RNA product bands at the last time point. Increasing times (a) 90, 180, 270, 360, 450 and 540 s and (b) 30, 60, 90, 180, 270 and 360 s. Data corresponds to four and three replicates experiments for HCV and CSFV, respectively.

conditions (Supplementary Figure S4). The results of this study showed that whereas CSFV RNA transcripts continue to undergo UV-C-induced cleavage in the absence of magnesium ions although with an important yield reduction these were required for the reaction of HCV RNA 1–130 and 1–249. Thus, after incubation with EDTA for 2 or 16 h, the cleavage yield decreased by up to 10.8% and 8.02% for HCV RNA 1–130, 24.1% and 20.9% for HCV RNA 1–245 and 58.6% and 63.5% for CSFV RNA 1–218 of the yield obtained in the control reaction.

The addition of Mg^{2+} to the depleted solution after incubation in EDTA for 2 or 16 h recovered essentially the entire initial cleavage yield in all cases (96.6% and 80.7% for HCV RNA 1–130, 74.5% and 62.1% for HCV RNA 1–245, and 89% and 78% for CSFV RNA 1–218).

The concomitant disappearance of the crosslink band X-link 2 in the absence of Mg^{2+} and the fact that Mg^{2+} has been reported to be required to maintain a single conformation of the 5'-UTR of HCV RNA (42), points to a more pronounced effect of Mg^{2+} in stabilizing HCV RNA structure than in CSFV RNA in the reactive region rather than to an effect on the reaction mechanism itself.

Further studies were then conducted, with HCV RNA 1–130 as substrate, in order to more exactly define the ionic and buffer conditions under which this cleavage can occur. Thus, UV irradiation of a set of four buffers commonly employed in our laboratory for RNA work, mainly the Tris-HCl, HEPES, Tris-HCl/HEPES and phosphate based buffers listed in the 'Material and Methods' section, resulted in cleavage in all conditions with a similar or lower efficiency to that obtained with our standard buffer (0.01 M Tris-HCl, pH 7.6, containing 10 mM $MgCl_2$), except for the phosphate buffer, which lacks Mg^{2+} and provided no appreciable cleavage (data not shown). We subsequently tested the UV standard reaction in the presence of increasing concentrations of K^+ , NH_4^+ and Mg^{2+} and Tris-HCl, pH 7.6, under a wide range of concentrations (Supplementary Figure S5). Again, cleavage occurred at all Mg^{2+} concentrations tested with the usual efficiency, whereas the reaction was linearly inhibited by the presence of NH_4^+ and considerably inhibited at over 20 mM Tris-HCl and 200 mM K^+ . Taken together, these findings ruled out the reliance of this reaction on the buffer component, and at the same time that it seemed unlikely that modification of our standard cleavage conditions could improve cleavage.

Structural elements required for the self-cleavage reaction

Deletion and mutation. Shortened HCV and CSFV RNAs transcribed from T7-synthetic DNA templates were assayed for UV-C reactivity. For HCV, the single structural domains and motifs that constitute the first 1–130 nt until loss of self-cleavage were eliminated either individually or consecutively (Table 1). The shortest RNA tested and found to be cleaved by UV-C light covered nucleotides G₆₈–G₁₀₀ for HCV and U₃₄–G₆₃ for CSFV; these will hereafter be referred to as minimal substrates. Same time course irradiation of the minimal substrate showed no difference in rate of self-cleavage with respect to its

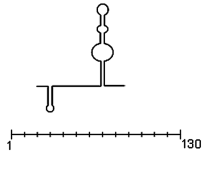
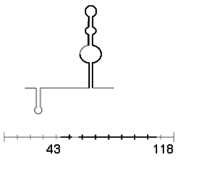
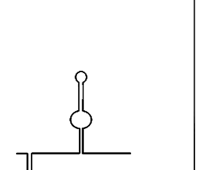
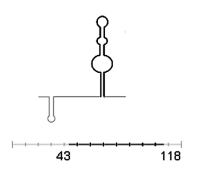
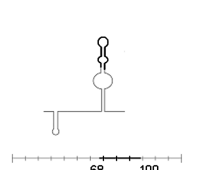
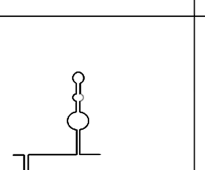
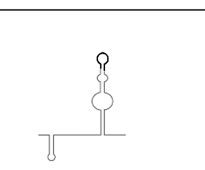
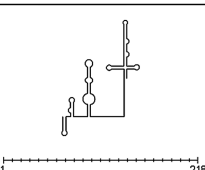

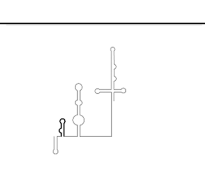
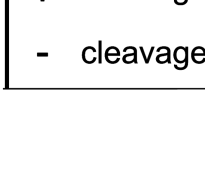
corresponding larger 1–130 RNA for HCV (Supplementary Figure S6a). This probably indicates that the HCV minimal RNA substrate molecules, are folding themselves into a similar conformation(s) to the original substrate in the absence of flanking sequences.

Next, to investigate whether the internal and/or apical loop motifs of HCV RNA stem-loop II (C₄₃–G₁₁₈) are involved in UV-C-induced self-cleavage in HCV RNA, a set of RNA transcripts from synthetic T7-DNA templates carrying sequence substitutions in these regions, obtained by modifying the sequences corresponding to basal stem-loop IIa, loop E, and the apical stem-loop II, were tested (Table 1). As expected from the sequence-deletion results (see above), basal stem-loop IIa, where an UV-C-induced crosslink was identified previously (27), did not affect the UV-C-induced self-cleavage reaction. Likewise, the results indicated that the E-loop motif is involved in the self-cleavage reaction but that the sequence in the apical loop is not. Two sequence modifications of the E-loop region in the context of a standard HCV RNA 1–130 sized fragment were tested. In one of these modifications the three central bases of the left strand of the E-loop sequence were changed, and in the other the bulged-out 'G94' was eliminated (Table 1). E-loop integrity was a requirement for UV-C-induced self-cleavage and that elimination of the single 'G' from HCV RNA prevents UV-C-induced self-cleavage (Supplementary Figure S7a).

Unlike the highly conserved and well-known structure of HCV RNA, several representations have been proposed for the secondary structure of the 5'-region of the CSFV RNA (43,44) genome. Thus, instead of following a stepwise fragment-deletion strategy guided by the structural information, a T7 *in vitro* RNA transcript similar in size to the HCV minimal fragment surrounding the self-cleavage site and including a predicted internal loop was tested directly. The reaction was performed in parallel with two *in vitro* transcripts carrying either two mutations or a deletion of 3 nt within the putative internal loop. All transcripts showed similar reactivity (Supplementary Figure S7b), thus indicating that a short 32-nt sized RNA is enough to support self-cleavage and that the internal loop does not participate in the reaction. These results initially appear to rule out structural similarities between both viral self-reactive domains. Nevertheless, it cannot be ruled out that the reactive RNA structures do not coincide with those described in the literature, especially in the case of CSFV RNA.

One intriguing observation was that the intensity of both crosslink bands of HCV RNA 1–130 seemed to correlate negatively with the intensity of the cleavage product over the time course of the reaction (indicated as X-link 1 and 2 in Supplementary Figure S2). The more intense cross-link (X-link 1) was previously mapped in the basal part of domain II (27), whereas, although the lower intensity, cross-link band (X-link 2) has not been characterized, it probably occurs at the E-loop of domain II. Both crosslinking bands were gel-purified individually and re-subjected to UV irradiation in a single time point (180 s). Crosslink photoreversion to substrate, a phenomenon previously described by Branch *et al.* (45),

Table 1. Schematic representation of shortened and sequence-modified HCV and CSFV RNA transcripts and their sensitivity to UV-C light

		Deletion	Mutation	Mutation
HCV				
		+	+	-
			51 GGAACUACU 50 ↓ GG - CU	1 GUUAGUAUG 130 ↓ GUUUUCUG
		+	+	-
			43 UCUAGCCAUGG 118 78 ↓ 88 UCUUCGGG	
		+		-
			43 GUUAGUAU 118 90 ↓ 97 GUCAAAU	1 GUUAGUAUG 130 ↓ GUUAUAUG
		-	-	-
CSFV			34 GATACAC 46 37 ↓ 43 GAGAGAC	
		+	+	
			34 GATACAC 46 37 ↓ 43 GA - AC	
		+	+	

+ cleavage detected
- cleavage no detected

reached 38.9% and 45.5% for X-links 1 and 2, respectively, alongside the appearance of the characteristic UV-cleavage products. The percentage of cleavage products arising from the original substrate and the X-link 1 band was 3.6% and 4.25%, respectively, whereas in a different experiment the percentage of product obtained from the original substrate and X-link 2 was 5.6% and 1.95%, respectively, thus indicating that neither of the cross-linked products is an intermediary in the cleavage reaction and

that the RNA conformation adopted by the material in X-link-2 does not appear to be a good substrate for cleavage.

RNA self-cleavage is oxidative and not mediated by solution hydroxyl radical

The key experimental questions regarding the viral RNA cleavages obtained in the reactions involving UV-C light

concern (i) a demonstration that such cleavages are induced by UV-C irradiation and are not a special case of chemical or thermal fragility of RNA at the cleavage site, and (ii) confirming that self-cleavage of RNA is a result of the direct action of UV-C light itself by excluding the indirect action of solution radicals that might be generated by ionization of water after UV-C irradiation. (iii) Also of interest is to determine if a similar cleavage reaction could happen *in vivo*.

The cleavage reaction involves oxidation of RNA by UV-C light. Since the UV dependence of specific and reproducible single self-cleavages in highly structured RNA molecules is unprecedented, we first investigated whether the viral RNA-cleavage reactions induced by UV irradiation in the viral transcripts are caused by oxidation, as would be expected with UV-C light. We then ruled out a physicochemical instability of our transcripts at the cleavage site.

Inhibition of RNA UV-C-induced reactions by antioxidant agents. DTT is a commonly used protector in RNA-based reactions. For the RNA self-cleavage inhibition assay, 10000 dpm of [α - 32 P]-labeled HCV RNA 1–130 and CSFV RNA 1–218 was incubated in standard buffer containing increasing concentrations of DTT, from 1 to 500 μ M. Three replicates were performed for the DTT inhibition reactions. Half inhibition was reached at low concentration of DTT, such as: 80 μ M for HCV and 150 μ M for CSFV with DTT (Figure 6). Interestingly, neither of the HCV RNA crosslinking bands were affected by the presence of DTT at the concentration tested.

Finally, to rule-out that the scissile bonds were ‘somehow’ particularly labile bonds, attempts were made to decouple these RNA self-cleavage reactions from UV-C irradiation. A number of reaction conditions known to activate ribozymes or to increase chemical degradation of RNA were tested and shown to be unable to support the reactions in the absence of UV-C irradiation. Modifications included an increase in pH, Mg^{2+} concentration, time and reaction temperature, which were the same as those originally tested during identification of the plant viroid ribozyme by Foster *et al.* (46). No RNA cleavage was detected at any condition (Supplementary Figure S8).

UV-cleavage is not stimulated by solution radicals

Sensitivity of viral RNAs to OH \cdot radicals in solution. The reported ionization of nucleic acid bases on irradiation >210 nm are due to photon excitation of the nucleic acid bases (direct mechanism), while <180 nm photolysis of the solvent (indirect mechanism) seemed to be the main cause (15,47,48). This might be because water only begins to absorb significantly in the far UV (48). In spite of that, we subsequently showed that the free radicals generated in solution by the Fenton reaction, which mimics the effects of those generated by ionizing radiation (10,49), are not responsible for mediating the UV-C-specific effect on viral RNAs. These radicals include the highly reactive hydroxyl species OH \cdot but also superoxide species O $_2^{\cdot-}$ (39), the most damaging being the hydroxyl radical (50). The reaction

was first titrated for internally labeled HCV RNA 1–130 and CSFV RNA 1–218 at 5 s and 2 min at 1% H $_2$ O $_2$ (data not shown). It was subsequently performed with increasing concentrations of H $_2$ O $_2$ (1, 1.5 and 2%) for 2 min, then run in polyacrylamide gels in parallel to standard UV-C reactions. No specific cleavage band was observed in either of the two viral RNAs (Figure 7a). As more than one cleavage in long internally labeled transcripts might hide a specific cleavage, Fenton reactions were performed using the shortened transcripts. All reactions were performed in our standard buffer in the presence of 2% H $_2$ O $_2$ for 2 min. RNA fragments were labeled at the 5'-end for HCV RNA 68–100 and the 3'-end for both HCV 68–100 and CSFV 34–63, and the Fenton reaction products were resolved in parallel with a standard UV-C cleavage and alkali degradation reaction in high percentage polyacrylamide gels (15–20%) (Figure 7b–d). The displacement of the band ladder obtained for the Fenton reaction products with respect to the alkali degradation products is due to the presence of an extra phosphate group at the newly generated 5'-ends in the oxidative reaction. It was found that, in general, solution radicals degraded the viral RNAs in a very unspecific manner, with no increase in reactivity at the UV-cleavage site, thereby ruling out the possibility that the structure of the RNA at the cleavage site is particularly sensitive to solution radicals. The resistance of base G $_{71}$ to radical attack, together with an increase in the sensitivity of G $_{94}$, were of particular interest due to the fact that both bases belong to the E-loop structure of HCV stem-loop II, thereby indicating that our Fenton reaction is able to correctly distinguish tertiary structural elements. The degradation of CSFV RNA 34–63 was far more homogenous, probably due to its lack of a stable tertiary structure.

These findings strongly suggest that UV-C light absorption and subsequent energy dissipation on the RNA directly promotes RNA cleavage.

Self-cleavage reaction does not occur during the viral life cycle. We analyzed whether the viral self-cleavages described here could mimic an oxidative cellular process that occurs either in the normal viral life cycle or under oxidative stress conditions. Thus, we determined, using the RACE technique, whether any RNA species of the expected length for the RNA self-cleavage could be observed *in vitro* in the total RNA extracted from an HCV-infected tissue sample from a human liver after transplantation for end-stage liver cirrhosis and in total RNA from CSFV-infected porcine PK-15 cells. We also tested CSFV-infected cell cultures subjected to different H $_2$ O $_2$ oxidative stress regimes, exactly as described previously (51). However, no product bands representative of self-cleavage were observed under these conditions (data not shown).

Characterization of the chemical nature of the end groups of the UV-C reaction products

In the case of DNA, determination of the chemical nature of the new ends generated upon oxidative

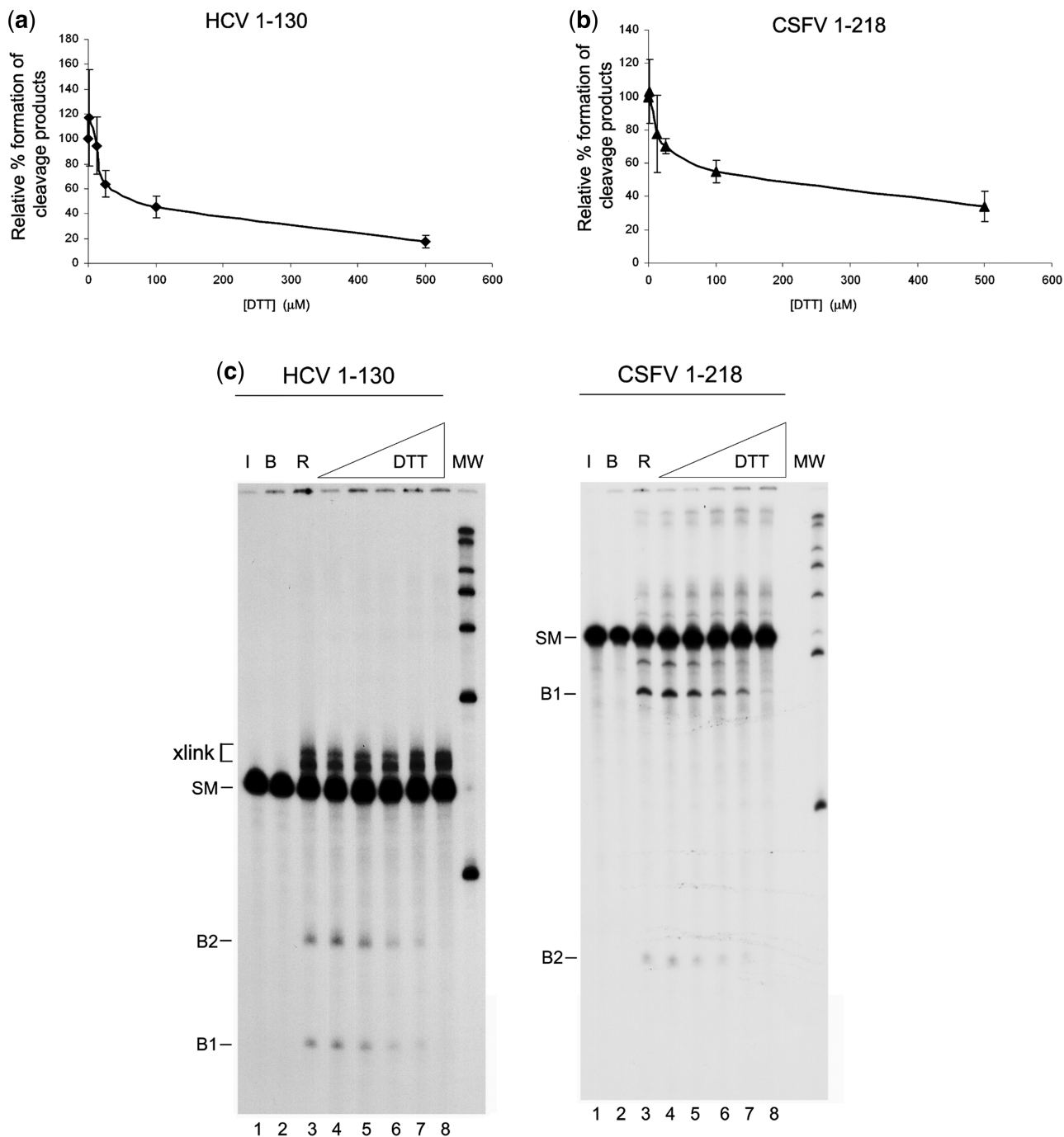


Figure 6. DTT inhibits UV-C-induced cleavage of viral RNA. Graphical representation of HCV RNA 1–130 (a) and CSFV RNA 1–218 (b). Standard reactions using a constant concentration of HCV or CSFV RNA were performed in the presence of increasing concentrations of DTT: 0, 1, 12.5, 25, 100 and 500 μM. Data were collected for three replicates. (c) Autoradiograms of one of the replicates of HCV RNA 1–130 (left panel) and CSFV RNA 1–218 (right panel) in the presence of DTT. A 10-μl aliquot containing 10 000 dpm of viral RNA was irradiated under standard conditions for 360 s. Lane 1: the RNA used in the reaction maintained on ice. Lane 2: the RNA incubated in buffer. Lanes 3 irradiated without DTT. Lanes 4–8: RNA irradiated with increasing concentrations of DTT.

cleavage can help to determine the type of oxidative reaction involved, in light of the large amount of experimental data available with which a comparison can be made (11,12,52,53). In contrast, the amount of information regarding the chemistry of the ends generated by oxidative processes in RNA is more limited (11).

Determination of the end generated can help in the comparison of the ends generated in experiments in which a radical is generated directly on the base (19,20) and to rule out other types of non-oxidative cleavage. In particular, contaminating RNases almost invariably cleave to yield 5'-hydroxyl and 2'-3' cyclic or 3'-phosphate end groups.

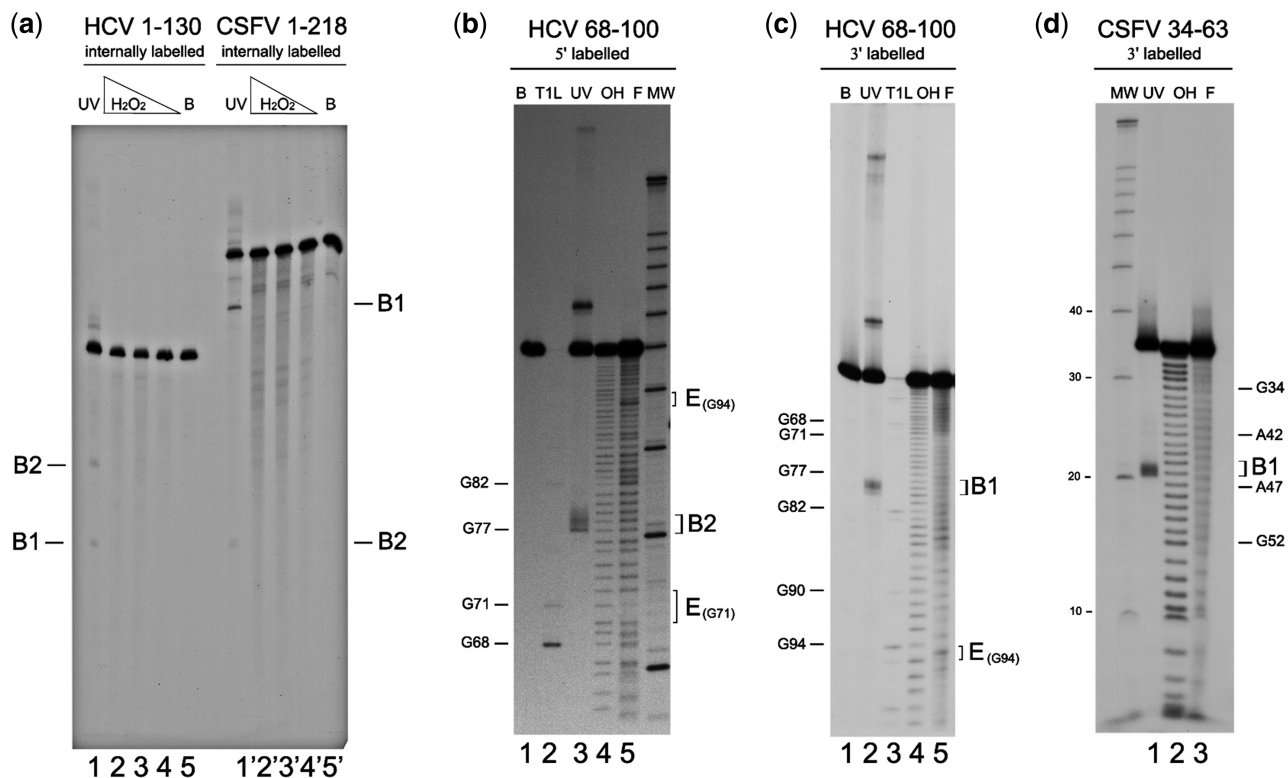


Figure 7. Solution radicals generated by the Fenton reaction do not mimic viral RNA cleavages. (a) A total of 10 000 dpm of internally labeled HCV RNA 1–130 (lanes 1–5) and CSFV 1–218 RNA (lanes 1'–5') was used to evaluate the effect of the Fenton reaction performed with increasing concentrations of H_2O_2 . Lanes 1 and 1' show the RNAs irradiated for 90 s, and lanes 5 and 5' the RNAs maintained on standard buffer. Lanes 2 and 2', 3 and 3', 4 and 4' show the RNA incubated in the presence of Fe^{2+} -EDTA and 1%, 1.5% and 2% H_2O_2 (Fenton reaction), respectively, for 2 min at 37°C. (b) The Fenton reaction at 2% H_2O_2 was performed using 5'-end labeled HCV shortened RNA 68–100. Lane 1: RNA maintained on standard buffer; lane 2: denatured RNA partially degraded with RNase T1; lane 3: standard UV-C reaction; lane 4: partial degradation with alkali; lane 5: partial degradation with Fenton reaction; or (c) 3'-end labeled HCV RNA 68–100. Lane 1: RNA maintained on standard buffer; lane 2: UV-C standard reaction; lane 3: partial RNase T1 degradation; lane 4: partial degradation with alkali; lane 5: Fenton degradation; and (d) 3'-end labeled CSFV RNA 34–63. Lane 1: UV-C standard reaction; lane 2: partial alkali degradation; lane 3: Fenton reaction. Guanosine positions are indicated on the left of the gels. 'E' indicates the position of E-loop. Low and high reactive positions 'G₉₄' and 'G₇₁' for the Fenton reaction within the E-loop are indicated on the right of panels b and c.

Two methods were employed for this purpose, namely enzymatic methods that specifically recognize the hydroxyl or phosphate groups and MALDI TOF spectrometry which allows direct detection of the end-group. Only a subset of enzymatic experiments was carried out for CSFV RNA.

Enzymatic assays for HCV 1–130 and CSFV 1–218. A set of specific enzymes was employed for each end-group determination along with gel-purified product fragments from the self-cleavage of HCV RNA 1–130 and CSFV RNA 1–218. The RNA substrates were labeled internally with [α - ^{32}P]GTP at low specific activity to allow the detection of further radioactive incorporation in subsequent tests. All the reactions were treated with proteinase K and SDS and ethanol precipitated before gel loading.

For determination of the newly generated 3'-end, we used the bacteriophage T4 RNA ligase which readily labels the new 3'-ends of HCV and CSFV RNA with [$5'$ - ^{32}P]pCp without any pre-treatment (Figure 8a). The increase in label with respect to the samples not treated with the ligase was 3.4- and 96.6-fold for HCV and CSFV RNA, respectively. Nevertheless, the labeling intensity

increased considerably if the RNA products were previously treated with a phosphatase (57.7- and 864.2-fold for HCV and CSFV RNA, respectively). The labeling intensity ratio for the bands in non-phosphatase/phosphatase treated reactions was 6.5% and 11.2% for CSFV RNA, thus indicating that the UV-C cleavage reaction probably results in a mixture of products ending mainly in 3'-P but also in a minor 3'-OH fraction for both viral RNAs.

Additional evidence for the chemical composition of the newly generated 3'-ends was obtained by the observed ability of poly-(A) RNA polymerase and poly-(U) RNA polymerase to add a poly-(A) or poly-(U) tail to the new 3'-end in the presence of [α - ^{32}P]ATP or [α - ^{32}P]UTP in the presence or absence of prior treatment of the RNA substrate with phosphatase (Figure 8b). Again, the reaction proceeded to a greater extent after treatment of the RNA with the phosphatase. The pattern was similar for both viral RNAs.

For the newly generated 5'-extreme, Figure 9a shows that polynucleotide kinase can label the new 5'-end of HCV and CSFV RNA with [γ - ^{32}P]ATP, preferentially after 5'-phosphate removal. Likewise, Figure 9b shows that bacteriophage T4 RNA ligase can cyclise these HCV

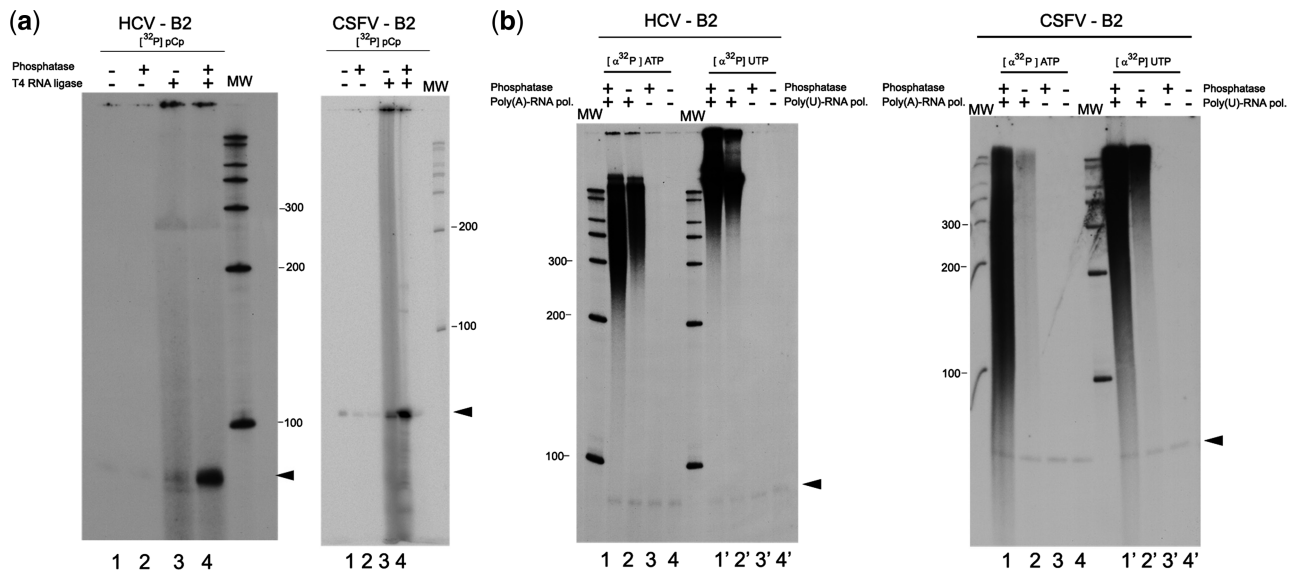


Figure 8. Enzymatic determination of the new 3'-end of HCV and CSFV RNA end-groups produced by UV-C-induced self-cleavage. (a) T4 RNA ligase treatment of gel-purified HCV RNA 1–130 (left panel) and CSFV RNA 1–218 (right panel) cleavage product band B2. B2 RNAs [4000 dpm (10^5 dpm/ μ g)] were incubated with T4 RNA ligase and [5'- 32 P]pCp. Lane 1: control reaction with B2 RNA incubated in SAP phosphatase buffer, then in ligase buffer and [5'- 32 P]pCp in the absence of any enzyme; Lane 2: control reaction of B2 RNA treated the same as in lane 1 but incubated with the phosphatase; Lane 3: B2 RNA incubated with T4 RNA ligase without previous dephosphorylation; Lane 4: complete reaction of B2 RNA incubated with the ligase after being treated with the phosphatase. (b) Addition of [32 P]-labeled poly (A) or poly (U) to bands B2 of HCV (left panel) and CSFV (right panel) with *E. coli* poly (A) polymerase or *Schizosaccharomyces pombe* poly (U) polymerase. A total of 4000 dpm RNA (10^5 dpm/ μ g) was used for both viral RNAs. A total of 20 μ Ci of the labeled nucleotide (ATP or UTP) was distributed for the four reactions. Lanes 1 and 2: B2 RNA incubated with the poly (A) polymerase after being treated or not with shrimp alkaline phosphatase, respectively. Lanes 3 and 4: control reactions of B2 RNA treated or not with the phosphatase but without incubation with the polymerase. Lanes 1' 2' 3' and 4' same as above, but using poly (U) polymerase. MW is a molecular weight marker.

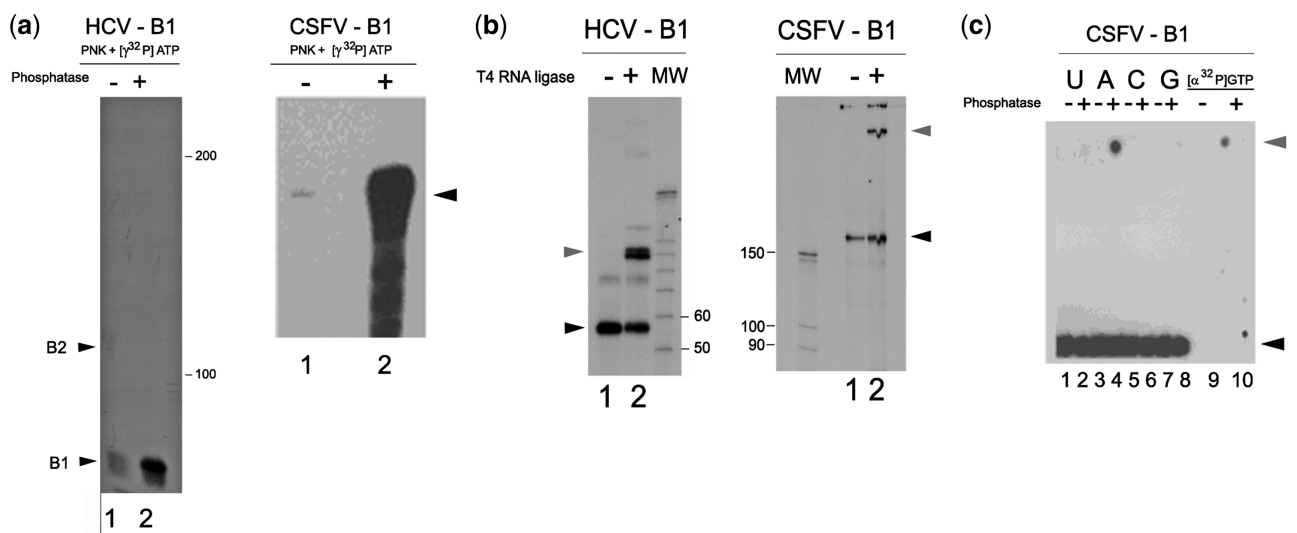


Figure 9. Enzymatic determination of the new 5'-end of HCV and CSFV RNA end-groups produced by UV-C-induced self-cleavage. (a) Phosphatase-dependent 5'-terminal labeling of both HCV RNA 1–130 cleavage product (B1) (left panel) and CSFV RNA 1–218 cleavage product (B1) (right panel) by polynucleotide kinase. Aliquots (10 000 dpm) of product bands (10^5 dpm/ μ g) were treated with polynucleotide kinase and [γ - 32 P]ATP, after treatment with Artichoke Phosphatase (lane 2) or without phosphatase pre-treatment (lane 1). (b) Cyclization of HCV (left panel) and CSFV (right panel) RNA product bands B1 by T4 RNA ligase [with 10 000 dpm (10^5 dpm/ μ g) RNA]. Lanes 1: HCV and CSFV B1 bands incubated without T4 RNA ligase; lanes 2: complete reaction (cyclized RNA: upper band). (c) Phosphatase treatment of singly labeled CSFV. Calf alkaline phosphatase was used to treat CSFV band B1 aliquots (50 000 dpm of 107 dpm/ μ g), followed by high-voltage electrophoresis at pH 1.9 on Whatman DE81 DEAE paper (16). B1 RNA is at the bottom and free phosphate at the top. 'U', 'A', 'C' and 'G' indicate RNAs labeled with [α - 32 P]UTP, ATP, CTP or GTP, respectively, whereas ' α - 32 P]GTP' indicates a control containing 1000 dpm of pure [α - 32 P]GTP.

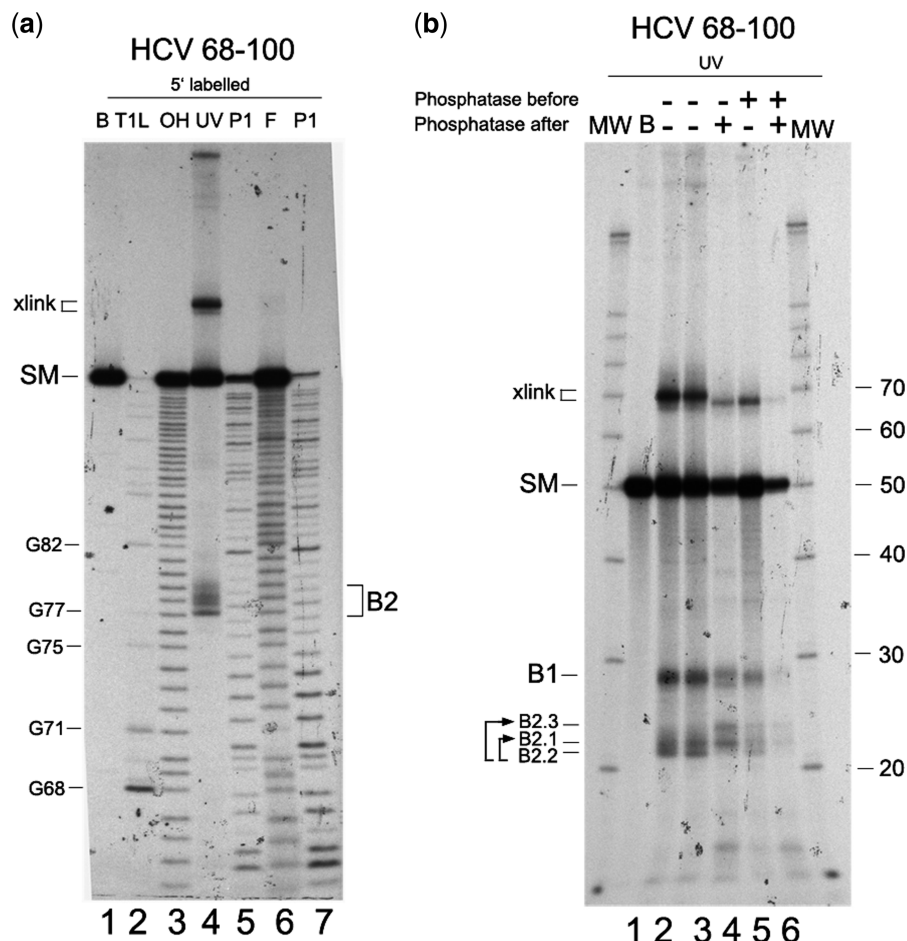


Figure 10. End-group determination of HCV self-cleavage products using a combination of enzymatic and electrophoretic methods and a shortened RNA. Analysis of end group generated during 360 s UV-C irradiation induced cleavage of end labeled (panel a) or internally labeled RNA (panel b) at low specific radioactive labeling. **(a)** Comparison of the position of UV-C cleavage bands for the 5'-labeled HCV RNA 68–100 (lane 4), relative to the RNase T1 sequencing ladder (lane 2), alkali partial degradation (lane 3), RNase P1 partial cleavage (lanes 5 and 7) and Fenton reaction lane 6. Lane 1 is the RNA entered in the reaction. **(b)** Changes in the electrophoretic mobility of HCV RNA 68–100 UV-C cleavage products in 15% polyacrylamide gels after treatment with phosphatase (SAP). UV-C irradiation was always performed under standard conditions; when the RNA was incubated with the other buffered solution, it was subsequently cleaned by precipitation before irradiation. Lane 1: RNA incubated on standard buffer; lane 2: RNA incubated in phosphatase buffer and subsequently irradiated with UV-C light; lane 3: a standard UV-C reaction; lane 4: RNA treated with phosphatase after UV-C irradiation; lane 5: RNA treated with phosphatase before UV-C irradiation; lane 6: RNA treated with SAP before and after UV-C irradiation. MW indicates molecular weight markers. Different length B2.1 and B2.2 bands are indicated. B2.3 indicates a product of dephosphorilation.

and CSFV fragments by linking the new 5'-phosphate to the original 3'-hydroxyl end. In the case of CSFV RNA, phosphatase treatment of the singly labeled (ATP, CTP, GTP and UTP) CSFV band B1 indicated that radioactive phosphate is released only from [α - 32 P]ATP-labeled RNA, thereby proving the presence of a new 5'-phosphate on an A-residue (Figure 9c).

Combined enzymatic and electrophoretic assays for HCV RNA 68–100. Oligonucleotides with hydroxyl termini can be identified by their slower electrophoretic mobility relative to phosphate-terminated strands. Thus, the minimal RNA fragment, namely HCV 68–100, was subjected to a standard UV-C reaction and its products electrophoresed in parallel to a set of standards containing different chemical groups at their 3'- and 5'-ends. These were obtained after alkali treatment, the Fenton

reaction, and RNase P1 treatment, which produced RNAs with 2'-3'cyclic P/5'-OH; 3'-P/5'-P; and 3'-OH/5'-P ends, respectively (Figure 10a). The fast moving product band from the UV-C reaction, and 'the minus one', migrate in positions G₇₇ and U₇₈ and can be aligned with those from the Fenton reaction. Likewise, the band that migrates between positions G₇₇ and U₈₀ can best be aligned with the 3'-OH terminated products generated by RNase P1, especially if a small so-called 'smiling' effect seen in the bands running on the gel is taken into account. This effect is visible when the migration of the product bands in the two lanes corresponding to RNase P1 degradation products is compared.

A standard UV-C reaction using a 5'-end labeled HCV 68–100 was run in parallel to a phosphatase-treated reaction, either before or after UV-C irradiation, and the electrophoretic mobility of the products determined

(Figure 10b). Phosphatase treatment before irradiation did not cause any change in mobility, thus indicating that the original 5'-terminal nucleotide pppG was protected. After UV-C irradiation, however, changes included mobility retardation of the band containing the new 5'-termini (band B1) and disappearance of the fast migrating band containing the new 3'-end B2.2. These results suggest that the new 5'-end of band B1 contains a 5'-phosphate group and that the fast migrating B2.2 band containing the new 3'-ends also contains a phosphate group.

As it is unlikely that dephosphorylation of the B2.2 fragment causes such a pronounced retardation in the electrophoresis mobility to the position of the newly observed B2.3 band, a simultaneous band retardation whereby B2.2 moves to the B2.1 position and B2.1 to the B2.3 position is more probable (indicated with arrows in the gel of Figure 10b). This would be indicative that both B2.2 and B2.1 contained a 3'-phosphate end.

The newly generated 5'-end-group of gel-purified bands B1, and the 3'-end-group from gel-purified B2.1 and B2.2, were further evaluated in a phosphatase/kinase or phosphatase/ligase assay (Supplementary Figure S9a and S9b). The new 5'-end in B1 was only labeled if it had previously been dephosphorylated, thus indicating the presence of a phosphate group. The results for the 3'-end indicated that the two purified bands (B2.1) and (B2.2) were labeled with the T4 RNA ligase without phosphatase pretreatment with a yield of 33.9% and 21.5% of the previously treated sample, respectively, thus indicating that both B2.1 and B2.2 contained products with 3'-P and, to a lesser degree, 3'-OH.

Mass spectrometry. A synthetic oligonucleotide corresponding to positions 68–100 of HCV RNA was employed. Figure 11 show the base peak chromatograms of HCV RNA 68–100 before and after irradiation with UV-C light or of bands B1 and B2 after purification by electrophoresis. The Mongo Oligo Mass Calculator was used to determine the theoretical mass of the RNA fragments considering the masses of different types of 5'- and 3'-termini. The observed values and calculated values can be found in the table within the figure. Figure 11a shows the spectrum of the RNA substrate, which includes peaks corresponding to full-length substrate with one, two or three negative charges. After UV-irradiation product peaks can be observed in two regions of the spectrum (Figure 11b), one corresponding to the size of electrophoretic band B2 (~3300–3800 Da) and the other to the size of band B1 (6500–7500 Da). Analysis of the gel-purified product for the shorter band (B2) was necessary because of coincidence with peaks arising directly from the molecular mass peak with three negative charges. Figure 11c and d show the spectra for the gel-purified bands. The major peak intensity for band B2 was for the oligonucleotide ending at 3'-₇₇G-p, and, with less intensity but similarly represented, those ending at either 3'-₇₈U-p and 3'-₇₈U-OH. Minor peaks of higher molecular mass could be found at 3'-₇₉C-p and 3'-₈₀U-p. A broad peak containing minor peaks and valleys was observed for Band B1. These started at ~5'p-C₇₉ and ended at 5'p-U₈₀. The most intense of these peaks corresponded probably to the

sodium adduct of 5'p-C₇₉. Most of the peaks in between probably therefore correspond to degradation products of the ribonucleotide at C₇₉.

UV-B

We decided to test whether cleavage could also occur in the presence of UV-B light that arrives at living organisms in the form of sunlight; in contrast to UV-C which is absorbed by the earth's atmosphere. Thus, using the minimal substrate fragments for both viral RNAs, a linear cleavage reaction was observed upon exposure to longer wavelength UV-B (312 nm) irradiation, although at a much slower rate (Supplementary Figure S10).

DISCUSSION

Herein, we report a novel photo-induced ribozyme reaction in which the 5'-region of HCV and a related viral pathogen (CSFV) are selectively cleaved. Our finding connects the field of ribozymes and that of nucleic acid reactivity to UV light, two fields of research with >25 and 40 years of history, respectively.

RNA structure at the cleavage site

HCV RNA cleavage required the integrity of an E-loop motif. A unique mutation at 'G₉₄' or deletion of right strand of the E-loop inhibited cleavage (Table 1 and Supplementary Figure S7a). The E-loop structure is a well-known tertiary structural RNA element initially characterized by its unusual ability to absorb UV radiation (21,25,26) that is involved in several RNA–RNA crosslinking. Nevertheless, despite of CSFV RNA does contains a well defined E-loop structure between positions 70 and 127, with same sequence to that of HCV RNA, and in a similar position in the global RNA conformation (54) the flanking region is not reactive to UV-C. Sequence comparison between the two structured CSFV and HCV RNAs reveals that differences map at the dsRNA sequence spanning the E-loop and the apical loop [see Figure 1 of Locker and colleagues (54)], indicating that the sequence of the double strand region is involved in HCV self-cleavage, and that besides the canonical E-loop structure is related to UV-C RNA reactivity but its presence does not ensures RNA self-cleavage. In contrast, the reactive region of CSFV RNA did not require a neighboring E-loop, or even an internal loop, thus indicating either the presence of a distinct RNA structure to that of HCV RNA that is able to self-cleave, or that the active conformation was a subpopulation with a different structure from the secondary structure proposed in the literature (43,44). Various alternative local conformations that are more or less susceptible to UV-light crosslinking in ribosomal RNA have been described (55).

Despite the RNA structure at the cleavage sites in both viral RNAs seems to be dissimilar, the reaction share several important characteristics.

Substrate size. RNA substrates could be reduced to ~33 nt, this indicates that the reaction might be relevant to RNA world scenarios.

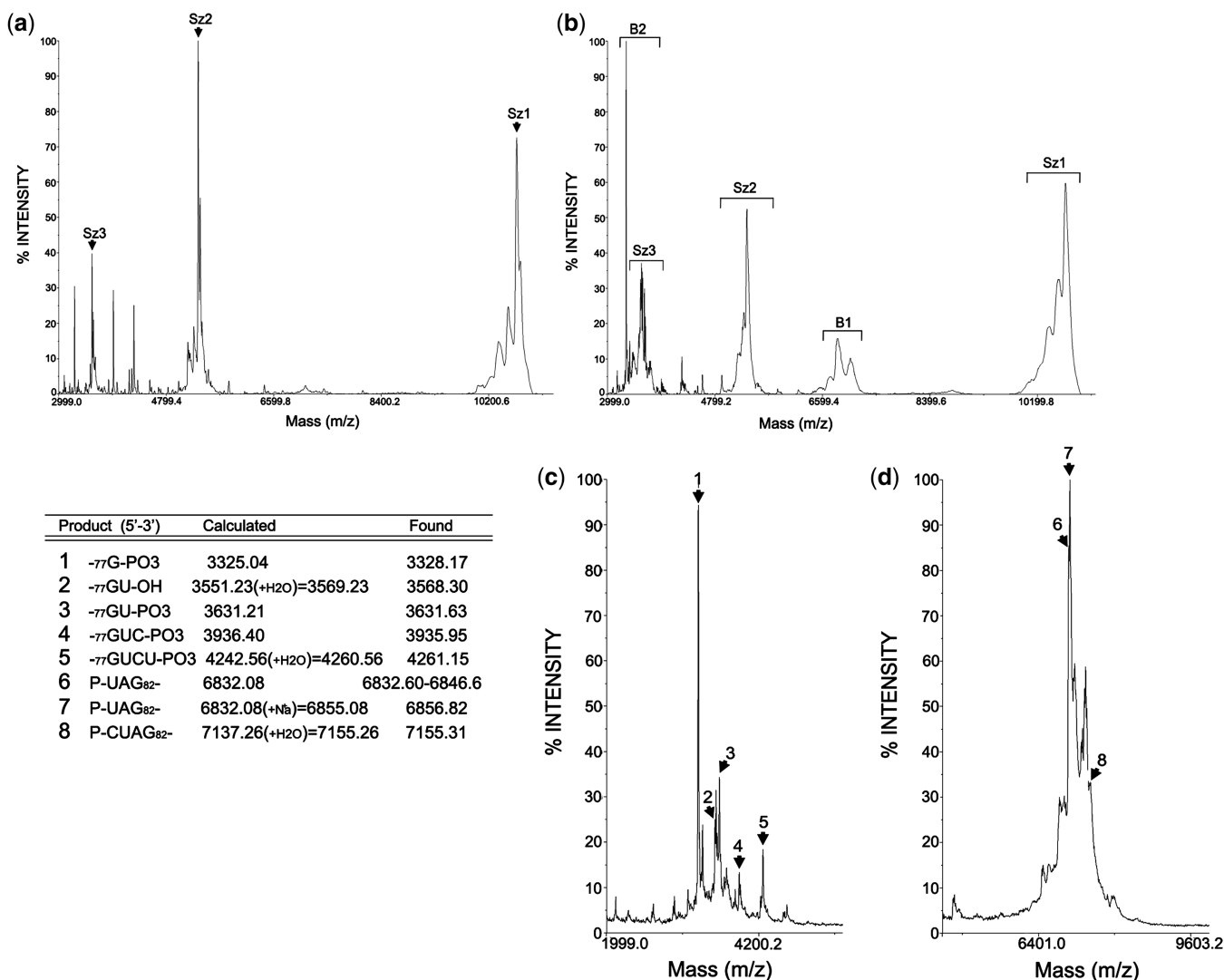


Figure 11. MALDI-TOF MS analysis of HCV 68–100 UV-C cleavage products. Spectra from (a) control HCV RNA 68–100, (b) HCV RNA 68–100 irradiated with UV-C in a standard reaction, (c) B2 RNA gel-purified products, and (d) B1 RNA gel-purified products. Sz1 corresponds to the expected mass/+1charge for RNA 68–100; Sz2 and Sz3 correspond to the expected mass/+2 or +3 charge. The substrate peak as well as the expected B1 and B2 peaks are indicated as Sz, B1 and B2, respectively. The major product oligoribonucleotide peaks in (c) and (d) are indicated by arrows with peak numbers and these were assigned to oligoribonucleotide fragments calculated theoretically using the MONGO oligonucleotide program. These results are contained in the Table within the figure.

Cleavage efficiency. This was found to be reproducible, but low, in long transcripts. This limited cleavage efficiency could be due either to competitive non-specific degradation of RNA caused by UV-C irradiation or, as previously mentioned, that the active structures represent only a minor subpopulation of the RNA structures (56). The fact that a higher cleavage efficiency was obtained for the minimal HCV substrate after irradiation for longer times is probably due to reduced random UV-C-induced cleavage (Supplementary Figure S6b), which is RNA length dependent. However, it is also possible that the minimal substrate adopts a more homogenous RNA structure.

Cleavage specificity. In contrast to transesterification or hydrolytic cleavage, at least one base/sugar is degraded

during oxidative cleavage (11). In the recent case of a chemically generated, position specific, base-radical in an RNA oligonucleotide (19,20), which is a very convenient situation to initiate a site specific RNA oxidative cleavage, it has been found that cleavage at the base generated radical coexisted with inter-nucleotide cleavage at the nucleotide 5' to the position of the base generated radical, being the proportion dependent on the single or double nature of the oligonucleotide employed. This allowed two product fragments whose 3'- and 5'-ends are contiguous in the original RNA sequence, as if no nucleotide had been degraded, to be detected in the reaction product mix. Our cleavage specificity is very close to this example, at least for the principal cleavage products for both HCV and CSFV RNAs, although minor represented products extend to neighbor bases in

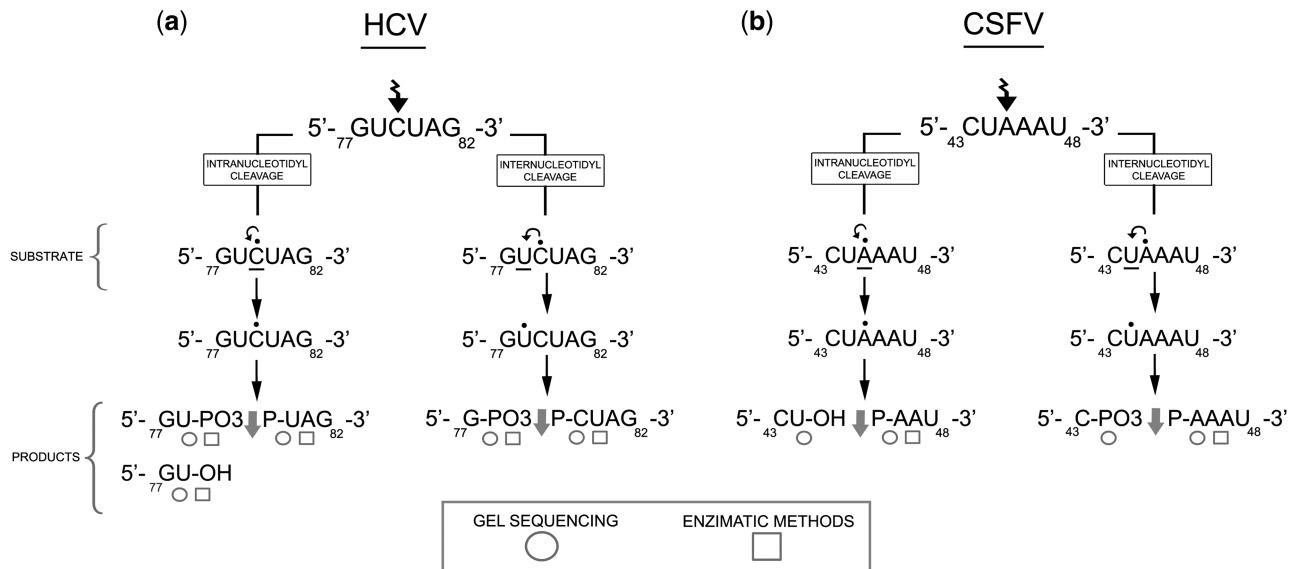


Figure 12. Schematic diagram showing the cleavage site and expected products for both viral RNAs. The cleavage site and the end groups generated upon UV-C irradiation were proposed on the basis that both intra- (left-hand side) and inter-strand (right-hand side) cleavage are occurring. The sequence surrounding the cleavage site is represented: (a) HCV RNA, (b) CSFV RNA. Here we compile the information from several figures. White circles indicate cleavage position and terminal group from sequencing gels. White squares indicate the chemistry of the terminal group obtained through enzymatic methods. All products represented in the figure were identified by mass spectrometry, except those 3'-ends from CSFV RNA. The underlined bases are the ones found to be fragmented by many sites during analysis of the mass spectra. Hypothetically, a dot over the base indicates the proposed position where the radical was generated. The accompanying arrow indicates the base where damage is initiated.

HCV RNA. Also, is similar to flavin-dependent photocleavage of RNA (34), and departs completely from unspecific degradation generated by solution radicals as can be observed in Figure 7b–d.

Cleavage products. Despite, we probed that RNA cleavage was of oxidative nature, and released the characteristic product fragments ending with 3'- and 5'-phosphate groups, we found that a minor fraction of molecules carried 3'-OH at the new generated termini. Product fragments carrying this 3'-OH end-group might be compatible with routes of RNA synthesis and metabolism.

Reaction mechanism

The reaction is oxidative as it is inhibited by DTT at a concentration 50–150 μM , 25- to 100-fold lower than that usually employed in protecting other types of RNA cleavage reactions. As we were able to demonstrate that the cleavage site is not a hot spot for the Fenton reaction, it is likely that a base radical is formed directly by photoionization of the base. Nevertheless, it cannot be completely ruled out that the particular RNA structures involved here could react differently to OH^\bullet radicals generated in solution by the Fenton reaction and those generated residually by UV-254 irradiation in close proximity to the RNA chain. In any of the cases, the base-radical could then abstract a proton from the sugar at position C2, followed by beta phosphate elimination and RNA cleavage (11). Hence, the HCV RNA fragment products with a phosphate group at the 3'-(HCV U₇₈) and 5'-ends (HCV U₈₀) found here are consistent with a classic nucleic acid oxidative mechanism if the base

attacked is HCV C₇₉. However, if a similar mechanism of inter-nucleotide strand cleavage to that described by Jacobs *et al.* (19,20) is acting, the radical at HCV C₇₉ would also generate fragments displaced one position toward the 5'-end with respect to those described above (inter-nucleotidyl strand cleavage), in this case 3'-HCV G₇₇-p and 5'-HCV p-C₇₉. Alternatively, the minus one 3'-products could be the result of a delta-elimination following beta-elimination. However, this reaction is slower than in DNA at abasic RNA sites (57), thus meaning that the mechanism proposed by Jacobs *et al.* (19,20) would be favored. As far as CSFV RNA is concerned, and similarly to HCV, if A₄₅ is the damaged base, the new 5'-end bases generated by intra- and inter-strand cleavage would be pA₄₆ and pA₄₅, respectively, whereas, although we lack mass spectrometry data, these are compatible with 32-P release only from the [α -³²P]A-labeled B1-band after phosphatase treatment (Figure 9c) as well as with the increased gel mobility of two 3'-end labeled band products in relation to the hydroxyl standard (Figure 4b). Residues C₄₃p and U₄₄OH can be observed for the new 3'-end. However, if U₄₄p is present, it only appears as a very faint electrophoresis band. Figure 12 diagrammatically summarizes this interpretation.

UV-B sensitivity. We found a decreased reactivity but still detectable under irradiation at 310 nm for longer exposure period, up to 15 min. This sensitivity may have relevance if reactive motifs that we found here might be found in viral organism subjected to long sunshine exposure as might be the plant virus and viroids, or in structural or messengers RNA from human tissues that might be related to sun exposition related diseases (58).

RNA archaeology. Early RNA life forms may have had the ability to use the abundantly available energy from UV radiation to carry out specific steps, thereby promoting the development of genetic systems or regulation of day/night activity. The RNA structures able to carry out this reaction might be remnants of an ancient UV-related biological function and could thus prove to be significant for the study of biochemical evolution. It could even be possible that long structured RNAs previously studied for UV-C induced crosslinks, such as ribosomal RNAs (59) viroid (21) or viroid-like RNAs (45) and RNase P RNA (41) may hide structures able to self-cleave as the ones presented here.

SUPPLEMENTARY DATA

Supplementary Data are available at NAR Online: Supplementary Figures 1–10.

ACKNOWLEDGEMENTS

The original observations and initial RNA fingerprinting characterization of UV-C-induced RNA self-cleavage were performed by our late friend and colleague Hugh D. Robertson with help from Alita Lyons. All work performed by A.B. was undertaken in Hugh D. Robertson's laboratory. The authors thank Antonio Larios from IPBLN for assistance in Mass Spectrometry. The authors would also like to thank Dr. Marc M Greenberg from Johns Hopkins University at Baltimore for his scientific support on RNA oxidative chemistry.

FUNDING

The Spanish Ministry of Science and Innovation (BIO2007-60106) and (BIO2010-15121); Autonomous Community of Andalucía (Proyecto Excelencia CVI-03050) and FISS (CIBERehd); Work in the IPBLN-CSIC was funded with FEDER funds from the EU. Funding for open access charge: Autonomous Community of Andalucía (Proyecto Excelencia CVI-03050).

Conflict of interest statement. None declared.

REFERENCES

- Pyle, A.M. (1993) Ribozymes: a distinct class of metalloenzymes. *Science*, **261**, 709–714.
- Valadkhan, S. and Manley, J.L. (2001) Splicing-related catalysis by protein-free snRNAs. *Nature*, **413**, 701–707.
- Sharp, P.A. (2001) RNA interference—2001. *Genes Dev.*, **15**, 485–490.
- Gesteland, R.F., Cech, T. and Atkins, J.F. (1999) *The RNA World*, 2nd edn. Cold Spring Harbor Press, New York.
- Wedekind, J.E. and McKay, D.B. (1999) Crystal structure of a lead-dependent ribozyme revealing metal binding sites relevant to catalysis. *Nat. Struct. Biol.*, **6**, 261–268.
- Correll, C.C., Munishkin, A., Chan, Y.L., Ren, Z., Wool, I.G. and Steitz, T.A. (1998) Crystal structure of the ribosomal RNA domain essential for binding elongation factors. *Proc. Natl Acad. Sci. USA*, **95**, 13436–13441.
- Martinez-Salas, E., Pacheco, A., Serrano, P. and Fernandez, N. (2008) New insights into internal ribosome entry site elements relevant for viral gene expression. *J. Gen. Virol.*, **89**, 611–626.
- Fraser, C.S. and Doudna, J.A. (2007) Structural and mechanistic insights into hepatitis C viral translation initiation. *Nat. Rev. Microbiol.*, **5**, 29–38.
- Fletcher, S.P. and Jackson, R.J. (2002) Pestivirus internal ribosome entry site (IRES) structure and function: elements in the 5' untranslated region important for IRES function. *J. Virol.*, **76**, 5024–5033.
- Pogozelski, W.K. and Tullius, T.D. (1998) Oxidative strand scission of nucleic acids: routes initiated by hydrogen abstraction from the sugar moiety. *Chem. Rev.*, **98**, 1089–1108.
- Burrows, C.J. and Muller, J.G. (1998) Oxidative nucleobase modifications leading to strand scission. *Chem. Rev.*, **98**, 1109–1152.
- Cadet, J. and Vigny, P. (1990) Photochemistry and nucleic acids. In Morrison, H. (ed.), *Bio-organic Photochemistry*. John Wiley & Sons, New York, pp. 1–272.
- Remsen, J.F., Miller, N. and Cerutti, P.A. (1970) Photohydration of uridine in the RNA of coliphage R17. II. The relationship between ultraviolet inactivation and uridine photohydration. *Proc. Natl Acad. Sci. USA*, **65**, 460–466.
- Coahran, D.R., Buzzell, A. and Lauffer, M.A. (1962) The effect of ultraviolet irradiation on nucleic acid isolated from tobacco mosaic virus. *Biochim. Biophys. Acta*, **55**, 755–767.
- Jericevic, Z., Kucan, I. and Chambers, R.W. (1982) Photochemical cleavage of phosphodiester bonds in oligoribonucleotides. *Biochemistry*, **21**, 6563–6567.
- Gorner, H. (1994) Photochemistry of DNA and related biomolecules: quantum yields and consequences of photoionization. *J. Photochem. Photobiol. B*, **26**, 117–139.
- Crespo-Hernandez, C.E. and Arce, R. (2002) Photoionization of DNA and RNA bases, nucleosides and nucleotides through a combination of one- and two-photon pathways upon 266 nm nanosecond laser excitation. *Photochem. Photobiol.*, **76**, 259–267.
- Newman, C.A., Resendiz, M.J., Szczepanski, J.T. and Greenberg, M.M. (2009) Photochemical generation and reactivity of the 5,6-dihydrouridin-6-yl radical. *J. Org. Chem.*, **74**, 7007–7012.
- Jacobs, A.C., Resendiz, M. and Greenberg, M.M. (2010) Direct strand scission from a nucleobase radical in RNA. *J. Am. Chem. Soc.*, **132**, 3668–3669.
- Jacobs, A.C., Resendiz, M. and Greenberg, M.M. (2011) Product and mechanistic analysis of the reactivity of a C6-pyrimidine radical in RNA. *J. Am. Chem. Soc.*, **133**, 5152–5159.
- Branch, A.D., Benenfeld, B.J. and Robertson, H.D. (1985) Ultraviolet light-induced crosslinking reveals a unique region of local tertiary structure in potato spindle tuber viroid and HeLa 5S RNA. *Proc. Natl Acad. Sci. USA*, **82**, 6590–6594.
- Branch, A.D., Benenfeld, B.J., Paul, C.P. and Robertson, H.D. (1989) Analysis of ultraviolet-induced RNA-RNA cross-links: a means for probing RNA structure-function relationships. *Methods Enzymol.*, **180**, 418–442.
- Downs, W.D. and Cech, T.R. (1990) An ultraviolet-inducible adenosine-adenosine cross-link reflects the catalytic structure of the Tetrahymena ribozyme. *Biochemistry*, **29**, 5605–5613.
- Butcher, S.E. and Burke, J.M. (1994) A photo-cross-linkable tertiary structure motif found in functionally distinct RNA molecules is essential for catalytic function of the hairpin ribozyme. *Biochemistry*, **33**, 992–999.
- Leontis, N.B. and Westhof, E. (1998) A common motif organizes the structure of multi-helix loops in 16 S and 23 S ribosomal RNAs. *J. Mol. Biol.*, **283**, 571–583.
- Wimberly, B., Varani, G. and Tinoco, I. Jr (1993) The conformation of loop E of eukaryotic 5S ribosomal RNA. *Biochemistry*, **32**, 1078–1087.
- Lyons, A.J., Lytle, J.R., Gomez, J. and Robertson, H.D. (2001) Hepatitis C virus internal ribosome entry site RNA contains a tertiary structural element in a functional domain of stem-loop II. *Nucleic Acids Res.*, **29**, 2535–2541.

28. Bevilacqua, P.C. and Yajima, R. (2006) Nucleobase catalysis in ribozyme mechanism. *Curr Opin Chem. Biol.*, **10**, 455–464.
29. Wilcox, J.L., Ahluwalia, A.K. and Bevilacqua, P.C. (2011) Charged nucleobases and their potential for RNA catalysis. *Acc. Chem. Res.*, in press, doi:10.1021/ar2000452.
30. Fedor, M.J. (2009) Comparative enzymology and structural biology of RNA self-cleavage. *Annu. Rev. Biophys.*, **38**, 271–299.
31. Cochrane, J.C. and Strobel, S.A. (2008) Catalytic strategies of self-cleaving ribozymes. *Acc. Chem. Res.*, **41**, 1027–1035.
32. Chinnappen, D.J. and Sen, D. (2004) A deoxyribozyme that harnesses light to repair thymine dimers in DNA. *Proc. Natl Acad. Sci. USA*, **101**, 65–69.
33. Sen, D. and Gilbert, W. (1990) A sodium-potassium switch in the formation of four-stranded G4-DNA. *Nature*, **344**, 410–414.
34. Burgstaller, P., Hermann, T., Huber, C., Westhof, E. and Famulok, M. (1997) Isoalloxazine derivatives promote photocleavage of natural RNAs at G.U base pairs embedded within helices. *Nucleic Acids Res.*, **25**, 4018–4027.
35. Diaz-Toledano, R., Ariza-Mateos, A., Birk, A., Martinez-Garcia, B. and Gomez, J. (2009) In vitro characterization of a miR-122-sensitive double-helical switch element in the 5' region of hepatitis C virus RNA. *Nucleic Acids Res.*, **37**, 5498–5510.
36. Milligan, J.F. and Uhlenbeck, O.C. (1989) Synthesis of small RNAs using T7 RNA polymerase. *Methods Enzymol.*, **180**, 51–62.
37. Branch, A.D., Benenfeld, B.J. and Robertson, H.D. (1989) RNA fingerprinting. *Methods Enzymol.*, **180**, 130–154.
38. Kieft, J.S., Costantino, D.A., Filbin, M.E., Hammond, J. and Pflugsten, J.S. (2007) Structural methods for studying IRES function. *Methods Enzymol.*, **430**, 333–371.
39. Gutteridge, J.M., Maidt, L. and Poyer, L. (1990) Superoxide dismutase and Fenton chemistry. Reaction of ferric-EDTA complex and ferric-bipyridyl complex with hydrogen peroxide without the apparent formation of iron(II). *Biochem. J.*, **269**, 169–174.
40. Knapp, G. (1989) Enzymatic approaches to probing of RNA secondary and tertiary structure. *Methods Enzymol.*, **180**, 192–212.
41. Guerrier-Takada, C., Lumelsky, N. and Altman, S. (1989) Specific interactions in RNA enzyme-substrate complexes. *Science*, **246**, 1578–1584.
42. Kieft, J.S., Zhou, K., Jubin, R., Murray, M.G., Lau, J.Y. and Doudna, J.A. (1999) The hepatitis C virus internal ribosome entry site adopts an ion-dependent tertiary fold. *J. Mol. Biol.*, **292**, 513–529.
43. Deng, R. and Brock, K.V. (1993) 5' and 3' untranslated regions of pestivirus genome: primary and secondary structure analyses. *Nucleic Acids Res.*, **21**, 1949–1957.
44. Le, S.Y., Liu, W.M. and Maizel, J.V. Jr (1998) Phylogenetic evidence for the improved RNA higher-order structure in internal ribosome entry sequences of HCV and pestiviruses. *Virus Genes*, **17**, 279–295.
45. Branch, A.D., Levine, B.J. and Polaskova, J.A. (1995) An RNA tertiary structure of the hepatitis delta agent contains UV-sensitive bases U-712 and U-865 and can form in a bimolecular complex. *Nucleic Acids Res.*, **23**, 491–499.
46. Forster, A.C. and Symons, R.H. (1987) Self-cleavage of plus and minus RNAs of a virusoid and a structural model for the active sites. *Cell*, **49**, 211–220.
47. Takakura, K., Ishikawa, M. and Ito, T. (1987) Action spectrum for the induction of single-strand breaks in DNA in buffered aqueous solution in the wavelength range from 150 to 272 nm: dual mechanism. *Int. J. Radiat. Biol. Relat. Stud. Phys. Chem. Med.*, **52**, 667–675.
48. Croke, D.T., Blau, W., OhUigin, C., Kelly, J.M. and McConnell, D.J. (1988) Photolysis of phosphodiester bonds in plasmid DNA by high intensity UV laser irradiation. *Photochem. Photobiol.*, **47**, 527–536.
49. Adilakshmi, T., Lease, R.A. and Woodson, S.A. (2006) Hydroxyl radical footprinting in vivo: mapping macromolecular structures with synchrotron radiation. *Nucleic Acids Res.*, **34**, e64.
50. Melvin, T., Plumb, M.A., Botchway, S.W., O'Neill, P. and Parker, A.W. (1995) 193 nm light induces single strand breakage of DNA predominantly at guanine. *Photochem. Photobiol.*, **61**, 584–591.
51. Thompson, D.M., Lu, C., Green, P.J. and Parker, R. (2008) tRNA cleavage is a conserved response to oxidative stress in eukaryotes. *RNA*, **14**, 2095–2103.
52. Cadet, J., Douki, T. and Ravanat, J.L. (2010) Oxidatively generated base damage to cellular DNA. *Free Radic. Biol. Med.*, **49**, 9–21.
53. Armitage, B. (1998) Photocleavage of nucleic acids. *Chem. Rev.*, **98**, 1171–1200.
54. Locker, N., Easton, L.E. and Lukavsky, P.J. (2007) HCV and CSFV IRES domain II mediate eIF2 release during 80S ribosome assembly. *EMBO J.*, **26**, 795–805.
55. Huggins, W., Ghosh, S.K., Nanda, K. and Wollenzien, P. (2005) Internucleotide movements during formation of 16 S rRNA-rRNA photocrosslinks and their connection to the 30 S subunit conformational dynamics. *J. Mol. Biol.*, **354**, 358–374.
56. Schuster, P. (1997) Genotypes with phenotypes: adventures in an RNA toy world. *Biophys. Chem.*, **66**, 75–110.
57. Kupfer, P.A. and Leumann, C.J. (2007) The chemical stability of abasic RNA compared to abasic DNA. *Nucleic Acids Res.*, **35**, 58–68.
58. Wurtmann, E.J. and Wolin, S.L. (2009) RNA under attack: cellular handling of RNA damage. *Crit. Rev. Biochem. Mol. Biol.*, **44**, 34–49.
59. Shapkina, T., Lappi, S., Franzen, S. and Wollenzien, P. (2004) Efficiency and pattern of UV pulse laser-induced RNA-RNA cross-linking in the ribosome. *Nucleic Acids Res.*, **32**, 1518–1526.
60. Brown, E.A., Zhang, H., Ping, L.H. and Lemon, S.M. (1992) Secondary structure of the 5' nontranslated regions of hepatitis C virus and pestivirus genomic RNAs. *Nucleic Acids Res.*, **20**, 5041–5045.
61. Lukavsky, P.J., Kim, I., Otto, G.A. and Puglisi, J.D. (2003) Structure of HCV IRES domain II determined by NMR. *Nat. Struct. Biol.*, **10**, 1033–1038.
62. Wang, T.H., Rijnbrand, R.C. and Lemon, S.M. (2000) Core protein-coding sequence, but not core protein, modulates the efficiency of cap-independent translation directed by the internal ribosome entry site of hepatitis C virus. *J. Virol.*, **74**, 11347–11358.

Additional Figure 1. Specificity of UV-C-induced cross-linking and self-cleavage of HCV RNA is maintained in different transcript lengths: 1-130, 1-249 and 1-402. (a) Gel purified [α - 32 P]-labeled HCV transcripts were treated (“+”) or not (“-”) with UV-C light for 180 s, separated on 8% denaturing polyacrylamide gels, and visualized by autoradiography. Lanes 1-2: RNA 1-130, lanes 3-4: RNA 1-249, and lanes 5-6: RNA 1-402. SM is indicated in the right of the gel. Bands B1 and band B2 carrying the original 5’end pppG is indicated in the left. (b) RNA fingerprinting analysis of the 5’ p-B2 product of UV-C-induced self-cleavage of HCV RNAs 1-130, 1-249 and 1-402. The coincident pattern of spots in the three two-dimensional fingerprints indicates that the self-cleavage reaction conserves its specificity for the three RNA transcripts studied. The directions of the first and second dimension separations are indicated at the bottom right by horizontal and vertical arrows, respectively.

Additional Figure 2 Kinetic analysis of UV-C-induced cleavage in HCV RNA 1-130 and CSFV RNA 1-218. The autoradiograms of 6% denaturing polyacrylamide gels showing one of the four assays performed at 10000 dpm. (a) HCV RNA 1-130. Lane 1: RNA maintained in ice; Lane 2: RNA incubated in reaction buffer. Left panel: Lanes 3 to 8: HCV RNA irradiated for 90, 180, 270, 360, 450, and 540 seconds respectively. (b) The same for CSFV RNA 1-218 irradiated for 30, 60, 90, 180, 270, and 360 seconds respectively. MW are molecular weights.

Additional Figure 3 (a) The data of the cleavage reaction for all concentrations : 5.000, 10.000 and 50.000 dpms for HCV and (b) 2.000, 5.000, 10.000 and 50.000 for CSFV was fitted to a polynomic model. For HCV and CSFV equations are: $f(x) = -0.0502 + 0.0149x + 1,4637E-5x^2 - 3,68857E-8x^3$ and $f(x) = 0.828727 + 0.0671164x - 4.97184E-5x^2 - 8.41759E-8x^3$ respectively. R2 for both equations were 0.9992 and 0.9993 respectively.

Additional Figure 4. Effect of pre-incubation with EDTA on the self-cleavage reaction in HCV and CSFV RNAs. Briefly, HCV or CSFV RNA transcripts were incubated by preheating at 90°C in 0.04 M Tris-HCl, pH 7.6, 2 mM EDTA, and then allowed to cool to room temperature and subsequently cooled to 4°C, at which temperature they were maintained for either two hours or overnight. The transcripts were then exposed to UV-C irradiation for 3 min either with or without the addition of 20 mM MgCl₂. **(a and b):** HCV RNA 1-130 and 1-249. **(c):** CSFV RNA 1-218. Lane 1: RNA kept on ice; lane 2: RNA incubated in standard buffer; lane 3: RNA irradiated 180 s. Lanes 4-9: Effect of pre-incubation with EDTA. Aliquots of RNA were incubated; or 2 hours (lanes 4-6) or 16 hours (lanes 7-9) in 0.04 M Tris-HCl, pH 7.6, 2 mM EDTA. They were then kept on ice (lanes 4 and 7); treated for 180 s with UV-C radiation (lanes 5 and 8); or treated with UV-C radiation for 180 s after addition of 20 mM MgCl₂ (lanes 6, 9).

Additional Figure 5. Ability of HCV RNA 1-130 to self-cleave in the presence of monovalent NH₄⁺ and K⁺, divalent Mg²⁺ ions, and Tris-HCl during irradiation. 10,000 dpm of HCV 1-130 RNA substrate in 10 µl aliquots in 10 mM Tris-HCl, pH 7.6, 10 mM MgCl₂ (standard conditions) were irradiated for 360 s, after being supplemented with **(a)** from 0 to 600 mM of ammonium acetate, **(b)** 0 to 500 mM KCl and **(c)** 0 to 90 mM MgCl₂, and **(d)** 0 to 90 mM Tris-HCl, pH 7.6. The reactions were then fractionated in 6% polyacrylamide gel containing 7 M urea. Data were collected from single experiments, quantified with the use of a PhosphorImager, and represented as the cleavage percentage of a standard reaction.

Additional Figure 6. Timecourses of UV-C induced cleavage of shortened HCV RNAs. **(a)** Graph showing the increase in cleavage of HCV 1-130 RNA and the shortened fragment HCV 68-100 with time of exposure to UV-C light: 90, 180, 270, 360, 450 and 540 s. **(b)** One additional kinetic assay for 3' end labeled HCV 68-100 extended over 30 mins of irradiation run in 20% polyacrylamide gel. Lane 1: RNA maintained on ice. Lane 2: RNA maintained on standard buffer. Lanes 3 to 8: RNA irradiated during: 3, 9, 18, 24 and 30 mins.

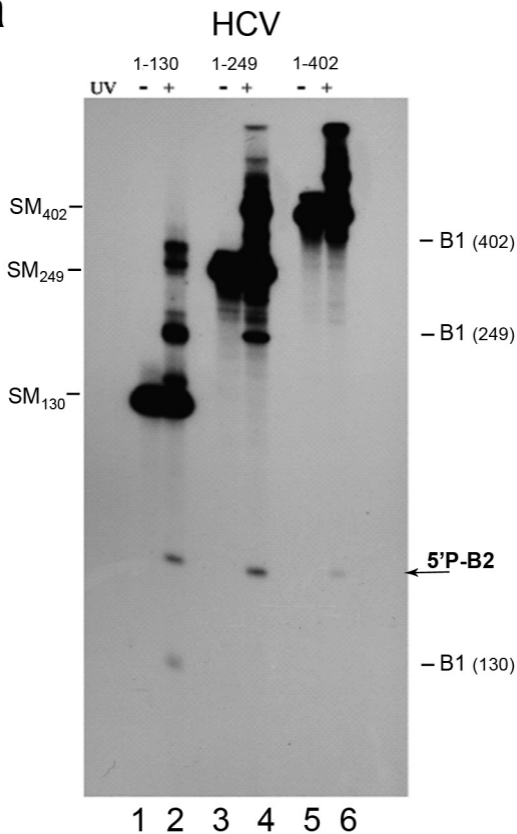
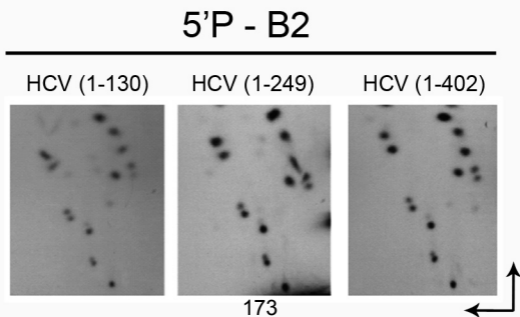
Additional Figure 7. Integrity of the E loop in HCV 1-30 RNA is a requisite for the self-cleavage reaction, whereas no internal loop is required for CSFV RNA cleavage. (a) 10% polyacrylamide gel electrophoresis analysis of HCV 1-130 self-cleavage. Lanes 1 and 2: wt sequence; lanes 3 and 4: a “G94” deleted sequence (Δ “G94”). Lanes 5 and 6: a mutant sequence “Mut 1” in which the upstream sequence of the E-loop $_{93}\text{AGU}_{95}$ has been substituted by the $_{93}\text{UUC}_{95}$ sequence. Lanes 1, 3, and 5 are control reactions in which the RNA was incubated in buffer. The RNA in lanes 2, 4, and 6 was irradiated for 90 s. The slightly slow migration of the deleted and mutated sequences in lanes 3 to 6 in relation to wt sequences is due to additional nucleotides flanking the HCV sequence derived from the plasmid polylinker after cloning. The secondary structures of wt and the “ Δ G94” and “ $_{93}\text{UUC}_{95}$ ” mutants are shown in Table 1 of the main text. **(b)** 20% polyacrylamide gel electrophoresis analysis of CSFV 34-63 self-cleavage. Lanes 1 and 2: wt sequence. Lanes 3 and 4: a three nucleotide deleted sequence (Δ U39-C41). Lanes 5 and 6: a two mutated position “Mut 2” $_{39}\text{UAC}_{41} \rightarrow _{39}\text{GAG}_{41}$. The RNAs in lanes 1, 3 and 5 were incubated in standard buffer. The RNAs in lanes 2, 4, and 6 were irradiated for 90s.

Additional Figure 8. Varying the reactions conditions (time, temperature, pH, and Mg^{2+} concentration) in the absence of UV-C light does not promote self-cleavage. HCV 1-130 RNA (lanes 1–6) and CSFV1-218 RNA (lanes 7–12). Standard buffer conditions (MgCl_2 10 mM, Tris-HCl 10mM, pH 7.6) were employed in lanes 1, 2, 3, 6 and 7, 8, 9, 12. The RNA in lanes 1 and 7: were incubated for 10 min at 25 °C. Lanes 2 and 8: 50 min at 25 °C. Lanes 3 and 9: 10 min at 40 °C. Variations in buffer composition: lanes 4 and 10: MgCl_2 50 mM, Tris-HCl 10 mM, pH 7.6. Lanes 5 and 11: MgCl_2 10 mM, Tris-HCl 10 mM, pH 9. Lanes 6 and 12: RNAs were irradiated under standard conditions UV-C at 0 °C for 180 s.

Additional Figure 9. End-group determination of purified product bands B1 and B2 from the shortened HCV 68-100 RNA fragment. (a) Band B1 was

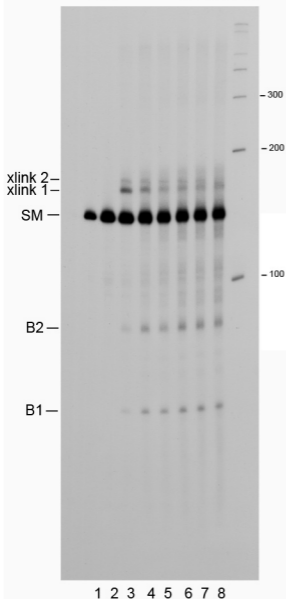
excised from the gel in two halves: a fast migrating half (B1f) and a slow migrating half (B1s). 5000 dpm (10^5 dpm/ μ g) aliquots of each B1 moiety were treated with T4 polynucleotide kinase and [γ - 32 P]ATP prior to dephosphorylation with phosphatase. Lane 1 and 1': RNA maintained on ice; lane 2 and 2': phosphatase and kinase treated RNA; lane 3 and 3': kinase incubated without previous dephosphorylation. A radioactive signal of band products B1f and B1s in lanes 1, 1', 3 and 3' can be seen if the sample loaded in lane 2 is diluted 30-fold and with longer gel exposure (data not shown). **(b)** Two bands from B2 products (B2.1 and B2.2) were "individually" isolated from the gel and their capacity to be labeled with T4 RNA ligase and [$5'$ - 32 P]pCp assayed. Lane 1: control reaction with B2.1 RNA incubated in phosphatase buffer, proteinase K/SDS treated, precipitated in EtOH and incubated in ligase buffer and [$5'$ - 32 P]pCp for 4 days at 4°C in the absence of any enzyme; Lane 2: control reaction of B2.1 RNA treated as in lane 1 but incubated with the phosphatase; Lane 3: B2.1 RNA incubated with T4 RNA ligase without prior dephosphorylation; Lane 4: complete reaction of B2.1 RNA incubated with the ligase after being treated with the phosphatase. Lanes 1', 2' 3' and 4' the same but with band B2.2.

Additional Figure 10. Comparison of UV-C and UV-B in HCV RNA self-cleavage. **(a)** The HCV 1-249 RNA substrate in 0.01 M Tris-HCl, pH 7.6, 10 mM MgCl₂, was either kept on ice (lanes 1 and 3) or irradiated with UV-C (lane 2) or UV-B (lane 4; as indicated by "+" signs) for 180 s and then electrophoresed on a 6% polyacrylamide gel. The left panel shows the autoradiograph obtained after light exposure (2 h), in which UV-B-induced cross-linking of the substrate can be seen above the starting material band, although the cleavage products are not detectable. The right panel shows an overnight (24 h) exposure covering the region of the gel from the starting material down through the positions of the two UV cleavage bands, thus allowing the UV-B cleavage products to be discerned in the right panel. **(b)** Graphical representation of the time course of UV-B-induced self-cleavage of shortened substrates HCV RNA 68-100 and CSFV RNA 34-63. The data were obtained from single experiments.

a**b****Supplementary Figure 1**

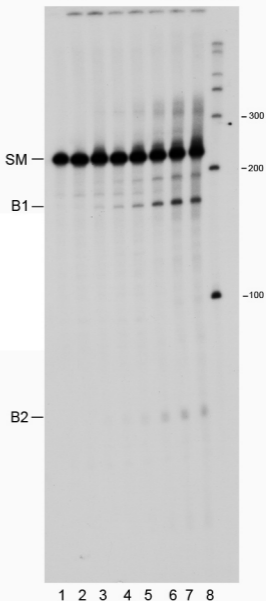
HCV 1-130

I B → time (seconds) → 540 MW



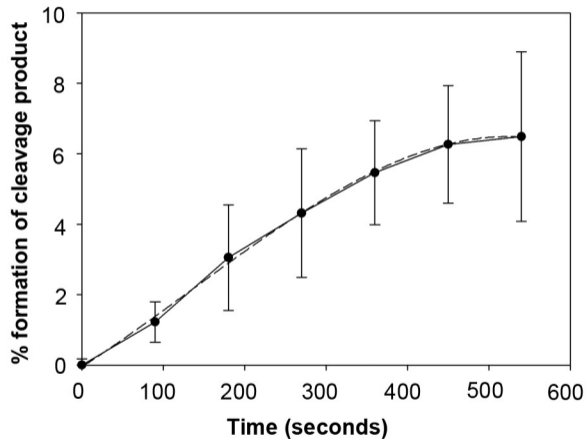
CSFV 1-218

I B → time (seconds) → 360 MW

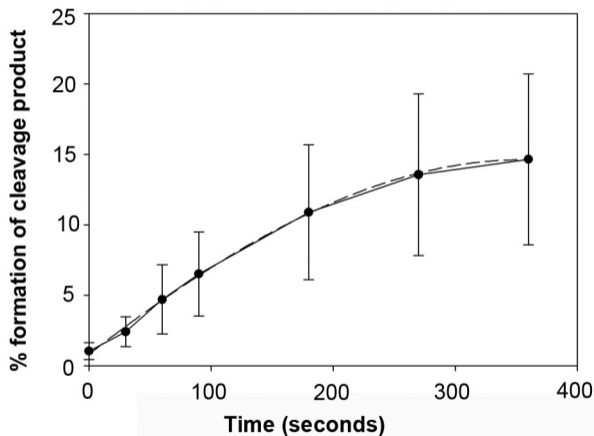


174

HCV 1-130 /UV-C

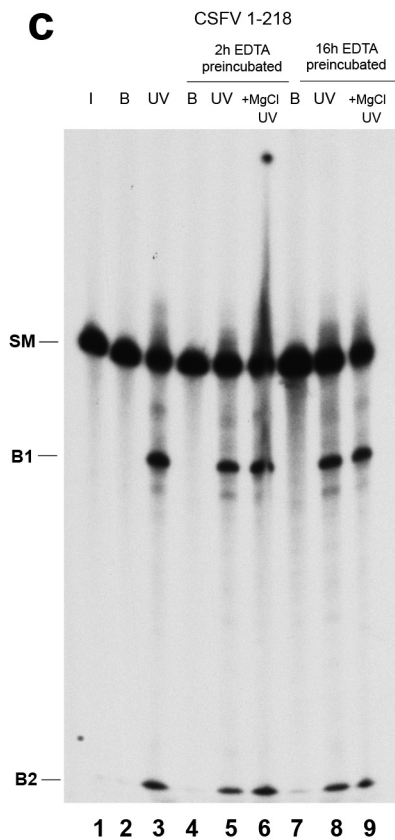
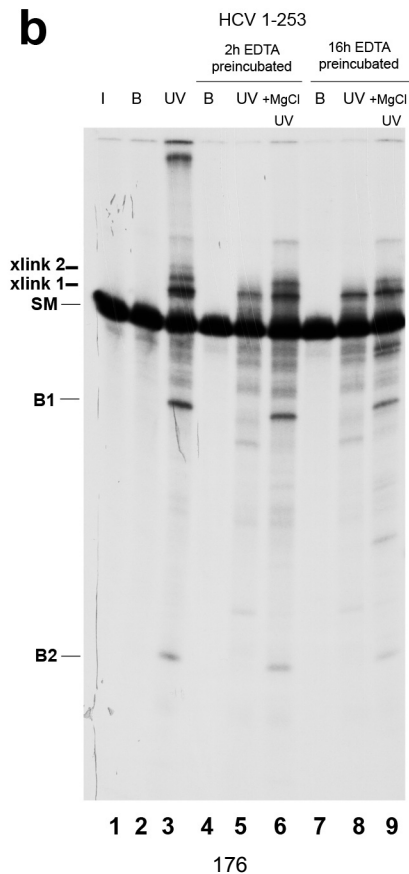
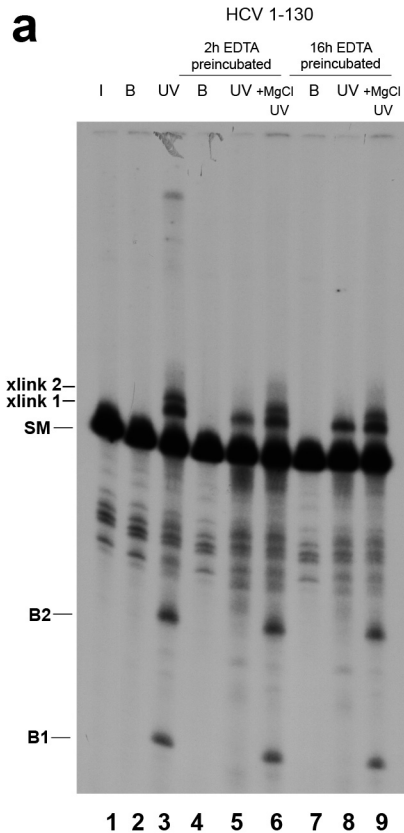


CSFV 1-218 /UV-C

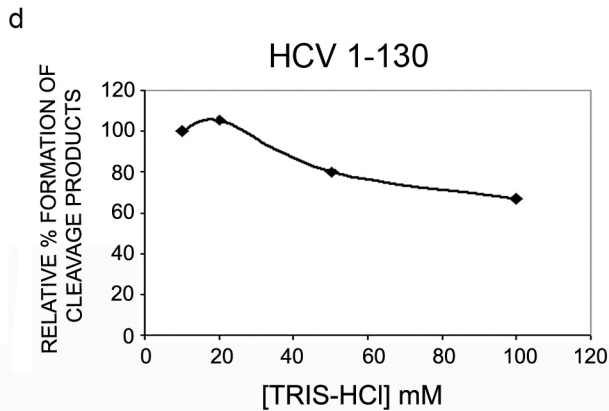
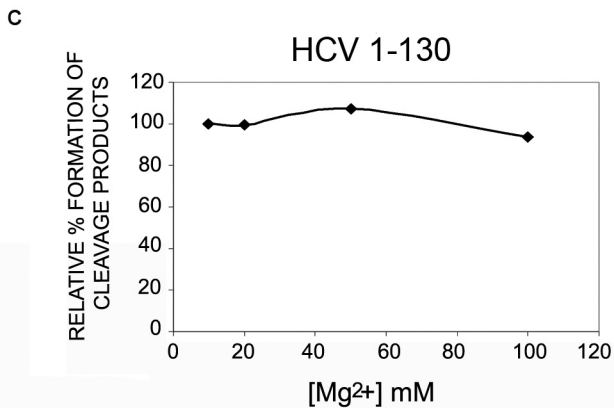
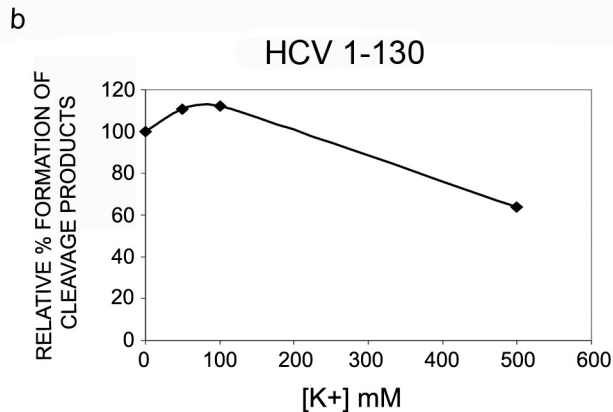
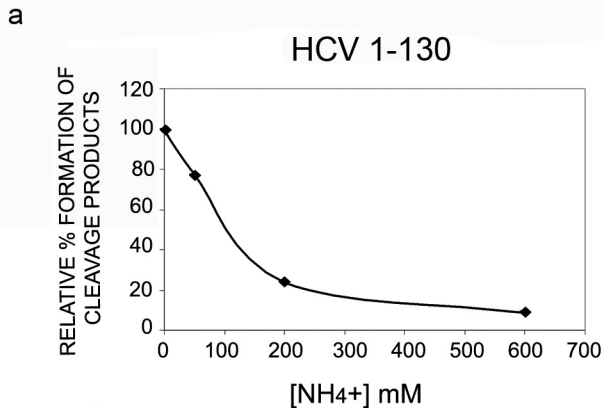


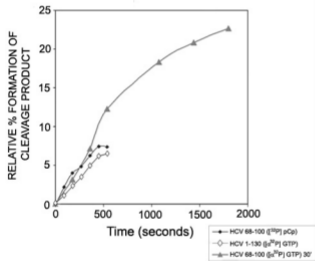
175

--- Arithmetic mean from experimental
— Polynomic equation

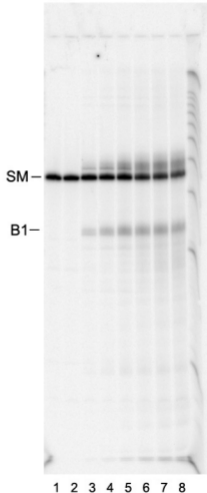


176



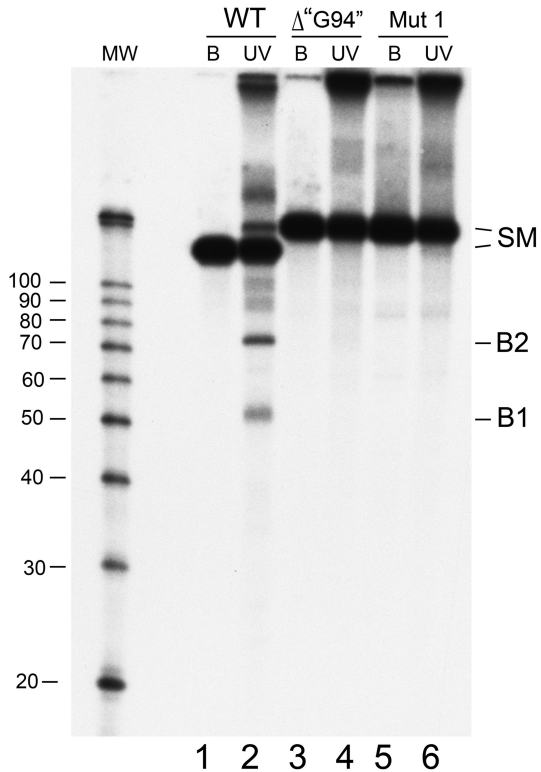
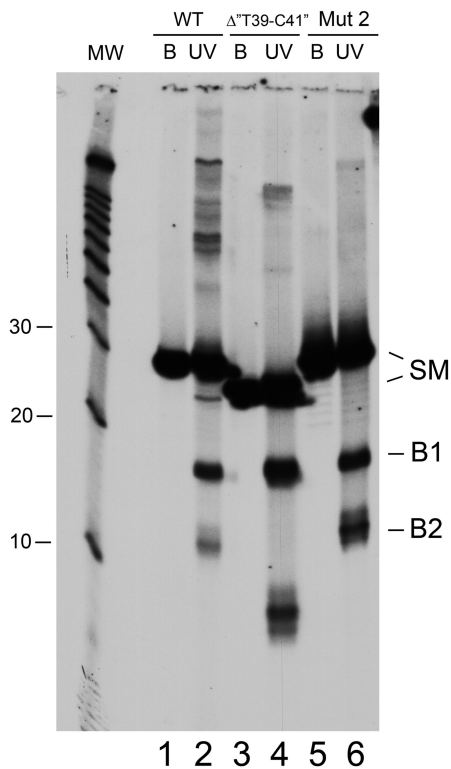
a**b** HCV 68-100
[^{32}P] pCp

time (min) → 30 MW



178

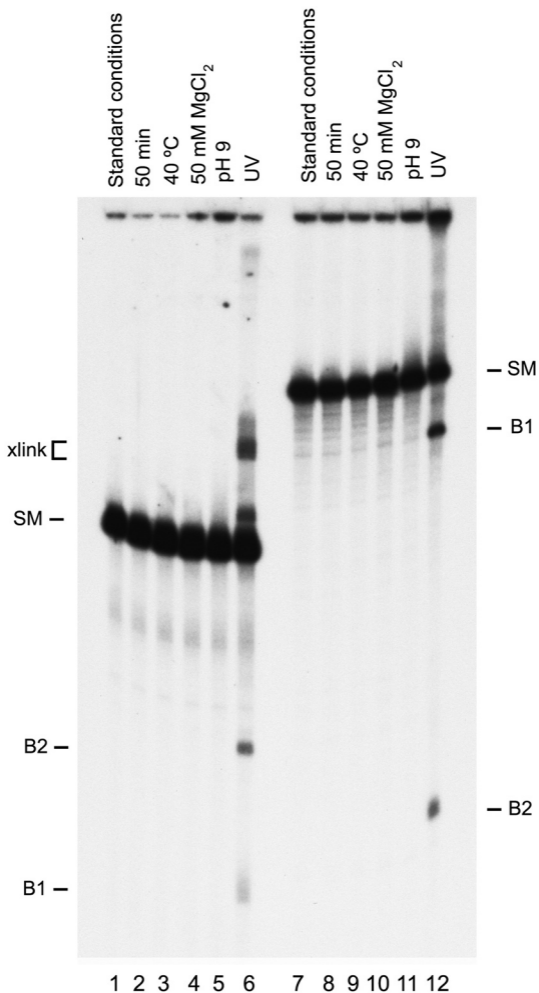
Supplementary Figure 6

a**HCV 1-130****b****CSFV 34-63**

179

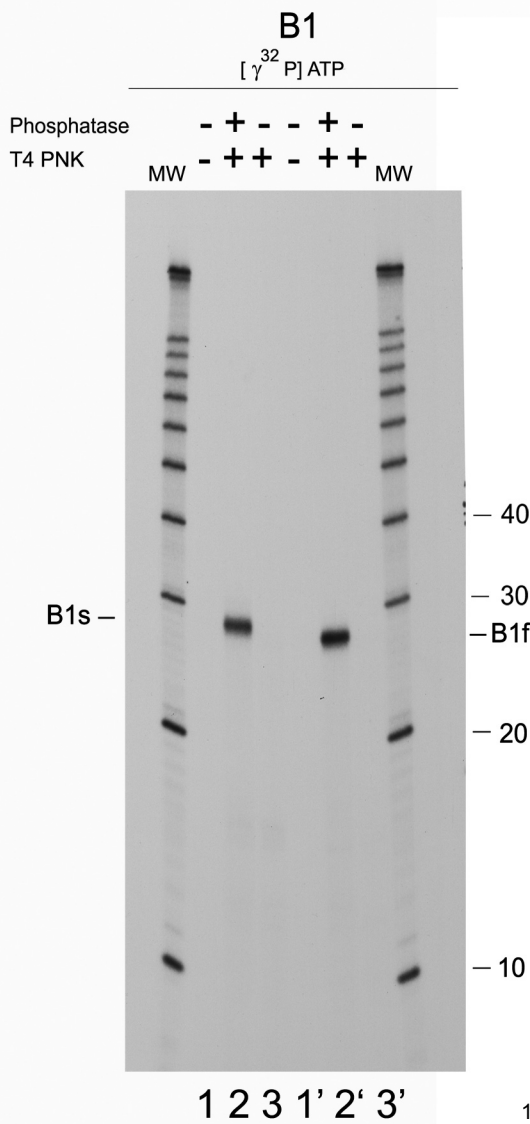
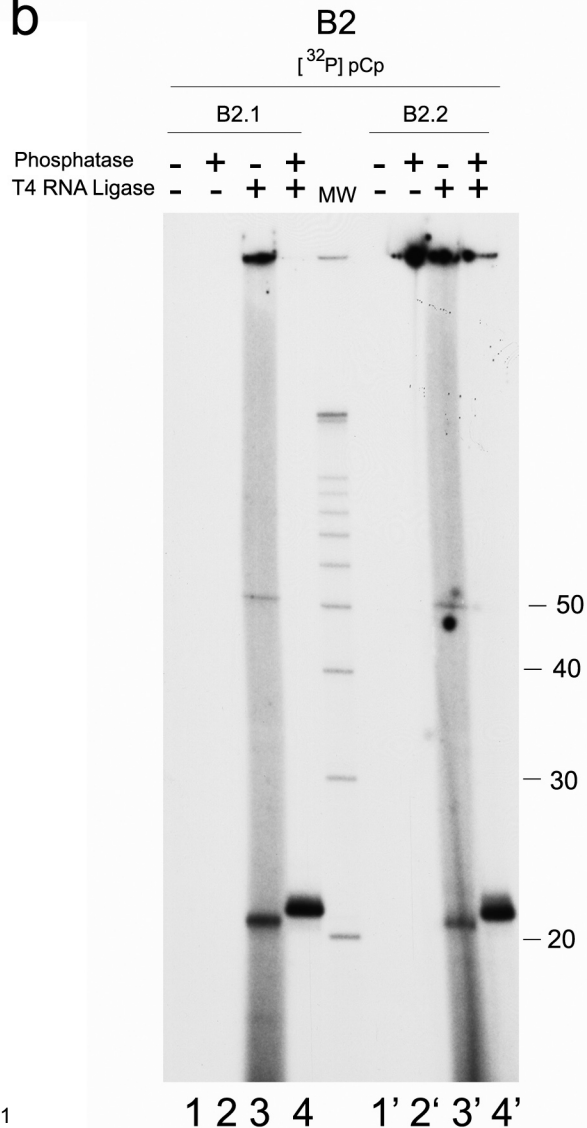
HCV 1-130

CSFV 1-218

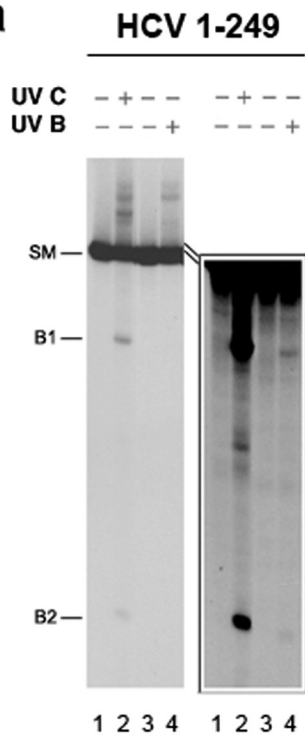
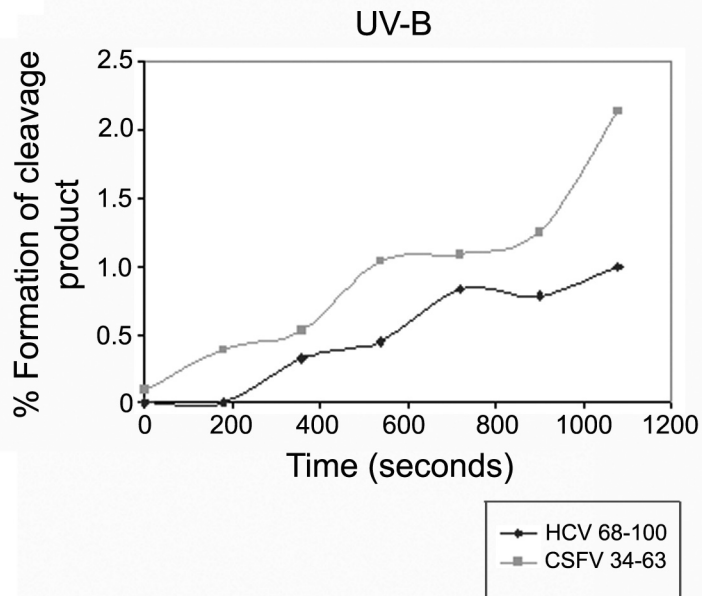


180

Supplementary Figure 8

a**b**

181

a**b**

A magnesium-induced RNA conformational switch at the internal ribosome entry site of hepatitis C virus genome visualized by atomic force microscopy

Ana García-Sacristán^{1,2}, Miguel Moreno^{1,†}, Ascensión Ariza-Mateos^{2,3,†},
Elena López-Camacho^{1,4}, Rosa M. Jáudenes¹, Luis Vázquez⁴, Jordi Gómez^{2,3}, José
Ángel Martín-Gago^{1,4} and Carlos Briones^{1,2,*}

¹Department of Molecular Evolution, Centro de Astrobiología (CSIC-INTA), Torrejón de Ardoz, Madrid 28850, Spain, ²Centro de Investigaciones Biomédicas en Red de Enfermedades Hepáticas y Digestivas, (CIBERehd), Spain, ³Laboratory of RNA Archaeology, Instituto de Parasitología y Biomedicina ‘López-Neyra’ (CSIC), Parque Tecnológico Ciencias de la Salud, Armilla, Granada 18016, Spain and ⁴Instituto de Ciencia de Materiales de Madrid (CSIC), Cantoblanco, Madrid 28049, Spain

Received August 27, 2013; Revised November 27, 2014; Accepted November 29, 2014

ABSTRACT

The 5' untranslated region of hepatitis C virus (HCV) genomic RNA contains an internal ribosome entry site (IRES) element, composed of domains II–IV, which is required for cap-independent translation initiation. Little information on the 3D structure of the whole functional HCV IRES is still available. Here, we use atomic force microscopy to visualize the HCV IRES conformation in its natural sequence context, which includes the upstream domain I and the essential, downstream domains V and VI. The 574 nt-long molecule analyzed underwent an unexpected, Mg²⁺-induced switch between two alternative conformations: from ‘open’, elongated morphologies at 0–2 mM Mg²⁺ concentration to a ‘closed’, comma-shaped conformation at 4–6 mM Mg²⁺. This sharp transition, confirmed by gel-shift analysis and partial RNase T1 cleavage, was hindered by the microRNA miR-122. The comma-shaped IRES-574 molecules visualized at 4–6 mM Mg²⁺ in the absence of miR-122 showed two arms. Our data support that the first arm would contain domain III, while the second one would be composed of domains (I–II)+(V–VI) thanks to a long-range RNA interaction between the I–II spacer and the basal region of domain VI. This reinforces the previously described structural continuity between the HCV IRES and its flanking domains I, V and VI.

INTRODUCTION

Hepatitis C virus (HCV) is the major etiological agent of chronic liver disease. There is no HCV vaccine and the traditional treatment based on a combination of alpha-interferon (IFN) and ribavirin (RBV) failed in about half of the patients. The need for new, alternative therapeutic approaches has encouraged the exploration of HCV life cycle as well as the development of direct-acting antiviral agents that have substantially increased sustained virologic response, what suggests that IFN-free regimens could lead to HCV eradication (1). With this aim, a thorough study of the native structure of the HCV genomic RNA is currently required, since certain structural/functional RNA elements, in particular those present at the 5' and 3' untranslated regions (UTR), are promising targets for antiviral therapy (2,3).

The 5' UTR of HCV is highly conserved among all the viral genotypes and contains an internal ribosome entry site (IRES) element that drives cap-independent initiation of translation of the viral polyprotein (4,5). The minimum sequence required for HCV IRES activity spans nucleotides (nts) 39–371 of the viral genome (6,7), and contains domains II to IV followed by the first 27 nts of the core coding sequence (4). Its secondary structure has been proposed using *in silico* RNA folding, covariation sequence analysis and biochemical methods (4,6,8–12) (Figure 1). The structures of individual HCV IRES domains or subdomains have been studied using techniques with atomic resolution (such as X-ray diffraction (XRD) and nuclear magnetic resonance (NMR)) (5,13–16), while electron microscopy (EM) has been used to visualize the structure of HCV IRES in its free form (17) and bound to the ribosome (18). A model of

*To whom correspondence should be addressed. Tel: +34 91 5206411; Fax: +34 91 5201074; Email: cbriones@cab.inta-csic.es

†Miguel Moreno and Ascensión Ariza-Mateos contributed equally to the paper as second authors.

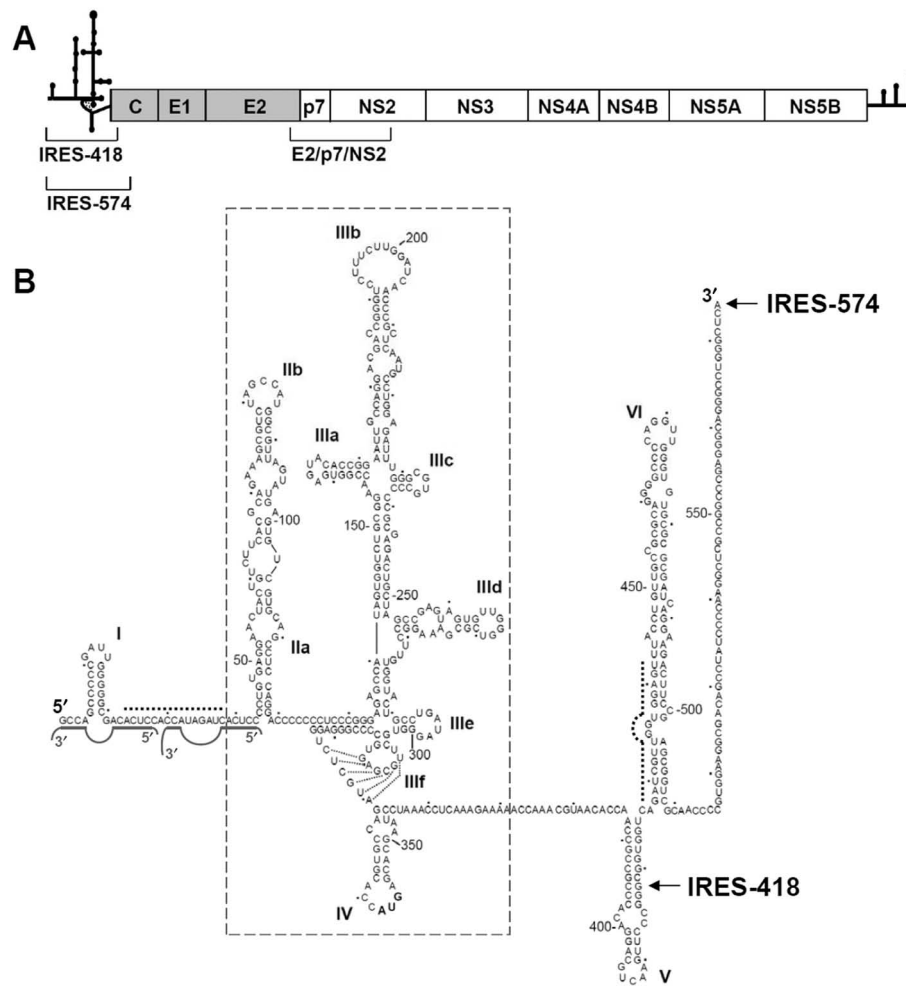


Figure 1. HCV IRES in its natural sequence context. (A) Schematic representation of the 9.6-Kb-long, ssRNA HCV genome. The secondary structures of the 5' UTR and 3' UTR are schematized. The structural (gray background) and non-structural (white background) proteins within the viral polyprotein are boxed. The regions corresponding to the IRES-418, IRES-574 and E2/p7/NS2 transcripts are shown. (B) Sequence and secondary structure of the 5' UTR of HCV, previously deduced by different bioinformatic, biochemical and biophysical methods. Nucleotides are numbered every 50 residues, and domains/subdomains are labeled from I to VI. HCV IRES domains II to IV are boxed. The last residues of the IRES-418 and IRES-574 molecules used in this work are marked with arrows. Dashed lines show the complementary sequences at the I-II spacer (nts 24–38) and the basal region of domain VI (nts 428–442), while the two miR-122-binding sites are marked with solid gray lines.

the HCV IRES structure in solution, based on small-angle X-ray scattering (SAXS) in combination with molecular dynamics simulations, has been also published (19).

HCV IRES is flanked upstream by a short stem-loop termed domain I, which is connected with domain II through a 23-nt-long ssRNA spacer region. Additionally, two downstream, structured domains termed V and VI (spanning nts 388–510 of the viral genome and located within the core coding sequence (20)), are essential for HCV viability (21) through a still unknown RNA structure-based mechanism. Phylogenetic (22), functional (23) and structural (24) studies have shown that a 15-nt-long sequence at the I-II spacer region can anneal with a complementary sequence at the basal region of domain VI (Figure 1), thus promoting a 'closed' conformation of the HCV IRES. This long-range RNA interaction is destabilized upon binding of the most abundant liver-specific microRNA, miR-122, which also interacts with the I-II spacer region by binding to two seed sites located 8 or 9 nts apart, depending on the viral

isolate (25,26), and promotes the switch to an 'open' IRES conformation (27). However, the transition from 'open' to 'closed' (or vice versa) HCV IRES conformations has not been described in the absence of any effector RNA or protein molecule.

At the functional level, miR-122 binding has been associated to several effects including the increase of HCV RNA stability (28,29), reduction of the 5' decay rates of the viral genome in infected cells (30) and stimulation of IRES-mediated translation (31). However, the distinct effects of miR-122 on translation observed *in vitro* and in cell culture (32,33) make it difficult to associate different HCV IRES conformations with miR-122 activities and to assess the role of miR-122 in the viral life cycle (34,35). This encourages the acquisition of additional structural and functional data on the interaction of miR-122 with HCV IRES in different experimental conditions.

RNA folding depends on the concentration of cations around the negatively charged phosphate backbone. Due

to its high charge density, Mg^{2+} ions stabilize RNA tertiary structure more efficiently than other divalent or monovalent cations (36), thus being essential for the functional folding of large RNAs (37,38). The Mg^{2+} concentration required for optimal HCV IRES activity in translation-competent extracts ranges from 1 to 2.5 mM (39). HCV IRES can promote translation initiation at 2.5 mM Mg^{2+} without requiring the complete set of initiation factors, and it is able to drive initiation factor-independent translation at 5 mM Mg^{2+} (40). Although the Mg^{2+} -dependent secondary structure of the minimal HCV IRES (domains II–IV) has already been investigated (10), new technological approaches are needed to visualize the effect of Mg^{2+} on the tertiary fold of the HCV IRES in its natural sequence context.

Atomic force microscopy (AFM) is a powerful nanotechnology-based tool for the structural analysis of a wide range of biological entities. It provides a 3D surface profile of the imaged sample without requiring any staining or coating, thus being less destructive and disruptive than EM. The nanometer resolution of this technique is optimal for the visualization of nucleic acid molecules (41–45), including RNA and RNA-protein complexes (46–49). AFM is increasingly being used in virology (50–53) and low-resolution images of the whole HCV genomic RNA have been published (54,55). However, AFM has not yet been applied to the structural characterization of either viral 5' UTR regions or viral/cellular IRES elements. Here, we analyze by AFM the Mg^{2+} -induced RNA folding of the HCV IRES in two constructions that contain either domains I–IV or I–VI. AFM results, in combination with gel-shift analysis and partial RNase T1 digestion, have allowed us to unveil a sharp magnesium-induced switch from an 'open' to a 'closed' conformation of the HCV IRES in its natural sequence context (domains I–VI), this transition being partially hindered by the presence of miR-122 in the medium.

MATERIALS AND METHODS

RNA synthesis

HCV RNA transcripts were obtained from the plasmid pN(1–4728) that contains the subgenomic region of HCV genotype 1b (GenBank accession number AF139594) spanning nts 1–4728, preceded by the T7 promoter (56). The IRES-418 construction (nts 1–418, IRES domains I–IV) and the E2/p7/NS2 fragment (nts 2478–3107) were obtained by polymerase chain reaction (PCR) amplification of pN(1–4728). The forward primer 1b/2a-5'-T71(+) (5'-TAATACGACTCACTATAGGACCCGCCC CGATTGGGGCGA-3', where the underlined sequence corresponds to the T7 RNA polymerase promoter), and the reverse primer 1b-C393(-) (5'-CCGGAATTCC CCGGGAAGTTCGACGTCCTGTGGGC-3') were used for the amplification of IRES-418, while 1b-NS2T7–2487(+) (5'-TAATACGACTCACTATAGGGAGTATGT CGTGTGCTT-3') and 1b-NS2–3087(-) (5'-AGCGCG TACGAAGTACGGCA-3') (11) allowed the PCR amplification of E2/p7/NS2. All high pressure liquid chromatography (HPLC) grade primers were purchased to IBA GmbH. In turn, the IRES-574 fragment (nts 1–574, IRES

domains I–VI) was obtained by digestion of pN(1–4728) with the restriction enzyme *BspI* (NEB). All the DNA fragments were purified by QIAquick Gel Extraction Kit (Qiagen) and eluted in water. These DNA templates (0.5–1 μ g) were *in vitro* transcribed using AmpliScribe T7 RNA polymerase (Epicentre) at 37°C for 4 h. After DNase I treatment, RNA was purified by precipitation with 2.5 M ammonium acetate and 2.5 volumes of absolute ethanol, and finally resuspended in diethylpyrocarbonate (DEPC)-treated water. The integrity of the RNA transcripts was checked in a denaturing 4% polyacrylamide gel, and the concentration of the transcribed RNA was determined by absorbance at 260 nm.

Control RNA molecule for AFM experiments

The dsRNA molecule used as a control for measuring the height of the A-RNA duplex adsorbed onto mica surfaces modified with (3-aminopropyl)triethoxysilane (APTES) was the 4579-bp-long genomic RNA of the totivirus L-A (57) (kindly provided by Dr. Rosa Esteban, Instituto de Microbiología Bioquímica, CSIC/USAL, Spain), with a theoretical length of 1236 nm.

RNA folding in different Mg^{2+} -containing buffers

RNA transcripts were resuspended at 2–3 nM concentration in folding buffer (100 mM NaCl and 100 mM HEPES pH 7.5) either magnesium-free or supplemented with 2, 4, 6 or 10 mM $MgCl_2$. The RNAs were heated at 90°C for 5 min, cooled on ice for 5 min and incubated at 37°C for 20 min. The use of other renaturation protocols did not affect the results. Control experiments were performed by incubating IRES-574 in 80% formamide at 90°C for 5 min, and cooling on ice for 5 min. A folding buffer in which sodium cations were replaced by ammonium ones (100 mM NH_4Cl , 100 mM HEPES pH 7.5 and 10 mM $MgCl_2$) was also used.

MicroRNA-122 annealing assay

The miR-122 RNA sequence (5'-UGGAGUGUGACAAUGGUGUUUGU-3') was synthesized and HPLC-purified by IBA GmbH. HCV IRES-574 was folded under different concentrations of Mg^{2+} as described above, incubated (at a concentration of 3 nM) with 15 nM miR-122 at 37°C for 20 min, and the mixture was successively transferred to ice.

RNA adsorption on mica surfaces

We used APTES-modified mica (58), a method that drives a tight enough immobilization of RNA via electrostatic interactions without damaging RNA molecules. This approach avoided the use of Mg^{2+} or other divalent cations as a bridge to immobilize the negatively charged RNA (59), since they would interfere with our envisaged study. Freshly cleaved muscovite mica Hi-Grade V2 (Monocomp Instrumentation) was treated with a 0.1% solution of APTES (SIGMA-Aldrich) for 15 min, washed with 2-propanol, rinsed with ultrapure, DEPC-treated milliQ water and dried at 37°C. Then, 30 μ l of the RNA sample at 2–3 nM concentration

was deposited onto the treated mica disc and incubated in a humidity chamber for 20 min at room temperature ($22 \pm 2^\circ\text{C}$). The RNA-containing mica discs were gently washed with ultrapure, DEPC-treated milliQ water and finally air-dried. A minimum of three independent samples of each HCV IRES preparation (IRES-418, IRES-574 and IRES-574/miR-122 complex) at each buffer composition was imaged.

AFM imaging

Samples were imaged in air, at room temperature, with two commercial AFM microscopes: PicoSPM (Agilent) and Nanoscope IIIa (Veeco). Their performance was equivalent in the analyzed samples, as assessed after measuring different control preparations of either IRES-574 molecules or IRES-574/miR-122 complexes in parallel using both microscopes (data not shown). Acoustic tapping mode AFM was performed using silicon cantilevers (Nanosensors and Bruker) with spring constants of 0.5–9.5 N/m and resonance frequency in the 50–80 KHz range. Two different kinds of tips, with nominal curvature radius of 2 and 10 nm, were used to obtain different levels of resolution during the image acquisition. The set-points used were kept relatively low, in the 0.3–0.6 V range, in order to use soft imaging conditions. The images (from 512×512 to 2048×2048 pixels) were recorded at a scan rate of 1 line per second and processed using WSxM v3.1 software (Nanotec) (60). The average length of the RNA molecules was measured using the same software. In the case of branched shapes, the length of every imaged arm of the molecule was measured, and the total length was computed. The number of analyzed IRES molecules in each buffer condition was at least 100 for IRES-574 samples, and at least 50 for IRES-574/miR-122 complexes. The angle between the arms of the selected IRES-574 molecules was measured with Image-J software (61).

Statistical analysis

The non-parametric Kolmogorov–Smirnov test was used to check the data sets for normality. A non-parametric Mann–Whitney test was applied to IRES-574 at different Mg^{2+} concentration. The independent samples *t*-test was also applied to the IRES-574, IRES-574/miR-122 and E2/p7/NS2 samples incubated under different ionic conditions.

RNA analysis by native gel electrophoresis

Purified RNA transcripts were internally radiolabeled with [α - ^{32}P]-GTP (specific radioactivity of 107 dpm/ μg) as described (62). After folding under different concentrations of Mg^{2+} , the IRES-574 molecule was left on ice for at least 10 min and resuspended at a final 3 nM concentration (3 nM IRES-574 and 15 nM IRES for IRES-574/miR-122 complexes) in loading buffer (previously described in (27)) containing 60% glycerol, $1 \times$ TMN, 0.4 $\mu\text{g}/\mu\text{l}$ yeast tRNA (Ambion), 0.4% (w/v) xylene cyanol and 0.4% (w/v) bromophenol blue. The samples were loaded into 0.8-mm thick, non-denaturing 6% polyacrylamide (acrylamide:bis-acrylamide ratio 1:19) gels containing 50 mM Tris-Ac pH

8.3 and 10 mM $\text{NH}_4(\text{OAc})$. The gels were run at 12 mA (constant intensity) for 24 h at 4°C , and autoradiographed. Product bands were scanned in a Phosphorimager (Storm 820, GE) and quantified with Image Quant 5.2 software (GE). The percentage of formation of each conformer *X* was calculated as follows: % conformer *X* = (signal conformer *X* / Σ signals of all conformers) \times 100. Mean values and standard deviations were calculated from three independent experiments.

RNase T1 and RNase III cleavage assays

Previous studies ((27) and data not shown) showed that the optimal conditions for RNase T1 (Calbiochem) partial digestion of the IRES-574 molecule were 0.001 $\mu\text{g}/\mu\text{l}$ of enzyme (concentrations assayed: 0.01, 0.001, 0.0001, 0.00001 $\mu\text{g}/\mu\text{l}$), in a 20-min reaction at 37°C . [^{32}P]pCp 3'-end labeled IRES-574 RNA (27) was resuspended in each of the following control conditions: in water and kept on ice for 2 h, to check the RNA integrity (sample 'I'); in standard folding buffer supplemented with 2 mM ethylenediaminetetraacetic acid (EDTA) (samples '0*' mM Mg^{2+}) and in folding buffer without Mg^{2+} (samples '0' mM Mg^{2+}), after preheating to 90°C and slowly cooling to room temperature. RNase T1-digested samples were previously resuspended in the corresponding folding buffer (in the presence of 0–10 mM Mg^{2+}), pre-heated to 90°C for 1 min and cooled to room temperature. Note that 300 cpm of labeled and digested RNA were loaded in each lane. Adequate band separation was achieved when bromophenol blue dye reached 80% of the length of a 7M urea-containing denaturing 4% polyacrylamide gel. IRES-574 molecules incubated with 0.0001 $\mu\text{g}/\mu\text{l}$ RNase T1 under denaturing conditions were used as an electrophoretic mobility control (sample 'D'). Reference bands were identified from previous studies (10,27). RNase T1 digestion bands that decrease their intensity with increasing Mg^{2+} concentration, consistently detected in different gels and exposure times, were identified.

Commercial *Escherichia coli* RNase III (Ambion), a nuclease specific for dsRNA, was used to cleave the internally labeled (24) HCV-574 molecule. Digestion was performed on renatured HCV RNA under 'secondary conditions of cleavage': RNA substrate was pre-heated at 90°C for 1 min, before the addition of reaction buffer [10 mM HEPES-KOH, pH 7.5, 100 mM $\text{NH}_4(\text{OAc})$ and 10 mM $\text{Mg}(\text{OAc})_2$] and cooled to room temperature. Cleavage reactions were performed at 37°C for 1 h in a volume of 10 μl , in the presence of 20 U RNasin, 0.0005 U/ μl (final concentration) of RNase III and 2 $\mu\text{g}/\mu\text{l}$ of yeast tRNA. Note that 300 cpm of digested RNA were loaded in the corresponding gel lane. Digestion products corresponding to fragments spanning nts 1–439 and 27–574 of the IRES-574 molecule, previously characterized by direct RNA fingerprinting analysis and other classical RNA sequencing techniques (24,27), were used as size markers.

RESULTS

AFM analysis of HCV IRES in denaturing conditions

A systematic AFM study of HCV IRES molecules adsorbed onto APTES-treated mica surfaces (58) (Supplementary Figure S1) was performed using an RNA transcript encompassing nts 1–574 (domains I–VI) of HCV genome, termed IRES-574 (Figure 1). The theoretical length of the unfolded IRES-574 molecule is 155 nm, assuming that each ribonucleotide unit is 0.27-nm long in an A-RNA helical conformation with a pitch of 3.0 nm and 11 nts per turn. The AFM analysis of the IRES-574 in 80% formamide (Supplementary Figure S2) evidenced that part of its secondary structure is highly stable under harsh denaturing conditions, since the imaged molecules showed 65–80% of the theoretical molecular length. This observation agrees with a previous report on the preservation of secondary structure elements of the hepatitis delta virus ribozyme in 95% formamide (63).

The measured height of the IRES-574 molecule in formamide varied between 1.3 and 2.2 nm (Supplementary Figure S2D). To experimentally check the height of a control linear dsRNA molecule adsorbed onto mica-APTES, we chose the whole genomic RNA of the totivirus L-A (Supplementary Figure S3A). The height of this molecule was 1.2–1.4 nm (Supplementary Figure S3B). Therefore, the height range of the imaged IRES-574 molecule in formamide might correspond to dsRNA regions lying on the surface, together with other elements of non-denatured secondary structure in different orientations.

AFM analysis of the Mg^{2+} -induced IRES-574 folding process

To analyze the influence of Mg^{2+} on IRES-574 folding, different preparations of the molecule in buffers containing 100 mM Na^+ supplemented with rising Mg^{2+} concentrations (0, 2, 4, 6 and 10 mM) were visualized by AFM. Tapping mode AFM images of more than 100 molecules under each ionic condition showed that the increase of Mg^{2+} concentration induced conformational changes in IRES-574, while molecular aggregation or dimerization was not observed. Supplementary Figure S4 shows a selection of 12 individual molecules imaged at each Mg^{2+} concentration, and Figure 2 summarizes the observed effect of Mg^{2+} on the conformational rearrangement of the molecule.

IRES-574 molecules incubated in a buffer lacking Mg^{2+} ions showed an elongated, zigzag shape with one to three bumps (Figure 2A and Supplementary Figure S4A), likely corresponding to regions that preserved their secondary structure in the absence of Mg^{2+} , in agreement with previous data on minimal HCV IRES (10) and also consistent with a recent analysis of the Mg^{2+} -dependent folding of picornavirus IRES (64). At 2 mM Mg^{2+} , the imaged shapes showed a large variability even within the same preparation: a majority of elongated morphologies similar to those found at 0 mM Mg^{2+} (Figure 2B) coexisted with some heterogeneous, more compact molecules with 2–4 arms protruding from a central axis (Supplementary Figure S4B) that could inform about certain Mg^{2+} -driven tertiary interactions (36,38). A neat increase in the homogeneity and compactness of the imaged molecules was found in

the presence of 4 mM Mg^{2+} (Figure 2C and Supplementary Figure S4C). This ionic condition promoted the unexpected formation of compact, comma-shaped molecules in which two arms could be distinguished: a bulky one and a flatter one. Both arms were 15–20 nm long, and the angle between them ranged between 110° and 150°, with a maximum in the interval 117°–127° (Supplementary Figure S5). Similar angles could also be measured in the fraction of non-elongated molecules imaged at 2 mM Mg^{2+} and even in some molecules at 0 mM Mg^{2+} (see examples in Supplementary Figure S4A and B). The trend toward a further RNA compaction was maintained in the presence of 6 mM Mg^{2+} (Figure 2D and Supplementary Figure S4D), with morphologies analogous to those found at 4 mM Mg^{2+} together with some more compact, elliptical-shaped molecules. Finally, in the presence of 10 mM Mg^{2+} only compact molecules with a highly uniform elliptical shape were observed (Figure 2E and Supplementary Figure S4E). Overall, this analysis evidenced that the main structural switch in the IRES-574 conformation occurred between 2 and 4 mM Mg^{2+} concentration.

To quantitatively study the Mg^{2+} -induced folding process, the average end-to-end distance of 100 IRES-574 molecules was measured for each Mg^{2+} concentration (Figure 3). At 0 mM Mg^{2+} , molecules with lengths in the range of 25–135 nm were imaged (Figure 3A), most of them being in the interval of 60–80 nm (Figure 3B). Their median length was 63 nm, about 40% of the theoretical length of the molecule. This confirmed that a significant number of RNA secondary structure elements are preserved in the presence of 100 mM Na^+ . IRES-574 molecules under 2 mM Mg^{2+} also showed a broad length distribution between 25 and 120 nm, the majority of them being in the intervals of 40–60 and 60–80 nm. Their median length was 61 nm. A clear shift in the length distribution was found at 4 mM Mg^{2+} : the molecules were imaged in a narrower interval of 14–93 nm, with a clear peak in the interval of 20–40 nm and a computed median length of 28 nm. Thus, a greater than 2-fold reduction in the median length was produced when Mg^{2+} concentration increased from 2 to 4 mM, in agreement with the qualitative data derived from Figure 2 and Supplementary Figure S4. In the presence of 6 mM Mg^{2+} , the length distribution of the IRES-574 molecules decreased to 12–70 nm while their median length was slightly higher (32 nm). Finally, the additional compaction of the imaged molecules at 10 mM Mg^{2+} was reflected in a very narrow length distribution of the molecules (14–50 nm), concentrated in the interval of 20–40 nm and showing a median length of 25 nm. Along this process, the only statistically significant reductions of the average lengths occurred in the transitions 2–4 and 6–10 mM Mg^{2+} (Figure 3A).

As a control experiment, we analyzed the eventual influence of Mg^{2+} concentration on the folding of a coding region of the HCV genome with a length similar to that of IRES-574: the E2/p7/NS2 junction, spanning nts 2487–3087 of the viral genome (Figure 1A). The results depicted in Supplementary Figure S6 showed that the HCV IRES element, whose biological function relies on its tridimensional structure, is much more dependent on the Mg^{2+} concentration than a coding region of the same length within

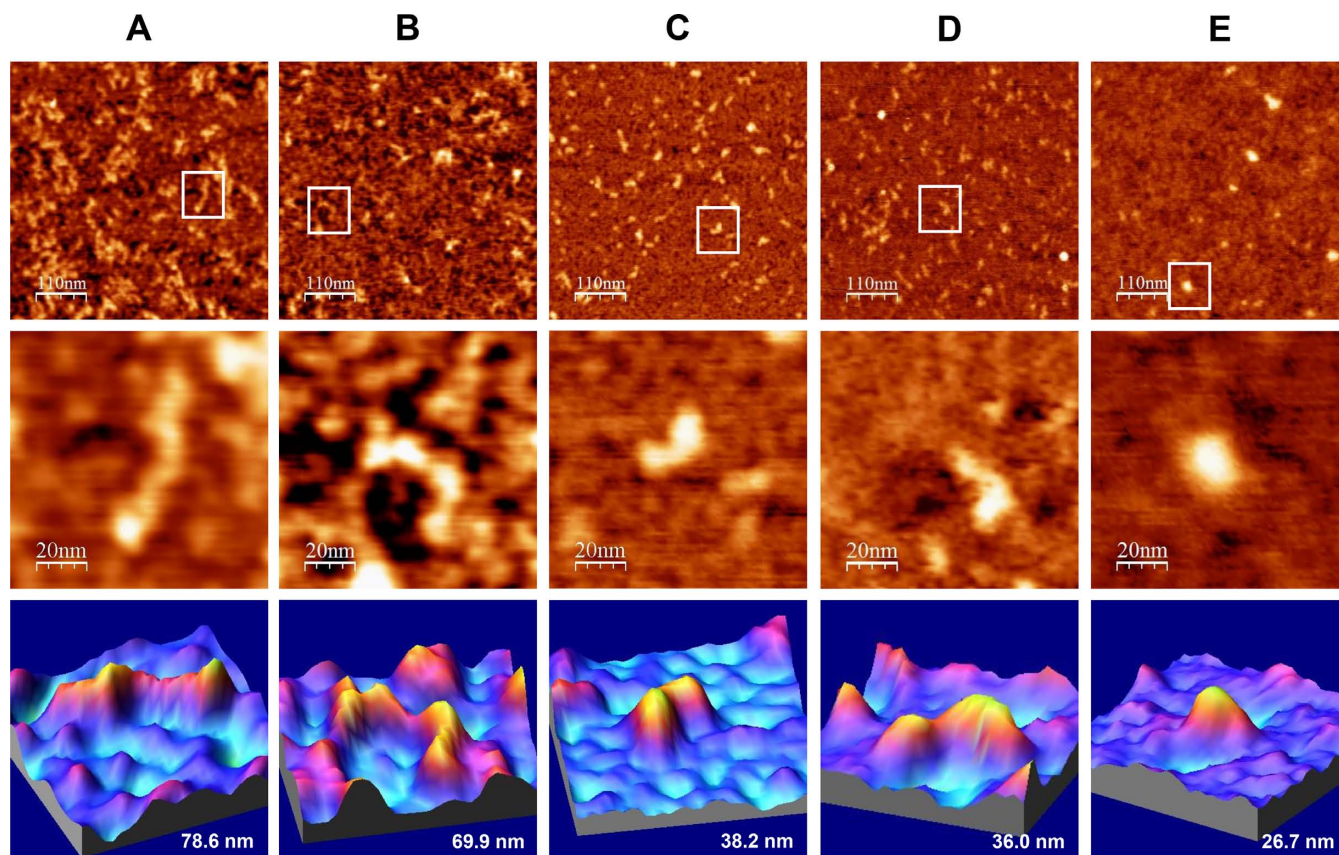


Figure 2. AFM images of IRES-574 molecules in a folding buffer supplemented with increasing Mg^{2+} concentration. IRES-574 RNA molecules were incubated in a buffer containing 100 mM Na^+ , either without Mg^{2+} (panel A) or supplemented with 2, 4, 6 and 10 mM Mg^{2+} (panels B, C, D and E, respectively). In all panels, top row contains large AFM images of molecules deposited onto a pre-treated mica-APTES surface (550×550 nm, scale bar of 110 nm), medium row shows a zoom area containing a selected molecule (100×100 nm image, scale bar of 20 nm), and the bottom row depicts a 3D representation of the selected molecule, showing its measured length. The nominal curvature radius of the AFM tips was 2 nm. Overall, this figure shows the Mg^{2+} -induced IRES-574 folding process and reveals a major conformational switch when Mg^{2+} concentration increases from 2 to 4 mM.

the same viral genome. We were also interested in analyzing whether two monovalent cations, Na^+ and NH_4^+ , might show a differential effect on the folding of IRES-574 molecule in the presence of 10 mM Mg^{2+} . The molecules incubated in a buffer containing 100 mM NH_4^+ (equivalent to that previously used in RNase III cleavage experiments that supported a ‘closed’ conformation of the HCV IRES including domains I–VI (24)) showed elliptical morphologies that were less compact than those folded in the presence of 100 mM Na^+ (Supplementary Figure S7). This observation agrees with previous results evidencing that the lower charge density of ammonium with respect to sodium makes the former cation less efficient than the latter one in promoting RNA folding (36,65).

AFM analysis of a 418-nt-long HCV IRES transcript in the presence of 4 mM Mg^{2+}

We also analyzed by AFM an RNA molecule spanning nts 1–418 of HCV genome (molecule termed IRES-418). It contained the IRES domains II–IV flanked upstream by domain I and, downstream, by the first 76 nts of the core coding region (Figure 1). Most of the imaged IRES-418 molecules in the presence of 4 mM Mg^{2+} showed elongated conformations together with branched shapes where three

arms of different lengths protruded from a central axis, some of which exhibited a characteristic ‘ λ -like’ shape (Figure 4).

Monitoring the Mg^{2+} -induced folding of IRES-574 by gel-shift

To deepen into the conformational rearrangements imaged by AFM in the IRES-574 molecules, two complementary techniques for RNA structural analysis were used: gel-shift and ssRNA-specific digestions. Native gel electrophoresis allowed the identification of only four major bands, corresponding to conformers termed C1 to C4 (Figure 5A). Among them, C1 and C2 were minority under all the buffer conditions assayed, while the fast-migrating conformers C3 and C4 were the most abundant. The band intensity was quantified in three independent experiments, and the ratio of each conformer was graphically represented (Figure 5B). In the absence of Mg^{2+} (both with and without added EDTA, see Materials and Methods) the most intense band was C3 (mean of 71.7% and 76.1% in lanes 2 and 3 of Figure 5A, respectively), followed by C4 (18.3% and 14.8%, respectively). Thus, the use of EDTA to remove the residual Mg^{2+} ions eventually trapped into the IRES-574 molecule showed a very limited effect in our experimental conditions. In turn,

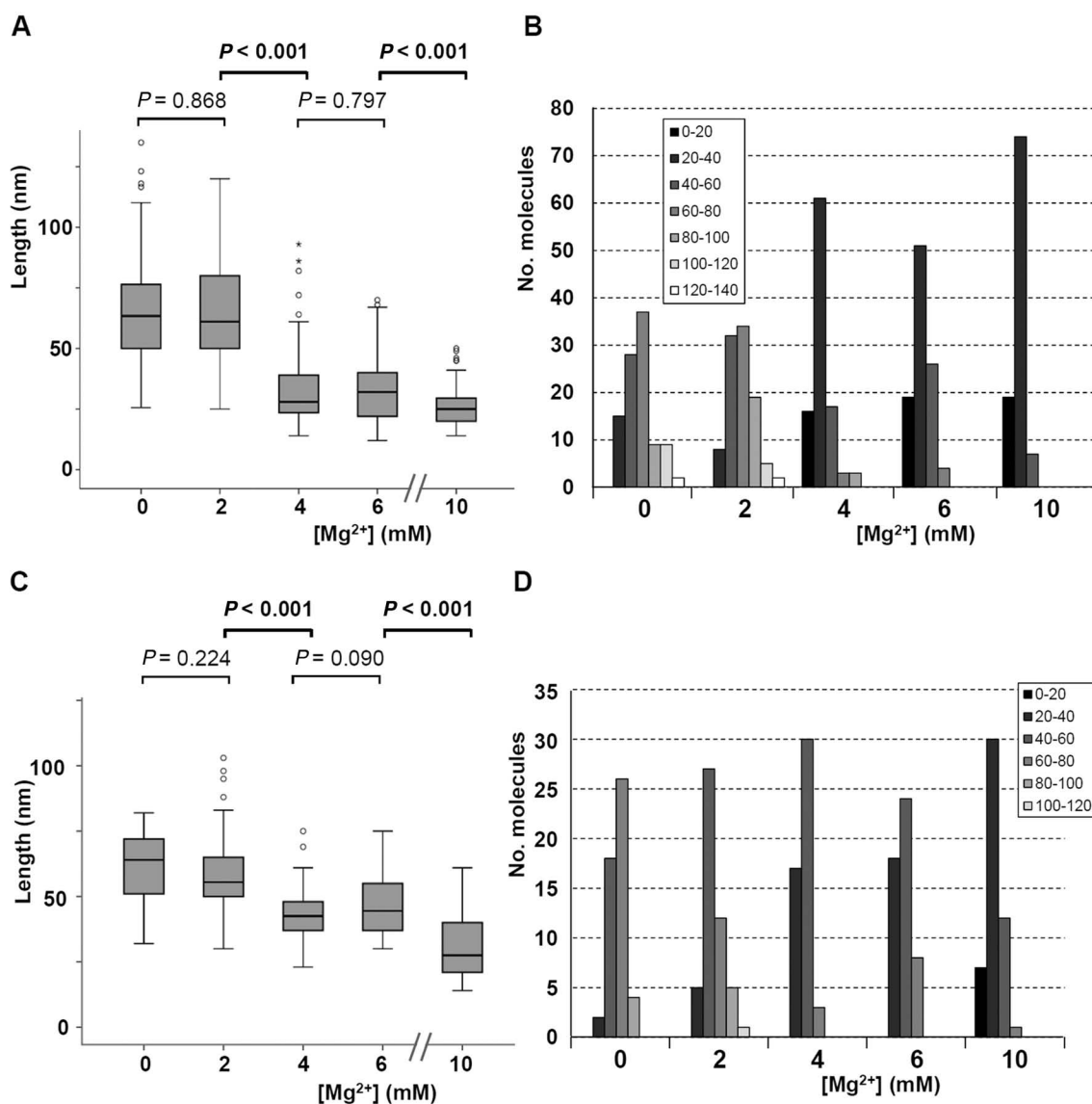


Figure 3. Length distribution of IRES-574 molecules at different Mg^{2+} concentrations. (A) Length distribution (computed over 100 molecules) of the IRES-574 molecule in folding buffer supplemented with 0, 2, 4, 6 and 10 mM Mg^{2+} concentration is depicted in a box plot. Boxes represent 25–75 percentile range, vertical lines span 10–90 percentile range and horizontal bar within the box represent the median. Outlier values are depicted as circles (mild outliers) and asterisks (extreme outliers). Statistical P -values corresponding to the average length of RNA molecules for 0 versus 2, 2 versus 4, 4 versus 6 and 6 versus 10 Mg^{2+} concentration are shown: statistically significant differences ($P < 0.001$) are marked in bold. (B) Distribution of molecular length versus Mg^{2+} concentration, computed for 100 IRES-574 molecules at each buffer composition. Box: intervals of molecular length (nm). (C) Length distribution (computed over 50 molecules) of the IRES-574/miR-122 complex at 0, 2, 4, 6 and 10 mM Mg^{2+} concentration depicted in a box plot, as detailed in panel A. (D) Distribution of molecular length versus Mg^{2+} concentration, computed for 50 IRES-574/miR-122 complexes in each condition. Box: intervals of molecular length (nm).

when the folding buffer contained 2 mM Mg^{2+} a reduction of the amount of C3 was observed concomitantly to the increase of C4, their relative intensities equalizing (45.7% and 46.3%, respectively). The increase of Mg^{2+} up to 4 mM completed the observed shift between C3 and C4 (rates of 25.3% and 66.3%, respectively). A further increase of Mg^{2+} up to 6 mM produced slight variations (21.5% of C3 and 69.4% of C4) while the dominance of the most compact conformer was again reinforced at 10 mM Mg^{2+} (19.9% of C3 and 71.0% of C4).

Analysis of the folding process of IRES-574 by partial RNase T1 cleavage

Partial RNase T1 cleavage assays were carried out on IRES-574 molecules under different Mg^{2+} concentrations. Nuclease T1 cuts after G nts in ssRNA regions, being a sensitive method to detect global rearrangements in RNA structure that introduce steric hindrance. Since the Mg^{2+} -dependent IRES structure has been previously analyzed for domains II and III in the context of a 332-nt-long molecule (10), we focused our study on the effect of Mg^{2+} on the 574-long transcript that also included domains I, IV, V and

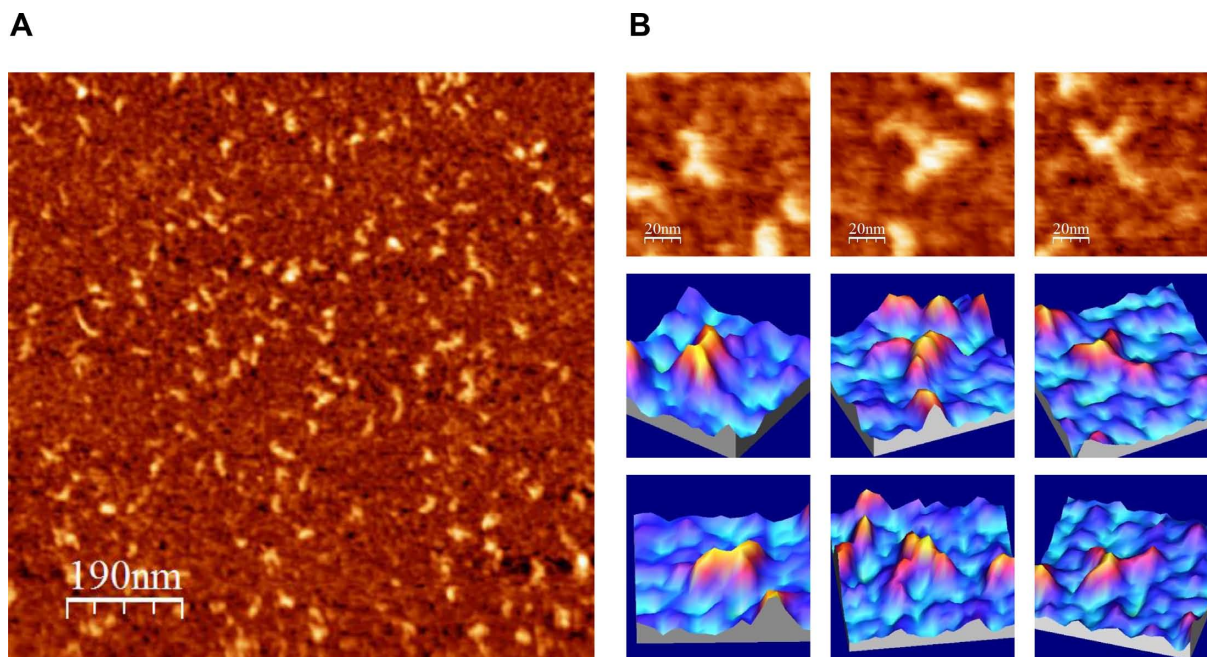


Figure 4. AFM images of IRES-418 molecules in a folding buffer containing 4 mM Mg^{2+} . (A) Large AFM image (1000 × 1000 nm) of molecules deposited onto a mica-APTES surface. (B) AFM images (100 × 100 nm) of three selected molecules (top row) and their corresponding 3D representations from two view angles (middle and bottom rows). The nominal curvature radius of the AFM tips was 2 nm.

VI. The partial digestion of IRES-574 molecules (Figure 6) showed a defined cleavage pattern in the absence of added divalent ions, which changed as a result of the presence of increasing Mg^{2+} concentrations. The samples without Mg^{2+} (lanes 4 and 5 of Figure 6A) showed that the cleavage yield of the EDTA-treated molecule (lane 4) was slightly lower than that of the sample without EDTA (lane 5). Thus, it is likely that the total absence of Mg^{2+} ions in the EDTA-containing buffer impaired the activity of the nuclease. Upon addition of Mg^{2+} , the overall reactivity of IRES-574 decreased (lanes 6–9), thus reflecting a progressive Mg^{2+} -induced compaction of the molecule, in agreement with previous results (10). However, several regions of the molecule, in particular, certain hairpin loops, remained accessible to the nuclease.

We chose the electrophoretic bands that could be used as a reference to identify the nts whose reactivity to RNase T1 cleavage was affected by the Mg^{2+} concentration. Among them, positions 82, 163, 200–201 and 266–268 corresponded to the highly accessible Gs located at the apical loops of subdomains IIb, IIIa, IIIb and IIIc, respectively (10), while reactive positions between nts 350 and 475 were detected in other previous work (27) (Figure 6A). Additional reference bands were identified as the eventually accessible Gs between positions 268 and 350: 283, 295, 299, 307, 309, 311, 328 and 331 (the latter G was previously shown to be a reactive nucleotide despite being paired in the secondary structure models (10)). This allowed us to identify the main Gs that changed their reactivity to RNase T1 as a result of the Mg^{2+} -driven compaction of the IRES-574 molecule. Additionally, a longer electrophoretic run allowed resolving the upper part of the gel showed at Figure

6A, corresponding to the 5'-end of the HCV IRES (Figure 6B).

The first observation was that the region encompassing nts 379–460 showed a very low reactivity to RNase T1 even in the absence of Mg^{2+} , which is indicative of the high stability of the RNA stems present at domains V and VI, as well as the protection of two Gs (at positions 435 and 436) whose accessibility might have been predicted from the secondary structure of the HCV IRES (Figure 1). This exemplifies that in the absence of added Mg^{2+} certain elements of secondary structure are stabilized by the monovalent cations present in the buffer, as imaged by AFM. On the contrary, certain nts in the analyzed region (including G350, G367, G460–G464 and G473–G475) remain highly reactive to RNase T1 digestion in folding buffers containing Mg^{2+} concentrations in the range 0–10 mM.

The conformational changes induced by Mg^{2+} (lanes 5–9 of Figure 6A, and lanes 6–10 of Figure 6B) were accompanied by a decrease in the intensity of at least nine RNase T1 bands. This effect was detected when Mg^{2+} concentration increased from 0 to 2 mM (bands G295–G299, G307–G309–G311, G328, G428, G469 and G470 in Figure 6A; G35 in Figure 6B) and from 2 to 4 mM (G331 and G379, Figure 6A). Among them, the most pronounced protections from RNase T1 cleavage was found in bands G295–G299, G307–G309–G311, G328, G469 and G470. In all the positions showing Mg^{2+} -dependent reactivity, the band intensities were similar at 4, 6 and 10 mM Mg^{2+} , what suggests that the main conformational rearrangement of the IRES-574 molecule is already completed at 4 mM Mg^{2+} , in agreement with our previous AFM and gel-shift results. The nts whose reactivity to RNase T1 is affected by Mg^{2+} are located at the spacer region between domains I and II (G35), the IIIef/IV

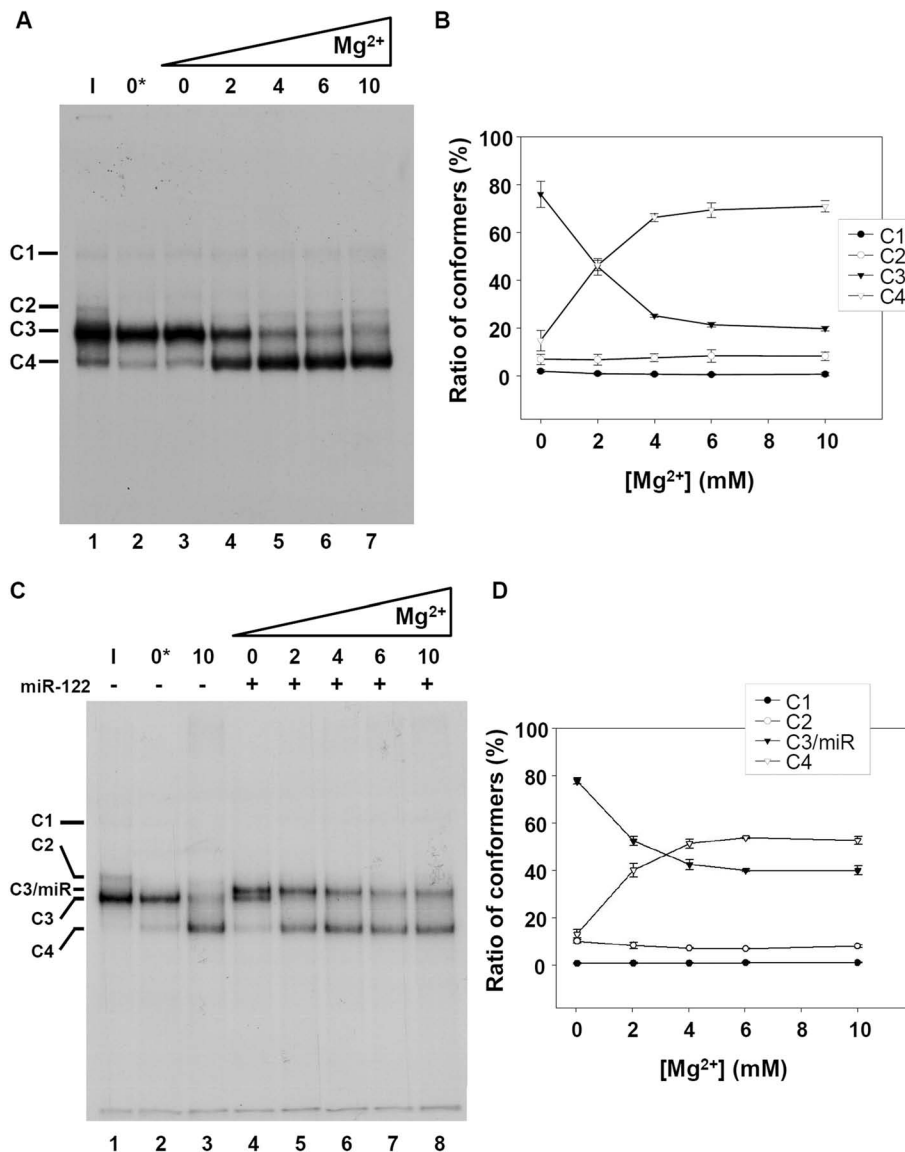


Figure 5. Native gel electrophoresis of the HCV IRES-574 at different Mg^{2+} concentrations. (A) Autoradiography of a non-denaturing 6% polyacrylamide gel. Internally labeled IRES-574 RNA was resuspended at 3 nM in each of the following conditions: in water and kept on ice for 10 min, as a control of intact RNA (sample 'I', lane 1); in standard folding buffer supplemented with 2 mM EDTA (sample '0*' mM Mg^{2+} , lane 2); in folding buffer alone (sample '0' mM Mg^{2+} , lane 3); in folding buffer containing Mg^{2+} at a final concentration of 2, 4, 6 and 10 mM (lanes 4–7). Resuspended RNA in lanes 2–7 was pre-heated to 90°C for 1 min and slowly cooled down to room temperature. Four conformers, labeled as C1 to C4, are detected at different ratios in all the lanes. (B) Quantification of the percentage of formation of each conformer at 0, 2, 4, 6 and 10 mM Mg^{2+} in three independent experiments analogous to that showed in panel A (lanes 3–7). Mean values and standard deviations are shown. (C) Same as panel A showing the effect of the interaction of miR-122 with IRES-574: ice-incubated control IRES-574 RNA (sample 'I', lane 1); IRES-574 alone in buffer supplemented with EDTA (sample '0*' mM Mg^{2+} , lane 2); IRES-574 in folding buffer containing Mg^{2+} at 10 mM concentration (lane 3); IRES-574 (at 3 nM concentration) incubated with miR-122 (at 15 nM concentration) in folding buffer either lacking Mg^{2+} (lane 4) or in the presence of increasing concentrations of Mg^{2+} from 2 to 10 mM (lanes 5–8). Five conformers (labeled as C1, C2, C3/miR, C3 and C4) were observed in total. (D) Quantification of the percentage of formation of conformers C1, C2, C3/miR and C4 at 0–10 mM Mg^{2+} in three independent experiments analogous to that showed in panel C (lanes 4–8). Mean values and standard deviations are shown.

pseudo-knot (G295-G299, G307-G309-G311 and G328), the basal region of domain IV (G331), the spacer between domains IV and V (G379), the basis of domain VI (G428) and the apical loop of this domain (G469 and G470), as depicted in Figure 6C.

Effect of miR-122 on the Mg^{2+} -induced conformational switch of IRES-574

The microRNA miR-122 interacts with two tandem binding sites in the I-II spacer region of the HCV IRES (25,26) (Figure 1) and induce switching of the IRES element in its natural sequence context (domains I–VI) between two alternative conformers: from a quick migrating form associated

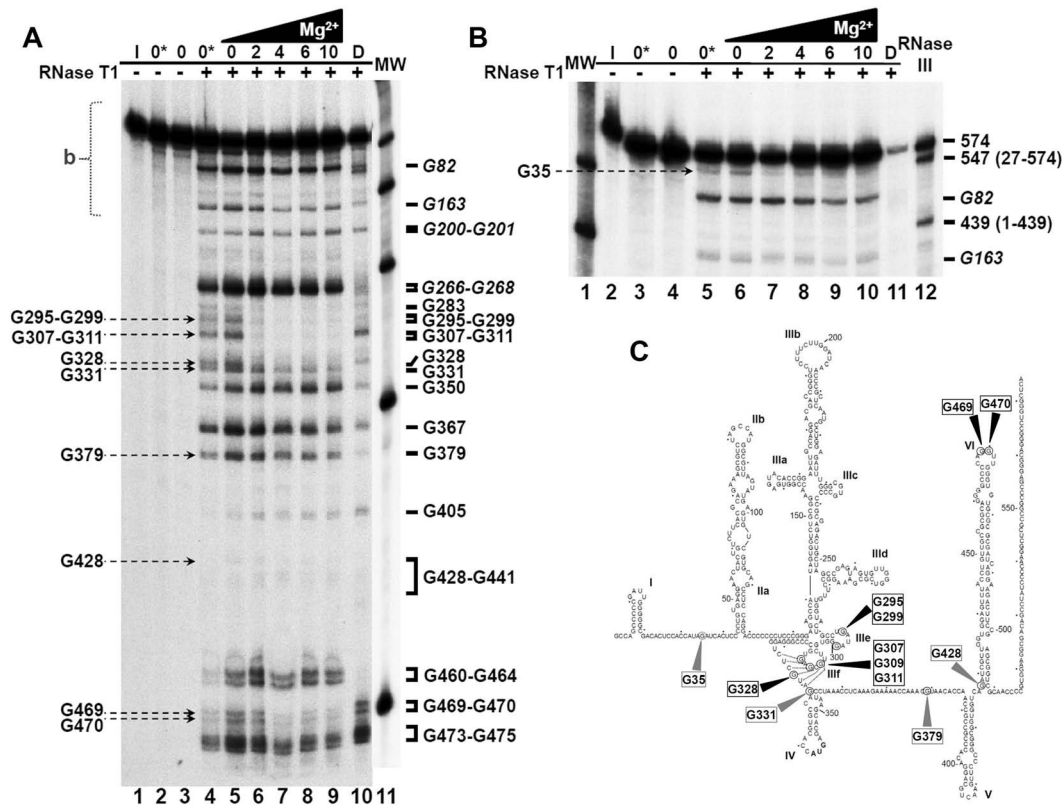


Figure 6. Mg^{2+} -induced protection from RNase T1 cleavage. (A) Partial RNase T1 cleavage of 3'-end labeled IRES-574 resolved in a denaturing gel. Undigested control samples (lanes 1–3) are described in the Materials and Methods section. Lanes 4–9 correspond to samples resuspended in folding buffer either without Mg^{2+} (lanes 4 and 5) or supplemented with 2, 4, 6 and 10 mM Mg^{2+} (lanes 6–9, respectively), renatured and digested by RNase T1. Electrophoretic mobility control: sample 'D' (see Materials and Methods), lane 10. Molecular weight (100–500 nt) markers ('MW') corresponding to a less exposed gel were added as lane 11. Reference bands are shown on the right of the gel. Bands that decrease their intensity with increasing Mg^{2+} are identified by arrows on the left. (B) A longer electrophoretic run used to resolve the upper region marked with 'b' in panel A. MW markers are shown in lane 11. Lanes 2–11 correspond to lanes 1–10 in panel A. Control RNase III digestion fragments spanning nts 1–439 and 27–574 of the IRES-574 molecule are shown in lane 12. Reference positions 82 and 163 (10) are also marked. The band corresponding to nt G35, which decreases its intensity with increasing Mg^{2+} concentration, is identified on the left. (C) Secondary structure of the HCV IRES-574 molecule, showing the positions of the RNase T1 cleavage sites corresponding to the bands identified in panels A and B. Nucleotides that either decrease their intensity or virtually disappear with increasing Mg^{2+} concentration are marked with grey and black arrowheads, respectively.

with a 'closed' conformation to a slow migrating one corresponding to an 'open' conformation) (27). Thus, the possibility that the conformational effect of Mg^{2+} on IRES-574 folding was inversely related to that of miR-122 deserved a detailed analysis by AFM and gel-shift. First, IRES-574 at 3 nM concentration was titrated using native gel electrophoresis with a range of miR-122 concentrations (from 0.5 to 150 nM) in the folding buffer containing 6 mM Mg^{2+} . As a 15 nM concentration of miR-122 was found to initiate the linear phase of the saturation curve from 'closed' to 'open' conformations (data not shown), such conditions (corresponding to an IRES-574:miR-122 ratio of 1:5) were used for subsequent AFM and gel-shift experiments.

The visualization by AFM of IRES-574/miR-122 complexes in buffers containing 100 mM Na^+ and 0–10 mM Mg^{2+} was performed as described above. As a control experiment, the miR-122 molecule alone (whose 23-nt-long sequence corresponds to a theoretical length of 6.2 nm) was imaged at 15 nM concentration under different ionic conditions, showing a uniform and elliptical shape of 10–14 nm in length (Supplementary Figure S8). Therefore, unbound

miR-122 and IRES-574 molecules were clearly distinguishable in the analyzed AFM images (see examples at Figure 7E and Supplementary Figure S9), while neither dimerization nor molecular aggregation were observed.

AFM images of IRES-574/miR-122 complexes in the folding buffer lacking Mg^{2+} ions showed a majority of elongated and angular shapes similar to those previously found in the absence of miR-122 (Figure 7A and Supplementary Figure S9A). Their median length (computed over 50 IRES-574 molecules) was 64 nm (Figure 3C), and most of the imaged molecules were in the length interval of 60–80 nm (Figure 3D). Elongated and zigzagging molecules were also imaged at 2 mM Mg^{2+} (Figure 7B and Supplementary Figure S9B), with a median length of 56 nm (Figure 3C) and the majority of them being 40–60 nm long (Figure 3D). In contrast to the observation in the absence of miR-122, the complex IRES-574/miR-122 at 4 mM Mg^{2+} did not show uniform, comma-shaped images, but a heterogeneous distribution of partially elongated and branched shapes together with a fraction of more compact ones (Figure 7C and Supplementary Figure S9C). The majority of their molecular

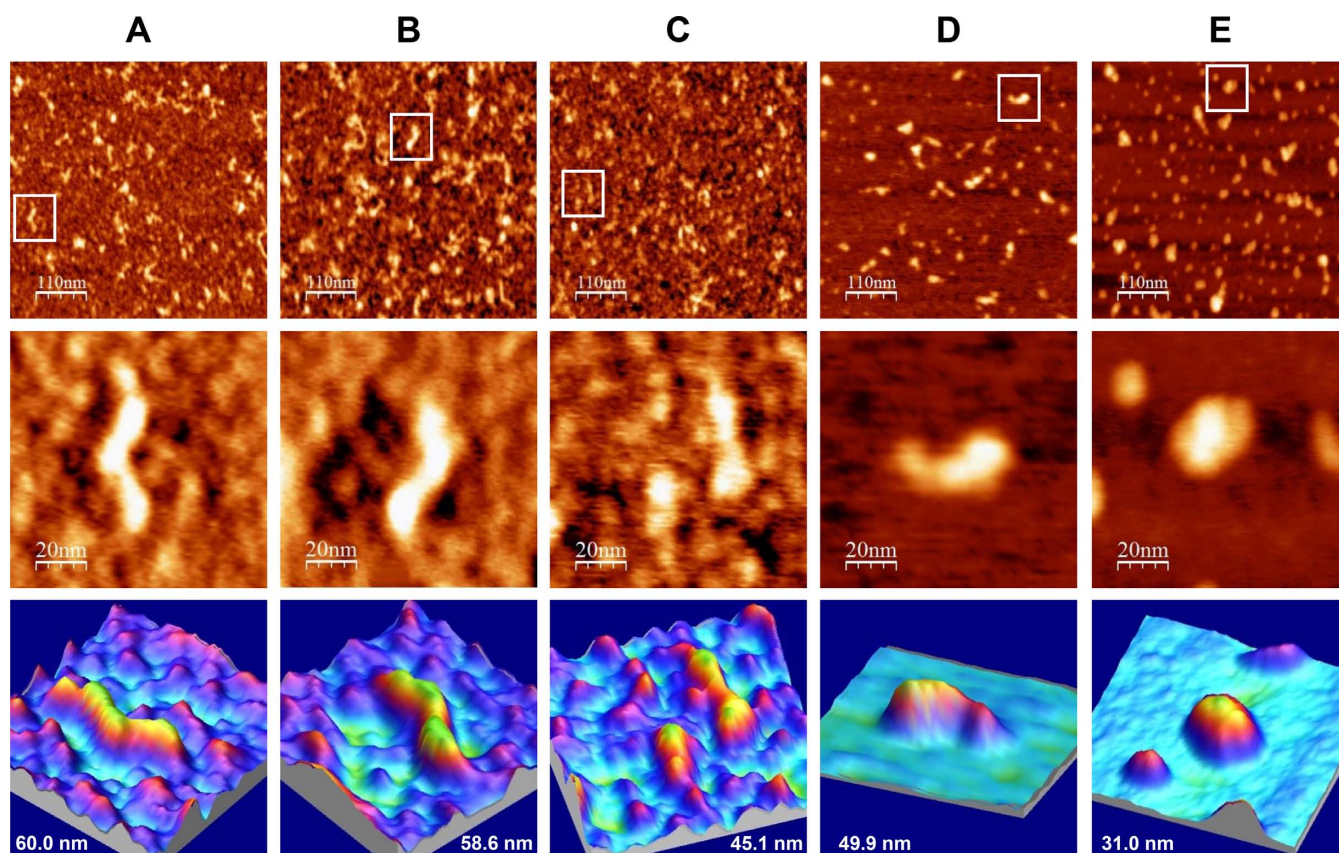


Figure 7. AFM images of IRES-574/miR-122 complexes in a folding buffer supplemented with increasing Mg^{2+} concentration. IRES-574 RNA molecules were folded in a buffer containing 100 mM Na^+ , either without Mg^{2+} (panel A) or supplemented with 2, 4, 6 and 10 mM Mg^{2+} (panels B, C, D and E, respectively) and incubated with miR-122 (see Materials and Methods). Large AFM images (550×550 nm, top row), zoom areas containing a selected molecule (100×100 nm images, middle row) and 3D representations of the selected molecule showing its measured length (bottom row) are shown. The middle and bottom row at panel C show an open and a closed IRES-574 conformer coexisting at 4 mM Mg^{2+} , the depicted length corresponding to the open one. Two miR-122 molecules are imaged at panel E (10 mM Mg^{2+}) together with a compact IRES-574 conformer. The nominal curvature radius of the AFM tips was 2 nm.

lengths belonged to the interval of 40–60 nm, with a computed median value of 43 nm (Figure 3C and D). Thus, the decrease in the median length associated to the transition from 2 to 4 mM Mg^{2+} was 13 nm (23% of the length at 2 mM), while the previously observed shortening in the absence of miR-122 (Figure 3A) was 33 nm (54% of the length at 2 mM). However, both decreases showed statistically significant differences at the level of the average molecular length. The coexistence of partially elongated and compact shapes was also imaged at 6 mM Mg^{2+} (Figure 7D and Supplementary Figure S9D): most of the molecular lengths were still found in the interval of 40–60 nm, with a median value of 45 nm (Figure 3C and D). Among the molecules observed in the presence of 2, 4 and 6 mM Mg^{2+} , examples with 3 to 4 arms, analogous to those found in the absence of miR-122 at 2 mM Mg^{2+} , were imaged, as well as additional morphologies including triangles, F- and C-shaped molecules (Supplementary Figure S9B–D). Finally, the maximum Mg^{2+} concentration assayed (10 mM) promoted a clear and statistically supported compaction of the imaged molecules to a median length of 28 nm (Figure 3C and D), with a majority of 20–40 nm long structures (Figure

3D) showing triangular, elliptical and round shapes (Figure 7E and Supplementary Figure S9E).

The effect on IRES-574 conformation of increasing Mg^{2+} concentration from 0 to 10 mM in the presence of miR-122 was also analyzed by gel-shift (Figure 5C and D) as described above, and the results were compared to those previously obtained in the absence of miR-122 (Figure 5A and B). In the absence of miR-122 and Mg^{2+} (lane 2 of Figure 5C, equivalent to lane 2 of Figure 5A) a single band, corresponding to the slow migrating form (conformer C3), was observed. The addition of miR-122 (lane 4 of Figure 5C), displaced more than one half of the total signal to a slightly slower migrating band, which corresponded to the IRES-574/miR-122 complex (conformer termed ‘C3/miR’), leaving a residual band with an electrophoretic mobility equivalent to that of the unbound IRES-574 molecule (C3). The presence of 2 mM Mg^{2+} in the folding buffer (lane 5 of Figure 5C) virtually eliminated the fraction of unbound IRES-574, thus showing that the divalent ion promoted the annealing of miR-122 (present in a 5:1 excess) with the available IRES-574 molecules. The relative band intensity of the conformer C3/miR (quantified in three independent experiments and graphically represented in Figure 5D)

showed a mean value of 52.1% of the total signal. Also, a fast migrating band (conformer C4) increased its mean ratio from 12.6% in the absence of Mg^{2+} to 39.7% at 2 mM Mg^{2+} . Thus, the Mg^{2+} -driven promotion of a 'closed' conformation of IRES-574 occurred in a smaller fraction of molecules with respect to the previous observation in the absence of miR-122 (see Figure 5B). The further addition of Mg^{2+} increased the mean ratio of C4 versus C3/miR conformers to 51.0%:42.1%, 53.4%:39.6% and 52.3%:39.5% at 4, 6 and 10 mM Mg^{2+} , respectively (Figure 5D). Therefore, two main differences were observed with respect to the situation found in the absence of miR-122 (compare Figure 5B and D): (i) when miR-122 was present in the medium, the Mg^{2+} concentration at which the two major conformers (C3/miR and C4) reached an equal representation was 3 mM, a value higher than that for the equilibrium between C3 and C4 in the absence of miR-122 (2 mM Mg^{2+}); (ii) miR-122 affected the equilibrium between 'open' and 'closed' conformations at 4–10 mM Mg^{2+} in such a way that the 'closed' conformer was still predominant over the 'open' one, though to a lesser extent than in the absence of the microRNA (roughly a 5:4 ratio versus a 7:2 ratio).

DISCUSSION

In this work, we used AFM for visualizing the Mg^{2+} -induced conformational rearrangement of a 574-nt-long RNA molecule that includes the HCV IRES element together with its flanking domains I, V and VI. The quantitative analysis of the molecular lengths measured at each Mg^{2+} concentration revealed a two-regime behavior in the IRES-574 folding. A sharp conformational switch was monitored from a heterogeneous distribution of elongated shapes at 0–2 mM Mg^{2+} to a uniform population of compact structures at 4–6–10 mM Mg^{2+} . It is reasonable to assume that the alternative conformations imaged at 2 mM Mg^{2+} reflect the relative movements of rigid parts (defined by stable secondary structures) instead of the presence of disordered regions, in agreement with previous analysis of the IRES domains II–IV at 2.5 mM Mg^{2+} (19). Thus, a fraction of the imaged shapes at 2 mM Mg^{2+} could allow the identification of some of the folded, individual IRES domains, while the morphologies imaged at 4 and 6 mM Mg^{2+} would eventually reveal long-range RNA interactions among the preformed domains. In our system, 2 mM Mg^{2+} could represent the divalent cation concentration at which some compact or 'collapsed' RNA intermediate conformations appear before the proper tertiary structure is acquired, by analogy to certain group I introns where the transition from collapsed RNA conformations to their functional tertiary structures occurs at 2–3 mM Mg^{2+} (66).

Gel-shift analysis confirmed the existence of a switch between two major, alternative conformations of the IRES-574 molecule. The stepwise increase of Mg^{2+} concentration from 0 to 4 mM completely shifted the ratio between such RNA conformers toward the most compact one, both of them being equally represented at 2 mM Mg^{2+} . A previous study showed that the HCV IRES containing domains II–IV folded into a unique, extended structure with certain degree of flexibility at 2.5 mM Mg^{2+} (10). This fact suggests that the presence of two major conformers in the molecule

IRES-574 at 2 mM Mg^{2+} is likely due to the conformational flexibility allowed by the flanking domains I, V and VI.

The AFM analysis of the shorter transcript IRES-418 (containing domains I–IV) showed that this molecule can adopt three-arms morphologies at 4 mM Mg^{2+} , including λ -shaped conformations. These molecular shapes are consistent with those derived from a previous TEM analysis (17) of the HCV IRES (nts 1–380) at 5 mM Mg^{2+} , and from a SAXS-based model (19) of a shorter version of the HCV IRES (nts 39–371) at 2.5 mM Mg^{2+} . Both approaches showed molecules with three main arms protruding from a central axis, what has been interpreted as a structure based on a flexible pseudo-knot that constitutes a hinge between IRES domains II, III and IV (14). The comparison of our AFM images with such previous data allowed us to hypothesize that the IRES domains II–IV might be assigned as depicted in Figure 8A. Hence, the bended arm corresponding to the upper part of the λ -like imaged shapes (showing a characteristic angular morphology previously revealed by NMR (13), also identified in a SAXS-based model of the HCV IRES (19) and in the cryo-EM map of the HCV IRES bound to the 40S ribosomal subunit (18)) would correspond to domain II. In turn, the bulky and straight arm would contain the apical part of domain III (subdomains IIIabc (16)). The comparison of our data with the SAXS-based model (19) also suggests that the third, shorter arm imaged by AFM could be assigned to either subdomain IIIcd or domain IV plus the core-coding sequence fragment. The putative domain I cannot be identified by AFM in any of the molecules, however, it is assumed to be placed next to the basal region of domain II.

Although it is evident that further experiments will be needed to unambiguously identify individual IRES domains in the molecules imaged by AFM, the three-arms conformation of the IRES-418 at 4 mM Mg^{2+} helped us interpret a fraction of the AFM images of the IRES-574 molecule at 2 mM Mg^{2+} , in which three or four arms have been imaged (two representative examples are shown in Figure 8B and C). According to our model, domains II and III could be distinguished, while the downstream domains V–VI might either be placed in the central region of the molecule close to the pseudo-knot (Figure 8B) or (thanks to the flexibility provided by the ssRNA spacer between domains IV and V) partially protrude from such central region as one or two extra arms (Figure 8C). In turn, the compact two-arms, comma-shaped morphology showed by most of the IRES-574 molecules at 4 and 6 mM Mg^{2+} (Figure 8D) would suggest the presence of a long-range interaction of the downstream domains V–VI with either domains I–II or domain III. The comparison of the images in Figure 8 and Supplementary Figure S4 with previously published data (17,19) would favor the former possibility. Therefore, we hypothesize that, in the IRES-574 molecule, the downstream domains V (likely excluding its apical region, which is also present in the IRES-418 molecule, see Figure 1) and/or VI could interact with the arm composed of domains I–II provided that Mg^{2+} concentration is at least 2 mM, this interaction being favored at 4 mM Mg^{2+} .

In order to test this hypothesis, a complementary analysis of the IRES-574 molecule was performed by RNase

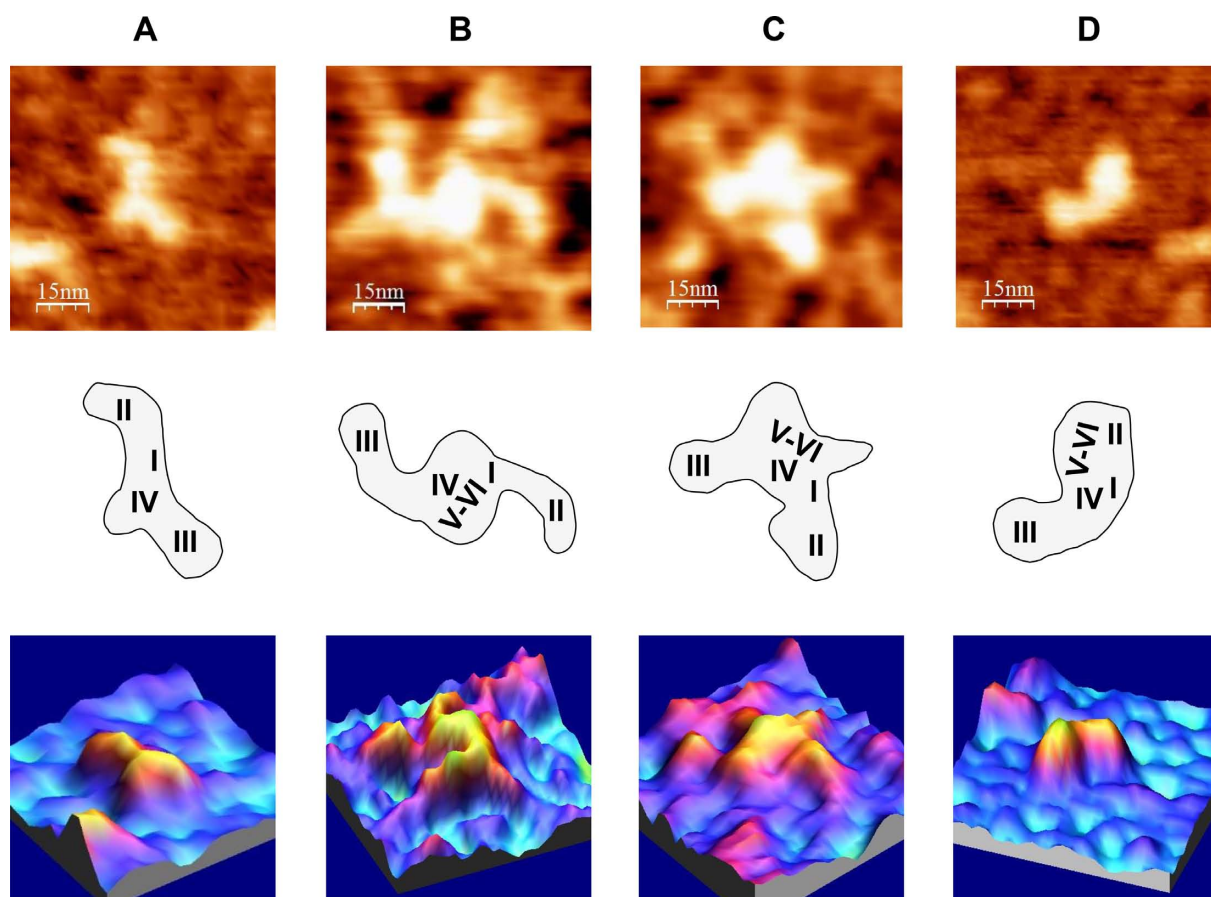


Figure 8. AFM images of HCV IRES-containing RNA molecules under different ionic conditions, in the absence of miR-122. (A) IRES-418 molecule at 4 mM Mg^{2+} . (B) and (C) Two examples of IRES-574 molecules at 2 mM Mg^{2+} . (D) IRES-574 molecule at 4 mM Mg^{2+} . AFM images (75×75 nm) of the selected molecule (top row), schematic representations of the molecule showing the suggested assignment of IRES domains (middle row) and 3D representations of the selected molecules (bottom row) are shown. The nominal curvature radius of the AFM tips was 2 nm.

T1 probing. Our results showed that the main transition in the observed conformational rearrangements was produced between 0 and 4 mM Mg^{2+} concentration: the intensity of at least nine RNase T1 bands (corresponding to 12 reactive Gs) decreased, and such a protection was already evident at 2 mM Mg^{2+} in seven bands (10 Gs). The protected positions at 2 mM Mg^{2+} included six Gs directly involved in the formation of the IIIef/IV pseudo-knot (14). The requirement of at least 0.25 mM Mg^{2+} for the establishment of this key tertiary interaction has been shown in the HCV IRES containing domains II–IV (10). Therefore, it seems evident that the formation of the central pseudo-knot is not affected by the presence of the flanking domains I, V and VI. Among the remaining six protected Gs, two of them (G35 and G428) are placed at the I-II spacer region and at the basis of domain VI, respectively. Notably, they lie at both strands of a previously proposed long-range annealing motif (involving sequences at nts 24–38 and 428–442, Figure 1) that could promote a ‘closed’ conformation of HCV IRES in its natural sequence context (22–24). This fact suggested that such a long-range RNA interaction could be involved in the Mg^{2+} -induced conformational switch reported in IRES-574.

The conformational rearrangement of the IRES-574 molecule produced between 0 and 4 mM Mg^{2+} (both conformers being in equilibrium at 2 mM Mg^{2+}) could rely, first, on the formation of the IIIef/IV pseudo-knot, which affects the central region of the IRES element including the basis of domain IV. Concomitantly, this tertiary interaction would allow the long-range RNA interaction involving domains I-II and domains V-VI. In the model we are envisaging, such interactions could be responsible for the main conformers visualized by AFM and quantified by gel-shift analysis: (i) elongated molecules at 0 mM Mg^{2+} , where only intra-domain, stable secondary structure elements are present; (ii) molecules with heterogeneous and angular shapes at 2 mM Mg^{2+} , including topologies with three arms, likely corresponding to domains I-II, III and V-VI, which protrude from a central region defined by the IIIef/IV pseudo-knot; (iii) homogeneous, comma-shaped molecules at 4–6 mM Mg^{2+} showing two arms, the first of them being likely composed of the interacting domains (I-II) + (V-VI) and the second one containing domain III alone.

The angle formed between the two IRES-574 arms at 4 mM Mg^{2+} showed a maximum in the interval of 117° – 127° . Previous studies indicated that the dominant motion

in HCV IRES is the in-plane movement of domains II and III toward and away from each other (19). Thus, it is reasonable to assume that, while in the IRES molecule than contains domains II–IV imaged by EM (17) the maximum angle between domains II and III lies in the interval 100° – 110° , the presence in IRES-574 of a bulky arm composed of the interacting domains (I-II) + (V-VI) displaces the maximum in the distribution of the angles formed with domain III toward higher values.

The AFM and gel-shift analyses performed in the presence of miR-122 supported the involvement of the miR-122-binding site at the I-II spacer region in the reported molecular switch. AFM images showed that, under Mg^{2+} concentrations of 0 and 10 mM Mg^{2+} , the distribution of molecular lengths and shapes was similar in IRES-574 molecules and in IRES-574/miR-122 complexes. However, the sharp conformational switch imaged in IRES-574 molecules when Mg^{2+} concentration increased from 2 to 4 mM was not evident in the presence of miR-122, since the IRES-574/miR-122 complex folded in heterogeneous shapes of different lengths in the interval of 2–6 mM Mg^{2+} concentration. The results of gel-shift analyses were in agreement with the equilibrium between ‘open’ and ‘closed’ conformations of the IRES-574/miR-122 complex in buffers containing Mg^{2+} concentrations higher than 2 mM.

Previously, a transition from ‘closed’ to ‘open’ IRES-574 conformation was demonstrated in the presence of miR-122 (27). Here, we show that this transition can also be promoted by Mg^{2+} , though in the opposite direction: while miR-122 favours the ‘open’ form, the increasing Mg^{2+} displaces the equilibrium toward the ‘closed’ conformer. Remarkably, both effectors have been described to affect HCV IRES-dependent initiation of translation *in vitro*: the presence of miR-122 stimulates the process (31), while the increase of Mg^{2+} concentration up to 5 mM allows IRES-dependent translation initiation in the absence of initiation factors (40). Therefore, in the frame of the many regulated functions in which the interactions between miR-122 and HCV IRES may participate (32–35), the data reported here point toward the existence of a bidirectional conformational switch stimulated (in opposite directions) by two effectors of very different nature.

Gel-shift analysis showed that ‘open’ and ‘closed’ conformations of IRES-574 are in equilibrium at 2 mM Mg^{2+} in the absence of miR-122, and at 3 mM Mg^{2+} when the microRNA is present in the medium. These values are higher than the closely regulated 0.5–1 mM concentration (0.59 mM in rat hepatocytes) of free Mg^{2+} in the eukaryotic cytoplasm (67–69), where positively charged RNA-binding proteins and other effectors also modulate the functional structure of HCV IRES. However, such a 2–3 mM Mg^{2+} concentrations correspond to the 2.5 mM value at which HCV IRES can promote the initiation of translation in the absence of the complete set of initiation factors (40) and define the upper limit of the Mg^{2+} concentration that allows IRES activity in translation-competent extracts (2.5 mM (39)). Therefore, the Mg^{2+} -induced ‘open’/‘closed’ switch reported here could be of relevance for IRES-dependent translation initiation *in vitro* under different experimental settings. Our results also support that the complementary sequences present at the I-II spacer and at the basal region

of domain VI are prone to establish a long-range RNA interaction provided that the ionic or biochemical environment of the folded HCV 5′ UTR allows a compatible tertiary structure. The structural data reported here provide further insights on the conformational plasticity of HCV IRES in its genomic context (22–24) and, as a result, encourage the development of novel HCV inhibitors based on small molecules targeting either the IRES regions essential for translation initiation (2,3) or the liver-specific microRNAs that act as enhancers of viral replication (70).

In summary, here we report for the first time the use of AFM to analyze the 3D structure of an IRES element. We have shown that, in its natural sequence context, HCV IRES can undergo a Mg^{2+} -induced molecular switch between two alternative conformations, such a structural rearrangement being hindered by the presence of miR-122 in the medium. Our data are compatible with those previously reported for HCV IRES domains II–IV based on chemical and enzymatic probing, EM and SAXS-derived models. Additionally, our results shed light on the 3D conformation of HCV IRES in its natural sequence context, thus reinforcing the previously suggested structural continuity between the domain I, the minimal HCV IRES element and (despite the apparent functional discontinuity between coding and non-coding sequences) the essential domains V and VI within the core coding region.

SUPPLEMENTARY DATA

Supplementary Data are available at NAR Online.

ACKNOWLEDGEMENT

The authors thank Dr. Victor M. González and Dr. Francisco J. López de Saro for preliminary analysis of the RNA conformation of IRES-574 molecules, and María Fernández-Algar for excellent technical assistance.

FUNDING

Spanish *Ministerio de Ciencia e Innovación* and *Ministerio de Economía y Competitividad* [BIO2010–20696 and BIO2013–47228-R to C.B.; MAT2011–26534 to J.A.M.-G.; BFU2010–11612-E to J.G.; FIS2012–38866-C05–05 to L.V.]; Spanish National Research Council [CSIC-200920I040 to C.B.]; *Comunidad de Madrid* [NANOAVANSENS S2013/MIT-3029 to L.V.]; FEDER funds from the European Union. CIBERehd is funded by the *Instituto de Salud Carlos III*. JAE-Doc postdoctoral fellowship from the CSIC Program *Junta de Ampliación de Estudios*, co-funded by the European Science Foundation [to M.M.]. Funding for open access charge: Spanish National Research Council (CSIC).

Conflict of interest statement. None declared.

REFERENCES

- Pawlotsky, J.-M. (2013) Treatment of chronic hepatitis C: current and future. *Curr. Topics Microbiol. Immunol.*, **369**, 321–342.
- Davis, D.R. and Seth, P.P. (2011) Therapeutic targeting of HCV internal ribosomal entry site RNA. *Antiviral Chem. Chemother.*, **21**, 117–128.

3. Romero-Lopez, C. and Berzal-Herranz, A. (2013) Unmasking the information encoded as structural motifs of viral RNA genomes: a potential antiviral target. *Rev. Med. Virol.*, **23**, 340–354.
4. Honda, M., Ping, L.H., Rijnbrand, R.C.A., Amphlett, E., Clarke, B., Rowlands, D. and Lemon, S.M. (1996) Structural requirements for initiation of translation by internal ribosome entry within genome-length hepatitis C virus RNA. *Virology*, **222**, 31–42.
5. Fraser, C.S. and Doudna, J.A. (2007) Structural and mechanistic insights into hepatitis C viral translation initiation. *Nat. Rev. Micro.*, **5**, 29–38.
6. Wang, C., Sarnow, P. and Siddiqui, A. (1993) Translation of human hepatitis C virus RNA in cultured cells is mediated by an internal ribosome-binding mechanism. *J. Virol.*, **67**, 3338–3344.
7. Honda, M., Beard, M.R., Ping, L.H. and Lemon, S.M. (1999) A phylogenetically conserved stem-loop structure at the 5' border of the internal ribosome entry site of hepatitis C virus is required for cap-independent viral translation. *J. Virol.*, **73**, 1165–1174.
8. Pang, P.S., Elazar, M., Pham, E.A. and Glenn, J.S. (2011) Simplified RNA secondary structure mapping by automation of SHAPE data analysis. *Nucleic Acids Res.*, **39**, e151.
9. Brown, E.A., Zhang, H.C., Ping, L.H. and Lemon, S.M. (1992) Secondary structure of the 5' nontranslated regions of hepatitis-c virus and pestivirus genomic RNAs. *Nucleic Acids Res.*, **20**, 5041–5045.
10. Kieft, J.S., Zhou, K., Jubin, R., Murray, M.G., Lau, J.Y.N. and Doudna, J.A. (1999) The hepatitis C virus internal ribosome entry site adopts an ion-dependent tertiary fold. *J. Mol. Biol.*, **292**, 513–529.
11. Martell, M., Briones, C., de Vicente, A., Piron, M., Esteban, J.I., Esteban, R., Guardia, J. and Gomez, J. (2004) Structural analysis of hepatitis C RNA genome using DNA microarrays. *Nucleic Acids Res.*, **32**, e90.
12. Romero-Lopez, C., Barroso-delJesus, A., Garcia-Sacristan, A., Briones, C. and Berzal-Herranz, A. (2012) The folding of the hepatitis C virus internal ribosome entry site depends on the 3'-end of the viral genome. *Nucleic Acids Res.*, **40**, 11697–11713.
13. Lukavsky, P.J., Kim, I., Otto, G.A. and Puglisi, J.D. (2003) Structure of HCV IRES domain II determined by NMR. *Nat. Struct. Mol. Biol.*, **10**, 1033–1038.
14. Berry, K.E., Waghay, S., Mortimer, S.A., Bai, Y. and Doudna, J.A. (2011) Crystal structure of the HCV IRES central domain reveals strategy for start-codon positioning. *Structure*, **19**, 1456–1466.
15. Kieft, J.S., Zhou, K.H., Grech, A., Jubin, R. and Doudna, J.A. (2002) Crystal structure of an RNA tertiary domain essential to HCV IRES-mediated translation initiation. *Nat. Struct. Biol.*, **9**, 370–374.
16. Collier, A.J., Gallego, J., Klinck, R., Cole, P.T., Harris, S.J., Harrison, G.P., Aboul-ela, F., Varani, G. and Walker, S. (2002) A conserved RNA structure within the HCV IRES eIF3-binding site. *Nat. Struct. Mol. Biol.*, **9**, 375–380.
17. Beales, L.P., Rowlands, D.J. and Holzenburg, A. (2001) The internal ribosome entry site (IRES) of hepatitis C virus visualized by electron microscopy. *RNA*, **7**, 661–670.
18. Spahn, C.M.T., Kieft, J.S., Grassucci, R.A., Penczek, P.A., Zhou, K.H., Doudna, J.A. and Frank, J. (2001) Hepatitis C virus IRES RNA-induced changes in the conformation of the 40S ribosomal subunit. *Science*, **291**, 1959–1962.
19. Perard, J., Leyrat, C., Baudin, F., Drouet, E. and Jamin, M. (2013) Structure of the full-length HCV IRES in solution. *Nat. Commun.*, **4**, 1612.
20. Tuplin, A., Evans, D.J. and Simmonds, P. (2004) Detailed mapping of RNA secondary structures in core and NS5B-encoding region sequences of hepatitis C virus by RNase cleavage and novel bioinformatic prediction methods. *J. Gen. Virol.*, **85**, 3037–3047.
21. McMullan, L.K., Grakoui, A., Evans, M.J., Mihalik, K., Puig, M., Branch, A.D., Feinstone, S.M. and Rice, C.M. (2007) Evidence for a functional RNA element in the hepatitis C virus core gene. *Proc. Natl. Acad. Sci. U.S.A.*, **104**, 2879–2884.
22. Honda, M., Rijnbrand, R., Abell, G., Kim, D.S. and Lemon, S.M. (1999) Natural variation in translational activities of the 5' nontranslated RNAs of hepatitis C virus genotypes 1a and 1b: Evidence for a long-range RNA-RNA interaction outside of the internal ribosomal entry site. *J. Virol.*, **73**, 4941–4951.
23. Kim, Y.K., Lee, S.H., Kim, C.S., Seol, S.K. and Jang, S.K. (2003) Long-range RNA-RNA interaction between the 5' nontranslated region and the core-coding sequences of hepatitis C virus modulates the IRES-dependent translation. *RNA-Publ. RNA Soc.*, **9**, 599–606.
24. Beguiristain, N., Robertson, H.D. and Gomez, J. (2005) RNase III cleavage demonstrates a long range RNA: RNA duplex element flanking the hepatitis C virus internal ribosome entry site. *Nucleic Acids Res.*, **33**, 5250–5261.
25. Jopling, C.L., Yi, M.K., Lancaster, A.M., Lemon, S.M. and Sarnow, P. (2005) Modulation of hepatitis C virus RNA abundance by a liver-specific microRNA. *Science*, **309**, 1577–1581.
26. Jopling, C.L., Schuetz, S. and Sarnow, P. (2008) Position-dependent function for a tandem microRNA miR-122-binding site located in the hepatitis C virus RNA genome. *Cell Host Microbe*, **4**, 77–85.
27. Diaz-Toledano, R., Ariza-Mateos, A., Birk, A., Martinez-Garcia, B. and Gomez, J. (2009) In vitro characterization of a miR-122-sensitive double-helical switch element in the 5' region of hepatitis C virus RNA. *Nucleic Acids Res.*, **37**, 5498–5510.
28. Machlin, E.S., Sarnow, P. and Sagan, S.M. (2011) Masking the 5' terminal nucleotides of the hepatitis C virus genome by an unconventional microRNA-target RNA complex. *Proc. Natl. Acad. Sci. U.S.A.*, **108**, 3193–3198.
29. Shimakami, T., Yamane, D., Welsch, C., Hensley, L., Jangra, R.K. and Lemon, S.M. (2012) Base pairing between hepatitis C virus RNA and microRNA 122 3' of its seed sequence is essential for genome stabilization and production of infectious virus. *J. Virol.*, **86**, 7372–7383.
30. Li, Y., Masaki, T., Yamane, D., McGivern, D.R. and Lemon, S.M. (2013) Competing and noncompeting activities of miR-122 and the 5' exonuclease Xrn1 in regulation of hepatitis C virus replication. *Proc. Natl. Acad. Sci. U.S.A.*, **110**, 1881–1886.
31. Henke, J.I., Goergen, D., Zheng, J., Song, Y., Schuetzler, C.G., Fehr, C., Juenemann, C. and Niepmann, M. (2008) MicroRNA-122 stimulates translation of hepatitis C virus RNA. *EMBO J.*, **27**, 3300–3310.
32. Goergen, D. and Niepmann, M. (2012) Stimulation of Hepatitis C Virus RNA translation by microRNA-122 occurs under different conditions in vivo and in vitro. *Virus Res.*, **167**, 343–352.
33. Pineiro, D. and Martinez-Salas, E. (2012) RNA structural elements of hepatitis C virus controlling viral RNA translation and the implications for viral pathogenesis. *Viruses-Basel*, **4**, 2233–2250.
34. Wilson, J.A. and Huys, A. (2013) miR-122 promotion of the hepatitis C virus life cycle: sound in the silence. *RNA*, **4**, 665–676.
35. Li, Y., Masaki, T. and Lemon, S.M. (2013) miR-122 and the Hepatitis C RNA genome: more than just stability. *RNA Biol.*, **10**, 919–923.
36. Draper, D.E. (2004) A guide to ions and RNA structure. *RNA*, **10**, 335–343.
37. Auffinger, P., Grover, N. and Westhof, E. (2011) Metal ion binding to RNA. *Metal Ions Life Sci.*, **9**, 1–35.
38. Bowman, J.C., Lenz, T.K., Hud, N.V. and Williams, L.D. (2012) Cations in charge: magnesium ions in RNA folding and catalysis. *Curr. Opin. Struct. Biol.*, **22**, 262–272.
39. Shenvi, C.L., Dong, K.C., Friedman, E.M., Hanson, J.A. and Cate, J.H.D. (2005) Accessibility of 18S rRNA in human 40S subunits and 80S ribosomes at physiological magnesium ion concentrations - implications for the study of ribosome dynamics. *RNA*, **11**, 1898–1908.
40. Lancaster, A.M., Jan, E. and Sarnow, P. (2006) Initiation factor-independent translation mediated by the hepatitis C virus internal ribosome entry site. *RNA*, **12**, 894–902.
41. Bustamante, C. and Keller, D. (1995) Scanning force microscopy in biology. *Phys. Today*, **48**, 32–38.
42. Hansma, H.G., Kasuya, K. and Oroudjev, E. (2004) Atomic force microscopy imaging and pulling of nucleic acids. *Curr. Opin. Struct. Biol.*, **14**, 380–385.
43. Hansma, H.G., Revenko, I., Kim, K. and Laney, D.E. (1996) Atomic force microscopy of long and short double-stranded, single-stranded and triple-stranded nucleic acids. *Nucleic Acids Res.*, **24**, 713–720.
44. Briones, C., Mateo-Marti, E., Gomez-Navarro, C., Parro, V., Roman, E. and Martin-Gago, J.A. (2004) Ordered self-assembled monolayers of peptide nucleic acids with DNA recognition capability. *Phys. Rev. Lett.*, **93**, 208103.
45. Neaves, K.J., Huppert, J.L., Henderson, R.M. and Edwardson, J.M. (2009) Direct visualization of G-quadruplexes in DNA using atomic force microscopy. *Nucleic Acids Res.*, **37**, 6269–6275.

46. Wells, S.E., Hillner, P.E., Vale, R.D. and Sachs, A.B. (1998) Circularization of mRNA by Eukaryotic Translation Initiation Factors. *Mol. Cell*, **2**, 135–140.
47. Hansma, H.G., Golan, R., Hsieh, W., Daubendiek, S.L. and Kool, E.T. (1999) Polymerase activities and RNA structures in the atomic force microscope. *J. Struct. Biol.*, **127**, 240–247.
48. Hansma, H.G., Oroudjev, E., Baudrey, S. and Jaeger, L. (2003) TectoRNA and 'kissing-loop' RNA: atomic force microscopy of self-assembling RNA structures. *J. Microsc.*, **212**, 273–279.
49. Basame, S., Wai-lun Li, P., Howard, G., Branciforte, D., Keller, D. and Martin, S.L. (2006) Spatial assembly and RNA binding stoichiometry of a LINE-1 protein essential for retrotransposition. *J. Mol. Biol.*, **357**, 351–357.
50. Giro, A., Bergia, A., Zuccheri, G., Bink, H.H., Pleij, C.W. and Samori, B. (2004) Single molecule studies of RNA secondary structure: AFM of TYMV viral RNA. *Microsc. Res. Tech.*, **65**, 235–245.
51. Alvarez, D.E., Lodeiro, M.F., Luduena, S.J., Pietrasanta, L.I. and Gamarnik, A.V. (2005) Long-range RNA-RNA interactions circularize the dengue virus genome. *J. Virol.*, **79**, 6631–6643.
52. Kuznetsov, Y.G., Daijogo, S., Zhou, J., Semler, B.L. and McPherson, A. (2005) Atomic force microscopy analysis of icosahedral virus RNA. *J. Mol. Biol.*, **347**, 41–52.
53. Kuznetsov, Y.G., Dowell, J.J., Gavira, J.A., Ng, J.D. and McPherson, A. (2010) Biophysical and atomic force microscopy characterization of the RNA from satellite tobacco mosaic virus. *Nucleic Acids Res.*, **38**, 8284–8294.
54. Sagan, S.M., Nasheri, N., Luebbert, C. and Pezacki, J.P. (2010) The efficacy of siRNAs against hepatitis C virus is strongly influenced by structure and target site accessibility. *Chem. Biol.*, **17**, 515–527.
55. Gilmore, J.L., Aizaki, H., Yoshida, A., Deguchi, K., Kumeta, M., Junghof, J., Wakita, T. and Takeyasu, K. (2014) Nanoimaging of ssRNA: genome architecture of the hepatitis C virus revealed by atomic force microscopy. *J. Nanomed. Nanotechnol.*, **S5**, 010.
56. Beard, M.R., Abell, G., Honda, M., Carroll, A., Gartland, M., Clarke, B., Suzuki, K., Lanford, R., Sangar, D.V. and Lemon, S.M. (1999) An infectious molecular clone of a Japanese genotype 1b hepatitis C virus. *Hepatology*, **30**, 316–324.
57. Icho, T. and Wickner, R.B. (1989) The double-stranded-RNA genome of yeast virus L-A encodes its own putative RNA-polymerase by fusing 2 open reading frames. *J. Biol. Chem.*, **264**, 6716–6723.
58. Lyubchenko, Y., Shlyakhtenko, L., Harrington, R., Oden, P. and Lindsay, S. (1993) Atomic force microscopy of long DNA - Imaging in air and under water. *Proc. Natl. Acad. Sci. U.S.A.*, **90**, 2137–2140.
59. Cheng, H., Zhang, K., Libera, J.A., de la Cruz, M.O. and Bedzyk, M.J. (2006) Polynucleotide adsorption to negatively charged surfaces in divalent salt solutions. *Biophys. J.*, **90**, 1164–1174.
60. Horcas, I., Fernandez, R., Gomez-Rodriguez, J.M., Colchero, J., Gomez-Herrero, J. and Baro, A.M. (2007) WSXM: A software for scanning probe microscopy and a tool for nanotechnology. *Rev. Sci. Instr.*, **78**, 013705.
61. Schneider, C.A., Rasband, W.S. and Eliceiri, K.W. (2012) NIH Image to ImageJ: 25 years of image analysis. *Nat. Methods*, **9**, 671–675.
62. Ariza-Mateos, A., Prieto-Vega, S., Diaz-Toledano, R., Birk, A., Szeto, H., Mena, I., Berzal-Herranz, A. and Gomez, J. (2012) RNA self-cleavage activated by ultraviolet light-induced oxidation. *Nucleic Acids Res.*, **40**, 1748–1766.
63. Duhamel, J., Liu, D.M., Evilia, C., Fleysh, N., Dinter-Gottlieb, G. and Lu, P. (1996) Secondary structure content of the HDV ribozyme in 95% formamide. *Nucleic Acids Res.*, **24**, 3911–3917.
64. Lozano, G., Fernandez, N. and Martinez-Salas, E. (2014) Magnesium-dependent folding of a picornavirus IRES element modulates RNA conformation and eIF4G interaction. *FEBS J.*, **281**, 3685–3700.
65. Chen, S.J. (2008) *Annual Review of Biophysics*. Annual Reviews, Palo Alto, Vol. **37**, pp. 197–214.
66. Woodson, S.A. (2005) Structure and assembly of group I introns. *Curr. Opin. Struct. Biol.*, **15**, 324–330.
67. Raju, B., Murphy, E., Levy, L.A., Hall, R.D. and London, R.E. (1989) A fluorescent indicator for measuring cytosolic free magnesium. *Am. J. Physiol.*, **256**, C540–C548.
68. Gaussin, V., Gailly, P., Gillis, J.M. and Hue, L. (1997) Fructose-induced increase in intracellular free Mg²⁺ ion concentration in rat hepatocytes: Relation with the enzymes of glycogen metabolism. *Biochem. J.*, **326**, 823–827.
69. Günther, T. (2007) Concentration, compartmentation and metabolic function of intracellular free Mg²⁺. *Magnes. Res.*, **19**, 225–236.
70. Lindow, M. and Kauppinen, S. (2012) Discovering the first microRNA-targeted drug. *J. Cell Biol.*, **199**, 407–412.

A magnesium-induced RNA conformational switch at the internal ribosome entry site of hepatitis C virus genome visualized by atomic force microscopy

Ana García-Sacristán^{1,2}, Miguel Moreno^{1,1}, Ascensión Ariza-Mateos^{2,3,1}, Elena López-Camacho^{1,4}, Rosa M. Jáudenes¹, Luis Vázquez⁴, Jordi Gómez^{2,3}, José Ángel Martín-Gago^{1,4} and Carlos Briones^{1,2,*}.

¹ Department of Molecular Evolution, Centro de Astrobiología (CSIC-INTA). Torrejón de Ardoz, Madrid, 28850, Spain.

² Centro de Investigaciones Biomédicas en Red de Enfermedades Hepáticas y Digestivas. (CIBERehd), Spain.

³ Laboratory of RNA Archaeology, Instituto de Parasitología y Biomedicina “López-Neyra” (CSIC), Parque Tecnológico Ciencias de la Salud, Armilla, Granada, 18016, Spain.

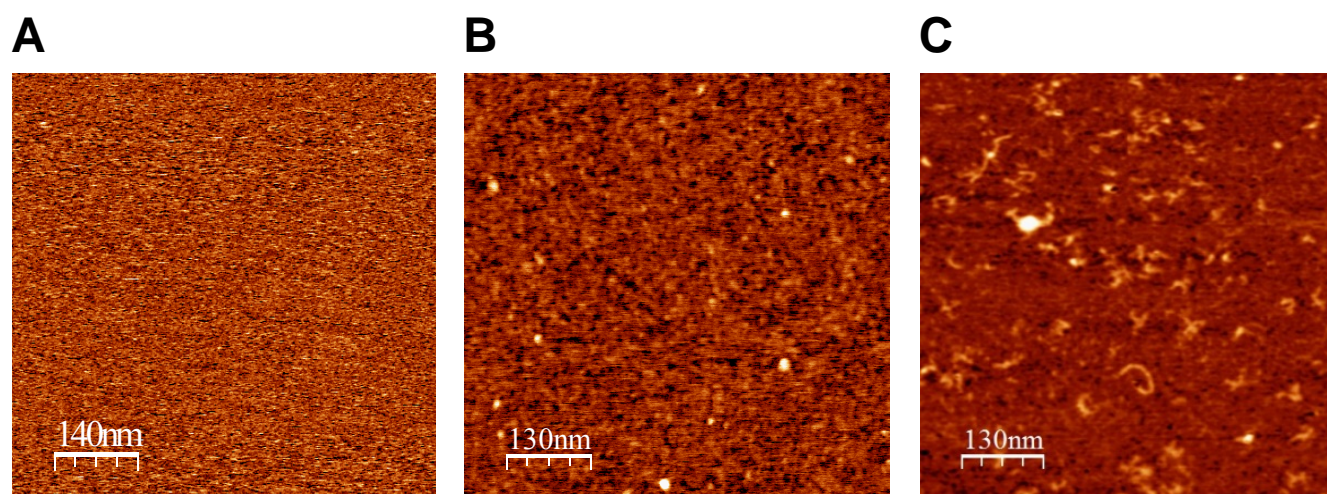
⁴ Instituto de Ciencia de Materiales de Madrid (CSIC). Cantoblanco, Madrid, 28049, Spain.

¹M.M. and A.A-M. contributed equally to this work.

* To whom correspondence should be addressed: Carlos Briones; Tel: +34 91 5206411; Fax: +34 91 5201074; E-mail: cbriones@cab.inta-csic.es

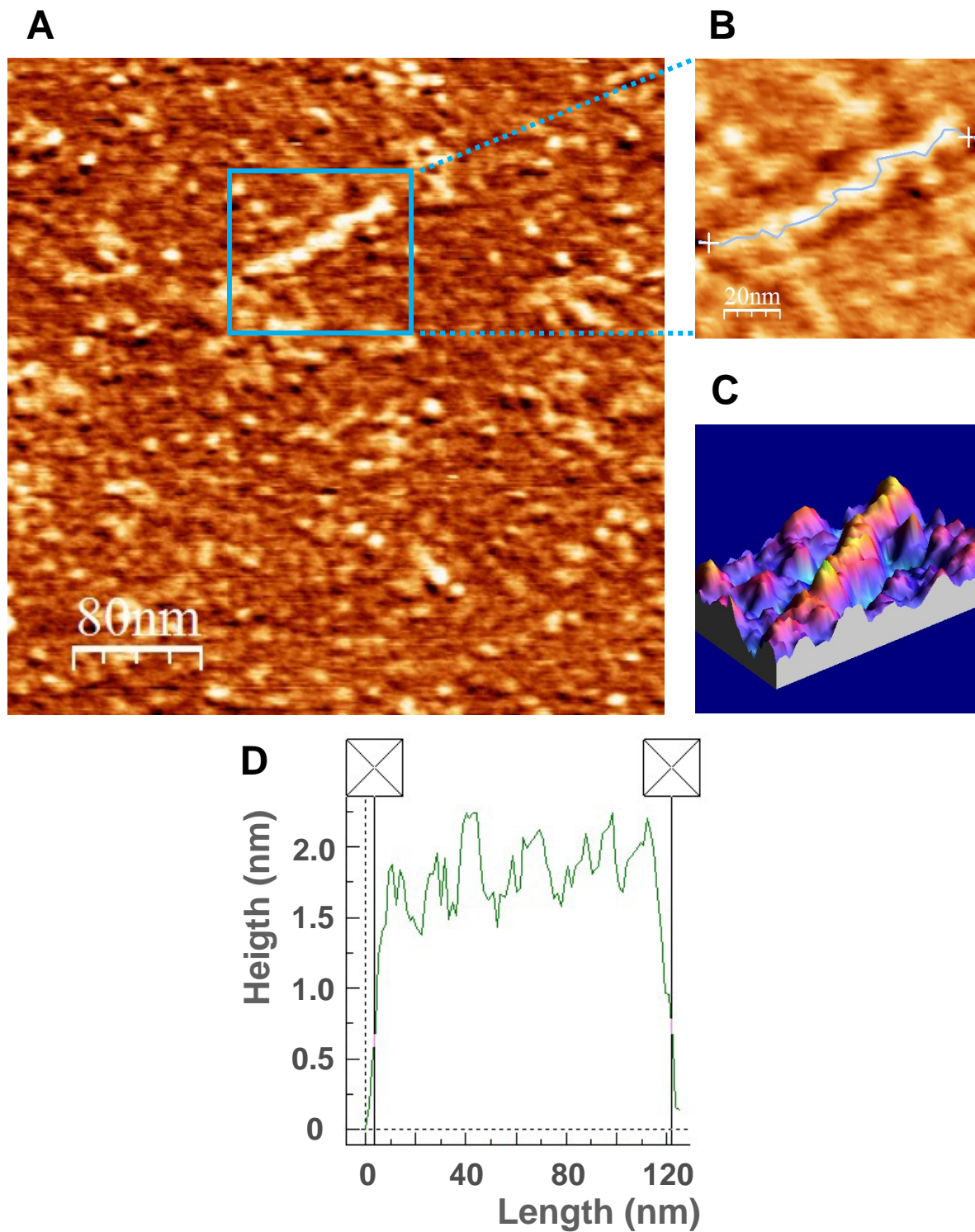
Supplementary Data

Supplementary Figure 1



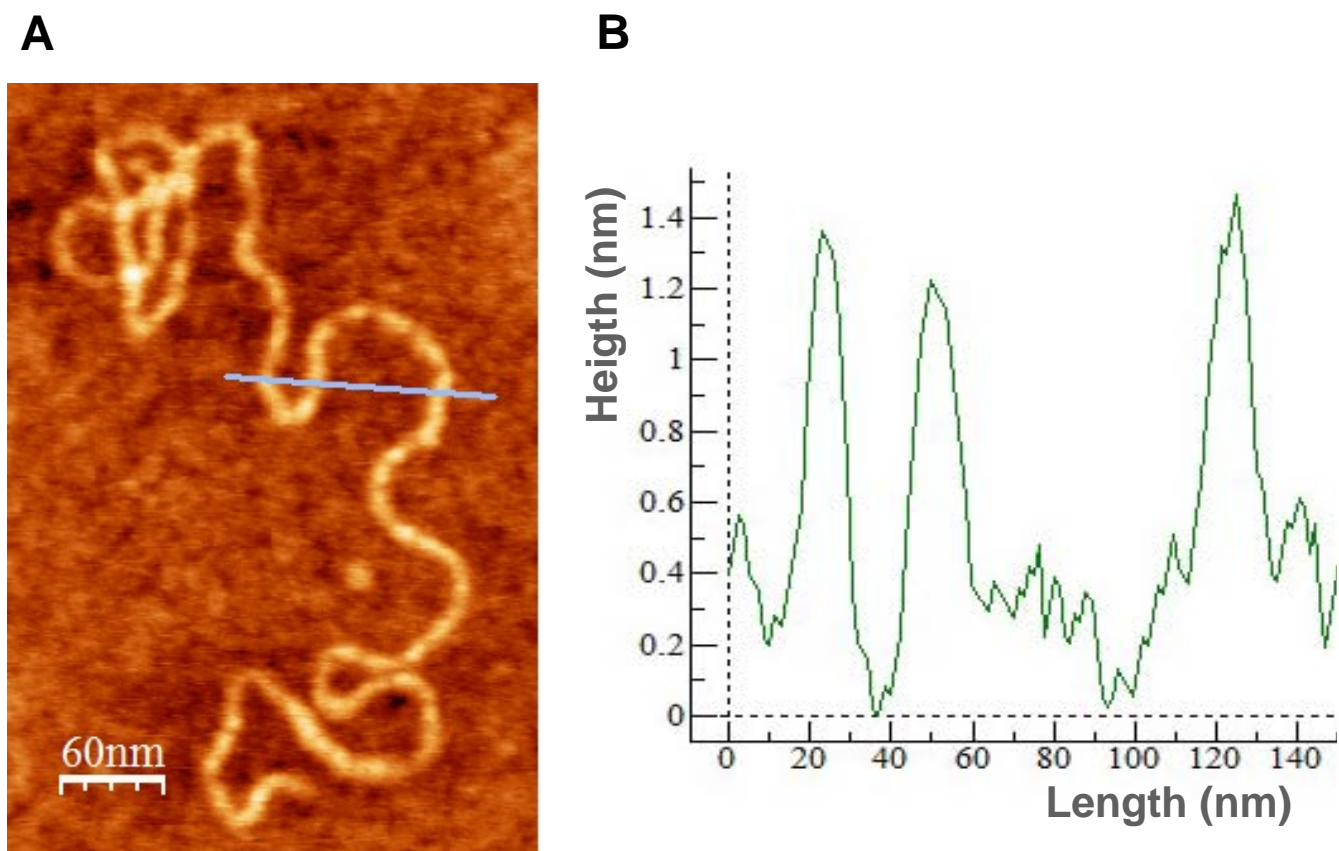
Supplementary Figure 1. Schematic representation of the adsorption process of RNA molecules onto (3-aminopropyl)triethoxysilane (APTES)-treated mica. (A) Freshly cleaved muscovite mica exposes a flat surface. (B) After treatment with APTES, the mica surface becomes positively charged. AFM images of mica-APTES surface show a root mean square (rms) roughness smaller than 0.65 nm, a low background value which allows distinguishing any biomolecule adsorbed onto the surface. (C) RNA deposited onto the mica-APTES surface interacts electrostatically with the charged surface. Preliminary experiments were carried out to check that the RNA preparation and AFM imaging did not damage or degrade the RNA molecules (data not shown). The nominal curvature radius of the AFM tips used for producing these images was 2 nm.

Supplementary Figure 2



Supplementary Figure 2. Tapping mode AFM image of denatured IRES-574 RNA molecules in 80% formamide. (A) AFM image (400x400 nm) of denatured IRES-574 molecules deposited onto a pretreated mica-APTES surface, using an AFM tip with nominal curvature radius of 2 nm. (B) Zoom image (100x100 nm) of the molecule boxed in panel A, with a profile line along its length. (C) 3D representation of the selected molecule. (D) Length profile recorded following the line drawn in panel B, showing a contour distance of 118 nm (76 % of the theoretical molecular length).

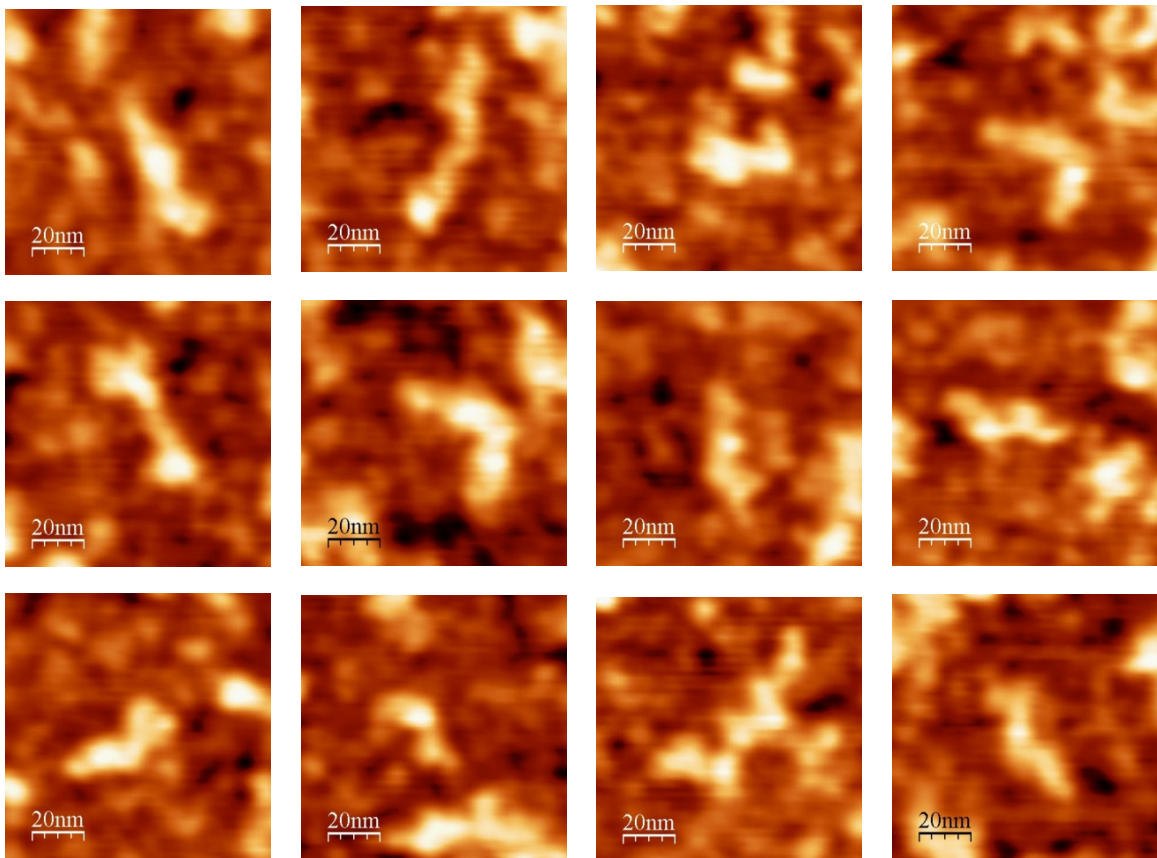
Supplementary Figure 3



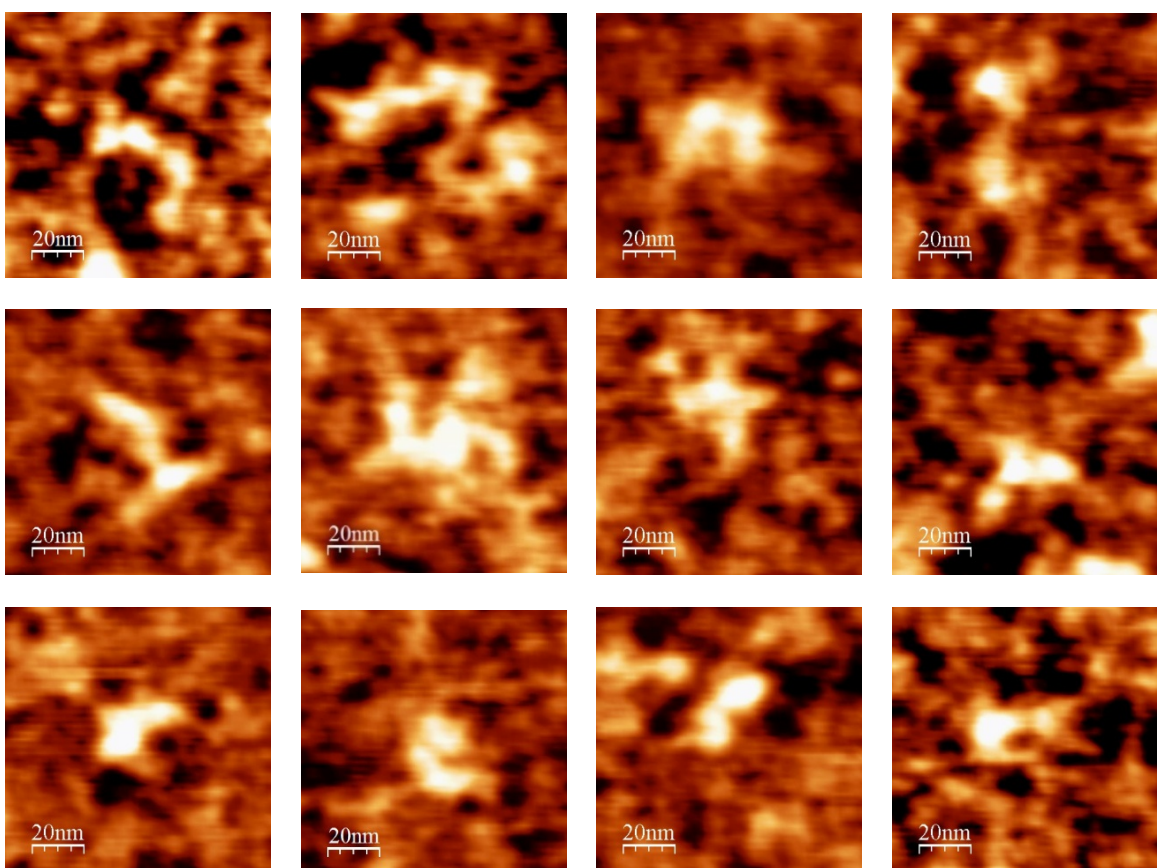
Supplementary Figure 3. AFM image of a control dsRNA molecule. (A) Tapping mode AFM image of the 4,579 bp-long genomic dsRNA of the totivirus L-A, using an AFM tip with nominal curvature radius of 2 nm. (B) Profile of the imaged molecule, showing a height of 1.2-1.4 nm, about 57% of the theoretical 2.3 nm diameter of the A-RNA double helix in solution. Such an apparent flattening of the molecule could be due to the pressure exerted by the AFM tip on the RNA sample. Other possible reasons why height values are lower than expected include the own roughness of the APTES films and the dry conditions of the imaging process.

Supplementary Figure 4

A

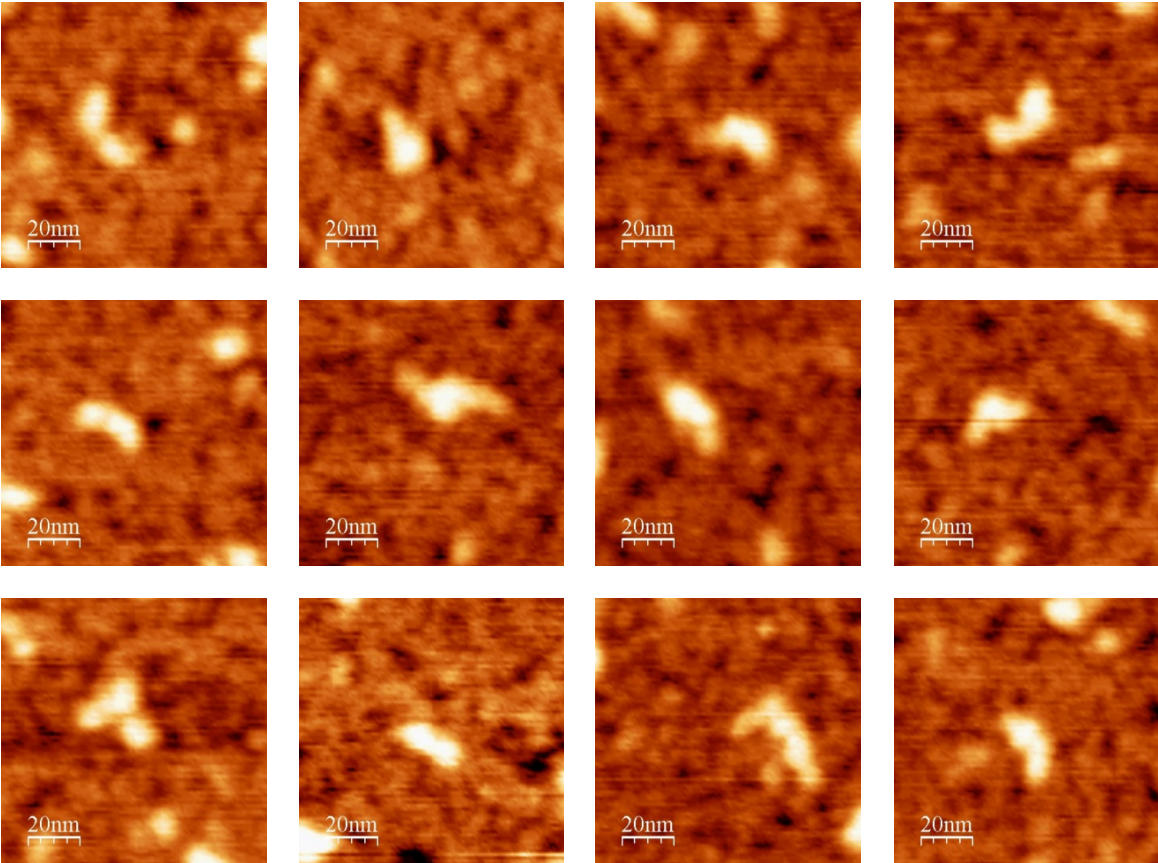


B

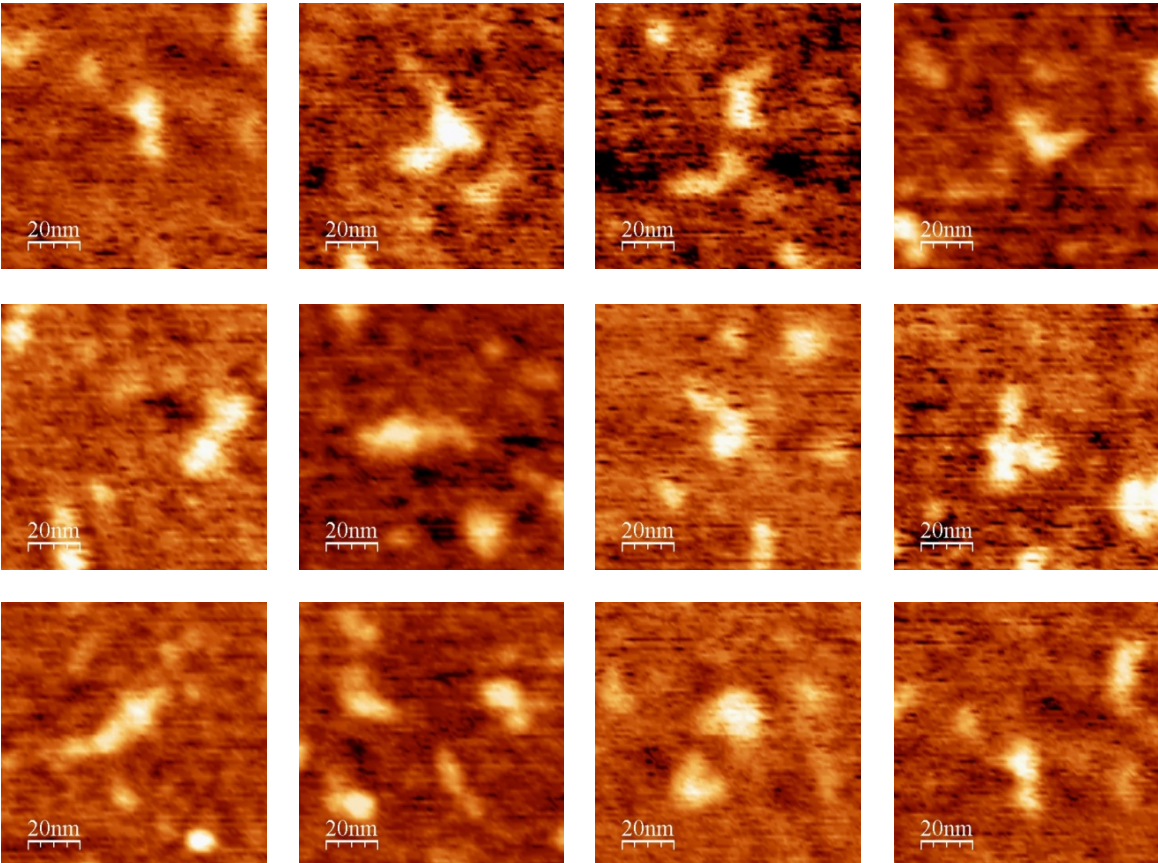


Supplementary Figure 4 (cont.)

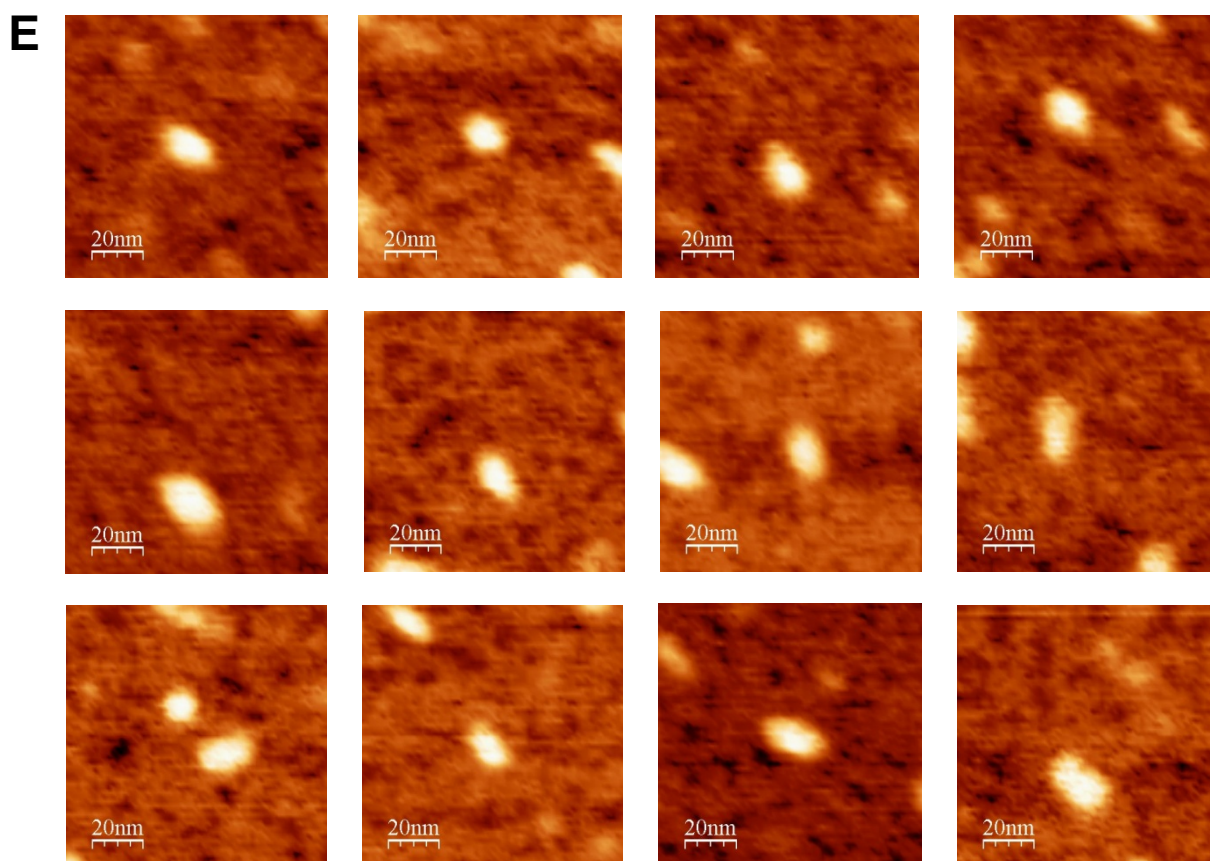
C



D

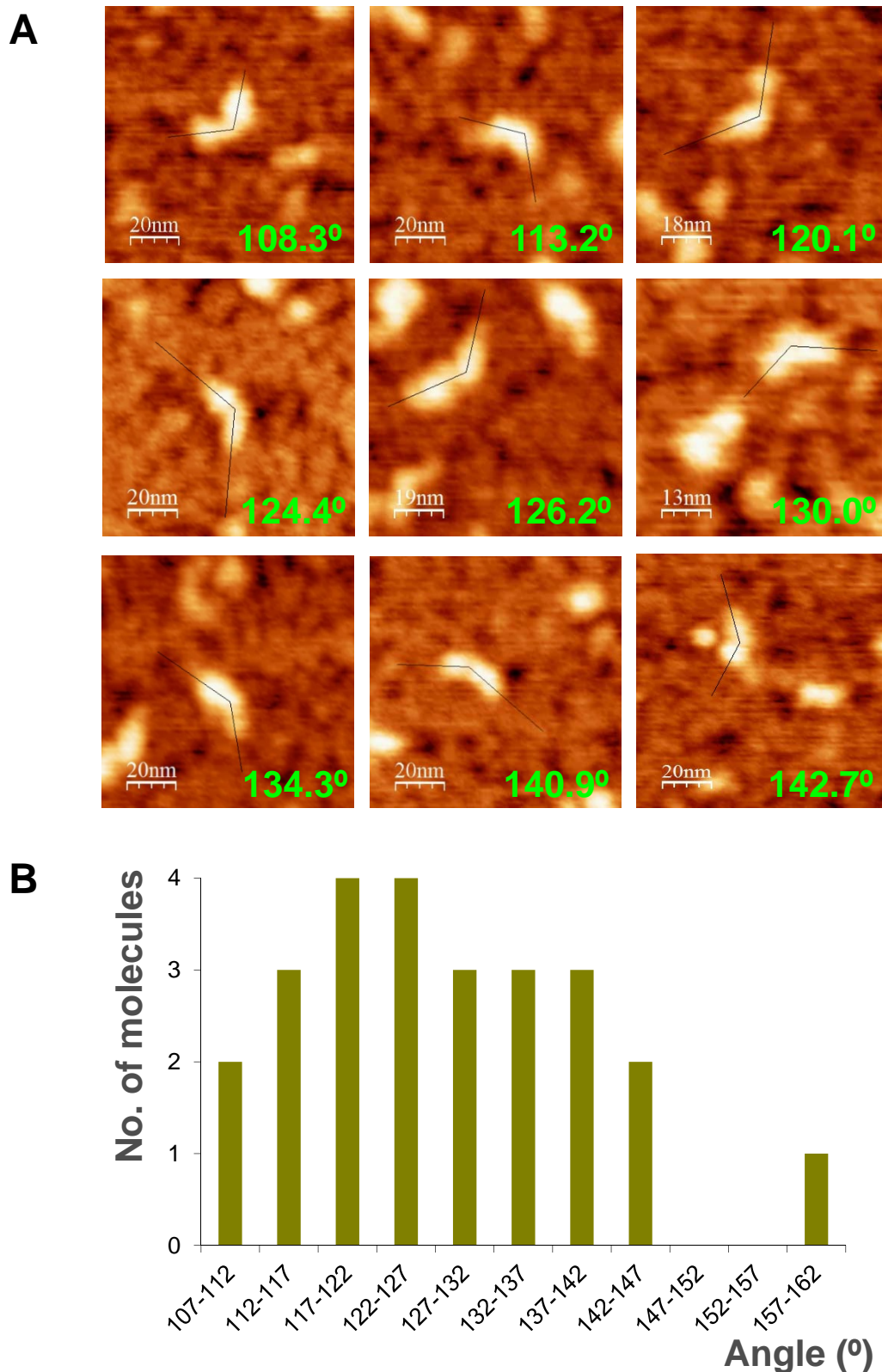


Supplementary Figure 4 (cont.)



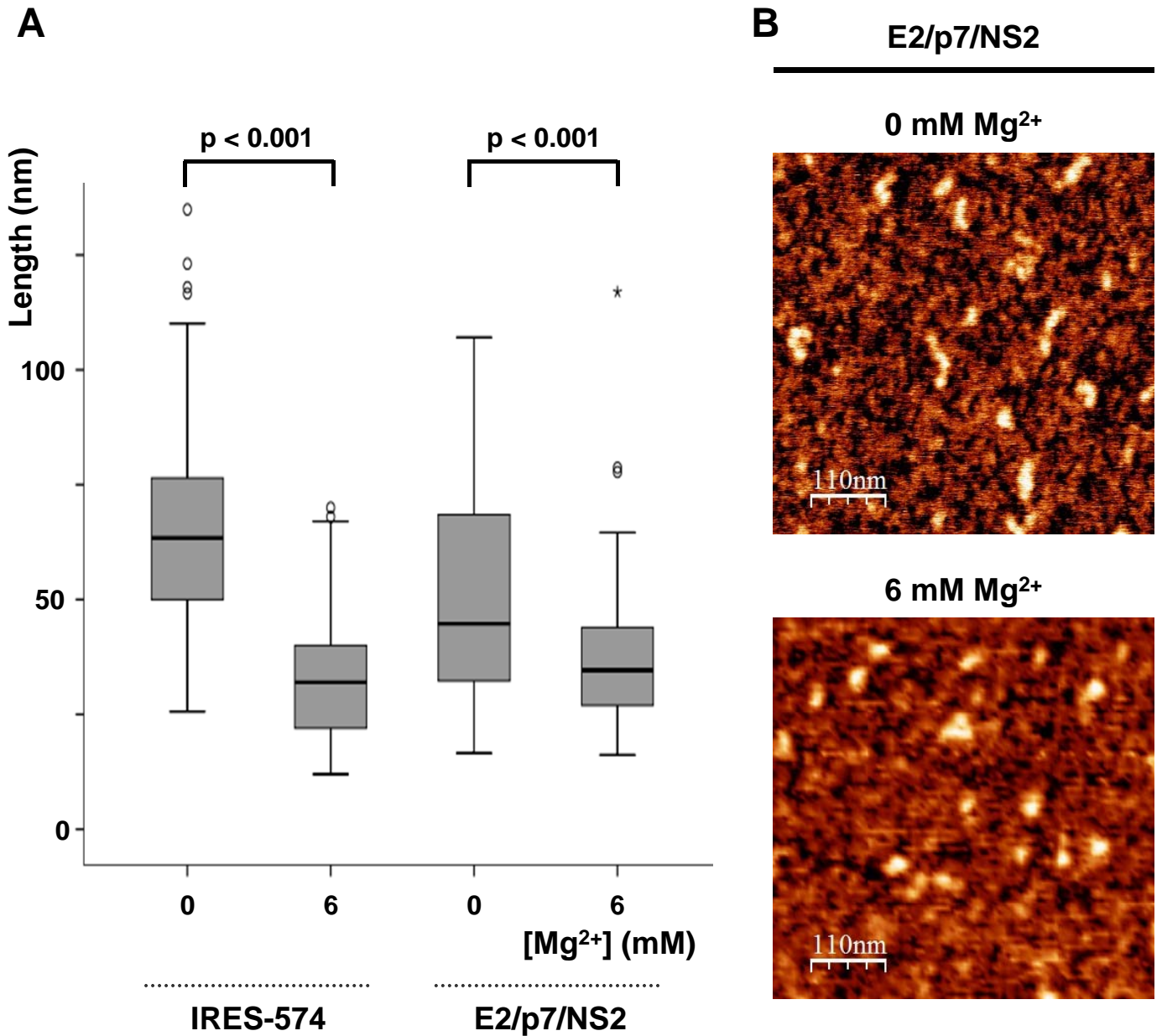
Supplementary Figure 4. Representative AFM images (100x100 nm) of individual IRES-574 molecules under different ionic conditions. (A) Molecules in folding buffer (100 mM NaCl and 100 mM HEPES pH 7.5) without added $MgCl_2$. Extended morphologies are observed, showing some bumps likely corresponding to elements of secondary structure. (B) Folding buffer supplemented with 2 mM Mg^{2+} . Extended shapes (upper row) coexist with molecules showing complex, branched morphologies where up to 4 arms protrude from a central axis (medium row), and angular molecules showing 2 arms (lower row). (C) Folding buffer supplemented with 4 mM Mg^{2+} . Compact, comma-shaped molecules are imaged. (D) Folding buffer supplemented with 6 mM Mg^{2+} . Morphologies analogous to those found at 4 mM Mg^{2+} are dominant, together with elliptical-shaped molecules. (E) Folding buffer supplemented with 10 mM Mg^{2+} . Very compact molecules with elliptical morphologies are imaged. The nominal curvature radius of the AFM tips was 2 nm. See main text for further details.

Supplementary Figure 5



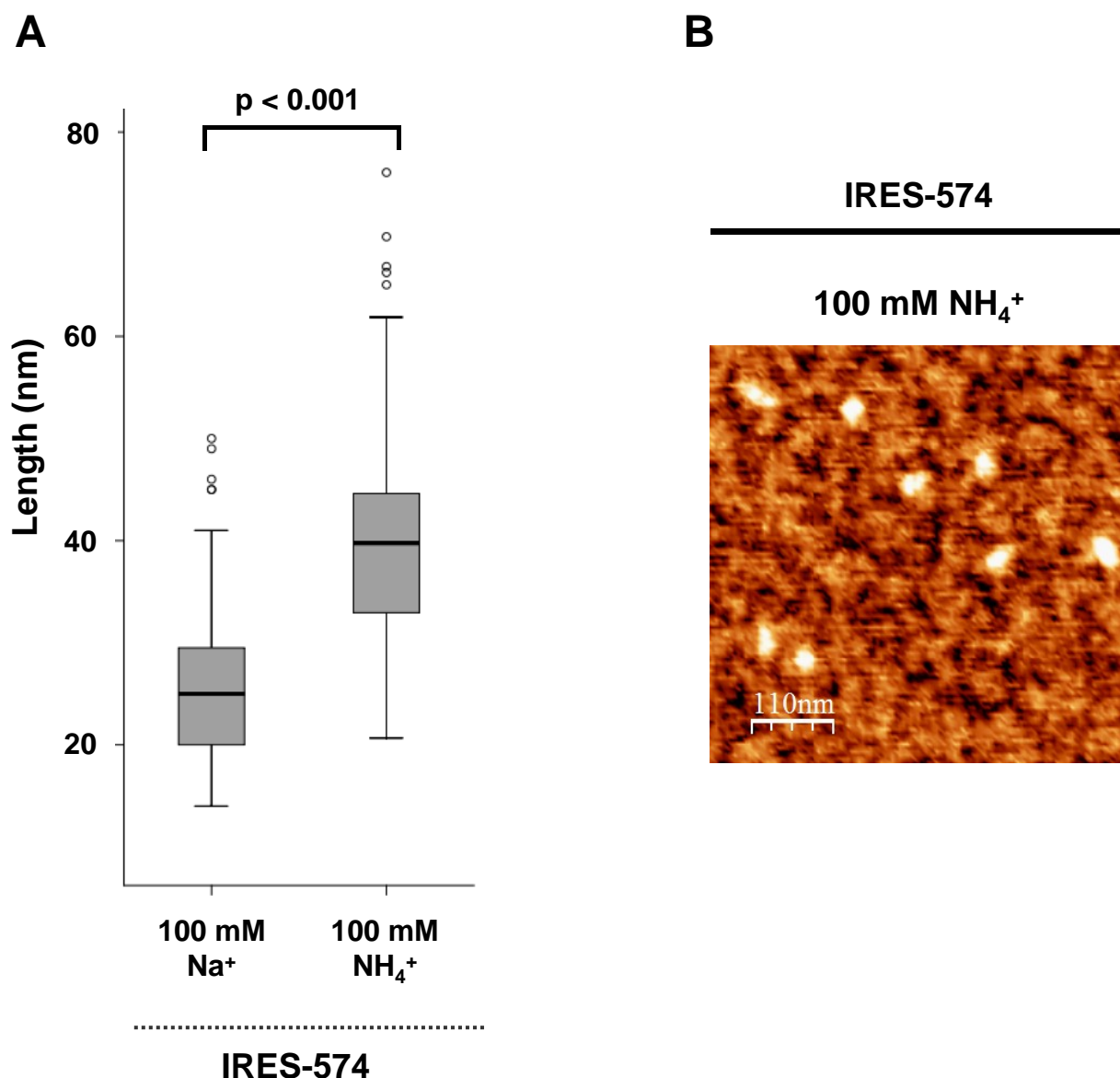
Supplementary Figure 5. Distribution of the angles formed between the two arms imaged in IRES-574 molecules at 4 mM Mg²⁺. (A) Selection of nine representative images (100x100 nm), showing the angle between the two imaged arms. The nominal curvature radius of the AFM tips was 2 nm. (B) Graphical representation of the angular distribution, computed over 25 molecules that showed the correct orientation on the surface.

Supplementary Figure 6



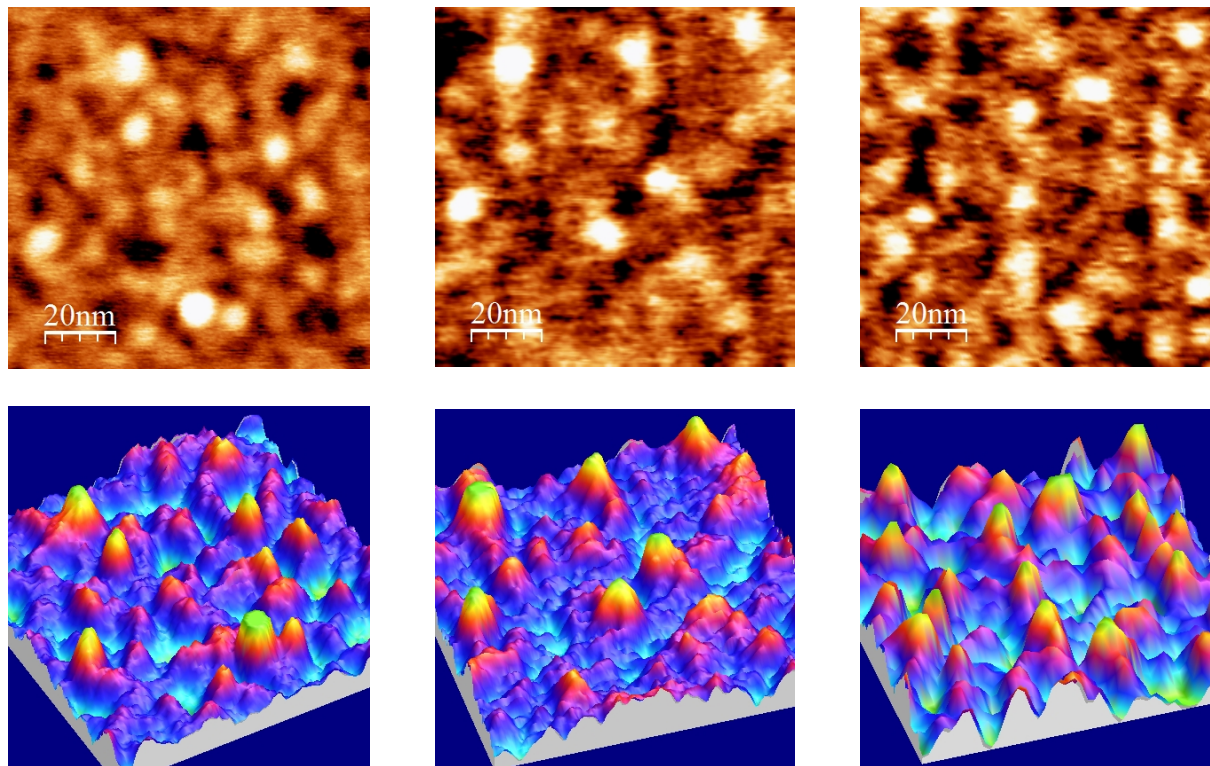
Supplementary Figure 6. Differential behavior of two HCV genomic regions in their Mg²⁺-induced folding. (A) Box plot of the length distribution (computed over 100 molecules) of the transcripts IRES-574 and E2/p7/NS2 in a folding buffer either in the absence of Mg²⁺ or supplemented with 6 mM Mg²⁺. Boxes represent 25-75 percentile range, vertical lines span 10-90 percentile range, and the horizontal bar within the box represent the median. Outlier values are depicted as circles (mild outliers) and asterisks (extreme outliers). Statistical p values are shown. Both sequences exhibited statistically significant reductions in their median length values when Mg²⁺ concentration was increased from 0 to 6 mM. However, this effect was much more pronounced in IRES-574 (49.2% reduction of the median values, from 63 to 32 nm) than in E2/p7/NS2 (24.4% reduction, from 45 to 34 nm). (B) Representative AFM images (550x550 nm) of E2/p7/NS2 molecules in folding buffer without Mg²⁺ (upper panel) and supplemented with 6 mM Mg²⁺ (lower panel). The nominal curvature radius of the AFM tips was 2 nm.

Supplementary Figure 7



Supplementary Figure 7. Differential compaction of the IRES-574 molecule induced by two monovalent cations. (A) Box plot of the length distribution (computed over 100 molecules) of the transcript IRES-574 incubated in folding buffer containing 100 mM HEPES pH 7.5 and 10 mM MgCl₂, supplemented with either 100 mM NaCl or 100 mM NH₄Cl. Boxes represent 25-75 percentile range, vertical lines span 10-90 percentile range, and horizontal bar within the box represent the median. Mild outlier values are depicted as circles, and statistical p values are shown. The lower compactness of the molecules incubated in NH₄⁺-containing buffer with respect to those folded under Na⁺ was evidenced by their median lengths (39.5 nm and 25 nm, respectively). (B) Representative AFM image (550x550 nm) of IRES-574 molecule in folding buffer containing 100 mM NH₄Cl. The nominal curvature radius of the AFM tip was 2 nm.

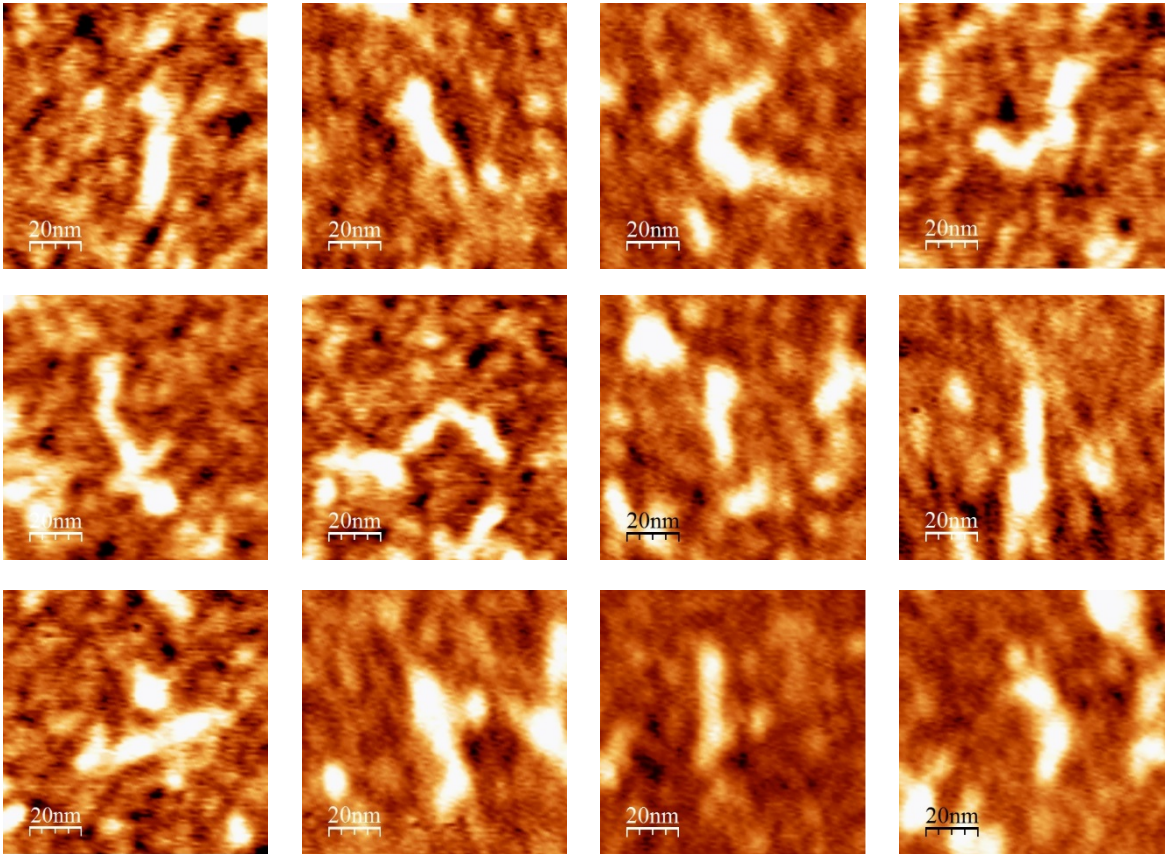
Supplementary Figure 8



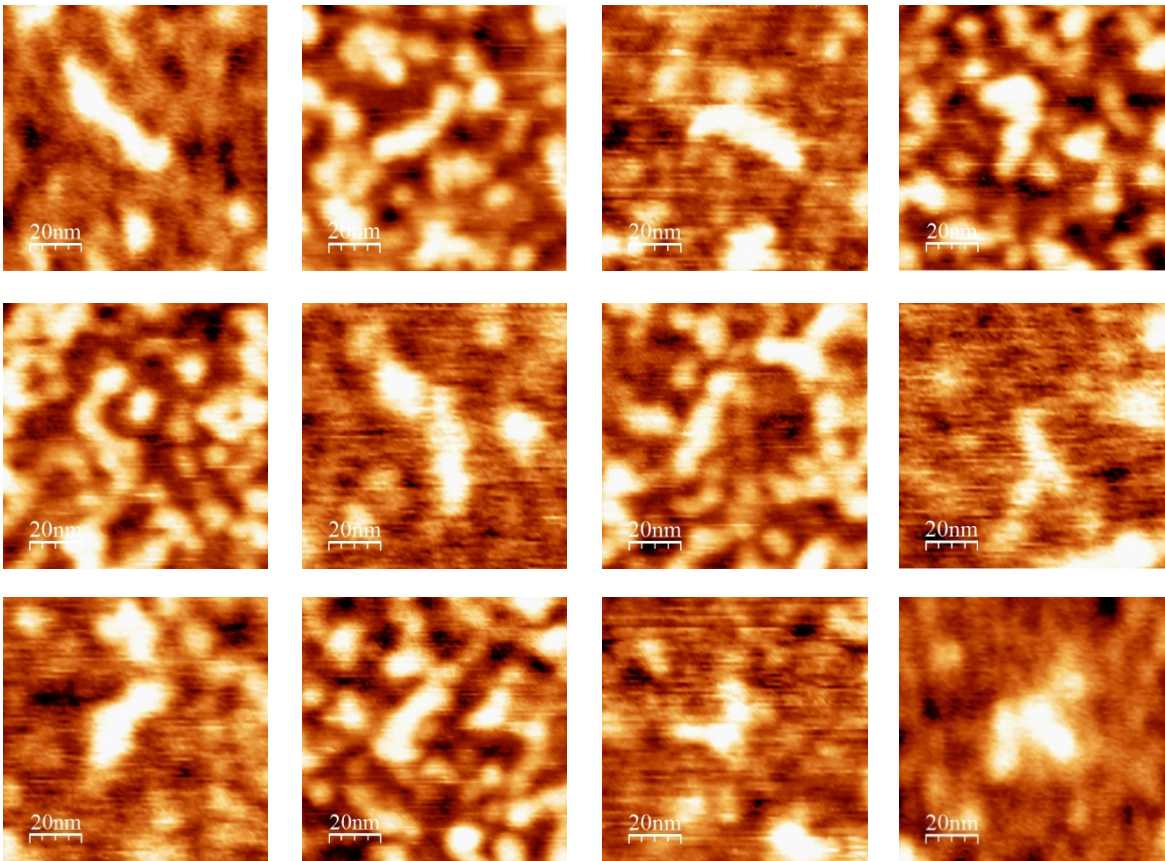
Supplementary Figure 8. AFM images of miR-122 molecules. MicroRNA miR-122 molecules at 15 nM concentration were incubated in a buffer composed of 100 mM NaCl, 100 mM HEPES pH 7.5, and 6 mM MgCl₂. Compact and elliptical shapes were imaged, with very homogeneous lengths of 10-14 nm. Three different AFM fields (100x100 nm) are shown, together with their corresponding 3D representation. The nominal curvature radius of the AFM tips was 2 nm.

Supplementary Figure 9

A

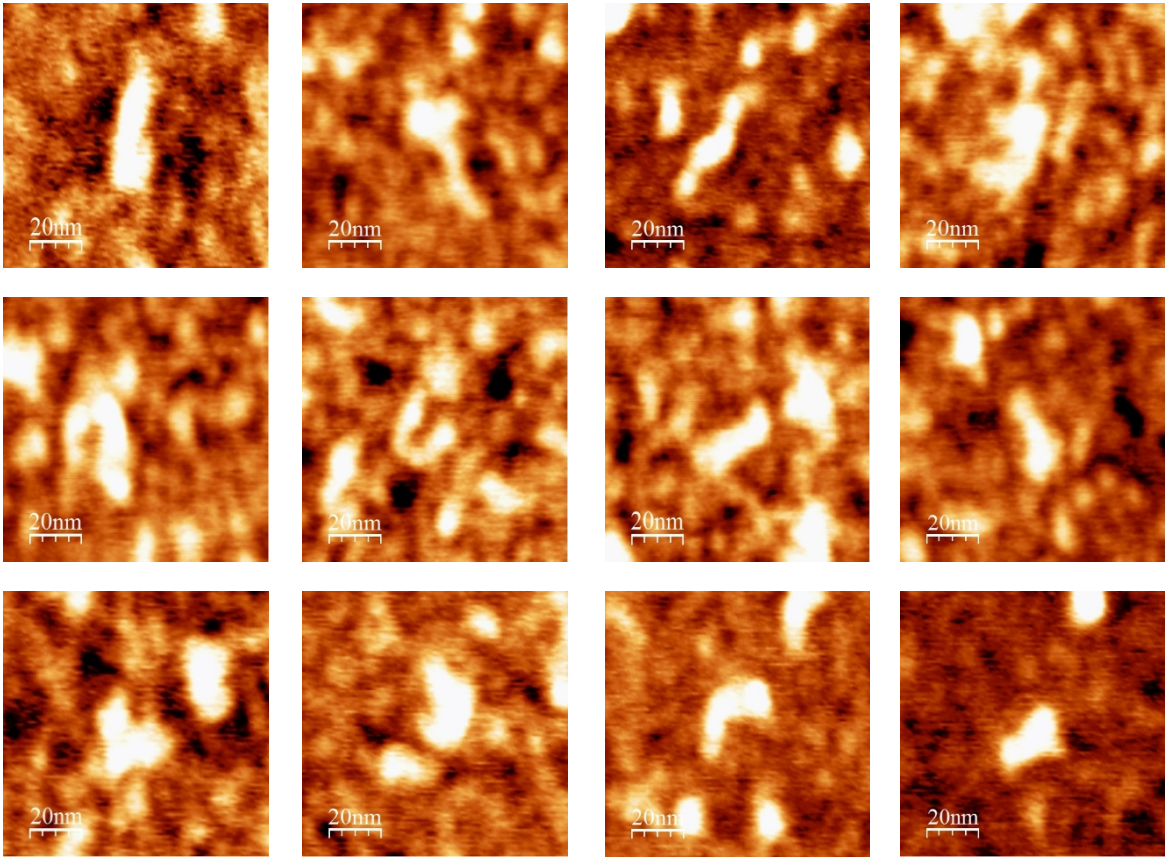


B

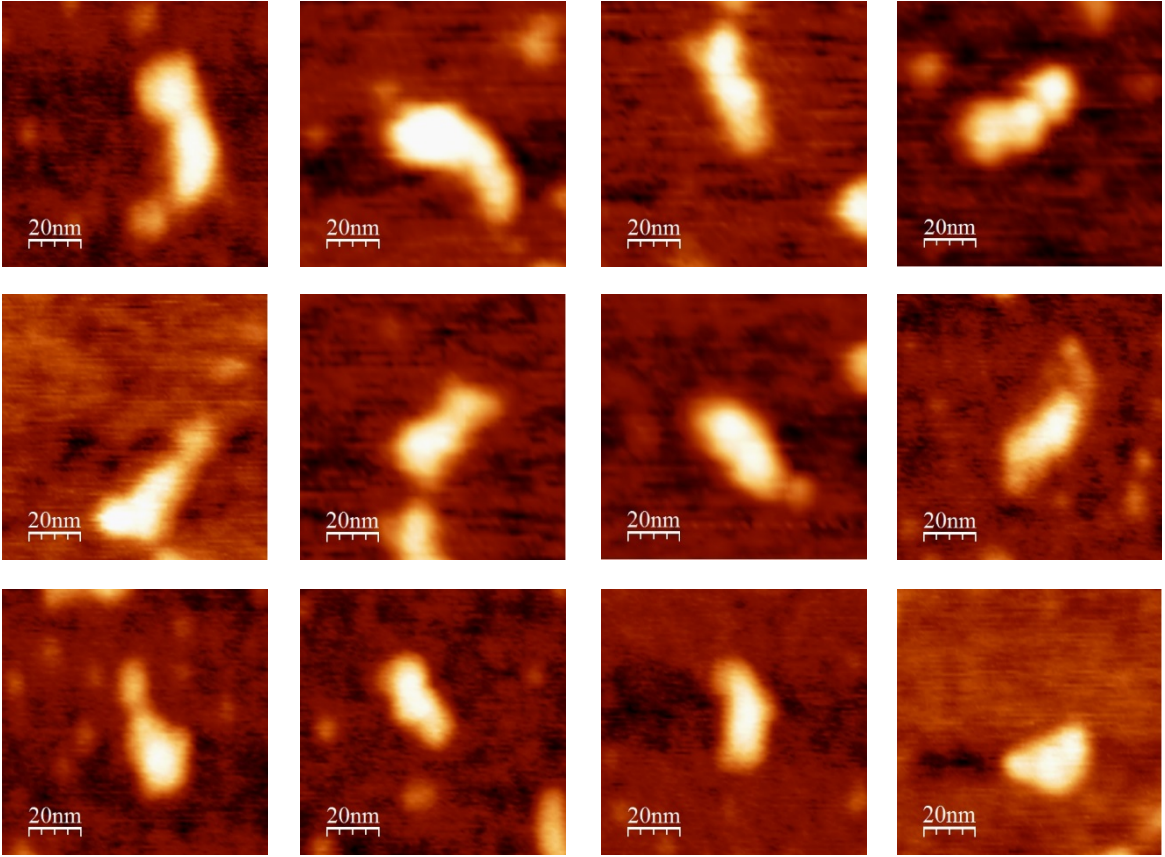


Supplementary Figure 9 (cont.)

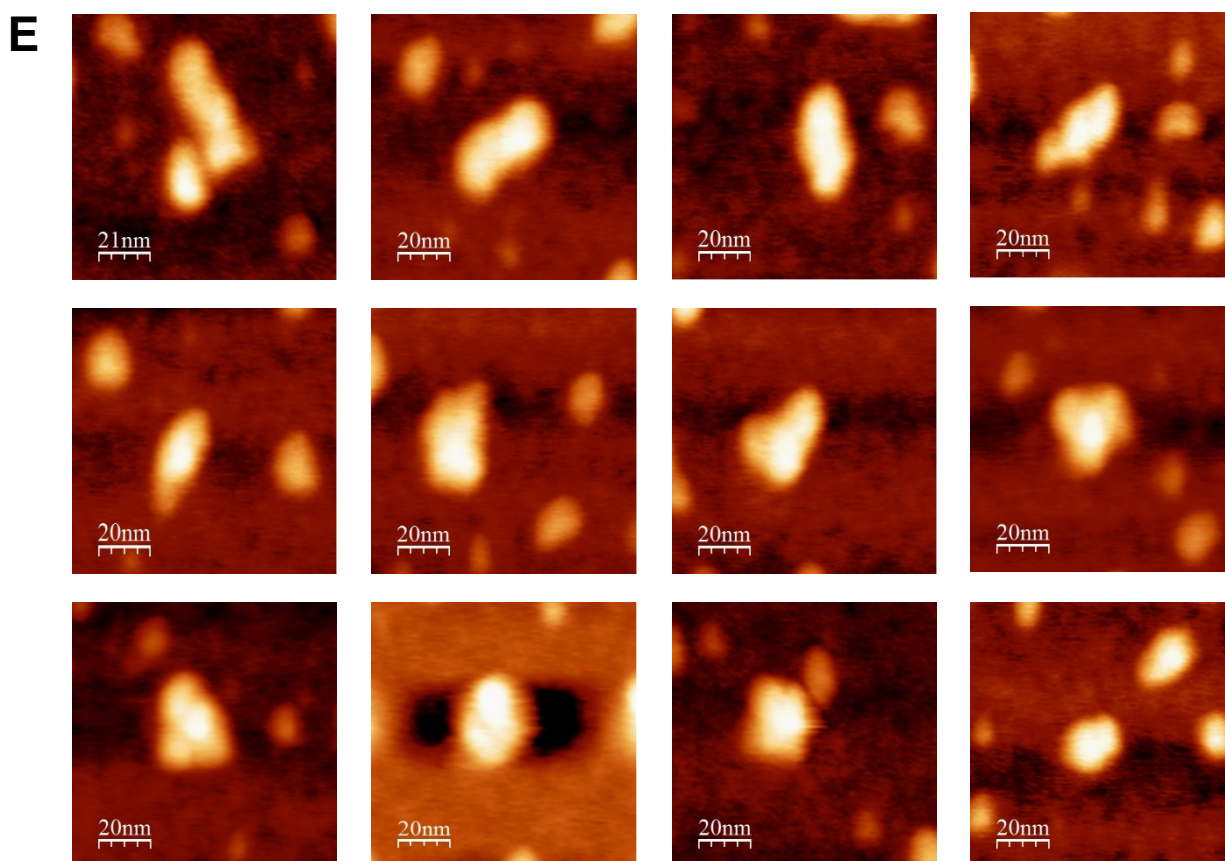
C



D



Supplementary Figure 9 (cont.)



Supplementary Figure 9. Representative AFM images (100x100 nm) of individual IRES-574/miR-122 complexes under different ionic conditions. (A) Molecules in folding buffer (100 mM NaCl and 100 mM HEPES pH 7.5) without added $MgCl_2$. Extended and angular morphologies are observed. **(B)** Folding buffer supplemented with 2 mM Mg^{2+} . Elongated and zigzagging molecules are imaged. **(C)** Folding buffer supplemented with 4 mM Mg^{2+} . Extended and angular shapes (upper-left panels) coexist with molecules showing branched morphologies, as well as a fraction of triangular and comma-shaped ones (lower-right panels). **(D)** Folding buffer supplemented with 6 mM Mg^{2+} . Partially elongated and angular molecules are imaged, together with comma-shaped and more compact molecules. **(E)** Folding buffer supplemented with 10 mM Mg^{2+} . Some short, linear molecules are imaged, although most of the AFM fields are dominated by compact morphologies with triangular and elliptical shapes. The nominal curvature radius of the AFM tips was 2 nm. See main text for further details.

Key role of IRES structural context and its dynamic transformations promoted by miR-122 in the formation of the hepatitis C virus IRES-40S binary complex.

Ascensión Ariza-Mateos^{1,2} and Jordi Gómez^{1,2}

1- Instituto de Parasitología y Biomedicina “Lopez-Neyra” CSIC. Spain

2- CIBERehd Centro de investigación en RED de enfermedades hepáticas y digestivas (ISCIII)

Abstract

The *RNA*₁₋₅₇₀ region of the hepatitis C virus genome includes the internal ribosome entry site (IRES) and its 5' and 3' flanking sequences. In this RNA fragment, the IRES adopts a closed configuration which switches to open after combining with the microRNA miR-122. In this study we have found that: i) *RNA*₁₋₅₇₀ forms two stable binary complexes with a ribosome 40S subunit. Each complex protects a specific group of sequences from RNase A depending on whether the *RNA*₁₋₅₇₀ is open or closed; ii) miR-122 binds in tandem at the 3' flank of the IRES. Binding kinetics are rapid at the 3' flank and domain IV opens directly, while binding at the 5' flank is slower and changes the base region of domains III and IV through the conformational transition from closed to open; and iii) the effect of the miR-122 binding together specifically favours the formation of the binary complex which transports *RNA*₁₋₅₇₀ in the open configuration in 15%, while it has no effect on the carrier of *RNA*₁₋₅₇₀ in the closed conformation. Thus, *RNA*₁₋₅₇₀ offers a structure-based level of regulation by miR-122 of any functions that the binary complex participates in which lack shortened RNA transcripts.

Introduction

The 5' region of the hepatitis C virus (HCV) genome comprises an internal ribosome entry site (IRES) between positions 44 and 372 (domains II to IV). It includes a double pseudoknot near the AUG start triplet, a 33-base sequence downstream within the CORE coding region and a wide range of local tertiary structural elements. The region overlapping the IRES-pseudoknot the AUG and 60-nts of the coding region, adopts a tRNA-like cloverleaf structure which is conserved in the animal pestiviruses. In turn, the IRES is part of an even higher order RNA structure formed by the annealing of both its flanking sequences: bases 428–442 (domain VI) within the coding region and the complementary 5' unstructured sequence 24–38 (domain I). This long-range annealing (LRA) motif constrains the IRES in a closed conformation between domains I and VI (Fig. 1) and implies that the IRES may form two stable secondary structures, closed (C) and open (O).

During translation initiation the 40S ribosomal subunit first binds to the HCV IRES to form an IRES–40S binary complex. This binary complex can also be formed in the absence of initiation factors, as in the case of a prokaryotic-like mode of pre-initiation. During incubation with purified 40S complexes, discrete regions of IRES domains II, III and IV appeared to be protected from RNase A digestion, chemical modification (Kieft, 2001) or blocked primer extension (Pestova, 1998 Genes Develop). Toeprinting experiments combined with robust mutation analysis determined that the pseudoknot region helps to specify the correct placement of the AUG initiator codon.

miR-122 is the most abundant micro-RNA in the liver; it is tissue specific and essential for HCV infection. miR-122 binds in tandem at two sites on the 5' IRES flank, S1 and S2 (nts 1–43) and plays a key role in stabilising the HCV genome, in promoting HCV translation and in switching from translation to replication. It has also been suggested that miR-122 has a direct influence on HCV replication and could be involved in masking the HCV genome from recognition by host antiviral proteins; a hypothesis that was comprehensively reviewed by J.A. Wilson (citas: JA Wilson). A third miR-122 binding position at the 3' IRES flank has been detected *in vitro*, but with no associated role.

Studies in parallel to those into HCV miR-122 function have demonstrated that miR-binding to S1 and S2 has the capacity to switch the IRES from the (C) to (O) conformations. While it is not clear how these two conformations may differ with respect to their functional properties, it is highly likely that changes in

IRES structure are decisive in determining the fate of full-length viral RNA, as is the case observed for other viral IRESes (Jackson R.J., 2000). Nevertheless, it is still unknown whether or not miR-122 binding and IRES C to O configuration transition have any effect on the actual IRES tertiary structure (and its potential consequences), at least in the first step of translation pre-initiation.

Initial IRES binding to 40S subunits has been characterised by other authors as a one-step mechanism without any metastable intermediates. However, once formed, 43S complexes are dynamic and may interconvert between more than one conformation, which have the same conformation at low Mg^{2+} concentrations or in the presence of a complete set of initiation factors. These forms have not been characterised further.

Here we demonstrate two of probably several factors that may be responsible for the difficult picture in the literature concerning the role of miR-122 in translation is the presence of two stable conformations for the pre-initiation complex and the activity of the binding in tandem of a second pair of miR-122 molecules at the 3' of the IRES when a fragment including both flanks of IRES (1-570) are considered.

Firstly we took a more detailed look at the formation of binary pre-initiation complexes between 40S subunits from HeLa cells and HCV IRES when using the 1–570 nts transcript, which can circularise. We then evaluated three different factors known to influence the IRES C to O conformation transition: separate removal of the 5' or 3' IRES flanking domains, incubation with miR-122 and changes in Mg^{2+} concentration. Purified 40S subunits interact with *RNA*₁₋₅₇₀ to produce two differentially migrating product complexes, revealing a fast (F) and a slow (S) band when examined by native gel electrophoresis; these two product complexes were determined to be isomers corresponding to the C and O forms, respectively, of the uncombined, free RNA. Each binary complex conformation protected both common and unshared regions of the viral IRES, indicating the 40S subunit took a different position. miR-122 binding stimulated S forms, but did not affect F forms.

Our second objective was to seek the specific structural change in IRES after miR-122 binding that may bear some relation to the different F and S forms. During the analysis we found a new binding site for miR-122, which we called S4. Here we report on the techniques used to prove that this is a specific binding located in the vicinity of S3 and which forms a tandem binding site downstream around the AUG

at the 3' IRES flank. This new binding site was characterised by fast annealing kinetics, which is one of the biophysical parameters that best correlates between *in vitro* and *in vivo* levels. Thus, mechanistic models based on the structural effects of miR-122 over binary complex formation should take into account not only the binding sites at the 5' IRES flank but also at the 3' flank. We therefore report a further dissection analysis of the structural effects of miR-122 binding at each IRES flank, by coupling the reaction of the structure-specific RNases P and Z in the presence or absence of different miR-122 binding sites and by varying the miR-122 concentration.

RNases P and Z recognise the IRES tRNA-like element, which is one of the IRES regions with differential protection from RNase A when present in the F and S forms. Thus, the correlation of tRNA-like structural changes recognised by RNases P and Z on one hand, and the need for these changes to produce F or S binary complexes on the other, gave us the opportunity to investigate IRES pre-initiation and how it works.

The mechanistic model is a kinetically controlled process in which miR-122 binds to the 3' IRES flank quickly, destabilising stem-loop IV and favouring 40S binding at domains III (left) and IV. Meanwhile, miR-122 binds to the 5' IRES flank more slowly, breaking LRA and favouring binding at right domain III/IV and domain II. This model may account for a number of seemingly contradictory or unrelated observations on HCV-IRES 40S binding.

Material and Methods

In vitro RNA transcription and internal labelling

HCV RNA transcripts were obtained from the plasmid vector pN(1–4728) Bluescript, which contains nt 1–4728 of HCV preceded by the bacteriophage T7 promoter, a gift from Dr Stanley Lemon, University of Texas, Galveston. This DNA template was used to generate a variety of shorter DNA fragments by PCR amplification. Upstream primers incorporated the T7 RNA polymerase promoters: 5'-TAATACGACTCACTATAGGGCCAGCCCCGATTGG-3' (when the sequence starts at nt 1) or 5'-TAATACGACTCACTATAGGGCCTGTGAGGAACTACT-3' (starting at nt 44). Downstream primers were 5'- CCCAGGCCCTGCCCTCGG-3' for HCV1-570 and HCV44-570; 5'- CCTGTGGGCGGCGGTTGGTGT-3' for HCV1-402 and HCV44-402; 5'-

TTTCTTTGAGGTTTAGGATT-3' for HCV1-370 and 5'-ACTCGCAAGCAC CCTATCAG-3' for HCV44-312.

The transcript of tRNA^{Tyr} precursor (pTyr) was produced from pUC19 Tyr, containing sequences of the naturally occurring pTyr found in *E. coli*, using the T7 promoter; a smaller pTyr precursor transcript (pATy-1A) (Lundberg U. RNA 1995) was obtained from the complementary reverse oligodeoxynucleotide

5'-
TGGTGGTGGGGGAAGGATTCGAACCTTCTCCCCACCACGGGGTAATGCTTTTTACTGGCCTG
CTCCCTTATCGGGAAGCCCTATAGTGAGTCGTATTA-3' including T7 promoter. And the tRNA^{Leu}
precursor RNA from *Bacillus subtilis* (trnD-Leu2) was transcribed by PCR from upstream primer 5'-
TAATACGACTCACTATAGGGGAGATACGACGTAAACTTGCC-3' and downstream primer 5'-
AGTCTGAAGCTTGCAGAAGAACTAGAAGAGGTGC-3', gifts from Dr Sydney R. Kushner.

The *in vitro* conditions used to obtain internally labelled RNAs using T7 RNA polymerase (Ambion) in the presence of [α -³²P]-labelled rNTPs (Perkin-Elmer) are described in Milligan J.F., Methods Enzymol. 180, 51-62; and in particular detail in Ariza-Mateos A. NAR, 2011. Unlabelled RNAs were transcribed with T7 RNA polymerase from MEGAshortscript™ kit (Ambion).

Unlabelled and internally labelled miR-122 and let-7b RNAs were transcribed under the same conditions. However, in this case the RNAs were purified with denaturing polyacrylamide gels rather than by cellulose CF-11 resin chromatography.

pT76803, digested with DraI, was used as the DNA template for the T7-dependent run-off transcription of cyanobacterial RNase P RNA from *Synechocystis sp.* and then purified.

5' and 3' end labelling

End labelling was performed as described previously (Díaz-Toledano R., NAR 2009).

Human and *Synechocystis sp.* RNase P cleavage assays

HCV-RNA substrates were folded and incubated at 37 °C for 20 min in the absence or presence of microRNA-122: 5'-UGGAGUGUGACAAUGGUGUUUGU-3' or let-7b: 5'-UGAGGUAGUAGGUUGUGUGGUU-3' (synthesised by Integrated DNA Technologies, Inc. and Exiqon, respectively) at concentrations of 15, 150 and 1500 nM. RNase P cleavage reaction human and bacterial ribozyme, product purification, analysis and quantification were all carried out exactly as

described by Nadal et al., for the human enzyme, or Sabariego et al., for the bacterial ribozyme (JBC 2002 and FEBS Lett. 2004 respectively).

Purification of *E. coli* RNase Z

The strain SK3188 transformed with the plasmid pUGK33, containing the *rnz/elaC* open reading frame encoding His-tagged RNase Z (six histidine codons), was a gift from Dr Sydney R. Kushner. (Perwez T. Molecular Microbiology 2006).

First, small-scale purification was performed to analyse the expression of RNase Z from 10 mL of kanamycin-free LB. RNase Z was then purified from 400 mL of LB containing 20 µg of kanamycin, following the method described by (Perwez T. Molecular Microbiology 2006) but with some modifications: the cell pellet obtained was washed in 20 mL of ice-cold resuspension/lysis buffer rather than 50 mL. After centrifugation and storage at -20 °C, the frozen cell pellet was resuspended in 5 mL of cold resuspension/lysis supplemented with 5 mM imidazole, 2 mM DTT and protease inhibitor.

RNase Z cleavage assays

Specificity and control assays were performed with increased concentrations of the standard substrate *trnD*-Leu2-RNA (235 nt) from *Bacillus subtilis* (Perwez T. Molecular Microbiology 2006). Cleavage reactions using pre-calibrated RNase Z were performed in 10 µL reaction volumes containing 4.2 nM substrate transcripts in a reaction buffer comprised of 20 mM Tris-HCl at pH 7.1, 10 mM KCl, 1 mM MgCl₂, 1 µM ZnCl₂ and 1.5 mM DTT (buffer Z), and also in the presence of 40 U RNasin[®] for 1 h at 37 °C. Calibration showed that the optimal RNase Z conditions for the HCV molecule were 1/9 of enzyme diluted with reaction buffer 1X at 37 °C for 1 h in the presence of 40 U RNasin. Samples were pretreated with proteinase K, denatured at 90 °C for 1 min and cooled on ice before loading onto polyacrylamide/7 M urea gels.

RNase H cleavage assays and determination of the cleavage points

RNase H (Ambion) cleavage assays (Díaz-Toledano R., NAR 2009) (Nadal A., JBC 2002) were carried out in the presence of different 20-mer DNA oligodeoxynucleotides with the same sequence as the microRNAs described above: miR-122 DNA (5'-TGGAGTGTGACAATGGTGTGTTTGT-3'), let-7b DNA

(5'-TGAGGTAGTAGGTTGTGTGGTT-3'). Kinetic assays were performed using the middle concentration of every DNA oligodeoxynucleotide (150 nM) up to 1 h.

Addition of a track of poly(U) or poly(X), either with specific terminal transferases of the new 3'-end products of RNase H or by cyclising those RNA products that present a new 5'-end with T4 RNA ligase, means we can use a complementary oligodeoxynucleotide to prime cDNA synthesis, followed by RT-PCR, cloning using pGEM[®]-T Easy (Promega) and Sanger sequencing analysis.

RNase T1 and RNase A cleavage assays

RNase T1 (Calbiochem) and RNase A (Ambion) digestion conditions for 100 cpm of HCV1-402 [32P]pCp 3'-end labelled fragment were 0.000 5 µg/µL and 0.000 1 µg/µL of enzyme, following protocols described previously by Díaz-Toledano, NAR 2009 (Díaz-Toledano CMLF 2014).

Dimethyl sulphate assays (chemical probing) and primer extension

Chemical modification was performed using DMS under denaturing conditions and following the procedures described by (Fernández-Miragall O. RNA 2003) and (Romero-López C. Nucleic Acids Research 2012) (Wells S.E. Methods in Enzymology 2000) (Brunel C. Methods in Enzymology 2000) but with some modifications: 1 µg of RNA was first denatured for 1 min at 90 °C and slowly cooled to room temperature with standard buffer, it was then incubated with 1 µL of DMS (freshly diluted 1:5 in ethanol) for 1 min at 20 °C in the presence of 2 µg of yeast tRNA (Ambion) as carrier in a 20 µL reaction volume, before finally stopping the incubation over ice. The methylated RNA was precipitated with 10% sodium acetate + glycogen at pH 5.2 and 2.5 vol. of ethanol, and then washed twice with 70% ethanol. The RNA was resuspended in 10 µL of water in preparation for primer extension analysis to detect the modified A and C residues.

DMS assays were performed in the presence of miR-122 after incubating folded RNA with miR-122, as described above.

Primer extension assays were performed using a 5' end-labelled 18-mer DNA oligodeoxynucleotide (5' GAACCGGACCGAAGCCCG-3') complementary to a sequence linked to a 3' end-labelled RNA-HCV1-402 (Wilkinson K.A. Nature protocols 2006). Extension reactions were carried out using 1 µg of methylated RNA with DMS and unmodified RNA in transcriptase buffer, 0.5 mM dNTPs, 5 mM DTT, 2 U RNasin and 10 U SuperScript[®] III RT (Invitrogen) for 1 h at 52 °C (based on Romero-López C.,

Nucleic Acids Research 2012). The enzyme was inactivated for 15 min at 70 °C, and the reaction loaded onto 10% polyacrylamide/7 M urea gel, in parallel to a sequence ladder performed with Thermo Sequenase™ Cycle Sequencing (USB).

Electrophoretic Mobility Shift Assays (EMSA)

HCV RNA fragments of different lengths were either internally labelled for use as migration control or unlabelled for use in the annealing reaction. The 5' end-labelled miR-122 or Let-7 RNA were used as probes. For non-denaturing gels, RNA pre-folding and incubation with miR-122 were performed as described by (García-Sacristán NAR 2014) (Díaz-Toledano NAR 2009). Samples were loaded in 0.8 mm thick gel and prepared with 6% polyacrylamide (acrylamide:bisacrylamide, 1:19), 50 mM Tris–Ac, pH 8.3 and 10 mM ammonium acetate. The gels were run at a constant amperage of 12 mA for 16 h (for miR-122 binding assays with different fragments of HCV-RNA) at 4 °C, and they were also autoradiographed.

Purification of 40S ribosomal subunit

40S ribosomal subunits were isolated from 1-2 g of HeLa cell pellets, following the method used by (Jan E. JBC 2002), but with several modifications: in cold conditions, HeLa spinner cells were washed in 10 vol. (with respect to pellet volume) of isotonic buffer (35 mM Hepes/KOH at pH 7.6, 146 mM NaCl, 11 mM glucose and protease inhibitors) at 1500 rpm for 5 min and 4 °C. The supernatant was removed by vacuum aspiration and the cell pellets were then incubated in 1.5 vol. of hypotonic buffer (20 mM Hepes/KOH at pH 7.6, 1 mM DTT, 1.5 mM magnesium acetate, 10 mM KCl and protease inhibitors) for 20 min at 4 °C. Cells were lysed over ice using a Dounce homogeniser (25 strokes). S10 buffer (100 mM Hepes/KOH pH 7.6, 25 mM DTT, 20 mM magnesium acetate, 600 mM KAcO and protease inhibitors) was added to the lysate and the mixture centrifuged at 10,000 xg for 10 min at 4 °C to remove debris. The supernatant (S10 fraction) was layered on sucrose cushion buffer A (20 mM Tris–HCl at pH 7.5, 6 mM magnesium acetate, 500 mM KCl, 1 M sucrose and 2 mM DTT) and centrifuged at 42,000 rpm for 4 h at 4 °C using a 70.1 Ti fixed angle rotor in a Sorvall centrifuge (Beckman) to obtain pellets with ribosomes. The ribosome pellets were resuspended in buffer B (20 mM Tris–HCl at pH 7.5, 6 mM magnesium acetate, 150 mM KCl, 100 mM sucrose, 2 mM DTT), treated with 4 mM puromycin to release the ribosomes from mRNA and salt washed with 0.5 M KCl. The dissociated ribosomal subunits were then

separated on a 10–30% (w/w) sucrose gradient by centrifuging in a SW41 swinging-bucket rotor (Beckman) at 28,000 rpm for 17 h and 4 °C. Fractions containing the 40S and 60S subunits were detected at 260 nm, pooled, concentrated, dialysed in buffer C (20 mM Tris–HCl at pH 7.5, 0.2 mM EDTA, 10 mM KCl, 1 mM MgCl₂, 1M sucrose and 1 mM DTT) using Amicon Ultra 10K and 50K (40S and 60S respectively) filter units and stored at –80 °C. The purity of the 40S and 60S subunits was examined by detecting rRNA using ethidium staining in agarose gel.

40S:HCV-RNA complex formation assays

0.6 nM HCV-RNA substrates were folded in standard buffer as before, but this time supplemented with 4 mM magnesium acetate instead of 10 mM. The HCV RNA was then either incubated alone or in the presence of 15, 150 and 1500 nM of miR-122 for 20 min at 37 °C before adding 40S subunits at a concentration of 15 nM in RNase P buffer. RNA-40S complexes were mixed with a loading buffer containing neither Mg²⁺ nor yeast tRNA and then loaded in 0.8 mm thick native gel with 4% polyacrylamide and TBM 1X buffer (34 mM Tris-base, 57 mM HEPES, 0.1 mM EDTA and 2.5 mM MgCl₂). The gels were run for 3 h at a constant amperage of 12 mA at 4 °C, and also autoradiographed (based on Lorsch J.R. EMBO J. 1999).

Thermodynamic assays

In order to evaluate the dissociation constant (K_d) of different fragments of unlabelled HCV-RNA (10 nM) bound at increasing concentrations of 5'-end-labelled miR-122 (0.04-50 nM). EMSAs were performed in the same way as were described above. Different HCV-RNA:miR-122 complexes were quantified by ImageQuant™ analysis, K_d values were calculated from hyperbolic curves plotted with SigmaPlot 8.0 software and data points were fitted to Klotz plots (semi-log plot) using GraphPad Prism 5 software. (Colas A., “Theory of Binding Data Analysis” Chapter 7. Invitrogen or Life Technologies) (Goodrich J.A., “Binding and Kinetics for Molecular Biologists” Cold Spring Harbor Laboratory Press. 2006)

Kinetic assays

The observed rate constant (K_{obs}) was measured using different fragments of unlabelled 0.6 nM HCV-RNA in order to follow the complex formation with 5'-end-labelled miR-122 (25 nM) over time in native gels. A plot of K_{obs} versus total free concentration of miR-122 gave a hyperbolic curve with the equation:

$$[\text{Complexes}] = [\text{complexes}_{\text{max}}] * (1 - e^{-k_{\text{obs}} * t})$$

K_{obs} was determined and plotted using SigmaPlot 8.0 software. (Goodrich J.A., “Binding and Kinetics for Molecular Biologists” Cold Spring Harbor Laboratory Press. 2006)

Quantification

Product bands in every gel were scanned in a PhosphorImager™ (Storm 820, GE) and quantified with ImageQuant™ 5.2 software (GE).

Results

1- Structural effects of the IRES flanking regions and miR-122 on HCV RNA₁₋₅₇₀ binding to 40S salt-washed ribosomal subunits.

HCV₁₋₅₇₀ resolved in two pre-initiation complexes using native gel electrophoresis.

Initial binding experiments involved the first 570 bases of HCV RNA using Electrophoretic Mobility-Shift Assays (EMSA). At the top of **Fig. 1** (ahora esta en la figura 17, falta cambiar) is a schematic drawing of the secondary structure of *RNA₁₋₅₇₀*. The autoradiogram in **Fig. 2A** shows that purified 40S ribosomal subunits (0.5 to 180 nM) bound efficiently to 0.6 nM of *RNA₁₋₅₇₀* as a substrate, producing two differentially migrating bands. The complex which migrated most rapidly was designated *F* and the slowest one *S* (indicated to the right of the lanes showing 40S-incubated RNA). 50% of the *F* complex was formed at 5–10 nM 40S and reached nearly 60% of the total count at the end of the reaction, while the reaction only produced about 20% of the *S* complex and required three times more 40S ribosome (**Fig. 2B**). After this unexpected result, we wanted to assess whether both product bands were preserved in shorter transcripts lacking either the 5' (*RNA₄₄₋₅₇₀*) or 3' (*RNA₁₋₄₀₂*) flanks of the IRES (**Fig. 1B**). Both, *F* and *S* bands were present in the two new transcripts (**Figs. 2C and E**), albeit in an inverse proportion in relation to *RNA₁₋₅₇₀*: *F* represented 20% in *RNA₁₋₄₀₂* and was less than 5% in *RNA₄₄₋₅₇₀* (**Figs. 2D and F**). Summing the intensity of both *F* and *S* complexed bands for each of the three transcripts *RNA₁₋₅₇₀*, *RNA₁₋₄₀₂*, and *RNA₄₄₋₅₇₀*, 50% of binding was reached at a concentration of 5–10 nM, 15 nM, and 15–30 nM of 40S, respectively. This indicated that *RNA₁₋₅₇₀* was the best substrate of the three for 40S ribosome (**Figs. 2 B, D and F**).

A set of control probing experiments were performed to rule out the possibility that the RNA contained in the *F* complex was a degradation sub-fragment of the RNA in *S*, (**Fig. S1a (Falta)**) and to measure the specificity of the 40S binding reactions (**Fig. S1b**).

miR-122 and let-7b effects promote 40S binding to RNA₁₋₅₇₀

Next, 0.6 nM of *RNA₁₋₅₇₀*, *RNA₁₋₄₀₂*, and *RNA₄₄₋₅₇₀* were incubated with increasing concentrations of miR-122 fragment (1.5–150 nM) to determine whether it could facilitate or impair 40S binding. In the absence of 40S, mixtures of *RNA₁₋₅₇₀* with increasing concentrations of miR-122 gave products which migrated slightly more slowly than the starting material as a consequence of miR-122-binding to RNA substrate sites (**Fig. 3A, lanes 4-6**), as described above. In the presence of 40S, the *S* band increased its intensity by around 15% with increasing concentrations of miR-122 while the *F* band was mostly unaffected (**Figs. 3A and B**). This indicates that the *S* band does not derive from the *F* band, but that it is formed directly from the unbound substrate. These data are the results from two different 40S purified extracts with a triplicate binding and gel shift analysis for each of them. Unlike complexes with *RNA₁₋₅₇₀*, the intensity of complexed bands of *RNA₁₋₄₀₂* and *RNA₄₄₋₅₇₀* were not affected by miR-122, except in the lanes with the highest miR-122 concentrations where some irregularities could be observed in repeated experiments (**Figs. 3C to D**).

A control reaction was performed using the cricket paralysis virus (CrPV) IRES (positions 1 to 185 nt), which is known to bind 40S, so that we could eliminate the possibility of miR-122 having a direct influence on 40S (**data not shown**).

From the foregoing results, it seems reasonable to conclude that the two IRES flanking domains are involved in the efficient recognition of *RNA₁₋₅₇₀* by 40S, in the predominance of the *F* band in the *RNA₁₋₅₇₀* complex as well as in the capacity of miR-122 to promote the *S* band.

Let-7b, whose binding site locates 3' to the IRES, but which has no binding site on the 5' IRES flank and was shown to be incapable of switching *RNA₁₋₅₇₀* from C to O forms, was also tested in a 40S binding assay. While it had no effect on the *S* band, it promoted the *F* band slightly (6%) (**Figs. S2A and B**).

Electrophoretic properties of the fast and slow binary complexes correlate with those of the closed and open conformation of free RNA₁₋₅₇₀.

We have previously shown that in native gels RNA_{1-570} in the C conformation migrates faster than in the O conformation (Díaz-Toledano, NAR 2009). We have also observed strict Mg^{2+} dependence on the ratio of C to O forms, either in the presence or absence of miR-122, with the C form being favoured by the presence of Mg^{2+} , as described in Figure X of Sacristan A et al., NAR 2015. Here we have evaluated how Mg^{2+} affects the ratio of RNA_{1-570} F and S complexes, either in the presence or absence of miR-122. In both cases, increasing Mg^{2+} concentration decreased the intensity of the S band and increased that of the F band. This effect occurred between 2 and 4 mM Mg^{2+} in the absence of miR-122 and was delayed to between 4 and 6 mM Mg^{2+} in the presence of miR-122 (**Fig. 4**).

The data in the previous section also provided a good correlation between the mobility of the RNA_{1-570} C and O forms and the intensity of the F and S bands produced by its binary complex because: (i) the section of RNA_{1-570} which carries the two flanking IRES sequences required to stabilise the C form is the fragment length in which only the F band clearly predominates; (ii) miR-122, which was shown to promote the O form in RNA_{1-570} , also promotes the S complex band.

Sucrose gradient sedimentation profiles of RNA_{1-570} and RNA_{44-570} with 40S subunits and protection patterns.

RNA_{1-570} and RNA_{44-570} binding to subunit 40S was analysed on sucrose gradients as described previously (Lytle A.R., RNA 2002). These transcripts were chosen because of their similar length and differential capacity to adopt the C conformation. RNA_{1-570} was also tested in the presence of miR-122. After collecting fractions from the sucrose gradient and measuring the radioactivity, the 40S: RNA_{1-570} profile revealed just a single peak (fractions 18 to 21). The peak including fractions 27–30 at the top of the gradient coincides with the position of the RNA_{1-570} transcript centrifuged alone (**Fig. 5**). Peaks for 40S: RNA_{44-570} and 40S: RNA_{1-570} + miR-122 were located in the same fractions as for 40S: RNA_{1-570} (**Fig. 5**). This indicates that the two complex bands detected by EMSA, F and S, are two conformations of the same complex. In particular, it rules out the possibility of a complex comprised of two 40S subunits bound to a single RNA transcript.

In another experiment, 40S: RNA_{1-570} and 40S: RNA_{44-570} complexes were treated with a high concentration of RNase A (**Fig. 6A**) Following digestion and sucrose gradient centrifugation, the fractions from the gradient containing each complex's radioactivity peak were pooled. The protected and labelled RNA

fragments from each complex were isolated and subjected to electrophoresis on a denaturing 15% polyacrylamide gel (**Fig. 6B**). The protected patterns of *RNA*₁₋₅₇₀ and *RNA*₄₄₋₅₇₀ were equivalent to the one described by Lytle and Robertson (RNA 2002), who provided a nucleotide sequence for each protected band by subjecting them to RNase T1 fingerprinting and secondary RNase analysis. Some of the most predominant protected products of *RNA*₁₋₅₇₀ and *RNA*₄₄₋₅₇₀ were common to both RNA fragments and others unique to each fragment or protected with different intensities. *RNA*₁₋₅₇₀ slightly protected the right strand of stem-loop II, the basal left and right strand of domain III and the pseudoknot, but it protects the basal left strand with a greater predominance than *RNA*₄₄₋₅₇₀. However, *RNA*₄₄₋₅₇₀ presented more pronounced protection of the right strand of domain III and the pseudoknot (**Fig. 1**), as well as the right strand of domain II, and it was unique in its protection of the left strand of domain II.

2- Map and biophysical properties of miR-122 binding sites in *RNA*₁₋₅₇₀.

A new miR-122 tandem binding site at the 3' flank of the IRES.

We analysed miR-122 binding to *RNA*₁₋₅₇₀, *RNA*₁₋₄₀₂ and *RNA*₄₄₋₅₇₀, and to some shorter fragments, *RNA*₁₋₃₇₀, *RNA*₄₄₋₃₇₀ and *RNA*₄₄₋₃₁₂, by EMSA. We then titrated the miR-122 binding to *RNA*₁₋₅₇₀ between a ratio range of 1:0.003 to 1:0.03, before choosing the lowest ratio that provided a signal for the next set of experiments. Binding reactions were performed using 40 nM of unlabelled RNAs. Labelled free RNA fragments (**Fig. 7B**, lanes 1–6) were used as electrophoretic mobility size markers and their unlabelled forms (**Fig. 7B**, lanes 7–12) as targets for γ -³²P-miR-122 binding. Four replicas were obtained with high reproducibility. According to expectations *RNA*₄₄₋₃₁₂, comprising the most central region of the six fragments tested and pictured in **Figure 7A**, did not form any complexes, while interestingly the other HCV RNA fragments, including those lacking the IRES 5' flank (domain I), i.e., *RNA*₄₄₋₃₇₀ and *RNA*₄₄₋₅₇₀, were still able to form complexes with miR-122 and at significant ratios (**Fig. 7B**). The percentage of binding to HCV RNAs which either contain (*RNA*₁₋₅₇₀, *RNA*₁₋₄₀₂ and *RNA*₁₋₃₇₀) or lack the IRES 5' flank (*RNA*₄₄₋₃₇₀ and *RNA*₄₄₋₅₇₀) showed that the presence of domain I increased the ratio of binding, but surprisingly by no more than 20% in comparison with those that did not contain the 5' region (**Fig. 7C**). Since miR-122 binding to central domains II and III of the HCV IRES found between positions 44 and 312 was negligible, then these results indicate that the 3' flank region of IRES is a binding region for

miR-122. This binding region could be further delimited to position 402, because the RNA_{1-402} fragment was the one retaining the maximum amount of miR-122. This sequence extends to the middle of stem-loop in domain V.

HCV conformations and miR-122 binding

Besides RNA_{1-570} being the largest fragment to contain all possible miR-122 binding sites, it also binds miR-122 to a lesser extent than its corresponding 3' end-shortened fragments – RNA_{1-370} and RNA_{1-402} – by 13% and 18%, respectively. This suggests that it is the C conformation adopted by RNA_{1-570} that hinders miR-122 binding. This observation can be attributed to the need for miR-122 to compete with long-range annealing (LRA) of the IRES flanking sequences, so that miR-122 can anneal to the 5' IRES flank. These quantitative measures together with results from previous sections imply that the 3' flank and the conformational status of the RNA fragment both contribute to the total miR-122 binding to RNA_{1-570} .

Qualitatively, the band migration patterns corresponding to each miR-122:RNA complex (**Fig. 7**, lanes 8–12) showed a subtle upward shift in mobility with respect to their corresponding RNA fragments, as expected. Nevertheless, the number of shifted bands for each RNA cannot be used to make a direct estimation of the number of binding sites for miR-122, because the same complex could be resolved in different band shifts as it might adopt different local or global conformations. Whatever the case may be, the miR-122: RNA_{1-570} band shift is very subtle compared to that of RNA_{1-570} . From our previous experience, C and O forms are separated clearly. The most intense band of miR-122: RNA_{1-570} runs faster than that of RNA_{1-402} ; this indicates that RNA_{1-570} + miR-122 is still in the C form. Therefore, this suggests that at the HCV RNA and miR-122 concentration ratios employed in these experiments, the miR-122 fragment bound predominantly at the 3' flank of the IRES.

miR-122 sequences involved in binding.

Using the same methodology as described above, we next analysed the binding of the seed sequence of miR-122 on its own (seed-122) and the miR-122 sequence in which all nucleotides of the seed sequence were mutated (mut-seed-122). The same set of HCV RNA fragments as before were tested using EMSA (**Figs. 7D and E**). As with the case of miR-122, neither of the probes bound to RNA_{44-312} , indicating that all binding could be attributed to the 5' or 3' IRES flanking sites. Seed-122 bound to RNA_{1-570} , RNA_{1-402}

and RNA_{1-370} , in agreement with published results, but did not bind detectably to RNA_{44-370} and RNA_{44-570} (**Fig. 7D**). Thus the presence of the seed-122 sequence is enough for recognition of the 5' IRES flank binding sites in domain I of HCV but not for binding to the 3' flank of the IRES. Mut-seed-122 was able to bind to RNA_{1-402} but not to RNA_{1-370} ; this implied that the short region found between positions 370 and 402 might anneal with miR-122 independently of its seed sequence. However mut-seed-122 binding was eliminated in RNA fragments with an extended 3' end RNA_{44-570} and RNA_{1-570} , forming stem-loops V and VI (**Fig. 7E**). This was interpreted as binding of miR-122 to the 3' IRES flank in RNA_{1-570} transcripts as being dependent on the seed sequence and no-seed regions of miR-122.

Rate of complex formation of the new tandem sites at the 3' IRES flank.

For a more detailed analysis of the relative contribution of the 3' IRES flank in terms of miR-122 interaction, the binding affinities for the complete RNA_{1-570} and RNA_{44-570} fragments which lacked the binding sites in the 5' IRES flank were determined and compared. RNA_{1-402} was also included in this analysis because akin to RNA_{1-570} it contains both IRES flanks, but unlike RNA_{1-570} it cannot circularise (**Fig. 1A**).

Results from several experiments covering three different parts of the concentration range were combined, HCV RNAs were unlabelled and miR-122 was 5' end radiolabelled. The semi-log plot in **Figure 8** represents the values for one experiment. The experiment was performed in triplicate for the central part of the curves and for the whole curve of fragment (44–570) containing the new 3' tandem binding site. Curves fitted well using a four-parameter sigmoidal model with Kds of 7.17 nM ($R^2:0.98$), 12.14 ($R^2:0.98$) and 68.69 ($R^2:0.99$) for RNA_{1-402} , RNA_{1-570} and RNA_{44-570} respectively.

The dissociation constant for the RNA_{44-570} :miR-122 complex was one order of magnitude higher than for the RNA_{1-402} :miR-122 complex. Nevertheless, the difference between Kds for RNA_{44-570} :miR-122 and RNA_{1-570} :miR-122 was reduced by half. Thus, the tandem sites in the 5' IRES flank were the major contributors to binding stability when the RNA was in the open conformation, but their relative contribution decreased when the RNA presented the closed conformation. This concurs with the observation that in the C conformation the 5' IRES flank miR-122 target sites are stabilised in a dsRNA element forming LRA. This deviation is accentuated in the parameter B_{max} , which reflects the total complex formation at saturation, with the RNA_{1-402} : RNA_{44-570} ratio being 1.26, while the RNA_{1-570} : RNA_{44-570}

ratio is 1.05. Thus, at miR-122 saturation, binding to the 3' IRES flank represents the major contribution to total binding. Hill plots for the RNA fragments provided values slightly higher than 1 for the three RNA fragments: 1.07 ± 0.03 ($R^2:0.98$), 1.11 ± 0.11 ($R^2:0.98$) and 1.05 ± 0.057 ($R^2:0.95$). Taking into account the error values, our data suggest that if any binding cooperativity occurs, then its relevance is low.

Kinetic analysis of miR-122 binding on different lengths of RNA transcript

It is well known that the efficacy of antisense RNAs and siRNA in living cells is related to *in vitro* annealing kinetics and that structural differences have a profound effect on the kinetics of RNA-RNA interactions. Accordingly, the kinetics for miR-122 binding to the three HCV RNAs analysed previously before were determined. Two sets of time points were obtained, for short (up to 15 min) and long (up to 45 min) reaction periods, and combined to obtain the complete curve. The values of K_{obs} for the truncated RNA_{1-402} and RNA_{44-570} fragments (**Fig. 9**) were 5.14 and 8.78, respectively. It is evident that there was rapid production of RNA:miR-122 in the first minute and a plateau was reached after 10 mins. Interestingly there was a significant decrease in the complex formation rate ($K_{obs}:0.81$) for the entire RNA_{1-570} fragment, taking around 20 min to near the plateau (**Fig. 9**). This suggests that miR-122 competes with LRA and gives rise to the reduced rate of kinetics for RNA_{1-570} .

The plotted data were fitted to a hyperbolic equation: $Y = Y_{max} (1 - e^{-K_{obs} x})$, where Y is the complex concentration (HCV RNA+miR-122) and Y_{max} is the complex's maximum concentration.

3- Enzymatic and chemical probing evidenced a tandem binding region for miR-122 within the 3' IRES flank. Precise sequence assignment of a new binding site, S4.

Comparative analysis of DMS treatment and RNases A and T1, partial digestion of RNA_{1-402} alone or pre-incubated with miR-122 or Let-7 RNA.

Base pairing of miR-122 to target HCV RNA may help to protect the HCV sequences involved in such contacts from digestion by single-stranded ribonucleases or modification by specific chemicals reagents. Direct determination of the protected bases was performed using 3' end-labelled RNA_{1-402} with [5'- ^{32}P]pCp and unlabelled miR-122 or micro-RNA let7b. Instead of the large RNA_{1-570} fragment, we used RNA_{1-402} to identify cleavages at base resolution based on the closer proximity of its 3' labelled end to the

putative miR-122 binding sites. Either with or without the addition of microRNAs miR-122 and Let-7, RNase A and T1 cleavage products were examined directly in denaturing polyacrylamide gel (**Fig. 10**). There were changes in reactivity at several positions, mostly bracketing between x-y and y-z for miR-122, or i-o for Let-7b. In the case of miR-122, DMS was also employed and probing modification products were visualised through primer extension analysis (**Fig. 11**). Changes were located specially at positions x-y with a lower intensity variation at position n-m.

These results confirm previous observations based on SHAPE analysis for an miR-122 target region detected overlapping the AUG start codon and also unveil a new neighbouring target site downstream, which we shall call S4. These two regions constitute a tandem binding site in the 3' IRES flank. To distinguish between the region containing the tandem S1 and S2 sites on the 5' IRES flank and that containing the tandem S3 and S4, we will refer to them as the proximal target site or S1/S2 and the distal target site or S3/S4.

For microRNA let7b, it should be noted that besides the highly overlapping recognition regions between miR-122 and let-7b at S3, they also present a different protection pattern.

Mapping miR-122 binding sites using RNase H in RNA₁₋₄₀₂ and RNA₁₋₅₇₀ and sequencing of the target sites.

We tried to collect further evidence of new miR-122 target regions using hybridisation to a DNA oligonucleotide (*d*)miR-122 (which has an identical sequence to miR-122) and RNase H cleavage of DNA:RNA hybrids predictably formed. To this end, *in vitro* RNA transcripts were internally labelled with [α -32P]GTP, or labelled at their 5' end with [γ -32P]GTP or their 3' ends with [α -32P]pCp during transcription. These hybrids were cleaved and then the migration products for the distinctly labelled products were studied with electrophoresis. This allowed us to determine that the main cleavages occurred at two separate regions in both RNA₁₋₅₇₀ and RNA₁₋₄₀₂. One of the cleavage regions was located near the 5' end in both RNA fragments, as expected for S1 and S2 binding sites. The others reside near the 3' end in the case of RNA₁₋₄₀₂ (where two nearby cleavages can be differentiated: a strong and a mild one), or at $\sim 2/3$ of the sequence length within the RNA₁₋₅₇₀. **Figure 12b** shows a linear schematic drawing of RNA₁₋₅₇₀ and RNA₁₋₄₀₂ indicating the observed cleavage products. PolyA or polyU tails were added to the 3' end of the major RNA cleavage products P1, P2, P3, P4 and P5 in order to generate a template for

the cDNA synthesis primer, this was then amplified by cPCR and the DNA fragments sub-cloned and sequenced (**Sup Fig. Falta**). It was observed that cleavages sites at the 3' IRES flank were located between x-y, corresponding to the S3 site observed previously, and between z-w, representing the new S4 site. For both *RNA₁₋₅₇₀* and *RNA₁₋₄₀₂*, the commonest position for cleavage sites in the sequenced clones corresponded to S4, at a 10:1 ratio with respect to S3, suggesting that S4 cleavage site was favoured by the RNase H cleavage region.

Specificity of the protection pattern to RNases T1 and A, and specificity of cleavage by RNase H

The effect of different concentrations of miR-122 and let-7 on the RNase T1 and A protection patterns and the RNase H cleavage pattern were assayed in order to provide evidence of the observed protection's specificity.

RNA₁₋₄₀₂ transcripts were pre-incubated with increasing concentrations (1.5, 15 and 150 nM) of miR-122 or let-7b, then partially digested with RNase T1 or A. All bases previously seen to change their sensitivity to RNase A or T1 in the presence of miR-122 and let-7b at 15 nM were observed to respond to miR-122 variations in a “dose-response” manner (**Fig. 13, panels A and B**). Additional bases in the region around the AUG were identified as reactive or protected at the highest concentration of microRNAs, see **Figure 13, panels A and B**, i.e., positions x-y, w-z and a-b. These were compatible with the S3, S4 and let-7b, respectively, binding sites observed previously.

RNase H activity was tested in both *RNA₁₋₅₇₀* and *RNA₁₋₄₀₂* (**Fig. 13, panels C and D**). The main cleavages of *RNA₁₋₄₀₂* were completed at the lowest (*d*)miR-122 concentration tested, while a gradual increase in cleavage was demonstrated in *RNA₁₋₅₇₀*. This means that *RNA₁₋₅₇₀* is clearly more resistant to RNase H at both proximal and distal target regions than *RNA₁₋₄₀₂*. In fact, 100 times more (*d*)miR-122 or (*d*)let-7b had to be added to the *RNA₁₋₅₇₀* cleavage reaction to reach approximately the same amount of cleavage as for the case of *RNA₁₋₄₀₂*. This in turn suggests that resistance to cleavage was due to an increased difficulty for (*d*)miR-122 to anneal to its target sites in *RNA₁₋₅₇₀* rather than steric hindrance of the enzyme in the larger fragment. Secondly, several other product bands were present at the highest (*d*)miR-122 or (*d*)let-7b concentration; these probably corresponded to secondary cleavages in the case of (*d*)miR-122 or hybridisation at other sites in the case of let-7b. These bands were not considered further.

The cleavage pattern for (*d*)let-7b was compared to that of (*d*)miR-122 in both *RNA*₁₋₄₀₂ and *RNA*₁₋₅₇₀ (Sup. Fig. 4). In *RNA*₁₋₅₇₀, a major band product was promoted by increasing the size of (*d*)let-7b, by about 350 bases, which had the expected size; this has a size in between of the two (*d*)miR-122 promoted cleavages around 340 and 380.

4. Probing the effect of miR-122 and let-7b on the tRNA-like domain of HCV RNA

Human RNase P specifically recognises a minimal fragment domain of 110 nt sequence around the AUG start codon and the pseudoknot, although at a lower efficacy than when the substrate is the whole IRES. The 5' half of this sequence was shown to be involved in the formation of the binary complex 40S:*RNA*₁₋₆₄₅ (Lytle et al. 2002). Only half of the counts protected in the F complex corresponded to this area, whereas in the S complex nearly all the protected counts were in this region. Therefore, the correlation between (a) RNase P's capacity to recognise the structure of this sequence in different conditions (presence or absence of microRNAs and different length fragments), and (b) the different forms adopted by these transcripts in the S or F forms, may provide information about this key motif in pre-initiation.

We used *in vitro* transcripts *RNA*₁₋₄₀₂, *RNA*₁₋₅₇₀ and *RNA*₄₄₋₅₇₀ to examine the effect of miR-122 and let-7b on the tRNA-like domain of HCV RNA. We coupled miR-122 at three different concentrations, 1.5, 15 and 150 nM, with three pre-tRNA cleaving activities in non-saturating conditions (Fig. 14). These activities were: human RNase P activity purified from HeLa cell extracts, RNase P ribozyme from cyanobacterial *Synechocystis sp.* transcribed *in vitro*, and the *E. coli* RNase Z purified from a recombinant source (Fig. S5). It has been shown that RNase P specifically cleaves HCV RNA near the authentic AUG start codon, while this work has purified and analysed RNase Z for the first time to determine whether it also cleaves specifically in the same region (Figs. S6A and B).

To control the effect that miR-122 itself might have on each of these activities, parallel reactions were performed with a standard substrate in the absence or presence of miR-122 at the same concentrations: *E. coli* pre-tRNA^{Tyr} (131 nts long) was used as the standard substrate for both RNase P activities and pre-tRNA^{Leu} (235-nts long), extracted from *B. Subtilis*, was used for RNase Z. The results are presented as histograms in Figure 15. The first group of bars in each panel corresponds to the control. We assumed that the activities were not modified by the presence of miR-122. 4.1. *miR-122 effects on tRNA-like recognition in fragment RNA*₁₋₅₇₀

The second group of bars in each panel of **Figure 15** shows that increasing miR-122 concentrations led to a direct increase in inhibition for both RNase P activities on RNA_{1-570} (panels a and b). Inhibition was complete for the *Synechocystis sp.* RNase P ribozyme reaction at the highest miR-122 concentration, whereas the effect was less pronounced for the human RNase P reaction. A slight stimulatory effect was observed for RNase Z. The amount of miR-122 required to inhibit half of the cleavage activity in the RNA_{1-570} reactions was x and y nM for human RNase P and RNase P ribozyme respectively. These results indicate that the elements in RNA_{1-570} , whether they are the tRNA-like motif, its tertiary structure or both, are modified by the binding of miR-122.

4.2. Conformational effects

RNA_{44-570} mimics the conformational effect of miR-122 binding at S1 and S2, concerning the issue that it has impeded the possibility of forming LRA. Compared to RNA_{1-570} , both human and cyanobacterial RNase P revealed a similar and considerable reduction in activity (**Figs. 15A and B**). RNase Z showed a mild reduction (**Fig. 15C**). This serves as a clear indication that structure-dependent nucleases in the closed conformation have a conformational preference for the tRNA-like motif.

4.3. miR-122 direct effects.

To evaluate the direct structural effects of miR-122 binding on tRNA-like recognition, the activities of the structural nucleases RNA_{44-570} , RNA_{1-402} and RNA_{1-370} with impeded LRA were compared in the presence of increasing concentrations of miR-122. Only a slight augmentation of RNase P activity was observed in RNA_{44-570} at the highest miR-122 concentration, while a slight inhibition was seen for the ribozyme and RNase Z activities. Unexpectedly, these effects were significantly increased in RNA_{1-402} as well as in RNA_{1-370} (**Fig. 15**). RNA_{1-370} was not tested with human RNase P because the fragment is shorter than the minimum size of substrate required for this enzyme. Thus, while binding to S3 and S4 alone seems to have a minimal impact on the tRNA-like motif, this effect is amplified by the presence of HCV domain I.

4.4. Let-7b effects.

In another set of reactions, let-7b's effect on the three activities was tested in RNA fragments RNA_{1-402} and RNA_{1-570} (**Fig. falta**). It has been proposed that let-7b binds in a region which mostly overlaps with the S3

region. We first used an RNase III assay to rule out the possibility that let-7b could alter LRA thus promoting the “C” to “O” conformational transition, as does miR-122 (**Sup. Fig. falta**). let-7 inhibited the cleavage of *RNA₁₋₄₀₂* and *RNA₁₋₅₇₀* by RNase P ribozyme and RNase Z activities to a similar degree as miR-122. Transcript let-7 also enhanced cleavage of *RNA₁₋₄₀₂* by human RNase P to a similar extent as miR-122. Distinct from our results for miR-122, let-7b did not inhibit cleavage of *RNA₁₋₅₇₀* by the human RNase P. This marked difference between let-7b and miR-122 on the RNase P could be attributed to let-7b's inability to disrupt the “C” conformation. This agrees with the effect that miR-122 binding at S1 and S2 has on tRNA-like structure recognition, through a conformational switch.

4.5. Specificity tests

Three mutant miR-122 sequences, carrying 1, 2 or 3 substituents in the middle of the seed sequence (described in footnote accompanying **Figure 16**), together with a wt miR-122 sequence were compared for RNase P cleavage accessibility of *RNA₁₋₅₇₀*. We used 15 nM of each mutant and the wt probes. Starting with the P ribozyme reaction, we observed that increasing the number of mutations within the miR-122 sequence counteracted the inhibitory effect of miR-122 and eventually abolished it in the case of the most mutated miR-122 sequence (mut 3) (**Fig. 16B**). The results for human RNase P of miR-122 with mutations in its seed sequence caused a similar reversion of cleavage inhibition as did the P ribozyme reaction; however, the cleavage products of mutant 3 were divided into two bands - one with typical electrophoretic mobility and a second band with a slower migration pattern (**Fig. 16D**). The new bands showed only a slight difference in migration in the gel, but they were more intense. We concluded that both bands corresponded to the same motif recognition, altered in the case of the by the presence of mutated miR-122. (**Falta la descripcion de las Figs. 16A y C**).

5. miR-122 destabilises binding of stem loop IV, whereas let-7b does not.

The stability of the stem of domain IV was demonstrated to be inversely related to the translational activity of HCV IRES (Honda and Lemon) and so it reasonable to test whether miR-122 or let-7b binding might destabilise the stem by hijacking base-pairing from the right stem's chain. Firstly, three consecutive 20-mer antisense oligodeoxynucleotides (ODN) (designed from the 339 to 390 region, where microRNAs miR-122 and let-7b bind), were individually assessed, at concentrations of 15, 150 and 1500 nM, to

analyse their effect on the accessibility to ODN-319 when used as a probe to target the left strand of stem IV in an RNase H assay. *RNA*₁₋₅₇₀ is not accessible to ODN-319, as noted in both gel shift analysis and RNase H assay (Lyons et al.). Here we observed that the presence of ODN-339 increased the accessibility to ODN-319, from uncleaved in the absence of ODN-339 to complete cleavage in its presence (data not shown). We also saw that this effect was suppressed/inhibited quickly (half cleavage was reached).

Subsequently, the accessibility to ODN-317 for both *RNA*₁₋₄₀₂ and *RNA*₁₋₅₇₀ (**Fig. 17D**) was determined in the presence of miR-122 by following a similar RNase H assay as mentioned earlier, and then titrated to exert its effect similar to ODN-339, but at a concentration 10 times lower. An identical effect was observed for *RNA*₁₋₃₇₀ (data not shown). As this shortened RNA fragment lacks S4, it implies that miR-122's effect was due to its binding to S3 and independent of S4's presence. Remarkably, transcript let-7b, whose binding site overlaps with that of miR-122 in S3, did not produce effects in parallel to those observed for miR-122 (**Fig. 17C**).

miR-122 had no effect on the stability of the upstream HCV-IRES pseudoknot between positions A₁₄₀-G₁₅₉ and C₂₉₃-C₃₃₃ (data not shown). We also determined that miR-122 facilitated cleavage by RNase H at target sites of ODNs 319 and 317, but not that of ODN-313; these sites, on ODNs 319, 317 and 313, disrupted the 7, 5 and 2 Watson-Crick pairs of stem IV, respectively. This suggests that, after binding to S3, miR-122 has a highly tuned role which specifically destabilises stem loop IV and exposes its left strand.

Direct effect of miR-122 on 40S binding

The above observations imply mechanistic differences between C and O RNAs in their interactions with 40S, but they may alternatively reflect direct effects of miR-122 in 40S binding. To address the second possibility, we examined the binding of the 40S subunit to *RNA*₁₋₅₇₀ mutants in the left strand of domain IV (**Fig. 18**). One of the mutants demonstrated a decreased stability in domain IV (*low stability*), while the other presented an increase in stability (*high stability*). Both mutants lacked an F band in the absence of miR-122. While in the presence of miR-122 the F band appeared in the *low stability* mutant, but not in the *high stability* mutant. Total 40S binding was similar in the wt and *low stability* mutants but was reduced in the *high stability* mutant. The binding profile for the *high stability* mutant was analysed by ultracentrifugation with sucrose gradient and provided the same result as ?.

Discussion

In this paper we have evaluated the effect of two different HCV IRES conformations, which differ in their sequence context modulated by miR-122, on the 40S ribosome binding process. We chose to limit our assay to pre-initiation of binary complex formation and just assay ribosome-protected fragments due to the highly complex nature of this first step. Nevertheless, we still benefited from results and models for the dynamics and structures involved in 40S binding to minimal-IRES sequences.

Two distinct stable 40S:*RNA*₁₋₅₇₀ pre-initiation complexes form *in vitro*.

We previously noted that HCV *RNA*₁₋₅₇₀ can adopt two different conformations, C and O, while miR-122 can compete with LRA and open the C form. Using native gel electrophoresis, a viral RNA fragment from positions 1 to 570 plus salt-washed and highly purified 40S ribosomes, we observed that two stable and distinct migration bands (F and S) coexist for the 40S pre-initiation complex, although in different amounts. Both complexes contained the intact fragments from RNA domains I-VI and they could not be distinguished as different peaks in density gradient centrifugation assays. This leads to the conclusion that the two bands discriminated in the non-denaturing gels are two conformers of the same complex, and not complexes containing additional 40S subunits. Other control experiments in addition to background literature led us to discard the possibility of 80S or ternary 40S+eIF3 complexes. Under our conditions the F and S forms are stable as they present sharp bands with little background in the intermediate gel region when evaluated by electrophoresis. We showed that the two forms correlate with two alternative base pairing arrangements on the substrate which are characteristic of the C or O conformations in the free RNA. The proportion of the F and S ribosomal-HCV complexes varied according to whether or not the viral RNA substrate was folded in conditions which favoured the C or O form of *RNA*₁₋₅₇₀ respectively. This result came from three different assays: 5' and 3' substrate truncation, miR-122 addition or Mg²⁺ concentration variation, and indicated that when LRA is impeded the complex mostly migrates as an S band and as an F band when it is favoured. Nevertheless, it is particularly noteworthy that even for the case in which annealing is impossible, e.g., the case of 5' or 3' IRES truncated fragments, then a low but reproducible proportion of complex migrates as the F form. Thus even though

LRA seemed a priori to be responsible for the complex's fast mobility, it later became clear that it was not an essential component for the compact conformation of the F form, as discussed below.

LRA favours the S form but is not an essential requisite

At least 80% of the free *RNA*₁₋₅₇₀ fragment, under our *in vitro* conditions, folds into the C conformation. This conformation provides a specific RNase III cleavage pattern which is clearly different from that of the O conformation. Using RNase III we have proven that when the RNA is either lacking the first forty 5' nts or in the presence of miR-122, then all populations of RNA molecules are present in the O conformation. Nevertheless, images of 40S binding on *RNA*₄₄₋₅₇₀ and *RNA*₁₋₄₀₂ that were unable to form LRA demonstrate that a percentage of the molecules were still in the F form. Thus, binding of the 40S ribosomal subunit might partially restore a closed-like conformation for the RNA fragment. Other interactions between IRES RNA domains distinct from LRA must be invoked to explain the predisposition for the C status. Studies using SHAPE or in-silico predictions describe several interactions between different IRES domains which might support the C status. If this is the case, then LRA would serve to stabilise the C conformation in a kind of overstabilisation by disulphide bonds in proteins.

Direct evidence for the two conformations and differences in HCV RNA protection.

We determined that 40S protects different positions on *RNA*₁₋₅₇₀ and *RNA*₄₄₋₅₇₀, giving rise to bands F and S respectively. This is direct proof of the presence of two different forms of the binary complex. Lytle and Robertson determined the sequences protected to RNase A of internally-labelled *RNA*₁₋₆₄₅. We previously commented that the concentration of Mg²⁺ used in their experiments provided an equimolar mixture of the RNAs in the C and O forms. Our current findings support those of Lytle and Robertson; the two forms we have exposed have two different protection patterns which, when combined, provide the pattern proposed by these authors. While in the F form, the 40S protected domain III; and while in the S conformation, two distant regions in the primary sequence were simultaneously protected, one in domain II and the other in domain III. Therefore viral RNAs and the 40S ribosome subunit have changed their respective locations during the F to S transition.

Effects of miR-122 on virus RNA binding and the conformational status of the consequent binary complex

Two phenomena were observed while carrying out experiments with miR-122. Firstly, the amount of S form increased in the presence of miR-122, but to a very limited extent, around ~ 15%. Secondly, this happened without decreasing the intensity of the major F form. Thus, while at the RNA level the O conformation proportionally increased at the expense of the C conformation by increasing miR-122 concentration, the 40S subunit disrupts this equilibrium displacement. Distinct possibilities could be proposed. If one considers the differential effect on 40S binding when LRA is disrupted by either deleting substrate binding sites S1/S2 or by competing with miR-122, then the most plausible possibility is that miR-122 binding to S1/S2 has a dual effect - it opens LRA, thus favouring 40S binding, but it alters other interactions which inhibit 40S binding in the S form. This could be due to local interactions proposed between the stem loop of domain I and a bulge in domain II. From experiments on the shortened 44-570 fragment lacking S1/S2, increasing miR-122 means we can eliminate the possibility that binding to S3/S4 inhibits the formation of the S conformation.

HCV-tRNA mimic fragments and 40S binding

The minimal tRNA-mimic fragment cleaved by human RNase P and the 40S ribosome binding site overlap in the region of the IRES pseudoknot and stem-loop IV. We evaluated three pre-tRNA processing activities which specifically recognise HCV tRNA-like structures and compared their activity on this element in order to examine its role in 40S binding. We tested whether the different IRES conformations required the tRNA-like motif to be recognised by these activities for it to be successfully recognised by 40S. We found that the three activities were able to distinguish between the different RNA substrate fragments -of different conformations- although not necessarily in an expected manner. The specific requirements by which each activity recognises a tRNA-like motif (i.e., cleavage polarity, structure determinants) may lead to important variations in the results, but they may also provide insights into the different conformations of the tRNA-like motif. For example, RNase Z, composed of a single small protein, might be less sensitive to steric effects than human RNase P, or the cyanobacterial RNase P ribozyme might suffer from electrostatic repulsion in larger RNAs. Another potential experimental complication was that different buffer conditions had to be used. Of the three activities tested here, human RNase P is the most

reliable for quantitative detection of the HCV tRNA-like motif because it uses similar buffer conditions as those for 40S binding, it consists of a large MW ribonucleoprotein and its minimal fragment substrate for HCV RNA is already known. Hence the discussion of the results is based on human RNase P activity and compared with the results for others activities.

Different conformations and sizes

We observed that tRNA-like motif recognition by human RNase P depended on the conformational status of the IRES and the presence of domain I. The latter observation was unexpected for two opposing reasons. Firstly because the domain I sequence is small, is located a long way from the tRNA-like sequence and there is insufficient evidence of interaction between domain I and the tRNA-like domain. And secondly because even though the presence of domain I has for a long time been known to inhibit translation, no structural explanation had yet been provided. Apart from the major occlusion of the tRNA-like domain in the O conformation, a lack of tRNA-like recognition in *RNA*₄₄₋₅₇₀ might be due to an excessive instability or because such a structure is stable but imperfect or sterically masked. Since RNase Z was able to cleave this fragment this may imply that the tRNA-like motif is still there, but its structure departs from the conformation adopted in the fragment *RNA*₁₋₅₇₀.

The fact that the HCV IRES can form two different structures which vary markedly in terms of tRNA-mimicry of the human RNase P ribonucleoprotein, as suggested above, may partly explain the different patterns of 40S binding on the C to O conformation transformation as well as the differential RNase A protection of the *RNA*₁₋₅₇₀ in the different conformations.

The effect of miR-122

The presence of miR-122 (15 nM) in the human RNase P reaction on *RNA*₁₋₅₇₀ provoked a similar cleavage reduction effect as the deletion of the 3' IRES flank, whereas in that given fragment (*RNA*₁₋₄₀₂), miR-122 slightly improved cleavage. While this may indicate that once the RNA has opened then miR-122 favours cleavage, it could also be interpreted that miR-122 binding to S1/S2 opens and decreases cleavage, while binding at S3/S4 favours it.

A model

Our investigation indicates that the global IRES in the C form displays the property of providing determinants and anti-determinants for both domain III 40S binding (while preventing domain II interaction) and facilitates dynamic structural changes of RNA from C to O conformations in the presence of miR-122 so that it may adopt the 40S binary complex.

Results elsewhere in the literature which are likely to play an important part in interpreting our results are: (i) only domain III, and not domain II, is a requisite for 40S binding; (ii) FRET experiments indicate that there is just a single way in the pre-initiation complex followed by dynamic conformational changes in minimal IRES; (iii) domain II not only bends but also rotates with respect to the central axis, so that it can align itself in parallel to the right strand of domain III; (iv) domain II is involved in tertiary interactions which induces a conformational change in 40S; and (v) miR-122.... A model of 40S interaction that accounts for these different experimental observations is summarised. The two alternative conformations are presented schematically.

Because domain II's access to the ribosome is impeded by the closed conformation adopted by RNA and since the RNA is initially in this C conformation, then domain III is the primary determinant for initial association. Breathing of LRA from C to O, or active competition for LRA by miR-122 opens the C conformation, allowing S to form - although at a lower proportion than when LRA strands are deleted. When LRA is disrupted, as is the case of *RNA*₄₄₋₅₇₀ and especially *RNA*₁₋₄₀₂, the slow form of the binary complex, despite its reduced molecular weight in comparison with the fast form of *RNA*₁₋₅₇₀, suggesting that the remarkably reduced gel mobility of the slow form results from its relatively open structure. This agrees with the reverse behaviour observed when increasing Mg^{2+} (Sacristan et al., XXXX). The IRES conformational transformation should be related to interactions described between domain stem loop-II and domain IV, modification of the 40S particle and the fact that stem loop II partially overlaps the E-stem, which happens in the minimal IRES when it is already in the O form.

Our original hypothesis that basal domain III and IV of HCV IRES included a folded structure resembling tRNA complexes can be summarised as follows: when stem-loop II sequences reach the vicinity of the E-site then the IRES structural transformation and miR-122 binding at S3/S4 may provide greater accessibility and stronger and more specific binding of the tRNA-like domain neighbouring the AUG start triplet into the E-site.

FIGURES

Figure 1: Secondary structure of the 5'-terminal region of *RNA*₁₋₅₇₀ and the size of RNA fragments employed. Nucleotides are numbered every 100 residues and major structural domains are depicted as domains I to VI. S1 to S4 are miR-122 binding sites described previously by other authors or during the present work. The dotted line connects the two complementary regions in *RNA*₁₋₅₇₀ which when annealed transform the IRES to the closed conformation. Below the diagram are the linear maps of the RNA fragments employed. Different lengths are shown with schematic bars. Nucleotides are indicated every 100 residues.

Figure 2: Characterising the binding of the 40S ribosomal subunit with closed and open IRES conformations.

Internally labelled transcripts *RNA*₁₋₅₇₀ (panel a), *RNA*₄₄₋₅₇₀ (panel b) and *RNA*₁₋₄₀₂ were incubated in buffer (lane 1) or with increasing concentrations of salt-washed ribosomal subunit 40S: 0.5, 5, 10, 15, 30 and 60 nM for lanes 2 to 7 respectively, and run in X% native gel electrophoresis. Two differentially migrating 40S:HCV complex bands: the fast (F) and slow (S) bands are indicated. Graphic representation of the percentage of binding for each RNA fragment in relation to the concentration of 40S is represented on the right of each corresponding gel.

Figure 3: 40S-RNA complex formation in presence of miR-122.

Panel a: Non-denaturing gel autoradiography of internally-labelled *RNA*₁₋₅₇₀. Lanes 1: RNA alone maintained on ice; Lane 2: incubated in standard buffer alone; Lane 3: incubated with 15 nM of ribosomal subunit 40S; Lanes 4-6: incubated in presence of increasing concentrations of miR-122; Lanes 7-9: the same as lanes 4-6 but in presence of 15 nM of ribosomal subunit 40S. Incubation with or without 40S was indicated with "+" or "-", respectively. Panel b: Bar chart of the percentage of 40S-*RNA*₁₋₅₇₀ complex formation from four replicates of panel a. Panels c/d, and e/f idem as panels a/b but with *RNA*₁₋₄₀₂ and *RNA*₄₄₋₅₇₀ respectively.

Figure 4: Effects of increased Mg^{2+} concentration on S40-RNA complex formation.

*RNA*₁₋₅₇₀ was internally labelled and incubated in the absence (lane 1) or in the presence of 40S (lanes 2 to 6), as well as in the absence (lane 2) or in increasing concentrations of Mg^{2+} x,y,z, for lanes 3 to 6, respectively. The same experiment was performed in the absence (panel a) or in the presence (panel b) of miR-122. Below each gel is a graph of their complex formation in function of Mg^{2+} .

Figure 5: Sucrose gradient sedimentation profiles for *RNA*₁₋₅₇₀ incubated alone or with 40S subunits in the absence or presence of miR-122. The profiles show the counts per minute plotted against the fraction number of the gradient. The first fraction is taken from the bottom of the gradient and the last is taken from the top. The RNA-40S and free RNA peaks are indicated.

Figure 6: 40S subunits protect common and distinct specific regions of *RNA*₁₋₅₇₀ when present in the C or O conformations.

Panel a: 15 to 30% sucrose gradient sedimentation profiles for *RNA*₁₋₅₇₀ and *RNA*₄₄₋₅₇₀ incubated with 40S subunits and subsequently treated, or not, with RNase A. Profiles show the counts per minute plotted against the fraction number of the gradient. Ribosomal complex and free RNA are indicated. Panel b: RNAs protected from sucrose gradient fractions were purified and visualised using denaturing acrylamide gel electrophoresis. Two different time expositions of the same gel provided correct visualisation of the lower and the upper portions of the gel. The protected fragments identified through fingerprinting and secondary analysis by Lytle and Robertson are shown on the right.

Figure 7: Binding of miR-122 to both 5' and 3' flanking sites of HCV IRES in *RNA*₁₋₅₇₀. Panel a: Lanes 1-6: internally-labelled fragments alone, indicated with “-”, served as migration control; lanes 7-12: unlabelled fragments but incubated 20 min at 37 °C with 12.5 nM of 5' end-labelled miR-122, indicated with “+”. b: Bar chart of the percentage of binding of miR-122 to the different length fragments from four replicates of panel b. c) and e) idem as panel b but using “seed-122” and “Mut-seed-122”, respectively, as the radiolabelled probe.

Figure 8: Comparison of HCV-RNA: miR-122 complex dissociation constants, determined by thermodynamic assays.

Binding affinities using cold HCV *RNA*₁₋₅₇₀, *RNA*₁₋₄₀₂ and *RNA*₄₄₋₅₇₀ at increasing concentrations of radiolabelled miR-122 were established by quantitative EMSA and represented with Klotz plot for one assay. HCV1-570 is represented by open circles (○), HCV1-402 with black inverse triangles (▼) and HCV44-570 with black circles (●). Dissociation constants are shown in the table below with the maximum complex concentrations (B_{max}) and R^2 values for three replicates with respect to the exponential phase.

Figure 9: Kinetic analysis of HCV-RNA:miR-122 complex formation rate.

a: values obtained from 5'end-labelled mir-122 binding to cold HCV RNA fragments 1-570, 1-402 and 44-570 are plotted versus time (min), showing the mean for three assays: HCV1-570 is depicted with (●), HCV1-402 with (○) and HCV44-570 with (▼). The observed rates (K_{obs}) for each length of HCV fragment are displayed in the table below, including B_{max} and R^2 values. b: shows the same curve for HCV44-570 as “panel a” but the y-axis has been amplified.

Figure 10: RNases T1 and A cleavage protection of HCV RNAs in the presence of miR-122 or let-7b.

Autoradiogram showing a parallel run in 10% sequencing gel of 3' end-labelled *RNA*₁₋₄₀₂ (100 cpm) cleaved with RNases T1 and A in the presence or absence of microRNAs miR-122 or let-7b at 15 nM. Lane 1 corresponds to HCV-RNA incubated in standard buffer alone. Lanes 2 and 3 are control mobility lanes obtained by treating the RNA with RNase T1 under denaturing conditions or with alkali, respectively. Lanes 4, 5 and 6 are the RNA probed with RNase T1. Lanes 7, 8, and 9 are the RNA treated with RNase A. Free RNA is in lanes 4 and 7, pre-incubated in the presence of miR-122 in lanes 5 and 8, or in the presence of let-7b in lanes 6 and 9. Cleavage and protection at relevant positions of RNases T1 and A are indicated at the left and right of the gel. Product bands with increased intensity after incubation with miR-122 and let-7b are represented by (●) and (▲), respectively. Protected cleavage, is represented by the open symbols (○) and (△). A lane with century markers (CM) is shown on the gel plate.

Figure 11: *RNA*₁₋₅₇₀ chemical probing of new binding sites.

Primer extension analysis using a 5' end-labelled primer complementary to the linker moiety of a cDNA of *RNA*₁₋₄₀₂ +linker, obtained by reverse transcription of an RNA, was pre-treated as follows: lane 5 with DMS, lane 6 with DMS in the presence of miR-122 and lane 7 without DMS pre-treatment. cDNA products were analysed on 10% denaturing gels in parallel with a DNA sequence ladder obtained with the same labelled primer, Lanes 1 to 4: specific for A,C,G and T bases respectively. Lanes with decade (DM) or century (CM) molecular weight markers are shown on the left and right of the gel respectively. Nucleotides modified by DMS at around the miR-122 S3 and S4 binding sites are shown on the right; the numbers refer to the nucleotide positions of the HCV genome. The numbers on the left indicate the position in the sequencing ladder around the S4 binding site; the arrows indicate the differences around the S3 binding site.

Figure 12: RNase H cleavage in the presence of miR-122.

a: cleavage reaction of HCV-RNAs with RNase H was run in parallel for differential transcripts of *RNA*₁₋₄₀₂ (lanes 1-9) and *RNA*₁₋₅₇₀ (lanes 10-18): internally radiolabelled (lanes 4-6 and 13-15); radiolabelled at the 5' end (lanes 1-3 and 10-12), or at the 3' end (lanes 7-9 and 16-18), respectively. RNAs were incubated in standard buffer without enzyme in lanes 1, 4, 7, 10, 13 and 16; treated with RNase H alone in lanes 2, 5, 8, 11, 14 and 17; or treated with RNase H in

the presence of 150 nM miR-122 ODN in lanes 3, 6, 9, 12, 15 and 18. The gel is flanked by two lanes corresponding to molecular weight markers (MW). The arrowheads on the left and right, respectively, indicate the cleavage positions on *RNA*₁₋₄₀₂ and *RNA*₁₋₅₇₀. The nucleotide position in the HCV-RNA sequence is given. Cleavage positions were obtained after eluting the radio-labelled band from the gel and then cloning and sequencing the cPCR product. b: schematic representation of fragments produced by RNase H after cleavage of both RNA fragments in the presence of miR-122 ODN.

Figure 13: Protection assays with RNases A, T1 and H by increasing miR-122 and let-7b.

a and b: autoradiograms showing 3' end-labelled *RNA*₁₋₄₀₂ treated with RNase A and RNase T1 respectively. Number 3 lanes corresponded to RNAs in the absence of microRNAs; lanes 4-6 and 7-9 were RNAs pre-incubated with increasing concentrations of miR-122 or let-7b: 1.5 nM, 15 nM and 150 nM, respectively; number 2 lanes were an alkali ladder; and number 1 lanes: denatured RNA partially degraded with RNase T1. Molecular weight markers are only shown in panel b.

c and d: RNase H cleavage products of internally-labelled HCV1-402 and HCV1-570 RNAs pre-annealed with ODN miR-122 (c) or, ODN let-7b (d). Denaturing gel autoradiograms: number 1 and 7 lanes: RNA alone kept on ice; number 2 and 8 lanes: RNA incubated in standard buffer; number 3 and 9 lanes: RNA treated with RNase H 0.5 U/μl with or without increasing concentrations of ODNs miR-122 or let-7b (HCV1-402: number 4-6 lanes and HCV1-570: 10-12 lanes), respectively. Molecular weight markers (MW) are shown on the left of panel (c) and on the right of panel (d).

Figure 14: Activity of tRNA processing RNases on different length fragments of HCV-RNA.

The HCV RNA fragments were *RNA*₁₋₅₇₀, *RNA*₁₋₄₀₂ and *RNA*₄₄₋₅₇₀. Autoradiogram of denaturing gel electrophoresis of internally-labelled RNAs treated with: a: human RNase P: lanes numbered 1 and 3 (both left and right panels) show RNAs incubated in standard buffer; lanes 2 and 4 were RNAs treated with enzyme. b: cyanobacterial RNase P ribozyme: lanes 1 and 2 show RNAs incubated with standard buffer; lanes 3 and 4 were treated with enzyme. c: RNase Z: lanes 1, 3, 5 and 7 show RNAs incubated with buffer Z; lanes 2, 4, 6 and 8 were treated with enzyme. The product bands are indicated by arrows.

Figure 15: miR-122's effect on the accessibility of the tRNA-like motif by structure-dependent nucleases on HCV-RNA.

Bar graphs representing cleavage product yield from truncated fragments of HCV-RNA on 3' and 5' ends. The first set of bars corresponds to a specific control used to check the effect of miR-122 on each nuclease. *E. coli* pATy-1A and Tyr-tRNA precursors were employed in panels a and b respectively. *Bacillus subtilis* tRNA-leu precursor was employed in panel c. The rest of the panels were HCV RNA fragments, where white bars indicate nuclease reaction without miR-122 and the increasing intensity of grey colour represents increasing concentrations of miR-122. Each assay was repeated thrice, except for *RNA*₄₄₋₅₇₀ (just once).

Figure 16: Effects of miR-122 mutations on the recognition of the tRNA-like motif by RNases P on HCV1-570 RNA.

miR-122 sequence wild type, seed-sequence alone (seed-122) and mutants 1, 2 and 3 in seed sequence. Seed sequence mutations are indicated in bold and underlined. a: dose-response assay in the presence of miR-122 versus seed-122 on internally-labelled *RNA*₁₋₅₇₀ cleaves by cyanobacterial RNase P. Lane 1: RNA incubated on ice; lane 2: RNA incubated in standard buffer; lane 3: RNA treated with enzyme alone; and lanes 4-6: RNA in the presence of increasing concentrations of miR-122 or lanes 7-9: in the presence of seed-122 at final concentrations of 1.5 nM, 15 nM and 150 nM, respectively. b: cyanobacterial RNase P reaction in the presence of seed-sequence mutants. Lane 1: RNA alone incubated on ice; lane 2: RNA incubated in standard buffer; lane 3: RNA treated with cyanobacterial RNase P alone; or with miR-122: wild type (lane 4), mut 1 (lane 5), mut 2 (lane 6) and mut 3 (lane 7) at a final concentration of 15 nM. c and d: idem panels a and b, respectively, but with human RNase P. Panel c was only performed in the presence of increasing concentrations of seed-122. Molecular weight markers (MW) are shown on the right of each gel.

Figure 17: Accessibility change (or conformational change) in domain IV through direct binding of miR-122 at 3' flanking site S3.

a: schematic drawing of RNA_{1-570} , indicating a subset of 20-base ODNs, each one complementary to an HCV IRES or its 3' flanking region; the numbers represent the first complementary base at 5'. Autoradiograms of 4% denaturing gel electrophoresis of internally-labelled RNA fragments treated with RNase H following incubation with 20-base ODNs. b: Differential RNase H cleavage reaction of RNA_{1-402} in the presence of ODNs 313 or 317. Lane 1: RNA alone kept on ice; lane 2: RNA incubated in standard buffer without enzyme; lane 3: RNA treated with RNase H alone; lanes 4-6: RNA treated with RNase H in the presence of 150 nM miR-122 RNA, 313 and 317 respectively; lanes 7-9: treated with RNase H in the presence of increasing concentrations of miR-122 and with 150 nM 313 and lanes 10-12: idem as ?? with oligo 317. Molecular weight markers are shown as MW. c: RNase H cleavage reaction of RNA_{1-570} in the presence of ODN 317 and microRNAs miR-122 or let-7b. Lanes 1-4 and 6 are the same as in panel b; lane 5: RNA treated with RNase H in the presence of 150 nM let-7b; lanes 7-9: idem lanes 10-12 of panel b; lanes 10-12: the same as in lanes 7-9 but incubated with increasing concentrations of let-7b. d) and e) same as panel (c) but using RNAs truncated at the 3' (RNA_{1-402} and RNA_{1-370}) or 5' end (RNA_{44-570}), respectively. Only miR-122 was tested in these fragments.

Figure 18: Effect of HCV-domain IV mutations on the accessibility of ribosomal subunit 40S.

a and b: autoradiograms of non-denaturing gel electrophoresis of internally-labelled RNA_{1-570} mutants in domain IV. RNA_{1-570} low stability mutant (panel a) and high stability mutant (panel b). Lanes 1: RNA alone kept on ice; lane 2: RNA incubated in standard buffer; lane 3: RNA incubated with 15 nM of ribosomal subunit 40S; lanes 4-6: RNA incubated in the presence of increasing concentrations of miR-122; lanes 7-9: the same as lanes 4-6 but further incubated with 15 nM of ribosomal subunit 40S. c and d: bar charts of the percentage of 40S-HCV mutant complex formation from three repetitions of panels a and b, respectively.

Supplementary Figure 1: specificity of 40S-HCV IRES binary complex formation.

Lanes 1 and 2: internally-labelled RNA_{1-570} was incubated alone on ice or with binding buffer under reaction conditions, respectively. Lane 7: idem as lane 2 but in the presence of miR-122. Lanes 3 and 8: RNA_{1-570} with the 40S ribosomal subunit alone and in the presence of miR-122; lanes 4 and 9: idem, but incubated with purified 60S ribosomal subunits; and lane 6: incubated with both 40S and 60S subunits. Lane 5: binding reaction in the presence of 40S and EDTA.

Supplementary Figure 2: 40S-RNA complex formation in the presence of let-7b1.

Panel a: non-denaturing gel autoradiogram of internally-labelled *RNA*₁₋₅₇₀. Lane 1: RNA alone kept on ice; lane 2: RNA incubated in standard buffer alone; lane 3: RNA incubated with 15 nM of 40S; lanes 4-6: RNA incubated in the presence of increasing concentrations of let-7b; lanes 7-9: the same as lanes 4-6 but in the presence of 15 nM of 40S. Incubation with or without 40S was indicated with “+” or “-”, respectively. Panel b: bar charts of the percentage of 40S-*RNA*₁₋₅₇₀ complex.

Supplementary Figure 3: comparison of miR-122 and let-7b RNase H cleavage sites on HCV-RNA.

Autoradiogram showing internally-labelled *RNA*₁₋₄₀₂ (lanes 1-5) and *RNA*₁₋₅₇₀ (6-10). Lanes 1 and 6 are RNAs incubated on ice; lanes 2 and 7: RNA incubated in standard buffer and under reaction conditions; lanes 3 and 8 respectively: RNAs were treated with 0.05 U/ μ L RNase H alone or with 150 nM of either miR-122 ODN in lanes 4 and 9 or let-7b ODN in lanes 5 and 10. Molecular weight markers (MW) are shown on the right.

Supplementary Figure 4: *E. coli* RNase Z purification.

a: SDS-PAGE gel electrophoresis of the starting material and chromatography fractions collected during RNase Z activity purification. Lanes 1-4 and lanes 5-8 correspond to two purifications carried out in the presence of 2.5 mM or 5 mM of imidazole respectively. Lanes 1 and 5 are the crude extract (CE), lanes 2 and 6 are the flow through (FT), lanes 3 and 7 are the first wash (*W*₁) and lanes 4 and 8 are the elution steps (EL). Was used a specific MW to proteins. b: analysis of purified *E. coli* RNase Z activity using trnD-Leu2 RNA from *B. subtilis* as a substrate. Lane 1: internally-labelled trnD-Leu2 RNA kept on ice; lane 2: as lane 1 but in buffer Z and under reaction conditions; lanes 3-5 were treated with decreasing dilutions of RNase Z extract: 1/1, 1/3 and 1/9, respectively.

Supplementary Figure S5: *E. coli* RNase Z activity cleaves HCV RNA near AUG start codon. Autoradiogram of 4% denaturing polyacrylamide gel electrophoresis showing: a: competitive inhibition of internally radiolabelled *RNA*₁₋₄₀₂ cleavage by *E. coli* RNase Z in the presence of increasing concentrations of trnD-Leu2 (precursor of tRNA-Leu extracted from *B. subtilis*). Lane 1: internally-labelled RNA kept on ice; lane 2: RNA incubated in buffer Z; lane 3: RNA incubated with RNase Z; and lanes 4-8: RNA in the presence of increasing concentrations of ptRNA-Leu2: 2.1 nM, 4.2 nM, 21 nM, 42 nM and 210 nM respectively. Molecular weight markers (MW) are shown on the right of the gel. b: direct determination of RNase Z cleavage positions on HCV by RNA sequencing reactions of 3' end-labelled *RNA*₁₋₄₀₂. Lane 1: RNA incubated on ice; lane 2: RNA incubated in buffer Z; lane 3: partial degradation with alkali; lanes 4 and 5: RNA treated with increased concentrations of RNase Z (R1 and R2); and lane 6: RNA partially degraded with RNase T1. Molecular weight markers (MW) are on the right.

FIGURA 1

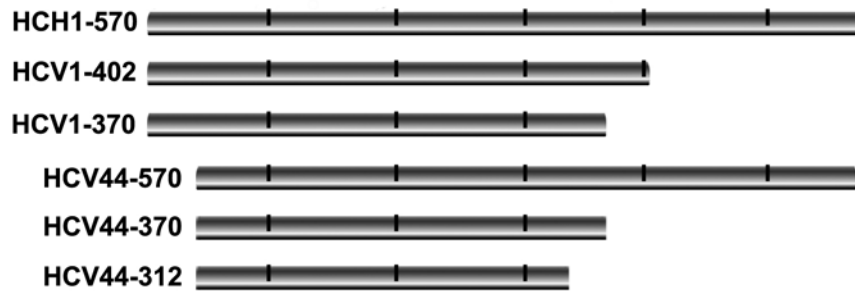
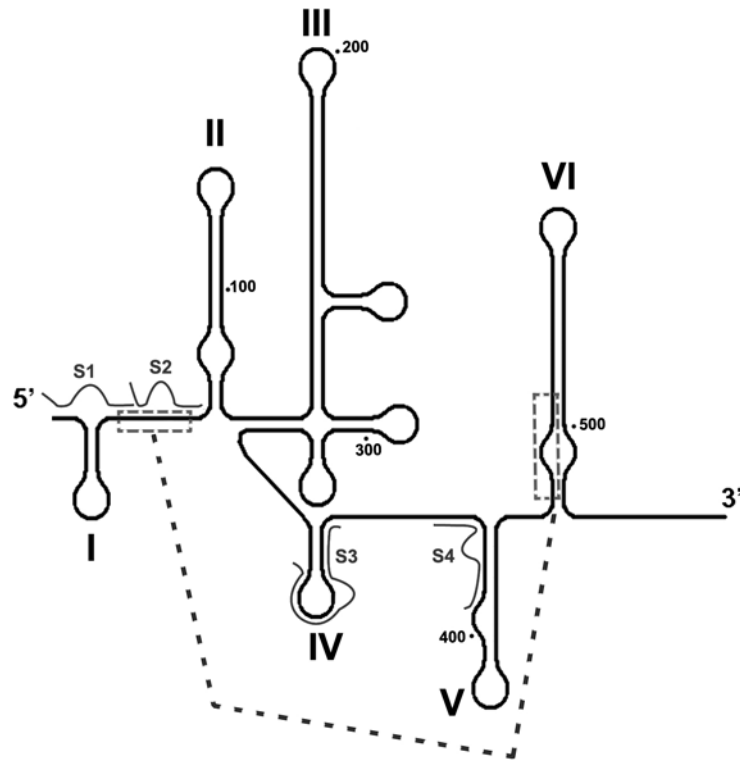


FIGURA 2

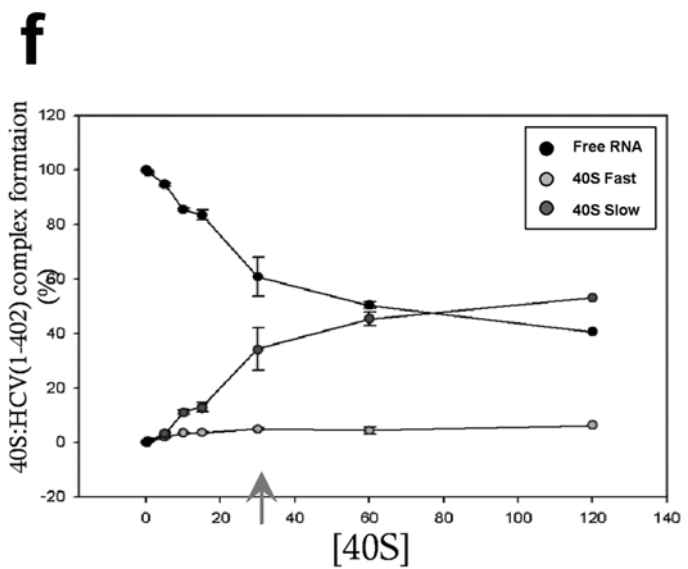
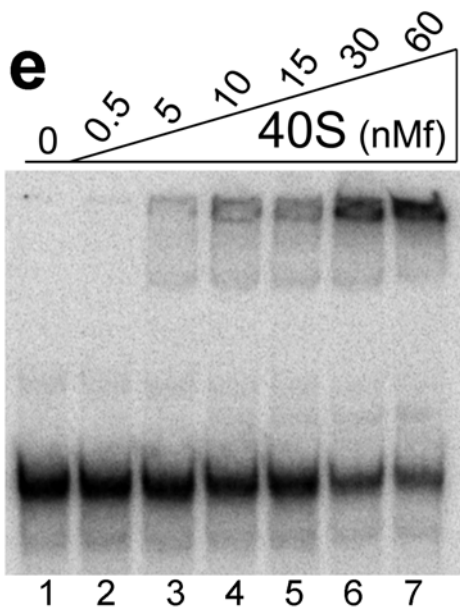
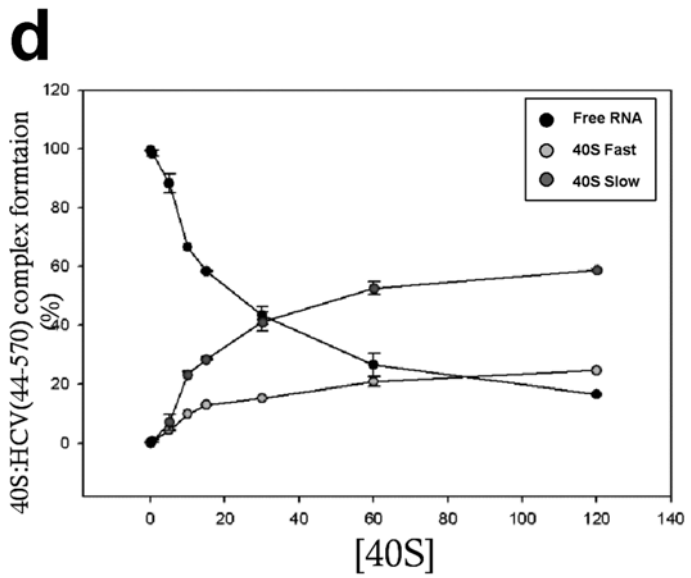
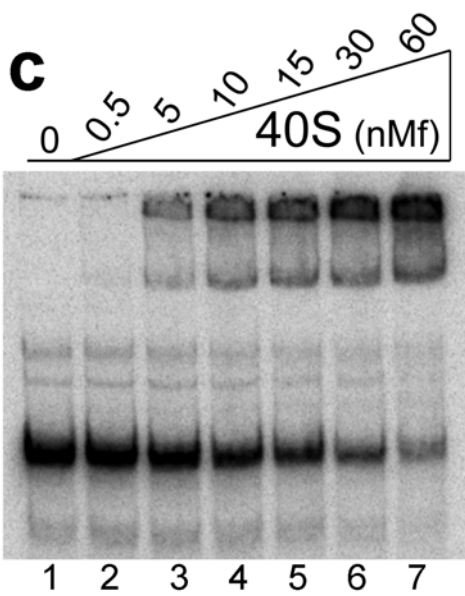
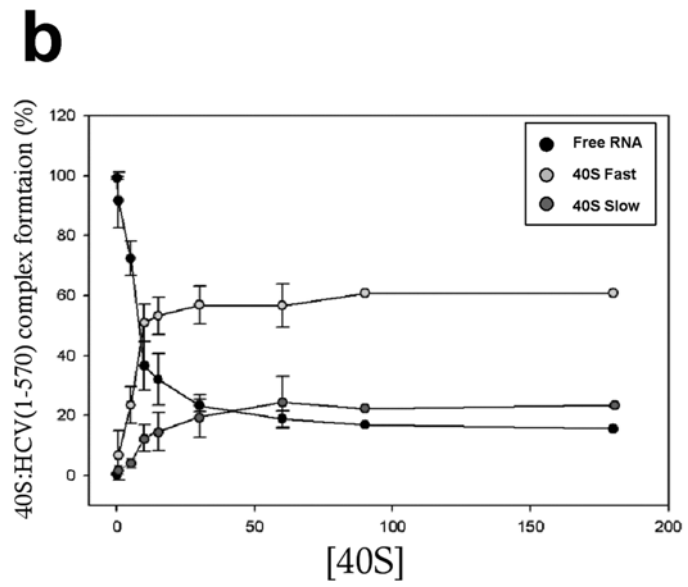
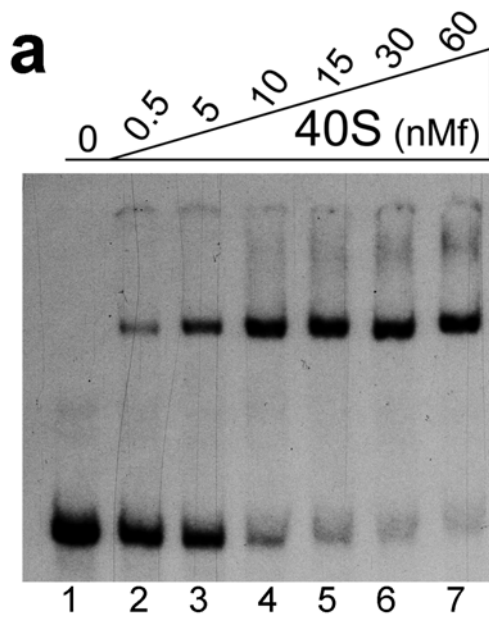


FIGURA 3

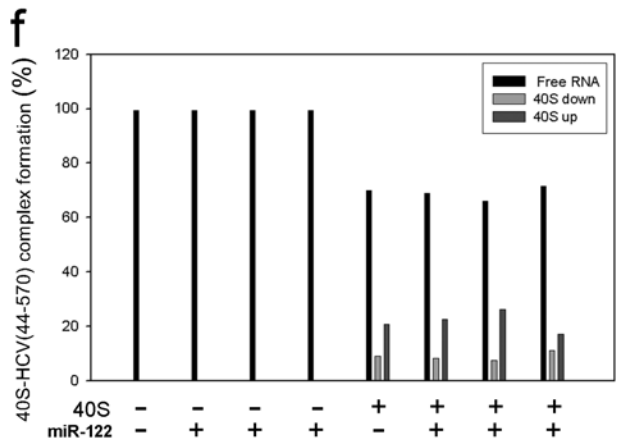
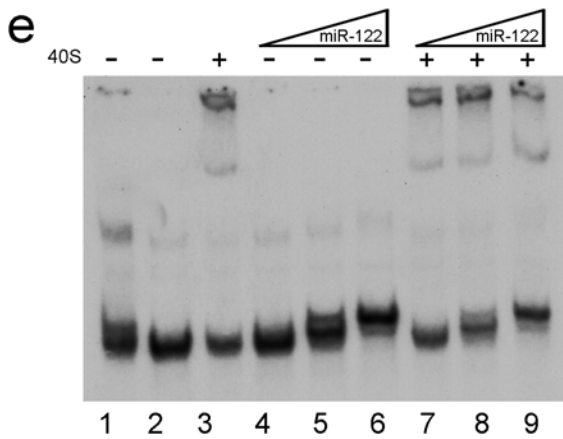
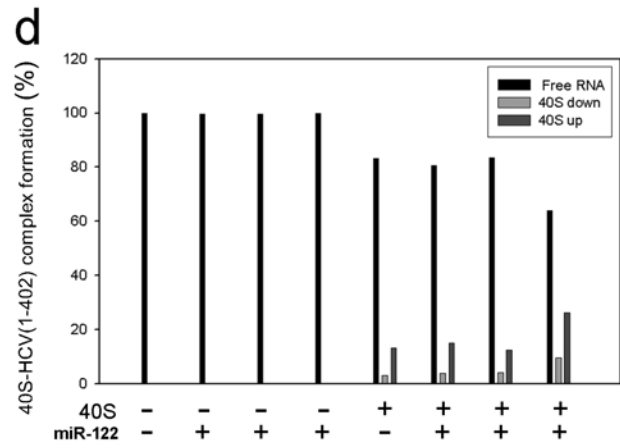
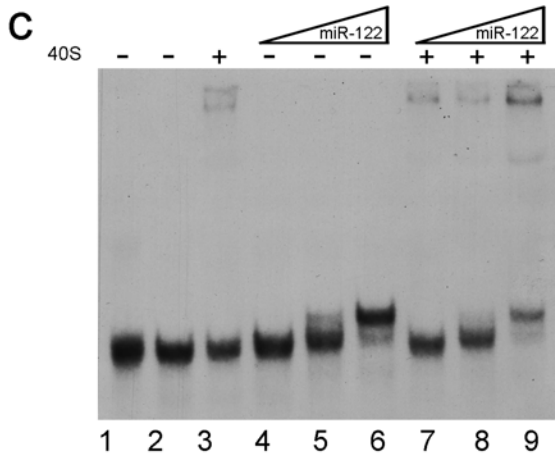
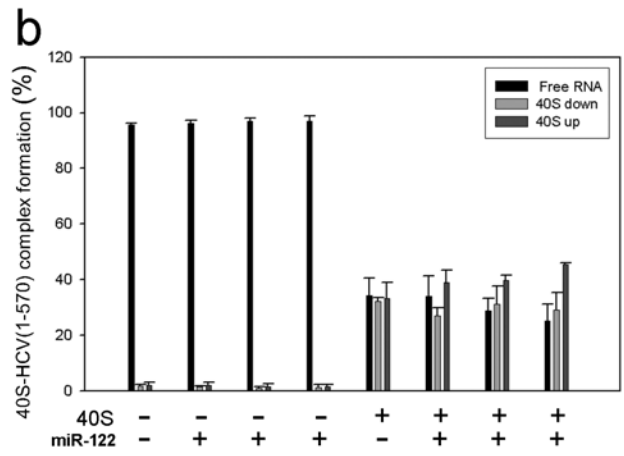
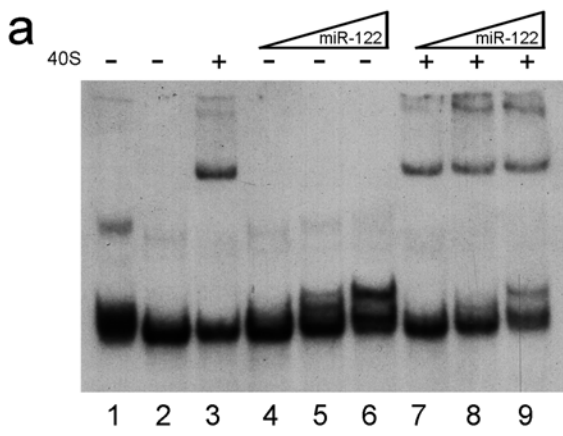


FIGURA 4

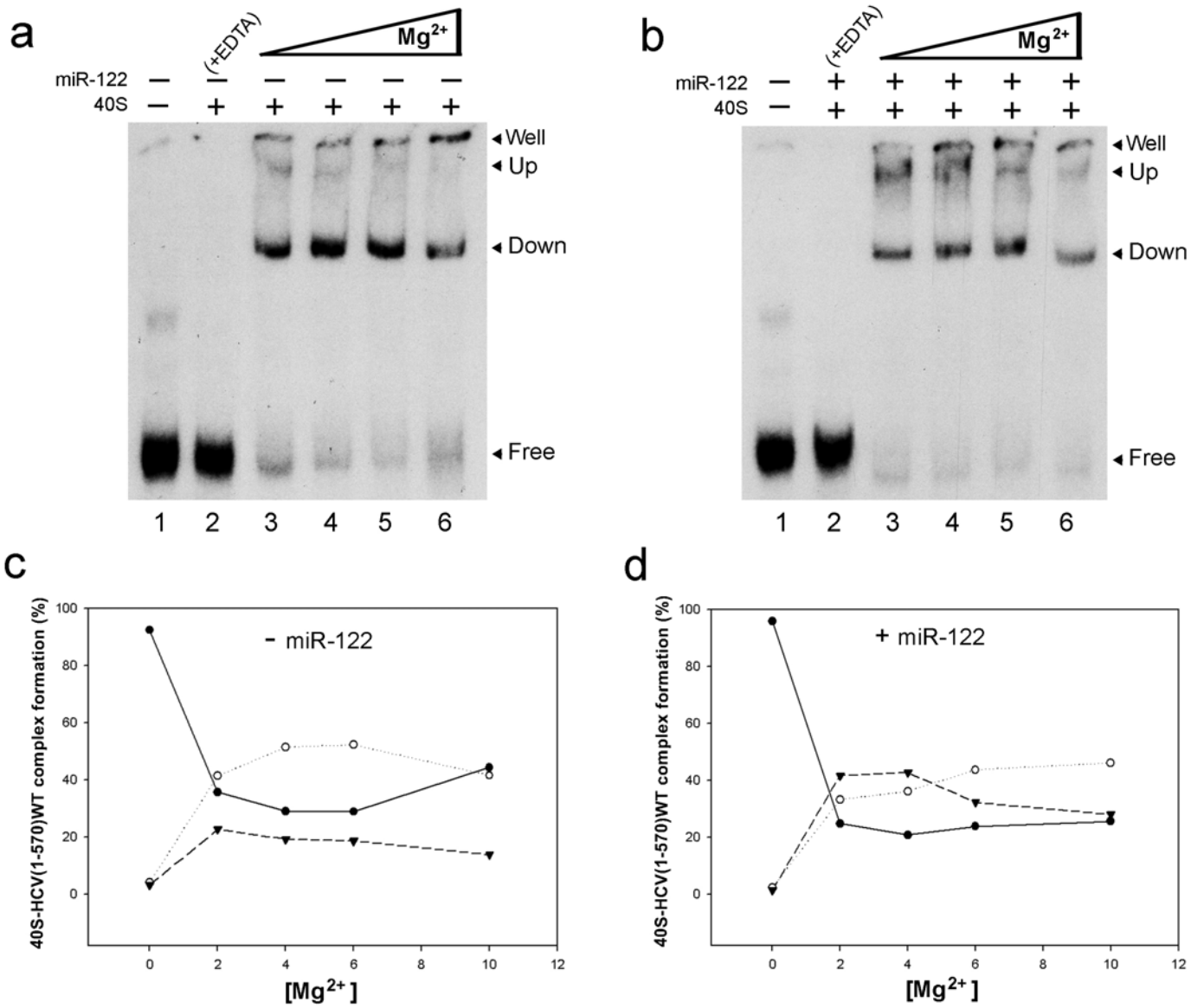


FIGURA 5

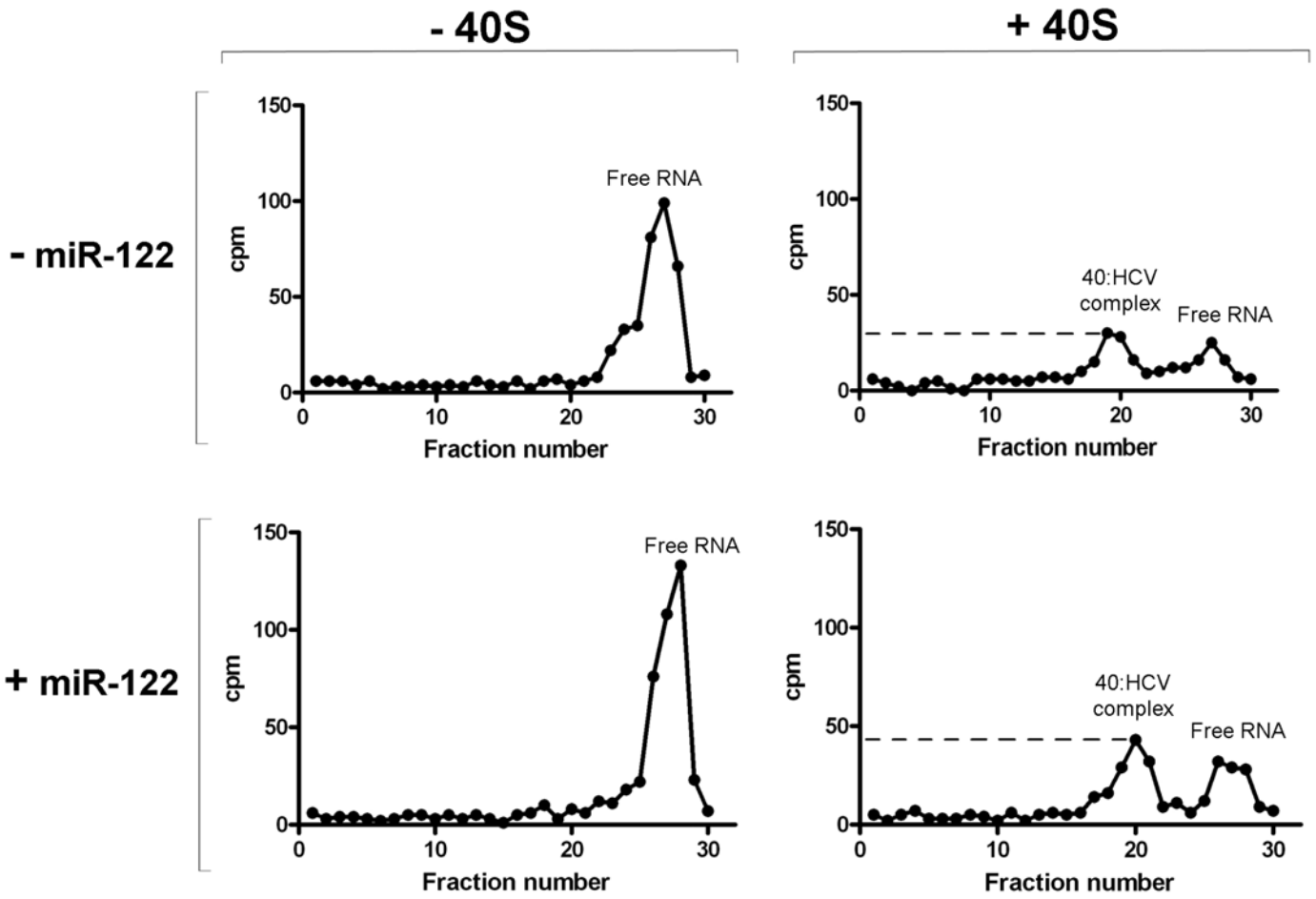


FIGURA 6

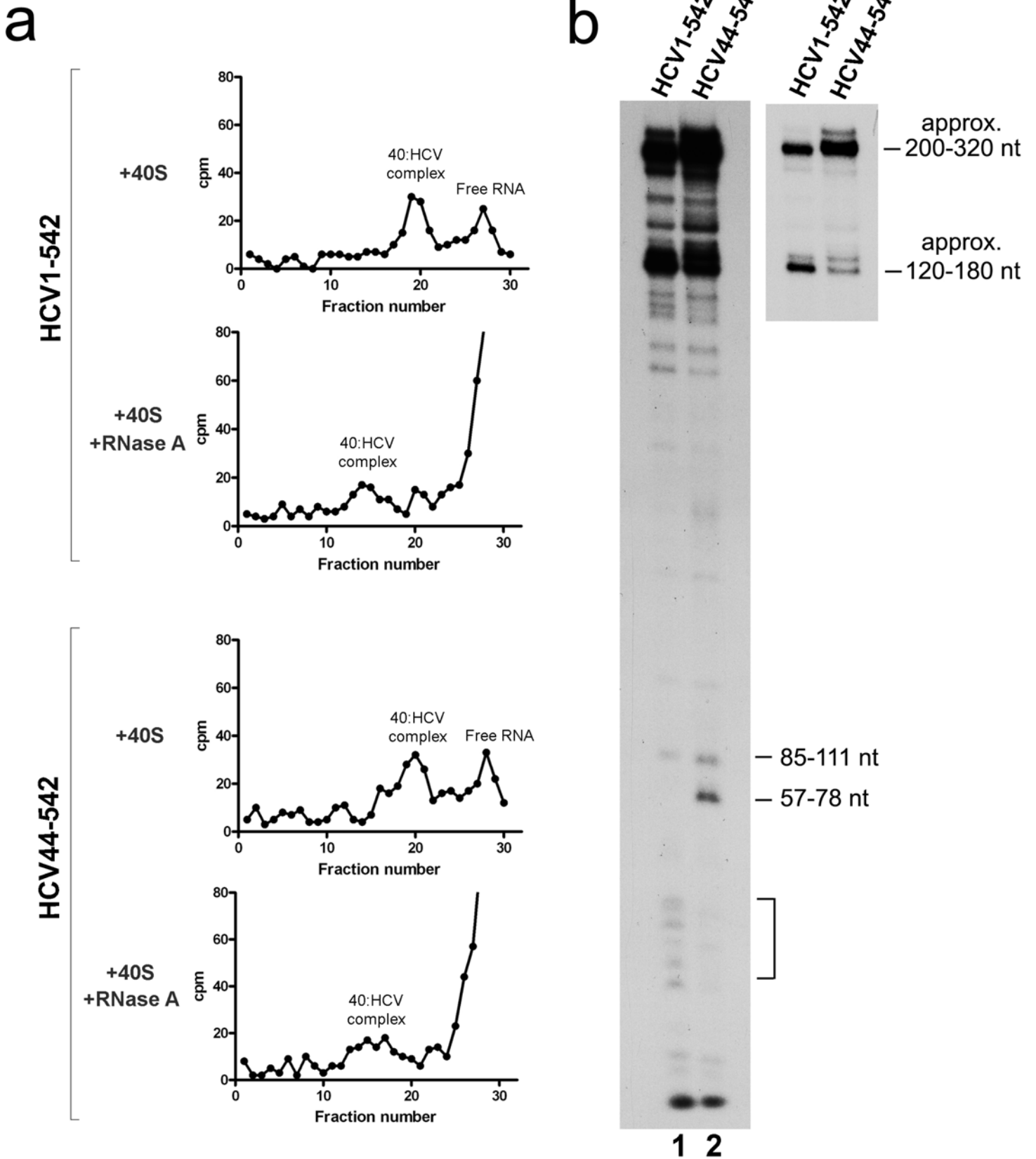


FIGURA 7

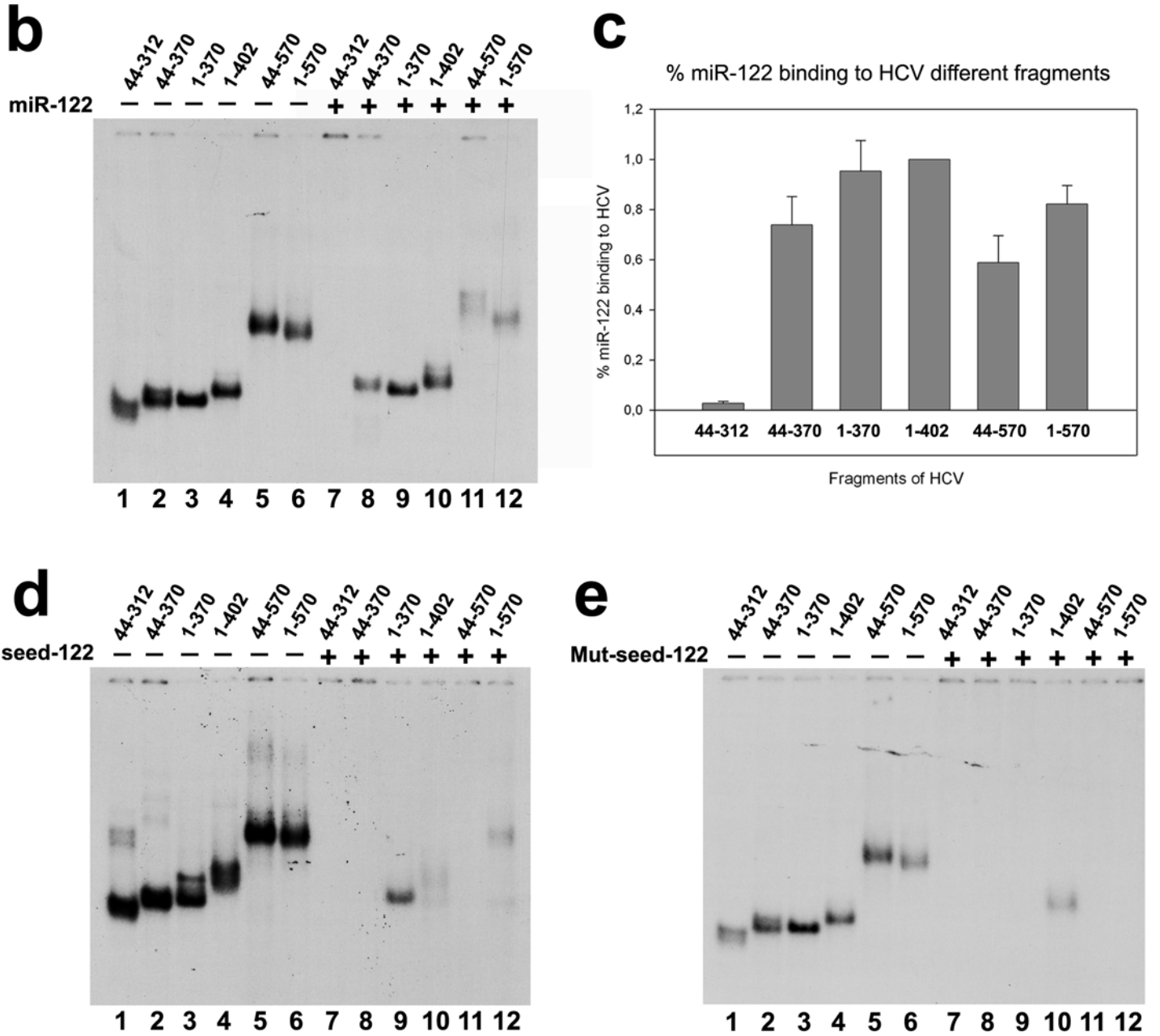
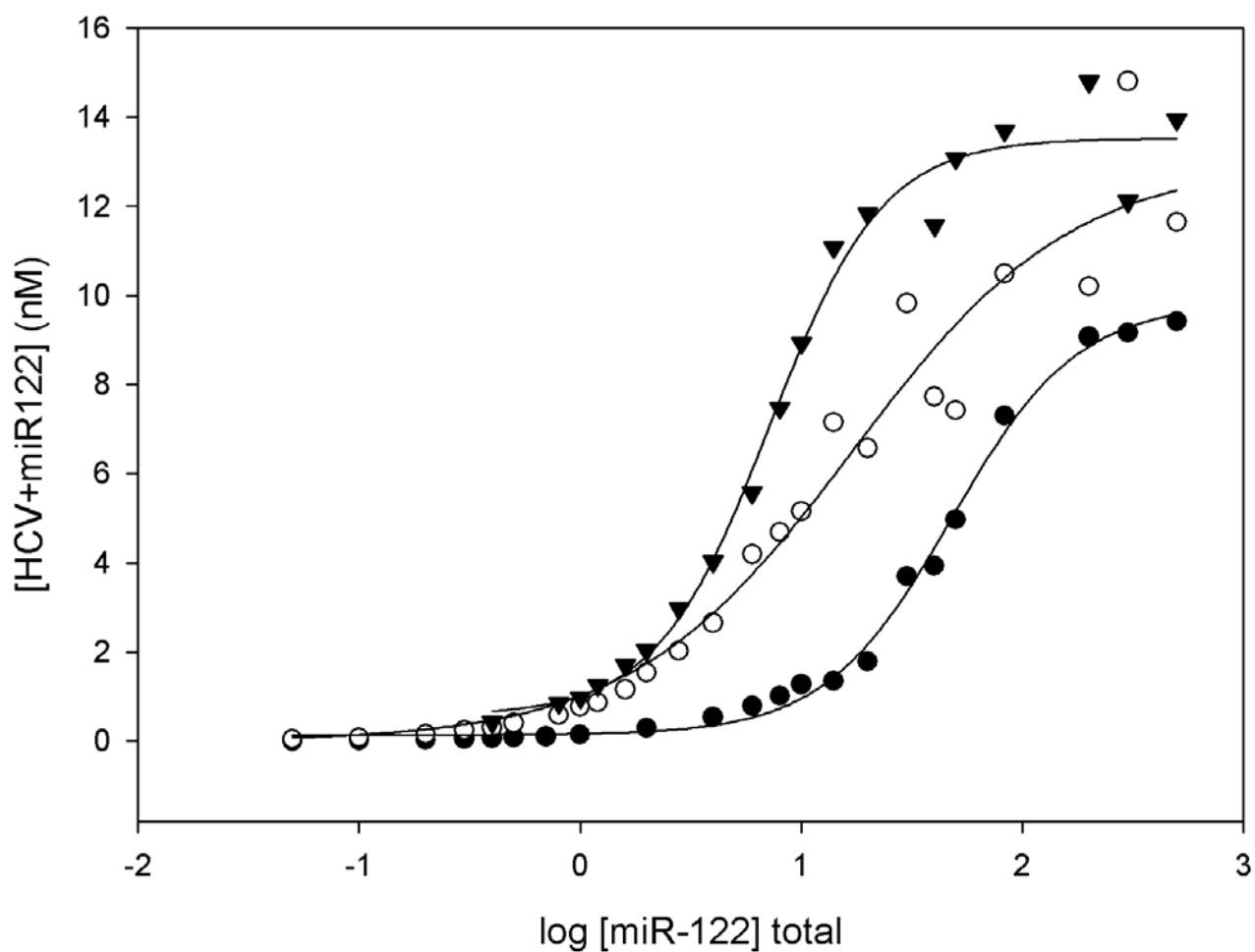


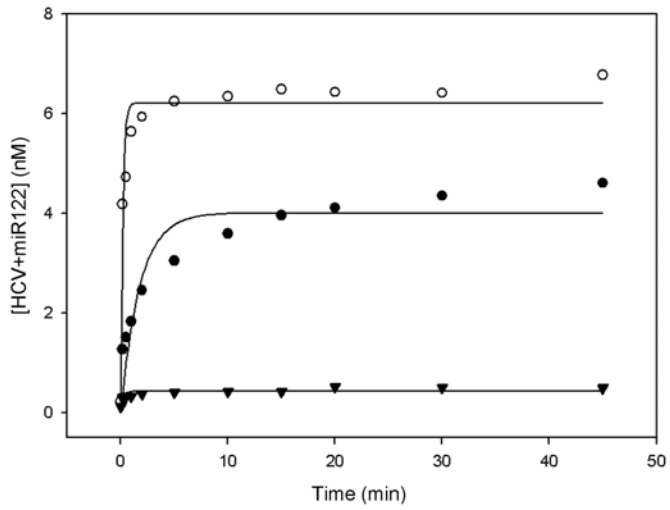
FIGURA 8



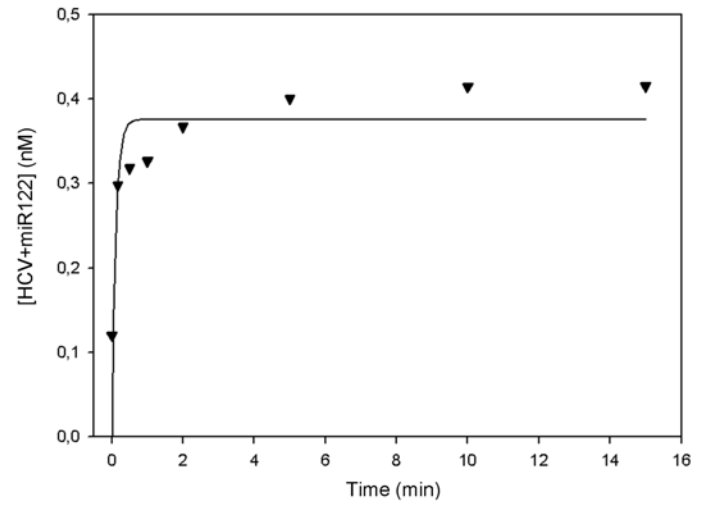
		Kd (nM)	Bmax (nM)	R ²
●	HCV 44-570	68.69 ± 1.11	10.70 ± 0.44	0.9947
○	HCV 1-570	12.14 ± 1.17	11.27 ± 0.57	0.9814
▼	HCV 1-402	7.17 ± 1.09	13.52 ± 0.33	0.9857

FIGURA 9

a



b



		Kobs	Bmax	R ²
▼	HCV 44-570	8.78 ± 4.48	0.38 ± 0.03	0.6435
●	HCV 1-570	0.56 ± 0.14	4.01 ± 0.22	0.8885
○	HCV 1-402	5.14 ± 1.06	6.21 ± 0.18	0.9360

FIGURA 10

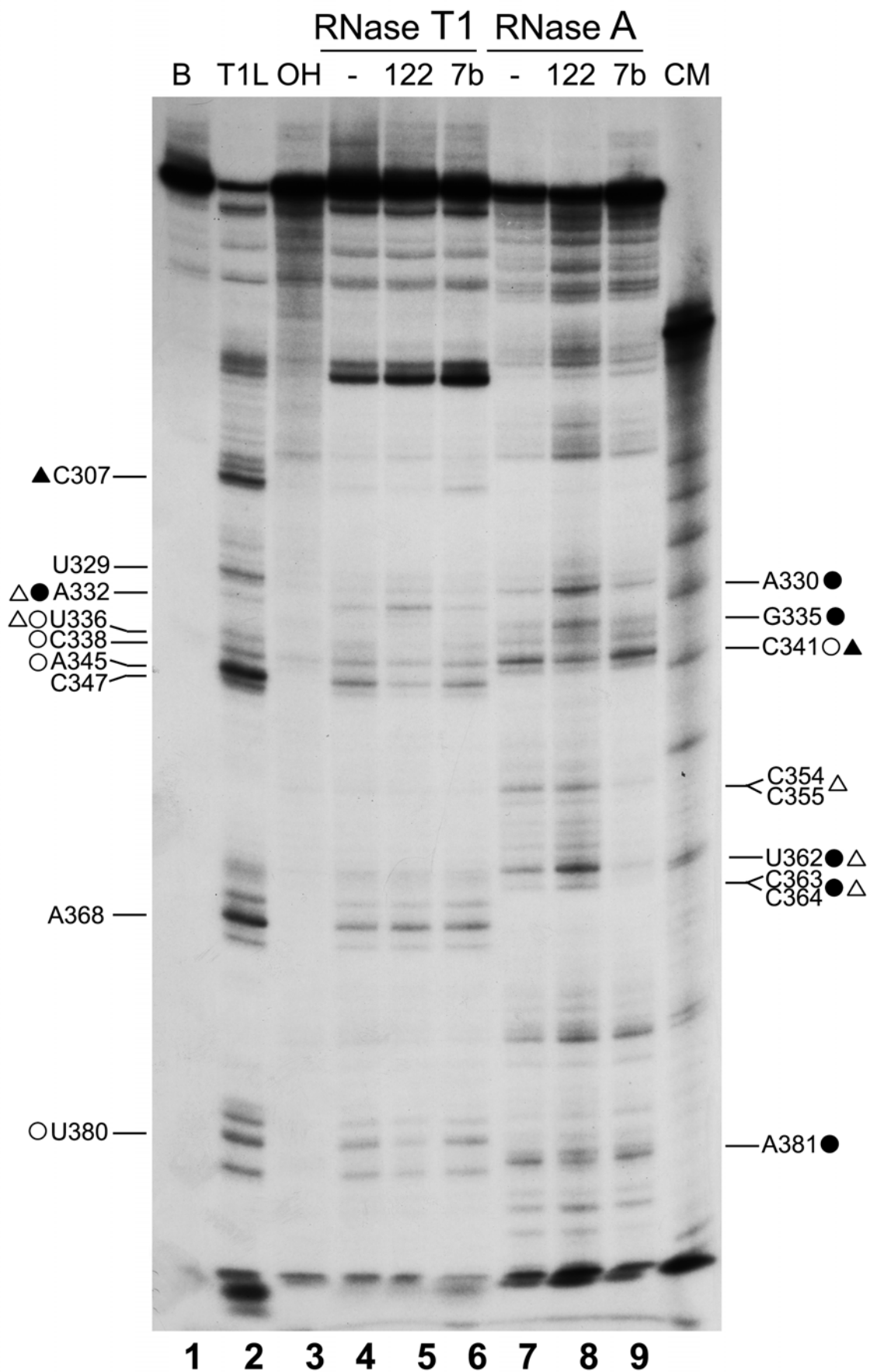


FIGURA 11

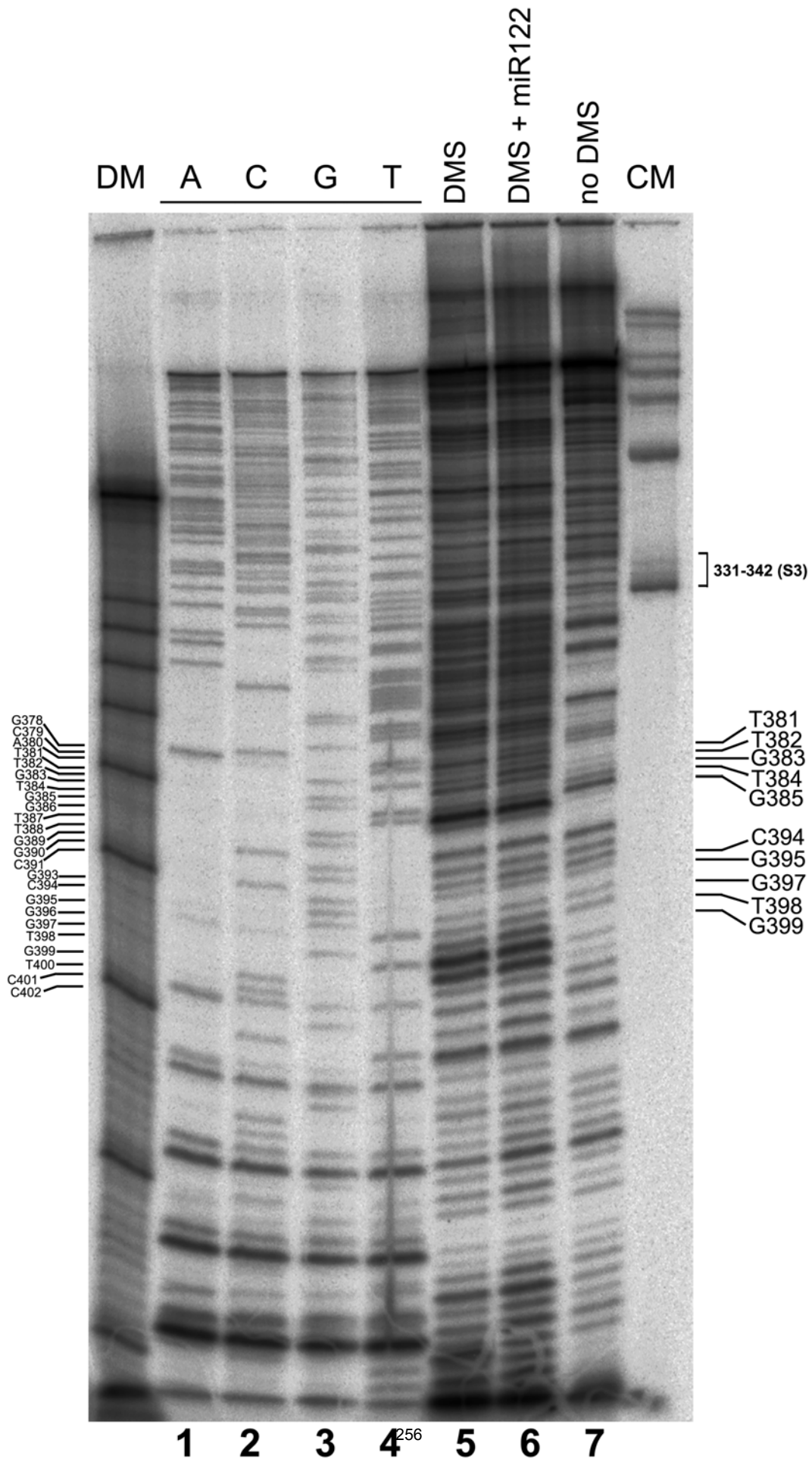
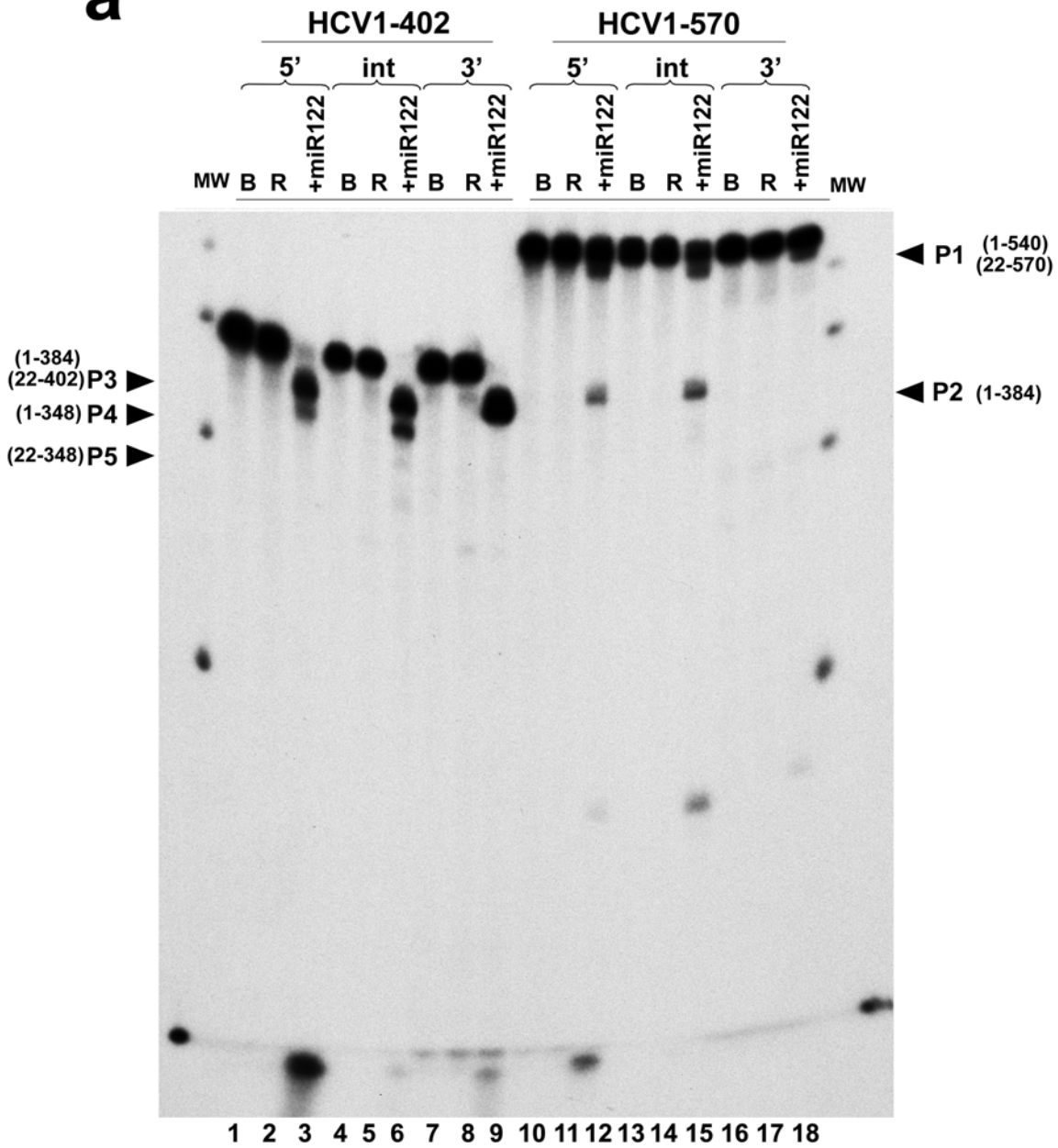


FIGURA 12

a



b

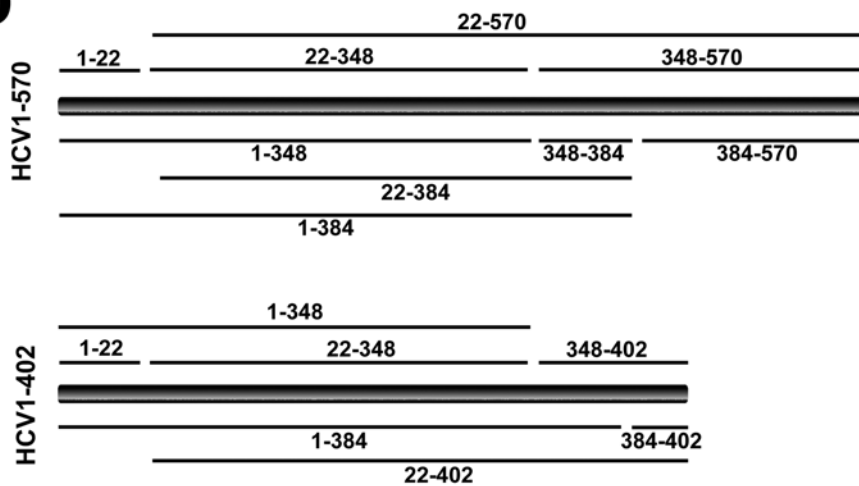


FIGURA 13

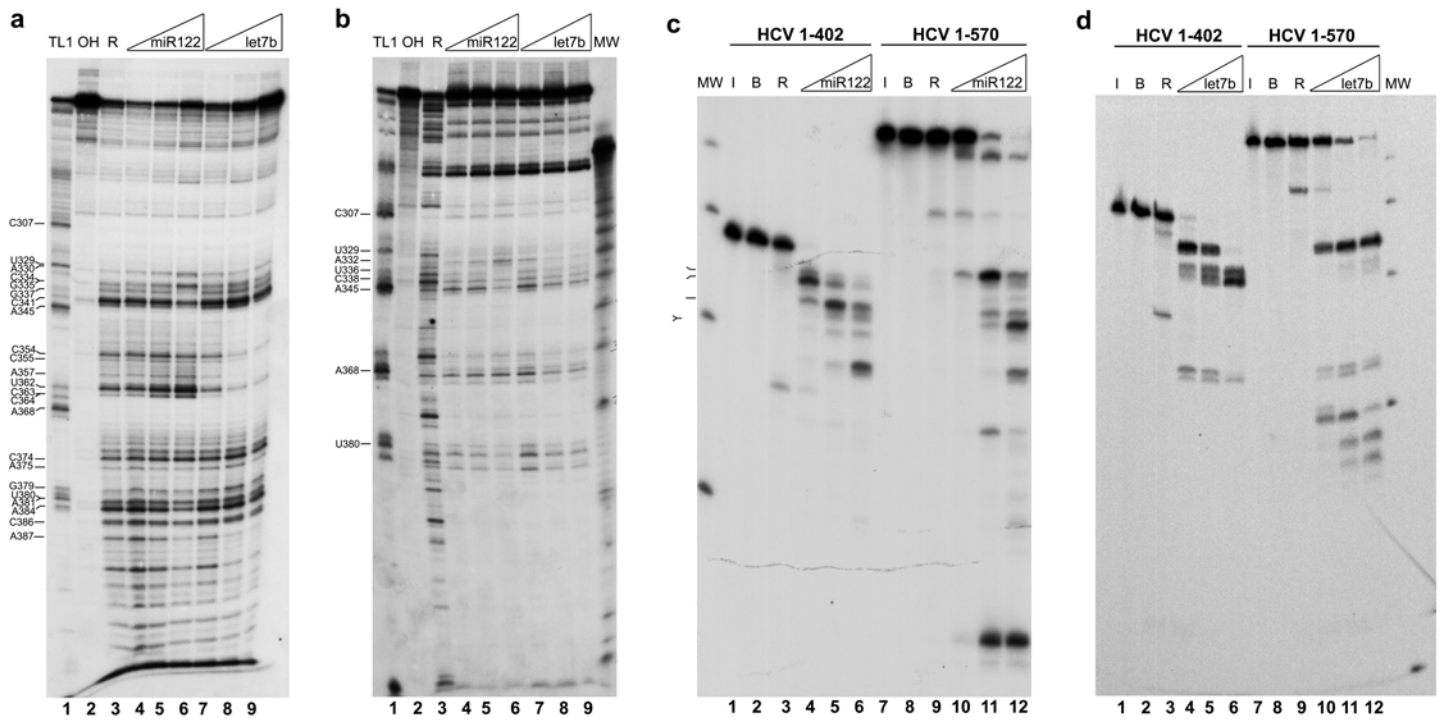


FIGURA 14

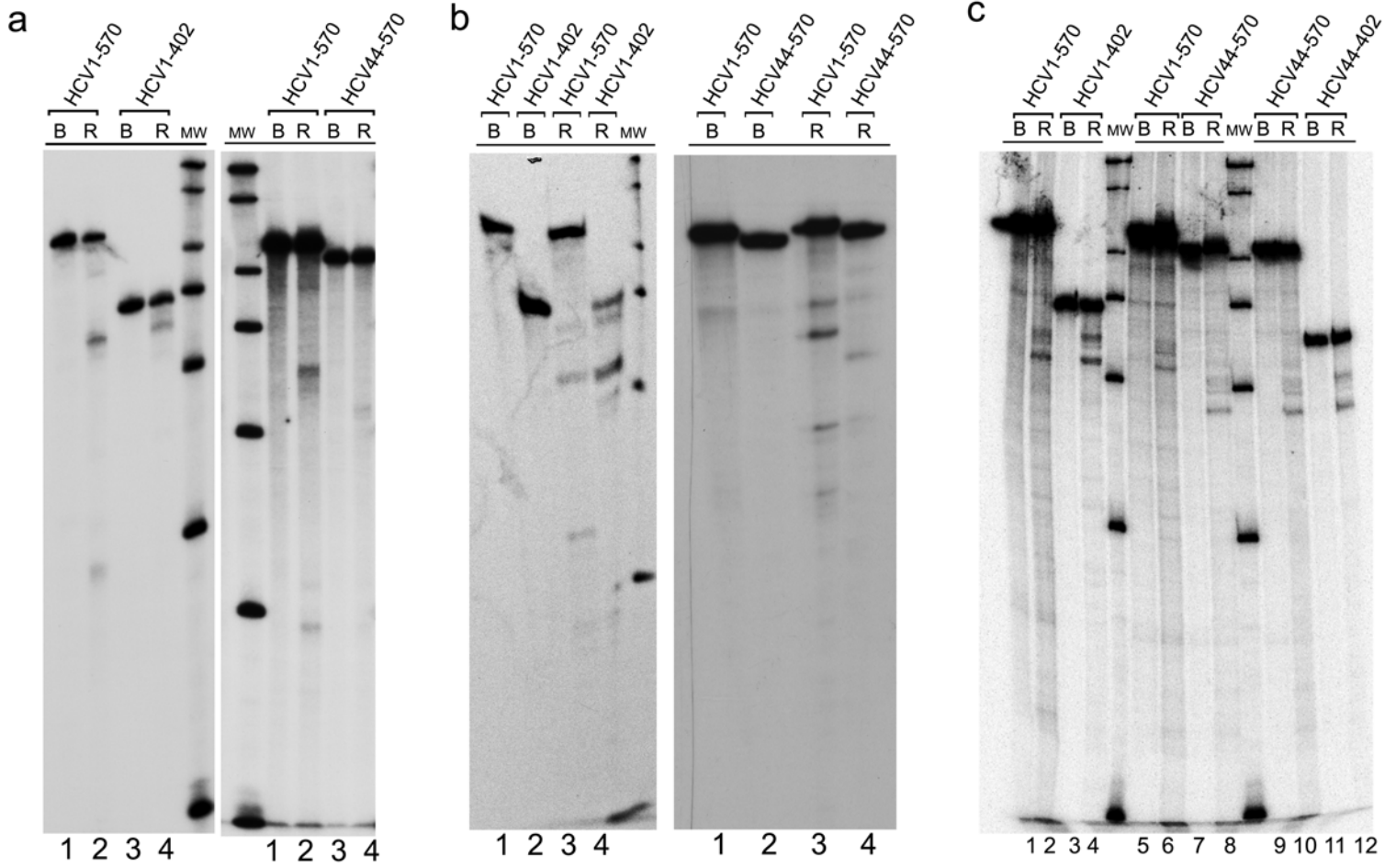


FIGURA 15

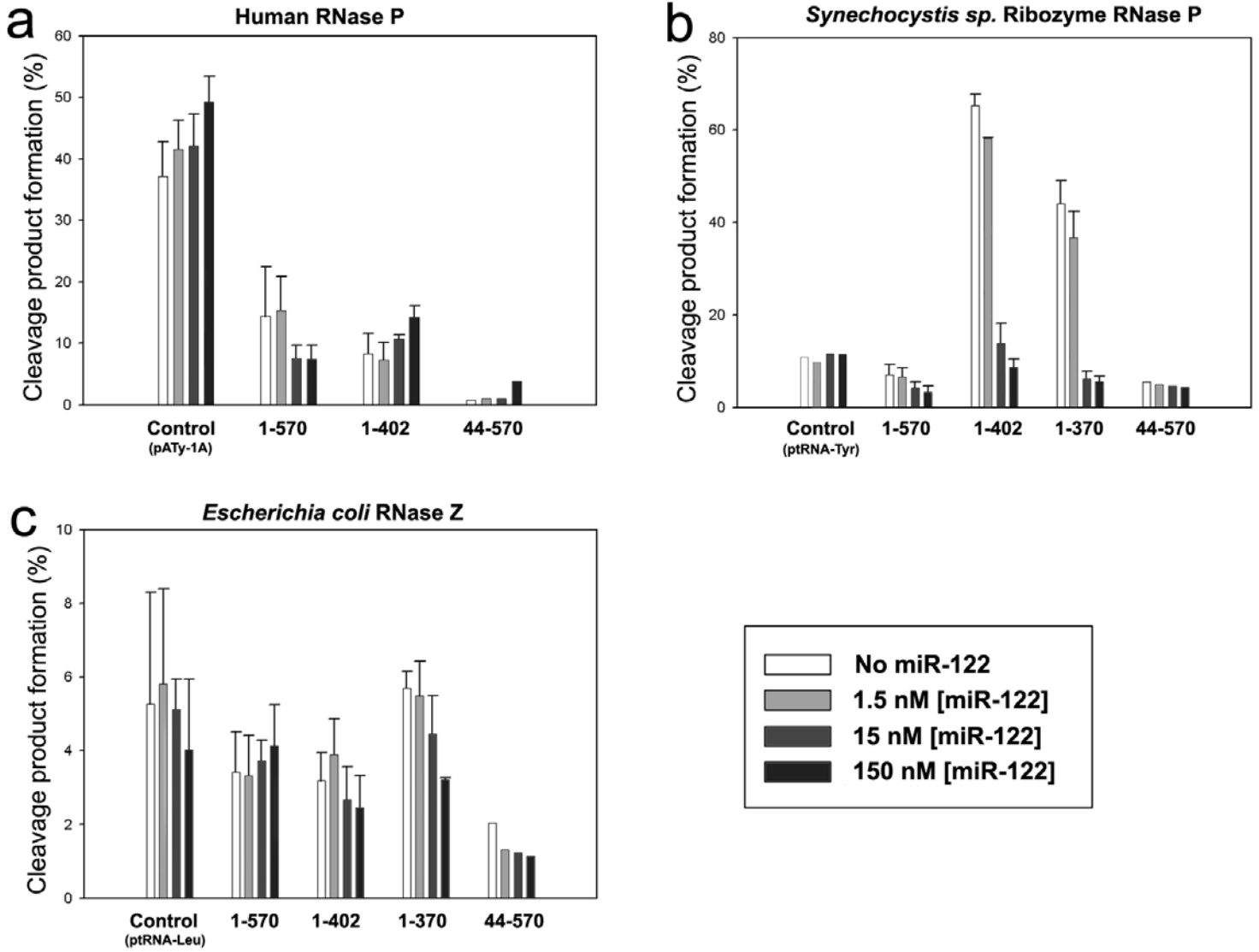


FIGURA 16

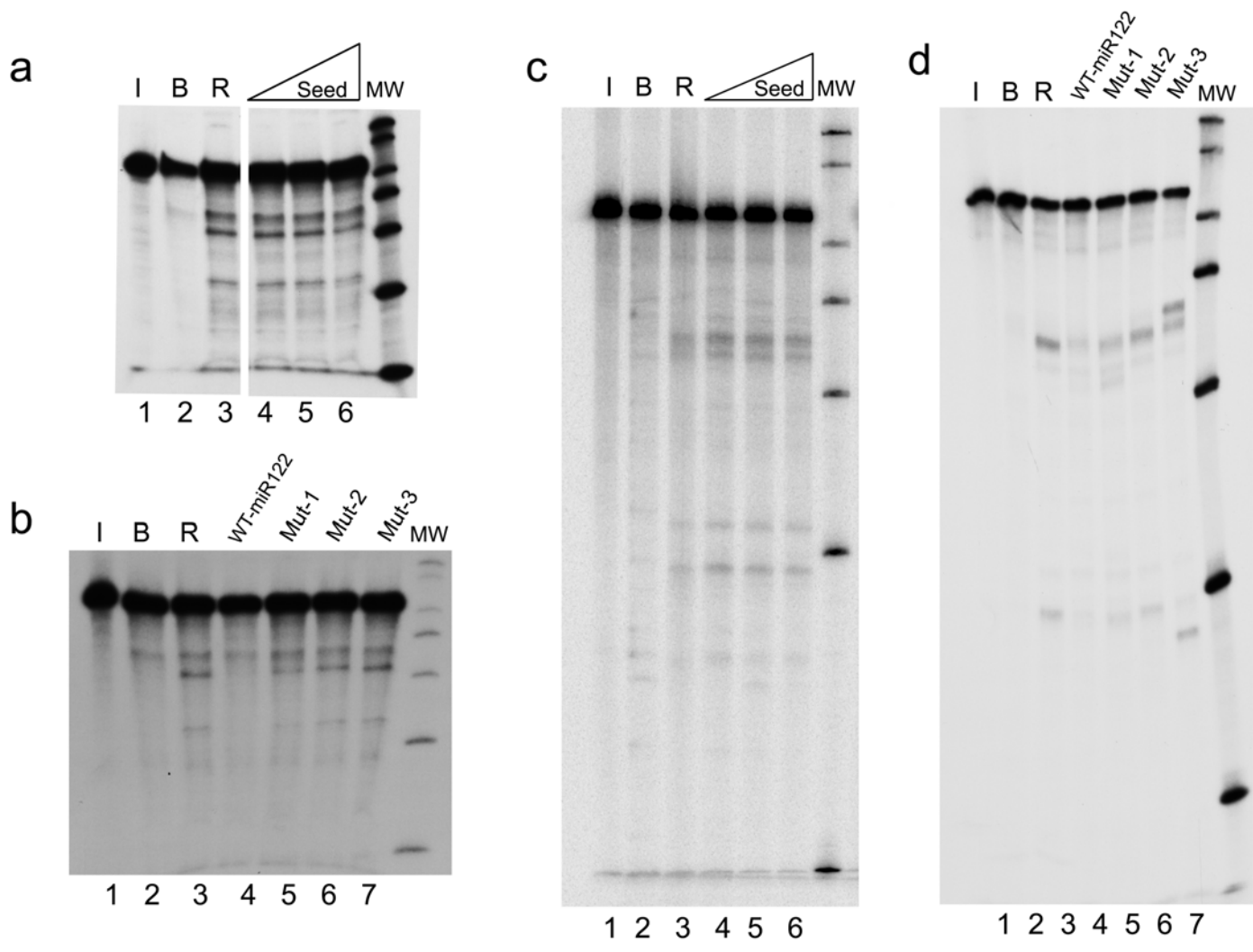


FIGURA 17

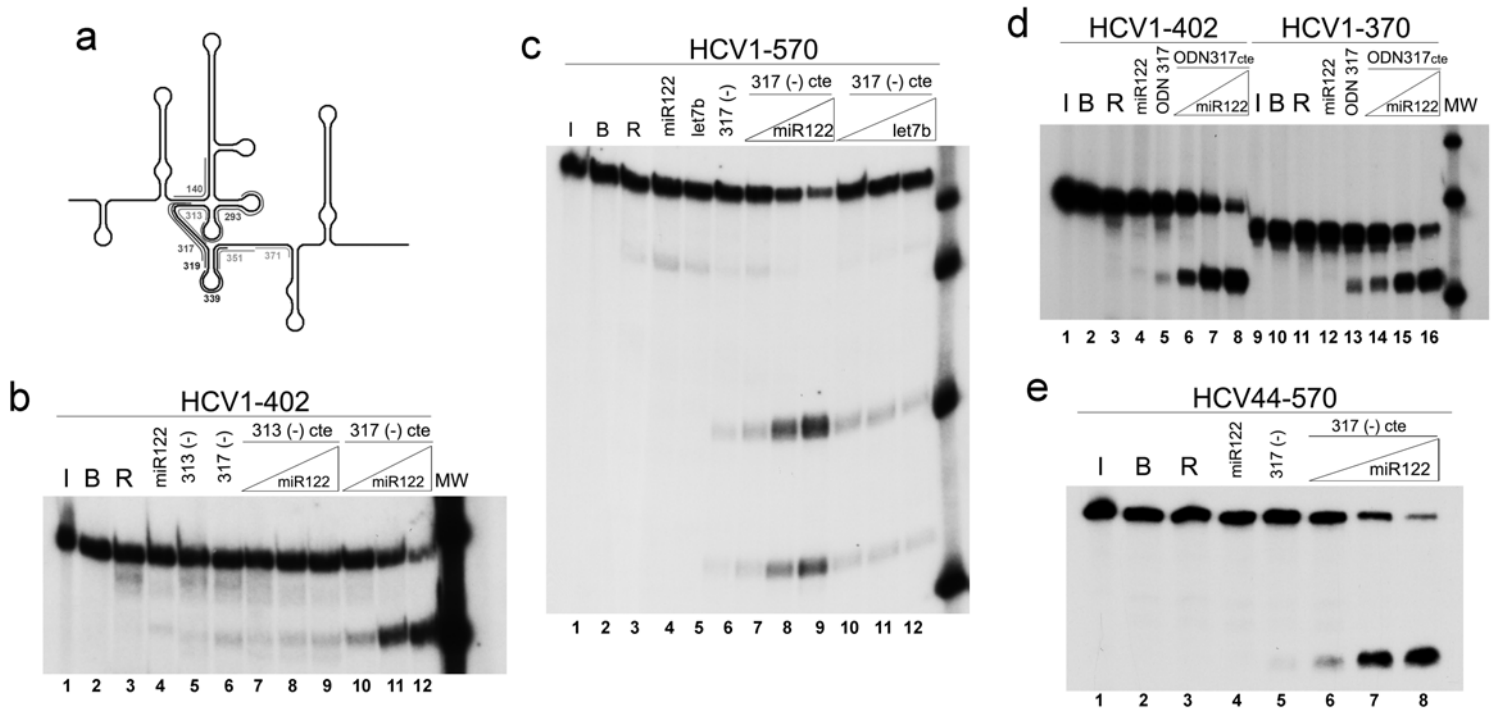
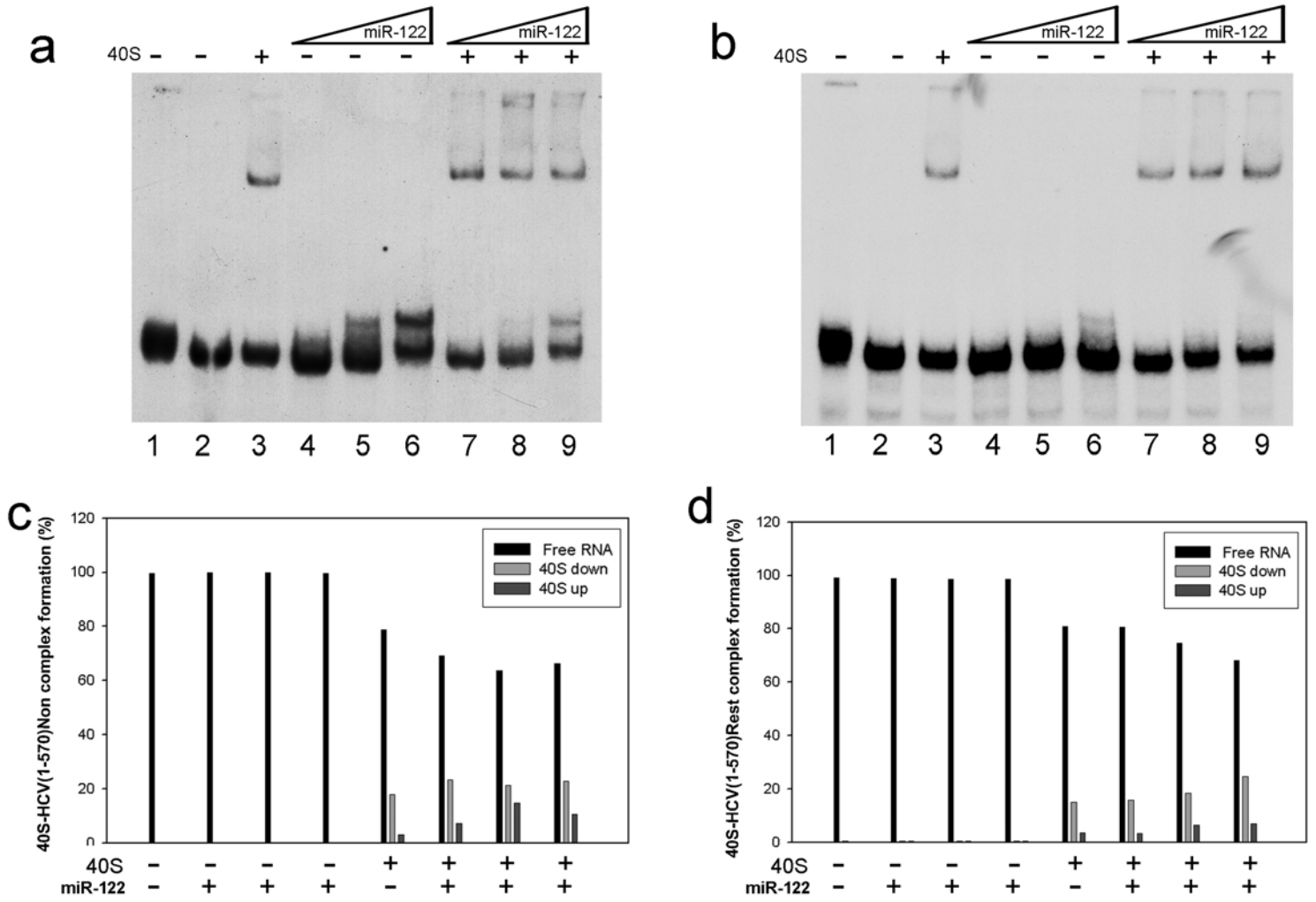
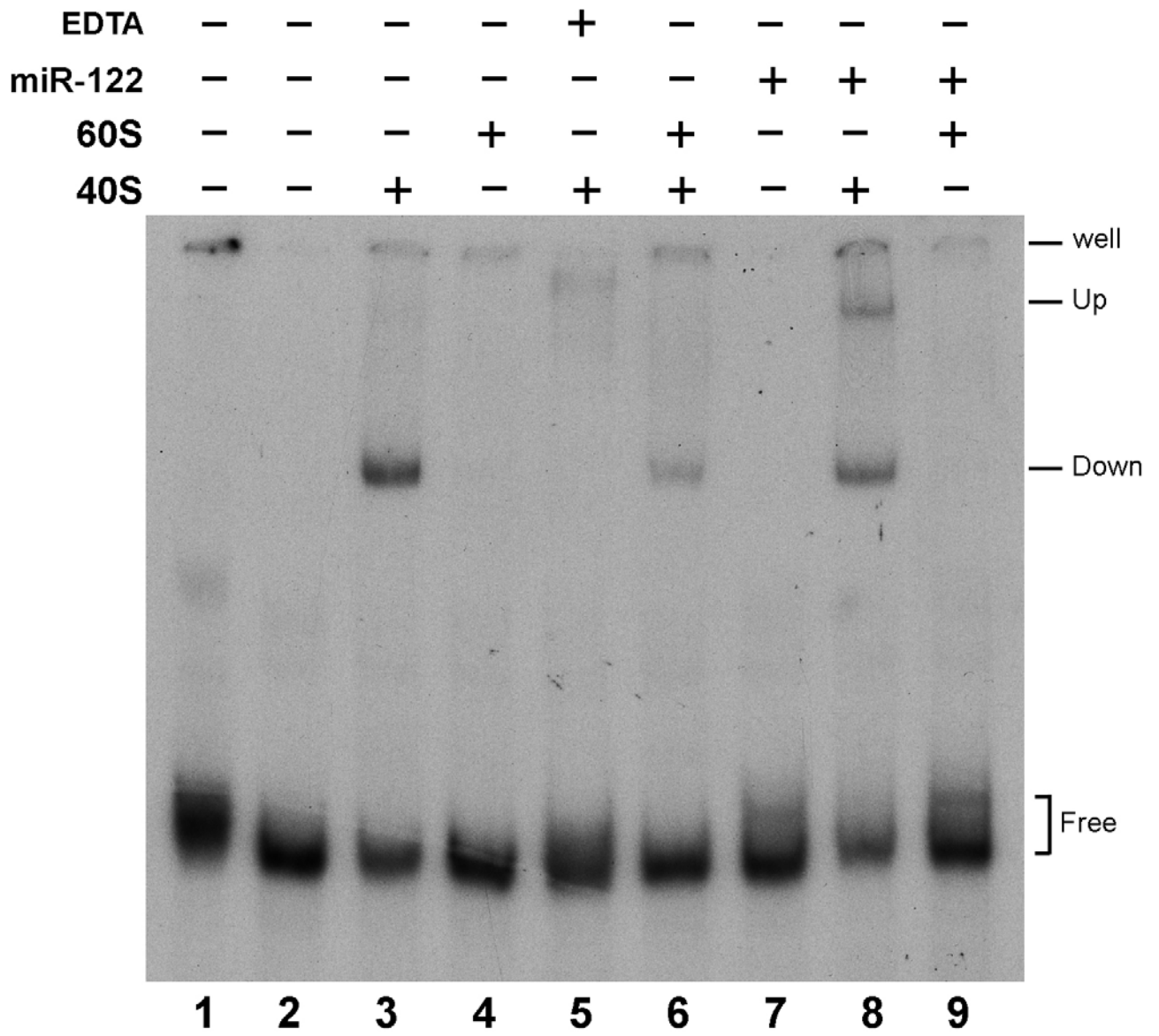


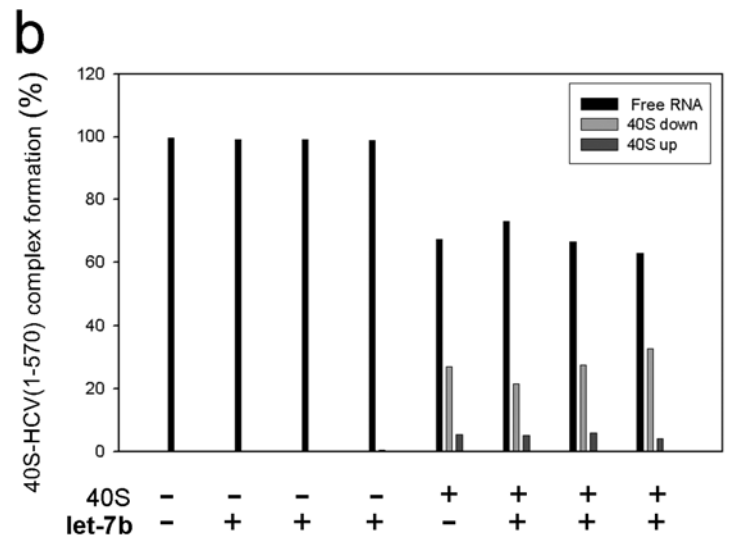
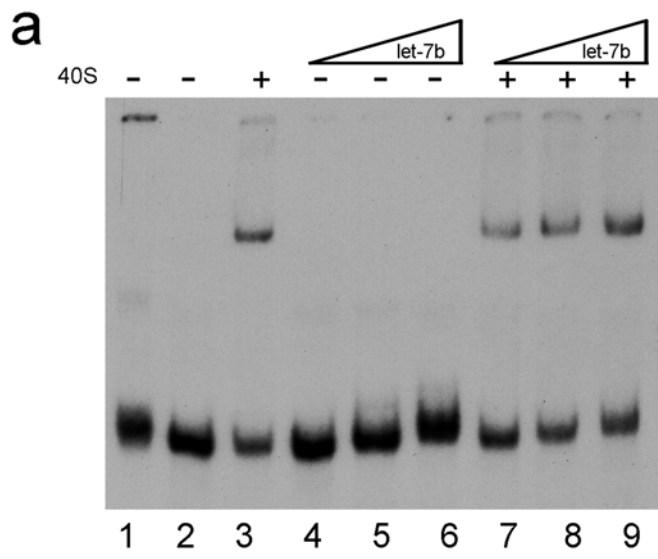
FIGURA 18



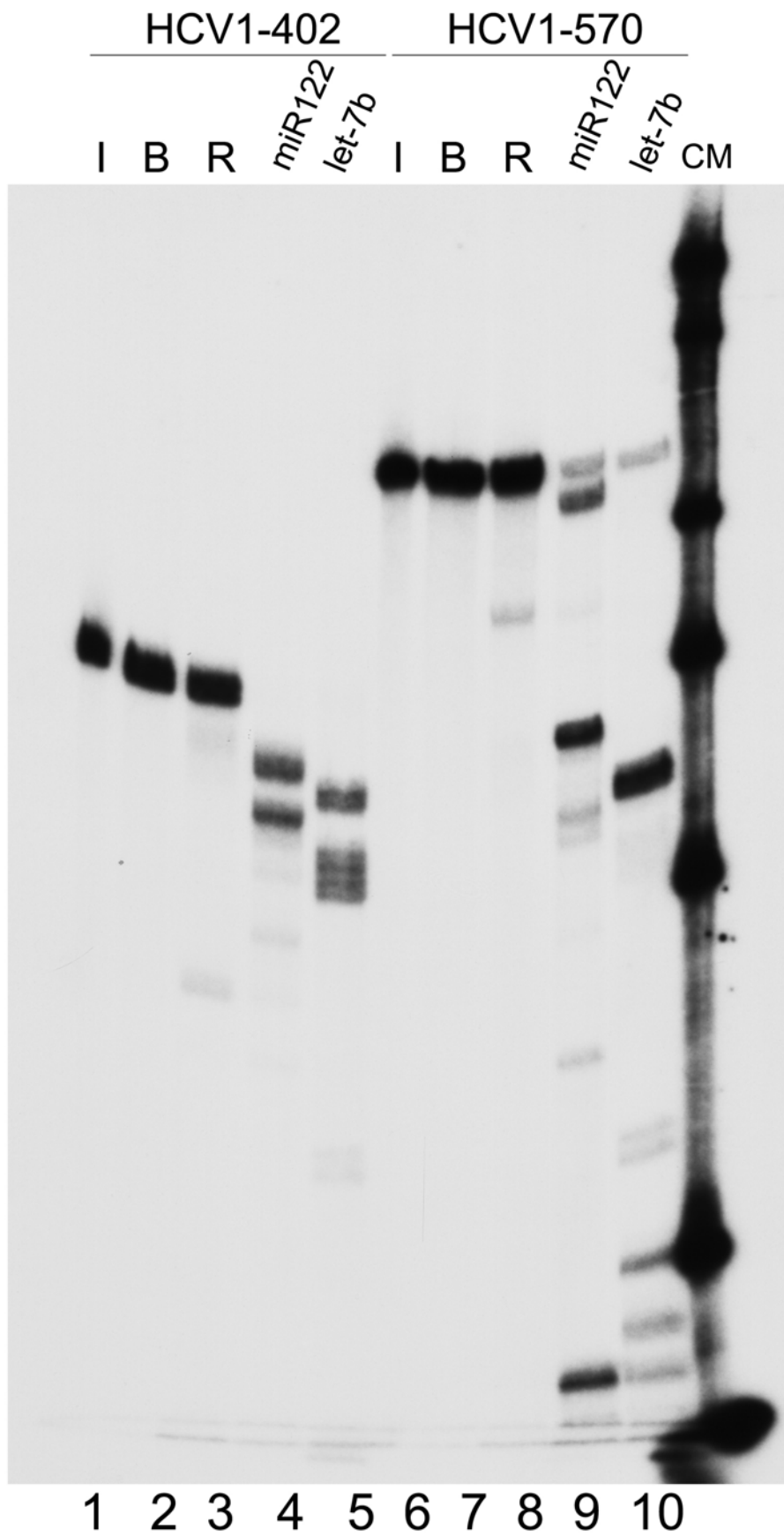
SUPP FIG 1b



SUPP FIG 2

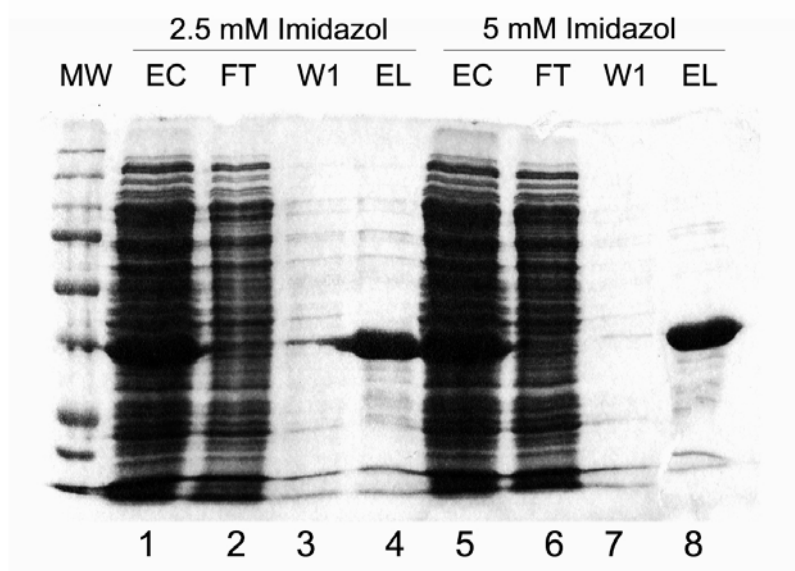


SUPP FIG 4



SUPP FIG 5

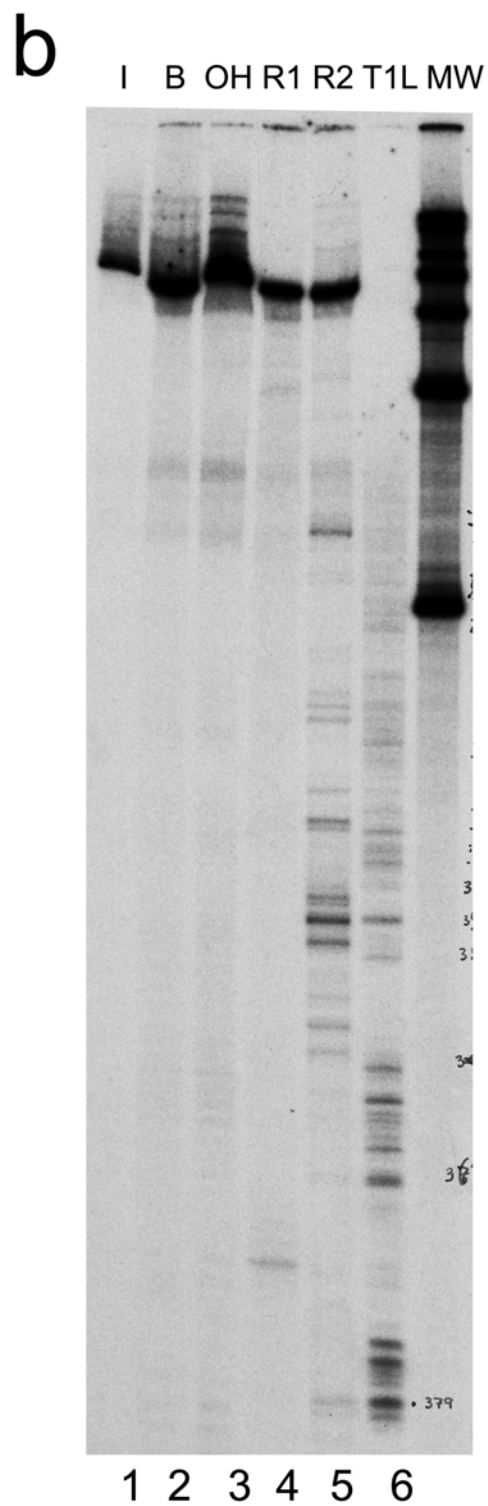
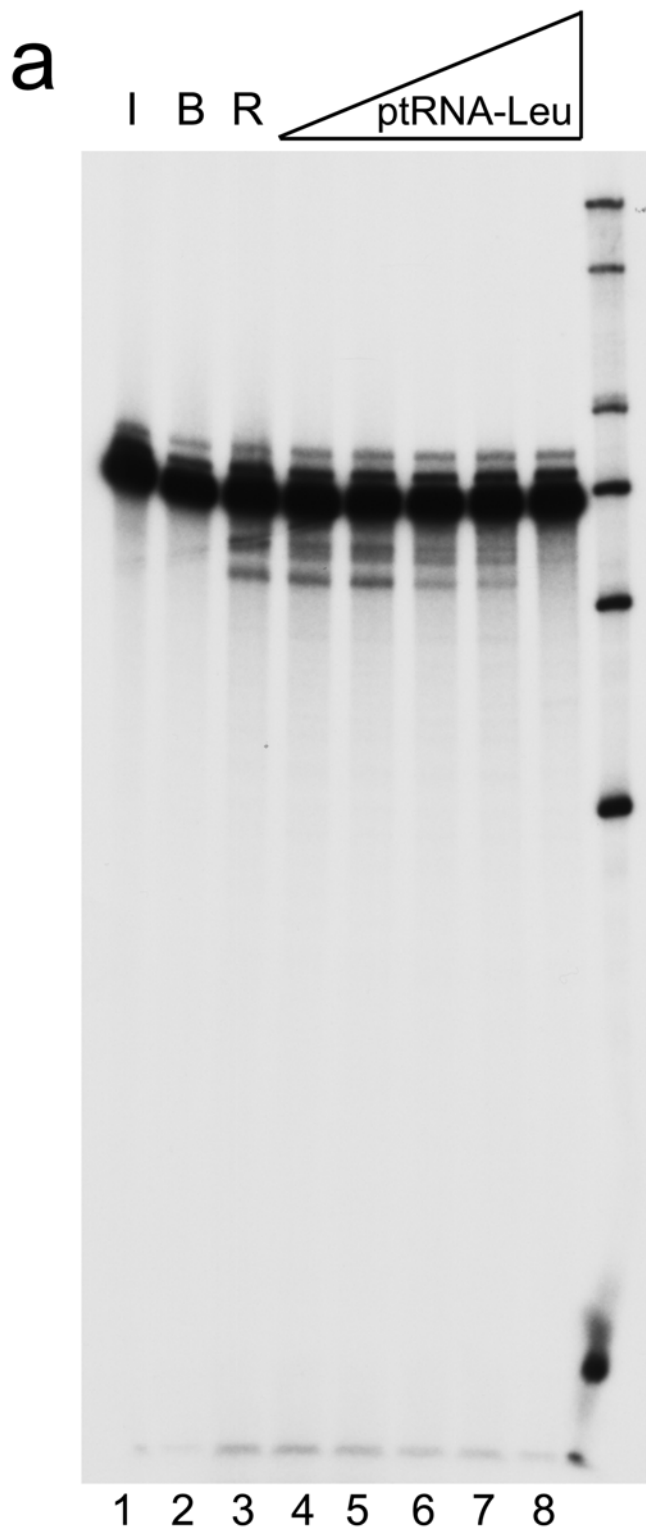
a



b



SUPP FIG 6



Virus is a Signal for the Host Cell

Jordi Gómez^{1,2} · Ascensión Ariza-Mateos^{1,2} ·
Isabel Cacho^{1,2}

Received: 13 March 2015 / Accepted: 25 June 2015

© The Author(s) 2015. This article is published with open access at Springerlink.com

Abstract Currently, the concept of the cell as a society or an ecosystem of molecular elements is gaining increasing acceptance. The basic idea arose in the 19th century, from the surmise that there is not just a single unit underlying an individual's appearance, but a plurality of entities with both collaborative and conflicting relationships. The following hypothesis is based around this model. The incompatible activities taking place between different original elements, which were subsumed into the first cell and could not be eliminated, had to be controlled very closely. Similarly, a strong level of control had to be developed over many cellular elements after the cell changed its genome to DNA. We assume that at least some of those original RNA agents and other biomolecules which carry incompatibilities and risks, are retained within current cells, although they are now under strict control. A virus functions as a signal informing these repressed cellular RNAs and other elements of ancient origin how to restore suppressed degrees of molecular freedom, favoring pre-existing molecular affinities and activities, re-establishing ancient molecular webs of interactions, and giving fragments of ancient coded information (mostly in the form of RNA structural motifs) the opportunity to be re-expressed. Collectively, these newly activated mechanisms lead to different possibilities for pathological cell states. All these processes are opposed by cell-control mechanisms. Thus, in this new scenario, the battle is considered intracellular rather than between the virus and the cell. And so the virus is treated as the signal that precipitates the cell's change from a latent to an active pathological state.

Ascensión Ariza-Mateos and Isabel Cacho contributed equally to this work.

✉ Jordi Gómez
jgomez@ipb.csic.es

¹ Laboratory of RNA Archeology, Instituto de Parasitología y Biomedicina 'López-Neyra', Consejo Superior de Investigaciones Científicas, Armilla 18100 Granada, Spain

² Centro de Investigación Biomedicina En Red de enfermedades hepáticas y digestivas, Barcelona, Spain

Keywords Molecular struggle · tRNA-like · IRES · Roux · Nietzsche · Eigen

Introduction

The unitary nature of the cell was criticized from a mechanistic and Darwinian perspective by one of the great scientists of the nineteenth century, Wilhelm Roux, in his 1881 book *The Struggle of the Parts in the Organism (Der Kampf der Teile im Organismus)* (Roux 2012). In this work, Roux proposed that the struggle must not only take place between organisms of the same species, but also on other, lower levels, such as the cellular or molecular levels. Examples at the cellular level could include the outgrowth of a cellular clone expressing a specific antibody after an antigen presentation or the selection of subsets of neuronal webs during development (Heams 2012). At the subcellular level these include the sequestered functional chloroplasts that can still be found in sea slugs which use them as a source of stored food reserves for sustenance during starvation periods (Christa et al. 2014a, b). The “molecular struggle” has also been related to several different forms of “intragenomic conflicts”, where genes do not follow the same laws of transmission (Heams 2012; Crespi and Nosil 2013); in the hypothetical genome reduction occurring during organelle (Baptiste and Gribaldo 2003) or other endosymbiosis (Husnik et al. 2013); or, possibly, for potential antagonist interaction between biomolecules within the same cell, for example in addiction modules in bacteria (Villarreal and Witzany 2013; Villarreal 2009).

Roux’s idea was taken up by Nietzsche, who integrated it into his metaphysical circuits: “Although the “units” are required to tell the tale, this doesn’t mean that such units “exist”. The concept of the unity is derived from our concept of “I”, which is our oldest article of faith. If we never considered ourselves as units, we would never have reached the concept of “thing”. Maybe we have been warned too late that our conception of “I” does not guarantee anything that can be referred to as a real unit” (Nietzsche 1968, Aphorism 520). Nietzsche suggest an ontology for interpreting organisms as a temporary result of a never-ending conflict, either inner or with the external world (Tauber 1994; Stiegler 2001).”Continuous becoming does not allow us to speak of individuals, etc.: the number of beings varies constantly...” (Nietzsche 1968, Aphorism 628). For Nietzsche, the most frequent changes would result from integrating the new and adapting it to what already existed (compressively reviewed in Stiegler 2001). Science has not yet provided a theoretical formulation capable of meeting the experimental exploration challenge of the Nietzschean view of his “being”: a metamorphic and active subject in directing its own becoming in contraposition to the passive Darwinian “unit of selection”. Nevertheless at present something is changing, new theoretical expressions oppose classical hierarchical ontology and, active and “far-seen” agents are being seriously considered (Eigen and Biebricher 1988; Gómez and Cacho 2001; Villarreal 2009; Baptiste and Dupre 2013; Sharov 2014; Noble 2015).

In general, viral infection is considered in terms of a relationship between two elements: the virus and host cell, or virus and the ribosome (Forterre and Prangishvili 2009). However, there might be problems for these clear splits as experts recognize the fact that the origin of the cell’s constitution is still a great enigma in biology (Koonin 2014). Moreover, since viruses were first discovered, experts have still not reached agreement as to whether they are by-products of cell evolution or living organisms that

pre-date cells (Moreira and López-García 2009; Villarreal and Witzany 2010). In our opinion, new data from virology also disrupts the theory of the cell as a coherent unit which tries to defend itself against infection: recently, it has been demonstrated that among genes induced by interferon (the paradigm of antiviral defense) nearly a third of them activate rather than suppress infection in a large set of (+) single-strand RNA viruses (Schoggins et al. 2014).

The Hypothesis

Unity of Pathological and Healthy States

Here, we propose a conceptual inversion. We begin by accepting the fact that the cell contains a multitude of factors and activities integrated into its subcellular groupings and molecular networks which are repressed. These factors (if expressed and coordinated) may cause genomic or cytoplasmic alterations, and then, the cell would acquire a range of distinct pathological states. That is to say, we accept that within the cell there are multiple grave dangers, and a healthy cell includes multiple potential pathologies. We will refer to this healthy condition as the latent pathological state of the cell. Necessarily, it may be argued that the cell is derived from a pathology-repressing molecular organization: the cell would not have existed if numerous incompatible activities of the original RNAs and other biomolecules were capable of avoiding diffusion, being under hierarchical organization, compartmentalization, being thermodynamically disadvantaged, kinetically slowed, time-synchronized, covalently modified, and so on. This surmise is necessary when the overall objective is to permit only the expression of the compatible qualities and coherent signals and codes (Barbieri 2008), i.e., those which foster collaboration between the different molecules that were finally enclosed within the cell. There may have been a new, significant wave of repression during the move from the RNA world to DNA genomes, in which, for example, many RNA activities that appeared to participate in the replication of RNA could subsequently have turned out to be problematic or toxic. Thus, in the case of viral infections, the hypothesis contends that cellular pathology does not necessarily follow the entry of the virus, except as a symptom, as a visualization of the fact that the pathology is actually occurring. Instead, our hypothesis is that molecular structures, their activities, and the majority of the information that makes up this new pathological state does not follow the entry of the virus and is not a consequence of viral activity, but exactly the opposite; that latent pathology within the cell must be placed ahead of it, as the basis of the infection. In other words, it is what makes infection possible. The basis of the infection is already there because it is also the basis of the cell itself, “basis” in the sense of “origin”: this latent pathological cellular state would have been there all along since the beginning of the cell, and in its very development.

Virus as Signal

To argue that the virus is a signal, or better, a folder full of signals, several conditions must be met. The first condition required for something to be considered a signal in a system is the existence of differentiated states which can communicate their difference

through space and time (Yair 2011). The pathological state of the cell is different from the one we have characterized as the latent-pathological state of the cell (the healthy cell), and the virus seems to be the vehicle and the information (the signal) charged with transmitting this difference. We are moving from a dual model of virus infections (virus ↔ cell) to a triadic model (virus ↔ pathological state ↔ transformation of the latent-pathological state into a pathological state) somewhat related to the Peirce's triadic sign (signal ↔ object ↔ interpretant) (Marty 1990). In our hypothesis, the signal is the virus; the object, the origin and the cause of the virus, is the pathological state; and the interpretant is the transformation, which is induced by the virus, from a latent-pathological state (the apparently healthy cell capable of receiving the signal) into a new pathological state: is a self-transformation signaled by the virus.

The second condition which must be met is that the virus signal is subject to interpretation according to biochemical and molecular biology rules, through which the cell is informed that another molecular organization (i.e., the pathological state) is possible (semantic aspect). This interpretative aspect distinguishes the virus activity from that of a chemical process. The transmission of the viral information can be blocked in the initial phase of infection, or indeed at any point throughout the process. The viral process is not a chemical reaction determined from the outset. Moreover, many environmental and historical and contextual factors (i.e., temperature, history of previous infections, co-infections, cellular genetic instability, tissue cellular heterogeneity, etc.) intervene crucially in the development of viral signal interpretation. So, although the virus may transmit to healthy cells the information that another state is possible, this information must be contextually interpreted (pragmatic aspect) (Witzany 2006). In each new round of virus-cell entry, the interpretant results, eventually, in a very similar new pathological state (object 2) to that from which the virus signal derives (object 1), but it is not exactly the same. For RNA viruses two factors contribute to these subtle differences: firstly, each virus that infects a target cell is composed of a subset of genetic variants from a swarm of variants from the infected donor cell (del Portillo et al. 2011) (Jung et al. 2002); secondly, the cellular context: each cell might be subtly different, either for *in vitro* cell virus cultures (de la Torre et al. 1988) or for *in vivo* infections (Korber et al. 1994). Cells maintained in culture suffer from genetic instability, while an infected organism is essentially a mosaic of different environments (cells, cell types and physiological conditions), and the virus multiplication rate is strictly dependent on the environment (Domingo and Holland 1997). Moreover, in rare cases, the interpretant may lead to quite a different situation, for example, when a cell that is newly infected by a cytolytic virus does not develop a cytolytic infection but rather a persistent infection. Again, the reason for this could lie either with the virus (Labadie et al. 2004) or the host cells (de la Torre et al. 1985; Martin Hernandez et al. 1994). Other examples of drastic differences between object and interpretant are tropism changes promoted by changes of a virus's use of cell receptors, and pathogenicity changes caused by substitutions in the viral polymerase and protease (Baranowski et al. 2001; Baranowski et al. 2003). Thus, virus signal meaning and evolution of meaning do not depend on the inherent properties of virus signal reproduction (i.e., high error rate) alone, but also in cellular contextual factors.

Thirdly, the grammatical rules, via which the RNA virus signal acquires meaning for those confronted elements within the cell, should be compatible with those we may presuppose to have applied to the RNA elements present at the origin of the cell. At least, high variation rates and limited message size, an inherent feature of RNA viruses,

are accomplished (Martell et al. 1992; Domingo 2007). The analogy between language and the original RNA quasi-species structure (Eigen 1988), similar to that found in present-day RNA viruses, has already been put forward by Nowak (Nowak 2002).

We hypothesize that these pathological states are somehow equivalent to one of the cell's ancient states. Each virally-dictated pathological state partially restores an early critical life situation. Viruses are signals derived from the biomolecules, activities and structures of life that existed in the remote past, but which are still present in our cells although in a fragmented, disjointed and inhibited form. In our hypothesis these pre-pathological states would be sustained by hidden agents, awaiting the arrival of an appropriate virus signal that tells them how to self-organize, express themselves, and so on.

Discussion

Evolutionary Forces That Might Maintain the Virus Signal

If viruses are signals, what selection forces could have acted to keep interpretation mechanisms within the cell that result, in many cases, in the death of that same cell? We come back to two selective forces, one is negative in character, and the other is positive. Negative selection forces would have preserved a risky feature or structure inside the cell in cases when, in addition to its potential toxic effects, it was also involved in activities that were essential to the cell. So instead of eliminating it, the cell somehow would have blocked its toxic properties. In fact, it is supposed that the most primitive molecular features are retained through selective pressure applied to their multiple connections and functions, which appeared as the complexity of cells increased in evolution. The presence of competing, at the time cooperating self-replicating agents and their swarms of associated biomolecules, might be sustained by their important contribution to fitness, rather than the pernicious effect of competition or mutual toxicity. Thus, the cell would have remained rooted in a state of tension, of latent internal conflict between its components, while it became more and more complex. This force would have retained the capability of the cell to interact/interpret the RNA virus signal since it first appeared. On the other hand, with regard to positive selection forces, we can conceive that in some cases, the cells having fortuitously incorporated stricter control mechanisms over their own internal elements would resist a new virus. In our hypothesis, this means that those cells would reaffirm cell unity when threatened with internal disintegration, generating the possibility for those new control systems to take over the metabolic networks affecting cell division and/or cell death, and/or acting to deal with situations of stress, and in any case conferring a competitive advantage over those cells which had never encountered that particular virus. In this sense, viral signals would favor cell complexity.

A particular virus signal that partially cuts off the communication between swarms of distinct cellular agents might lead to two different evolutionary effects: (i) in very primitive RNA-based cells more or less sensitive to the virus, the semiotic partitioning of a polymorphic population might lead to sympatric speciation; (ii) those cells that had developed immunity to the viral action would at least persist, and while contributing to the fitness of a polymorphic population they might subsequently be selected during a situation of stress or another type of infection. On the other hand, the high rates of RNA virus mutation may continuously introduce new challenges and lead to the selection of

new solutions for the cells, for further application elsewhere and in future selection scenarios. Thus, sustained internal conflicts between cellular agents together with continuously arriving variants of virus signals create a trend towards increasing redundant cohesion mechanisms and cellular complexity. Lack of continuous viral infection (in the long term), would lead to the spontaneous atrophy of such redundant connections and interactions among cellular agents, weakening the cells and being eliminated via selection. It would therefore be possible to propose virus-cell relationships as an example of non-genetic, ecological inheritance (Danchin et al. 2011).

Hidden Potential of RNA Signals

Studies in the 1970s indicated that rabbit reticulocyte ribosomes could bind to and protect authentic initiation regions of the bacterial phage ϕ 1 mRNA (Legon et al. 1977) and that eukaryotic viral RNAs, such as poliovirus, were translated into *E. coli* translation extracts (Rekosh et al. 1970). These studies indicated that at least a few signalling features within an mRNA strand, which can lead to ribosome recognition, should be common to prokaryotes and eukaryotes for initiation of protein synthesis (Legon et al. 1977). Recently, in the context of a non-canonical mechanism of translation initiation of Cricket Paralysis Virus (CrPV) (Dicistroviridae), Colussi (Colussi et al. 2015) found an RNA structural element capable of operating in both bacterial and eukaryotic translation systems, albeit with a different mechanism. It is likely that these events reflect neither the replication cycle of this virus in two such different hosts nor the canonical action of other bacteriophage mRNAs. Rather, it is more likely that the bacterial ribosome's potential to bind the eukaryotic signal is reporting a very ancient type of interaction that has been preserved by other unknown means. These 5' mRNA tRNA-like elements were found inside the viral mRNA as part of the internal ribosome entry site of the hepatitis C virus (Nadal et al. 2002) and then subsequently generalized to other viruses including animal pestivirus, picornaviruses and Cricket Paralysis Virus (CrPV) (Dicistroviridae) (Jan et al. 2003; Lyons and Robertson 2003). Very recently, we have identified and characterized structural elements bearing tRNA properties within human mRNA species (Díaz-Toledano and Gómez 2015) and in particular, in one of the characterized mRNAs, these structural elements coincide with what is known as a "cytoplasmic accumulation region". Thus, what we find is: (1) the unexpected potential of a viral tRNA-like motif to retain "eventually" very ancient properties; (2) the resemblance structural RNA signals within cellular mRNAs have with tRNA. These may acquire the capacity to bind 40S ribosomal subunits or other unexpected activities after viral entry (for example, if the viral tRNA-like motif sponges out factors normally interacting with the tRNA-like-signals within cellular mRNAs, releasing them to carry out other activities); and (3) the ancient and central role of tRNAs in cell life. All together this could suggest the potential for a tRNA-like entity, or agent, capable of reproducing and representing (at least partially) a primordial form of early life in our present day cells.

How to Support the Hypothesis Experimentally

The focus should be on identifying potentially hidden ontological entities within the cell at the molecular level by taking advantage of a viral infection. This involves, first,

seeking out new structures and activities for ancient cellular RNAs that are acquired upon entry of the virus into the cell. Second comes the characterization of new interactions between these RNAs (e.g., ribosomal RNAs, or their degradation fragments after viral infection, RNA from RNase P; Signal Recognition Particle RNA, tRNAs, and other non-coding RNAs), nucleotides, cofactors and other cellular biomolecules that favor the multiplication of the virus. Third, it should be tested whether, after the entry of the virus, any of the cellular molecules identified rebel against the establishment of control over cellular unity. Then, there must be exploration of the relationships between these cellular molecules that both favor viral multiplication, and actively participate in disrupting the cellular *status quo*. The robustness of these “alliances” between similar viruses should be examined using examples from different genera. Fourth, the origins of these alliances should be traced back, if possible, to try to theoretically identify the ancient “beings” still living in our cells. The fifth and final step is to experimentally disrupt and reconstitute these beings (or parts of them), to prove their actual existence. If all this could be accomplished, a new antiviral strategy could be developed.

CIBERehd: Centro de Investigación Biomédica en Red de Enfermedades Hepáticas y Digestivas (ISCIII). CSIC: Consejo Superior de Investigaciones Científicas.

Acknowledgments We thank Drs. Esteban Domingo, Carlos Briones, Purificación Lopez-García, Alexei A. Sharov and unknown referees for helpful advices.

Compliance with Ethical Standards The authors declare that they have no competing interests. The work was funded by the National Ministry of Competitiveness (which includes science and development) BFU2012-35898, Proyecto Excelencia Junta de Andalucía CVI-03050 and CIBERehd (Centro de Investigación en Red de Enfermedades Hepáticas y Digestivas) to A-AM.

Open Access This article is distributed under the terms of the Creative Commons Attribution 4.0 International License (<http://creativecommons.org/licenses/by/4.0/>), which permits unrestricted use, distribution, and reproduction in any medium, provided you give appropriate credit to the original author(s) and the source, provide a link to the Creative Commons license, and indicate if changes were made.

References

- Bapteste, E., & Dupre, J. (2013). Towards a processual microbial ontology. *Biology and Philosophy*, *28*(2), 379–404.
- Bapteste, E., & Gribaldo, S. (2003). The genome reduction hypothesis and the phylogeny of eukaryotes. *Trends in Genetics*, *19*(12), 696–700.
- Baranowski, E., Ruiz-Jarabo, C. M., & Domingo, E. (2001). Evolution of cell recognition by viruses. *Science*, *292*(5519), 1102–1105.
- Baranowski, E., Ruiz-Jarabo, C. M., Pariente, N., Verdaguier, N., & Domingo, E. (2003). Evolution of cell recognition by viruses: a source of biological novelty with medical implications. *Advances in Virus Research*, *62*, 19–111.
- Barbieri, M. (2008). Biosemiotics: a new understanding of life. *Naturwissenschaften*, *95*(7), 577–599.
- Colussi, T. M., Costantino, D. A., Zhu, J., Donohue, J. P., Korostelev, A. A., Jaafar, Z. A., et al. (2015). Initiation of translation in bacteria by a structured eukaryotic IRES RNA. *Nature*, *519*, 110–113.
- Crespi, B., & Nisil, P. (2013). Conflictual speciation: species formation via genomic conflict. *Trends in Ecology & Evolution*, *28*(1), 48–57.
- Christa, G., de Vries, J., Jahns, P., & Gould, S. B. (2014a). Switching off photosynthesis: The dark side of sacoglossan slugs. *Communicative & Integrative Biology*, *7*(1), e28029.

- Christa, G., Handeler, K., Schaberle, T. F., König, G. M., & Wagele, H. (2014b). Identification of sequestered chloroplasts in photosynthetic and non-photosynthetic sacoglossan sea slugs (Mollusca, Gastropoda). *Front Zool*, *11*(1), 15.
- Danchin, E., Charmantier, A., Champagne, F. A., Mesoudi, A., Pujol, B., & Blanchet, S. (2011). Beyond DNA: integrating inclusive inheritance into an extended theory of evolution. *Nature Reviews Genetics*, *12*(7), 475–486.
- de la Torre, J. C., Davila, M., Sobrino, F., Ortin, J., & Domingo, E. (1985). Establishment of cell lines persistently infected with foot-and-mouth disease virus. *Virology*, *145*(1), 24–35.
- de la Torre, J. C., Martínez-Salas, E., Diez, J., Villaverde, A., Gebauer, F., Rocha, E., et al. (1988). Coevolution of cells and viruses in a persistent infection of foot-and-mouth disease virus in cell culture. *Journal of Virology*, *62*(6), 2050–2058.
- del Portillo, A., Tripodi, J., Najfeld, V., Wodarz, D., Levy, D. N., & Chen, B. K. (2011). Multiploid inheritance of HIV-1 during cell-to-cell infection. *Journal of Virology*, *85*(14), 7169–7176.
- Díaz-Toledano, R., & Gómez, J. (2015). Messenger RNAs bearing tRNA-like features exemplified by interferon alfa 5 mRNA. *Cellular and Molecular Life Sciences*. doi:10.1007/s00018-015-1908-0.
- Domingo, E. (2007). *Virus Evolution* (5th ed., Vol. I, Fields Virology). New York: Wlaters Kluwer/Lippincott Williams & Wilkins.
- Domingo, E., & Holland, J. J. (1997). RNA virus mutations and fitness for survival. *Annual Review of Microbiology*, *51*, 151–178.
- Eigen, M., and Biebricher, CK. (1988). *Sequence space and quasispecies distribution* (RNA genetics. Vol III, Variability of RNA genomes). Boca Raton: CRC press.
- Forster, P., & Prangishvili, D. (2009). The great billion-year war between ribosome- and capsid-encoding organisms (cells and viruses) as the major source of evolutionary novelties. *Annals of the New York Academy of Sciences*, *1178*, 65–77.
- Gómez, J., & Cacho, I. (2001). Can Nietzsche power relationships be experimentally approached with theoretical and viral quasispecies? *Contributions to Science*, *2*(1), 103–108. <http://www.cat-science.com>. ISSN: 2013-410X; 1575-6343.
- Heams, T. (2012). Selection within organisms in the nineteenth century: Wilhelm Roux's complex legacy. *Progress in Biophysics and Molecular Biology*, *110*(1), 24–33.
- Husnik, F., Nikoh, N., Koga, R., Ross, L., Duncan, R. P., Fujie, M., et al. (2013). Horizontal gene transfer from diverse bacteria to an insect genome enables a tripartite nested mealybug symbiosis. *Cell*, *153*(7), 1567–1578.
- Jan, E., Kinzy, T. G., & Samow, P. (2003). Divergent tRNA-like element supports initiation, elongation, and termination of protein biosynthesis. *Proceedings of the National Academy of Sciences of the United States of America*, *100*(26), 15410–15415.
- Jung, A., Maier, R., Vartanian, J. P., Bocharov, G., Jung, V., Fischer, U., et al. (2002). Recombination: Multiply infected spleen cells in HIV patients. *Nature*, *418*(6894), 144.
- Koonin, E. V. (2014). The origins of cellular life. *Antonie Van Leeuwenhoek*, *106*(1), 27–41.
- Korber, B. T., Kunstman, K. J., Patterson, B. K., Furtado, M., McEvilly, M. M., Levy, R., et al. (1994). Genetic differences between blood- and brain-derived viral sequences from human immunodeficiency virus type 1-infected patients: evidence of conserved elements in the V3 region of the envelope protein of brain-derived sequences. *Journal of Virology*, *68*(11), 7467–7481.
- Labadie, K., Pelletier, I., Saulnier, A., Martin, J., & Colbere-Garapin, F. (2004). Poliovirus mutants excreted by a chronically infected hypogammaglobulinemic patient establish persistent infections in human intestinal cells. *Virology*, *318*(1), 66–78.
- Legon, S., Model, P., & Robertson, H. D. (1977). Interaction of rabbit reticulocyte ribosomes with bacteriophage f1 mRNA and of Escherichia coli ribosomes with rabbit globin mRNA. *Proceedings of the National Academy of Sciences of the United States of America*, *74*(7), 2692–2696.
- Lyons, A. J., & Robertson, H. D. (2003). Detection of tRNA-like structure through RNase P cleavage of viral internal ribosome entry site RNAs near the AUG start triplet. *The Journal of Biological Chemistry*, *278*(29), 26844–26850.
- Martell, M., Esteban, J. I., Quer, J., Genesca, J., Weiner, A., Esteban, R., et al. (1992). Hepatitis C virus (HCV) circulates as a population of different but closely related genomes: quasispecies nature of HCV genome distribution. *Journal of Virology*, *66*(5), 3225–3229.
- Martin Hernandez, A. M., Carrillo, E. C., Sevilla, N., & Domingo, E. (1994). Rapid cell variation can determine the establishment of a persistent viral infection. *Proceedings of the National Academy of Sciences of the United States of America*, *91*(9), 3705–3709.
- Marty, R. (1990). *L'Algèbre des signes: Essai de sémiotique scientifique d'après C.S. Peirce* (Foundations of Semiotics 24): John Benjamin Publishin Company.

- Moreira, D., & López-García, P. (2009). Ten reasons to exclude viruses from the tree of life. *Nature Reviews Microbiology*, 7(4), 306–311.
- Nadal, A., Martell, M., Lytle, J. R., Lyons, A. J., Robertson, H. D., Cabot, B., et al. (2002). Specific cleavage of hepatitis C virus RNA genome by human RNase P. *The Journal of Biological Chemistry*, 277(34), 30606–30613.
- Nietzsche, F. (1968). *The will to power*. New York: Ed. Random House.
- Noble, D. (2015). Evolution beyond neo-Darwinism: a new conceptual framework. *The Journal of Experimental Biology*, 218(Pt 1), 7–13.
- Nowak, M. (2002). From quasispecies to universal grammar. *Zeitschrift für Physikalische Chemie*, 216, 5–20.
- Rekosh, D. M., Lodish, H., & Baltimore, D. (1970). Protein synthesis in *Escherichia coli* extracts programmed by poliovirus RNA. *Journal of Molecular Biology*, 54(2), 327–340.
- Roux, W. (2012). *La lutte des parties dans l'organisme (original 1881)* (Collection “Sciences & philosophie”). Paris.
- Schoggins, J. W., MacDuff, D. A., Imanaka, N., Gainey, M. D., Shrestha, B., Eitson, J. L., et al. (2014). Pan-viral specificity of IFN-induced genes reveals new roles for cGAS in innate immunity. *Nature*, 505(7485), 691–695.
- Sharov, A. A. (2014). Evolutionary constraints or opportunities? *Biosystems*, 120C, 21–30.
- Stiegler, B. (2001). La vie comme “lutte interne des parties de l'organisme”. In *Nietzsche et la biologie* (1re ed., pp. 127). Paris: Presses Universitaires de France.
- Tauber, A. I. (1994). *The immune self: theory or metaphor? The self as organism: A philosophical consideration*. New York: Cambridge University press.
- Villarreal, L. P. (2009). *Origin of group identity: Viruses, addiction and cooperation*. Irvine: Springer.
- Villarreal, L. P., & Witzany, G. (2010). Viruses are essential agents within the roots and stem of the tree of life. *Journal of Theoretical Biology*, 262(4), 698–710.
- Villarreal, P., & Witzany, G. (2013). The DNA Habitat and its RNA Inhabitants: At the Dawn of RNA sociology. *Genomics Insights*, 6, 1–12.
- Witzany, G. (2006). From Umwelt to Mitwelt: Natural laws versus rule-governed sign-mediated interactions (rsi's). *Semiotica*, 158, 425–438.
- Yair, N. (2011). Why do we need signs in biology? In C. Emenche and K. Kull (Ed.), *Towards a semiotic biology* (pp. 1–297). London: Imperial College Press.

DISCUSIÓN

Importancia del análisis estructural del IRES de HCV junto a sus regiones 5' y 3' flanqueantes

En este trabajo, se han analizado y estudiado nuevos elementos estructurales del RNA de HCV en un fragmento que contiene los primeros 570 nucleótidos del genoma del virus. En este fragmento se incluye la totalidad de la región 5'UTR y el primer tercio de la secuencia que codifica para la proteína *core* del virus. Esta región contiene un elemento IRES, altamente estructurado y muy conservado a nivel de su estructura secundaria entre miembros del género *Hepacivirus* y *Pestivirus* (Brown, Zhang et al. 1992; Honda, Beard et al. 1999). En el desarrollo de esta Tesis, se ha determinado una serie de cambios estructurales, hasta el momento no identificados, gracias a la incorporación de las regiones flanqueantes del IRES en su análisis estructural.

Grupos que han trabajado con este fragmento, han determinado el anillamiento a larga distancia entre la región basal del dominio VI y la región que separa los dominios I y II, dejando al IRES en una forma cerrada (Honda, Rijnbrand et al. 1999) (Tuplin, Evans et al. 2004; Beguiristain, Robertson et al. 2005). Ensayos de unión del RNA de HCV con el miR-122 han permitido demostrar en esta Tesis que la unión del miR-122 en sus dianas S1 y S2, entre los dominios I y II, es capaz de competir con la formación de ese anillamiento a larga distancia, pasando de la conformación cerrada a una forma abierta que favorece la integridad estructural de los dominios V y VI, *in vitro* (Diaz-Toledano, Ariza-Mateos et al. 2009).

Es importante resaltar, que la mayoría de grupos han excluido los dominios I, V y VI tanto de ensayos estructurales como funcionales del IRES. Se han centrado únicamente en los dominios que componen el IRES: dominios II, III y IV que conforman la unidad funcional mínima para el estudio del IRES.

El dominio I de la región 5'-UTR, en el flanco 3', se ha relacionado con una disminución de los niveles de traducción del virus, aunque aún no ha podido determinarse el modo en el que afecta a la función del IRES (Rijnbrand, Bredenbeek et al. 1995; Honda, Ping et al. 1996). El tallo-lazo que forma el dominio I presenta un tallo altamente estable formado por apareamientos G:C y un bucle apical que podría establecer algún tipo de interacción con algún otro elemento estructural. Ensayos de SHAPE de la región 5'UTR mostraron que la delección del dominio I incrementó la accesibilidad del bucle interno del subdominio IIa, sin embargo, si existe la relación entre ambos dominios permanece

aún por vislumbrar(Mortimer and Doudna 2013). Continúa la controversia en el papel que juegan los dominios estructurales V y VI, localizados en el flanco 3' del IRES. La supresión de la integridad estructural de cualquiera de los dos dominios conduce a la represión de la replicación y traducción(Vassilaki, Friebe et al. 2008). El papel regulador de ambos dominios en la función del IRES se muestra reforzado por el alto grado de conservación de la estructura y secuencia entre los diferentes genotipos de HCV(McMullan, Grakoui et al. 2007). En esta Tesis se ha conseguido determinar una nueva diana para el miR-122 localizada en la última porción de la región espaciadora entre los dominios IV y V (S4), interaccionando tanto a través de su secuencia *seed* como *no-seed*. La interacción del miR-122 en S4 podría incrementar la estabilidad de los dominios V y VI en la forma abierta del IRES y dificultar su extensión para formar el anillamiento a larga distancia. Este cambio conformacional desde la forma abierta a la cerrada se detectó también como dos confórmeros de diferente migración en EMSA, al cambiar las condiciones de Mg^{2+} en el medio de reacción. Al ir incrementando la concentración de Mg^{2+} las estructuras terciarias del RNA se originan y estabilizan, como ocurrió con el pseudonudo(Kieft, Zhou et al. 1999). Igualmente, el cambio de la forma abierta a la forma cerrada fue dependiente de la presencia de Mg^{2+} (Garcia-Sacristan, Moreno et al.).

Por otro lado, la presencia de los dominios que flanquean en 5' y 3' al IRES de HCV ha permitido determinar dos formas de complejo binario en las que la subunidad ribosomal 40S se encuentra unida de forma diferente: Una forma de migración más lenta en EMSA, que correspondería a la forma abierta, donde la subunidad ribosomal 40S está unida a los dominios II y III; y otra forma de migración más rápida, asociada a la forma cerrada, donde la subunidad ribosomal se uniría principalmente al dominio III. Esto podría indicar que el dominio II no se encuentra unido a la subunidad ribosomal 40S en la forma cerrada al encontrar algún tipo de limitación conformacional que impida su torsión hacia el dominio IV, como ha sido descrito que sucede en el inicio de traducción del IRES de HCV(Spahn, Kieft et al. 2001; Lukavsky, Kim et al. 2003).

Mediante ensayos de corte con la RNasa P humana, hemos detectado mayor rendimiento de corte de la estructura tipo-tRNA en el fragmento del RNA de HCV que presenta la forma cerrada (HCV1-570). Esto indicaría que la presencia de los dominios

flanqueantes, al permitir el anillamiento a larga distancia, favorece el reconocimiento de la estructura tipo-tRNA hacia la RNasa P humana. O bien porque contribuya en el plegamiento del motivo tipo-tRNA o porque deje más accesible las regiones del tRNA que reconoce el enzima (Swerdlow and Guthrie 1984; Lee and Knapp 1985; Maraia and Lamichhane 2011).

En cualquier caso, nuestro estudio ha tenido únicamente un carácter estructural, enfocado en profundizar en las interacciones y cambios conformacionales que suceden en la región 5' del RNA de HCV. Destacamos que las regiones que flanquean al IRES contribuyen a establecer un dominio aún más complejo de IRES, que lo dota de un cambio conformacional y que conlleva asociado distintas formas en las que es protegido por el ribosoma.

Análisis de elementos estructurales en el RNA de HCV a nivel operativo

En el desarrollo de esta Tesis se ha abordado el estudio de la estructura del RNA de HCV utilizando la actividad biológica de una serie de agentes celulares que establecen o podrían establecer relación con el virus durante la infección. La mayoría de ensayos destinados a estudiar la estructura y los cambios conformacionales del RNA suelen llevarse a cabo mediante diferentes herramientas de carácter químico (DMS) o enzimático (RNasas T1, V1, A) que inciden sobre el propio RNA y aportan una información directa de la estructura de éste. Sin embargo, en este estudio se obtuvo información de la relación de cada uno de los diferentes agentes bioquímicos y biofísicos utilizados con el RNA de HCV, a través de su actividad biológica. La actividad biológica de un agente, se definiría como la función o funciones que ejerce en la célula. De esta manera, la información que aporta un agente biológico al investigador está relacionada con la actividad que lo define. Un claro ejemplo utilizado en este trabajo, es la RNasa P, que reconoce estructuras tipo-tRNA, debido a su actividad biológica relacionada con el procesamiento de los precursores del tRNA. La principal ventaja que aporta este tipo de estudio es la extrapolación de la información que aporta el agente bioquímico y biofísico a otros RNAs. Sin embargo, en aquellos casos donde ya era conocida la actividad que ejerce alguno de estos agentes sobre el RNA de HCV, se

complementó mediante el estudio con herramientas clásicas específicas para el estudio del RNA.

Entre los agentes utilizados, destacan los microRNAs miR-122 y let-7b, ambos, íntimamente relacionados con el ciclo replicativo del virus. Es de resaltar el miR-122 ya que está relacionado con el tropismo celular, aporta estabilidad a su genoma e interviene regulando la replicación y traducción viral. La utilización del miR-122 permitió identificar el cambio conformacional de la forma cerrada a la forma abierta, debido a la interacción del miR-122 en las dianas S1 y S2 que compiten con el anillamiento a larga distancia, aportando un patrón de corte de la RNasa III diferente en presencia o ausencia del microRNA. Tras la identificación de este cambio conformacional, las herramientas empleadas para su confirmación consistieron en ensayos de corte con las RNasas específicas de simple (RNasa T1) y doble cadena (RNasa V1). La presencia del miR-122 también permitió identificar un nuevo cambio conformacional en el dominio IV, mediante ensayos de corte con la RNasa H. Tras la unión del miR-122 en la diana S3 se mejoró la hibridación del oligonucleótido de DNA 317, con su secuencia complementaria en el dominio IV, para la cual ya había sido descrito que presentaba dificultades en su accesibilidad. De manera que, el miR-122 podría estar abriendo el tallo del dominio IV y facilitando la entrada del oligonucleótido 317. Este cambio conformacional se confirmó y apoyó con la detección de las posiciones directamente implicadas en ausencia y presencia del miRNA, mediante análisis de la propia estructura del RNA con DMS, la RNasas A y T1, y a través de mutaciones puntuales en el tallo del dominio IV (Non y Rest). Por el momento, la función del mir-122 en S3 no ha sido determinada, sin embargo, el cambio conformacional local que origina en el dominio IV, donde se localiza el codón de inicio de la traducción, podría tener algún tipo de relación con el inicio de la traducción y el posicionamiento del codón AUG iniciador. Se desconoce si la presencia del miR-122 en S3 podría suponer un obstáculo para la traducción o si en alguna etapa del inicio de traducción es capaz de separarse y contribuir positivamente en el proceso. Por otro lado, la diana para let-7b en el dominio IV del RNA-HCV no permitió este cambio conformacional. Esto podría ser debido a que let-7b, a diferencia del miR-122, se une unos nucleótidos aguas abajo de donde lo hace el miR-122 y no participando en esa desnaturalización del tallo del dominio IV. El miR-122 también fue capaz de

incrementar la unión de la subunidad ribosomal 40S por el IRES de HCV en la forma abierta del complejo con el fragmento 1-570, capaz de formar el anillamiento a larga distancia. Al no ocurrir con los fragmentos delecionados en los extremos 5' (HCV44-570) y 3' (HCV1-402), que ya se muestran abiertos desde un principio, resaltaría la importancia de los dominios flanqueantes I, V y VI en la formación del complejo binario y podría explicar la discrepancia de resultados en relación al papel del miR-122 en la traducción viral. La utilización del miR-122 en estos ensayos ha permitido comparar los cambios estructurales que sufre el RNA de HCV en su ausencia y presencia. El papel estructural del miR-122 ha sido utilizado para obtener información de otros agentes biológicos que también fueron utilizados al modular la información que transmitieron. La concordancia de información aportada por la combinación de diferentes agentes biológicos ha dado más peso a los resultados obtenidos.

El HCV utiliza las subunidades ribosomales del hepatocito para llevar a cabo la síntesis de sus proteínas virales mediante una traducción dependiente de IRES. En este trabajo se utilizaron las subunidades ribosomales 40S procedentes de células HeLa, cuyo comportamiento, unión y cambios conformacionales en el IRES de HCV es el mismo que el de subunidades procedentes de células hepáticas Huh-7. La elección de subunidades 40S a partir de células HeLa permitieron comparar los resultados obtenidos con la mayoría de ensayos ya publicados en relación a la unión del RNA de HCV y la subunidad 40S, realizados también con subunidades procedentes de células HeLa. Los ensayos de unión de la subunidad ribosomal 40S con los diferentes fragmentos del RNA de HCV permitieron detectar dos formas de complejo RNA-HCV:40S mediante EMSA, asociadas con las formas abierta (migración más lenta) y cerrada (migración más rápida) del RNA de HCV. En los ensayos de unión de las subunidades 40S con fragmentos del RNA de HCV delecionados en sus extremos 5' y 3', que están impedidos en la formación del anillamiento a larga distancia, sorprendió la presencia de las dos bandas de complejo en el fragmento 44-570, no esperada. Esto podría indicar que otras interacciones estructurales no identificadas contribuirían en la estabilización de la forma cerrada, adicionales al anillamiento a larga distancia. La identificación de ambas conformaciones del complejo RNA-HCV:40S permitió determinar las diferencias en la secuencia protegida por la subunidad 40S en ambas

formas, mediante ensayos de digestión total con la RNasa A y fraccionamiento en gradiente de sacarosa.

Una de las herramientas utilizadas para la identificación de estructuras tipo-tRNA es la capacidad de la RNasa P para el reconocimiento y procesamiento de estas estructuras. En este trabajo se utilizó la RNasa P humana y la subunidad ribozima de la RNasa P de la cianobacteria *Synechocystis sp.* La identificación de la estructura tipo-tRNA del IRES de HCV ya había sido descrita con cada una de las dos enzimas. Aquí se utilizó la RNasa P para analizar los cambios de accesibilidad a este motivo tipo-tRNA inducidos por cambios estructurales en el RNA 1-570 en distintas condiciones.

Resultados de interés fueron obtenidos con la RNasa P humana. La forma cerrada del RNA de HCV permitió un incremento de la accesibilidad del motivo tipo-tRNA por la RNasa P humana, que no fue apreciado en fragmentos delecionados del RNA, ni en presencia del miR-122. Sin embargo, el efecto del miR-122 no fue siempre negativo: cuando el RNA se encontró ya en la forma abierta, entonces, el miR-122 estimuló el procesamiento por la RNasa P. Lo que podría estar ocurriendo es que la unión del miR-122 provocaría dos cambios conformacionales diferentes que afectarían a la accesibilidad de la estructura tipo-tRNA: (1) la interacción del miR-122 en las dianas S1/S2 provoca un cambio conformacional a larga distancia pasando de la forma cerrada a la abierta, que presentaría peor accesibilidad por la RNasa P humana; (2) la unión directa del miR-122 al dominio IV (S3) provoca un cambio conformacional local que desestabiliza el tallo de este dominio, pudiendo contribuir positivamente al plegamiento o la exposición de la estructura tipo-tRNA por la RNasa P humana.

La accesibilidad del motivo tipo-tRNA se analizó también con la ribozima de la RNasa P de *Synechocystis*. La unión del miR-122 provocó en todos los fragmentos utilizados una disminución de la accesibilidad de la ribozima por el motivo tipo-tRNA, independientemente de presentarse en la forma abierta o cerrada.

En este trabajo se utilizó también la RNasa Z de *E. coli* para confirmar la presencia de la estructura tipo-tRNA mediante un agente de diferente naturaleza a la RNasa P. Este sería el primer indicio de que la RNasa Z reconoce y procesa el motivo tipo-tRNA de HCV. Tras la secuenciación de los diferentes productos de corte de la RNasa Z el corte quedó definido en la cadena 5' del tallo del dominio IV. Los ensayos de corte en presencia de miR-122 mostraron una disminución de la accesibilidad de la RNasa Z por

el motivo tipo-tRNA. Los resultados de inhibición del corte tanto de la ribozima de *Synechocystis*, como con la RNasa Z en presencia del miR-122, podrían ser debidos a que el miR-122 al unirse a su diana S3 en el dominio IV, estaría ocupando las posiciones de reconocimiento y corte de ambas enzimas. Esto no ocurrió con la RNasa P humana que presenta su sitio de corte en la región espaciadora de los dominios IV y V (nt 373).

El ión magnesio es otro agente bioquímico utilizado en este trabajo y que resulta imprescindible en la formación y estabilidad de las estructura terciarias. Cambios en la concentración de Mg^{2+} de 0 a 10 mM en reacción permitió confirmar la dependencia de Mg^{2+} en la formación del pseudonudo, el anillamiento a larga distancia y el cambio de conformación local del dominio IV, mediante EMSA y ensayos de digestión parcial con la RNasa T1 en condiciones nativas. La unión del miR-122 en cada una de sus dianas en ambos flancos del IRES, supuso la necesidad de utilizar mayor concentración de Mg^{2+} en reacción para contrarrestar los cambios conformacionales que origina el miR-122. Esto supondría que el miR-122 y el Mg^{2+} presentan efectos opuestos en relación a los cambios conformacionales, donde el Mg^{2+} tiende a compactar las estructuras de RNA estabilizando las estructuras terciarias y el miR-122 competiría con la formación de las estructuras terciarias relacionadas con sus sitios de unión. De tal manera, cambios en la concentración de Mg^{2+} en reacciones de unión del RNA-HCV con la subunidad 40S, ayudó a confirmar que las dos bandas complejos obtenidas por EMSA correspondían a dos conformaciones del RNA-HCV unidas a la subunidad 40S.

La capacidad de la radiación UV para formar *crosslink* en el bucle-E del dominio II del RNA de HCV permitió determinar un autocorte inducido directamente por la radiación del UV-C.. Sin embargo, el corte específico por acción de la radiación UV en el RNA del CSFV resultó independiente del bucle-E. Indicando un mecanismo de autocorte también oxidativo como ocurrió en HCV, pero originado de manera independiente al bucle-E. De manera que, el mecanismo de corte directo por acción de la radiación UV podría ser un mecanismo regulador reminiscente de un mundo RNA donde la radiación UV fue más intensa debido a la ausencia de la capa de ozono.

La información aportada por cada uno de estos agentes y la interrelación de ellos en ciertos ensayos, como fueron los ensayos comparativos en ausencia o presencia del miR-122, o el cambio de la concentración de Mg^{2+} en los ensayos con cada uno de los otros agentes implicados, permitió identificar y mejorar la caracterización de elementos estructurales en el RNA de HCV.

Correlación con otros RNAs similares

En otros RNAs de *Flavivirus* relacionados con HCV, como es el caso del RNA del *Pestivirus* CSFV, los dominios II y III del IRES presentan alta similitud estructural, incluyendo a los diferentes cambios conformacionales que experimenta en relación al papel funcional del IRES. El dominio II del IRES de CSFV tiene la capacidad de doblarse mediante su bucle interno y aproximar el bucle apical al codón de inicio de traducción. La formación de un pseudonudo en la vecindad del codón de inicio, al igual que sucede para HCV, complementa al dominio II en el posicionamiento del codón de inicio AUG en el surco de descodificación en la subunidad ribosomal 40S durante el inicio de traducción. Todos estos datos apoyan la importancia del estudio de la actividad de los diferentes agentes que interaccionan con el RNA para conocer las estructuras y los cambios estructurales. La actividad de cada agente será la misma ante elementos estructurales idénticos o similares. La caracterización de nuevos elementos estructurales a través de estos agentes aportaría información del posible papel funcional de esas nuevas estructuras.

Las diferentes estructuras que forman la región de estudio, en este caso, el RNA de HCV 1-570, consistirían en una serie de marcas o señales que podrían repetirse a lo largo de los diferentes RNAs y ser identificados por cada uno de los agentes bioquímicos y biofísicos. De manera que, la especificidad que presentan esos agentes celulares por cada una de las diferentes estructuras presentes en los RNAs virales es la información que resulta de interés.

CONCLUSIONES

1. Mediante ensayos de corte con las RNasas que reconocen simple (RNasa T1) y doble (RNasa V1) cadena se determinaron cambios en la estructura del RNA de HCV 1-570 por la unión del microRNA hepático miR-122 en los sitios S1 y S2. Estos cambios se corresponden con un cambio conformacional de la forma cerrada a la forma abierta.
2. El incremento de la concentración de magnesio en reacción, favorece el cambio conformacional de la forma abierta a la forma cerrada.
3. Se ha determinado un nuevo sitio de unión para el miR-122, llamado S4; que junto al sitio de unión S3, forman un sitio de unión en tándem para el miR-122 en el flanco 3' del IRES. De manera que, el IRES se presenta flanqueado por dos sitios de unión en tándem para el miR-122 en los flancos 5' (S1 y S2) y 3' (S3 y S4).
4. Estudios termodinámicos y cinéticos de la unión del miR-122 al RNA-HCV han determinado que el miR-122 interacciona con mayor afinidad en el flanco 5' del IRES (S1 y S2), pero con mayor rapidez al flanco 3' del IRES (S3 y S4).
5. La unión del miR-122 en el flanco 5' del IRES (S1 y S2) es dependiente de la presencia de la secuencia *seed*. Mientras que la unión en el flanco 3' del IRES es dependiente de la secuencia *no-seed* para S4 y dependiente de la longitud completa del miR-122 para S3.
6. La unión directa del miR-122 en el dominio IV provoca un cambio conformacional local que produce la desestabilización del tallo del dominio. Este cambio conformacional incrementa la accesibilidad del oligonucleótido de DNA 317 por su secuencia complementaria el dominio IV.
7. Los cambios conformacionales promovidos por la unión del miR-122 en flanco 3' ó 5' del IRES modifican el reconocimiento de la estructura tipo-tRNA por las RNasas dependientes de estructura RNasas P y Z:
 - 7.1. Incrementa la accesibilidad y/o el reconocimiento por la RNasa P humana en la forma abierta, y la dificulta en la forma cerrada.
 - 7.2. La ribozima de la RNasa P de la cianobacteria *Synechocystis* y la RNasa Z disminuyen la accesibilidad por la estructura tipo-tRNA tanto en la forma abierta como cerrada.
8. La RNasa P humana presenta mayor accesibilidad por la estructura tipo-tRNA en la forma abierta que en la cerrada.

9. La unión del miR-122 en el dominio IV (S3) no desestabiliza el pseudonudo presente en el IRES de HCV.
10. Se han identificado dos conformaciones del complejo formado por 40S:HCV-RNA "Rápida" y "Lenta" que corresponden respectivamente a las formas "Abierta" y "Cerrada" del RNA de HCV.
11. La unión del miR-122 es capaz de incrementar la unión de la subunidad ribosomal 40S en la conformación abierta.
12. Las regiones del IRES de HCV protegidas por la subunidad ribosomal 40S varían entre las conformaciones abierta y cerrada. En la forma abierta están protegidos los dominios II y III, mientras que en la forma cerrada se protege el dominio III.
13. Se ha identificado un autocorte específico por acción directa de la radiación UV-C en los RNAs de HCV y CSFV.
14. El autocorte por acción de la luz UV ocurre en las posiciones C₇₉ y en la U₇₈ 5' adyacente del dominio IIb del RNA de HCV y en las posiciones A₄₅ y en la U₄₄ 5' adyacente del dominio Ib del RNA del CSFV.
15. El autocorte inducido por la radiación UV en el RNA de HCV es dependiente de la presencia de un bucle-E, a diferencia del RNA de CSFV que es capaz de cortarse en ausencia del bucle-E.
16. El autocorte producido por la radiación directa de UV-C en el RNA de HCV se lleva a cabo mediante un mecanismo oxidativo independiente de la generación de radicales libres en el medio.
17. Los nuevos extremos generados tras el autocorte por la radiación UV-C, tanto en el RNA de HCV como en el de CSFV, son principalmente 5'-P y 3'-P y en menor medida 3'-OH.
18. La radiación UV-B es capaz de producir el autocorte en el RNA de HCV con mucha menos eficiencia que la radiación UV-C.

BIBLIOGRAFÍA

- Bai, Y., K. Zhou, et al. (2013). "Hepatitis C virus 3'UTR regulates viral translation through direct interactions with the host translation machinery." Nucleic Acids Res **41**(16): 7861-74.
- Barth, H. (2015). "Hepatitis C virus: Is it time to say goodbye yet? Perspectives and challenges for the next decade." World J Hepatol **7**(5): 725-37.
- Beguiristain, N., H. D. Robertson, et al. (2005). "RNase III cleavage demonstrates a long range RNA: RNA duplex element flanking the hepatitis C virus internal ribosome entry site." Nucleic Acids Res **33**(16): 5250-61.
- Berry, K. E., S. Waghray, et al. (2010). "The HCV IRES pseudoknot positions the initiation codon on the 40S ribosomal subunit." Rna **16**(8): 1559-69.
- Berry, K. E., S. Waghray, et al. (2011). "Crystal structure of the HCV IRES central domain reveals strategy for start-codon positioning." Structure **19**(10): 1456-66.
- Boehringer, D., R. Thermann, et al. (2005). "Structure of the hepatitis C virus IRES bound to the human 80S ribosome: remodeling of the HCV IRES." Structure **13**(11): 1695-706.
- Boerneke, M. A. and T. Hermann (2015). "Ligand-responsive RNA mechanical switches." RNA Biol **12**(8): 780-6.
- Bradrick, S. S., S. Nagyal, et al. (2013). "A miRNA-responsive cell-free translation system facilitates isolation of hepatitis C virus miRNP complexes." Rna **19**(8): 1159-69.
- Branch, A. D., B. J. Benenfeld, et al. (1985). "Ultraviolet light-induced crosslinking reveals a unique region of local tertiary structure in potato spindle tuber viroid and HeLa 5S RNA." Proc Natl Acad Sci U S A **82**(19): 6590-4.
- Branch, A. D., B. J. Levine, et al. (1995). "An RNA tertiary structure of the hepatitis delta agent contains UV-sensitive bases U-712 and U-865 and can form in a bimolecular complex." Nucleic Acids Res **23**(3): 491-9.
- Brannvall, M. and L. A. Kirsebom (2001). "Metal ion cooperativity in ribozyme cleavage of RNA." Proc Natl Acad Sci U S A **98**(23): 12943-7.
- Brodersen, P. and O. Voinnet (2009). "Revisiting the principles of microRNA target recognition and mode of action." Nat Rev Mol Cell Biol **10**(2): 141-8.
- Brown, E. A., H. Zhang, et al. (1992). "Secondary structure of the 5' nontranslated regions of hepatitis C virus and pestivirus genomic RNAs." Nucleic Acids Res **20**(19): 5041-5.
- Buck, A. H., A. V. Kazantsev, et al. (2005). "Structural perspective on the activation of RNase P RNA by protein." Nat Struct Mol Biol **12**(11): 958-64.

- Burgstaller, P., T. Hermann, et al. (1997). "Isoalloxazine derivatives promote photocleavage of natural RNAs at G.U base pairs embedded within helices." Nucleic Acids Res **25**(20): 4018-27.
- Burrows, C. J. and J. G. Muller (1998). "Oxidative Nucleobase Modifications Leading to Strand Scission." Chem Rev **98**(3): 1109-1152.
- Cadet, J., T. Douki, et al. (2015). "Oxidatively generated damage to cellular DNA by UVB and UVA radiation." Photochem Photobiol **91**(1): 140-55.
- Candeias, L. P., P. O'Neill, et al. (1992). "Ionization of polynucleotides and DNA in aqueous solution by 193 nm pulsed laser light: identification of base-derived radicals." Int J Radiat Biol **61**(1): 15-20.
- Castano, J. G., J. A. Tobian, et al. (1985). "Purification and characterization of an endonuclease from *Xenopus laevis* ovaries which accurately processes the 3' terminus of human pre-tRNA-Met(i) (3' pre-tRNase)." J Biol Chem **260**(15): 9002-8.
- Catanese, M. T. and M. Dorner (2015). "Advances in experimental systems to study hepatitis C virus in vitro and in vivo." Virology **479-480C**: 221-233.
- Cerutti, P. A., N. Miller, et al. (1969). "Photohydration of uridine in the RNA of coliphage R17. I. Reductive assay for uridine photohydration." Proc Natl Acad Sci U S A **64**(2): 731-8.
- Coahran, D. R., A. Buzzell, et al. (1962). "The effect of ultraviolet irradiation on nucleic acid isolated from tobacco mosaic virus." Biochim Biophys Acta **55**: 755-67.
- Conrad, K. D., F. Giering, et al. (2013). "MicroRNA-122 dependent binding of Ago2 protein to hepatitis C virus RNA is associated with enhanced RNA stability and translation stimulation." PLoS One **8**(2): e56272.
- Conrad, K. D. and M. Niepmann (2013). "The role of microRNAs in hepatitis C virus RNA replication." Arch Virol **159**(5): 849-62.
- Correll, C. C., B. Freeborn, et al. (1997). "Metals, motifs, and recognition in the crystal structure of a 5S rRNA domain." Cell **91**(5): 705-12.
- Cox, E. M., S. M. Sagan, et al. (2013). "Enhancement of hepatitis C viral RNA abundance by precursor miR-122 molecules." Rna **19**(12): 1825-32.
- Crespo-Hernandez, C. E. and R. Arce (2002). "Photoionization of DNA and RNA bases, nucleosides and nucleotides through a combination of one- and two-photon pathways upon 266 nm nanosecond laser excitation." Photochem Photobiol **76**(3): 259-67.
- Czech, B. and G. J. Hannon (2011). "Small RNA sorting: matchmaking for Argonautes." Nat Rev Genet **12**(1): 19-31.

- Chen, J. L. and N. R. Pace (1997). "Identification of the universally conserved core of ribonuclease P RNA." Rna **3**(6): 557-60.
- Cheng, J. C., Y. J. Yeh, et al. (2012). "Let-7b is a novel regulator of hepatitis C virus replication." Cell Mol Life Sci **69**(15): 2621-33.
- Chinnapen, D. J. and D. Sen (2004). "A deoxyribozyme that harnesses light to repair thymine dimers in DNA." Proc Natl Acad Sci U S A **101**(1): 65-9.
- Chu, S., R. H. Archer, et al. (1994). "The RNA of RNase MRP is required for normal processing of ribosomal RNA." Proc Natl Acad Sci U S A **91**(2): 659-63.
- Daoud, R., L. Forget, et al. (2011). "Yeast mitochondrial RNase P, RNase Z and the RNA degradosome are part of a stable supercomplex." Nucleic Acids Res **40**(4): 1728-36.
- Deng, R. and K. V. Brock (1993). "5' and 3' untranslated regions of pestivirus genome: primary and secondary structure analyses." Nucleic Acids Res **21**(8): 1949-57.
- Diaz-Toledano, R., A. Ariza-Mateos, et al. (2009). "In vitro characterization of a miR-122-sensitive double-helical switch element in the 5' region of hepatitis C virus RNA." Nucleic Acids Res **37**(16): 5498-510.
- Diaz-Toledano, R. and J. Gomez (2015). "Messenger RNAs bearing tRNA-like features exemplified by interferon alfa 5 mRNA." Cell Mol Life Sci.
- Dobrov, E. N., Z. Arbieva, et al. (1989). "UV laser induced RNA-protein crosslinks and RNA chain breaks in tobacco mosaic virus RNA in situ." Photochem Photobiol **49**(5): 595-8.
- Dreher, T. W. (2009). "Role of tRNA-like structures in controlling plant virus replication." Virus Res **139**(2): 217-29.
- Dreher, T. W. (2010). "Viral tRNAs and tRNA-like structures." Wiley Interdiscip Rev RNA **1**(3): 402-14.
- Dubrovsky, E. B., V. A. Dubrovskaya, et al. (2004). "Drosophila RNase Z processes mitochondrial and nuclear pre-tRNA 3' ends in vivo." Nucleic Acids Res **32**(1): 255-62.
- Dutta, T., A. Malhotra, et al. (2013). "How a CCA sequence protects mature tRNAs and tRNA precursors from action of the processing enzyme RNase BN/RNase Z." J Biol Chem **288**(42): 30636-44.
- Edgil, D. and E. Harris (2006). "End-to-end communication in the modulation of translation by mammalian RNA viruses." Virus Res **119**(1): 43-51.
- Evans, D., S. M. Marquez, et al. (2006). "RNase P: interface of the RNA and protein worlds." Trends Biochem Sci **31**(6): 333-41.

- Fehr, C., K. D. Conrad, et al. (2012). "Differential stimulation of hepatitis C virus RNA translation by microRNA-122 in different cell cycle phases." Cell Cycle **11**(2): 277-85.
- Fernandez-Hernando, C., C. M. Ramirez, et al. (2013). "MicroRNAs in metabolic disease." Arterioscler Thromb Vasc Biol **33**(2): 178-85.
- Filbin, M. E. and J. S. Kieft (2011). "HCV IRES domain IIb affects the configuration of coding RNA in the 40S subunit's decoding groove." Rna **17**(7): 1258-73.
- Filbin, M. E., B. S. Vollmar, et al. (2013). "HCV IRES manipulates the ribosome to promote the switch from translation initiation to elongation." Nat Struct Mol Biol **20**(2): 150-8.
- Fletcher, S. P., I. K. Ali, et al. (2002). "The influence of viral coding sequences on pestivirus IRES activity reveals further parallels with translation initiation in prokaryotes." Rna **8**(12): 1558-71.
- Fletcher, S. P. and R. J. Jackson (2002). "Pestivirus internal ribosome entry site (IRES) structure and function: elements in the 5' untranslated region important for IRES function." J Virol **76**(10): 5024-33.
- Fricke, M., N. Dunnes, et al. (2015). "Conserved RNA secondary structures and long-range interactions in hepatitis C viruses." Rna.
- Friebe, P., J. Boudet, et al. (2005). "Kissing-loop interaction in the 3' end of the hepatitis C virus genome essential for RNA replication." J Virol **79**(1): 380-92.
- Friebe, P., V. Lohmann, et al. (2001). "Sequences in the 5' nontranslated region of hepatitis C virus required for RNA replication." J Virol **75**(24): 12047-57.
- Friis, M. B., T. B. Rasmussen, et al. (2012). "Modulation of translation initiation efficiency in classical swine fever virus." J Virol **86**(16): 8681-92.
- Fuchs, G., A. N. Petrov, et al. (2014). "Kinetic pathway of 40S ribosomal subunit recruitment to hepatitis C virus internal ribosome entry site." Proc Natl Acad Sci U S A **112**(2): 319-25.
- Garcia-Sacristan, A., M. Moreno, et al. "A magnesium-induced RNA conformational switch at the internal ribosome entry site of hepatitis C virus genome visualized by atomic force microscopy." Nucleic Acids Res **43**(1): 565-80.
- Gardiner, K. J., T. L. Marsh, et al. (1985). "Ion dependence of the Bacillus subtilis RNase P reaction." J Biol Chem **260**(9): 5415-9.
- Gebert, L. F., M. A. Rebhan, et al. (2013). "Miravirsin (SPC3649) can inhibit the biogenesis of miR-122." Nucleic Acids Res **42**(1): 609-21.
- Giege, R., M. Frugier, et al. (1998). "tRNA mimics." Curr Opin Struct Biol **8**(3): 286-93.

- Gobert, A., B. Gutmann, et al. (2010). "A single Arabidopsis organellar protein has RNase P activity." Nat Struct Mol Biol **17**(6): 740-4.
- Goergen, D. and M. Niepmann (2012). "Stimulation of Hepatitis C Virus RNA translation by microRNA-122 occurs under different conditions in vivo and in vitro." Virus Res **167**(2): 343-52.
- Gopalan, V., A. Vioque, et al. (2002). "RNase P: variations and uses." J Biol Chem **277**(9): 6759-62.
- Gorner, H. (1994). "Photochemistry of DNA and related biomolecules: quantum yields and consequences of photoionization." J Photochem Photobiol B **26**(2): 117-39.
- Griffiths-Jones, S., H. K. Saini, et al. (2008). "miRBase: tools for microRNA genomics." Nucleic Acids Res **36**(Database issue): D154-8.
- Guerrier-Takada, C., K. Gardiner, et al. (1983). "The RNA moiety of ribonuclease P is the catalytic subunit of the enzyme." Cell **35**(3 Pt 2): 849-57.
- Gutmann, B., A. Gobert, et al. (2012). "PRORP proteins support RNase P activity in both organelles and the nucleus in Arabidopsis." Genes Dev **26**(10): 1022-7.
- Haas, E. S., A. B. Banta, et al. (1996). "Structure and evolution of ribonuclease P RNA in Gram-positive bacteria." Nucleic Acids Res **24**(23): 4775-82.
- Haas, E. S. and J. W. Brown (1998). "Evolutionary variation in bacterial RNase P RNAs." Nucleic Acids Res **26**(18): 4093-9.
- Hall, T. A. and J. W. Brown (2002). "Archaeal RNase P has multiple protein subunits homologous to eukaryotic nuclear RNase P proteins." Rna **8**(3): 296-306.
- Hammond, S. M. (2015). "An overview of microRNAs." Adv Drug Deliv Rev **87**: 3-14.
- Hartmann, R. K., M. Gossringer, et al. (2009). "The making of tRNAs and more - RNase P and tRNase Z." Prog Mol Biol Transl Sci **85**: 319-68.
- Hellen, C. U. and T. V. Pestova (1999). "Translation of hepatitis C virus RNA." J Viral Hepat **6**(2): 79-87.
- Henke, J. I., D. Goergen, et al. (2008). "microRNA-122 stimulates translation of hepatitis C virus RNA." Embo J **27**(24): 3300-10.
- Hoffmann, T. W., G. Duverlie, et al. (2012). "MicroRNAs and hepatitis C virus: toward the end of miR-122 supremacy." Virology **9**: 109.
- Holzmann, J., P. Frank, et al. (2008). "RNase P without RNA: identification and functional reconstitution of the human mitochondrial tRNA processing enzyme." Cell **135**(3): 462-74.

- Honda, M., M. R. Beard, et al. (1999). "A phylogenetically conserved stem-loop structure at the 5' border of the internal ribosome entry site of hepatitis C virus is required for cap-independent viral translation." *J Virol* **73**(2): 1165-74.
- Honda, M., E. A. Brown, et al. (1996). "Stability of a stem-loop involving the initiator AUG controls the efficiency of internal initiation of translation on hepatitis C virus RNA." *Rna* **2**(10): 955-68.
- Honda, M., L. H. Ping, et al. (1996). "Structural requirements for initiation of translation by internal ribosome entry within genome-length hepatitis C virus RNA." *Virology* **222**(1): 31-42.
- Honda, M., R. Rijnbrand, et al. (1999). "Natural variation in translational activities of the 5' nontranslated RNAs of hepatitis C virus genotypes 1a and 1b: evidence for a long-range RNA-RNA interaction outside of the internal ribosomal entry site." *J Virol* **73**(6): 4941-51.
- Hoofnagle, J. H. (2002). "Course and outcome of hepatitis C." *Hepatology* **36**(5 Suppl 1): S21-9.
- Hsu, W. L., C. L. Chen, et al. (2014). "The untranslated regions of classic swine fever virus RNA trigger apoptosis." *PLoS One* **9**(2): e88863.
- Ishii, R., A. Minagawa, et al. (2005). "Crystal structure of the tRNA 3' processing endoribonuclease tRNase Z from *Thermotoga maritima*." *J Biol Chem* **280**(14): 14138-44.
- Jackson, R. J., C. U. Hellen, et al. (2010). "The mechanism of eukaryotic translation initiation and principles of its regulation." *Nat Rev Mol Cell Biol* **11**(2): 113-27.
- Jacobs, A. C., M. J. Resendiz, et al. (2010). "Direct strand scission from a nucleobase radical in RNA." *J Am Chem Soc* **132**(11): 3668-9.
- Jacobs, A. C., M. J. Resendiz, et al. (2011). "Product and mechanistic analysis of the reactivity of a C6-pyrimidine radical in RNA." *J Am Chem Soc* **133**(13): 5152-9.
- Jangra, R. K., M. Yi, et al. (2010). "Regulation of hepatitis C virus translation and infectious virus production by the microRNA miR-122." *J Virol* **84**(13): 6615-25.
- Jarrous, N. (2002). "Human ribonuclease P: subunits, function, and intranuclear localization." *Rna* **8**(1): 1-7.
- Jarrous, N. and V. Gopalan (2010). "Archaeal/eukaryal RNase P: subunits, functions and RNA diversification." *Nucleic Acids Res* **38**(22): 7885-94.
- Jarrous, N. and R. Reiner (2007). "Human RNase P: a tRNA-processing enzyme and transcription factor." *Nucleic Acids Res* **35**(11): 3519-24.

- Jarrous, N., J. S. Wolenski, et al. (1999). "Localization in the nucleolus and coiled bodies of protein subunits of the ribonucleoprotein ribonuclease P." J Cell Biol **146**(3): 559-72.
- Jericevic, Z., I. Kucan, et al. (1982). "Photochemical cleavage of phosphodiester bonds in oligoribonucleotides." Biochemistry **21**(25): 6563-7.
- Jopling, C. (2012). "Liver-specific microRNA-122: Biogenesis and function." RNA Biol **9**(2): 137-42.
- Jopling, C. L., S. Schutz, et al. (2008). "Position-dependent function for a tandem microRNA miR-122-binding site located in the hepatitis C virus RNA genome." Cell Host Microbe **4**(1): 77-85.
- Jopling, C. L., M. Yi, et al. (2005). "Modulation of hepatitis C virus RNA abundance by a liver-specific MicroRNA." Science **309**(5740): 1577-81.
- Joyce, M. A. and D. L. Tyrrell (2010). "The cell biology of hepatitis C virus." Microbes Infect **12**(4): 263-71.
- Kazantsev, A. V. and N. R. Pace (2006). "Bacterial RNase P: a new view of an ancient enzyme." Nat Rev Microbiol **4**(10): 729-40.
- Khawaja, A., V. Vopalensky, et al. (2014). "Understanding the potential of hepatitis C virus internal ribosome entry site domains to modulate translation initiation via their structure and function." Wiley Interdiscip Rev RNA **6**(2): 211-24.
- Kieft, J. S. (2008). "Viral IRES RNA structures and ribosome interactions." Trends Biochem Sci **33**(6): 274-83.
- Kieft, J. S., K. Zhou, et al. (2001). "Mechanism of ribosome recruitment by hepatitis C IRES RNA." Rna **7**(2): 194-206.
- Kieft, J. S., K. Zhou, et al. (1999). "The hepatitis C virus internal ribosome entry site adopts an ion-dependent tertiary fold." J Mol Biol **292**(3): 513-29.
- Kim, Y. K., S. H. Lee, et al. (2003). "Long-range RNA-RNA interaction between the 5' nontranslated region and the core-coding sequences of hepatitis C virus modulates the IRES-dependent translation." Rna **9**(5): 599-606.
- Kirsebom, L. A. (2007). "RNase P RNA mediated cleavage: substrate recognition and catalysis." Biochimie **89**(10): 1183-94.
- Klinck, R., E. Westhof, et al. (2000). "A potential RNA drug target in the hepatitis C virus internal ribosomal entry site." Rna **6**(10): 1423-31.
- Kolupaeva, V. G., T. V. Pestova, et al. (2000). "Ribosomal binding to the internal ribosomal entry site of classical swine fever virus." Rna **6**(12): 1791-807.

- Kostecky, B., E. Pohl, et al. (2006). "The crystal structure of the zinc phosphodiesterase from *Escherichia coli* provides insight into function and cooperativity of tRNase Z-family proteins." J Bacteriol **188**(4): 1607-14.
- Kundu, L. M., U. Linne, et al. (2004). "RNA is more UV resistant than DNA: the formation of UV-induced DNA lesions is strongly sequence and conformation dependent." Chemistry **10**(22): 5697-705.
- Kupfer, P. A. and C. J. Leumann (2007). "The chemical stability of abasic RNA compared to abasic DNA." Nucleic Acids Res **35**(1): 58-68.
- Lafontaine, D. L. (2015). "Noncoding RNAs in eukaryotic ribosome biogenesis and function." Nat Struct Mol Biol **22**(1): 11-9.
- Lafuente, E., R. Ramos, et al. (2002). "Long-range RNA-RNA interactions between distant regions of the hepatitis C virus internal ribosome entry site element." J Gen Virol **83**(Pt 5): 1113-21.
- Lai, L. B., A. Vioque, et al. (2010). "Unexpected diversity of RNase P, an ancient tRNA processing enzyme: challenges and prospects." FEBS Lett **584**(2): 287-96.
- Lavender, C. A., F. Ding, et al. (2010). "Robust and generic RNA modeling using inferred constraints: a structure for the hepatitis C virus IRES pseudoknot domain." Biochemistry **49**(24): 4931-3.
- Le, S. Y., W. M. Liu, et al. (1998). "Phylogenetic evidence for the improved RNA higher-order structure in internal ribosome entry sequences of HCV and pestiviruses." Virus Genes **17**(3): 279-95.
- Lechner, M., W. Rossmann, et al. (2015). "Distribution of Ribonucleoprotein and Protein-Only RNase P in Eukarya." Mol Biol Evol.
- Lee, M. C. and G. Knapp (1985). "Transfer RNA splicing in *Saccharomyces cerevisiae*. Secondary and tertiary structures of the substrates." J Biol Chem **260**(5): 3108-15.
- Leifer, I., N. Ruggli, et al. (2013). "Approaches to define the viral genetic basis of classical swine fever virus virulence." Virology **438**(2): 51-5.
- Leontis, N. B. and E. Westhof (1998). "The 5S rRNA loop E: chemical probing and phylogenetic data versus crystal structure." Rna **4**(9): 1134-53.
- Leontis, N. B. and E. Westhof (1998). "A common motif organizes the structure of multi-helix loops in 16 S and 23 S ribosomal RNAs." J Mol Biol **283**(3): 571-83.
- Li de la Sierra-Gallay, I., O. Pellegrini, et al. (2005). "Structural basis for substrate binding, cleavage and allostery in the tRNA maturase RNase Z." Nature **433**(7026): 657-61.

- Li, Y., T. Masaki, et al. (2013). "miR-122 and the Hepatitis C RNA genome: more than just stability." RNA Biol **10**(6): 919-23.
- Li, Y., T. Masaki, et al. (2012). "Competing and noncompeting activities of miR-122 and the 5' exonuclease Xrn1 in regulation of hepatitis C virus replication." Proc Natl Acad Sci U S A **110**(5): 1881-6.
- Locker, N., L. E. Easton, et al. (2007). "HCV and CSFV IRES domain II mediate eIF2 release during 80S ribosome assembly." Embo J **26**(3): 795-805.
- Loria, A. and T. Pan (1996). "Domain structure of the ribozyme from eubacterial ribonuclease P." Rna **2**(6): 551-63.
- Lukavsky, P. J., I. Kim, et al. (2003). "Structure of HCV IRES domain II determined by NMR." Nat Struct Biol **10**(12): 1033-8.
- Lukavsky, P. J., G. A. Otto, et al. (2000). "Structures of two RNA domains essential for hepatitis C virus internal ribosome entry site function." Nat Struct Biol **7**(12): 1105-10.
- Luna, J. M., T. K. Scheel, et al. (2015). "Hepatitis C virus RNA functionally sequesters miR-122." Cell **160**(6): 1099-110.
- Lundblad, E. W. and S. Altman (2010). "Inhibition of gene expression by RNase P." N Biotechnol **27**(3): 212-21.
- Lyons, A. J., J. R. Lytle, et al. (2001). "Hepatitis C virus internal ribosome entry site RNA contains a tertiary structural element in a functional domain of stem-loop II." Nucleic Acids Res **29**(12): 2535-41.
- Lyons, A. J. and H. D. Robertson (2003). "Detection of tRNA-like structure through RNase P cleavage of viral internal ribosome entry site RNAs near the AUG start triplet." J Biol Chem **278**(29): 26844-50.
- Lytle, J. R., L. Wu, et al. (2002). "Domains on the hepatitis C virus internal ribosome entry site for 40s subunit binding." Rna **8**(8): 1045-55.
- Macejak, D. G. and P. Sarnow (1991). "Internal initiation of translation mediated by the 5' leader of a cellular mRNA." Nature **353**(6339): 90-4.
- Maizels, N. and A. M. Weiner (1994). "Phylogeny from function: evidence from the molecular fossil record that tRNA originated in replication, not translation." Proc Natl Acad Sci U S A **91**(15): 6729-34.
- Malygin, A. A., O. A. Kossinova, et al. (2013). "HCV IRES interacts with the 18S rRNA to activate the 40S ribosome for subsequent steps of translation initiation." Nucleic Acids Res **41**(18): 8706-14.
- Mans, R. M., C. W. Pleij, et al. (1991). "tRNA-like structures. Structure, function and evolutionary significance." Eur J Biochem **201**(2): 303-24.

- Maraia, R. J. and T. N. Lamichhane (2011). "3' processing of eukaryotic precursor tRNAs." Wiley Interdiscip Rev RNA **2**(3): 362-75.
- Marmur, J. and L. Grossman (1961). "Ultraviolet light induced linking of deoxyribonucleic acid strands and its reversal by photoreactivating enzyme." Proc Natl Acad Sci U S A **47**: 778-87.
- Martell, M., J. I. Esteban, et al. (1992). "Hepatitis C virus (HCV) circulates as a population of different but closely related genomes: quasispecies nature of HCV genome distribution." J Virol **66**(5): 3225-9.
- Masaki, T., K. C. Arend, et al. (2015). "miR-122 stimulates hepatitis C virus RNA synthesis by altering the balance of viral RNAs engaged in replication versus translation." Cell Host Microbe **17**(2): 217-28.
- Masquida, B. and E. Westhof (2011). "RNase P: at last, the key finds its lock." Rna **17**(9): 1615-8.
- Matsuda, D. and V. P. Mauro (2014). "Base pairing between hepatitis C virus RNA and 18S rRNA is required for IRES-dependent translation initiation in vivo." Proc Natl Acad Sci U S A **111**(43): 15385-9.
- McMullan, L. K., A. Grakoui, et al. (2007). "Evidence for a functional RNA element in the hepatitis C virus core gene." Proc Natl Acad Sci U S A **104**(8): 2879-84.
- Melvin, T., S. M. Cunniffe, et al. (1998). "Guanine is the target for direct ionisation damage in DNA, as detected using excision enzymes." Nucleic Acids Res **26**(21): 4935-42.
- Messina, J. P., I. Humphreys, et al. (2014). "Global distribution and prevalence of hepatitis C virus genotypes." Hepatology **61**(1): 77-87.
- Minagawa, A., H. Takaku, et al. (2004). "A novel endonucleolytic mechanism to generate the CCA 3' termini of tRNA molecules in *Thermotoga maritima*." J Biol Chem **279**(15): 15688-97.
- Moennig, V. (2000). "Introduction to classical swine fever: virus, disease and control policy." Vet Microbiol **73**(2-3): 93-102.
- Mondragon, A. (2013). "Structural studies of RNase P." Annu Rev Biophys **42**: 537-57.
- Moradpour, D. and F. Penin (2013). "Hepatitis C virus proteins: from structure to function." Curr Top Microbiol Immunol **369**: 113-42.
- Mortimer, S. A. and J. A. Doudna (2013). "Unconventional miR-122 binding stabilizes the HCV genome by forming a trimolecular RNA structure." Nucleic Acids Res **41**(7): 4230-40.

- Mulkiyanian, A. Y., D. A. Cherepanov, et al. (2003). "Survival of the fittest before the beginning of life: selection of the first oligonucleotide-like polymers by UV light." BMC Evol Biol **3**: 12.
- Murakami, Y., H. H. Aly, et al. (2009). "Regulation of the hepatitis C virus genome replication by miR-199a." J Hepatol **50**(3): 453-60.
- Nadal, A., M. Martell, et al. (2002). "Specific cleavage of hepatitis C virus RNA genome by human RNase P." J Biol Chem **277**(34): 30606-13.
- Nasheri, N., R. Singaravelu, et al. (2011). "Competing roles of microRNA-122 recognition elements in hepatitis C virus RNA." Virology **410**(2): 336-44.
- Newcomer, B. W. and M. D. Givens (2013). "Approved and experimental countermeasures against pestiviral diseases: Bovine viral diarrhea, classical swine fever and border disease." Antiviral Res **100**(1): 133-50.
- Niepmann, M. (2009). "Activation of hepatitis C virus translation by a liver-specific microRNA." Cell Cycle **8**(10): 1473-7.
- Niranjanakumari, S., T. Stams, et al. (1998). "Protein component of the ribozyme ribonuclease P alters substrate recognition by directly contacting precursor tRNA." Proc Natl Acad Sci U S A **95**(26): 15212-7.
- Nissen, P., M. Kjeldgaard, et al. (2000). "Macromolecular mimicry." Embo J **19**(4): 489-95.
- Nordlund, T. M. (2007). "Sequence, structure and energy transfer in DNA." Photochem Photobiol **83**(3): 625-36.
- Odom, D. T. and J. K. Barton (2001). "Long-range oxidative damage in DNA/RNA duplexes." Biochemistry **40**(30): 8727-37.
- Ottensmeyer, F. P. and G. F. Whitmore (1968). "Coding properties of ultraviolet photoproducts of uracil. I. Binding studies and polypeptide synthesis." J Mol Biol **38**(1): 1-16.
- Pace, N. R. and J. W. Brown (1995). "Evolutionary perspective on the structure and function of ribonuclease P, a ribozyme." J Bacteriol **177**(8): 1919-28.
- Pan, T., A. Loria, et al. (1995). "Probing of tertiary interactions in RNA: 2'-hydroxyl-base contacts between the RNase P RNA and pre-tRNA." Proc Natl Acad Sci U S A **92**(26): 12510-4.
- Panek, J., M. Kolar, et al. (2013). "An evolutionary conserved pattern of 18S rRNA sequence complementarity to mRNA 5' UTRs and its implications for eukaryotic gene translation regulation." Nucleic Acids Res **41**(16): 7625-34.
- Pang, P. S., E. A. Pham, et al. (2011). "Structural map of a microRNA-122: hepatitis C virus complex." J Virol **86**(2): 1250-4.

- Paton, D. J., A. McGoldrick, et al. (2000). "Genetic typing of classical swine fever virus." Vet Microbiol **73**(2-3): 137-57.
- Pavlova, L. V., M. Gossringer, et al. (2012). "tRNA processing by protein-only versus RNA-based RNase P: kinetic analysis reveals mechanistic differences." ChemBiochem **13**(15): 2270-6.
- Pellegrini, O., J. Nezzar, et al. (2003). "Endonucleolytic processing of CCA-less tRNA precursors by RNase Z in *Bacillus subtilis*." Embo J **22**(17): 4534-43.
- Pelletier, J., G. Kaplan, et al. (1988). "Cap-independent translation of poliovirus mRNA is conferred by sequence elements within the 5' noncoding region." Mol Cell Biol **8**(3): 1103-12.
- Peng, W. T., M. D. Robinson, et al. (2003). "A panoramic view of yeast noncoding RNA processing." Cell **113**(7): 919-33.
- Perard, J., C. Leyrat, et al. (2013). "Structure of the full-length HCV IRES in solution." Nat Commun **4**: 1612.
- Perwez, T. and S. R. Kushner (2006). "RNase Z in *Escherichia coli* plays a significant role in mRNA decay." Mol Microbiol **60**(3): 723-37.
- Pfaender, S., R. J. Brown, et al. (2014). "Natural reservoirs for homologs of hepatitis C virus." Emerg Microbes Infect **3**(3): e21.
- Pineiro, D. and E. Martinez-Salas (2012). "RNA structural elements of hepatitis C virus controlling viral RNA translation and the implications for viral pathogenesis." Viruses **4**(10): 2233-50.
- Pogozelski, W. K. and T. D. Tullius (1998). "Oxidative Strand Scission of Nucleic Acids: Routes Initiated by Hydrogen Abstraction from the Sugar Moiety." Chem Rev **98**(3): 1089-1108.
- Poole, T. L., C. Wang, et al. (1995). "Pestivirus translation initiation occurs by internal ribosome entry." Virology **206**(1): 750-4.
- Redko, Y., I. Li de la Sierra-Gallay, et al. (2007). "When all's zed and done: the structure and function of RNase Z in prokaryotes." Nat Rev Microbiol **5**(4): 278-86.
- Rice, C. M. and M. Saeed (2014). "Hepatitis C: Treatment triumphs." Nature **510**(7503): 43-4.
- Rijnbrand, R., P. Bredenbeek, et al. (1995). "Almost the entire 5' non-translated region of hepatitis C virus is required for cap-independent translation." FEBS Lett **365**(2-3): 115-9.
- Rijnbrand, R., T. van der Straaten, et al. (1997). "Internal entry of ribosomes is directed by the 5' noncoding region of classical swine fever virus and is

- dependent on the presence of an RNA pseudoknot upstream of the initiation codon." J Virol **71**(1): 451-7.
- Roberts, A. P., A. P. Lewis, et al. (2011). "miR-122 activates hepatitis C virus translation by a specialized mechanism requiring particular RNA components." Nucleic Acids Res.
- Roberts, A. P., A. P. Lewis, et al. (2011). "The role of microRNAs in viral infection." Prog Mol Biol Transl Sci **102**: 101-39.
- Robertson, H. D., S. Altman, et al. (1972). "Purification and properties of a specific Escherichia coli ribonuclease which cleaves a tyrosine transfer ribonucleic acid precursor." J Biol Chem **247**(16): 5243-51.
- Romero-Lopez, C., A. Barroso-Deljesus, et al. (2012). "The folding of the hepatitis C virus internal ribosome entry site depends on the 3'-end of the viral genome." Nucleic Acids Res **40**(22): 11697-713.
- Rosenstein, B. S. and J. M. Ducore (1983). "Induction of DNA strand breaks in normal human fibroblasts exposed to monochromatic ultraviolet and visible wavelengths in the 240-546 nm range." Photochem Photobiol **38**(1): 51-5.
- Rossmannith, W. (2011). "Localization of human RNase Z isoforms: dual nuclear/mitochondrial targeting of the ELAC2 gene product by alternative translation initiation." PLoS One **6**(4): e19152.
- Rossmannith, W. (2011). "Of P and Z: mitochondrial tRNA processing enzymes." Biochim Biophys Acta **1819**(9-10): 1017-26.
- Rossmannith, W. and R. M. Karwan (1998). "Characterization of human mitochondrial RNase P: novel aspects in tRNA processing." Biochem Biophys Res Commun **247**(2): 234-41.
- Roush, S. and F. J. Slack (2008). "The let-7 family of microRNAs." Trends Cell Biol **18**(10): 505-16.
- Sabariegos, R., A. Nadal, et al. (2004). "Catalytic RNase P RNA from Synechocystis sp. cleaves the hepatitis C virus RNA near the AUG start codon." FEBS Lett **577**(3): 517-22.
- Sagan, S. M., J. Chahal, et al. (2015). "cis-Acting RNA elements in the hepatitis C virus RNA genome." Virus Res.
- Sagan, S. M., P. Sarnow, et al. (2013). "Modulation of GB virus B RNA abundance by microRNA-122: dependence on and escape from microRNA-122 restriction." J Virol **87**(13): 7338-47.
- Schiffer, S., S. Rosch, et al. (2003). "Recombinant RNase Z does not recognize CCA as part of the tRNA and its cleavage efficiency is influenced by acceptor stem length." Biol Chem **384**(3): 333-42.

- Shapkina, T., S. Lappi, et al. (2004). "Efficiency and pattern of UV pulse laser-induced RNA-RNA cross-linking in the ribosome." Nucleic Acids Res **32**(4): 1518-26.
- Shimakami, T., D. Yamane, et al. (2011). "Stabilization of hepatitis C virus RNA by an Ago2-miR-122 complex." Proc Natl Acad Sci U S A **109**(3): 941-6.
- Shimakami, T., D. Yamane, et al. (2012). "Base pairing between hepatitis C virus RNA and microRNA 122 3' of its seed sequence is essential for genome stabilization and production of infectious virus." J Virol **86**(13): 7372-83.
- Simmonds, P. (2013). "The origin of hepatitis C virus." Curr Top Microbiol Immunol **369**: 1-15.
- Spahn, C. M., J. S. Kieft, et al. (2001). "Hepatitis C virus IRES RNA-induced changes in the conformation of the 40s ribosomal subunit." Science **291**(5510): 1959-62.
- Suzuki, T., K. Ishii, et al. (2007). "Hepatitis C viral life cycle." Adv Drug Deliv Rev **59**(12): 1200-12.
- Svard, S. G., U. Kagardt, et al. (1996). "Phylogenetic comparative mutational analysis of the base-pairing between RNase P RNA and its substrate." Rna **2**(5): 463-72.
- Swerdlow, H. and C. Guthrie (1984). "Structure of intron-containing tRNA precursors. Analysis of solution conformation using chemical and enzymatic probes." J Biol Chem **259**(8): 5197-207.
- Takada, T., Y. Otsuka, et al. (2011). "Electron transfer through RNA: chemical probing of dual distance dependence." Bioorg Med Chem **19**(22): 6881-4.
- Takaku, H., A. Minagawa, et al. (2004). "The N-terminal half-domain of the long form of tRNase Z is required for the RNase 65 activity." Nucleic Acids Res **32**(15): 4429-38.
- Takakura, K., M. Ishikawa, et al. (1987). "Action spectrum for the induction of single-strand breaks in DNA in buffered aqueous solution in the wavelength range from 150 to 272 nm: dual mechanism." Int J Radiat Biol Relat Stud Phys Chem Med **52**(5): 667-75.
- Takaya, T., C. Su, et al. (2008). "UV excitation of single DNA and RNA strands produces high yields of exciplex states between two stacked bases." Proc Natl Acad Sci U S A **105**(30): 10285-90.
- Tavtigian, S. V., J. Simard, et al. (2001). "A candidate prostate cancer susceptibility gene at chromosome 17p." Nat Genet **27**(2): 172-80.
- Terenin, I. M., S. E. Dmitriev, et al. (2008). "Eukaryotic translation initiation machinery can operate in a bacterial-like mode without eIF2." Nat Struct Mol Biol **15**(8): 836-41.

- Thibault, P. A., A. Huys, et al. (2015). "Regulation of Hepatitis C Virus Genome Replication by Xrn1 and MicroRNA-122 Binding to Individual Sites in the 5' Untranslated Region." J Virol **89**(12): 6294-311.
- Thomas, B. C., X. Li, et al. (2000). "Chloroplast ribonuclease P does not utilize the ribozyme-type pre-tRNA cleavage mechanism." Rna **6**(4): 545-53.
- Thorp, H. H. (2000). "The importance of being r: greater oxidative stability of RNA compared with DNA." Chem Biol **7**(2): R33-6.
- Tinoco, I., Jr. and C. Bustamante (1999). "How RNA folds." J Mol Biol **293**(2): 271-81.
- Tsukiyama-Kohara, K., N. Iizuka, et al. (1992). "Internal ribosome entry site within hepatitis C virus RNA." J Virol **66**(3): 1476-83.
- Tuplin, A., M. Struthers, et al. (2015). "Inhibition of HCV translation by disrupting the structure and interactions of the viral CRE and 3' X-tail." Nucleic Acids Res **43**(5): 2914-26.
- Tuplin, A., M. Struthers, et al. (2012). "A twist in the tail: SHAPE mapping of long-range interactions and structural rearrangements of RNA elements involved in HCV replication." Nucleic Acids Res **40**(14): 6908-21.
- Vassilaki, N., P. Friebe, et al. (2008). "Role of the hepatitis C virus core+1 open reading frame and core cis-acting RNA elements in viral RNA translation and replication." J Virol **82**(23): 11503-15.
- Vogel, A., O. Schilling, et al. (2002). "ElaC encodes a novel binuclear zinc phosphodiesterase." J Biol Chem **277**(32): 29078-85.
- Vogel, A., O. Schilling, et al. (2005). "The tRNase Z family of proteins: physiological functions, substrate specificity and structural properties." Biol Chem **386**(12): 1253-64.
- Walker, S. C. and D. R. Engelke (2006). "Ribonuclease P: the evolution of an ancient RNA enzyme." Crit Rev Biochem Mol Biol **41**(2): 77-102.
- Wang, C., S. Y. Le, et al. (1995). "An RNA pseudoknot is an essential structural element of the internal ribosome entry site located within the hepatitis C virus 5' noncoding region." Rna **1**(5): 526-37.
- Wang, T. H., R. C. Rijnbrand, et al. (2000). "Core protein-coding sequence, but not core protein, modulates the efficiency of cap-independent translation directed by the internal ribosome entry site of hepatitis C virus." J Virol **74**(23): 11347-58.
- Waters, E., M. J. Hohn, et al. (2003). "The genome of *Nanoarchaeum equitans*: insights into early archaeal evolution and derived parasitism." Proc Natl Acad Sci U S A **100**(22): 12984-8.

- Weiner, A. M. (2004). "tRNA maturation: RNA polymerization without a nucleic acid template." Curr Biol **14**(20): R883-5.
- Werner, M., E. Rosa, et al. (1998). "Short oligonucleotides as external guide sequences for site-specific cleavage of RNA molecules with human RNase P." Rna **4**(7): 847-55.
- Wilson, J. A. and A. Huys (2013). "miR-122 promotion of the hepatitis C virus life cycle: sound in the silence." Wiley Interdiscip Rev RNA **4**(6): 665-76.
- Wilson, J. A. and S. M. Sagan (2014). "Hepatitis C virus and human miR-122: insights from the bench to the clinic." Curr Opin Virol **7**: 11-8.
- Wimberly, B., G. Varani, et al. (1993). "The conformation of loop E of eukaryotic 5S ribosomal RNA." Biochemistry **32**(4): 1078-87.
- Wu, J., W. Liu, et al. (2015). "A Structural Overview of RNA-Dependent RNA Polymerases from the Flaviviridae Family." Int J Mol Sci **16**(6): 12943-57.
- Wu, S., E. Kikovska, et al. (2012). "Cleavage mediated by the catalytic domain of bacterial RNase P RNA." J Mol Biol **422**(2): 204-14.
- Wurtmann, E. J. and S. L. Wolin (2009). "RNA under attack: cellular handling of RNA damage." Crit Rev Biochem Mol Biol **44**(1): 34-49.
- Yanagi, M., M. St Claire, et al. (1999). "In vivo analysis of the 3' untranslated region of the hepatitis C virus after in vitro mutagenesis of an infectious cDNA clone." Proc Natl Acad Sci U S A **96**(5): 2291-5.
- Yot, P., M. Pinck, et al. (1970). "Valine-specific tRNA-like structure in turnip yellow mosaic virus RNA." Proc Natl Acad Sci U S A **67**(3): 1345-52.
- Yuan, Y. and S. Altman (1995). "Substrate recognition by human RNase P: identification of small, model substrates for the enzyme." Embo J **14**(1): 159-68.
- Zhang, C., A. Huys, et al. (2012). "Requirements for human Dicer and TRBP in microRNA-122 regulation of HCV translation and RNA abundance." Virology **433**(2): 479-88.

